Selenium isotope systematics of mid-ocean-ridge basalts and implications for the long-term volatile and chalcophile record of the crust–mantle system

Dissertation

der Mathematisch-Naturwissenschaftlichen Fakultät

der Eberhard Karls Universität Tübingen

zur Erlangung des Grades eines

Doktors der Naturwissenschaften

(Dr. rer. nat.)

vorgelegt von

MSc Aierken Yierpan

aus Xinjiang Uyghur Autonomous Region, China

Tübingen

2019

Gedruckt mit Genehmigung der Mathematisch-Naturwissenschaftlichen Fakultät der Eberhard Karls Universität Tübingen.

Tag der mündlichen Qualifikation:	22.11.2019
Dekan:	Prof. Dr. Wolfgang Rosenstiel
1. Berichterstatter:	Dr. Stephan König
2. Berichterstatter:	Prof. Dr. Ronny Schönberg
3. Berichterstatter:	Prof. Dr. Raúl Fonseca (Ruhr-Universität Bochum)

Acknowledgements

This work presented here was financially supported by the ERC Starting Grant O_2RIGIN (636808) to Stephan König.

First of all, I am truly grateful that Stephan decided to have me as his PhD student. I still remember the day I came to Tübingen for my interview. I was walking across the Neckarbrücke, thinking how great it would be if I had an opportunity to work with you in the next few years in this lovely city. Thank you for your continued guidance and encouragement throughout this work. Without your patience, it would not have been possible to get through probably one of my toughest days when I lost my passport right before the flight back home to Kashgar. I also want to thank you for your time and availability for the long and stimulating discussions we had, which always helped me develop new and creative scientific ideas at various stages of my PhD study.

I sincerely appreciate the support and guidance I received from Ronny Schoenberg over the years. I benefited greatly from each of our conversations because of your enthusiasm for research as well as your unique and brilliant perspectives to solve scientific problems. I always think of the old paper (in Japanese) you gave me when we were having analytical difficulties with Se and Te separation. I really enjoyed working in your group and gained profitable experience in dealing with the Neptune. I am proud of the many accomplishments we have achieved together.

I would like to thank Timon Kurzawa for being an important part of my great PhD journey. It was a great pleasure to know you and work with you. We experienced so many difficult times together while developing the analytical protocols. You were always there and listened to me whenever I wanted to talk about personal or scientific issues. Thanks to you, I always could maintain positive and joyful attitudes towards whatever I do.

A special thanks goes to Jabrane Labidi for being involved in all of my studies and giving me constructive feedback. You always had a way of clarifying things and your advice always improved the discussion. I really enjoyed when we brainstorm scientific ideas together. I consider myself very lucky to have had the chance to work with you.

I thank Elmar Reitter, Michael Babechuk, Bernd Steinhilber, Ilka Kleinhanns, Martin Wille and Heinrich Taubald for their continued and dedicated support in the lab throughout the study. Mike made the Te analysis on iCAP so much easier thanks to his deep and unique insights into the analytical technique. Martin was willing to help and was able to give me suggestions whenever I felt stuck. Thank you Elmar for always being there regardless of the busy schedule! It would have been impossible for me to complete the projects in a timely manner without your support. You are such a nice person!

I am very much thankful to Laure Dosso for providing the Pacific–Antarctic ridge basalts, Katherine A. Kelley for the northern Mid-Atlantic ridge basalts and Ilka Kleinhanns for the Västervik granitoid samples.

I thank Maria Varas-Reus for generous support during the lab work as well as for the great organizations during each of our travel for conferences.

I thank Daniel Schöckle, Benjamin Eickmann and Frantz-Gerard Ossa Ossa for helping me further understand some important geochemical processes and element cycling in low-temperature environments. Thanks a lot for taking the time to share your knowledge with me!

I also thank Johannes Redlinger, Mona Schiller, Regina Neubauer and Felix Brey for the assistance in the lab over the years. I also benefited from the scientific discussions with Johannes and Mona during the course of their Bachelor's and Master's thesis.

I further thank all other members of the Isotope Geochemistry Group in Tübingen, especially Gülüm Albut, Florian Kurzweil, Sümeyya Eroglu, Carolina Rosca, Julius Havsteen, Yunfeng Wang, Luise Wagner and Lucile Roué. Thank you for encouraging me and supporting me during the last four years. It was fantastic to work with all of you guys!

Finally, I would like to express my gratitude to my family: my wife, my daughter, my mother and my brother. I just want to say thank you for being in my life. This work is also dedicated to the loving memory of those who left me forever.

Abstract

Selenium is a chalcophile, moderately volatile and redox-sensitive element. The Se isotopic and elemental systematics of mantle-derived rocks and melts may therefore provide new approaches to study the terrestrial volatile origin and evolution as well as secular changes of redox conditions across the surface and mantle reservoirs.

Selenium is significantly depleted in the Earth's mantle compared to other similarly volatile lithophile elements because of its incorporation into the core. Consequently, Se is present in mantle samples at low concentration levels (ng/g). This poses analytical challenges for Se isotopic studies of the igneous system. This dissertation presents an analytical protocol suitable for precise and accurate determination of Se isotope and Se and Te abundances of igneous rocks from the same sample digest (Chapter 1). The Se–Te elemental systematics provide an essential petrogenetic context for interpretation of the Se isotope systematics. Chapter 2 reports the first Se isotope and Se–Te elemental data for basaltic glasses from the Pacific–Antarctic ridge (PAR). These MORBs are derived from ridge sections devoid of plume influences and represent a first-order mantle source homogeneity. The magmatic differentiation involving concurrent sulfide segregation results in significant chalcophile element fractionation but no measurable Se isotopic variation. Secondary processes such as high-temperature hydrothermal sulfide assimilation does not affect Se isotopes or Se–Te abundances. Forward modelling of mantle melting yields two distinct source Se–Te contents due to the different sulfide–silicate melt partition coefficient data published in the literature. Regardless, it shows that chalcophile element behavior in the upper mantle is controlled by sulfide liquid–silicate melt partitioning, consistent with recent experimental constraints. This further suggests that, from the MORB perspective, Se–Te systematics of worldwide lithospheric lherzolites (with near-chondritic Se/Te ratios) reflect significant, if not complete, metasomatic overprinting rather than the primitive signature of the silicate mantle. Finally, because of the lack of Se isotopic fractionation between sulfide phases and silicate melt, the Se isotope systematics of MORB reflects a source signature. The PAR MORB average $\delta^{82/76}$Se overlaps with chondritic values but shows offset towards lighter values relative to worldwide basaltic lavas (Chapter 1). These subtle but significant Se isotopic variations within the PAR suite and between other igneous samples might reflect isotopic heterogeneity of the mantle. This is investigated by analyzing Se isotope compositions of representative basaltic glasses from the Mid-Atlantic ridge (MAR; Chapter 3). The southern section of the MAR displays a significant source heterogeneity due to

the localized interaction between the ridge and Shona and Discovery mantle plumes that incorporate a variety of recycled components. The depleted basalts free of plume contributions show similar $\delta^{82/76}$Se values to the PAR MORB average. In contrast, basalts enriched by recycled components (originating mainly from the Discovery plume) show heavier $\delta^{82/76}$Se values, correlated with δ^{34}S and ^{87}Sr/^{86}Sr ratios. This illustrates a simple binary mixing between the depleted mantle and enriched components. The latter is shown here to mainly reflect subducted marine sediments that are Se-rich compared to the mantle. The calculated Se content and $\delta^{82/76}$Se for the sediment endmember well match the average composition of the Proterozoic sediments, in agreement with the previous S isotope study. The inferred Se content of the pyrite in the subducting sediment is similar to or higher than the literature value for the Proterozoic sediment-hosted pyrites. These results, from the mantle perspective, are in favor of the recently proposed high O_2 level in the mid-Proterozoic atmosphere. This in turn implies that, together with atmospheric O_2, other factors such as nutrient element availability also played a critical role in the evolution of complex life during the 'Boring Billion'.

Zusammenfassung

Selen ist ein chalkophiles, mäßig flüchtiges und redoxempfindliches Element. Die isotopische und elementare Selensystematik von Gesteinen und Schmelzen des Erdmantels könnte daher neue Ansätze zur Untersuchung des Ursprungs und der Entwicklung der Redoxbedingungen der Erdoberfläche und der Erdmantelreservoire liefern.

Selen ist im Erdmantel im Vergleich zu anderen ähnlich flüchtigen und lithophilen Elementen aufgrund seines Einbaus in den Kern erheblich abgereichert. Folglich ist Se in Mantelproben in geringen Konzentrationen (ng/g) vorhanden. Dies ist eine analytische Herausforderung für Selenisotopenstudien des Mantelsystems. In dieser Dissertation wird ein Analyseprotokoll vorgestellt, das zur präzisen und genauen Bestimmung von Selenisotopen und Se-Te Konzentrationen magmatischer Gesteine aus demselben Probenaufschluss geeignet ist (Kapitel 1). Die elementare Se-Te Systematik liefert einen wesentlichen petrogenetischen Kontext für die Interpretation der Selenisotopie. In Kapitel 2 werden die ersten Daten zu Selenisotopen und elementaren Se-Te Konzentrationen von Basaltgläsern des pazifisch-antarktischen Kamm (PAR) aufgeführt. Diese MORBs stammen aus Rückenabschnitten, die keine Plume-Einflüsse aufweisen, und repräsentieren daher eine Mantelquellenhomogenität erster Ordnung. Die magmatische Differenzierung unter gleichzeitiger Sulfidabtrennung führt zu einer signifikanten Fraktionierung der chalkophilen Elemente, jedoch zu keiner messbaren Variation der Selenisotopie. Sekundäre Prozesse wie die Hochtemperatur-Hydrothermalsulfidassimilation beeinflussen weder die Selenisotopie noch die Se-Te-Konzentrationen. Die Vorwärtsmodellierung des Mantelschmelzens liefert aufgrund der in der Literatur veröffentlichten unterschiedlichen Daten zum Sulfid-Silikat-Schmelzverteilungskoeffizienten zwei unterschiedliche Se-Te-Gehalte. Unabhängig davon zeigt sich, dass das Verhalten von chalkophilen Elementen im oberen Mantel durch die Verteilung der Sulfid-Flüssigkeits-Silikat-Schmelze gesteuert wird, was den jüngsten experimentellen Ergebnissen entspricht. Dies legt ferner nahe, dass aus der MORB-Perspektive die Se-Te Systematik weltweiter lithosphärischer Lherzolite (mit nahezu chondritischen Se/Te-Verhältnissen) eine signifikante, wenn nicht vollständige metasomatische Überprägung und nicht die primitive Signatur des Silikatmantels widerspiegelt. Schließlich spiegelt die Selenisotopensystematik von MORB aufgrund des Fehlens einer Selenisotopenfraktionierung zwischen Sulfidphasen und Silikatschmelze eine Quellensignatur wider. Der PAR-MORB Durchschnitt $\delta^{82/76}$Se-Wert überlappt mit chondritischen Werten, zeigt jedoch einen Versatz zu

leichteren Werten im Vergleich zu weltweiten Basaltlaven (Kapitel 1). Diese subtilen, aber signifikanten Selenisotopenvariationen innerhalb der PAR-Suite und zwischen anderen magmatischen Proben könnten die Isotopenheterogenität des Mantels widerspiegeln. Dies wird untersucht, indem Selenisotopenzusammensetzungen von repräsentativen Basaltgläsern des mittelatlantischen Rückens analysiert werden (MAR; Kapitel 3). Der südliche Abschnitt des MAR weist aufgrund der lokalen Wechselwirkung zwischen dem Rücken und den Shona- und Discovery-Mantelplume, die eine Vielzahl von recycelten Bestandteilen enthält, eine signifikante Quellenheterogenität auf. Die abgereicherten Basalte, die frei von Plumebeiträgen sind, zeigen ähnliche $\delta^{82/76}$Se wie der PAR-MORB Durchschnittswert. Im Gegensatz dazu weisen mit recycelten Bestandteilen angereicherte Basalte (die hauptsächlich aus dem Discovery Plumee stammen) schwerere $\delta^{82/76}$Se-Werte auf, die mit δ^{34}S- und ^{87}Sr/^{86}Sr-Verhältnissen positiv korrelieren. Dies zeigt eine einfache binäre Mischung zwischen dem abgereicherten Mantel und den angereicherten Bestandteilen. Letztere spiegeln hier hauptsächlich abgeleitete marine Sedimente wider, die im Vergleich zum Mantel Se-reich sind. Der berechnete Se-Gehalt und $\delta^{82/76}$Se-Wert für das Sedimentendglied stimmen gut mit der durchschnittlichen Zusammensetzung der Proterozoikum-Sedimente überein, in Übereinstimmung mit der vorherigen Schwefelisotopenstudie. Der abgeleitete Se-Gehalt des Pyrits im subduzierenden Sediment ist ähnlich oder höher als der Literaturwert für die Pyrite im Sediment des Proterozoikum. Diese Ergebnisse sprechen aus der Perspektive des Erdmantels für den kürzlich vorgeschlagenen hohen O_2-Gehalt in der Atmosphäre des mittleren Proterozoikums. Dies wiederum impliziert, dass neben dem atmosphärischen O_2 eher andere Faktoren wie die geringere Verfügbarkeit von Nährstoffen eine entscheidende Rolle bei der verlangsamten Entwicklung des komplexen Lebens während der ‘Boring Billion’ spielten.

Table of contents

Introduction

Volatile elements are key ingredients for life. Origin of terrestrial volatiles and their secular evolution in Earth's reservoirs through time has been the subject of scientific debate over the last few decades. Volatile distribution between the Earth's surface and interior is intimately connected to variations in physical and chemical properties of each reservoir, both controlled by geodynamic processes. The moderately volatile and redox-sensitive Se isotope system may provide new perspectives to understand how these processes influence the volatile element budget and development of redox conditions across different reservoirs.

Selenium is classified as a moderately volatile and chalcophile element during planetary formation and its stable gas species H_2Se in the solar nebula condenses into troilite (FeS) with a 50% condensation temperature of 701 K at 10^{-4} bar (Fig. I; Lodders, 2003; Lodders et al., 2009; Wood et al., 2019). In the upper mantle, Se and Te are mainly hosted by Fe–Ni–Cu base metal sulfides and platinum-group minerals (e.g., Guo et al., 1999; Hattori et al., 2002; Lorand and Alard, 2010; König et al., 2015; Lorand and Luguet, 2016). The current estimate of the primitive mantle Se abundance (~80 ng/g) is ca. 40 times lower compared to the Earth's general depletion trend displayed by moderately volatile lithophile elements (Fig. I; McDonough and Sun, 1995; Allègre et al., 2001; McDonough, 2003; Wang and Becker, 2013; Palme and O'Neill, 2014; Wood et al., 2019). Still, the Se abundance is ca. 2 orders of magnitude higher than that predicted by extrapolation of metal–silicate partitioning experiments conducted at <20 GPa to core formation conditions ($D_{Se}^{met.-sil.} = 10^4$; Rose-Weston et al., 2009). The primitive mantle budget of Se, together with S and Te, has been suggested to be established by addition of chondrite-like late veneer after core formation was completed (Fig. I; Kimura et al., 1974; Chou, 1978; Morgan, 1986; McDonough and Sun, 1995; Rose-Weston et al., 2009; Albarède, 2009; Wang and Becker, 2013). However, the non-chondritic S isotope composition of the mantle ($\delta^{34}S = -1.40 \pm 0.50‰$; 1 s.d.) requires that the mantle S budget mainly records core–mantle differentiation rather than a post-core formation S addition (Labidi et al., 2013, 2014, 2016). This is supported by recent metal–silicate partitioning ($D_S^{met.-sil.}$) data obtained at pressure and temperature conditions directly relevant for core segregation (46–91 GPa), with $D_S^{met.-sil.}$ of ~10–55 versus ~1000 predicted previously by Rose-Weston et al. (2009). Meanwhile, it has been debated whether the near-chondritic (relative to CI chondrites; S/Se = 2635 ± 227; Se/Te = 8.9 ± 0.9; Lodders et al., 2009) S–Se–Te elemental ratios in worlwide lherzolites (S/Se = 2690 ± 700; Se/Te = 7.9 ± 1.6; 1 s.d.; Wang and Becker, 2013) represent the

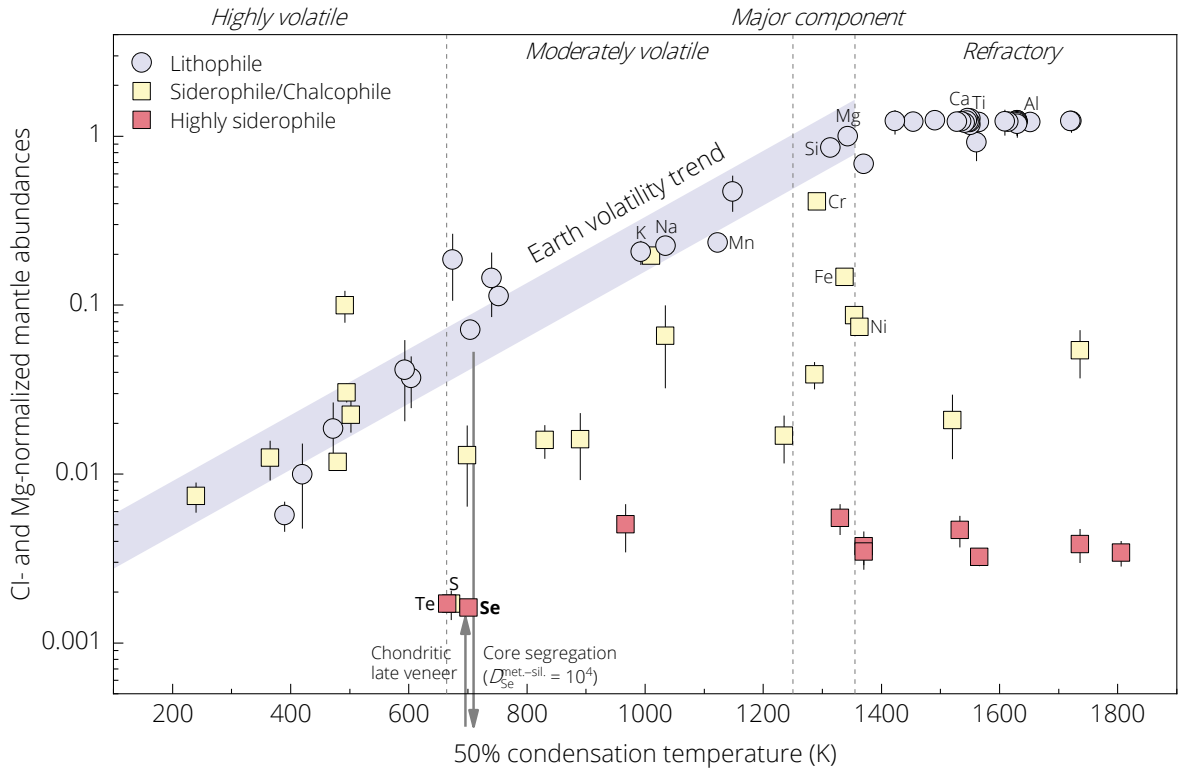

Fig. I Abundances of elements in the primitive mantle normalized to those of CI chondrites and Mg plotted against their volatility expressed by the 50% condensation temperature at a total nebular pressure of 10^{-4} bar (modified after Palme and O'Neill, 2014; Wood et al., 2019). The metal–silicate partition coefficient of Se ($D_{Se}^{met.-sil.}$) during core-mantle differentiation is from Rose-Weston et al. (2009).

primary signature of the primitive mantle since these samples from the lithospheric mantle are often considered metasomatized, especially by Se–Te-rich base metal sulfides and (associated) platinum-group minerals (Lorand and Alard, 2010; Lorand et al., 2003, 2004, 2010; Luguet et al., 2003, 2004, 2015; König et al., 2014, 2015; Harvey et al., 2015).

In this context, stable Se isotope systematics of mantle-derived rocks and melts may offer new insights into the origin of S, Se and Te as well as other highly siderophile or volatile elements in the terrestrial mantle. If the primitive mantle Se budget was established by chondrite-like late veneer components and if no subsequent Se isotope fractionation occurred in the mantle, a chondritic mantle Se isotope composition (Vollstaedt et al., 2016) would be expected. Investigation of Se isotope systematics in high-temperature systems has been limited to meteorites and silicate rock standards (Krouse and Thode, 1962; Rouxel et al., 2002, 2004; Layton-Matthews et al., 2006) mainly due to difficulties in chemical sample processing and instrumental analysis of samples with low Se concentrations (ng/g) such as mantle-derived rocks (e.g., ~20–100 ng/g in lherzolites and <~10 ng/g in harzburgites; König et al., 2012, 2014;

Wang and Becker, 2013; Wang et al., 2013) and melts (e.g., ~100–200 ng/g in MORBs; Hertogen et al., 1980; Lissner et al., 2014). In contrast, surface samples such as soils and sediments are commonly Se-rich (μg/g level). Due to the redox-sensitive characteristics of Se and distinct redox-dependent mobility of Se species in aqueous solutions (e.g., Krouse and Thode, 1962; Cutter and Bruland, 1984; Johnson et al., 1999; Johnson, 2004; Johnson and Bullen, 2004; Stüeken et al., 2017), Se isotope measurements have received increasing interest in studies regarding low-temperature environments (Johnson et al., 1999; Johnson and Bullen, 2003; Herbel et al., 2000, 2002; Ellis et al., 2003; Clark and Johnson, 2010; Schilling et al., 2011a, 2011b, 2014; Mitchell et al., 2012, 2016; Stüeken et al., 2013, 2015a, 2015b; Pogge Von Strandmann et al., 2014, 2015; Zhu et al., 2014; Wen et al., 2014; Kipp et al., 2017; Koehler et al., 2018). These studies demonstrated that Se isotopes can be used as a useful tracer of changes in the ocean-atmosphere redox conditions. Therefore, a combined Se isotope record of the mantle and surface samples may provide new constraints on the cycles of redox-sensitive volatiles across different terrestrial reservoirs.

On the other hand, Se–Te elemental systematics of mantle-derived melts such as mid-ocean ridge basalts may provide a complementary and broader picture regarding the composition of the asthenospheric mantle, provided that Se–Te elemental behavior in igneous systems is well constrained. Also, this would provide a necessary petrogenetic context to interpret the Se isotopic behavior during mantle processes such as partial melting, magmatic differentiation and metasomatic addition of base metal sulfides because both Se and Te behave as chalcophile elements but show contrasting partitioning behavior into different sulfide phases (sulfide liquid and monosulfide solid solution; Brenan, 2015; König et al., 2015). So far, only a few studies reported Se and/or Te concentrations of MORBs (Hertogen et al., 1980; Yi et al., 2000; Jenner et al., 2010, 2015; Lissner et al., 2014). The Se and Te elemental behavior during MORB differentiation is relatively well-understood and they are dominantly controlled by sulfide liquid segregation during differentiation (e.g., Peach et al., 1990; Patten et al., 2013; Brenan, 2015; Kiseeva et al., 2017). However, significant discrepancies exist regarding their absolute and relative partitioning during mantle melting from studies of peridotites and MORB melts, which has been explained by the presence of distinct equilibrium sulfide phases (see above) during mantle melting (Lorand and Alard, 2010; Wang et al., 2013; Wang and Becker, 2015a; Lissner et al., 2014; König et al., 2014, 2015; Brenan, 2015). Therefore, the Se and Te behavior in MORB petrogenesis requires further investigations, as a prerequisite for understanding the Se isotopic behavior in igneous systems.

In this cumulative dissertation, Chapter 1 describes a series of comparative sample dissolution and Se and Te purification experiments on international rock standards and discusses in detail some of the major issues regarding sample processing for isotopic/elemental analyses, including sample heterogeneity ('nugget effect'), Se and Te extraction efficiency, sample-spike equilibration, Se and Te volatility and quantitative separation of interferences such as Ge and hydride formation-buffering metals. Based on these tests, a sample digestion and refined chemical separation technique is presented. It yields high Se and Te recoveries and enables Se isotope and Se–Te elemental analyses from the same rock digest using double spike MC-ICP-MS (following instrumental protocol reported by Kurzawa et al. 2017) and isotope dilution quadrupole ICP-MS, respectively. Replicate analyses of basaltic rock standards demonstrate that precise and accurate Se isotope and Se–Te concentration data can be obtained using small sample sizes. This analytical method hence allows for extending the limited dataset of Se isotope and Se–Te elemental abundances of low-ng level samples relevant to study the terrestrial igneous reservoirs.

Chapter 2 presents the first Se isotope and new Se–Te elemental data for a suite of MORB glasses (N = 27) collected from the Pacific–Antarctic ridge (PAR; 65–56°S and 53–41°S). Compared to previous Se–Te studies (Hertogen et al., 1980; Lissner et al., 2014), these ridge sections are free of plume influence and represent a first-order homogeneous depleted mantle source (with respect to major elements; Vlastélic et al., 2000; Hamelin et al., 2010). It is thus an ideal sample set for quantitatively constraining the Se–Te elemental behavior during MORB differentiation and partial melting using recently published experimental sulfide phase–silicate melt partitioning data (Brenan, 2015; Kiseeva et al., 2017) and investigating potential Se isotopic fractionation during these mantle processes. Besides, this sample suite allows for examination of the role of high-temperature hydrothermal fluid and/or sulfide assimilation (during crustal differentiation) on the Se isotope and Se–Te elemental abundances. This secondary process was previously shown to significantly affect S isotopes (Labidi et al., 2014). Finally, a reliable estimation of the Se isotope composition and Se-Te concentrations of the depleted MORB source mantle is provided. Such a characterization provides a background for future Se isotope studies in igneous systems and contributes new constraints on planetary accretion models regarding the terrestrial volatile delivery.

In chapter 3, Se isotope systematics of a suite of representative MORB glasses (N = 18) from the southern and northern Mid-Atlantic ridge (MAR) are investigated. The southern MAR basalts exhibit significant mantle heterogeneity with respect to radiogenic isotopes due to the

localized interaction between the ridge and Discovery and Shona hotspots (Douglass et al., 1999; Andres et al., 2002; Escrig et al., 2005). These previous studies suggested that a variety of recycled components were incorporated in the mantle sources of the enriched basalts. Sulfur isotope systematics show large variations in $\delta^{34}S$ values that are linearly correlated with $^{87}Sr/^{86}Sr$ and $^{143}Nd/^{144}Nd$ ratios, which requires that the enriched components in the southern MAR mantle source primarily reflect a subducted sediment signature (Labidi et al., 2013). In this context, given the distinct range of Se isotopic variations and Se abundances between the mantle and marine sediments, the enriched MAR basalts allow for investigating the role of crustal recycling on the mantle Se isotope record. The sample suite also includes 2 depleted basalts from each sections of the MAR free of plume influence (White et al., 1978; Douglass et al., 1999) to be compared with the PAR depleted MORB. Additionally, this chapter reports on the first $\delta^{82/76}Se$ analyses of 3 well-characterized granitoids from the Västervik area in Sweden (Kleinhanns et al., 2015), which resemble materials derived from the continental crust. All these new $\delta^{82/76}Se$ data, combined with the data for the PAR basalts (Chapter 2) and marine sediments in the literature, are used to estimate the Se isotope composition of the depleted mantle and to examine the extent and origin of Se isotopic heterogeneity in the upper mantle. Isotopic signatures of the redox-sensitive element Se in mantle-derived melts may thus be used to study secular changes of the surface redox conditions from the mantle perspective.

The results of this dissertation aim at providing novel constraints on the origin and evolution of redox-sensitive volatile and chalcophile elements in the crust–mantle system and the secular changes in the redox conditions across Earth's reservoirs through geological time.

Chapter 1

Chemical sample processing for combined selenium isotope and selenium–tellurium elemental investigation of the Earth's igneous reservoirs

Abstract

The redox-sensitive, chalcophile and volatile Se stable isotope system offers new perspectives to investigate the origin and evolution of terrestrial volatiles and the roles of magmatic and recycling processes in the development of the redox contrast between Earth's reservoirs. Selenium isotope systematics become more robust in a well-constrained petrogenetic context as can be inferred from Se–Te elemental signatures of sulfides and igneous rocks. In this study, we present a high-yield chemical sample processing method that allows the determination of Se–Te concentrations and Se isotope composition from the same sample digest of silicate rocks by hydride generation isotope dilution (ID) quadrupole inductively-coupled plasma mass spectrometry (ICP-MS) and double spike (DS) multicollector (MC)-ICP-MS, respectively. Our procedure yields ~80% Se–Te recoveries with quantitative separation of relevant interfering elements such as Ge and HG-buffering metals. Replicate analyses of selected international reference materials yield uncertainties better than 0.11‰ (2 s.d.) on $\delta^{82/76}$Se and 3% (r.s.d.) on Se concentration for DS MC-ICP-MS determinations for as low as ~10 ng sample Se. The precision of Se–Te concentration measurements by ID ICP-MS is better than 3% and 5% (r.s.d.) for total amounts of ~0.5–1 ng Se and ~0.2–0.5 ng Te, respectively. The basaltic reference materials have variable Se–Te contents, but their $\delta^{82/76}$Se values are rather uniform (on average 0.23 ± 0.14‰; 2 s.d.) and different from the chondritic value. This altogether provides the methodology and potential to extend the limited dataset of coupled Se isotope and Se–Te elemental systematics of samples relevant to study the terrestrial igneous inventory.

1.1 Introduction

Selenium and tellurium are moderately volatile (Lodders, 2003) and chalcophile elements (Guo et al., 1999; Hattori et al., 2002). They are present in the mantle at 2–3 orders of magnitude higher concentrations than expected from metal–silicate partitioning experiments performed at low pressure (<20 GPa; Rose-Weston et al., 2009). The broadly chondritic S–Se–Te elemental ratios in fertile peridotites (Wang & Becker, 2013) have been attributed to late accretion (i.e. the late veneer; Kimura et al., 1974; Morgan, 1986; McDonough & Sun, 1995). However, the sub-chondritic $\delta^{34}S$ of the silicate Earth indicates that the mantle S budget probably records core formation with limited sulfide incorporation rather than a post-core formation accretionary S addition (Labidi et al., 2013, 2016; Labidi & Cartigny, 2016). Moreover, some authors argue that the observed Se–Te signature of fertile peridotites are not primitive features of the mantle because peridotites are generally affected by secondary magmatic processes (Harvey et al., 2015; König et al., 2014, 2015a, 2015b; Luguet et al., 2015).

Systematics of Se isotopes may contribute to placing constraints on these possible scenarios. If the Se budget was dominated by late-accreted materials and if no subsequent Se isotope fractionation of the upper mantle occurred, a chondritic Se isotope composition (Labidi et al., 2018; Vollstaedt et al., 2016) would be expected for the upper mantle. However, the scarcity of data sets regarding Se isotopes in mantle-derived rocks limits reasonable conclusions regarding either process. In order to evaluate the origin of Se isotope signatures in igneous rocks, the Se–Te elemental systematics are very useful. This is because of the chalcophile behaviours of both Se and Te with complementary partitioning into residual monosulfide solid solution vs metasomatic sulfide liquid, respectively (Brenan, 2015; König et al., 2014). Using Se–Te elemental systematics thus helps interpret isotopic signatures of Se in a constrained petrogenetic context, including partial melting, magmatic differentiation and metasomatic addition of base metal sulfides (e.g., Harvey et al., 2015; Jenner et al., 2015; König et al., 2014; Lissner et al., 2014; Luguet et al., 2015). Therefore, a combination of the Se–Te abundances and Se isotope analysis of igneous rocks may be useful for investigating the intrinsic origin and budget of these elements in the silicate Earth and during evolution of its reservoirs. Yet, to date, no such combined studies exist.

Following pioneering studies (Hertogen et al., 1980; Lorand & Alard, 2010; Morgan, 1986;), analytical advancements for combined Se–Te elemental analyses of silicate rocks have been made by hydride generation (HG) isotope dilution (ID) inductively-coupled plasma mass

spectrometry (ICP-MS) measurements coupled with chemical purification such as thiol cotton fiber/powder (TCF/TCP) chemistry (König et al., 2012) and ion exchange chromatography (Wang et al., 2013). Different sample digestion techniques have been used: (1) inverse *aqua regia* digestion in a high-pressure asher (HPA-S) for peridotites (König et al., 2012; Wang & Becker, 2013, 2014; Wang et al., 2013), pyroxenites (Wang & Becker, 2015) and basalts (Wang et al., 2013); (2) hotplate HF digestion in perfluoroalkoxy alkane (PFA) beakers for peridotites (König et al., 2012, 2014, 2015a; Luguet et al., 2015) and basalts (Forrest et al., 2009; König et al., 2014; Lissner et al., 2014); (3) HF digestion in HPA-S or pressure bombs for a wide range of matrices, including peridotites, basalts and Martian meteorites (Wang et al., 2015; Wang & Becker, 2017); (4) inverse *aqua regia* (HPA-S) digestion followed by a hotplate HF-desilicification for peridotites (Harvey et al., 2015; König et al., 2012). While there are several rather comprehensive studies regarding different chemical sample processing and associated limitations for analyses of highly siderophile element (HSE) abundances in mafic and ultramafic rocks (e.g., Dale et al., 2012; Day et. al., 2016; Ishikawa et al., 2014; Li et al., 2015; Meisel et al., 2003), few studies conducted comparative sample digestion experiments for Se–Te analyses (König et al., 2012, Wang & Becker, 2014; Wang et al., 2015).

Due to significant isotopic fractionation during Se oxyanion reduction (Krouse & Thode, 1962; Rees & Thode, 1966), Se isotope measurements have received increasing interest in biogeochemistry (Clark & Johnson, 2010; Ellis et al., 2003; Herbel et al., 2000, 2002; Johnson et al., 1999; Schilling et al., 2011a) and paleoenvironmental studies (Kipp et al., 2017; Layton-Matthews et al., 2013; Mitchell et al., 2012, 2016; Pogge Von Strandmann et al., 2015; Rouxel et al., 2004; Stüeken et al., 2015a, b; Zhu et al., 2014). Following important analytical advancements (Elwaer & Hintelmann, 2008; Layton-Matthews et al., 2006; Pogge von Strandmann et al., 2014; Rouxel et al., 2002; Stüeken et al., 2013; Zhu et al., 2008), Kurzawa et al. (2017) provided a precise and accurate measuring method for $\delta^{82/76}$Se with a consumption of as low as 5 ng Se, which allows the Se isotope determination of geological samples with low ng g^{-1} Se levels. To do so, it is necessary to establish a matrix-matched sample digestion and purification method that necessarily includes (1) complete Se extraction, (2) high chemistry recovery and (3) quantitative separation of HG-buffering transition metals and Ge that potentially causes significant isobaric interferences on ^{74}Se (e.g., Pogge von Strandmann et al., 2014; Stüeken et al., 2013).

In this study, we aim to combine the instrumental protocol for Se isotope analysis described by Kurzawa et al. (2017) with Se–Te concentration determinations by ID ICP-MS from a single

digest of igneous rocks. We report on a series of comparative experiments on the international basaltic reference material BHVO-2 and discuss some of the major issues regarding sample digestion, such as sample heterogeneity, Se–Te extraction efficiency, sample-spike equilibration and Se–Te volatility. We present a suitable sample digestion and refined chemical purification method with high Se–Te recoveries, which enables precise and accurate Se isotope and Se–Te elemental analyses from the same rock digest using small amounts of sample materials. Our ultimate goal is to extend the limited data set of Se isotope composition and Se–Te concentrations of mantle-derived rocks in order to place firm constraints on the behavior of these elements in magmatic processes and their message regarding the origin and evolution of Earth's volatiles.

1.2 Reagents, samples and method

1.2.1 Reagents

Hydrochloric, hydrofluoric and nitric acids (Emsure®, Merck) used in this study were distilled using Savillex DST-1000 sub-boiling Teflon stills. All diluted acids were prepared with 18.2 MΩ·cm water and titrated on a molarity basis. All PFA vials were fluxed successively in reagent grade 3 M HCl, 5 M HNO_3 and 18.2 MΩ·cm H_2O at 120 °C for more than 48 h prior to use. The reducing solution for HG (0.1 M $NaBH_4$ in 0.07 M NaOH) was prepared fresh before each analytical session by dissolving sodium borohydride (analytical grade, Merck) and sodium hydroxide monohydrate (Suprapur®, Merck) in 18.2 MΩ·cm H_2O. Selenium standard solutions of NIST SRM 3149 and MH 495 (in 2 M HCl) were used for MC-ICP-MS analysis with concentrations of 15 or 30 ng mL^{-1}. The standard solutions used for ID ICP-MS measurements were diluted from NIST SRM 3149 and NIST SRM 3156 stock solutions to 0.5 ng mL^{-1}. A calibrated Se double spike (~52% ^{74}Se and ~47% ^{77}Se in 0.1 M HNO_3; Kurzawa et al., 2017) and Te single spike (~92% ^{125}Te in 1 M HNO_3; König et al., 2012) were used for our analyses.

1.2.2 Samples

Given the few studies regarding Se isotopes in mantle geochemistry, limited data of igneous reference materials measured by several working groups are available so far. In this study, we mainly used the international reference material BHVO-2 (Hawaiian basalt; splits

#2375, #2481 and #3323) from the United States Geological Survey (USGS) for our sample digestion and chemical purification experiments because relatively consistent isotope dilution Se–Te concentration data are recently published for this material by different laboratories (König et al., 2012; Wang et al., 2015). The newly established sample processing scheme was then applied to other reference materials such as BCR-2 (Columbia River flood basalt, USGS), BE-N (continental intraplate basalt, Service d'Analyse des Roches et des Minéraux, France), BIR-1a (Icelandic basalt, USGS) and W-2a (diabase, USGS) to allow inter-laboratory comparison of future studies on a larger number of natural samples.

All reference materials used were supplied as finely ground powders. The BHVO-2 standard has a fairly wide range of particle sizes (supporting information Figure S1.1). To compare the Se–Te extraction efficiency of the HPA-S digestion between sample powders with different particle sizes, we reground two independent BHVO-2 splits (~6 g each) using a micro mill (Fritsch Pulverisette 7 classic line). Particle size distribution of the reground material was determined using a laser particle sizer (Analysette 22 NanoTec) in the Application Laboratory of Fritsch, Germany. König et al. (2015a) demonstrated large whole-rock Se–Te concentration heterogeneities in peridotites. This was investigated for basalts in this study by analysis of BHVO-2 sieved fractions of <25 μm and >25 μm. Both fractions were further reground to preclude any potential sampling and digestion bias. All reground powders have particles ≤5 μm (supporting information Figure S1.1).

1.2.3 Sample Digestion

The extraction efficiency of the HPA-S technique for coupled Se isotope and Se–Te concentration analyses from the same sample digest was assessed using BHVO-2 under varying conditions, including sample size, acid volume, digestion temperature (supporting information Table S1.1) and particle size (supporting information Figure S1.1). A conventional hotplate HF digestion (König et al., 2012) was performed in parallel for comparison. We additionally carried out a series of extensive HF digestion experiments on BHVO-2 and BCR-2 following different protocols to evaluate some of the most common digestion related issues such as sample heterogeneity, sample-spike equilibration, effect of insoluble fluoride complexes and Se–Te volatility, with the aim to identify the most suitable digestion method for our routine analyses.

1.2.3.1 HPA-S (inverse *aqua regia*) digestion

The HPA-S (Anton Paar^{TM}, Graz) digestion was performed following the basic procedure outlined by Kurzawa et al. (2017). Briefly, about 0.2–1.1 g of BHVO-2 powder (n = 31) together with Se DS or Te single spike solutions were weighed into quartz glass vials and mixed with 2.5–10 mL inverse *aqua regia* (14.5 M HNO_3 and 10.5 M HCl, molar ratio 3:1). The digestion was carried out at 100 bar and different temperatures (220, 280, 320 °C) with a constant duration of 16 h. After the digestion, the supernatant was processed for Se–Te purification based on the protocol of Wang et al. (2013). The solid residue (n = 7) was analyzed for its Se content in order to assess Se extraction efficiency from the rock powder and potential Se degassing during ashing. To do so, the residue was first fluxed multiple (1–3) times with 18.2 MΩ·cm water in an ultrasonic bath for 30 min. After centrifugation for 15 min, the supernatant water was discarded and the residue was then transferred to a PFA beaker and dried down at 65 °C. The dry residue was carefully weighed with Se DS and processed following the HF digestion protocols described below.

1.2.3.2 Hotplate HF digestion

Sample powders ranging in weight from 0.05–1.2 g were mixed with Se and Te spike solutions and digested using a HF–HNO_3 mixture (1:5 volume ratio) in PFA beakers on a hotplate at 120 °C or 85 °C for 24 h. Solutions were subsequently evaporated at 65 °C. After this point, BHVO-2 and BCR-2 samples that were digested at 120 °C (n = 50 and 11, respectively) were processed following the protocol used by König et al. (2012) before the chemical purification. Briefly, the dry dissolved samples were taken up in 6 M HCl, heated at 100–130 °C for > 24 h, dried down at 65 °C and re-dissolved in 6 M HCl. The fluoride precipitates were removed via centrifugation and the supernatant solution was used for the subsequent TCF/TCP chemistry or chromatography. In order to examine the effect of insoluble fluorides for Se–Te analysis, additional HCl, HNO_3 and $HClO_4$ treatments were performed for several BHVO-2 (n = 4) in high-pressure PTFE vials with pressure bombs in an oven at 190 °C for 48 h to fully dissolve fluoride complexes (Cotta & Enzweiler, 2012; Langmyhr, 1967; Yokoyama et al., 1999). All HCl and HNO_3 solutions were evaporated to complete dryness at 65 °C. The $HClO_4$ solution was evaporated at 130 °C until ~10% solution remained in order to avoid potential Se loss (Stüeken et al., 2013) and directly taken up in 4 M HCl before chromatographic purification.

For all other samples that were digested at 85 °C, a modified protocol (i.e., our routine procedure) was used in combination with our ion exchange chromatography. The dry sample residues were dissolved and heated in 8 mL 6 M HCl at 130 °C on a hotplate for a minimum of 48 h, during which they were treated twice in an ultrasonic bath for 30 min. No visible fluoride precipitates were inspected at this point (for up to 0.55 g sample). Samples were subsequently evaporated to dryness at 85 °C, followed by two successive dissolutions and complete evaporations with 1 mL 10.5 M HCl. Finally, samples were taken up in 5 mL 4 M HCl and centrifuged for 10 min to separate transparent silica gels (e.g., Luais, 2012; Rouxel et al., 2006) prior to chromatographic purification.

In order to quantify and compare potential loss of Se–Te during the evaporation of HCl solutions, 7 BHVO-2 samples were digested and spiked only after the evaporation of 8 mL 6 M HCl and 2 mL 10.5 M HCl solutions to complete dryness at 65 (n = 4) or 85 °C (n = 3).

1.2.4 Chemical purification of Se and Te

1.2.4.1 TCF and TCP chemistry

Several BHVO-2 (n = 26) and BCR-2 (n = 4) samples with weights 0.25–1 g were digested with HF–HNO_3 and used for Se separation via TCF or TCP chemistry. The TCF and TCP batches (n = 5 and 1, respectively) were prepared from commercially available medical-grade cotton fiber and powder with analytical-grade thioglycolic acid, acetic anhydride, acetic acid and sulfuric acid (Merck) based on the methods described by König et al. (2012). Selenium was purified through columns filled with 0.15–0.3 g TCF and TCP (depending on the sample size) following the procedure of Rouxel et al. (2002) and Vollstaedt et al. (2016), respectively. After the separation and evaporation at 65 °C, a dark residue was observed. It was repeatedly treated with ~200 µL of 14.5 M HNO_3 and 30% H_2O_2 to remove residual organic matter. This step was followed by dissolution of the Se fractions in 1 mL 2 M HCl and centrifugation for 15 min. The supernatant was passed through a pre-cleaned 0.45 µm syringe filter (Millex®, Merck) to further eliminate residual fine organic particles (Vollstaedt et al., 2016) and then measured for Se isotope composition.

1.2.4.2 Ion exchange chromatography

When comparing the Se–Te extraction efficiencies of the HPA-S (inverse *aqua regia*) and hotplate HF digestions, BHVO-2 samples were purified for Se and/or Te using the ion exchange chromatography developed by Wang et al. (2013). This method was recently demonstrated to be applicable to high-precision analysis of Se isotopes in shales and basalts after the HPA-S digestion (Kurzawa et al., 2017). In contrast to HPA-S (inverse *aqua regia*) digestion that produces a relatively simple matrix (only ~12 wt.% of the BHVO-2 powder was dissolved; n = 13; supporting information Table S1.1; also see Xu et al., 2012), HF digestion results in whole-rock dissolution, posing additional difficulties on the ion exchange chromatography in terms of Se–Te recovery and separation of interference elements.

We tested existing purification protocols (supporting information Table S1.2) and propose an improved method in combination with our established HF digestion procedure. The new method utilized polypropylene columns (0.9 cm diameter and 8 cm bed height; Triskem, France) filled with 7 mL resin bed volume of Eichrom AG1-X8 (100–200 mesh chloride form) and Eichrom AG 50W-X8 (100–200 mesh hydrogen form) anion and cation exchange resins, respectively. A fresh resin bed, pre-cleaned following a general laboratory procedure (e.g., successive cleaning with H_2O, HNO_3 and HCl), was used for each separation procedure. The columns were calibrated with 7 mL resin for up to 0.45 g mafic matrix. A complete procedure and elution profiles of Se–Te from NIST SRM 3149 and 3156 as well as BHVO-2 for each individual fraction (2.5 mL) are shown in Figure 1.1 and supporting information Table S1.3.

In the first stage, the anion exchange resin was cleaned with 10 mL 18.2 MΩ·cm water and conditioned with 10 mL 4 M HCl. The sample solution (5 mL 4 M HCl) was then loaded onto the column, followed by an addition of 9 mL 4 M HCl. Tellurium and iron are strongly retained by the resin in ≥2 M HCl (Fehr et al., 2004; Fornadel et al., 2014; Loss et al., 1990; Yi et al., 1998), whereas selenium is not adsorbed at HCl molarities of 4–7 M (Schönbächler and Fehr, 2014; Wang & Becker, 2014; Wang et al., 2015). The Se fraction was collected in 14 mL 4 M HCl together with most matrix elements and subsequently evaporated at 85 °C to complete dryness. Rinsing the resin with 10 mL of 2 M HCl–5 M HF mixture eluted almost all Fe while assuring complete retention of Te, probably as chloro- and fluoro-complexes. The resin was further rinsed with 4 mL 0.4 M HCl to elute residual Fe before collecting Te with 14 mL 0.4 M HCl. Separation of Fe may also be achieved by elution with 5 M HF only (Faris, 1960; Fehr et al., 2004; Wang et al., 2013), but we found that in that case, large amounts of

eluent (>25 mL of 0.4 M HCl or 1 M HNO_3) were necessary to quantitatively elute Te. Besides, weak HCl was preferred over HNO_3 for Te elution as the latter more readily destroys the persistent $FeCl_4^-$ complex in the resin (Schoenberg & von Blanckenburg, 2005), resulting in more Fe in the Te eluate. Finally, the Te fractions were dried down at 85 °C to incipient dryness and directly taken up in 1 mL 2 M HCl for concentration analysis.

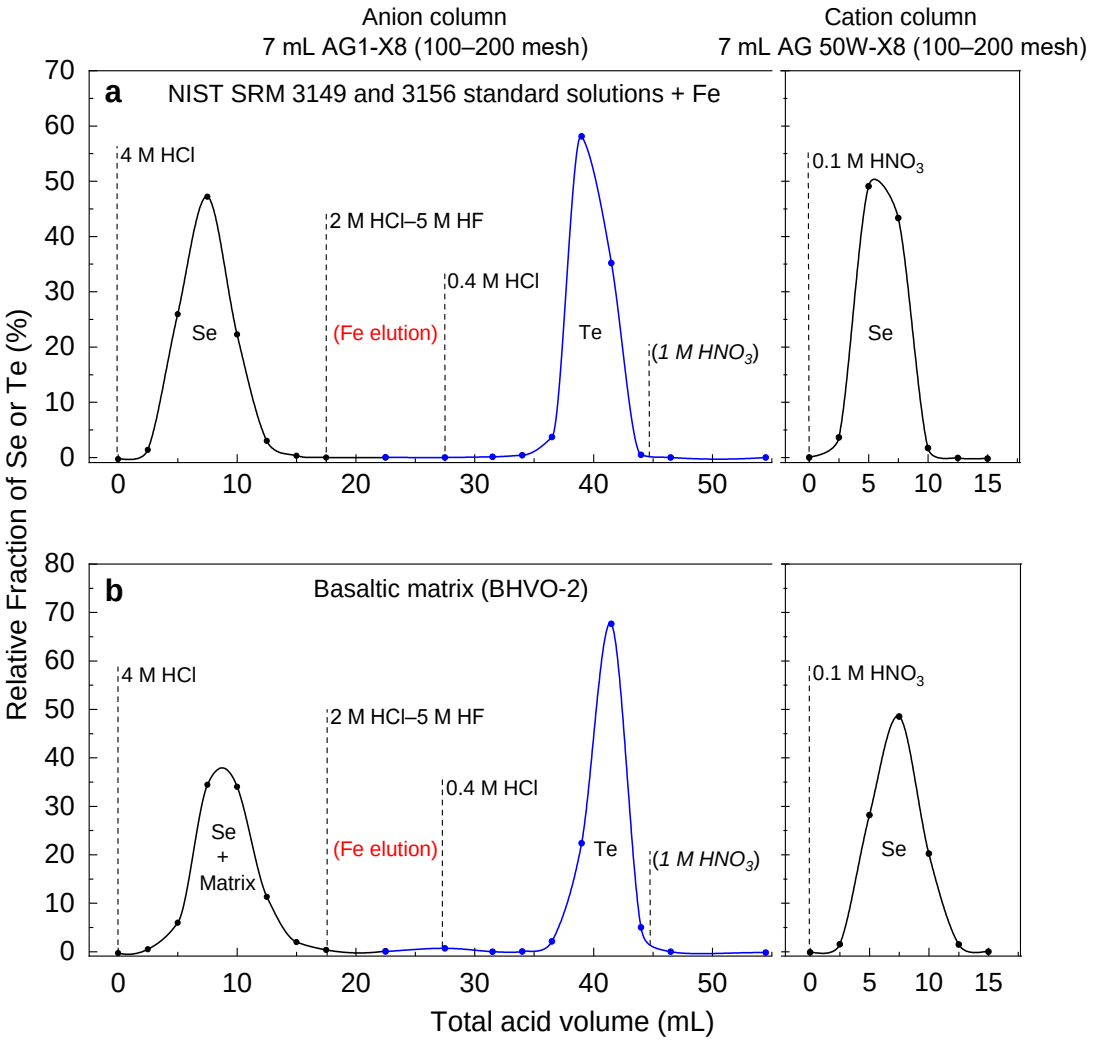

Figure 1.1 Elution profiles for Se (black line) and Te (blue line) from (a) standard solutions NIST SRM 3149 and 3156 and (b) BHVO-2 after the hotplate HF digestion using 7 mL of AG1-X8 and AG 50W-X8 anion and cation resins (100–200 mesh) following the newly established protocol in this study. The dashed lines represent the eluent we used. The relative fractions of Se and Te were determined at each 2.5 mL eluent (for 2 M HCl–5 M HF and 1 M HNO3, 5 and 8 mL of fractions were collected, respectively) using ID method (supporting information Table S1.3). The Se–Te yields were determined twice on some collection cuts and the yield repeatabilities are <1% (r.s.d.). The Te elution with 1 M HNO3 (Fehr et al., 2004; Wang et al., 2013) was additionally performed to check the complete desorption of Te from the resin during the column calibration.

Complete separation of Fe from Te eluate is crucial as Fe significantly inhibits H_2Te formation during the analysis, reducing signal intensity (Yu et al., 1983). This effect was quantified by analyses of Fe-doped (ICP Fe standard solution, 1000 μg mL^{-1}) NIST SRM 3156 solutions (0.5 ng mL^{-1}), with Fe/Te mass ratio ranging between ~10^3 and 10^6 (supporting information Table S1.4).

In the second stage, the dry Se fraction was dissolved in 5 mL 0.1 M HNO_3 and placed in an ultrasonic bath for 30 min. When observed, insoluble fluorides were separated via 10-min centrifugation. Selenium was then purified through the cation column following the procedure established by Wang et al. (2015) with small modifications. Briefly, the resin was rinsed with water and conditioned with 0.1 M HNO_3. The sample solution was then loaded onto the column, and Se was collected with another 9 mL 0.1 M HNO_3. In these conditions, other species such as the HG-buffering transition metals Co^{2+}, Ni^{2+}, Cu^{2+} and Pb^{2+} (Vijan & Leung, 1980; Welz & Melcher, 1984; Yu et al., 1983) are quantitatively retained on the resin (Davies, 2012). The Se fractions were dried down at 85 °C, followed by another complete dry-down in 2 mL 10.5 M HCl to remove extant NO_3^-. Finally, they were taken up in 1 mL 2 M HCl, from which an aliquot (100 μL) was measured to verify that all Ge was removed (see Section 1.2.5.1). In case of remaining Ge, the dry-down step at 85 °C was repeated (1–2 times) until a final 1 mL 2 M HCl solution was ready for Se isotope analysis. Note that in dependence on PFA beaker size, hotplate heating increments and laminar flow cooling effects, the specific temperature settings required for adequate hotplate temperatures may slightly vary in different laboratories. At this stage, we emphasize that the optimum temperature window (between 85 and 90 °C) is crucial for eliminating Ge from the sample solution while minimizing Se loss (see Section 1.4.2).

1.2.5 Instrumental analysis

1.2.5.1 DS MC-ICP-MS analysis

Analysis of Se isotope composition was performed on a ThermoFisher Scientific NeptunePlus™ MC-ICP-MS coupled with a HGX-200 (Cetac) hydride generator at the laboratory of the Isotope Geochemistry Group, University of Tübingen, Germany. Measurements were run in low-resolution mode with a Ni-Jet sample cone and Ni skimmer H-cone. Typical operating parameters, analytical procedure, interference corrections and double-

spike inversion protocols were previously described in detail by Kurzawa et al. (2017). For most analyses in this study, ~10–35 ng mL^{-1} sample Se was used, which generated ^{82}Se signal intensities of ~350–1150 mV using a $10^{11}\,\Omega$ amplifier resistor with an uptake rate of 0.181 mL min^{-1} under typical running conditions. The background level (typically ~3 mV on ^{82}Se) was determined on pure 2 M HCl before each standard and sample solution for on-peak-zero corrections. Washout times were typically 5 min. Selenium isotope ratios are expressed in the δ-notation relative to NIST SRM 3149 as per mil (‰) deviation following:

$$\delta^{82/76}Se_{Sample} = \left(\frac{^{82/76}Se_{Sample}}{^{82/76}Se_{NIST\ SRM\ 3149}} - 1 \right) \times 1000$$

The $\delta^{82/76}Se$ values of sample and inter-laboratory standard MH 495 are always corrected against the average $\delta^{82/76}Se$ value of two bracketing (concentration-matched) NIST SRM 3149 standards with 15 and 30 ng mL^{-1} Se. Kurzawa et al. (2017) reported a long-term external reproducibility of 0.11‰ (2 s.d.) on $\delta^{82/76}Se$ using 15 ng mL^{-1} NIST SRM 3149 standard solution. The MH 495 standard analyzed together with the samples in this study yields mean $\delta^{82/76}Se$ values of −3.24 ± 0.10‰ (2 s.d., n = 46) and −3.26 ± 0.06‰ (2 s.d., n = 32) for 15 and 30 ng mL^{-1} solutions, respectively (supporting information Table S1.5). This is in accordance with the value of −3.27 ± 0.13‰ (2 s.d., n = 100; on 15 ng mL^{-1} solution) reported by Kurzawa et al. (2017) and is within the range of previously published values (Carignan & Wen, 2007; Vollstaedt et al., 2016; Zhu et al., 2008).

Germanium is the main isobaric interference from the sample matrix in Se isotope analysis, but it cannot be fully separated from Se by our chromatography with the range of eluent molarities tested (e.g., 4–7 M HCl and 0.06–0.2 M HNO_3; but see Schilling et al., 2011b, 2014). However, it is efficiently eliminated during the evaporation of all HCl solutions at 85 °C (see Section 1.4.2). As a result, we observed $^{72}Ge/^{82}Se$ signal ratios <0.0002 (i.e., Ge/Se <0.0001) from all sample solutions with digested sample sizes <0.45 g, allowing us to fully neglect a ^{74}Ge interference correction. Note that the occurrence of As, Se and Br hydrides could also represent significant interferences (Pogge von Strandmann et al., 2014; Stüeken et al., 2013; Vollstaedt et al., 2016). However, all relevant hydride interferences are suppressed to undetectable levels by adding a controlled flux of methane in the plasma during the measurement (for details, see Floor et al., 2011; Kurzawa et al., 2017), and no further corrections were made after the on-peak-zero correction.

1.2.5.2 ID ICP-MS analysis

The Se and Te ID concentration measurements were carried out on a ThermoFisher Scientific iCAP-Qc quadrupole ICP-MS at the laboratory of the Isotope Geochemistry Group, University of Tübingen, Germany. For most analyses, aliquots of purified Se and Te fractions were prepared separately in 1 mL 2 M HCl to have 0.5–1.0 ng mL^{-1} Se and 0.15–0.5 ng mL^{-1} Te. Some sample unknowns were analyzed for Se concentrations directly after removing only Fe by the anion resin in order to swiftly obtain Se concentrations for adequate spiking for Se isotope analysis on new digests. The sample solutions were mixed with 2 M HCl and 0.1 M $NaBH_4$–0.07 M NaOH in a hydrideICP HG system (ESI) to reduce Se^{4+} and Te^{4+} oxyanions to their hydride forms, which were transported by Ar (~1.08 L min^{-1}) to the plasma through a quartz cyclonic spray chamber. Measurements were performed in the iCAP-Qc STD mode to maximize signal sensitivity on the analyte isotopes, due to the reduction in sensitivity that can accompany the use of He kinetic energy discrimination (Chew et al., 2014). Each individual analysis consisted of 420 measurements of 3 points per peak of ^{77}Se and ^{78}Se for Se and ^{125}Te and ^{126}Te for Te with a dwell time of 0.03 s starting from the point of signal stabilization, which was usually achieved after ~1.2 min from the start of sample uptake. Every analytical session includes 4 standard solutions (0.5 ng mL^{-1} NIST SRM 3149 and 3156) measured before and after the sample unknowns. Under typical operating conditions with an uptake rate of ~0.41 mL/min, these standard solutions yield intensities of ~40,000 cps on ^{78}Se and ~55,000 cps on ^{126}Te, whereas the reagent blank (i.e., pure 2 M HCl) generally yields less than 13% and 3% of the respective signals. Unlike the HPA-S vial blanks that can sometimes be up to ~1 ng (Kurzawa et al., 2017), total procedural blanks (n = 10) from our established sample preparation procedures always yielded Se–Te signals that are indistinguishable from the background level on pure 2 M HCl. Taking the detection limit of the quadrupole ICP-MS as three times the standard deviation for each measured isotope in the reagent blank (Long & Winefordner, 1983), the maximum detection limits of the isotope dilution analysis calculated following the approach of Yu et al. (2002) are ~0.05 and ~0.007 ng mL^{-1} for Se and Te, respectively (for the comparison of ID detection limits on an Element XR sector field ICP-MS, see Wang & Becker, 2014).

A typical washout time of 2.5 min for solutions with Se concentrations of up to 5 ng mL^{-1} Se efficiently flushed the HG system. On the contrary, efficiency of Te washout was in some cases compromised by memory effects after ~10 samples. Elevated background levels may occur (up to 10 times the initial level), especially when Te fractions contain residual Fe

after the purification. Note that our refined chromatographic protocol for Fe separation (by a HF–HCl mixture) efficiently addressed this issue (see Section 1.2.4.2). When still necessary in some cases, a prolonged >45 min washout was performed. Fehr et al. (2005) also reported long washout times of up to 60 min during Te isotope analysis using a desolvating nebulizer system. The primary source of the memory was identified as Te accumulation on the quartz injector and torch, which were cleaned with 0.1 M of HNO_3 or 0.5 M HCl for ~24 h after every 2 analytical sessions in order to ensure Te concentration data quality.

Selenium and tellurium concentrations of the samples were calculated using $^{77}Se/^{78}Se$ and $^{125}Te/^{126}Te$ ratios obtained after on-peak-zero and instrumental mass bias correction using the measured and natural ratios (Meija et al., 2016) of the NIST SRM 3149 and 3156 solutions. Although the Se and Te concentrations of these standards (both 0.5 ng mL^{-1}) in some cases do not overlap with the full range of sample concentrations (0.5–1.0 ng mL^{-1} Se and 0.15–0.5 ng mL^{-1} Te), we did not observe any associated uncertainty propagation on the corrected isotopic ratios, although the blank levels on each of the monitored masses are different. This might be due to the high washout efficiency for both Se and Te (with <10 samples in a session). The Se–Te analysis may in theory be affected by multiple isobaric and polyatomic interferences at monitored masses, but no further corrections were considered necessary. This is because any existing matrix-based oxides (e.g., $^{62}Ni^{16}O$, $^{109}Ag^{16}O$, $^{110}Pd^{16}O$ and $^{110}Cd^{16}O$) are prevented from entering the plasma by the hydride generator, whereas interferences from the carrier gas, analyte and cones (e.g., $^{40}Ar^{37}Cl$, $^{40}Ar^{38}Ar$, ^{78}Kr, $^{86}Kr^{40}Ar$, ^{126}Xe and $^{62}Ni^{16}O$) are considered to be constant over the course of a session and hence eliminated by the on-peak-zero correction. To evaluate the quantities of potential hydride interferences such as ^{76}GeH, ^{77}SeH, ^{124}SnH and ^{125}TeH, we monitored signal intensities at m/z 82, 83, 130 and 131 for ^{82}Se, ^{82}SeH, ^{130}Te and ^{130}TeH in 3 standard and BHVO-2 solutions containing 0.5–1.5 ng mL^{-1} Se and Te. The signals obtained at m/z 83 and 131 were identical to background levels within the Se and Te concentration range tested. Assuming $SeH^+/Se^+ = GeH^+/Ge^+$ and $TeH^+/Te^+ = SnH^+/Sn^+$, our results suggest that negligible interferences are generated from these hydrides.

The precision of the Se–Te concentration analyses is evaluated by replicate analyses of BHVO-2 with a wide range of sample sizes (~0.08–1.10 g) from different HF digestion batches (n = 61 and 24 for Se and Te, respectively) and chemical separation procedures (Figure 1.2 and supporting information Table S1.6). Despite these different methods applied, BHVO-2 yields consistent Se–Te concentrations with an average of 169 ± 3 ng g^{-1} Se (1 s.d., n = 61) and 14.2 ± 0.3 ng g^{-1} Te (1 s.d., n = 24; Figure 1.2). Based on these replicate analyses, the

intermediate precision of our method for Se–Te concentration determination is estimated to be ~2% (expressed in r.s.d.). For comparison, some Se concentrations were determined on both quadrupole ICP-MS (by ID) and MC-ICP-MS (by DS inversion) using aliquots from the same sample digest and show excellent agreement (within ~3% variation) for all samples (supporting information Figure S1.2).

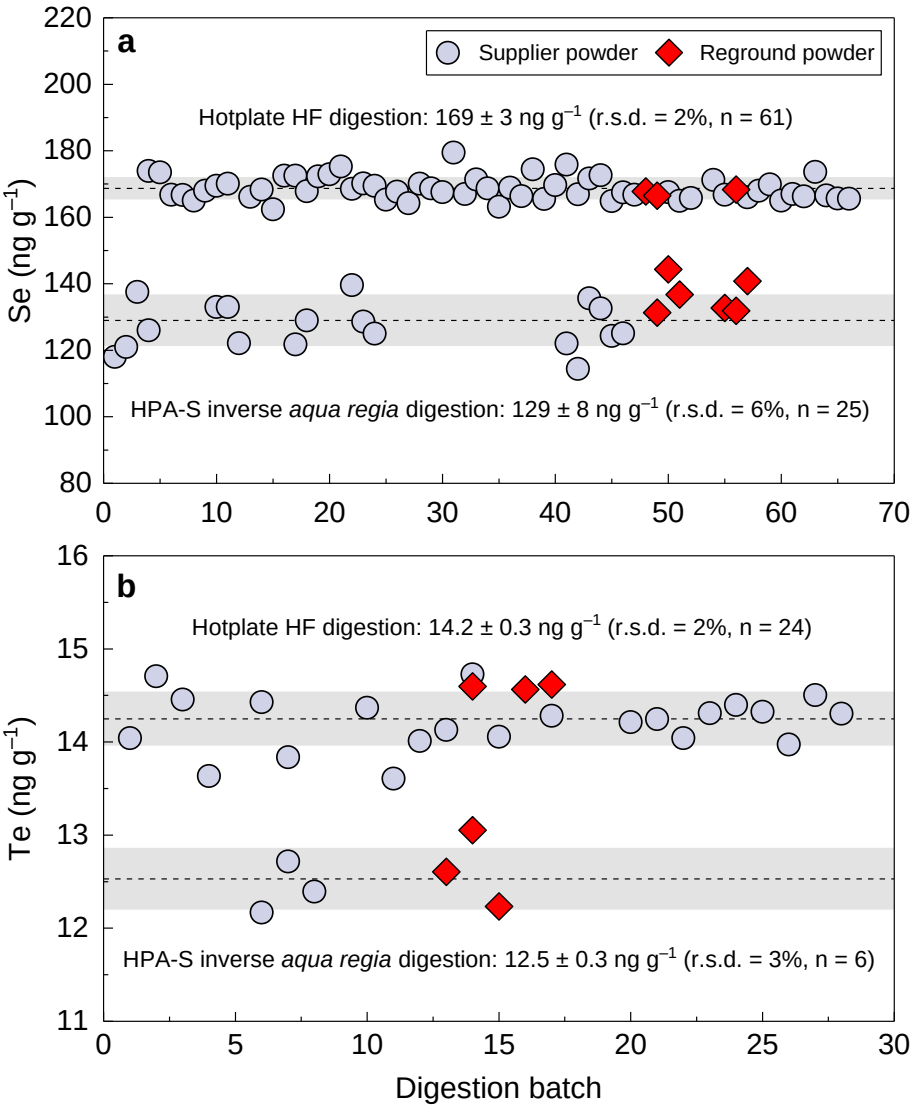

Figure 1.2 BHVO-2 Se and Te concentrations analyzed from the HPA-S (inverse *aqua regia*) and different hotplate HF digestion procedures over the course of 18 months. These samples cover a wide range of sample sizes (~0.08–1.1 g). The sample size distributions are reported in supporting information Tables S1.1 and S1.6. Note that the reground sample powder shows the same Se and Te extraction efficiencies from the HPA-S digestion with the original/supplier powder, although they show quite distinct particle size distributions (supporting information Figure S1.1).

1.3 Results

1.3.1 Recoveries of Se and Te

Selenium and tellurium recoveries for BHVO-2 at different stages after digestion and chemical purification procedures are determined by the ID approach and/or comparing signal intensities against NIST SRM 3149 and 3156 standard solutions. Results are listed in supporting information Table S1.2. Selenium recoveries from the TCF and TCP chemistry are systematically low for BHVO-2 (<20%, n = 26) as well as BCR-2 (<15%, n = 4). Only Se concentrations were analyzed for these samples. Although this purification chemistry has the advantage of quantitatively separating Ge from Se (Rouxel et al., 2002), this technique was not pursued for subsequent Se isotope analysis due to the poor and variable Se recoveries obtained for basalts by several TCF and TCP batches (n = 5 and 1, respectively).

Selenium recoveries for BHVO-2 (digested with HF–HNO_3) from the new chromatographic purification procedure are 73–87% (n = 5) and 92–100% (n = 5) from the anion and cation exchange column, respectively, with a total procedural recovery of 70–83% (n = 16). The observed and expected signal intensities from samples relative to NIST SRM 3149 standard solutions show that the H_2Se formation efficiency exceeds 90% for all sample solutions after the 2-stage purification, indicating a near-quantitative removal of HG-buffering metals.

For Te in BHVO-2, we obtain 85–93% (n = 5) and 68–89% (n = 11) column chemistry and overall recovery, respectively. The lower overall recovery is mainly caused by the residual Fe that in some cases was not fully separated from Te, thereby inhibiting H_2Te formation. Analysis of Fe-doped standard solutions (see Section 1.2.4.2) shows that Te signals are highly sensitive to the amount of Fe: up to 40% signal loss can occur with Fe/Te = 5000 (Figure 1.3 and supporting information Table S1.4). Based on the difference between the (anion) column and overall recovery (i.e., ~15% signal suppression), an average Fe/Te ratio of ~1000–2000 is estimated for the BHVO-2 Te fraction. Low Te recoveries (10–30%) from peridotites observed by Wang et al. (2013) might also be due to the incomplete separation of Fe.

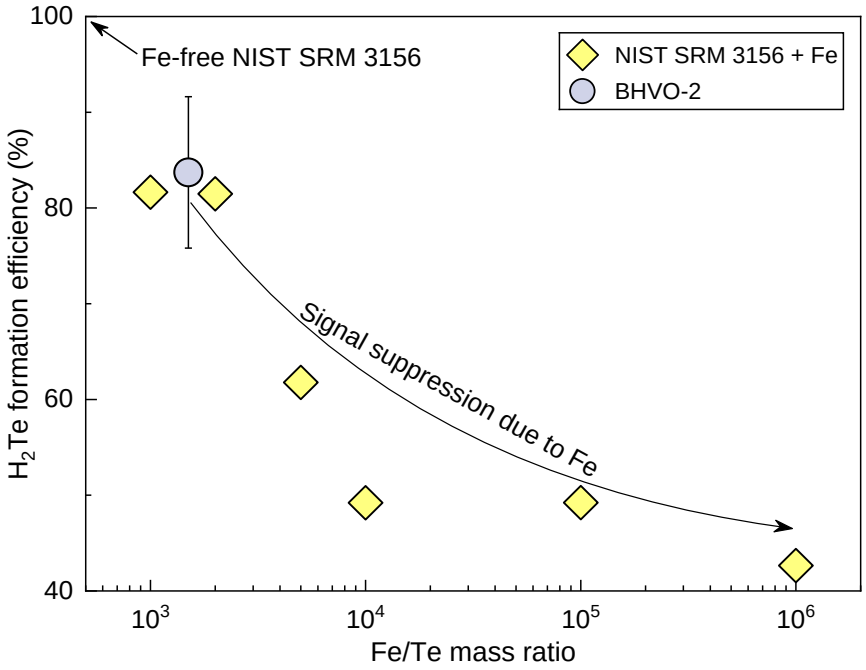

Figure 1.3 Effect of Fe on the hydride (H_2Te) formation efficiency in the hydride generator. The H_2Te formation yields of Fe-doped solutions are calculated by comparing signal intensities against those of pure NIST SRM 3156 standard solutions (0.5 ng mL^{-1}). It shows that H_2Te formation is highly sensitive to the amount of coexisting Fe. Based on this, the purified Te fraction from BHVO-2 (~15% difference between the column and overall recovery) is estimated to have residual Fe with Fe/Te mass ratio of ~1000–2000, which mainly accounts for the ~15% signal suppression.

Overall, total procedural recoveries of Se and Te for all other samples (<0.45 g) are ~80% and ~75%, respectively. The Se and Te elution peaks can shift in the presence of matrix (see NIST SRM 3149 and 3156 versus BHVO-2 in Figure 1.1). However, in comparison to pure standard solution, the Se recoveries for BHVO-2 are only ~10% lower after anion and identical after cation column chemistry. The Te column recovery is even identical between standard and matrix-bearing solutions (supporting information Table S1.3). This tentatively suggests that our chromatographic purification method is only slightly (if any) matrix-dependent.

As for the HCl evaporation experiments (see Section 1.2.3.2), we obtain 99–103% (n = 4) and 87–91% (n = 3) Se recoveries (determined by the ID method) from BHVO-2 when performing the evaporation at 65 and 85 °C, respectively. Two BHVO-2 samples spiked after the evaporation with ~10% Se loss at 85 °C yield higher $\delta^{82/76}$Se (0.42 ± 0.04‰; 2 s.d.) compared to our average value of BHVO-2 that are spiked prior to the digestion (Table 1.1). We obtain Te recoveries of ~100% at both evaporation temperatures for BHVO-2 (n = 5), as well as NIST SRM 3156 standard solutions (n = 5).

1.3.2 Se–Te concentrations

The BHVO-2 supplier and reground powders from the HPA-S digestions were analyzed for Se isotopes (hence also Se concentrations) or Te concentrations in order to evaluate Se and Te extraction efficiencies (supporting information Table S1.1). They yield average concentrations of 129 ± 8 ng g^{-1} Se (1 s.d., n = 25) and 12.5 ± 0.3 ng g^{-1} Te (1 s.d., n = 6). The reground powder alone yields 136 ± 5 ng g^{-1} Se (1 s.d., n = 6) and 12.7 ± 0.3 ng g^{-1} Te (1 s.d., n = 3), indistinguishable from the HPA-S total averages. These values display higher variations and are distinctly lower compared to the values from the HF-based digestions of BHVO-2 with average concentrations of 169 ± 3 ng g^{-1} Se (1 s.d., n = 61) and 14.2 ± 0.3 ng g^{-1} Te (1 s.d., n = 24; Figure 1.2). Note that the Se concentration of the solid residue after the HPA-S procedure is on average 37 ± 3 ng g^{-1} (1 s.d., n = 7; supporting information Table S1.1). When added to the HPA-S extracted fractions, this yields 173 ± 7 ng g^{-1} (1 s.d., n = 7), which matches the bulk BHVO-2 average (169 ± 3 ng g^{-1}; 1 s.d., n = 61) obtained from the HF digestion.

The Se–Te concentrations of reference materials obtained after the newly established sample digestion and purification protocols are listed in Table 1.1. Additional Se–Te concentration data for BHVO-2 and Se concentration data for BCR-2, BE-N, and W-2a from the HF-based digestion experiments using different purification protocols can be found in supporting information Table S1.6. The calculated uncertainties (r.s.d.) on all samples are better than ~3% and ~5% for Se and Te concentrations, respectively. Despite limited literature data, our BHVO-2 Se–Te concentrations overlap with the values of ~170 ng g^{-1} Se and ~11.9–14.4 ng g^{-1} Te reported by König et al. (2012) and Wang et al. (2015). The reason why these two studies obtained similar Se (169 ± 3 ng g^{-1} and 170 ± 22 ng g^{-1}; 1 s.d.) but different Te concentrations (11.9 ± 0.7 ng g^{-1} and 14.4 ± 0.3 ng g^{-1}; 1 s.d.) for BHVO-2 remains unclear. We therefore compared our data with the combined range of these published data. Overall, our Se–Te concentrations of most samples are fairly comparable to the published data, but some significant differences are also observed (Table 1.1). For example, W-2a in this study yields Se concentration (107 ± 1 ng g^{-1}; 1 s.d., n = 8) that is significantly different from the published value of 5.2 ng g^{-1} (Forrest et al., 2009) but similar to the average value of 91 ± 13 ng g^{-1} (1 s.d.) from Savard et al. (2009). Also, BE-N Te concentration (1.02 ± 0.05 ng g^{-1}) is ~25–30% higher than those published by Lissner et al. (2014) and König et al. (2014). About ~7% relative difference is observed for BCR-2 Te data between this study and Lissner et al. (2014).

The BHVO-2 grain separates of >25 μm and <25 μm analyzed after the HF digestion yields distinct concentrations: 134 ± 2 and 200 ± 5 ng g^{-1} Se and 10.6 ± 0.4 and 18.9 ± 0.5 ng g^{-1} Te (all 1 s.d.; supporting information Table S1.7). Mass balance calculation of the bulk-rock Se–Te concentrations using weight fractions of these separates yields 167 ± 3 ng g^{-1} Se (1 s.d.) and 14.8 ± 0.3 ng g^{-1} Te (1 s.d.), in agreement with the average measured concentrations.

Table 1.1 Combined selenium isotope compositions and Se–Te concentrations of selected international reference materials analyzed from the same sample digests following the newly established hotplate HF digestion and chromatographic purification protocols in this study.

Samples		Se concentration[a] (ng g^{-1})	Se analyzed (ng)	$\delta^{82/76}$Se (‰)	2 s.e.[b] (‰)	Te concentration (ng g^{-1})
BHVO-2 (basalt)		171	14	0.21	0.06	14.3
		170	36	0.26	0.04	14.3
		167	12	0.18	0.11	14.3
		168	35	0.10	0.04	14.1
		168	37	0.14	0.04	14.2
		166	9	0.20	0.11	14.0
		166	20	0.16	0.06	14.1
		166	23	0.16	0.06	14.4
	Average	*169*		0.18		*14.2*
	Uncertainty[c]	*3*		0.10		*0.3*
König et al. (2012)		169 ± 3				11.9 ± 0.7
Wang et al. (2015)		170 ± 22				14.4 ± 0.3
BCR-2 (basalt)		76	15	0.28	0.06	2.50
		77	14	0.31	0.07	2.53
		78	13	0.36	0.07	2.46
		78	16	0.23	0.06	2.66
		77	17	0.25	0.06	2.52
	Average	*76*		0.29		2.54
	Uncertainty[c]	*1*		0.10		0.08
Makishima and Nakamura (2009)		82 ± 7				3.20 ± 0.04
Lissner et al. (2014)		78 ± 3				2.73 ± 0.06
Kurzawa et al. (2017)		71 ± 4		0.18 ± 0.03		
BE-N (basalt)		65	19	0.18	0.06	1.06
		66	20	0.16	0.05	1.04
		66	20	0.14	0.06	1.05
		65	20	0.20	0.05	1.03
		65	19	0.07	0.06	0.94
	Average	*66*		0.15		1.02
	Uncertainty[c]	*1*		0.10		0.05

Samples		Se concentration[a] (ng g^{-1})	Se analyzed (ng)	$\delta^{82/76}$Se (‰)	2 s.e.[b] (‰)	Te concentration (ng g^{-1})
Rouxel et al. (2002)		57		0.37 ± 0.32[d]		
Savard et al. (2009)		70 ± 9				
Lissner et al. (2014)		65 ± 1				0.82 ± 0.01
König et al. (2014)		67 ± 3				0.78 ± 0.10
BIR-1a (basalt)		14.9	18	0.25	0.08	5.86
		14.5	10	0.31	0.08	5.81
		15.4	18	0.28	0.08	5.85
		15.5	19	0.22	0.07	5.62
		14.5	12	0.36	0.08	5.98
	Average	15.0		0.28		5.82
	Uncertainty[c]	0.5		0.11		0.13
Yi et al. (1998)						5.70 ± 0.15
Forrest et al. (2009)		11–11.2				3.5–5.3
König et al. (2012)		14.2 ± 1.0				4.79 ± 0.17
W-2a (diabase)		107	21	−0.04	0.05	1.64
		108	27	−0.13	0.04	1.67
		108	41	−0.09	0.04	1.68
		107	30	−0.10	0.04	1.69
		108	18	−0.15	0.07	1.83
		106	24	0.00	0.05	1.75
	Average	*107*		−0.09		1.71
	Uncertainty[c]	*1*		0.11		0.07
Yi et al. (1998)						1.84 ± 0.05
Savard et al. (2009)		91 ± 13				
Forrest et al. (2009)		5.2				1.6

Italics refer to the average Se and Te concentrations and 1 s.d. calculated using the data in this table and all the additional Se and/or Te concentrations analyzed in this study from supporting information Table S1.6.
[a] Selenium concentrations in this table are obtained from the double-spike inversion.
[b] Internal precision of a sample run (over 40 cycles) is reported as 2 standard error (2 s.e.).
[c] All uncertainties are 2 s.d. and 1 s.d. for the average $\delta^{82/76}$Se and Se–Te concentrations, respectively.
[d] $\delta^{82/76}$Se data from Rouxel et al. (2002) is converted relative to NIST SRM 3149 following the approach of Carignan and Wen (2007).

1.3.3 Se isotopic composition

The Se isotope compositions of BHVO-2 analyzed using the HPA-S and HF digestion techniques are listed in Table 1.1 and supporting information Table S1.1 and presented in Figure 1.4. Although the ID concentrations are significantly different as mentioned above, the $\delta^{82/76}$Se values for the bulk-rock BHVO-2 from the HF digestion and extracted fractions from

the HPA-S digestion are indistinguishable: 0.18 ± 0.10‰ (2 s.d., n = 8) and 0.22 ± 0.10‰ (2 s.d., n = 12), respectively.

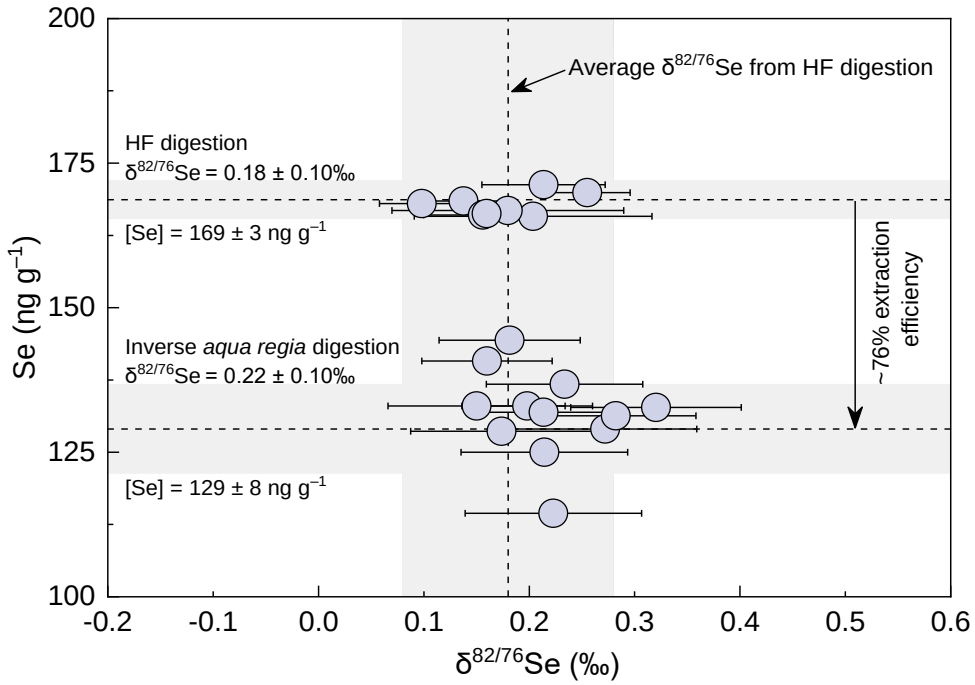

Figure 1.4 The $\delta^{82/76}$Se value and Se concentrations of BHVO-2 obtained from the HPA-S (inverse *aqua regia*) and hotplate HF digestions. Horizontal error bars are internal precisions (2 s.e.) on $\delta^{82/76}$Se for a single analysis (40 cycles). The horizontal dashed lines and shaded fields represent average ID concentrations ± 1 s.d. obtained using each digestion method (Figure 1.1). The vertical dashed line and shaded field represent the bulk-rock average $\delta^{82/76}$Se value ± 2 s.d. that is obtained from HF digestions. Despite the systematically low Se extraction efficiency of the HPA-S digestion (~76% relative to the HF digestion), the extracted fraction yields identical $\delta^{82/76}$Se value to that of the bulk rock.

The bulk-rock Se isotope compositions of all international reference materials processed following the newly established sample processing scheme are listed in Table 1.1 and presented in Figure 1.5. Existing literature data for silicates, chondrites and troilites are also shown for comparison (Kurzawa et al., 2017; Labidi et al., 2018; Rouxel et al., 2002; Vollstaedt et al., 2016). The 2 s.d. uncertainties on $\delta^{82/76}$Se estimated over at least 5 different sample digestion batches are ≤0.11‰ for all samples. When the ^{82}Se signal is below 200 mV (~6.5 ng mL^{-1} Se), the internal precision (2 standard error, 2 s.e.) becomes higher than the analytical uncertainty. However, a minimum of 6.5 ng Se still permits a high-precision Se isotope analysis (e.g., Kurzawa et al., 2017). In this study, more than 15 ng Se (up to 40 ng) was used for most analyses and the internal precision of a sample run is generally better than 0.06‰ (over 40

cycles). The $\delta^{82/76}$Se values of these reference materials range between −0.09 ± 0.11‰ (W-2a; 2 s.d., n = 6) and 0.29 ± 0.10‰ (BCR-2; 2 s.d., n = 5). The $\delta^{82/76}$Se value obtained for BE-N is 0.15 ± 0.10‰ (2 s.d., n = 5), similar within uncertainties to the previously published value of 0.37 ± 0.32‰ (relative to NIST SRM 3149; 2 s.d., n = 1; Rouxel et al., 2002; for the conversion, see Carignan & Wen, 2007). After HF digestion, BCR-2 yields comparable $\delta^{82/76}$Se within uncertainty to that obtained from HPA-S (inverse *aqua regia*) digestion (0.18 ± 0.03‰; 2 s.d., n = 3) by Kurzawa et al. (2017). The diabase W-2a yields distinctly lower $\delta^{82/76}$Se that does not overlap with any basaltic values.

1.4 Discussion

1.4.1 Comparison of the HPA-S (inverse *aqua regia*) and hotplate HF digestion

1.4.1.1 Se–Te extraction efficiency

Selenium and tellurium are chalcophile elements and considered to be primarily hosted by base metal sulfides and platinum group minerals in mantle rocks (Guo et al., 1999; Hattori et al., 2002; Lorand & Alard, 2010; König et al., 2015a). As these accessory phases are easily dissolved in inverse *aqua regia* at high temperature (e.g., Day et al., 2016; Li et al., 2015), a complete extraction of Se–Te from peridotites would be expected after HPA-S digestion. Despite heterogeneous distribution of sulfides in peridotites, several authors reported similar Se and/or Te abundances for peridotites using HPA-S or HF-based digestions (König et al., 2012, 2014, 2015a; Lissner et al., 2014; Wang et al., 2013, 2015; Wang & Becker, 2014). It is noteworthy that these groups analyzed UB-N (serpentinized lherzolite, SARM) as a reference material and obtained similar Se–Te abundances within uncertainties, regardless of whether silicate phases were dissolved by HF. This observation, together with the analytical results of a harzburgite sample (König et al., 2012), strongly argues for the quantitative control of the peridotite Se–Te budget by sulfides. In chondrites, Se also appears to be fully hosted by sulfides (Labidi et al., 2018; Vollstaedt et al., 2016; and references therein). The HPA-S (inverse *aqua regia*) digestion thus has been employed as an ideal digestion technique for combined determination of S–Se–Te and HSE abundances of mantle rocks, bulk chondrites and components of chondrites (Kadlag & Becker, 2015, 2016; Wang & Becker, 2013).

On the other hand, few comparative digestion experiments have been done on basalts. The basaltic reference material BHVO-1 (no longer commercially available from USGS) yields similar Se–Te ID concentrations from HPA-S (inverse *aqua regia*) and HF-based digestions (Makishima & Nakamura, 2009; Wang & Becker, 2014; Wang et al., 2015). Two previous studies (Kurzawa et al., 2017; Lissner et al., 2014) and this study obtain similar Se ID concentrations within uncertainty for another basaltic reference material BCR-2 (USGS) using these digestion techniques. However, basalts can have crystalline and glassy components. Selenium and tellurium, similar to sulfur, may be exsolved in sulfides and/or dissolved in the glassy matrices (e.g., Wykes et al., 2011, 2015). In this case, liberation of the dissolved Se–Te fractions requires HF-desilicification.

Relative to our BHVO-2 Se–Te concentrations obtained from HF digestion, the HPA-S digestion extracted 76 ± 5% and 88 ± 3% (1 s.d.) of the bulk-rock Se and Te, respectively (Figure 1.2). Note that the Se concentrations of the solid residue and extracted fractions of BHVO-2 after the HPA-S procedure sum up to the BHVO-2 bulk-rock average obtained after hotplate HF digestion (Section 1.3.2). The extraction efficiency of the HPA-S for Se seems independent from the sample size (~0.08–1.1 g), acid volume (2.5–10 mL) and ashing temperature (220–320 °C; see supporting information Table S1.1). Some sulfides can be enclosed in coarse silicate grains and remain shielded from acid digestion (Day et al., 2016). However, we observed nearly identical Se–Te extraction efficiency on both the supplier and reground powders (Figure 1.2 and supporting information Figure S1.1). This suggests that the population of exposed sulfides does not increase with decreasing particle sizes of the powder. Unless the sulfide grains are systematically smaller than silicate grains in the reground powder that ranges between 0.5 and 5 μm (Moore & Calk, 1971), our observation might suggest that most sulfides in BHVO-2 are quantitatively dissolved during the digestion. Similarly, all oxide phases are sufficiently dissolved in inverse *aqua regia* at high-temperature (Li et al., 2015). Therefore, we suggest that the unextracted portions of Se and Te from BHVO-2, which systematically represent ~25% and ~12% of the bulk-rock budget, are either dissolved in the glass matrix or hosted in the crystal lattice of silicate minerals (also see Chau & Riley, 1965; Hall & Pelchat, 1997a).

The results of this study support that the extraction of Se and Te from basalts using inverse *aqua regia* may depend on the sample matrix and partitioning of these elements between silicate phases (crystals and glass) and sulfides (e.g., Brenan, 2015; Kiseeva & Wood, 2017; Kiseeva et al., 2017), as previously suggested for some HSEs (e.g., Dale et al., 2012; Ishikawa et al.,

2014; Li et al., 2015). Therefore, the HPA-S (inverse *aqua regia*) digestion without HF-desilicification has to be used with caution for analyses of bulk-rock Se–Te concentrations and/or Se isotope composition of basalts and potentially other silicate melts.

1.4.1.2 Effect of insoluble fluorides during HF digestion

A typical disadvantage associated with HF-based digestion compared to the inverse *aqua regia* digestion is that many elements tend to coprecipitate with fluorides (e.g, Cotta & Enzweiler, 2012; Meisel et al., 2003; Takei et al., 2001; Yokoyama et al., 1999). Some authors speculated that Se and Te do not coprecipitate with fluorides but are dissolved in the supernatant HF solution as oxyanions (Makishima & Nakamura, 2009). Indeed, we did not observe any measurable Se or Te from fluoride precipitates (n = 5) that were separated and completely dissolved by multiple HCl treatments. Moreover, the low uncertainties and consistency of the BHVO-2 Se–Te ID concentrations obtained between different HF digestion procedures (see Section 1.2.3.2) seem to suggest a complete sample-spike equilibrium in the presence of fluoride precipitates, supporting that Se and Te do not coprecipitate with fluorides.

1.4.2 Volatile loss of Se–Te during the sample processing

Accurate determination of Se–Te and other volatile elements (such as S, Ge, As and Sb) in silicate rocks can be compromised by evaporative loss during solution treatment as hydride or halide species (Makishima et al., 2009). Formation of these species can be suppressed by the addition of strongly oxidizing $HCl–HNO_3$ or $HBr–HNO_3$ mixtures to the digestion acid (e.g., Hall & Pelchat, 1997a, b; Makishima & Nakamura, 2009). A combination of the inverse *aqua regia* digestion in HPA-S and the ID method may thus promote sample-spike equilibration and minimize analytical bias associated with the effects of Se–Te loss (König et al., 2012; Wang & Becker, 2014). In our experiment, the Se concentrations of the dissolved phases and residue of BHVO-2 from the HPA-S procedure sum up to 97 ± 6% (1 s.d., n = 7) of the bulk-rock Se concentration by ID. This suggests that Se degassing, if any, is efficiently prevented before equilibration of the dissolved sample fraction and spike.

Following HF digestion, Se and Te are probably present as aqueous oxyanions of Se^{4+} and/or Se^{6+} and Te^{4+} in the solution (Hall & Pelchat, 1997a; Kuldvere, 1989; Stüeken et al., 2013). During subsequent evaporation at 65 °C, these species may not be prone to degassing as

volatile fluorides in the presence of rock matrix and HNO_3 (Marin et al., 2001; Makishima & Nakamura, 2009; but see Yi et al., 1998). Note that our HCl evaporation experiment conducted at 65 °C (after the evaporation of HF–HNO_3) yields full Se–Te recoveries from BHVO-2. This observation, together with the intermediate precision of our BHVO-2 Se–Te concentration data (r.s.d. = ~2%; Figure 1.2), suggests that both elements are not subject to evaporative losses following the HF digestion.

As for the subsequent HCl treatment for dissolving insoluble fluorides and converting total Se to Se^{4+} (Hill et al., 1995; Hall & Pelchat, 1997a), Se loss may indeed occur (Chau & Riley, 1965). This might be due to the formation of (1) volatile Se compounds such as hydride (H_2Se) and chlorides (Kurzawa et al., 2017; Schirmer et al., 2014; Vollstaedt et al., 2016) and/or (2) insoluble Se^0 (Langner, 2000; Marin et al., 2001; Tokunaga et al., 2013) that is unreactive with $NaBH_4$ during the analysis (Hall & Pelchat, 1997a). It has been suggested that evaporation of HCl solutions needs to be conducted below 80 °C to prevent Se loss (Layton-Matthews et al., 2006; Rouxel et al., 2002). However, despite the potential Se losses, we necessarily dried down all HCl solutions to complete dryness at 85 °C in order to quantitatively eliminate Ge as volatile $GeCl_4$ (boiling point 84 °C; see Lopez-Molinero et al., 2001; Luais, 2012; Makishima & Nakamura, 2009; Rouxel et al., 2006). Note that the double spike approach corrects for any isotopic fractionation associated with loss of Se as detailed by Kurzawa et al. (2017). We observed between negligible and up to 10% Se losses from BHVO-2 after multiple evaporations of HCl solutions at 65 and 85 °C, respectively (see Section 1.3.1). Kurzawa et al. (2017) reported large Se losses (up to 51%) from NIST SRM 3149 solution even at 65 °C. This indicates that the behavior of Se species in HCl in fact largely depends on the presence of sample matrix. On the other hand, we observed negligible evaporative Te losses from both standard (NIST SRM 3156) and BHVO-2 matrix solutions at 65 and 85 °C, reflecting different chemical behaviors of Se and Te in aqueous solutions (McPhail, 1995).

1.4.3 Sample heterogeneity

The reproducibility of HSE analysis is known to be compromised by sample heterogeneity (Meisel & Horan, 2016; and references therein). Similarly, based on the literature, Se–Te concentrations for a given sample can show large variabilities between replicate digestions (e.g., Forrest et al., 2009; König et al., 2012; Wang et al., 2015). This is more pronounced in peridotites even with a large sample size (up to 3 g; König et al., 2012). Furthermore, grain size

experiments on a harzburgite showed that coarse and fine fractions have quite different Se–Te concentrations and Se/Te ratios, emphasizing the importance of the mineralogy and sample size selection for precise Se–Te determinations in peridotites (König et al., 2015a).

The Se–Te concentrations of our BHVO-2 sieved fractions of >25 μm and <25 μm illustrate a similar sample heterogeneity in this basaltic reference material (supporting information Table S1.7). The Se/Te ratio of the fine fraction (10.6 ± 0.4) is lower than that of the coarse fraction (12.6 ± 0.5) and the bulk rock (11.9 ± 0.7; all 1 s.d.). For peridotites, the complementary Se/Te ratios in different grain separates are explained by the predominant stabilization of metasomatic Te-rich phases (e.g., tellurides) along interstitial grain boundaries after melt depletion (König et al., 2015a). In the case of basalt BHVO-2, it probably indicates predominant settling of tellurides or other high Te-bearing host phases (with lower Se/Te) along grain boundaries during cooling and crystallization of the melt.

Despite the heterogeneous distribution of Se–Te rich phases within the matrix, the variabilities of Se–Te concentrations obtained for bulk-rock BHVO-2 powders are always lower than ~3% (r.s.d.) at a range of sample sizes (~0.08–1.1 g; see supporting information Table S1.6 and Figure 1.2). Although the level of heterogeneity is predicted to be sample specific (Wang et al., 2015), low variabilities are also observed under intermediate precision conditions for the measured Se–Te concentrations (r.s.d. <5%) and $\delta^{82/76}$Se values (2 s.d. ≤0.11‰) in all reference materials with a wide range of Se–Te contents (~15–170 ng g^{-1} Se and ~1–14 ng g^{-1} Te). This suggests that the effect of sample heterogeneity might not be significant in Se–Te analysis of a melt-like matrix with digestion of down to 0.1 g sample powder.

1.4.4 The Se isotopic composition of igneous rocks

Identical $\delta^{82/76}$Se values after the HPA-S (inverse *aqua regia*) and hotplate HF digestions might indicate a Se isotopic homogeneity within a basaltic matrix (e.g., BHVO-2), despite seemingly different Se host phases as indicated by systematically lower and relatively variable Se concentrations obtained after the HPA-S digestion (Figure 1.4). However, for accurate analyses of combined Se isotope and Se concentration of bulk basalts, the use of HF is required to achieve complete Se extraction (see Section 1.4.1.1).

With the method presented, the $\delta^{82/76}$Se values of all analyzed reference materials are indistinguishable within 2 s.d. uncertainties from the previous estimate for the igneous silicate

Earth (0.33 ± 0.32‰; 2 s.d. analytical precision; Rouxel et al., 2002; Figure 1.5). Based on the basaltic reference materials and refined analytical precision (~0.11 ‰; 2 s.d.), we obtain an estimate of 0.23 ± 0.14‰ (2 s.d. of the mean). Interestingly, the basalts displaying this narrow

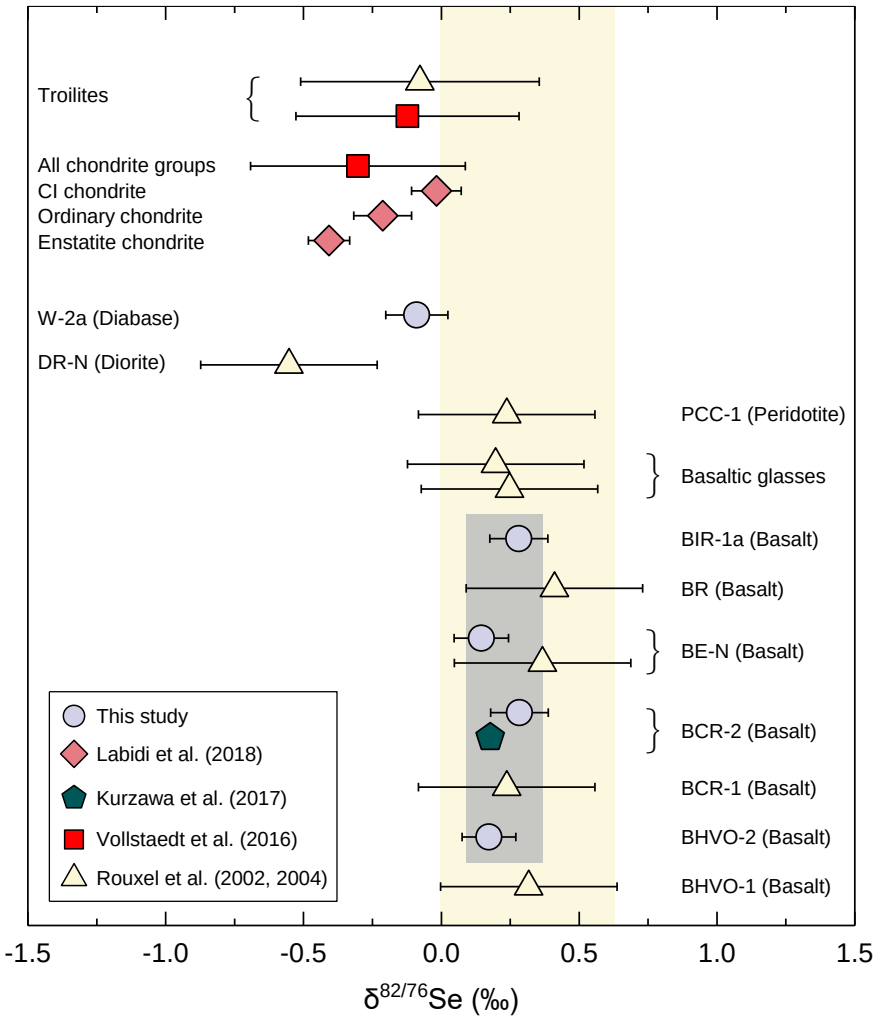

Figure 1.5 The $\delta^{82/76}$Se values of reference materials analyzed using our newly established HF digestion and chromatographic purification protocols. Also shown for comparison are literature data for silicate rocks (Kurzawa et al., 2017; Rouxel et al., 2002, 2004), chondrites and troilites (Rouxel et al., 2002; Vollstaedt et al., 2016), as well as each chondrite group (Labidi et al., 2018). Literature data is converted to $\delta^{82/76}$Se relative to NIST SRM 3149 (Carignan & Wen, 2007). Horizontal error bars on our data represent 2 s.d. uncertainties estimated over at least 5 digestion batches and are well within our analytical precision of ~0.11‰. The grey shaded box represents the range for $\delta^{82/76}$Se values of analyzed basalts (0.23 ± 0.14‰), which is smaller but still falls in the previously constrained range (light-yellow shaded field) for the igneous silicate Earth (0.33 ± 0.32‰; Rouxel et al., 2002). Note that the range conservatively takes into account the 2 s.d. of the mean or, where larger, 2 s.d. analytical uncertainty.

range of $\delta^{82/76}$Se are from diverse geodynamic settings (e.g., ocean islands, plume-influenced mid-ocean ridges and continental settings). Despite markedly different Se–Te elemental systematics of these basalts (Table 1.1), their similar Se isotopic compositions overlapping with those of a peridotite (Rouxel et al., 2002) and basaltic glasses (from a lava lake near the Lucky Strike hydrothermal field; Rouxel et al., 2004) may either reflect their isotopically homogeneous source or secondary processes (e.g., Lissner et al., 2014; Jenner et al., 2015) that result in similar Se isotope and different Se–Te elemental signatures. On the same note, we point out that the resolvable differences of $\delta^{82/76}$Se values between these basalts and a diabase (W-2a) as well as a diorite (DR-N; Rouxel et al., 2002; Figure 1.5) require further investigation of different types of igneous rocks in order to assess if and how the respective emplacements or subtle petrogenetic differences have an effect on Se isotopes.

Despite some overlap within uncertainties, we note that the average $\delta^{82/76}$Se of basalts analyzed so far are higher than the average chondritic values of -0.30 ± 0.39‰ (2 s.d.; Vollstaedt et al., 2016) and -0.21 ± 0.31‰ (2 s.d.; Labidi et al., 2018). Perhaps more significantly, some basalts (BHVO-2 and BE-N) show $\delta^{82/76}$Se values similar to the estimate for carbonaceous chondrites (-0.01 ± 0.09‰; 2 s.d.), but all basalts show Se isotope signatures significantly different from those of ordinary and enstatite chondrites (-0.21 ± 0.10‰ and -0.40 ± 0.07‰, respectively; 2 s.d.; Labidi et al. 2018). However, a substantially extended data set on terrestrial melts and mantle rocks is still required to fully understand Se isotope variations in magmatic systems before constraining the isotopic composition of the bulk silicate Earth (BSE). This is a prerequisite for understanding the Se isotope and Se–Te elemental perspective on the origin and evolution of the Earth's volatiles.

1.5 Conclusion

This study presents a new and simplified chemical sample processing scheme that enables combined high-precision analyses of Se stable isotopes and Se–Te elemental abundances from the same rock digest of significantly small sample amounts using as low as ~6.5 ng Se by DS MC-ICP-MS (Kurzawa et al., 2017) and ~0.5 ng Se and ~0.15 ng Te by ID (quadrupole) ICP-MS. The method includes a hotplate HF digestion and refined chromatographic purification that yields low blanks and high procedural recoveries of Se and Te (~80%). A complete separation of isobarically interfering Ge from Se is achieved via evaporation of HCl solutions at 85 °C. At the same time, previous equilibration of sample and ^{77}Se–^{74}Se double spike enables correction

for any Se isotopic fractionation associated with minor Se losses. Low variability under intermediate precision conditions was obtained for each sample over at least 5 digestion batches, with calculated uncertainties better than ~0.11‰ (2 s.d.) on $\delta^{82/76}$Se and 3% and 5% (r.s.d.) on Se and Te concentrations, respectively. The selected reference materials (BHVO-2, BIR-1a, BCR-2, BE-N and W-2a) are therefore considered to be rather homogeneous when digested strategically and recommended as Se isotope reference materials in future studies concerning igneous systems.

Although an identical $\delta^{82/76}$Se value of BHVO-2 is observed using the HPA-S (inverse *aqua regia*) and HF digestion techniques, the former cannot fully extract Se and Te depending on the sample matrix and has to be used with caution in bulk-rock Se isotope and/or Se–Te abundance analyses of basaltic matrices. The presented sample preparation procedure in this study is optimized for basalts, but may be readily applied to other silicate matrices (e.g., ultramafic samples with resistant alloys) by employing HPA-S digestion followed by a hotplate HF-desilisification.

The basalts analyzed in this study have markedly distinct Se and Te contents, yet their Se isotopic compositions fall within the range of the igneous silicate Earth previously estimated by Rouxel et al. (2002) but exhibit a smaller variation with an average of 0.23 ± 0.14‰ (2 s.d.). Despite the demonstrated differences of $\delta^{82/76}$Se between these basalts and main chondrite groups (Labidi et al., 2018; Vollstaedt et al., 2016), more systematic studies are required to investigate natural Se isotope variations in igneous systems in order to place firm constraints on the BSE and planetary-scale processes. At this point, the observed $\delta^{82/76}$Se variations indicate the potential of Se isotopes as a future tracer for the origin and evolution of volatiles in the mantle.

Chapter 2

Selenium isotope and S-Se-Te elemental systematics along the Pacific-Antarctic ridge: Role of mantle processes

Abstract

The selenium stable isotope system emerges as a new potential tracer of volatile origin and evolution of the terrestrial planets. Accurate determination of the mantle Se isotope composition requires an assessment of Se isotopic behavior in magmatic processes and potential variations across all mantle reservoirs. Here we report the first high-precision Se isotope and Se–Te abundance data for a suite of basaltic glasses from the Pacific–Antarctic ridge. These MORBs display a narrow range in $\delta^{82/76}$Se values (deviation of ^{82}Se/^{76}Se relative to NIST SRM 3149) between −0.30 ± 0.09‰ and −0.05 ± 0.09‰, with an average of −0.16 ± 0.13‰ (2 s.d., n = 27). We quantify the main processes relevant to MORB petrogenesis in order to better understand the Se–Te elemental behavior in the mantle and investigate if these are systematically related to Se isotope variations.

We show that both Se isotopes and S–Se–Te abundances of MORB melts remain unaffected by assimilation of high-temperature hydrothermal fluids and sulfides, whereas the latter has been shown to overprint the ^{34}S/^{32}S ratios. MORB differentiation involving sulfide segregation (sulfide liquid and monosulfide solid solution) significantly fractionates Se and Te (Se/Te ratio ~45 to 190), with no systematic Se isotope variation. The Se–Te contents of the primary MORB melt corrected for magmatic differentiation can be successfully reproduced by near-fractional decompression melting of a mantle with 170–200 μg g^{-1} S (as sulfide liquid), which has either (1) "fertile lherzolite-like" Se–Te contents (80 ± 17 and 11 ± 1.7 ng g^{-1}, respectively; 1 s.d.) or (2) distinctly lower Se (49 ± 11 ng g^{-1}) and Te (3.5 ± 1.3 ng g^{-1}) contents depending on the choice of experimental partition coefficients published by different studies. Regardless, our model shows that Se–Te systematics of "fertile" lithospheric peridotites preserve little primary melt depletion signatures and reflect significant, if not complete, metasomatic overprinting. Finally, based on the observed negligible Se isotopic fractionation between sulfide phase and silicate melt, we suggest that MORBs preserve their mantle source

isotopic signature ($\delta^{82/76}Se = -0.16 \pm 0.13‰$). Our MORB average is similar within uncertainty to chondritic values but significantly lighter than previously published $\delta^{82/76}Se$ data for basalts from a variety of geodynamic settings. The subtle but significant Se isotope variation observed within the investigated MORB suite (up to ~0.25‰) and between other mantle samples analyzed so far may reflect intrinsic source heterogeneity and potential isotopic differences across various mantle reservoirs.

2.1 Introduction

The current primitive mantle (PM) abundances of the moderately volatile and chalcophile elements Se (~80 ng g^{-1}) and Te (~11 ng g^{-1}) are 35–45 times lower compared to the Earth's general volatile depletion trend (McDonough and Sun, 1995; Allègre et al., 2001; McDonough, 2003; Wang and Becker, 2013; Palme and O'Neill, 2014). Because extrapolation of metal–silicate partitioning experiments at 1–19 GPa to core formation conditions predicts near-complete Se–Te removal from the silicate mantle (Rose-Weston et al., 2009), the mantle abundances of Se–Te, together with that of S, have been explained to be established by a chondritic late veneer addition after core formation (Morgan, 1986; McDonough and Sun, 1995; Rose-Weston et al., 2009; Wang and Becker, 2013). However, the non-chondritic $^{34}S/^{32}S$ ratio of the mantle and recent S partitioning experiments suggest that a major fraction of mantle S budget reflects metal–silicate equilibration (Labidi et al., 2013; Suer et al., 2017). Meanwhile, it has been debated whether the broadly-chondritic relative abundances of S–Se–Te in lherzolites are representative of the PM composition (Wang and Becker, 2013) since these samples from the lithospheric mantle are often considered metasomatized, especially by Se–Te-rich base metal sulfides and associated platinum-group minerals (Lorand and Alard, 2010; Lorand et al., 2003, 2004, 2010; Luguet et al., 2003, 2004, 2015; König et al., 2014, 2015; Harvey et al., 2015). In this context, mantle-derived melts such as mid-ocean ridge basalts (MORBs) may provide a complementary and broader picture regarding the composition of the asthenospheric mantle, provided that Se–Te elemental behavior in mantle processes is well constrained.

There are only few studies concerning Se and/or Te elemental systematics in MORB (Hertogen et al., 1980; Yi et al., 2000; Jenner et al., 2010, 2015; Lissner et al., 2014). Because of their strong partitioning into base metal sulfides (Guo et al., 1999; Hattori et al., 2002; Peach et al., 1990; Barnes et al., 2009; Patten et al., 2013; Brenan, 2015; Kiseeva et al., 2017), Se–Te

abundances and ratios in basaltic melts are strongly controlled by sulfide phase–silicate melt partitioning (Hertogen et al., 1980; Lissner et al., 2014). Hertogen et al. (1980) first observed distinctly higher Se/Te ratios and broadly similar Te contents in worldwide MORBs compared to mantle rocks and suggested a higher apparent compatibility of Te relative to Se during partial melting. This appears consistent with observations from lherzolites, pyroxenites (Wang et al., 2013; Wang and Becker, 2013, 2015a), and sulfides in sub-arc mantle xenoliths (Hattori et al., 2002) but inconsistent with observations from refractory harzburgites and platinum group minerals (König et al., 2012, 2014, 2015). Lissner et al. (2014) investigated the Se–Te systematics in enriched- and depleted-MORBs from a restricted section of the southern Mid-Atlantic ridge and suggested an incompatible behavior of both elements and a higher incompatibility of Te during partial melting. This relative partitioning seems to be reversed during magmatic differentiation (Lissner et al., 2014). These observations might be partly attributed to contrasting relative partitioning of Se–Te in different sulfide phases and platinum-group minerals (e.g., Helmy et al., 2010; Liu and Brenan, 2015; Brenan, 2015; König et al., 2015) during different mantle processes. Previous evidence for Se and Te behavior in MORB petrogenesis remains ambiguous and warrants further work.

On the other hand, Se isotopes might provide new perspectives on the origin of S–Se–Te as well as other highly siderophile or volatile elements on Earth. Due to analytical difficulties (e.g., Yierpan et al. 2018), only few studies reported Se isotope composition ($\delta^{82/76}$Se; deviation of ^{82}Se/^{76}Se relative NIST SRM 3149) of mantle rocks/melts, which are limited to geological reference materials (Rouxel et al., 2002; Kurzawa et al., 2017; Yierpan et al., 2018). Compared to the chondrite average $\delta^{82/76}$Se of −0.30 ± 0.39‰ (Vollstaedt et al., 2016) and −0.21 ± 0.31‰ (2 s.d.; Labidi et al., 2018), previously analyzed basalts (n = 9) and one peridotite show heavier $\delta^{82/76}$Se with some marginal overlap. Labidi et al. (2018) reported resolvable mass-dependent Se isotope variations among main chondrite groups, ranging between −0.40 ± 0.07‰ (enstatite chondrite) and −0.01 ± 0.09‰ (CI-chondrite). Recent high-precision Se isotope analyses on a small number of different basalts show a rather restricted range in $\delta^{82/76}$Se (+0.21 ± 0.15‰, n = 4; Kurzawa et al., 2017; Yierpan et al., 2018). These rocks originate from a variety of geodynamic settings and cover a wide range of Se contents (~15–170 ng g^{-1}) and Se/Te ratios (~3–65), indicating various mantle sources and/or igneous differentiation histories (Yierpan et al., 2018). It thus remains unclear whether their $\delta^{82/76}$Se values readily represent a mantle source signature.

In this study, we present the first Se isotope compositions and new Se–Te abundances for a total of 27 fresh MORB glasses collected from the Pacific–Antarctic ridge (65–56°S and 53–41°S). Compared to the sampling areas in previous Se–Te studies (Hertogen et al., 1980; Lissner et al., 2014), these ridge sections are free of plume influence and represent melts derived from a source with first-order major element homogeneity (Vlastélic et al., 2000; Moreira et al., 2008; Hamelin et al., 2010). It is thus an ideal sample set for (1) better understanding Se–Te elemental behavior during mantle processes using recently published experimental sulfide–silicate melt partitioning data and (2) investigating effects of such processes on potential Se isotope fractionation in order to constrain the isotopic composition of the depleted mantle.

2.2 Samples and geological background

We have analyzed 27 on-axis MORB glasses from two sections of the Pacific–Antarctic ridge (PAR): 65–56°S (n = 10) and 53–41°S (n = 17) (Supplementary Fig. S2.1). These samples were collected from the PAR by the French research vessel *L'Atalante* during the cruises PACANTARCTIC 1 (65–56°S; Géli et al., 1997; Vlastélic et al., 1999) and PACANTARCTIC 2 (53–41°S; Klingelhoefer et al., 2006; Moreira et al., 2008; Hamelin et al., 2010). The PAR extends southward from the southern end of the Juan Fernandez microplate at 35°S,110°W (Francheteae et al., 1987) to the Macquarie triple junction at 62°S, 161°E (Falconer, 1972). The studied ridge sections are located to the north of the Vacquier Fracture Zone (FZ; ~53°S) and south of Udintsev FZ (~56–57°S; Supplementary Fig. S2.1), respectively, with the Eltanin FZ System in between (Watts et al., 1988; Géli et al., 1997; Castillo et al., 1998). The northern section is separated by the Menard FZ (~50°S), which is the major geological feature along the sampling area (Hamelin et al., 2010). Two ridge sections have half-spreading rates of 46–50 mm/year between 52 and 42°S (Lonsdale, 1994) and 27–37 mm/year between 65 and 55°S (Hamelin et al., 2010). The northern ridge section is one of the fastest spreading mid-ocean ridges (Moreira et al., 2008) and, therefore, shows a uniform axial high morphology along the crest (Klingelhoefer et al., 2006). In contrast, the southern section (slow to intermediate spreading ridge) displays variable axis morphologies, ranging from axial valley to axial high (Vlastélic et al., 2000; Ondréas et al., 2001). The oceanic crust beneath the PAR is estimated to be 6–7 km (Adams, 1964).

Previous analyses of He, Sr, Nd, Hf, and Pb isotopes show that the studied PAR sections are free from any plume-ridge interactions and reflect a regional-scale first-order mantle source

homogeneity (Vlastélic et al., 1999, 2000; Moreira et al., 2008; Hamelin et al., 2010, 2011). However, the ridge sections display clear latitudinal variations of radiogenic isotopes, with gradually increasing recycled crust component northwards (Hamelin et al., 2011). This is interpreted to be a subtle yet intrinsic source heterogeneity resulting from progressive mixing of a depleted MORB mantle and recycled oceanic crust. Besides, almost all PAR samples have experienced contamination by Cl-rich brines and/or hydrothermally altered crust during low-pressure magmatic differentiation, which results in significantly heavier S isotope composition if it is associated with hydrothermal sulfide assimilation (Clog et al., 2013; Labidi et al., 2014; Bezard et al., 2016).

2.3 Analytical methods

2.3.1 Selenium isotope and Se–Te elemental analyses

Most of the studied PAR basalts are in the form of fresh glass fragments. A few samples have plagioclase phenocrysts (<3 mm) and slightly altered yellowish crusts. After they were crushed, fresh chips (1–5 mm) were picked, washed with 18.2 MΩ·cm water in an ultrasonic bath and ground to fine powders. At least 2.5 g sample was used for grinding in order to preclude any potential effect of sample heterogeneity (Wang et al., 2015; Yierpan et al., 2018). One sample (PAC2 DR01-1) is represented by both glass rims and pillow interior, which were processed and analyzed separately.

All analyses were conducted at the University of Tübingen. Selenium isotope and Se–Te concentrations were determined from the same sample digest. Details of the chemistry and instrumental procedures are given in Kurzawa et al. (2017) and Yierpan et al. (2018). Briefly, Se contents of most sample unknowns were first determined via isotope dilution by estimating a spike–sample ratio of ~1 based on a general Se vs MgO or S trend previously shown for MORB (Lissner et al., 2014). For this procedure, only ~0.025 g of sample was digested and analyzed directly after separating Fe (see below; but with 2.5 mL resin and 6 N HCl). After Se content was determined, ~0.15–0.4 g of sample was mixed with ^{74}Se–^{77}Se double spike and ^{125}Te single spike to yield Se and Te spike–sample ratios of ~1 and ~0.6–1, respectively. Samples were then digested in a HF–HNO_3 mixture at 85°C and evaporated at 65°C. This is followed by heating in 6 N HCl at 130°C and complete evaporation at 85°C. In order to remove Ge while minimizing evaporative Se losses, samples were additionally dissolved and dried

down twice with 10.5 N HCl at 85°C in the presence of rock matrix. Selenium was purified by a two-stage column chemistry using 7 mL of Eichrom AG1-X8 and AG 50W-X8 (both 100–200 mesh) ion exchange resins (collected in 4 N HCl and 0.1 N HNO_3, respectively). The dry Se cuts were subsequently dissolved and evaporated in 10.5 N HCl. Tellurium was collected in 0.4 N HCl from the first column after eluting Se and most matrix elements with 4 N HCl and Fe with a 2 N HCl–5 N HF mixture. Finally, the dry Se and Te fractions were taken up in 1 mL 2 N HCl for analysis. Total procedural recoveries of Se and Te for MORBs are systematically ~85–95%, higher than that for reference materials (~80%; Yierpan et al., 2018). Procedural blanks (n = 5) yield signal intensities for each isotope indistinguishable from the background (2 N HCl), which are equivalent to ~0.05 and 0.01 ng for Se and Te, respectively.

Selenium isotopes were measured on a ThermoFisher Scientific NeptunePlus multi-collector inductively coupled plasma mass spectrometer (MC-ICP-MS) connected to a HGX-200 hydride generator. The double spike method was used to correct for isotopic fractionation during the chemistry and instrumental analysis. Each analysis was bracketed by 30 ng mL^{-1} spiked NIST SRM 3149 standard. The Se isotope composition is expressed using δ-notation relative to the international reference material NIST SRM 3149 following:

$$\delta^{82/76}Se_{Sample} = \frac{\left(^{82}Se/^{76}Se\right)_{Sample}}{\left(^{82}Se/^{76}Se\right)_{NIST\ SRM\ 3149}} - 1$$

$\delta^{82/76}$Se values are reported in ‰ units by multiplication with a factor of 1,000. In order to fully eliminate residual Ge that represents a significant isobaric interference (Stüeken et al., 2013; Pogge von Strandmann et al., 2014), post-chemistry Se fractions were additionally evaporated (1–2 times) in HCl at 85–90°C and monitored for Ge using sample aliquots before analysis (Luais, 2012; Yierpan et al., 2018). Each analyzed sample has $^{72}Ge/^{82}Se<0.0002$ (with <~10% evaporative Se loss). Hydride interferences of Se, Br, and ArAr are generally insignificant owing to the methane addition (Floor et al., 2011; Kurzawa et al., 2017) and associated corrections (mainly SeH) on $\delta^{82/76}$Se are typically ≤0.04‰. For most sample analyses, ~20–40 ng Se was used and the internal error (2 standard error, 2 s.e.) of a single measurement over 40 cycles is mostly <0.05‰. Analytical accuracy and precision were monitored by analyses of inter-laboratory standard MH-495 (30 ng mL^{-1}; Supplementary Table S2.1) and three reference materials (Table 2.1; Fig. 2.1). The MH-495 yields an average $\delta^{82/76}$Se of −3.24 ± 0.07‰ (2 s.d., n = 20), in excellent agreement with literature values (Zhu et al., 2008; Kurzawa et al., 2017; Labidi et al., 2018; Yierpan et al., 2018). The $\delta^{82/76}$Se values of BHVO-2

(+0.10 ± 0.11‰; 2 s.d., n = 4) and W-2a (0.00 ± 0.04‰; 2 s.e., n = 1) are comparable to the previously reported values of +0.18 ± 0.10‰ (2 s.d., n = 8) and −0.09 ± 0.11‰ (2 s.d., n = 6), respectively (Yierpan et al., 2018; Fig. 2.1). Two BCR-2 digestions yield $\delta^{82/76}$Se values (+0.18 ± 0.09‰ and +0.15 ± 0.07 ‰; 2 s.e.) that are identical to the average value from Kurzawa et al. (2017) (+0.18 ± 0.11‰; 2 s.d., n = 3) but somewhat lower than that from Yierpan et al. (2018) (+0.29 ± 0.10‰; 2 s.d., n = 5; Fig. 2.1). BCR-2 yields an overall average $\delta^{82/76}$Se of +0.23 ± 0.14‰ (2 s.d., n = 10), whose uncertainty is slightly higher than a typical external reproducibility of 0.10 to 0.12‰ (2 s.d.) on other reference materials (Fig. 2.1; Yierpan et al., 2018). Note that all these analyses were performed in the same lab (Fig. 2.1). Considering potentially smaller sample heterogeneity in a glass matrix relevant to this study, the external reproducibility for MORB was assessed by replicate analyses of a randomly selected moderately evolved sample (PAC2 DR33-1; 6.63 wt.% MgO) with different sample amounts (0.15–0.4 g; Table 2.1). We obtain a 2 s.d. uncertainty of 0.09‰ from 7 digestions and 9 measurements (4 different sessions over 6 months).

Table 2.1 Selenium isotope composition and Se–Te abundances of geological reference materials and a randomly selected PAR MORB glass reported in this study and literature.

Sample	Weight (g)	$\delta^{82/76}$Se (‰)	2 s.e.[a] (‰)	Se[b] (ng g^{-1})	Te (ng g^{-1})
BHVO-2	0.193	0.13	0.07	164	14.4
	0.201	0.15	0.05	168	14.2
	0.238	0.04	0.08	164	14.0
	0.400	0.06	0.08	165	14.3
Average		0.10 ± 0.11		165 ± 2	14.2 ± 0.2
Rouxel et al. (2002)[c]		0.32 ± 0.32 (n = 1)		74 (n = 1)	
Wang et al. (2015)				170 ± 22 (n = 3)	14.4 ± 0.3 (n = 3)
Yierpan et al. (2018)		0.18 ± 0.10 (n = 8)		169 ± 3 (n = 61)	14.2 ± 0.3 (n = 24)
BCR-2	0.406	0.18	0.09	78	2.65
	0.450	0.15	0.07	79	2.54
Rouxel et al. (2002)[c]		0.24 ± 0.32 (n = 1)		90 (n = 1)	
Lissner et al. (2014)				78 ± 3 (n = 5)	2.73 ± 0.06 (n = 5)
Kurzawa et al. (2017)		0.18 ± 0.11 (n = 3)		71 ± 4 (n = 3)	
Yierpan et al. (2018)		0.29 ± 0.10 (n = 5)		76 ± 1 (n = 18)	2.54 ± 0.08 (n = 5)
W-2a	0.454	0.00	0.04	105	1.78
Yierpan et al. (2018)		−0.09 ± 0.11 (n = 6)		107 ± 1 (n = 8)	1.71 ± 0.07 (n = 6)
PAC2 DR33-1	0.150	−0.16	0.03	201	2.14
	0.210 (a)[d]	−0.10	0.04	198	2.20
	0.210 (b)[d]	−0.11	0.07	198	
	0.232	−0.16	0.03	198	2.18
	0.238	−0.19	0.04	198	
	0.241	−0.18	0.03	197	2.23
	0.255	−0.22	0.03	199	2.27
	0.402 (a)[d]	−0.12	0.04	201	2.17
	0.402 (b)[d]	−0.10	0.05	201	
Average		−0.15 ± 0.09		199 ± 2	2.20 ± 0.05

Note: Uncertainties are 2 s.d. for $\delta^{82/76}$Se and 1 s.d. for Se–Te concentrations; numbers in parentheses denote different sample digestions; $\delta^{82/76}$Se data from Rouxel et al. (2002) are converted relative to NIST SRM 3149 (Carignan and Wen, 2007) considering error propagation (analytical and conversion errors); quoted uncertainties on $\delta^{82/76}$Se are conservatively represented by either the external reproducibility of the sample $\delta^{82/76}$Se or analytical precision as reported in the literature, whichever is larger.

[a] Internal uncertainty of each individual measurement (over 40 cycles) given in 2 standard error (2 s.e.).

[b] Selenium concentrations listed here were obtained by double spike inversion.

[c] Rouxel et al. (2002) analyzed BHVO-1 and BCR-1.

[d] Replicate analyses of the final sample solutions from the same digestion.

The isotope dilution concentrations for Te (and when necessary, also for Se; Table 2.2) were determined on a ThermoFisher Scientific iCAP-Qc quadrupole ICP-MS connected to an ESI hydrideICP hydride generator. Only ~0.1–0.3 ng Te and 0.5–1 ng Se (in 1 mL 2 N HCl) were used for each analysis. The analytical precision of our method was previously reported to be ~2–3% r.s.d. (relative standard deviation) for both Se and Te. All reference materials yield Se–Te concentrations that are in general agreement with the recently published data (Table 2.1; Lissner et al., 2014; Wang et al., 2015; Yierpan et al., 2018). The Se concentrations of MORBs obtained by double spike inversion and isotope dilution are always comparable within 2% and both reproduce at ~2% r.s.d. (Tables 2.1 and 2.2).

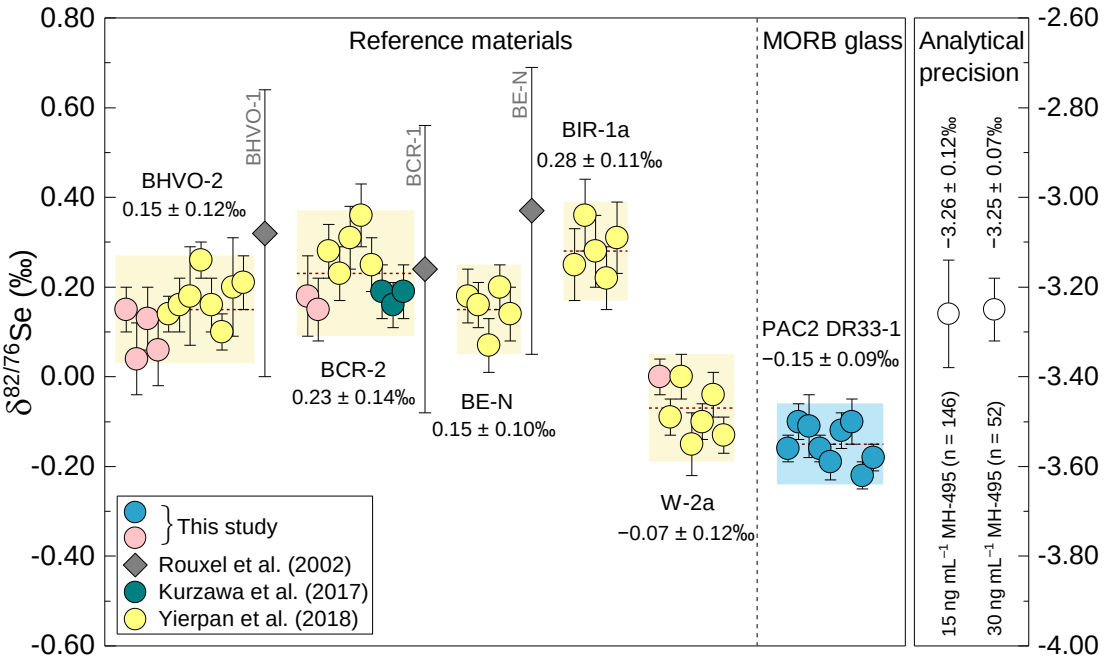

Fig. 2.1 Measurements of geological reference materials and a randomly selected moderately evolved PAR glass (PAC2 DR33-1; 6.63 wt.% MgO; Table 2.1) for assessing the external reproducibility (2 s.d.) on the sample $\delta^{82/76}$Se (left panel). Each symbol represents an individual measurement with the associated internal precision (2 s.e.; over 40 cycles). All sample digests were analyzed once, except for two MORB glass digestions that were aliquoted and analyzed twice. Our analytical accuracy and precision is evaluated by the long-term reproducibility of inter-

laboratory standard MH-495 (open circles; right panel), which yields −3.26 ± 0.12‰ and −3.25 ± 0.07‰ (2 s.d.) for 15 and 30 ng mL^{-1} solutions, respectively (Supplementary Table S2.1; this study; Kurzawa et al., 2017; Yierpan et al., 2018). Shown for comparison are literature data on reference materials reported by Kurzawa et al. (2017), Yierpan et al. (2018) (measurements in both studies were performed over the course of ~18 months at the University of Tübingen; all circles), and Rouxel et al. (2002) (diamonds). Interlaboratory comparison of $\delta^{82/76}$Se data on silicate samples remains difficult due to the limited Se isotope studies, and therefore BHVO-2 and BCR-2 are compared here with BHVO-1 and BCR-1 (only BE-N has been analyzed by two working groups). $\delta^{82/76}$Se from Rouxel et al. (2002) that were originally reported relative to MERCK standard are converted relative to NIST SRM 3149 following Carignan and Wen (2007) considering error propagation (analytical and conversion errors of 0.25‰ and 0.20‰, respectively).

2.3.2 Trace element analysis

Only a few trace element data have been published for the PAC1 samples (latitude 65–56°S), whereas the data for PAC2 samples (latitude 53–41°S) are relatively complete (Supplementary Table S2.2; Vlastélic et al., 2000; Hamelin et al., 2010; Clog et al., 2013; Labidi et al., 2014; Bezard et al., 2016). To fully characterize the samples, we report a more complete set of trace element data (43 elements). The measurements were performed at the University of Tübingen by solution ICP-MS following the method previously described by Babechuk et al. (2010) and Albut et al. (2018). About 0.02 g of sample powder was digested and diluted with 2% HNO_3 containing an internal standard solution (^{6}Li, In, Re, and Bi) to the analyte solution with a final dilution factor of ~10,000. Reproducibility and accuracy of trace element determinations were evaluated from the average data of BHVO-2 (quality control standard) from 14 analyses of 6 separate digestions (4 digested together with the PAR samples). Our BHVO-2 results (Supplementary Table S2.3) show uncertainties better than ~5% r.s.d. for all elements except for Mo, Sb, W, and Tl (~8–20%). Most data agree within ~5% with previously reported values (GeoReM; Jochum et al., 2005).

2.4 Results

2.4.1 Major/trace element composition

The trace element concentrations determined here, together with all available major/trace element, radiogenic/stable isotope data, are compiled in Supplementary Table S2.2. All samples are typical N-MORB (normal MORB) with $(La/Sm)_N$ ratios of 0.461–0.965 (normalized to PM;

McDonough and Sun, 1995), except PAC2 DR27-1 ($(La/Sm)_N$ = 1.227), which is the most evolved sample (4.52 wt.% MgO) and dredged from a seamount-ridge transition zone (Hamelin et al., 2010). The PM-normalized trace element patterns of PAR glasses are similar to that of the average N-MORB compiled by Gale et al. (2013) (Supplementary Fig. S2.2). Variations in major element compositions of the studied samples span the entire spectrum observed in PAR basalts from 65–56°S and 53–41°S, with MgO content from 8.85 to 4.52 wt.% (Supplementary Fig. S2.3). This MgO range is larger than that of MORBs previously investigated for Se–Te systematics (7.02–9.23 wt.%; Hertogen et al., 1980; Lissner et al., 2014). The most evolved glasses (MgO <5 wt.%; n = 3) have experienced titanomagnetite fractionation, evidenced by a decrease in Ti and Fe from the general trend after 5 wt.% MgO (Supplementary Fig. S2.3; Vlastélic et al., 2000; Hamelin et al., 2010). Similar abrupt drops are also consistently observed for concentrations of Zn, Ga, Mn (not shown), V, Sc, and Co in these evolved samples (e.g., Supplementary Fig. S2.2), probably resulted from the magnetite saturation and/or the induced sulfide segregation due to their strong partitioning into these phases (Nielsen et al., 1994; Toplis and Corgne, 2002; Righter et al., 2006; Dare et al., 2012, 2014; Labidi et al., 2014; Jenner et al., 2010, 2012, 2015).

Table 2.2 Selenium isotope composition, S–Se–Te abundances, and selected major element composition of the studied PAR glasses.

Sample	$\delta^{82/76}$Se (‰)	2 s.e.[a] (‰)	n[b]	Se (ng g^{-1})	s.d.[c] (ng g^{-1})	n[d]	Te (ng g^{-1})	s.d.[c] (ng g^{-1})	Se/Te	s.d.	S (µg g^{-1})	MgO (wt. %)	FeO_T (wt. %)
PAC1 CV02-g	−0.23	0.05	1	180	4	2	1.99	0.06	90	3	1171	7.74	10.5
PAC1 CV03-g	−0.19	0.05	1	158	1	3	3.19	0.10	50	2	938	8.57	8.60
PAC1 CV04-g	−0.15	0.04	1	176	4	1	4.10	0.12	43	2	940	8.78	8.55
PAC1 DR05-1g	−0.22	0.04	1	167	3	1	3.06	0.09	55	2	932	8.33	8.42
PAC1 DR06-g	−0.30	0.05	1	177	2	3	1.61	0.05	110	4	1351	6.93	11.2
PAC1 DR07-1g	−0.06	0.05	1	186	4	2	2.23	0.07	83	3	1301	6.83	10.7
PAC1DR10-1g	−0.24	0.08	1	170	3	3	2.68	0.08	63	2	1047	4.83	10.8
PAC1 DR11-1g	−0.10	0.05	1	174	3	1	3.06	0.09	57	2	1153	7.33	9.25
PAC1 DR12-1g	−0.15	0.04	1	165	3	2	3.70	0.11	45	2	968	8.85	8.49
PAC1 DR13-2g	−0.21	0.05	2	194	2	5	1.95	0.06	99	3	1259	7.42	11.0
PAC2 DR01-1 glass	−0.13	0.04	1	166	3	1	2.52	0.08	66	2	1116	7.30	9.67
PAC2 DR01-1 basalt	−0.18	0.05	1	167	3	1	2.39	0.07	70	2			
PAC2 DR04-2	−0.09	0.03	1	168	3	1	2.33	0.07	72	3	1199	7.08	10.5
PAC2 DR05-2g	−0.06	0.04	2	176	4	2	1.43	0.04	123	4	1339	6.52	12.1
PAC2 DR08-1	−0.15	0.04	1	194	4	1	2.76	0.08	70	2	1239	7.05	11.4
PAC2 DR20-1	−0.15	0.06	2	193	4	2	1.68	0.05	115	4	1550	4.60	12.8
PAC2 DR21-2	−0.17	0.04	2	198	4	2	1.97	0.06	101	4	1312	6.73	11.3
PAC2 DR22-1	−0.22	0.02	1	187	4	1	2.47	0.07	76	3	1172	7.25	10.5

Sample	$\delta^{82/76}$Se (‰)	2 s.e.[a] (‰)	n[b]	Se (ng g^{-1})	s.d.[c] (ng g^{-1})	n[d]	Te (ng g^{-1})	s.d.[c] (ng g^{-1})	Se/Te	s.d.	S (µg g^{-1})	MgO (wt. %)	FeO_T (wt. %)
PAC2 DR27-1	−0.14	0.04	2	219	4	2	1.16	0.03	189	6	1755	4.52	14.1
PAC2 DR28-2	−0.15	0.05	2	174	3	2	3.32	0.10	52	2	1112	7.85	10.0
PAC2 DR29-1	−0.05	0.07	1	210	4	2	2.07	0.06	101	4	1471	6.16	12.4
PAC2 DR30-1	−0.12	0.07	2	195	1	4	2.21	0.07	88	3	1348	7.00	11.2
PAC2 DR31-3	−0.09	0.07	2	193	4	2	3.17	0.10	61	2	1208	7.55	10.5
PAC2 DR32-1	−0.10	0.07	1	186	4	1	1.97	0.06	94	4	1321	6.80	11.3
PAC2 DR33-1	−0.15	0.08	7	199	1	9	2.20	0.05	90	2	1340	6.63	11.5
PAC2 DR34-1	−0.30	0.05	1	168	1	3	2.63	0.08	64	2	1094	8.00	9.39
PAC2 DR36-1	−0.13	0.08	2	194	1	5	2.26	0.07	86	3	1381	7.07	11.3
PAC2 DR38-1	−0.16	0.05	2	180	1	4	3.12	0.09	58	2	1244	8.35	9.72

Note: S data from Labidi et al. (2014); MgO and FeO_T (total Fe expressed as FeO) data from Vlastélic et al. (2000) and Hamelin et al. (2010).

[a] For replicate digestions, the highest 2 s.e. is reported.

[b] Number of digestions for combined Se isotope and Te concentration analyses.

[c] Uncertainties are 1 s.d. of the mean for n≥3 and conservatively estimated using the long-term external reproducibility of ~3% (Yierpan et al., 2018) for n<3.

[d] Total number of Se concentration determinations by double spike inversion and isotope dilution.

2.4.2 Selenium isotope composition and Se–Te abundances

The selenium isotope composition and Se–Te concentrations of the studied PAR samples are reported in Table 2.2 together with S (Labidi et al., 2014) and selected major element data. The uncertainties on $\delta^{82/76}$Se and Se–Te abundances throughout the text are given in 2 and 1 s.d., respectively. The PAR glasses display $\delta^{82/76}$Se values ranging between −0.30 ± 0.09‰ and −0.05 ± 0.09‰, with an average of $\delta^{82/76}$Se = −0.16 ± 0.13‰ (n = 27; Fig. 2.2 and Fig. 2.3). The differences in $\delta^{82/76}$Se between sample duplicates (n = 12) never exceeded the 2 s.d. external reproducibility of 0.09‰ (Table 2.1). The glassy rim and pillow interior of PAC2 DR01-1 that were analyzed separately yield identical $\delta^{82/76}$Se values within uncertainty (−0.13 ± 0.09‰ and −0.18 ± 0.09‰, respectively; Table 2.2). However, small but resolvable isotopic variations (up to 0.25 ± 0.13‰ in $\delta^{82/76}$Se) are observed between different samples (e.g., between PAC1 DR06-g and PAC2 DR29-1, with $\delta^{82/76}$Se of −0.30 ± 0.09‰ and −0.05 ± 0.09‰, respectively). These variations are not systematically related to the sample latitude or ridge axial depth (Fig. 2.2a and b). The average $\delta^{82/76}$Se of the two PAR sections (Fig. 2.2a) are identical within uncertainty: −0.14 ± 0.12‰ north of the Vacquier FZ (n = 17) and −0.19 ± 0.14‰ south of the Udintsev FZ (n = 10). $\delta^{82/76}$Se values of the samples are fairly constant over the wide range of Se abundances observed (158–219 ng g^{-1}; Fig. 2.2c).

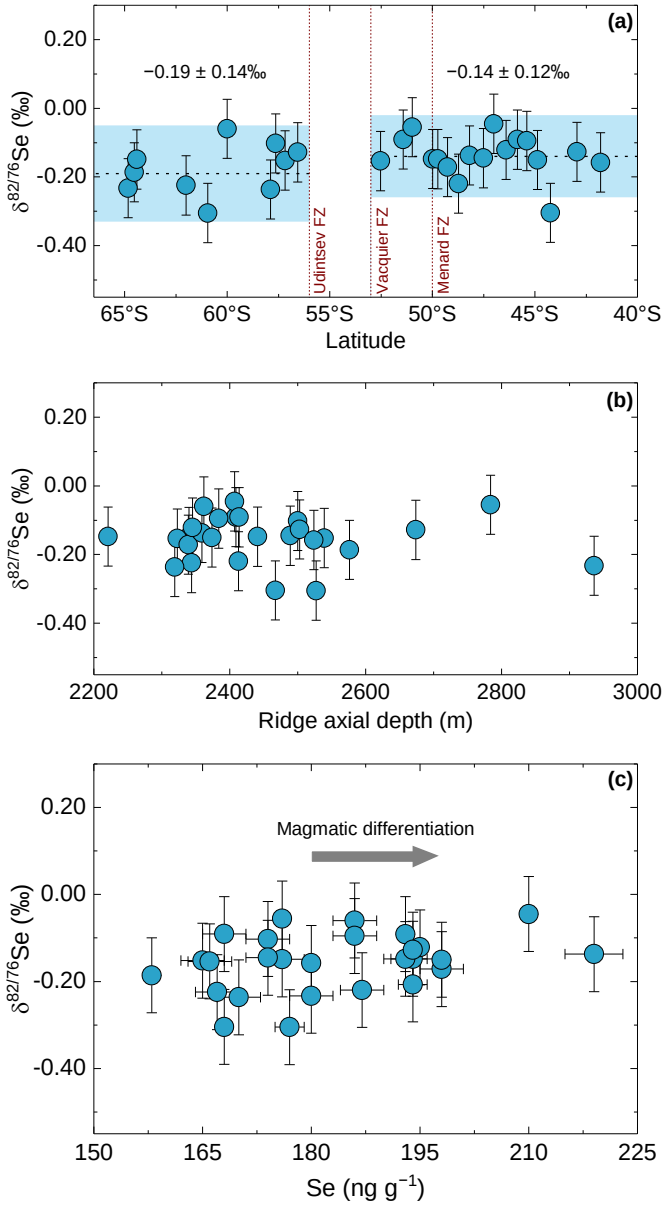

Fig. 2.2 Variation of Se isotope composition of PAR glasses with (a) sample latitude, (b) dredging depth, and (c) Se abundance. Two ridge sections (north of the Vacquier FZ and south of the Udintsev FZ) display identical average $\delta^{82/76}$Se values within uncertainty (a).

The MORBs show systematic offset towards lighter Se isotope composition compared to all previously analyzed basalts (average $\delta^{82/76}$Se between +0.21 ± 0.15‰ and +0.30 ± 0.32‰; n = 9) and one peridotite (+0.24 ± 0.32‰), with some marginal overlap with the latter (Fig. 2.3; Rouxel et al., 2002, 2004; Kurzawa et al., 2017; Yierpan et al., 2018; this study). The MORB average $\delta^{82/76}$Se (−0.16 ± 0.13‰) lies in the range of chondritic values of −0.30 ± 0.39‰ (n = 14; Vollstaedt et al., 2016) and −0.21 ± 0.31‰ (n = 20; Labidi et al., 2018) (Fig. 2.3). Specifically, it is similar within uncertainty to $\delta^{82/76}$Se values of ordinary chondrites (−0.21 ± 0.10‰; n = 9) and CO (−0.19 ± 0.07‰; n = 2), CV (−0.25 ± 0.12‰; n = 2), and CI (−0.01 ± 0.09‰; n = 2) carbonaceous chondrites, but distinct from that of enstatite chondrites (−0.40 ± 0.07‰; n = 3; Labidi et al., 2018; Fig. 2.3).

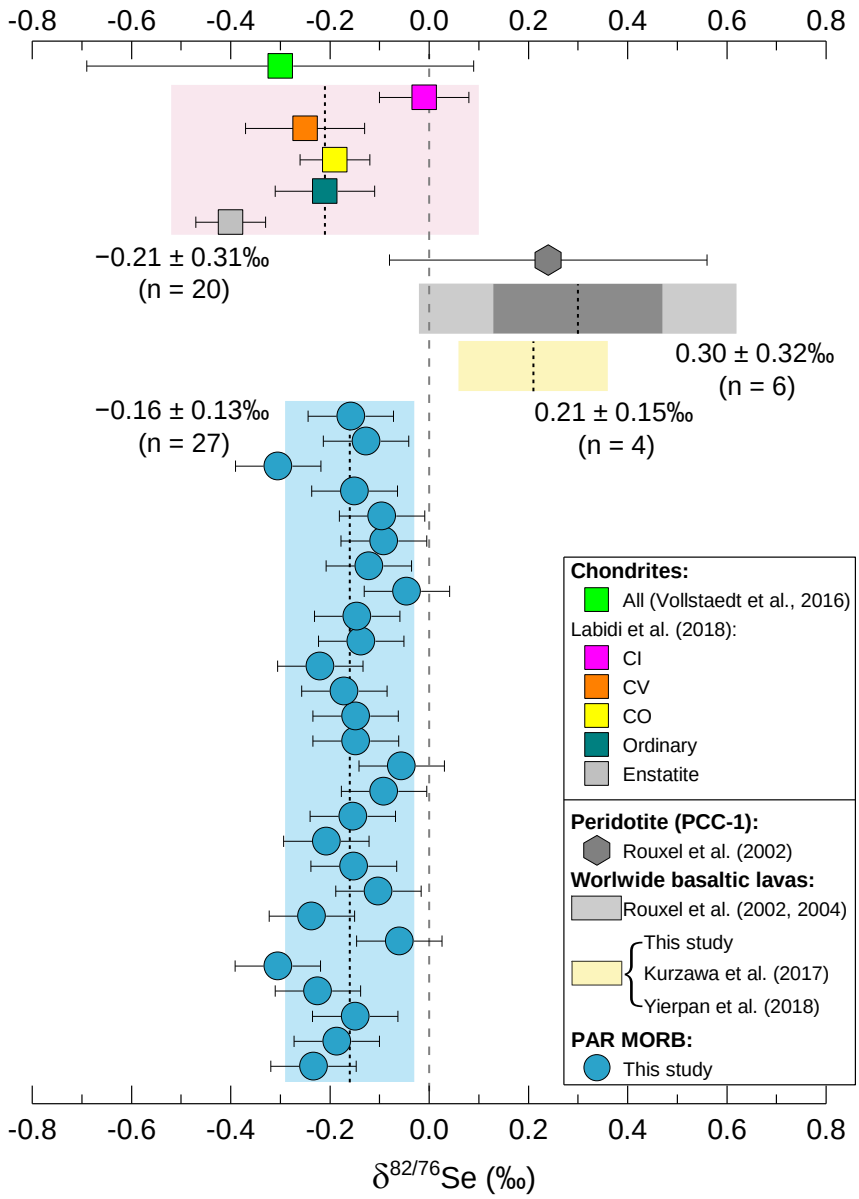

Fig. 2.3 Compilation of Se isotope compositions of PAR MORBs, terrestrial rock standards (7 basalts and 1 peridotite; Rouxel et al., 2002; Kurzawa et al., 2017; Yierpan et al., 2018; this study), basalts from a lava lake near the Lucky Strike hydrothermal field (n = 2; Rouxel et al., 2004), and main chondrite classes (Vollstaedt et al., 2016; Labidi et al., 2018). See Fig. 2.1 and Yierpan et al. (2018) for details on the measured basaltic rock standards. The peridotite analyzed by Rouxel et al. (2002) is a partially serpentinized harzburgite (PCC-1; Jain et al., 2000). Each shaded field represents the average $\delta^{82/76}$Se (black dashed line) with 2 s.d. uncertainties of chondrite and terrestrial rocks. Grey dashed line denotes $\delta^{82/76}$Se = 0‰. The overall chondrite average $\delta^{82/76}$Se from Labidi et al. (2018) includes all chondrite groups analyzed (enstatite, ordinary, and carbonaceous) except three weathered CV chondrites. The data from Rouxel et al. (2002, 2004) is converted relative to NIST SRM 3149 following the approach of Carignan and Wen (2007) while considering error propagation (analytical and conversion uncertainties); the light and dark grey fields represent the uncertainties of the mean with (0.32‰) and without (0.17‰) error prorogation, respectively.

Fig. 2.4 presents the variation of Se, Te, S, and Cu abundances and/or their ratios versus MgO contents of PAR basalts. The generally negative correlation of Se (from 158 ± 1 to 219 ± 4 ng g^{-1}) and positive correlations Te (from 4.10 ± 0.12 to 1.16 ± 0.03 ng g^{-1}) with MgO show their apparently contrasting compatibilities (Fig. 2.4a and b), which result in significant Se/Te fractionation (increasing from 42.9 ± 1.1 to 188.8 ± 4.7 with decreasing MgO content; Fig. 2.4c). Selenium in PAR MORBs seems to behave as an apparently incompatible element, opposite to observations from the southern Mid-Atlantic ridge (SMAR) basalts (Lissner et al., 2014). At a given MgO, PAR MORBs tend to have higher Se content than SMAR N-MORBs (Fig. 2.4a). Two samples from the Indian ocean have anomalously high Se contents (~330 ng g^{-1}) compared to the range in PAR and SMAR, but these samples have probably been affected by assimilation of wall-rock sulfide cumulates (Fig. 2.4a; Hertogen et al., 1980). Tellurium displays similarly apparent compatibility in a global context (Fig. 2.4b; Hertogen et al., 1980; Yi et al., 2000; Lissner et al., 2014). It is noteworthy, however, that Te contents in SMAR E-MORBs (i.e., enriched- and transitional-type MORBs) are generally higher than in N-MORBs, attributed to Te enrichment (relative to Se) in an E-MORB mantle source (Lissner et al., 2014). This is in agreement with the distinctly lower Se/Te and S/Te ratios of E-MORBs compared to N-MORBs over almost the entire melt evolution in both PAR and SMAR (Fig. 2.4c and e). Besides, the S/Se variations in these settings (Fig. 2.4d) appear to follow two distinct trends, with Se being more compatible relative to S in the SMAR melts than in PAR melts. The Cu/Se ratios in both PAR and SMAR for MgO contents above ~7–7.5 wt.% remain fairly constant and identical (418 ± 24 and 408 ± 22, respectively; Fig. 2.4f). The constant Cu/Se ratios were previously interpreted to reflect a similar geochemical behavior of these elements based on a relatively small data set (MgO ~7–9 wt.%; Lissner et al., 2014). Below ~7 wt.% MgO, the Cu/Se ratios of PAR basalts smoothly decrease from 346 to 178, indicating an overall higher compatibility of Cu.

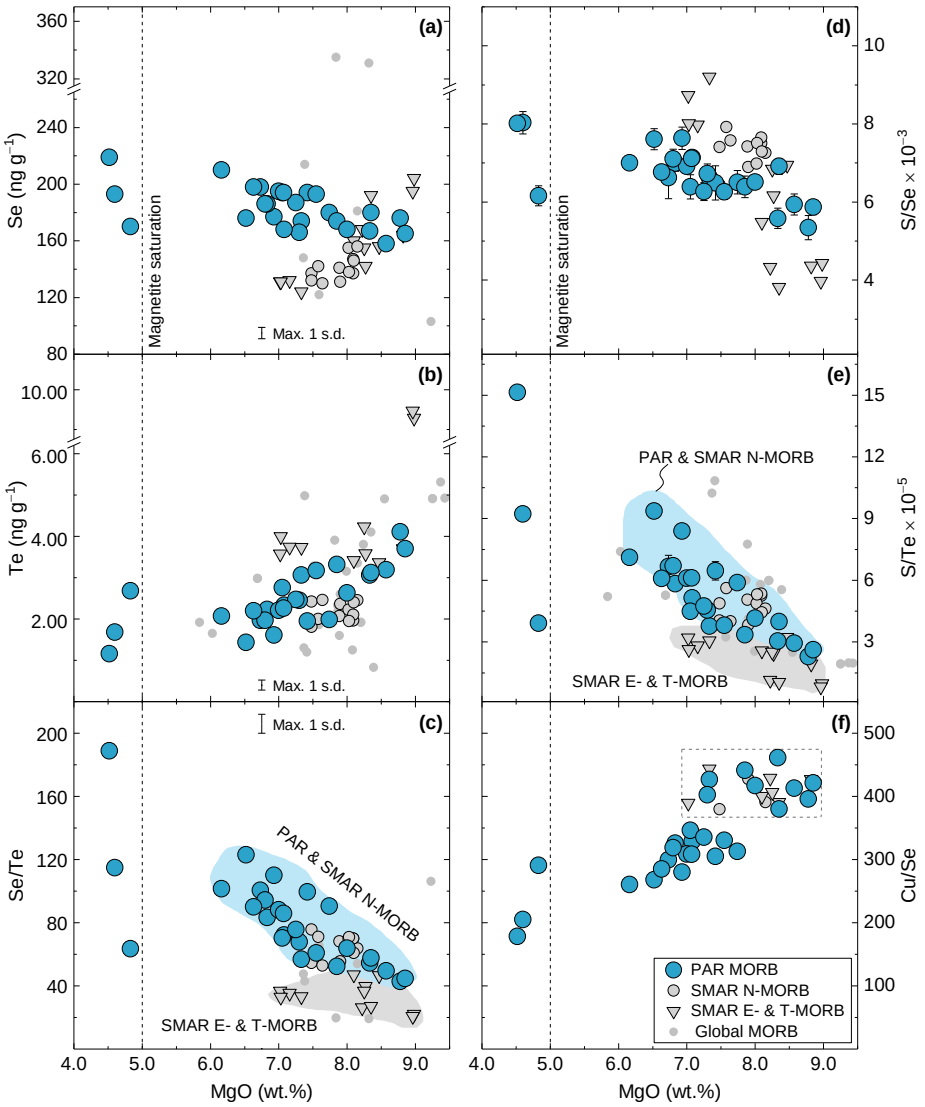

Fig. 2.4 Variations of Se, Te, S, and Cu abundances and/or their ratios with MgO content. Also shown for comparison are SMAR N- and E-MORBs (Lissner et al., 2014; E-MORB refers to all enriched- and transitional-type MORBs), as well as global MORBs from Hertogen et al. (1980) and Yi et al. (2000). The SMAR E-MORBs display distinctly lower Se/Te and S/Te ratios than that of N-MORBs from both PAR and SMAR over almost the entire magmatic differentiation (c and e), reflecting the Te-enrichment in E-MORB mantle source (Lissner et al., 2014). The Cu/Se ratio (f) in PAR and SMAR remains fairly constant and remarkably similar prior to ~7–7.5 wt.% MgO and PAR samples show a smooth decrease afterwards. The change of relative compatibility of Cu–Se may be related to the FeO content of the silicate melt as noted by Brenan (2015). The vertical dashed lines represent the onset of magnetite saturation (5 wt.% MgO) and associated sulfide segregation. Prior to this, the observed apparent compatibilities of these chalcophile elements (Te>Cu>Se>S) in the PAR suite indicate that they are predominantly controlled by fractionation of sulfide liquid, consistent with previous studies. At magnetite saturation, except the most evolved sample (PAC2 DR27-1) whose S solubility remains largely unaffected (Labidi et al., 2014), other two samples show consistent decrease in Se (a) and increase in Te (b) from the general trend (note the consistent decreases in FeO_T and TiO_2; Supplementary Fig. S2.3). The strong abrupt decrease in their Se/Te and S/Te ratios (c and e) is argued here as an indicator of the predominant appearance of crystalline MSS in the segregating sulfide assemblage from the MORB melt (see the text for details).

2.5 Discussion

2.5.1 Effects of non-magmatic processes on Se isotopes and S–Se–Te abundances

Non-magmatic processes that may potentially affect the S–Se–Te systematics of MORB melts generally include eruption-related degassing and assimilation of hydrothermal fluids during and/or after MORB differentiation in crustal magma chambers (Jenner et al., 2010; Floor and Román-Ross, 2012; Labidi et al., 2014; Lissner et al., 2014). All the studied PAR glasses are sulfide saturated as evidenced by the systematically observed immiscible sulfide droplets and the correlation between S and FeO contents (Labidi et al., 2014). The latter, together with the lack of correlation between S content and eruption depth (~2220–2950 m; Supplementary Table S2.2), also argues against eruptive S degassing (Moore and Fabbi, 1971; Moore and Schilling, 1973; Mathez, 1976; Wallace and Edmonds, 2011; Labidi et al., 2014). Little is known about the Se–Te gaseous species and their formation conditions in igneous systems. Similar to S, Se and Te are possibly dissolved in a silicate melt as Se^{2-} and Te^{2-} and/or Se^{4+} and Te^{4+} depending on the prevailing oxygen fugacity (e.g., Nagamori and Mackey, 1977; Fang and Lynch, 1987; Choi and Cho, 1997; Wykes et al., 2011). In the case of (PAR) MORB, S occurs almost exclusively as reduced S^{2-} and retained in the glass during submarine quenching (Labidi et al., 2014). Since transition of selenide and telluride to oxyanions requires higher redox potential relative to sulfide (Se>Te>S at a given temperature and pH; Yamamoto 1976; Brookins, 1988; McPhail, 1995; Johnson, 2004; König et al., 2019), we suggest that Se and Te are dissolved in MORB melts in the form of Se^{2-} and Te^{2-} and are (also) unlikely to degas during submarine eruption (also see Yi et al., 2000; Jenner et al., 2010; Lissner et al., 2014). This would be in accordance with the lack of a systematic variation of Se isotopes (Fig. 2.2b) and Se–Te contents (not shown) with the ridge axial depth (>2220 m).

The majority of PAR basalts have experienced interaction with chlorine-rich brines and/or hydrothermally altered materials during magmatic differentiation (Clog et al., 2013; Labidi et al., 2014). We have examined the potential effect of hydrothermal fluid contamination on Se isotopes and Se–Te concentrations using Cl/K ratio as an indicator of the extent of chlorine contamination because Cl and K are not fractionated during magmatic processes (Fig. 2.5; Michael and Cornell, 1998; Clog et al., 2013; Labidi et al., 2014). Previous studies on PAR samples show that this process did not significantly affect D/H ratios and stable Mo isotope

compositions (Clog et al., 2013; Bezard et al., 2016), but systematically shifted the S isotope compositions towards heavier values (>−0.5‰ in $\delta^{34}S_{V\text{-}CDT}$) when the chlorine contamination was associated with high-temperature (>300°C) hydrothermal sulfide assimilation (Fig. 2.5a; Labidi et al., 2014). Volcanogenic massive sulfides from sediment-starved environments (such as hydrothermal systems at mid-ocean ridges) show highly variable and mostly negative $\delta^{82/76}Se$ values from −4.75‰ to +0.7‰ (Rouxel et al., 2002, 2004; Layton-Matthews et al., 2013). However, we do not observe any systematic deviations in $\delta^{82/76}Se$ values of the samples that

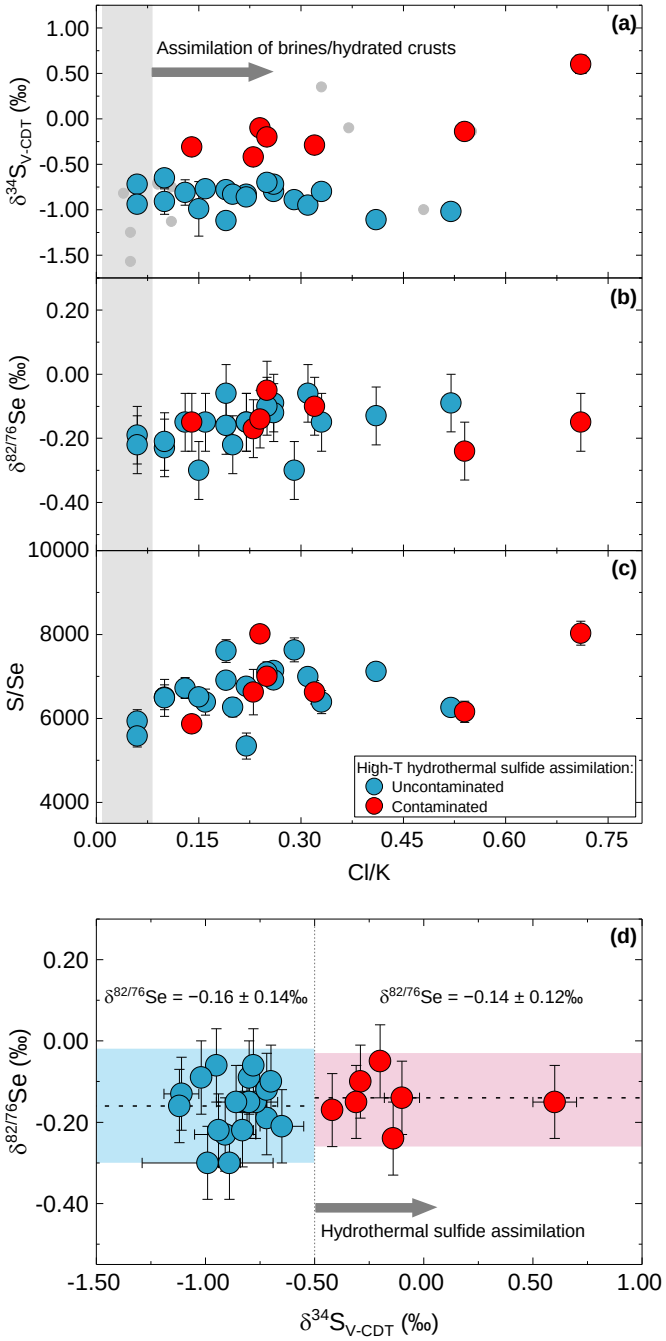

Fig. 2.5 Variations of $\delta^{34}S_{V\text{-}CDT}$ (a), $\delta^{82/76}Se$ (b) and S/Se ratios (c) with Cl/K that is used as a proxy for the extent of Cl contamination due to the interaction of the magma with brines and hydrothermally altered materials during magmatic differentiation (Michael and Cornell, 1998; Clog et al., 2013; Labidi et al., 2014). Note that Cl/K The grey shaded field represents the Cl/K ratio (0.01–0.08) of global MORBs that are unaffected by hydrothermal fluid assimilation (Michael and Cornell, 1998). The studied PAR basalts that have experienced high-T hydrothermal sulfide assimilation based on S isotope systematics (Labidi et al., 2014) are shown in red. Other PAR glass data (Labidi et al., 2014) are shown in grey circles (a). (d) shows the variation of $\delta^{82/76}Se$ with $\delta^{34}S_{V\text{-}CDT}$. Two shaded fields in (d) represent the average $\delta^{82/76}Se$ of two subsets of samples with and without assimilating hydrothermal sulfides.

show variable S assimilation (i.e., $\delta^{34}S_{V\text{-}CDT}$ heavier than −0.5‰; n = 7) from the general variation trend along Cl/K or $\delta^{34}S_{V\text{-}CDT}$ (Fig. 2.5b and d). The sample PAC2 DR20-1 with the highest $\delta^{34}S_{V\text{-}CDT}$ value of +0.60 ± 0.10‰ (1 s.d.; Supplementary Table S2.2), which represents the highest amount of S assimilation, shows "typical" $\delta^{82/76}Se$ of −0.15 ± 0.09‰ (Table 2.2; Fig. 2.5d). Average $\delta^{82/76}Se$ values of the two sample subsets (i.e., with and without sulfide assimilation) are identical within 2 s.d. uncertainty (−0.14 ± 0.12‰ and −0.16 ± 0.14‰, respectively). Also, there is no clear covariation between the Se isotope composition and degree of Cl contamination (Fig. 2.5b).

On the other hand, there seems to be an apparent increase in S/Se ratio with Cl/K from 0.06 to 0.41 (Fig. 2.5c). Highest S/Se ratios (~8,000) are also observed in two samples (PAC2 DR20-1 and PAC2 DR27-1) that have experienced S assimilation (Fig. 2.4d and 2.5c). Compared to MORBs (~3,800–9,200; Fig. 2.4d; Lissner et al., 2014; this study) and magmatic sulfides (~2,700–8,700; Patten et al., 2013, 2016), massive sulfides from sediment-starved hydrothermal systems have much more variable S/Se ratios (500–500,000), with lower values typical for sulfides near mid-ocean ridges due to the formation of selenide or Se-rich sulfides at high temperature conditions (Rouxel et al., 2004; Hannington et al., 2002; Layton-Matthews et al., 2008, 2013; Keith et al., 2016). Sulfur assimilation would not increase S abundance (hence S/Se ratio) of the melt due to sulfide saturation (Labidi et al., 2014; also see Section 2.5.2.2), but it may potentially increase the Se abundance because a MORB melt with ~8–14 wt.% FeO can dissolve ~0.15–0.25 wt.% Se (Wykes et al., 2015). Labidi et al. (2014) show that the highest $\delta^{34}S_{V\text{-}CDT}$ value (+0.60 ± 0.10‰; 1 s.d.) can be reproduced by mixing a MORB melt having 1,000 μg g^{-1} S and $\delta^{34}S_{V\text{-}CDT}$ = −1‰ with a maximum of 3.5 wt.% wall-rock having 10,000 μg g^{-1} S and $\delta^{34}S_{V\text{-}CDT}$ = +5‰. Assuming that the original melt has ~168 ng g^{-1} Se (at 1,000 μg g^{-1} S; from the general S–Se covariation), a final melt with the lowest S/Se = 5,867 ($\delta^{34}S_{V\text{-}CDT}$ = −0.31‰) observed in the contaminated samples (Fig. 2.5a and c) would require only ~3 ng g^{-1} increase in Se concentration to be associated with an assimilation of ~1.35 wt.% wall-rock. Note that a typical uncertainty of MORB Se concentration is also ~3 ng g^{-1} (Table 2.2). Therefore, we argue that the observed variation in S/Se ratios of PAR basalts (Fig. 2.5c) are not influenced by high-temperature hydrothermal sulfide assimilation but rather reflects magmatic differentiation (Fig. 2.4d; see below). Note that Cl contamination broadly scales with the degree of magmatic differentiation (Labidi et al., 2014), which readily accounts for the seemingly increasing S/Se with increasing Cl/K (Fig. 2.5c). The same conclusion may be reached for S/Te ratios (not shown) and hence the observed Te abundances. Lastly, alteration by seawater after

the eruption (e.g., Lissner et al., 2014) or during magmatic differentiation are not likely to influence the Se isotope or Se–Te elemental systematics of MORBs because of extremely low Se and Te concentrations in modern seawater at relevant depths (~200 and ~0.2 ng kg^{-1}, respectively; Cutter and Bruland, 1984; Cutter and Cutter, 2001; Lee and Edmond, 1985; Measures and Burton, 1980).

2.5.2 Se–Te elemental systematics during MORB differentiation

As chalcophile elements, Se and Te, together with S and Cu, are sensitive to progressive MORB differentiation involving a concurrent precipitation of immiscible sulfides (Fig. 2.4). This process accounts for the observed abundances and relative fractionation of Se–Te–S–Cu (Fig. 2.4) because these elements are all highly incompatible in silicate minerals but show different partitioning into sulfides (Barnes et al., 2009; Patten et al., 2013; Labidi et al., 2014; König et al., 2015; Brenan, 2015; Wang and Becker, 2015a; Kiseeva et al., 2017). Our data shows a relative compatibility into sulfides (prior to magnetite saturation; see below) in the order of Te>Cu>Se>S (Fig. 2.4; Cu/Te ratio increases with decreasing MgO; not shown), consistent with earlier studies. The difference in the relative compatibility of Se and Cu above and below ~7 wt.% MgO (see Section 2.4.2 and Fig. 2.4f) may be attributed to different FeO content of the silicate melt (Brenan, 2015).

All these elements are affected by magnetite saturation-triggered sulfide segregation after ~5 wt.% MgO (Fig. 2.4; also see Section 2.4.1), as previously observed for S in PAR MORB (Fig. 2.6a; Labidi et al., 2014) and other chalcophile elements in glasses from worldwide arc settings (Jenner et al., 2010, 2012, 2015) and Kilauea Iki lava lake (Greaney et al., 2017). One exception is PAC2 DR27-1, which is the most evolved sample (MgO 4.52 wt.%; Table 2.2) yet remains largely unaffected (Labidi et al., 2014). Compared to the extrapolated general differentiation trends prior to 5 wt.% MgO, there is a consistent decrease in S–Se and increase in Te concentrations in samples that have experienced magnetite-induced sulfide segregation (Fig. 2.4a and b, and Fig. 2.6a; Supplementary Fig. S2.3). This is amplified by consistent and abrupt decrease in Se/Te and S/Te (Fig. 2.4c and e).

Selenium and tellurium likely segregate from the silicate melt as Fe–Se and Fe–Te complexes analogous to Fe–S and thus their abundances in the melt should (also) be directly related to the FeO content. This is evidenced by the significant effect of FeO on the Se solubility in silicate melts (Fang and Lynch, 1987; Wykes et al., 2015) and on the partitioning of Se–Te

between sulfide and silicate melts (Choi and Cho, 1997; Brenan, 2015; Kiseeva et al., 2017). Indeed, PAR MORBs display strong covariations between FeO_T and Se–Te contents (Fig. 2.6b and c), similar to that observed for S (Labidi et al., 2014). Note that FeO_T monotonically increases with deceasing MgO prior to magnetite saturation (Supplementary Fig. S2.3). In the following sections, we first model Se–Te variations during MORB differentiation using FeO_T content as an index of crystal fractionation. We then estimate the primary melt Se–Te contents by correcting the observed concentrations for crystal + sulfide fractionation.

2.5.2.1 Modelling Se–Te variations and implications for chalcophile element partitioning

Details of the model calculations are given in Supplementary Material. Major element variations were modelled by alphaMELTS (fractional crystallization; Ghiorso and Sack, 1995; Smith and Asimow, 2005). The model curves for FeO_T yield the best match with the observed variation at 3 kbar and the resulting parameters were used subsequently (Supplementary Fig. S2.3). Bulk partition coefficients of Se and Te ($D^{bulk}_{Se\ or\ Te}$) were calculated using the mean sulfide fraction in the bulk segregated minerals ($X^{bulk\ min}_{sulf}$ = 0.14 ± 0.04 wt.%; based on S systematics; Labidi et al., 2014) and two sets of experimentally determined sulfide liquid–silicate melt partition coefficients ($D^{sulf\ liq–sil}_{Se\ or\ Te}$) considering the range of FeO contents of our samples: 450–650 for Se and 2600–3200 for Te (Kiseeva et al., 2017) and 1560 ± 410–1035 ± 360 for Se and 14430 ± 1680–9570 ± 1150 for Te (1 s.d.; $D^{sulf\ liq–sil}_{Se\ or\ Te}$ decreases with increasing FeO; Brenan, 2015). The Se–Te variations were then modelled by a combination of the fractional and batch crystallization laws because partitioning of a chalcophile element between the fractionated sulfide and silicate melt is probably an intermediate (between pure fractional and batch) equilibrium process (Rehkämper et al., 1999; Bézos et al., 2005; Yang et al., 2014; Lissner et al., 2014; Kiseeva and Wood, 2015). The partitioning mode is described by the parameter S_b, which is the mass fraction of sulfide displaying batch partitioning (Rehkämper et al., 1999).

Dependency of the modelled Se–Te variations on the mode of sulfide–silicate melt partitioning (i.e., S_b) is relatively small compared to that of other highly chalcophile elements (e.g., Rehkämper et al., 1999). This is indicated by similar observed sulfide phase–silicate melt partition coefficients ($D^{sulf–sil}_{Se\ or\ Te}$) at S_b of 0 and 1 (by inversion; Supplementary Material Eq. s2.2, s2.4, and s2.5; also see Bézos et al., 2005; Lissner et al.,2014), which yields $D^{sulf–sil}_{Se}$ of ~560 ± 190 and 530 ± 180 and $D^{sulf–sil}_{Te}$ of ~1600 ± 600 and 2200 ± 950, respectively (1 s.d.). With

S_b = 0.5 and $D_{Se\ or\ Te}^{sulf\ liq–sil}$ from Kiseeva et al. (2017), the calculated trends well reproduce the observed Se–Te variations across the PAR magmatic differentiation (Fig. 2.6b and c). On the other hand, the modelled trends using $D_{Se\ or\ Te}^{sulf\ liq–sil}$ from Brenan (2015) predict much higher

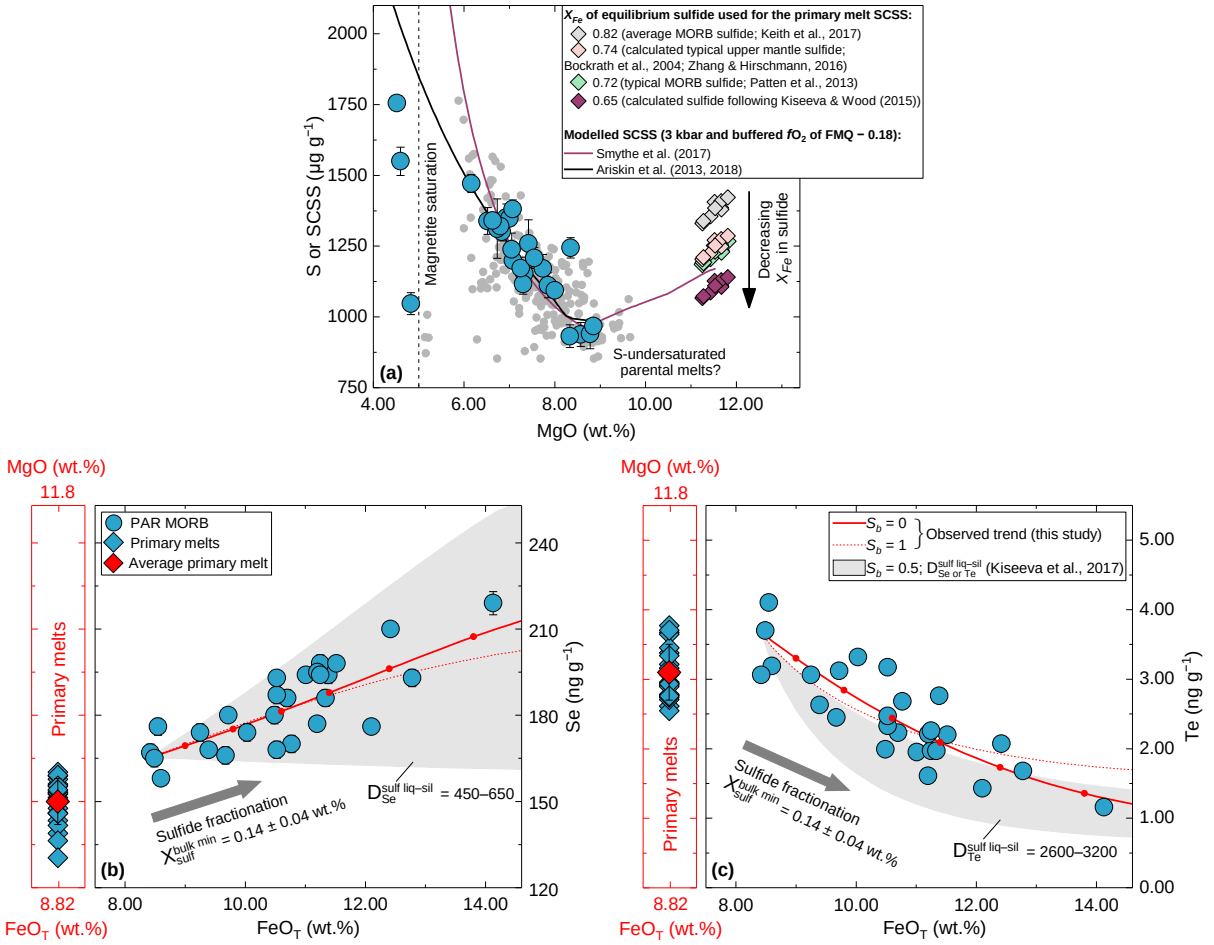

Fig. 2.6 Variations of S, Se, and Te abundances with MgO and/or FeO_T contents in PAR glasses. (a) shows the calculated SCSS (Smythe et al., 2017) for the primary melts (n = 10) as well as across the entire PAR magmatic differentiation following a similar approach of Ding and Dasgupta (2017). The primary melt major element compositions and their P–T conditions (on average ~10.2 kbar and 1325°C) of last equilibration with mantle olivine (Mg# = 0.90) are calculated using the algorithm of Lee et al. (2009). At this condition, their SCSS are calculated in combination with a variety of equilibrium sulfide compositions (X_{Fe} = 0.65–0.82; X_{Fe} = Fe/(Fe + Ni + Cu) atomic ratio) that might be found in the shallow mantle. It shows that even the lowest SCSS value with X_{Fe} = 0.63 (calculated sulfide composition in equilibrium with the most primitive glass PAC1 DR12-1g following Kiseeva and Wood (2015)) is still higher than the observed S contents of primitive PAR MORBs, implying that primary melts may be sulfide-undersaturated. The modelled SCSS (Smythe et al., 2017) across the entire PAR magmatic differentiation (from ~11.8 wt.% MgO) is calculated at 3 kbar (also see Fig. 2.7 and Supplementary Fig. S2.3) with X_{Fe} = 0.65 using major element compositions from alphaMELTS. Also shown for comparison is the SCSS from COMAGMAT (Ariskin et al., 2013, 2018) for the observed magmatic differentiation using Ni contents of the

silicate melts (other parameters from alphaMELTS; Supplementary Fig. S2.3). Both models are in good agreement with the observed S abundances in sulfide-saturated MORBs from the PAR and global oceanic spreading ridges (Jenner et al., 2012, 2015; Labidi et al., 2014; global MORB data from Jenner and O'Neill (2012); n = 233). (b) and (c) show the modelled Se–Te variations with the calculated $X_{sulf}^{bulk\ min}$ (based on S systematics; Labidi et al., 2014) and the experimentally determined $D_{Se\ or\ Te}^{sulf\ liq–sil}$ for basaltic melts with 8–11 wt.% FeO from Kiseeva et al. (2017), which well reproduces the observed Se–Te variations. Calculation assumes that Se–Te partitioning between the fractionated sulfide liquid and silicate melt is an intermediate equilibrium process between fractional and batch partitioning, with S_b = 0.5 (Rehkämper et al., 1999). The observed/empirical trends using the observed $D_{Se\ or\ Te}^{bulk}$ values with S_b of 0 and 1 were shown for comparison. Each tick mark represents 10% crystal fractionation step. Also shown in (b) and (c) are the primary PAR melt (~11.8 wt.% MgO) Se–Te contents corrected for sulfide + crystal fractionation during later differentiation (sulfide-saturated; MgO <8.85 wt.%) and for olivine fractionation during early differentiation (sulfide-undersaturated; 11.8–8.85 wt.% MgO).

$D_{Se\ or\ Te}^{bulk}$ and cannot properly describe the observed patterns with any S_b values (not shown). Based on the experiments of Brenan (2015), a lower apparent $D_{Te}^{sulf–sil}$ can be predicted if a significant fraction of the segregating sulfides is crystalline monosulfide solid solution (MSS) in which Te is significantly more incompatible relative to sulfide liquid ($D_{Te}^{MSS–sulf\ liq} \approx$ 0.02–0.08 and $D_{Te}^{MSS–sil}$ = 729; also see Helmy et al., 2010; Liu and Brenan, 2015); in this case, our observed $D_{Te}^{sulf–sil}$ at S_b = 1 would require 87 ± 6% of the sulfide phase to be MSS using an average $D_{Te}^{sulf\ liq–sil}$ = 11960 ± 1400 (see above). Such a high MSS fraction is however unlikely. At a pressure–temperature (P–T) range relevant to MORB differentiation (e.g., from ~1280 to 1160°C at 2–5 kbar until ~70% crystallization in most PAR melts; Fig. 2.7), segregated sulfide is at its liquidus near ~1050–1125°C according to sulfide melting experiments (Bockrath et al., 2004; Zhang Z. and Hirschmann, 2016) and empirical approximations on natural sulfides in MORB glasses (Patten et al., 2012). Although there is geochemical evidence that a certain proportion of MSS needs to be present in fractionating sulfides to explain the variations of some chalcophile elements (Li and Audétat, 2012), sulfide liquid is still the main (if not dominant) sulfide phase during much of MORB differentiation that occurs above the sulfide liquidus (e.g., Bézos et al., 2005; Jenner et al., 2010; Li and Audétat, 2012; Lissner et al., 2014; Brenan, 2015). Besides, the fact that the observed Se–Te variations are well reproduced with $D_{Se\ or\ Te}^{sulf\ liq–sil}$ from Kiseeva et al. (2017) argues against a significant control of MSS fractionation on Se–Te systematics of PAR glasses. Another alternative explanation for the observed low $D_{Te}^{sulf–sil}$ compared to $D_{Te}^{sulf\ liq–sil}$ from Brenan (2015) could be poor equilibration between sulfides and

silicate melt (i.e., R_{eff}<1) as previously proposed for partitioning of platinum-group elements in MORBs (Rehkämper et al., 1999; Bézos et al., 2005; Yang et al., 2014). However, the extent of sulfide–silicate equilibration in our case might not be properly assessed due to the difference in the experimental $D_{Se\ or\ Te}^{sulf\ liq–sil}$ published by Brenan (2015) and Kiseeva et al. (2017) for the range of FeO content of PAR basalts.

Finally, only for the highly evolved MORB melts (PAC1 DR10-1g and PAC2 DR20-1) that have experienced >70% crystallization and magnetite-triggered sulfide segregation (Fig. 2.6a; Supplementary Fig. S2.3), we suggest crystalline MSS to be the dominant fractionating sulfide phase to account for the observed abrupt drop in Se/Te (and S/Te) ratios (Fig. 2.4), considering $D_{Se}^{sulf\ liq–sil} < D_{Te}^{sulf\ liq–sil}$ and $D_{Se}^{MSS–sil} > D_{Te}^{MSS–sil}$ (Brenan, 2015). This was previously proposed for sulfide-saturated arc magmas based on Cu–Ag systematics (Jenner et al., 2010, 2012, 2015).

2.5.2.2 Primary melt Se–Te contents: Consideration of sulfide saturation

The primary melt major element composition was calculated following Lee et al. (2009) by adding liquidus olivine back into primitive samples with MgO >~8.5 wt.% (n = 10; Vlastélic et al., 2000; Hamelin et al., 2010) until the melts reach equilibrium with mantle olivine containing Mg# = 0.90 (Mg#: molar Mg/(Mg + Fe^{2+})). Assuming the glasses have $Fe^{2+}/\Sigma Fe$ = 0.87 (e.g., Bézos and Humler, 2005; Zhang H. L. et al., 2018), we obtain an average primary melt composition of ~11.8 wt.% MgO and ~8.8 wt.% FeO_T at ~10.2 kbar and ~1325°C after ~8.7% olivine addition. For the Se–Te contents, we applied a two-step correction. Considering all studied glasses are sulfide-saturated, based on the strong covariation paths of Se–Te with FeO_T (Fig. 2.6b and c) and FeO_T with MgO (Supplementary Fig. S2.3), the Se–Te contents were first corrected to FeO_T content (8.49 wt.%) of the most primitive sample (PAC1 DR12-1g; 8.85 wt.% MgO) following a linear regression scheme previously used for other elements (e.g., Klein and Langmuir, 1987; Bézos et al., 2005; Kelley et al., 2006; Lissner et al., 2014). This yields 164 ± 8 and 3.4 ± 0.4 ng g^{-1} Se and Te, respectively (melts experiencing magnetite saturation were excluded; see Fig. 2.4 and Supplementary Fig. S2.2 and S2.3). Further corrections (from 8.85 to 11.8 wt.% MgO) along some linear slope with MgO or Mg# depend on whether the more primitive melts are sulfide-saturated. Several global MORBs with MgO >9 wt.% (Jenner and O'Neill, 2012; Jenner et al., 2015) seem to display a clear absence of fractionation between chalcophile elements that have quite different $D^{sulf\ liq–sil}$ (e.g., Cu, As, Se,

Ag, In, Sn, Tl, and Pb; Li and Audétat, 2012; Patten et al., 2013; Kiseeva and Wood, 2015; Kiseeva et al., 2017), which might indicate a sulfide undersaturation in high-MgO basalts (also see Ding and Dasgupta, 2017).

In this regard, we calculated the S solubilities of the primary PAR melts at their last equilibration with the mantle (see above) using the recent sulfur content at sulfide saturation (SCSS) model of Smythe et al. (2017) while taking into account the effect of equilibrium sulfide chemistry (Fig. 2.6a). It shows that, with a wide range of sulfide compositions (42–51 wt.% Fe, 9–18 wt.% Ni, and 0.4–10 wt.% Cu; Bockrath et al., 2004; Patten et al., 2013; Kiseeva and Wood, 2015; Zhang Z. and Hirschmann, 2016; Keith et al., 2017), SCSS of the primary melts range from 1117 ± 44 to 1394 ± 55 μg g^{-1}, which decreases with decreasing X_{Fe} in sulfides (X_{Fe} = Fe/(Fe + Ni + Cu) molar ratio). Even the lowest SCSS seems to be still higher than the S contents of the primitive PAR glasses (932–968 μg g^{-1}; Labidi et al., 2014), implying that primary melts might be sulfide-undersaturated. The modelled SCSS (Smythe et al., 2017) across the entire magmatic evolution (with X_{Fe} = 0.65 at 3 kbar and fO_2 of FMQ − 0.18; Supplementary Material) shows that MORBs may have reached sulfide saturation during early differentiation (P from ~10.2 to 3 kbar and T from ~1325 to 1248°C; Fig. 2.7) due to the decreasing S solubility as well as olivine crystallization; they then remained sulfide-saturated, which also matches the model of Ariskin et al. (2013, 2018) that considers the effect of sulfide chemistry using Ni contents of the silicate melts (Fig. 2.6a). Both predictions are consistent with the observed sulfide saturation in the PAR as well as global spreading-ridge glasses (Jenner et al., 2012, 2015; Labidi et al., 2014; Smythe et al., 2017; but see Shimizu et al., 2016). Although primitive basalts (MgO >9–10 wt.%) were also suggested to be sulfide undersaturated based on a variety of S solubility models, these models can result in significant differences in SCSS (up to 1,000 μg g^{-1}) at a given condition (Saal et al., 2002; Ding and Dasgupta, 2017; and references therein). The model of Smythe et al. (2017), which we applied for our model primary melts, also carries large uncertainties (~25%). Here, we tentatively assume that parental PAR melts (MgO >8.85wt.%) are sulfide undersaturated and accordingly the Se–Te concentrations after the first-step correction were further corrected for ~8.7% olivine fractionation only. This yields average Se and Te concentrations of 150 ± 8 and 3.1 ± 0.4 ng g^{-1}, respectively, for PAR primary melts (Se/Te = 48.4 ± 6.8; n = 24; Fig. 2.6b and c). This Se/Te ratio would represent an upper limit if the primary melts are sulfide saturated. These estimates are significantly lower than for the SMAR N-MORB primary melts (230–254 and 9.0–11.3 ng g^{-1}, respectively; Se/Te = 22–26; Lissner et al., 2014). This discrepancy may be attributed to the difference in the observed Se–

Te variations (Fig. 2.4a, b, and c; Section 2.4.2) as well as the correction approach used between two studies. Additional uncertainties may also result from other complexities during MORB differentiation (e.g., Coogan and Dosso, 2016; Lissenberg and MacLeod, 2016; O'Neill and Jenner, 2012). Most importantly, the clear negative slope in Te versus MgO in PAR MORBs is not resolved in SMAR N-MORBs (Lissner et al., 2014) due to the smaller MgO range of the latter (Fig. 2.4b). A wider compositional range of N-MORB now proves to be more appropriate (this study) than coupled N- and E-MORB arrays (Lissner et al., 2014) in order to adequately correct for differentiation and recover the primary melt Se–Te contents.

2.5.3 Role of partial melting on Se–Te systematics and inferences on composition of the upper mantle

2.5.3.1 Partitioning behavior of Se–Te during mantle melting

In the upper mantle, Se and Te are mainly hosted by Fe–Ni–Cu base metal sulfides and platinum-group minerals (Guo et al., 1999; Hattori et al., 2002; Lorand and Alard, 2010; König et al., 2015; Lorand and Luguet, 2016). The behavior of Se–Te during mantle melting is thus predominantly controlled by fractionation between these phases and silicate melt. However, their absolute and relative partitioning during melting has been debated. Based on the apparent variation in Se–Te abundances of peridotites, some authors suggest a slightly more incompatible behavior of Se compared to Te, with both being moderately incompatible (Wang and Becker, 2013; Wang et al., 2013). This relative partitioning is however opposite to observations from highly depleted harzburgites (König et al., 2012, 2014, 2015; Luguet et al., 2015). Hertogen et al. (1980), from the MORB perspective, suggest that Se is much more incompatible than Te during melting, with Te being rather compatible. This was based on the observed lack of clear Se/Te fractionation during magmatic differentiation and distinctly higher Se/Te ratios of global MORBs compared to mantle rocks (Hertogen et al., 1980; and references therein). In fact, as shown for PAR and SMAR MORBs (Fig. 2.4c), significant Se/Te fractionation occurs during MORB differentiation. This was not evident from the relatively small sample suite of Hertogen et al. (1980) probably due to (1) different source composition (Section 2.4.2) and (2) different mode and rate of sulfide fractionation during low-P magmatic differentiation in different spreading ridges (e.g., Bézos et al., 2005; Yang et al., 2014; Lissner et al., 2014), which may result in different apparent fractionation of Se/Te among genetically

unrelated samples. Lissner et al. (2014) propose that both Se–Te are apparently incompatible during melting, with Te being more incompatible, although the empirical $D_{Se\ or\ Te}^{sulf\ liq–sil}$ they applied for modelling seem to suggest the opposite at low- to moderate-degree melting. Besides, both PAR and SMAR MORB data show that Te is much more compatible than Se during magmatic differentiation (Fig. 2.4c; Section 2.5.2.1), in accordance with experimental or empirical constraints (Peach et al., 1990; Patten et al., 2013; Lissner et al., 2014; Brenan, 2015; Wang and Becker, 2015a; Kiseeva et al., 2017).

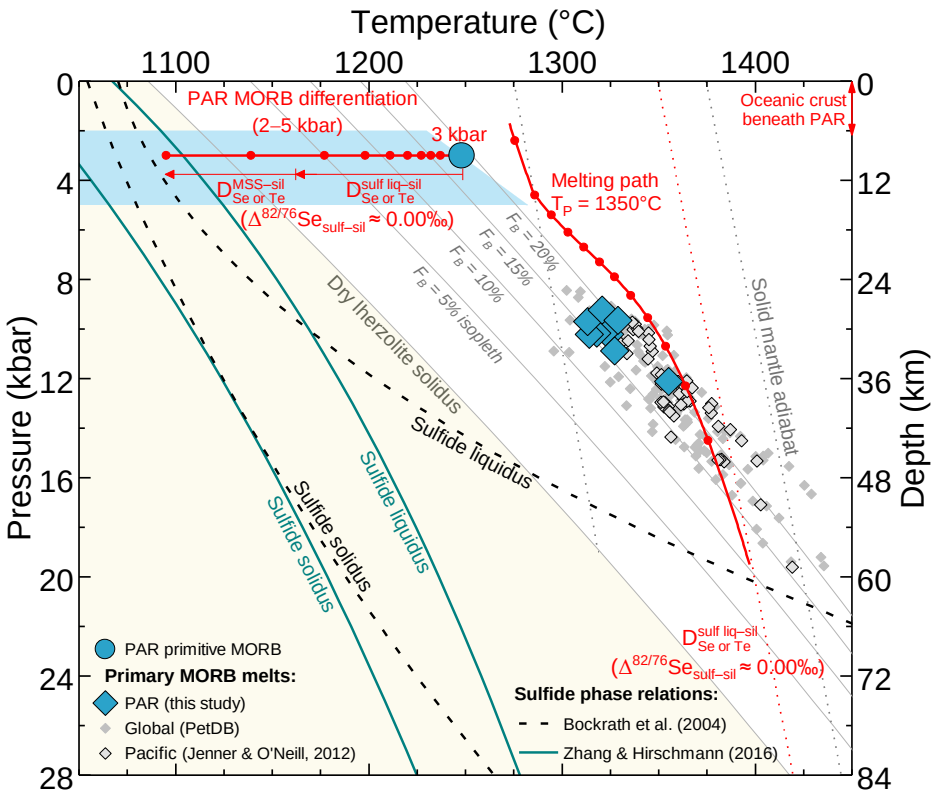

Fig. 2.7 P–T diagram showing the sulfide phase relations determined on a single sulfide composition (X_{Fe} = 0.74, metal/S = 0.93, and Ni/(Fe + Ni) = 0.25 molar ratio; Bockrath et al., 2004; Zhang Z. and Hirschmann, 2016) and modelled conditions of PAR MORB differentiation (isobaric fractional crystallization; also see Supplementary Fig. S2.3) and near-fractional isentropic decompression melting path of a depleted MORB mantle (Salters and Stracke, 2004) to the base of the PAR crust (6.5 Km; alphaMELTS; Ghiorso and Sack, 1995; Ghiorso et al., 2002; Smith and Asimow, 2005). Each tick mark indicates 10% crystal fractionation or 2% melting extent. Anhydrous lherzolite solidus and bulk melt fraction (F_B) isopleths are calculated after Katz et al. (2003). The P–T condition of primary melt–mantle equilibration was obtained by the thermobarometer of Lee et al. (2009) using primitive PAR MORBs (>8.5 wt.% MgO; n = 10; Vlastelic et al., 2000; Hamelin et al., 2010), suggesting that melting at a mantle potential temperature (T_P) of 1350°C (also see Ding and Dasgupta (2017) for other MORBs) may be adequate for our modelling purpose because each data point for an aggregate primary melt represents weighted average P–T of melt extraction from all mantle parcels across the triangular melting zone and thus lies below the

polybaric melting path (Asimow and Longhi, 2004; Lee et al., 2009). The primary melt P–T of MORBs from the Pacific (n = 55; Jenner and O'Neill, 2012) and other spreading-ridges (n = 157; PetDB) is shown for comparison. Both sulfide melting experiments (Bockrath et al., 2004; Zhang Z. and Hirschmann, 2016) suggest that sulfide liquid is the dominant fractionating phase across much of low-P MORB differentiation (red arrow), consistent with previous inferences from behavior of chalcophile elements (see Section 2.5.2.1). However, the sulfide liquidi estimated by these experiments distinctly vary at P–T conditions relevant to melting of a depleted mantle with typical T_P between ~1275°C and 1400°C. Under these conditions, a mantle sulfide may have similar metal/S ratio but much higher Ni/(Fe + Ni) (~0.40–0.65) compared to the sulfide mentioned above, resulting in an even lower solidus (Zhang Z. and Hirschmann, 2016; Zhang Z. et al., 2018). This implies that chalcophile element behavior during decompression melting is entirely controlled by sulfide liquid–silicate melt fractionation rather than MSS–sulfide liquid or MSS–silicate melt fractionation.

These discrepancies have been explained by the presence of different equilibrium sulfide assemblages (sulfide liquid and crystalline MSS) during MORB differentiation and mantle melting, which involve sulfide liquid–silicate melt partitioning and MSS–sulfide liquid/silicate melt partitioning, respectively (Lorand and Alard, 2010; Lissner et al., 2014; König et al., 2014, 2015; Brenan, 2015). This is because Te is much more incompatible in MSS relative to sulfide liquid than Se (with $D_{Se\ or\ Te}^{MSS-sulf\ liq}$ of ~0.56–0.75 and ~0.02–0.08 for Se and Te, respectively; Helmy et al., 2010; Liu and Brenan, 2015; Brenan, 2015). The presence of MSS in the MORB mantle was also experimentally shown and used to explain the partitioning behavior of chalcophile and highly siderophile elements during melting (e.g., Bockrath et al., 2004; Bézos et al., 2005; Ballhaus et al., 2006; Fischer-Gödde et al., 2011; Brenan, 2015). However, the sulfide liquidus (Fig. 2.7) determined by Bockrath et al. (2004) has been questioned (Hart and Gaetani, 2006; Fonseca et al., 2012; Mungall and Brenan, 2014; Zhang Z. and Hirschmann, 2016). Recent sulfide melting experiments using the same sulfide composition as in Bockrath et al. (2004) show that crystalline MSS is not stable in the convecting upper mantle (Fig. 2.7; Zhang Z. and Hirschmann, 2016; Zhang Z. et al., 2018), which indicates that behavior of chalcophile elements during the partial melting might be entirely controlled by sulfide liquid–silicate melt partitioning, in favour of earlier conclusions based on Cu–Ag systematics of mantle rocks and melts (Wang and Becker, 2015b; Jenner et al., 2015).

2.5.3.2 Melting model

In order to further understand the role of partial melting on the Se–Te systematics of MORB melts and mantle residues, we modelled the behavior of Se–Te in a triangular passive-flow near-

fractional melting regime, which was previously used to explain the Se–Te and highly siderophile element systematics of MORBs (e.g., Rehkämper et al., 1999; Lissner et al., 2014; Brenan, 2015). The modelling procedures and parameters are detailed in Supplementary Material and summarized in Table 2.3. Briefly, the melt major element compositions and P–T conditions for calculating the SCSS (Smythe et al., 2017) and $D_{Se\ or\ Te}^{sulf\ liq–sil}$ (as a function of FeO; Brenan, 2015; Kiseeva et al., 2017) were modelled with alphaMELTS front end (pMELTS mode; Ghiorso et al., 2002; Smith and Asimow, 2005) at a mantle potential temperature of 1350°C following a similar approach used by Ding and Dasgupta (2017) (Fig. 2.6). The depleted mantle composition was taken from Salters and Stracke (2004) assuming 0.2 wt.% Fe_2O_3 (e.g., Cottrell and Kelley, 2011). The average melting degree (F_B; Langmuir et al., 1992; Plank et al., 1995) of the samples was estimated using differentiation-corrected incompatible trace element concentrations by (1) solving the simple batch melting equation for F_B (e.g., Kelley et al., 2006) and (2) comparing the concentrations to the result from pMELTS (near-fractional melting). These two approaches yield consistent F_B of ~6.6–11.7% (average 8.5 ± 1.5%) and 6.5–9.5% (Supplementary Fig. S2.4), respectively, in agreement with the previous estimates for global MORBs (e.g., Klein and Langmuir, 1987; Salters and Stracke, 2004; Workman and Hart, 2005; Kimura et al., 2017). Three different upper mantle sulfide compositions were considered when calculating the SCSS of the partial melts (X_{Fe} = 0.44–0.74 and Ni/(Fe + Ni) = 0.25–0.53 at a constant (Fe + Ni + Cu)/S = 0.93; Supplementary Fig. S2.5). Considering a large number of input parameters in our model, in order to assure an internal consistency and reliability of our MORB mantle Se–Te estimates, we first modelled the variation of S and Cu during partial melting (Supplementary Fig. S2.5) because their mantle abundances (McDonough and Sun, 1995; Salters and Stracke, 2004; Lorand et al., 2013; Lorand and Luguet, 2016; Palme and O'Neill, 2014; Wang and Becker, 2013, 2015b) and behavior during mantle melting are relatively well established (e.g., Lee et al., 2009; Li and Audétat, 2012; Kiseeva and Wood, 2013, 2015; Ding and Dasgupta, 2017).

Our result shows that the PAR primary melt S concentrations are well reproduced for the estimated F_B of the samples using a range of source S content from "PM-like" 200 μg g^{-1} (e.g., Palme and O'Neill, 2014; Wang and Becker, 2013) to slightly lower 150 μg g^{-1} as estimated for the depleted MORB mantle (e.g., Luguet et al., 2003; Bézos et al., 2005; Nielsen et al., 2014; Lorand and Luguet, 2016) in combination with the SCSS model of Smythe et al. (2017) and equilibrium "sulfide B" (Supplementary Fig. S2.5a). Note that this sulfide chemistry is typical for lherzolite-hosted sulfides (e.g., Lorand and Luguet, 2016; Kiseeva et al., 2017) and

Table 2.3 Summary of model parameters used for the near-fractional melting of a MORB mantle.

		Note
PAR primary melts		
Major elements	~11.8 wt.% MgO, ~8.8 wt.% FeO_T, and Mg# = 73 (calculated average; n = 10)	Following Lee et al. (2009)
fO_2	ΔFMQ = −0.18 ($Fe^{2+}/\Sigma Fe$ = 0.87)	Bézos and Humler (2005); Zhang H. L. et al. (2018)
Equilibration P–T with Fo_{90} olivine	~10.2 kbar and ~1325°C (calculated average; n = 10)	Thermobarometer of Lee et al. (2009); Fig. 7
Equilibrium sulfide	Natural and calculated sulfide compositions (X_{Fe} = 0.82–0.65)	Fig. 6
S–Se–Te	874 ± 48 μg g^{-1} S, 150 ± 8 ng g^{-1} Se, and 3.1 ± 0.4 ng g^{-1} Te (1 s.d., n = 24)	Fig. 8 and 9; Supplementary Fig. S5 and S6
Se/Te	48.4 ± 6.8 (1 s.d., n = 24)	
Mantle source		
Major/trace elements	Depleted MORB Mantle (with 0.2 wt.% Fe_2O_3)	Salters and Stracke (2004); Cottrell and Kelley (2011)
Potential temperature (T_P)	1350°C	Following Lee et al. (2009); also see Ding and Dasgupta (2017)
Extraction P–T for each 1% melt increment	17.5–5.4 kbar and 1389–1294°C (for *F* 0–20%; pMELTs)	Ghiorso et al. (2002); Smith and Asimow (2005); Fig. 7
S	170–200 μg g^{-1}	E.g., Lorand and Luguet (2016)
Se–Te (Potential Source 1)	80 ng g^{-1} Se and 11 ng g^{-1} Te (fertile lherzolite)	Wang and Becker (2013)
Se–Te (Potential Source 2)	49 ± 11 ng g^{-1} Se and 3.5 ± 1.3 ng g^{-1} Te (resulting best-fit abundances)	Figs. 8–10
Experimental partition coefficients		
$D^{sulf\ liq–sil}$	(1) 1414–1900 for Se and 13199–16811 for Te (for equilibrium melts at *F* 0–20%)	Following Brenan (2015); increasing with decreasing FeO
$D^{sulf\ liq–sil}$	(2) 850 for Se and 3800 for Te	Kiseeva et al. (2017)
$D^{MSS–sil}$	883 for Se and 729 for Te	Brenan (2015)
Equilibrium sulfide	$Fe_{0.50}Ni_{0.36}Cu_{0.07}S_{1.00}$ (calculated "sulfide B"; X_{Fe} = 0.54; Ni/(Ni + Fe) = 0.42)	Supplementary Fig. S5
SCSS of the partial melts	960–821 μg g^{-1} (for an aggregate column-melt at *F* 0–20%)	Smythe et al. (2017); Supplementary Fig. S5
F_B	(1) 8.5 ± 1.5% (from trace element systematics; n = 24)	Following Kelley et al. (2006); Supplementary Fig. S4
F_B	(2) 6.5–9.5% (pMELTs forward modelling)	Fig. 8; Supplementary Fig. S4–S6

consistent with the suggested range of Ni/(Fe + Ni) value for a shallow mantle Cu-free sulfide liquid (0.4–0.6) by recent experiments (Zhang Z. et al., 2018) at the range of melting depth (~50–20 km; Fig. 2.7) and fO_2 (~FMQ; Cottrell and Kelley, 2011; Zhang H. L. et al., 2018) estimated for the PAR basalts. The corresponding model curves also show an excellent fit to the primary melt Cu concentrations with 170–200 μg g^{-1} S and 30 (or 24) μg g^{-1} Cu in the source (Supplementary Fig. S2.5b and c).

2.5.3.3 Modelling Se–Te variations in mantle melts and residues

Fig. 2.8 and Fig. 2.9a show that the Se–Te systematics of PAR primary melts (150 ± 8 and 3.1 ± 0.4 ng g^{-1} Se and Te, respectively; Se/Te = 48.4 ± 6.8; n = 24) can be successfully reproduced by melting of a sulfide liquid-bearing MORB mantle which has "fertile lherzolite-like" Se and Te contents (80 and 11 ng g^{-1}, respectively; estimated at 3.52 wt.% Al_2O_3; Wang and Becker, 2013) using experimental $D^{sulf\ liq–sil}_{Se\ or\ Te}$ from Brenan (2015) calculated at each 1% equilibrium melting (Table 2.3). With the same SCSS, the polybaric aggregate melts reach S-undersaturation at F_B from ~9.5% to 11.5%, increasing with increasing initial S content from 170 to 200 μg g^{-1} (also see Supplementary Fig. S2.5a). This corresponds to an extent of melting F from ~19% to 23% in the central melting column (i.e., F_{max}; Supplementary Material) and is consistent with the conclusion of previous studies using other empirical or experimental SCSS models (Luguet et al., 2003; Bézos et al., 2005; Lee et al., 2012; Lissner et al., 2014; Brenan, 2015). In the case of 180 μg g^{-1} S, a mantle column becomes sulfide-exhausted after ~20% melting. At any stage before sulfide exhaustion, Se is apparently much more incompatible than Te, with contrasting $D^{bulk}_{Se\ or\ Te}$ values of ~0.69–0.01 and ~6.38–0.11 for Se and Te, respectively (decreasing with ongoing partial melting). Therefore, a large Se/Te fractionation occurs between the melt and residue as long as sulfide liquid is present in the system (Fig. 2.8c). The estimated F_B for PAR MORBs (~6.6–11.7%) indicates that the primary aggregate melt is a mixture of melt increments derived from both sulfide-bearing (low-F) and sulfide-exhausted (high-F) mantle columns (also see Ding and Dasgupta, 2017), and therefore, the observed Se/Te fractionation in primary melts with respect to their source is largely accounted for by melting. This is in contrast to the observations from the primary SMAR melts, in which the relative partitioning of Se and Te is suggested to have played a minor role on the observed Se–Te variation (Lissner et al., 2014). This is because the SMAR partial melts are mostly derived from sulfide-free mantle owing to the relatively high F_B (12.8–17.2%) estimated by the authors, whereas sulfide exhaustion in their model occurs at around $F_B \approx 9\%$. However, as noted by

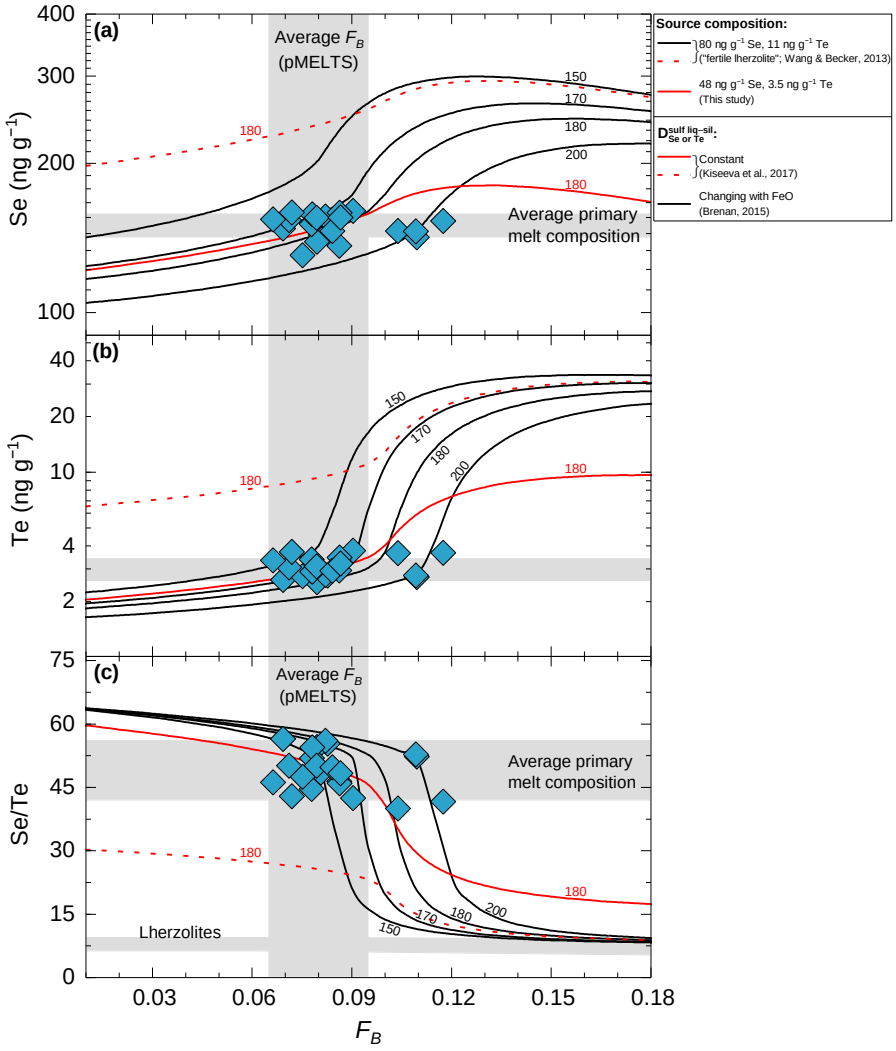

Fig. 2.8 Variations of Se (a) and Te (b) contents and Se/Te ratios (c) of the primary PAR melts (also see Fig. 2.6b and c) with their average degree of melting (F_B) estimated by batch melting equation using incompatible trace element systematics (~6.6–11.7%; Supplementary Fig. S2.4). The vertical and horizontal shaded field represent the range of F_B (6.5–9.5%) estimated from the forward modelling (near-fractional melting; pMLETS) and average primary melt composition (150 ± 8 and 3.1 ± 0.4 ng g^{-1} Se and Te, respectively; Se/Te = 48.4 ± 6.8). The variation in Se–Te concentrations were modelled for a triangular near-fractional melting regime (e.g., Rehkämper et al., 1999; Lissner et al., 2014; Brenan, 2015) using "fertile lherzolite-like" Se and Te contents (80 and 11 ng g^{-1}; Wang and Becker, 2013) and a range of S contents (150–200 µg g^{-1}) previously estimated for the primitive and/or depleted upper mantle (e.g., Luguet et al., 2003; Lorand et al., 2013; Lorand and Luguet, 2016; Bézos et al., 2005; Wang and Becker, 2013; Nielsen et al., 2014; Palme and O'Neill, 2014). $D^{sulf\ liq–sil}_{Se\ or\ Te}$ values are from Brenan (2015) and Kiseeva et al. (2017) (Table 2.3). The melt major element compositions and P–T conditions were modelled with pMELTS (see Fig. 2.7) and used to calculate $D^{sulf\ liq–sil}_{Se\ or\ Te}$ (as a function of FeO content of each equilibrium melt) and SCSS of the melt (Smythe et al., 2017) assuming the melt is in equilibrium with a calculated upper mantle sulfide ($Fe_{0.50}Ni_{0.36}Cu_{0.07}S_{1.00}$; Supplementary Fig. S2.5). (a), (b), and (c) show that the Se–Te systematics of the primary PAR melts can be broadly reproduced using the selected "fertile lherzolite-like" Se–Te contents (with 170–200 µg g^{-1} S) and $D^{sulf\ liq–sil}_{Se\ or\ Te}$ from Brenan (2015) (black lines). S-undersaturation in the aggregate melt

occurs at slightly different F_B (~9.5% to 11.5%) depending on the source S content (see Supplementary Fig. S2.5a). With the same starting composition, calculation using $D_{Se\ or\ Te}^{sulf\ liq–sil}$ of Kiseeva et al. (2017) overestimates the Se–Te contents of the melts (only shown for 180 μg g^{-1} S in the source for simplicity; red dashed lines) and only reproduces the observed variations with a significantly lowered source Se and Te contents (48 and 3.5 ng g^{-1}, respectively; red solid lines).

Kinzler and Grove (1993), the model of Niu and Batiza (1991) applied by Lissner et al. (2014) to estimate the melting extent of the SMAR MORB tends to produce somewhat higher values compared to other models using major element systematics. This may partly explain the different observations between our study and Lissner et al. (2014) regarding the effect of partial melting on the observed Se/Te fractionation in MORB. The modelling was also performed using experimental $D_{Se\ or\ Te}^{sulf\ liq–sil}$ of Kiseeva et al. (2017), from which the highest values were taken (850 and 3800 for Se and Te, respectively) considering the FeO content of the equilibrium melts (8.3–5.4 wt.%; Supplementary Material). However, these $D_{Se\ or\ Te}^{sulf\ liq–sil}$ overestimate the Se–Te contents of the melts with a "fertile lherzolite-like" starting Se–Te contents (with 180 μg g^{-1} S; Fig. 2.8a and b). A good match is obtained only after the source Se and Te contents are lowered to 48^{+5}_{-8} and $3.5^{+0.5}_{-0.9}$ ng g^{-1}, respectively (Fig. 2.8 and Fig. 2.9a). With this set of $D_{Se\ or\ Te}^{sulf\ liq–sil}$, we obtain 49 ± 11 ng g^{-1} Se and 3.5 ± 1.3 ng g^{-1} Te on average for the PAR mantle having 170–200 μg g^{-1} S. Considering the difference in experimental $D_{Se\ or\ Te}^{sulf\ liq–sil}$ between Brenan (2015) and Kiseeva et al. (2017), it is uncertain which Se–Te contents actually represent the mantle source composition (Fig. 2.9a).

The role of MSS–silicate melt partitioning on the behavior of Se–Te was investigated by incorporating varying proportions of MSS and sulfide liquid into the bulk sulfide assemblage in the mantle (180 μg g^{-1} S) using experimental $D_{Se\ or\ Te}^{MSS–sil}$ from Brenan (2015) and "fertile lherzolite-like" Se–Te contents for consistency (Supplementary Fig. S2.6). Due to the similar $D_{Se\ or\ Te}^{MSS–sil}$ of Se and Te (883 and 729, respectively), there is little Se/Te fractionation during the entire melting interval if crystalline MSS is the only controlling sulfide phase (also see Brenan, 2015); besides, both Se–Te concentrations are highly overestimated owing to their high apparent incompatibilities, with $D_{Se\ or\ Te}^{bulk}$ values of ~0.43–0.01 and 0.35–0.01 for Se and Te, respectively (Supplementary Fig. S2.6). It shows that Se–Te systematics of the melt can only be reproduced if sulfide liquid is the major controlling phase (>50%; in the case of 180 μg g^{-1} S in the source; Fig. 2.9a and Supplementary Fig. S2.6).

On the other hand, the modelled Se–Te contents of the residue shows that the variations of Se–Te abundances and Se/Te ratios of worldwide lherzolites (Fig. 2.9b and c) can be reproduced only when MSS is the dominant, if not only, sulfide phase (>90%) in the mantle. In this case, both Se and Te would be (apparently) incompatible, with Te being more incompatible (e.g., Brenan, 2015). As mentioned earlier, this absolute and relative partitioning during partial melting are in line with the conclusion of some studies (Lissner et al., 2014; König et al., 2014, 2015) but cannot be reconciled with our observations from the perspective of partial melts, which does not require the presence of "residual" crystalline MSS controlling Se–Te partitioning (Fig. 2.9a) as previously suggested by the Cu–Ag systematics (Jenner et al., 2015; Wang and Becker, 2015b) as well as recent sulfide melting experiments (Zhang Z. and Hirschmann, 2016; Zhang Z. et al., 2018; Fig. 2.7; Section 2.5.3.1). We argue that, from the melt perspective, secondary refertilization processes such as addition of metasomatic base metal sulfides and platinum-group minerals have significantly, if not completely, overprinted the original melt depletion signature of lherzolites (i.e., sulfide liquid–silicate melt fractionation; Fig. 2.9b and c), in line with the conclusions from studies of peridotites (Lorand and Alard, 2010; König et al., 2014, 2015; Luguet et al., 2015; Harvey et al., 2015). Note that this argument is independent of the choice of source Se–Te contents and published experimental $D^{sulf\ liq–sil}_{Se\ or\ Te}$. For instance, the residue composition was also calculated with a source having the maximum "fertile mantle" Se and Te contents (101 and 12.5 ng g^{-1}, respectively; estimated at 4.45 wt.% Al_2O_3; Wang and Becker, 2013) using $D^{bulk}_{Se\ or\ Te}$ from both studies (Brenan, 2015; Kiseeva et al., 2017). Results show that the modelled residue composition still hardly reconciles with the observed Se–Te variation in lherzolites, which likely represent a post-melt depletion refertilization trend (Fig. 2.9b and c). As for the highly depleted residue after sulfide exhaustion, little is known regarding the quantitative control of Se–Te host phases. Nevertheless, the increasing Se/Te ratios (>15; suprachondritic relative to CI chondrites; Lodders et al., 2009) with progressive melt depletion in refractory harzburgites, which represent the least metasomatically influenced peridotites (König et al., 2014; Luguet et al., 2015), probably reflects the relatively compatible behavior of Se that is preferentially incorporated in platinum-group minerals formed upon sulfide exhaustion (Luguet and Reisberg, 2016; Luguet et al., 2007; Fonseca et al., 2012; König et al., 2015).

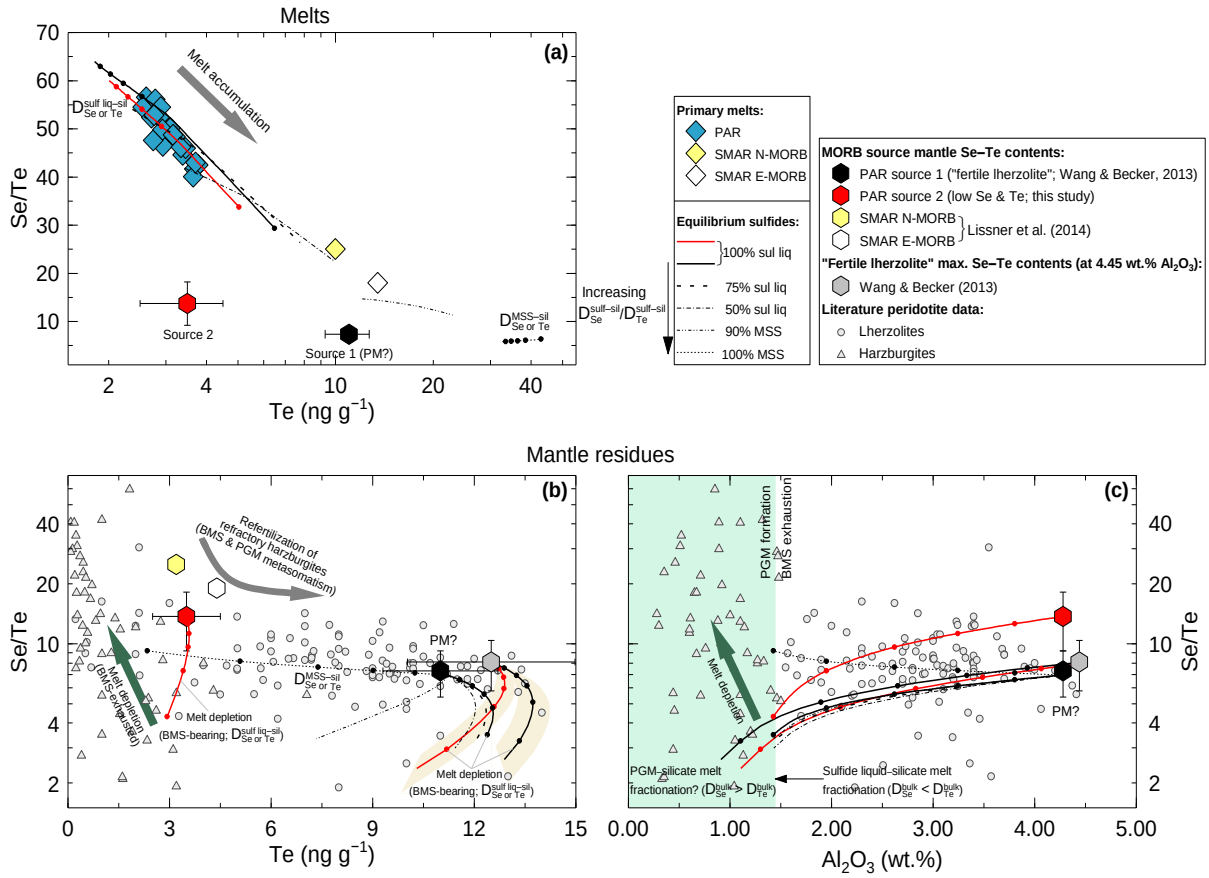

Fig. 2.9 Variations of Se/Te against (a) Te contents of the primary aggregate melts and (b) Te and (c) Al_2O_3 contents of the mantle residue. The red solid lines and all black lines correspond to the modelled melt composition with different proportions of sulfide liquid and crystalline MSS in the mantle having 180 μg g^{-1} S but two distinct Se and Te concentrations: (1) 80 ± 17 and 11 ± 1.7 ng g^{-1}, respectively ("fertile mantle"; estimated at 3.52 wt.% Al_2O_3; Wang and Becker, 2013), in combination with $D^{sulf\ liq–sil}_{Se\ or\ Te}$ (changing as a function of FeO contents of equilibrium melts) and/or $D^{MSS–sil}_{Se\ or\ Te}$ (constant) from Brenan (2015); and (2) 48 ± 8 and 3.5 ± 0.9 ng g^{-1}, respectively, which are the best-fit values from the modelling in combination with $D^{sulf\ liq–sil}_{Se\ or\ Te}$ (constant) from Kiseeva et al. (2017) (see Fig. 2.8 and Supplementary Fig. S2.6 for the modelling of partial melt composition). Each tick mark indicates 2% F_B (average degree of melting over a triangular melting zone) for the melts and 4% melting for a residual melting column (only shown for curves with 100% sulfide liquid or MSS). The modelling results are only shown until a mantle column becomes sulfide-exhausted, after which the remaining Se–Te budget is controlled by platinum-groups minerals (PGM; see the light blue shaded area in (c); Luguet et al., 2007; König et al., 2015). Additionally shown are the melting curves of a source with the maximum "fertile mantle" Se and Te contents (101 and 12.5 ng g^{-1}, respectively; estimated at 4.45 wt.% Al_2O_3 by Wang and Becker (2013)) using experimental $D^{sulf\ liq–sil}_{Se\ or\ Te}$ of (1) 1086 and 8789 (used in the melting model of Brenan (2015)) and (2) 850 and 3800 (same as above; Kiseeva et al., 2017) for Se and Te, respectively. For this modelling, major element compositions are from PM of McDonough and Sun (1995) and SCSS is calculated accordingly using parameters from pMELTS. The light yellow shaded areas in (c) are the range of residue compositions with a typical fertile mantle S content (200 ± 40 μg g^{-1}; e.g., Lorand, 1991; Palme and O'Neill, 2014). Our result shows that, regardless of the choice of source Se–Te contents and experimental $D^{sulf\ liq–sil}_{Se\ or\ Te}$ data, the Se–Te pattern displayed by lherzolites is inconsistent with melt

depletion involving sulfide liquid–silicate melt fractionation (all solid black and red lines; b and c), which is suggested here to control Se–Te partitioning during mantle melting ($D_{Se}^{bulk} << D_{Te}^{bulk}$; see text for more details). Shown for comparison are the Se–Te contents for the SMAR N- and E-MORB primary melts and mantle sources (Lissner et al., 2014). Lherzolite (>1.5 wt.% Al_2O_3) and harzburgite (<1.5 wt.% Al_2O_3) data are from Morgan (1986), Lorand and Alard (2010), Wang and Becker (2013), Wang et al. (2013), König et al. (2012, 2014, 2015), Luguet et al. (2015), and Harvey et al. (2015).

2.5.4. Role of magmatic processes on Se isotope systematics of MORB

Having established the Se (and Te) elemental behavior during partial melting and MORB differentiation, we now discuss the role of these magmatic processes on Se isotopes and estimate a reliable mantle source composition. Note that none of the (secondary) non-magmatic processes, including high-T hydrothermal fluid/sulfide assimilation during magmatic differentiation and volcanic degassing, have measurable effects on Se isotope composition of PAR glasses (Section 2.5.1).

Previous experiments reported significant Se isotopic fractionation (up to 19‰ in $^{82}Se/^{76}Se$) during abiotic reduction of Se oxyanions (SeO_3^{2-} and SeO_4^{2-}) at low temperature conditions (e.g., Krouse and Thode, 1962; Rees and Thode, 1966; Rashid and Krouse, 1985; Johnson et al., 1999; Johnson and Bullen, 2003; Mitchell et al., 2013). In contrast, there is little isotopic fractionation (<0.5‰) associated with oxidation of reduced Se species (Johnson et al., 1999; Johnson, 2004). As discussed in Section 2.5.1, Se is very likely dissolved in MORB melts as reduced Se^{2-}. Since MORB forms and evolves at fO_2 around FMQ buffer (Ballhaus, 1993; Bézos and Humler, 2005; Cottrell and Kelley, 2011; Labidi et al., 2014; Zhang H. L. et al., 2018), transition between Se^{4+} (with/without Se^{6+}) and Se^{2-} and hence associated Se isotopic fractionation, if any, is expected to be very subtle across the entire MORB evolution starting from the mantle source region.

Despite the narrow range in $\delta^{82/76}Se$ values of the PAR glasses (-0.16 ± 0.13‰ on average), subtle but resolvable differences (up to ~0.25‰ vs the external reproducibility of 0.09‰) is observed between some samples (Fig. 2.3). These differences seem to be unrelated to the sample latitude, tectonic discontinuity, or ridge axial depth (Fig. 2.2a and b; Supplementary Fig. S2.1). Hamelin et al. (2011) demonstrated clear latitudinal variations in radiogenic isotopes (He–Sr–Nd–Hf–Pb) along the studied PAR segments (65–56°S and 53–41°S), which is interpreted to result from progressive mixing of the depleted Pacific upper mantle and gradually increasing

amount of recycled oceanic crust component northwards. However, Se isotope compositions of the northern and southern PAR segments are essentially the same (−0.14 ± 0.12‰ and −0.19 ± 0.14‰, respectively; 2 s.d.) and show no clear latitudinal variation (Fig. 2.2a). There is also no covariation between $\delta^{82/76}$Se (or Se–Te contents) and radiogenic isotope ratios of the samples (not shown). Furthermore, the Se isotopic variations are not correlated with (1) Se content of the melt (158–219 ng g^{-1}; Fig. 2.2c), (2) magmatic differentiation index Mg# (0.68–0.40; Fig. 2.10a), or (3) Se/Te ratio (~43–189) that is demonstrated above as a direct indicator of sulfide liquid–silicate melt fractionation (Fig. 2.4c and Fig. 2.10b; Section 2.5.2.1). Besides, two highly evolved PAR glasses that show clear evidence of magnetite-triggered sulfide fractionation (PAC1DR10-1g and PAC2 DR20-1; Fig. 2.4c and e) have Se isotope compositions (−0.24 ± 0.09‰ and −0.15 ± 0.09‰) indistinguishable from those of less evolved samples (MgO >5wt.%). As discussed earlier, the predominantly fractionating sulfide phase in response to liquidus magnetite appearance after MgO <5wt.% is very likely crystalline MSS. Altogether, we suggest that there is no resolvable Se isotopic fractionation within uncertainty (0.09‰; 2 s.d.) during shallow-level magmatic differentiation that involves segregation of silicate crystals and sulfide liquid and/or MSS (i.e., $\Delta^{82/76}Se_{sulf-sil} \approx 0.00$‰). Effects of pressure on Se isotopic partitioning at mantle conditions relevant to MORB petrogenesis (Fig. 2.7) is expected to be negligible (Young et al., 2015), as in the case of S isotopes (Labidi and Cartigny, 2016). We therefore argue that there is negligible $^{82}Se/^{76}Se$ fractionation during partial melting of the upper mantle, which also involves equilibrium partitioning of Se between sulfide liquid (probably without MSS) and silicate melt (Fig. 2.8 and Fig. 2.9; Supplementary Fig. S2.5; see Section 2.5.3.3). Accordingly, we use the observed PAR MORB average $\delta^{82/76}$Se (−0.16 ± 0.13‰; n = 27) to represent the Se isotope composition of the primary melts (Mg# = 0.73) as well as the mantle source (Fig. 2.10a and b). The apparent Se isotope variation along the PAR (up to 0.25 ± 0.13‰; e.g., Fig. 2.2 and 2.3) thus likely reflects intrinsic mantle heterogeneity.

The $\delta^{82/76}$Se values of the PAR MORBs are systematically lighter than that of all other basaltic lavas from various geological settings (e.g., oceanic/continental intraplate basalts and plume-influenced ocean ridge basalts; Fig. 2.3; Rouxel et al., 2002; Kurzawa et al., 2017; Yierpan et al., 2018; this study). Four subaerial basalts analyzed by the same technique as in this study have variable Se (~15–170 ng g^{-1}) and Te (1.0–14.2 ng g^{-1}) contents with Se/Te ratios ~3–65 (Fig. 2.10b; Yierpan et al., 2018), implying that they may have different source compositions and/or experienced different degrees of partial melting and igneous differentiation (see Section 2.5.2 and 2.5.3). These petrogenetic processes however should result in no Se

isotopic fractionation as discussed above. Their non-chondritic and significantly heavier $\delta^{82/76}$Se (+0.21 ± 0.15‰) compared to MORB could thus reflect (1) so far unidentified effects of non-magmatic processes (such as subaerial eruption-related degassing; e.g., Floor and Román-Ross, 2012; Floor et al., 2013) and/or (2) Se isotopic variability among terrestrial igneous reservoirs ($\delta^{82/76}$Se between −0.16 ± 0.13‰ and +0.21 ± 0.15‰; Fig. 2.3 and 2.10b).

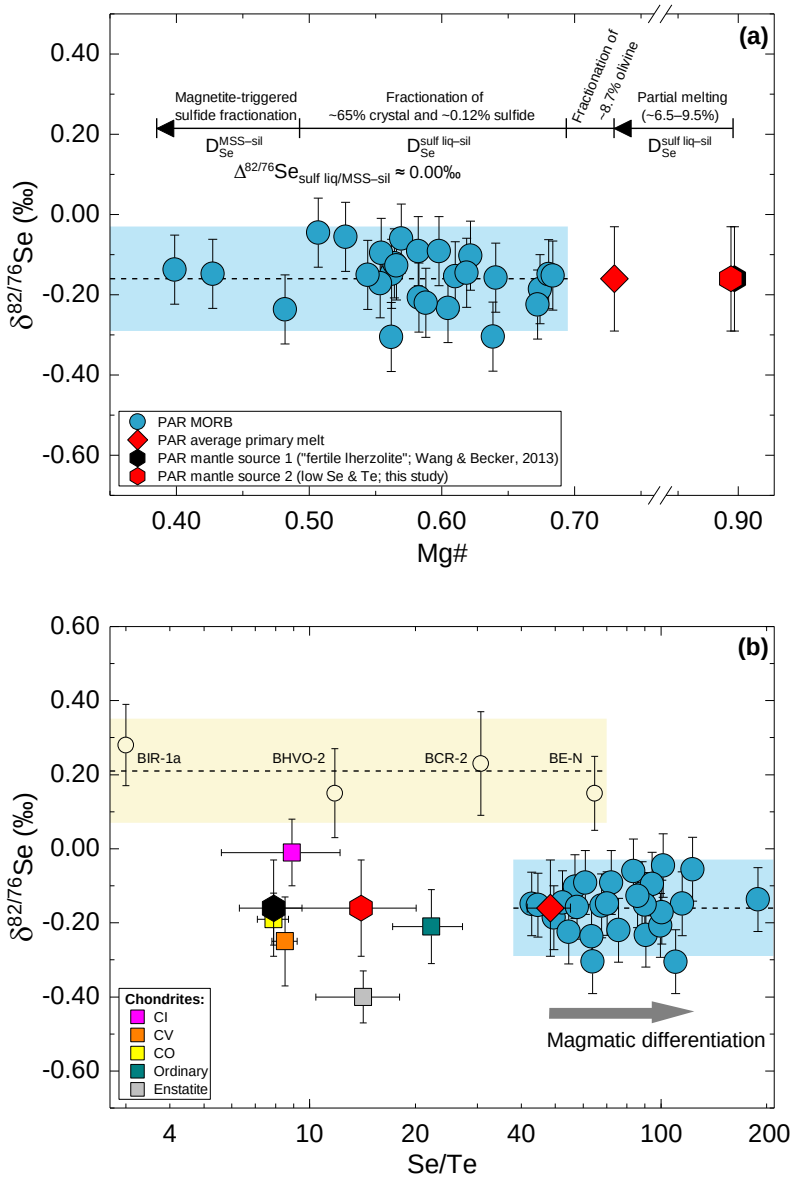

Fig. 2.10 $\delta^{82/76}$Se plotted against (a) Mg# and (b) Se/Te ratio across the entire MORB evolution according to our models of magmatic differentiation and partial melting. Also shown for comparison are $\delta^{82/76}$Se (± 2 s.d.) and Se/Te (± 1 s.d.) data for basaltic reference materials and main chondrite groups (also see Fig. 2.3). Each shaded field represents the average $\delta^{82/76}$Se with 2 s.d. uncertainty and range of Mg# (a) or Se/Te (b). The mass fractions of the fractionated crystals and sulfides are relative to the initial primary melt (a). Selenium isotope compositions of the primary PAR melt and MORB mantle source are represented by the average $\delta^{82/76}$Se value of all PAR glasses

(−0.16 ± 0.13‰; 2 s.d., n = 27) based on the demonstrated absence of Se isotope fractionation during Se partitioning between sulfide (liquid and/or crystalline MSS) and silicate melt ($\Delta^{82/76}Se_{sulf-sil} \approx 0.00$‰). Both mantle source compositions estimated for PAR MROBs were shown: 80 ± 17 and 11 ± 1.7 ng g^{-1} (source 1) and 49 ± 11 and 3.5 ± 1.3 ng g^{-1} (source 2) Se and Te, respectively (also see Fig. 2.8 and Fig. 2.9; symbols in (a) were slightly staggered for clarity). $\delta^{82/76}$Se and Se/Te ratios of all basaltic reference materials are from this study and Yierpan et al. (2018) and $\delta^{82/76}$Se of BCR-2 is also taken from Kurzawa et al. (2017) (also see Fig. 2.1). For chondrites, $\delta^{82/76}$Se are from Labidi et al. (2018) and the Se/Te ratios from Wasson and Kallemeyn (1988), Lodders et al. (2009), Schaefer and Fegley (2010), and Wang and Becker (2013).

2.5.5. Implications for the origin of Se and Te in the mantle

The upper mantle abundances of Se, Te, and S have been suggested to be primarily established by addition of volatile-rich chondritic late veneer after core formation (Wang and Becker, 2013) because these elements are predicted to behave as highly siderophile elements during core–mantle differentiation based on the extrapolation of low-P (1–19 GPa) metal–silicate partitioning experiments (Rose-Weston et al., 2009; Steenstra et al., 2017). However, this simple late-veneer origin of S cannot explain the non-chondritic S isotope composition of the mantle, which requires a significant portion of S in the pre-late veneer mantle (Labidi et al., 2013, 2016). This is further supported by more recent partitioning experiments on S (Boujibar et al., 2014; Suer et al., 2017). Suer et al. (2017) showed that S becomes less siderophile with increasing pressure than previously predicted, with the observed $D_S^{metal-silicate}$ of ~10–55 versus ~1000 predicted by Rose-Weston et al. (2009), at core forming condition (~40–55 GPa; Jackson et al., 2018). In this context, if the late veneer consisted of volatile-rich materials (e.g., McDonough and Sun, 1995; Wang and Becker, 2013), suprachondritic S/Se and S/Te ratios should be expected for the mantle because the Se–Te budget was primarily accounted for by late veneer; alternatively, if the pressure dependence of $D_{Se\ or\ Te}^{metal-silicate}$ determined at <20 GPa (Rose-Weston et al., 2009; Steenstra et al., 2017) was lowered at higher pressure (or temperature) to some extent as in the case of S (Suer et al., 2017) and other elements (e.g., Siebert et al., 2013), the possibility that mantle Se–Te budget represents metal–silicate equilibration would remain open (as suggested for the Moon; Steenstra et al., 2017).

As discussed earlier, lithospheric lherzolites that were used to estimate PM Se–Te abundances (Wang and Becker, 2013) preserve little primary melt depletion signature and very likely represent refertilized (previously-depleted) harzburgites (Fig. 2.9b and c; also see Le

Roux et al., 2007; König et al., 2014). Unlike Cu and Ag that show limited fractionation during different petrogenetic processes (e.g., mantle melting, refertilization, and melt transport; Wang and Becker, 2015b), different and non-systematic Se–Te fractionation occurs during these processes depending on the host assemblages controlling the Se–Te behavior (Fig. 2.4, 2.6, and 2.9b and c; Section 2.5.3.3). This implies that the near-chondritic Se/Te ratios (7.9 ± 1.6) in worldwide "fertile lherzolites", despite the broad correlation between Se–Te and lithophile elements such as Al and Ca (Wang and Becker, 2013), should be considered with great caution as primitive signature of PM.

Mantle melts provide an alternative approach to estimate composition of the asthenospheric mantle. The MORB mantle abundances of Se–Te and other strongly chalcophile elements (e.g., Cu; Supplementary Fig. S2.5) would be essentially identical to that of PM (Fig. 2.9b and c) because average depleted MORB mantle is only ~2–3% melt-depleted from PM (Menzies et al., 1977; Salters and Stracke, 2004; Workman and Hart, 2005; Bodinier and Godard, 2014). However, this approach critically depends on the modelling parameters (Section 2.5.2.2 and 5.3.3) and hence leads to different results (Fig. 2.8 and Fig. 2.9). We obtain two distinct possible source compositions for the PAR MORB: 80 ± 17 ng g^{-1} Se and 11 ± 1.7 ng g^{-1} Te (source 1; "fertile lherzolite-like"; Wang and Becker, 2013) vs 49 ± 11 ng g^{-1} Se and 3.5 ± 1.3 ng g^{-1} Te (source 2) due to the difference in $D_{Se\ or\ Te}^{sulf\ liq–sil}$ published by Brenan (2015) and Kiseeva et al. (2017), respectively (Table 2.3; Fig. 2.9 and Fig. 2.10). Note that only $D_{Se\ or\ Te}^{sulf\ liq–sil}$ from the latter study successfully reproduces the observed Se–Te variation during MORB differentiation (Fig. 2.6b and c; Section 2.5.2.1).

On the other hand, $\delta^{82/76}$Se of PAR MORB mantle (−0.16 ± 0.13‰) is well within the range of chondritic values of −0.30 ± 0.39‰ (Vollstaedt et al., 2016) and −0.21 ± 0.31‰ (Labidi et al., 2018) (Fig. 2.3). Combined with the possible Se/Te ratios (7.9 ± 1.6 and 14.0 ± 6.1 for source 1 and 2, respectively), $\delta^{82/76}$Se of the PAR mantle appears to overlap with that of both CI chondrites and volatile-depleted carbonaceous (CV and CO) and ordinary chondrites but show a significant offset from enstatite chondrites (Fig. 2.10b). Yet, the latter have been suggested to be the main constituent of the late veneer based on Ru and Os isotopes (e.g., Meisel et al., 1996; Dauphas, 2017; Fischer-Gödde and Kleine, 2017). Interestingly, all terrestrial rocks/melts show distinctly heavier $\delta^{82/76}$Se relative to enstatite chondrites (Fig. 2.3). At this stage, it is difficult to link the late veneer material to certain chondrite groups because a robust mantle $\delta^{82/76}$Se value remains to be established and little is known regarding the role of planetary

processes on moderately volatile Se isotopes (e.g., metal–silicate equilibration and vapor loss during accretionary growth of small planetesimals; Labidi et al., 2016; Hin et al., 2017; Norris and Wood, 2017). Our result obtained here however highlights the potential of Se isotopes to contribute new constraints on planetary accretion models regarding the Earth's volatile delivery.

2.6 Conclusion

We present the first high-precision Se isotope and Se–Te elemental data for MORB glasses from the PAR (65–56°S and 53–41°S) using recently developed analytical techniques (Kurzawa et al., 2017; Yierpan et al., 2018). Almost all PAR basalts have experienced high-temperature hydrothermal fluid assimilation during magmatic differentiation, which significantly overprints the S isotope composition when it is associated with assimilation of hydrothermal sulfides (Labidi et al., 2014). However, neither of these processes affects the Se isotope composition and S–Se–Te abundances. The observed S–Se–Te variation is dominantly controlled by MORB differentiation involving segregation of immiscible sulfide liquid, which are successfully reproduced using the experimentally determined $D_{Se\ or\ Te}^{sulf\ liq–sil}$ values from Kiseeva et al. (2017); in the highly evolved melts at magnetite saturation, the dominant fractionating sulfide phase is very likely crystalline MSS, indicated by the abrupt drop in Se/Te and S/Te ratios. The differentiation-corrected Se–Te contents of the primary MORB melts are well reproduced by near-fractional decompression melting of a mantle using experimental $D_{Se\ or\ Te}^{sulf\ liq–sil}$ (Brenan, 2015; Kiseeva et al., 2017) with a mantle source containing 170–200 μg g^{-1} S but distinct Se–Te contents ("fertile lherzolite-like" 80 ± 17 and 11 ± 1.7 ng g^{-1} vs 49 ± 11 and 3.5 ± 1.3 ng g^{-1} Se and Te, respectively) due to the significant difference in $D_{Se\ or\ Te}^{sulf\ liq–sil}$ reported by these groups. Nevertheless, our model suggests that sulfide liquid–silicate melt partitioning, rather than MSS–sulfide liquid or MSS–silicate melt partitioning, predominantly controls the partitioning behavior of chalcophile elements during melting of a MORB mantle, in accordance with recent sulfide melting experiments (Zhang Z. and Hirschmann, 2016; Zhang Z. et al., 2018). This reinforces the notion that Se–Te variations (with broadly-chondritic Se/Te ratios) in "static" lithospheric lherzolites reflect significant, if not complete, metasomatic overprinting (e.g., König et al., 2014), which in turn requires a reassessment of the current PM composition (Wang and Becker, 2013).

The observed Se isotope variation along the PAR (−0.30 ± 0.09‰–−0.05 ± 0.09‰; 2 s.d., n = 27) is not systematically related to magmatic differentiation involving sulfide liquid/MSS–

silicate melt partitioning or other geochemical parameters, indicating negligible $^{82}Se/^{76}Se$ fractionation within uncertainty during decompression melting. The Se isotope composition of the Pacific mantle is thus represented by the average $\delta^{82/76}Se$ of all MORBs ($-0.16 \pm 0.13‰$). This value is significantly lighter than previously reported $\delta^{82/76}Se$ for basalts and one peridotite from diverse geodynamic settings (Rouxel et al., 2002; Kurzawa et al., 2017; Yierpan et al., 2018); meanwhile, it overlaps with $\delta^{82/76}Se$ of carbonaceous (CI and volatile depleted CV and CO) and ordinary chondrites but shows a distinct offset from that of enstatite chondrites (Labidi et al., 2018). Selenium isotope variations between different mantle reservoirs and in additional non-magmatic processes can be resolved and further investigated in order to contribute constraints on the accretion history of terrestrial volatiles.

Chapter 3

Deep mantle Se isotope record of atmospheric oxygenation

Abstract

Selenium is a chalcophile and redox-sensitive element. Due to the contrasting chemical behavior of Se species and associated isotopic fractionation, both the Se abundance and isotopes in bulk sediment and its pyrite may trace temporal changes in surface redox conditions. Global marine sediments show significant Se isotope variation, with δ^{82}Se values (deviation in $^{82}Se/^{76}Se$ relative to NIST SRM 3149 standard) ranging between ~−3‰ and +3‰. In contrast, Se isotope variability in mantle-derived rocks and melts is limited yet still resolvable (δ^{82}Se values ~−0.3‰–+0.3‰). Because of the limited Se isotopic fractionation during high-temperature processes, recycling of crustal materials such as sediments might provide a viable explanation for the observed δ^{82}Se variation in mantle samples.

Here we report on high-precision Se isotope data for 18 representative MORB glasses from the Mid-Atlantic ridge, influenced locally by the Shona and Discovery plumes. Previous studies suggested that a variety of recycled components were incorporated in the sources of these basalts. Samples devoid of plume influences (N = 4) show similar δ^{82}Se values to the average previously reported for the Pacific-Antarctic ridge basalts. This suggests that the depleted mantle has a rather homogenous Se isotope composition of $\delta^{82}Se = -0.16 \pm 0.03$‰ (95% confidence interval, N = 31). In comparison, samples influenced by enriched components originating mainly from the Discovery plume show systematic offset (up to ~0.30‰ in δ^{82}Se) from the average depleted mantle towards heavier values. For the first time, we show that Se isotope ratios are correlated with sulfur isotope ratios, as well as radiogenic isotope tracers. This illustrates a simple binary mixing between the depleted mantle and subducted components, which must be of sedimentary origin. The calculated Se abundance and δ^{82}Se for the sediment endmember shows an excellent match to the literature average for the Proterozoic marine sediments, in agreement with the conclusion obtained from the S isotope systematics. Moreover, the inferred average Se abundance of the pyrite in the subducting sediment is similar to or higher than the literature value for the mid-Proterozoic sedimentary pyrites. Our findings,

from the mantle perspective, are in favor of the recently proposed high O_2 level in the Proterozoic atmosphere. This in turn implies that, together with the atmospheric oxygen, other factors such as the availability of nutrient elements also played critical role in the progressive evolution of complex life during the 'Boring Billion'.

3.1 Introduction

Selenium behaves as a chalcophile element in the magmatic systems (Peach et al., 1990; Guo et al., 1999; Hattori et al., 2002; Brenan, 2015). As a redox-sensitive element, Se is commonly present in a variety of oxidation states (−2, 0, +4, and +6) in different geological reservoirs (Howard, 1977; Cutter and Bruland, 1984; Elrashidi et al., 1987; McNeal and Balistrieri, 1989). The igneous inventory of Se is probably dominated by its reduced form (Se^{2-}), either partitioned into mantle/magmatic sulfides or dissolved in the silicate magma (Brenan, 2015; Yierpan et al., 2019). In comparison, Se in natural aqueous environments dominantly occurs as highly soluble selenate (SeO_4^{2-}) and selenite (SeO_3^{2-}) oxyanions under oxidizing conditions, and as insoluble Se^0 and pyrite-bound Se^{2-} as well as soluble organic Se^{2-} under reducing conditions (Cutter and Bruland, 1984; Cutter and Cutter, 2001; Johnson, 2004; Johnson and Bullen, 2004; Schilling et al., 2014). Transitions between different oxidation states can induce strong mass-dependent isotope fractionation, with the most significant isotopic variations (up to ~19‰ in $^{82}Se/^{76}Se$) observed during reduction reactions (Krouse and Thode, 1962; Rees and Thode, 1966; Rashid and Krouse, 1985; Johnson and Bullen, 2003). Therefore, together with the distinct redox-dependent mobility of Se species, the Se elemental and isotopic abundances in sediment and its pyrite can be used as a proxy to constrain changes in the redox conditions of the ocean and atmosphere (Johnson et al., 1999; Large et al., 2014).

Previous studies reported considerable variations in Se isotope data for global marine sediments, with $\delta^{82}Se$ values (deviation in $^{82}Se/^{76}Se$ relative to NIST SRM 3149 standard) ranging between ~−3‰ and +3‰ (N = 699; Fig. 3.1; Shore, 2010; Mitchell et al., 2012, 2016; Wen et al., 2014; Stüeken et al., 2015a, b; Pogge von Strandmann et al., 2015; Kipp et al., 2017; Koehler et al., 2018). Although modest compared to the experimental observations, variations in the shale $\delta^{82}Se$ record show an apparent secular change from the Precambrian to the Phanerozoic, reflecting oxygenation of the deep ocean (Fig. 3.1; Stüeken et al., 2015b; Mitchell et al., 2016). On the other hand, Se isotope variability in mantle-derived rocks and melts (such as MORB, peridotites, arc lavas, and other subaerial lavas), based on a rather limited dataset, is

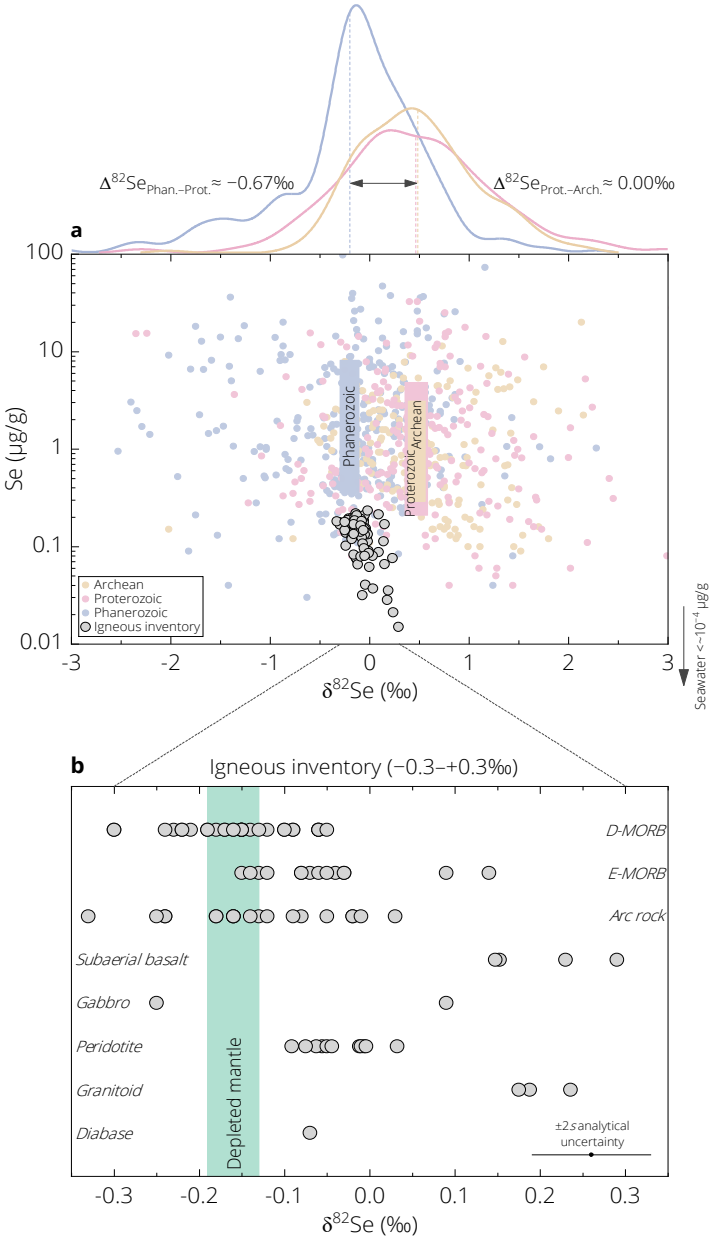

Fig. 3.1 Compiled dataset of the Se isotope compositions and Se abundances of marine sediments (N = 699) and mantle-derived rocks/melts (N = 72). All the previous analyses of marine sediments throughout the geological time are included (3250 Myr ago to present; Shore, 2010; Mitchell et al., 2012, 2016; Wen et al., 2014; Stüeken et al., 2015a, b; Pogge von Strandmann et al., 2015; Kipp et al., 2017; Koehler et al., 2018). The shaded boxes superimposed over the data in (a) represent the mean δ^{82}Se values (±95% *CI*) and log-normal mean Se abundances (±1*s*) of sediments from Archean (N = 191), Proterozoic (N = 210), and Phanerozoic (N = 298). The empirical distribution curves with mean δ^{82}Se values (dashed lines) of these groups (colour-coded) are shown in the upper panel (bin width = 0.5‰). For the mantle samples (i.e., igneous inventory), only the high-precision data obtained under intermediate precision condition (2*s* = ±0.07‰) are presented to allow comparison between samples from a variety of geodynamic settings (Kurzawa et al., 2017, 2019; Yierpan et al., 2018, 2019; Varas-Reus et al., 2019). The shaded field in (b) represents the isotope composition of the depleted mantle (−0.16 ± 0.03‰; 95% *CI*) estimated from the MAR and PAR depleted MORB δ^{82}Se data (N = 31).

much smaller yet still resolvable (δ^{82}Se values between ~−0.3‰ and +0.3‰; N = 72; Fig. 3.1; Rouxel et al., 2002; Kurzawa et al., 2017, 2019; Yierpan et al., 2018, 2019; Varas-Reus et al., 2019). These variations cannot be explained by mantle melting or crustal differentiation because there is no resolvable (at 0.09‰; 2s) Se isotope fractionation during these processes (Yierpan et al., 2019). Considering the contrasting differences in both Se isotopic compositions and abundances (e.g., $1.26^{+4.21}_{-0.97}$ μg/g in sediments and $0.12^{+0.11}_{-0.06}$ μg/g in mantle samples; log-normal mean) between the surface and igneous reservoirs (Fig. 3.1), recycling of surface materials via subduction could potentially introduce a Se isotope heterogeneity into the mantle. Similar mechanisms have been suggested for other redox-sensitive stable isotope systems such as S (Labidi et al., 2013, 2014, 2015; Beaudry et al., 2018), Fe (Williams and Bizimis, 2014; He et al., 2019; Nebel et al., 2019), Mo (Bezard et al., 2016; Willbold and Elliott, 2017), and U (Andersen et al., 2015).

In this work, we report new high-precision Se isotope and Se–Te abundance data for 18 well-characterized MORB glasses (N = 18) from the southern and northern sections of the Mid-Atlantic ridge (MAR; Supplementary Fig. S3.1). They include 14 enriched MORBs that incorporate recycled components in their mantle sources due to the interaction between the Discovery and Shona plumes and the southern MAR (Douglass et al., 1995, 1999). Sulfur isotope systematics of these basalts suggest that the enriched components are chiefly contributed by subducted marine sediments (Labidi et al., 2013). Given some similarities of S and Se with respect to the isotope and elemental behavior in both high- and low-temperature environments (e.g., Johnson and Bullen, 2004; König et al., 2019; Yierpan et al., 2019), the selected sample suite is ideal for investigating the influence of crustal recycling on the Se isotope signature of the mantle. This is supplemented by 2 depleted MORBs from each sections of the MAR devoid of plume contribution (Supplementary Fig. S3.1; White et al., 1978; Douglass et al., 1999). Additionally, we report on the first δ^{82}Se analyses of 3 well-characterized granitoids from the Västervik area in Sweden (Kleinhanns et al., 2015), resembling materials derived from the continental crust. All these new data combined with the published data for the Pacific-Antarctic ridge (PAR) basalts (depleted MORB; N = 27; Yierpan et al., 2019) are used to (1) determine the Se isotope composition of the depleted mantle and (2) investigate a potential Se isotope heterogeneity in the mantle and its origin. This may provide new means to trace the redox conditions of ancient surface environments using redox-sensitive isotope record from the mantle perspective.

3.2 Samples and background

The MORB samples analyzed here are quenched submarine lavas dredged from the southern (44°–53°S, S-MAR; N = 16) and northern (51°–52°N, N-MAR; N = 2) sections of the MAR during the *R/V Maurice Ewing* cruise EW93-09 and *R/V Trident* cruise TR138, respectively (White et al., 1978; Schilling et al., 1983; Douglass et al., 1995; 1999). Locations of the samples, mantle plumes, and relevant first-order tectonic discontinues (fracture zones) are shown in Supplementary Fig. S3.1. All these basalts were well characterized in terms of major- and trace-element abundances (Supplementary Fig. S3.2; Schilling et al., 1983; Dixon et al., 2002; le Roux et al., 2002a, b, c; Kelley et al., 2013) and radiogenic (Sr, Nd, Hf, Pb, and Os; Fig. 3.2; White et al., 1978; Douglass et al., 1999; Andres et al., 2002; Blichert-Toft et al., 2005; Escrig et al., 2005), noble gas (Moreira et al., 1995; Sarda et al., 2000), and S (Labidi et al., 2013) isotope compositions. The most prominent feature in the S-MAR is the localized interaction between the ambient asthenospheric mantle and two mantle plumes: the off-axis Discovery plume centered at 44.45°S, 6.45°W (~425 km away from the ridge) and the on-axis Shona plume centered between 50°–52.5°S, 6°W (Small, 1995; Douglass et al., 1995). A variety of recycled components have been proposed for these mantle plumes based on radiogenic isotope ratios (Fig. 3.2; see references above). Four distinct groups of S-MAR basalts can be identified: (1) depleted MORB (N = 2) from ridge segments unaffected by plumes (2) Discovery anomaly (N = 7) showing EM1 affinity with $^{87}Sr/^{86}Sr$ ratio up to 0.705728; (3) LOMU (low-μ, $\mu = {}^{238}U/^{204}Pb$) anomaly (N = 3) genetically linked to the Discovery plume but showing distinctly lower $^{206}Pb/^{204}Pb$ compared to Discovery anomaly basalts; (4) Shona anomaly (N = 4) with both EM1 and HIMU/high-μ affinities (most clearly seen in $^{206}Pb/^{204}Pb$–$^{87}Sr/^{86}Sr$ space; Fig. 3.2). The 49°S and 50°S fracture zones mark the boundaries between samples affected by the Discovery plume and Shona plume, whereas the Agulhas fracture zone offsets the Discovery anomaly samples (Douglass et al., 1995). In addition, the N-MAR samples (N = 2) are depleted MORBs from a restricted ridge segment that displays one of the most remarkable depletion signatures in the mantle (White et al., 1978; Fig. 3.2). All these MORB samples show a correspondingly wide range in their incompatible trace element compositions, with the primitive mantle-normalized $(La/Sm)_N$ ratios of 0.457–0.643 for depleted MORBs and 0.670–2.681 (mostly >1) for MORBs associated with plume enrichment (Supplementary Fig. S3.2)

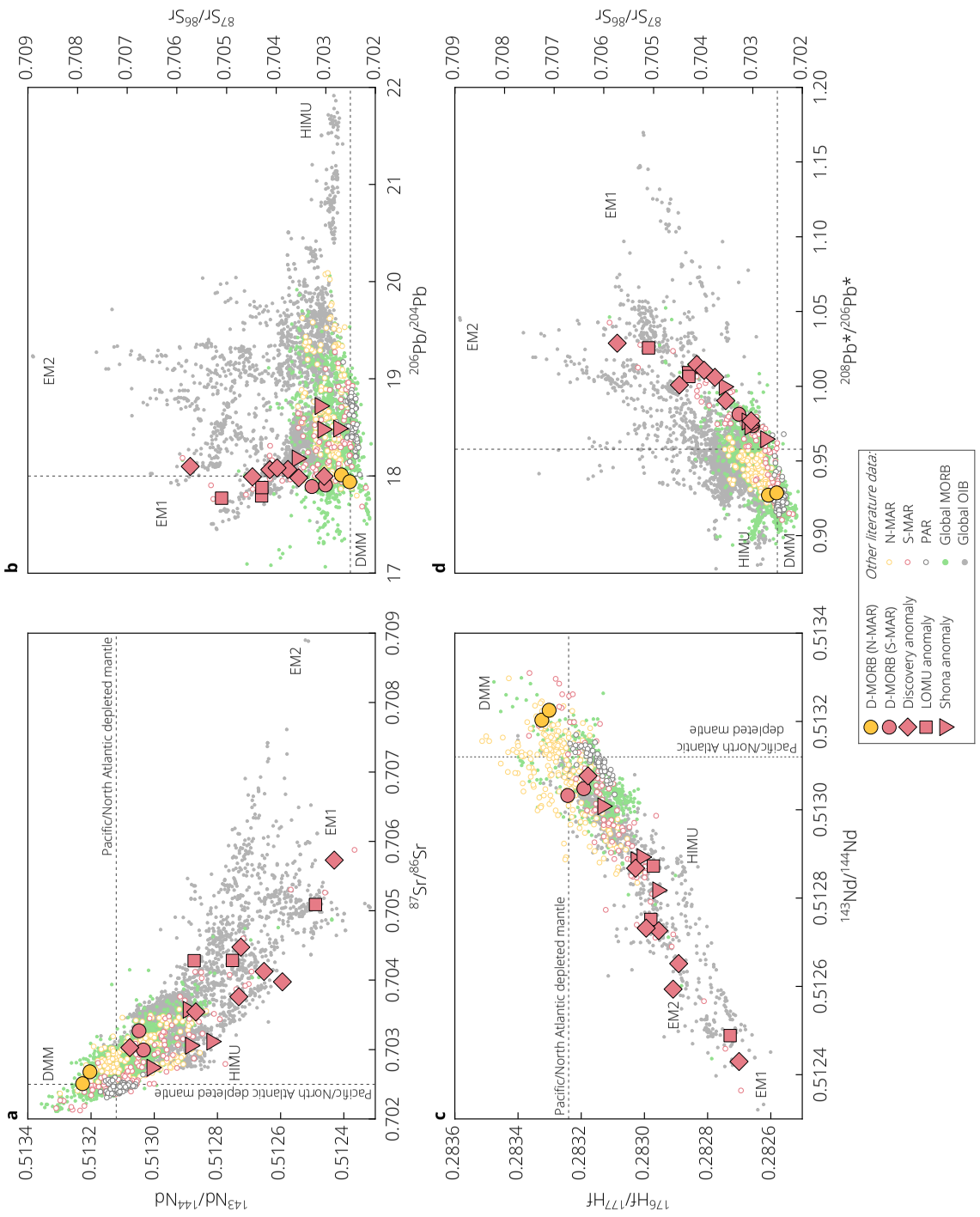

Fig. 3.2 A compilation of the radiogenic isotope data of the studied S- and N-MAR glasses in comparison with the literature data for global oceanic basalts (MORB and OIB; ocean-island basalt). The dashed lines represent the composition of the ambient depleted mantle beneath the Pacific and North Atlantic (Andres et al., 2002). $^{208}Pb^*/^{206}Pb^* = (^{208}Pb/^{204}Pb - 29.476)/(^{206}Pb/^{204}Pb - 9.307)$. Literature data comprise a more complete dataset for the entire MAR (S- and N-MAR basalts; pre-compiled by Agranier et al. (2005) and Labidi et al. (2013)) and the PAR (Vlastélic et al., 1999, 2000; Hamelin et al., 2010, 2011), superimposed onto the global MORB (pre-compiled by Stracke (2012)) and OIB data (taken from the PetDB database; http://www.earthchem.org).

On a large scale, the South Atlantic ambient depleted mantle is more enriched than the Pacific/North Atlantic depleted mantle due to the pervasive mantle pollution with DUPAL- or Indian Ocean-type mantle components (Fig. 3.2; Douglass et al., 1999; Andres et al., 2002; le Roux et al., 2002b; and references therein).

The well-characterized granitoid samples (Cordilleran-type) are from the Västervik area in the southeast Sweden, which is located between two main tectonic domains, Transscandinavian Igneous Belt and Svecofennian domain, in the Baltic Shield (Nolte et al., 2011; Kleinhanns et al., 2015). They have intrusion ages of ~1800 Ma (Kleinhanns et al., 2015) and therefore provide insights into the Se isotope composition of the Proterozoic continental crust.

3.3 Analytical techniques

3.3.1 Sample dissolution and chemical separation

The MORB samples analyzed here are optically fresh glasses. All samples were successively cleaned with 18.2 MΩ·cm H_2O and ethanol in an ultrasonic bath (for 15 min) before they were powdered in an agate mortar. The mortar was always cleaned twice with quartz (pro analysi, Merck) and ethanol before each grinding. The details of the subsequent sample dissolution are reported by Yierpan et al. (2018). Briefly, small amounts of sample unknowns (10–15 mg MORB and ~100 mg granitoids) were first analyzed for their Se contents via isotope dilution method (see next Section) after a simple dissolution and single-stage chemical separation procedure (e.g., Yierpan et al., 2019; Kurzawa et al., 2019). About 190–1500 mg sample powders (Table 3.1 and 3.2; Supplementary Table S3.1) were then mixed with adequate amounts of ^{74}Se–^{77}Se and ^{125}Te spikes and dissolved in a mixture of HF–HNO_3 at 85 °C. This is followed by evaporation at 65 °C and multiple successive treatments with HCl (heating at 130 °C and complete evaporation at 85 °C) in order to maximize Ge removal as $GeCl_4$ (Luais, 2012). Although there is concomitant Se loss in HCl matrix at temperatures higher than ~60 °C (Kurzawa et al., 2017; Yierpan et al., 2018), quantitative elimination of Ge is preferred because it is the major matrix-related isobaric interference.

The Se separation was performed via anion and cation exchange chromatography using 7 mL of new and pre-cleaned AG1-X8 and AG 50W-X8 resins (100–200 mesh, Eichrom). Two different protocols were followed during the first stage, namely ‘HCl chemistry’ and ‘HF

chemistry' (Table 3.1 and 3.2; Supplementary Table S3.1). The former was described in detail by Yierpan et al. (2018). Briefly, the dry samples were loaded onto the columns in 4 N HCl. Selenium and most matrix elements are eluted, whereas Fe and Te are retained in the resin. After eluting Fe with 2 N HCl–5 N HF mixture, Te was collected in 0.4 N HCl. The new 'HF chemistry' used in this work was modified from the Ge purification procedure of Rouxel et al. (2006). The dry samples were first converted into fluoride form by dissolution and evaporation in 1 mL 27 N HF at 65 °C. They were then taken up in 5 mL 1 N HF and centrifuged to separate the supernatant and insoluble fluorides, which contain large proportions of of Mg, Al, Ca, and other trace elements (Yokoyama et al., 1999; Rouxel et al., 2006; Cotta and Enzweiler, 2012) but not Se (Yierpan et al., 2018). After conditioning the resin with 10 mL 1 N HF, the supernatant solutions were loaded onto the columns, followed by addition of 9 mL 1 N HF. Selenium and some matrix fractions (Fe, alkalis, and some transition metals such as Co, Ni, and Cu) were eluted, whereas Ge, Al, and Ti were retained (Faris, 1960; Rouxel et al., 2006; Luais, 2012; this study). The Se cuts 14 mL 1 N HF) were finally evaporated at 65 °C. Subsequent to the first-stage separation following these two protocols, all Se cuts were further purified using the cation resin with 0.1 N HNO_3 following Yierpan et al. (2018). Samples processed through the 'HF chemistry' generally yielded Se recoveries of ~35–80%, overall lower compared to the 'HCl chemistry' (mostly >~80%; see Yierpan et al., 2019). These samples also arbitrarily contained residual Ge, as in the case of the 'HCl chemistry'. However, the 'HF chemistry' has the advantage that larger amounts of sample digests (up to ~1500 mg; Table 3.1 and 3.2) can be processed with 7 mL resin, in comparison to the 'HCl chemistry' (up to ~450 mg).

3.3.2 Elemental and isotopic analyses

All analyses were performed at the Isotope Geochemistry laboratory, Department of Geosciences, University of Tübingen. The Se and Te isotope dilution concentration data were obtained on a ThermoFisher Scientific iCAP-Qc quadrupole inductively coupled plasma mass spectrometer (ICP-MS) linked with an ESI hydrideICP hydride generator following the method of Yierpan et al. (2018). The Se isotope compositions were determined on a ThermoFisher Scientific NeptunePlus multi-collector ICP-MS linked with a HGX-200 hydride generator. The double spike approach allows for the correction of instrumental and chemistry-related mass fractionation. Details of the instrumental analysis and double spike conversion are outlined in Kurzawa et al. (2017). Before the final analyses, sample solutions (1 mL in 2 N HCl) were always monitored for residual Ge and further evaporated at 85 °C in case of any detectable Ge

(see Section 3.3.1). The procedural blank solutions (N = 4) were also checked at this stage, which yielded background signal intensities for all Se isotopes (also see Yierpan et al., 2019). Each sample analysis was bracketed by 30 ng/mL spiked NIST SRM 3149 standard solution and Se isotope composition is presented relative to the NIST SRM 3149 using δ^{82}Se notation. Most sample solutions contained 10–30 ng Se, which yields an internal error of <0.07‰ (95% confidence interval (*CI*) based on 40 cycles of integration) for an individual measurement (Table 3.1 and 3.2; Supplementary Table S3.1). Several MH-495 solutions (inter-laboratory standard; 30 ng/mL) were included in each analytical session to control the data quality. We obtain an average δ^{82}Se of −3.25 ± 0.07‰ (2*s*, n = 53), identical to the MH-495 data previously obtained under intermediate precision conditions (i.e., in the University of Tübingen; Supplementary Table S3.2; Yierpan et al., 2018, 2019; Kurzawa et al., 2019; Varas-Reus et al., 2019). Together, they allow us to estimate the 2*s* analytical precision of the method and yield an average δ^{82}Se = −3.25 ± 0.07‰ (2*s*, n = 200).

The international rock standards processed together with the samples are listed in Supplementary Table S3.1. The δ^{82}Se values of 4 USGS rock standards BHVO-2 (+0.14 ± 0.10‰; 2*s*, n = 4), BCR-2 (+0.27 ± 0.05‰; 95% *CI* internal error, n = 1), BIR-1a (+0.33 ± 0.06‰; 95% *CI* internal error, n = 1), and W-2a (−0.05 ± 0.10‰; 2*s*, n = 2) are all in excellent agreement with the published data: BHVO-2 (+0.15 ± 0.12‰; n = 12), BCR-2 (+0.23 ± 0.14‰; n = 10), BIR-1a (+0.28 ± 0.11‰; n = 5), and W-2a (−0.07 ± 0.12‰; n = 7) (uncertainties are 2*s* of the mean; Kurzawa et al., 2017; Yierpan et al., 2018, 2019). To extend the δ^{82}Se dataset for mantle samples we additionally report on analyses of other certified rock standards JGb-1, MRG-1, and JA-3. The external reproducibility of our method for non-glass matrices are evaluated by pooling over all replicate analyses of rock standards (each >3 times) under intermediate precision conditions (e.g., Hin et al., 2017):

$$s_p = \sqrt{\frac{\sum_{i=1}^{N}\sum_{j=1}^{n_i}\left(\delta_{ij} - \bar{\delta}_i\right)^2}{\sum_{i=1}^{N}(n_i - 1)}} \tag{3.1}$$

where s_p is the pooled standard deviation, N is the number of samples, n_i is the number of replicate analyses of a sample, and δ_{ij} and $\bar{\delta}_i$ represent the individual and average δ^{82}Se of a sample, respectively. This approach requires a homogeneity of variances across N groups of samples. This is validated by running a Bartlett's test over 5 samples and 48 analyses (47

digests), which yields a test statistic of 0.69 and *p*-value of 0.95. Finally, we obtain an external reproducibility of $2s_p$ = ±0.12‰ for non-glass samples (Supplementary Table S3.1).

A recent study on PAR MORB reported higher reproducibility of 0.09‰ for glass δ^{82}Se data (Yierpan et al., 2019). Here, we combine the replicate analyses (>3 times) of 3 MAR glasses, which were randomly selected and processed via two different separation protocols (Section 3.3.1), and the previously analyzed PAR glass, to re-evaluate the method reproducibility for glasses (Table 3.1). These groups of samples (N = 4, n_i = 23) pass the null hypothesis of the Bartlett's test with a test statistic of 1.57 and *p*-value of 0.67. Therefore, Eq. 3.1 can be used to calculate the pooled external reproducibility, which yields $2s_p$ = ±0.08‰ (Table 3.1). This is similar to the analytical precision (±0.07‰) and considerably lower than the reproducibility for non-glass matrices (±0.12‰), attesting to a significant sample homogeneity of glasses with respect to Se isotopes.

Table 3.1 Individual analyses of Se isotope composition of the Mid-Atlantic ridge basalts and a Pacific-Antarctic ridge basalt.

	Individual measurement				Mean[d]		
Sample	Sample weight digested (mg)	δ^{82}Se (‰)	Internal error (95% *CI*)[c]	Se (ng/g)	δ^{82}Se (‰)	Uncertainty	Se (ng/g)
South Atlantic ridge							
EW9309 41D-1g	308.28	-0.03	0.04	144	-0.06	0.08	144
	208.77	-0.08	0.08	145			
EW9309 40D-1g	315.88[a]	-0.23	0.05	146	-0.18	0.08	147
	316.42[b]	-0.17	0.10	147			
	316.42[b]	-0.15	0.05	147			
EW9309 34D-1g	302.36	-0.07	0.04	161	-0.07	0.08	160
EW9309 33D 1g	326.75	-0.06	0.04	126	-0.03	0.08	125
	249.38	0.01	0.06	125			
EW9309 28D-1g	315.52	-0.16	0.09	156	-0.14	0.08	156
	323.08[a]	-0.12	0.06	156			
EW9309 25D-1g	366.37	0.05	0.06	89	0.09	0.08	88
	349.07	0.16	0.11	88			
	279.17	0.08	0.08	89			
	282.61[a]	0.08	0.06	88			
EW9309 2D-1g	300.29	-0.10	0.06	132	-0.08	0.04	132
	275.94[b]	-0.05	0.06	132			
	275.94[b]	-0.08	0.07	132			
	215.94	-0.10	0.07	133			
EW9309 4D-3g	323.71	-0.04	0.04	153	-0.04	0.08	154
	312.54[a]	-0.03	0.07	153			
EW9309 5D 5g	327.89	-0.03	0.04	132	-0.06	0.08	132

Sample	Individual measurement				Mean[d]		
	Sample weight digested (mg)	δ^{82}Se (‰)	Internal error (95% *CI*)[c]	Se (ng/g)	δ^{82}Se (‰)	Uncertainty	Se (ng/g)
	294.06[a]	-0.09	0.10	133			
EW9309 7D-1g	326.18	0.09	0.05	112	0.14	0.08	113
	196.85	0.15	0.07	114			
	406.76[a]	0.18	0.09	113			
EW9309 8D-1g	320.42	-0.03	0.05	152	-0.05	0.08	152
	188.21	-0.04	0.07	152			
	299.23[a]	-0.08	0.03	153			
EW9309 9D-3g	257.39	-0.03	0.04	140	-0.03	0.04	139
	239.61	-0.04	0.04	139			
	244.32	-0.07	0.05	142			
	262.65	-0.01	0.04	136			
	260.52	0.03	0.06	137			
	356.77[a]	-0.04	0.04	139			
EW9309 15D-1g	339.95	-0.12	0.03	213	-0.13	0.08	209
	319.97[a]	-0.14	0.04	209			
EW9309 21D-1g	329.60	-0.11	0.04	165	-0.12	0.08	165
	309.97[a]	-0.13	0.06	165			
EW9309 23D-1g	303.32	-0.19	0.05	188	-0.15	0.08	186
	302.05[a,]	-0.10	0.07	188			
EW9309 22D-3g	307.20[b]	-0.10	0.05	183	-0.08	0.08	183
	307.20[b]	-0.06	0.05	183			
North Atlantic ridge							
TR138 09D-2g	403.57	-0.17	0.03	162	-0.17	0.08	166
TR138 08D-1g	401.88	-0.20	0.04	150	-0.19	0.08	150
	252.63	-0.18	0.05	150			
Pacific-Antarctic ridge							
PAC2 DR33-1	150	-0.16	0.03	201	-0.15	0.03	199
	210[b]	-0.10	0.04	198			
	210[b]	-0.11	0.07	198			
	232	-0.16	0.03	198			
	238	-0.19	0.04	198			
	241	-0.18	0.03	197			
	255	-0.22	0.03	199			
	402[b]	-0.12	0.04	201			
	402[b]	-0.10	0.05	201			

Note: the Pacific-Antarctic ridge glass data are from Yierpan et al. (2019).

[a] Sample digests processed through the new 'HF chemistry'. All other sample digests were processed through the 'HCl chemistry' following Yierpan et al. (2018).

[b] Different aliquots of a single sample digest measured separately.

[c] Internal error (95% confidence interval; *CI*) based on 40 cycles of integration in each individual measurement.

[d] Uncertainties on δ^{82}Se are 95% *CI* if the number of analyses n_i>3, or the $2s_p$ external reproducibility of 0.08‰ (estimated for glass matrices) if $n_i \leq 3$ (see Section 3.3.2 and 3.4). Uncertainties on Se abundances are ~2% two relative standard deviation (external reproducibility for glass matrices; this work and Yierpan et al., 2019). Se abundances include both isotope dilution (n_i = 1 for all samples) and double spike inversion data (see Section 3.3).

3.4 Results

Selenium isotope compositions and elemental abundances of MAR glasses and Västervik granitoids are reported in Table 3.1, 3.2, and 3.3. Supplementary Table S3.3 presents a compilation of Se isotope and Se–Te abundances (from this work) and major/trace element and radiogenic/stable isotope compositions (in the literature) of the studied MAR glasses (for the compiled datasets of the entire MAR section, see Agranier et al., 2005; Labidi et al., 2013; Kelley et al., 2013). The radiogenic isotope compositions of the samples are also presented in Fig. 3.2 together with the worldwide oceanic basalts, which shows the prominent regional heterogeneity beneath the MAR mantle (see Section 3.2).

Table 3.2 Selenium isotope and elemental abundances of the Västervik granitoids.

Sample	Granitoid group	Age (Ma)[a]	Sample weight digested (mg)[b]	δ^{82}Se (‰)[c]	Internal error (95% *CI*)	Se (ng/g)[c]
SES 3-05	Quartzmonzonite–Monzogranite	1803	1498.53	0.24	0.05	21.2
SES 19-05	Quartzmonzonite–Monzogranite	1812	1003.71	0.19	0.05	35.4
SES 1-96	Monzogranite	1809	1213.43	0.18	0.07	28.3

[a] U–Pb age from Kleinhanns et al. (2015).
[b] Samples were processed through the 'HF chemistry' (Section 3.3.1).
[c] External uncertainties on δ^{82}Se and Se contents are estimated with the external reproducibility of 0.12‰ ($2s_p$) and 4% two relative standard deviation calculated for non-glass samples (Section 3.3.2; Yierpan et al., 2018).

In the following (unless otherwise specified), the quoted uncertainty on a MORB δ^{82}Se value is ±95% *CI* for the mean if n_i>3, or the $2s_p$ external reproducibility of ±0.08‰ if $n_i \leq 3$ (see above; Table 3.1 and 3.2). Almost all the MAR samples have been analyzed more than once. Replicate analyses of a sample (glass and rock standard) processed by the two different separation protocols (Section 3.3.1) yield identical results within uncertainty, further attesting to the accuracy of our analytical procedure. The Se isotope composition of the MAR glasses (N = 18) vary from −0.19 ± 0.08‰ (TR138 08D-1g; N-MAR depleted MORB) to +0.14 ± 0.08‰ (EW9309 7D-1g; LOMU anomaly), extending the δ^{82}Se range observed for the PAR depleted MORBs (−0.30 ± 0.08‰–−0.05 ± 0.08‰; N = 27; Yierpan et al., 2019) towards heavier values (Fig. 3.1b). Similar observations have been made for the S isotope compositions of MORB glasses from these two ridges (Labidi et al., 2013, 2014). Systematic variations are observed among different groups of samples: δ^{82}Se values of D-MORBs from the S- and N-MAR (−0.19 ± 0.08‰–−0.06 ± 0.08‰; N = 4) and Shona anomaly MORBs (−0.15 ± 0.08‰–−0.08 ± 0.08‰; N = 4) both fall within the PAR δ^{82}Se range, whereas the majority of samples associated with the Discovery plume (i.e., Discovery and LOMU anomalies; N = 10) show

heavier values (e.g., EW9309 25D-1g and 7D-1g with δ^{82}Se of +0.09 ± 0.08‰ and +0.14 ± 0.08‰, respectively). The largest δ^{82}Se variation within the MAR basalts (~0.33‰) is significantly higher than the external reproducibility of the method. The calculated Mean Squared Weighted Deviation (MSWD) or reduced χ^2 for the entire MAR δ^{82}Se dataset is 4.71, which well exceeds the 95% confidence interval of 0.44–1.78 given by the χ^2 statistics. This suggests that the observed spread in Se isotope compositions of these MORBs cannot be accounted for by analytical uncertainties alone.

Table 3.3 Selenium, sulfur and radiogenic isotope compositions of the Mid-Atlantic ridge basalts.

Sample	Type	δ^{82}Se (‰)[a]	n[a]	$^{87}Sr/^{86}Sr$[b]	$^{143}Nd/^{144}Nd$[b]	δ^{34}S (‰)[b]
Southern Mid-Atlantic ridge						
EW9309 41D-1g	depleted MORB	−0.06 ± 0.08	2	0.703273	0.513048	−1.04
EW9309 40D-1g		−0.18 ± 0.08	2 (3)	0.702997	0.513033	−1.21
EW9309 34D-1g	Discovery anomaly	−0.07 ± 0.08	1	0.703544	0.512868	−1.23
EW9309 33D 1g		−0.03 ± 0.08	2	0.704475	0.512726	−0.58
EW9309 28D-1g		−0.14 ± 0.08	2	0.703028	0.513077	−0.83
EW9309 25D-1g		+0.09 ± 0.08	4	0.705728	0.512430	1.05
EW9309 2D-1g		−0.08 ± 0.04	3 (4)	0.704127	0.512652	−0.14
EW9309 4D-3g		−0.04 ± 0.08	2	0.703762	0.512732	−0.62
EW9309 5D 5g		−0.06 ± 0.08	2	0.703976	0.512594	−0.42
EW9309 7D-1g	LOMU anomaly	+0.14 ± 0.08	3	0.705093	0.512489	0.03
EW9309 8D-1g		−0.05 ± 0.08	3	0.704286	0.512752	−0.48
EW9309 9D-3g		−0.03 ± 0.04	6	0.704284	0.512873	−0.50
EW9309 15D-1g	Shona anomaly	−0.13 ± 0.08	2	0.702741	0.513008	−1.38
EW9309 21D-1g		−0.12 ± 0.08	2	0.703115	0.512818	−1.06
EW9309 23D-1g		−0.15 ± 0.08	2	0.703058	0.512886	−0.91
EW9309 22D-3g		−0.08 ± 0.08	1 (2)	0.703576	0.512893	−0.59
Northern Mid-Atlantic ridge						
TR138 09D-2g	depleted MORB	−0.17 ± 0.08	1	0.70268	0.513203	
TR138 08D-1g		−0.19 ± 0.08	2	0.70251	0.513226	
Pacific depleted mantle[c]		**−0.16 ± 0.03**		**0.70248 ± 0.00014**	**0.51311 ± 0.00003**	**−1.40 ± 0.5**
Depleted mantle[d]		**−0.16 ± 0.03**		**0.70211–0.70263**	**0.51310–0.51328**	**−1.40 ± 0.5**

[a] Uncertainties are 95% *CI* if the number of analyses n_i>3 or the $2s_p$ external reproducibility of 0.08‰ (estimated for glass matrices) if n_i≤3 (see Section 3.3.2 and 3.4); n = number of sample digestions; the number in parentheses refers to n_i.

[b] Literature data from White et al. (1978), Douglas et al. (1999), and Labidi et al. (2013).

[c] Represented by the average δ^{82}Se (±95% *CI*, N = 27; Yierpan et al., 2019) and Sr–Nd isotopic ratios (±95% *CI*, N = 66; Vlastélic et al., 1999, 2000; Hamelin et al., 2010, 2011) of all Pacific–Antarctic MORBs and the previously estimated δ^{34}S (±1*s*; Labidi et al., 2014) for the Pacific depleted mantle.

[d] δ^{82}Se (±95% *CI*, N = 31) is estimated using all depleted MORB data for the MAR and PAR; Sr–Nd isotopic ratios from Kimura et al. (2017) and δ^{34}S (±1*s*) from Labidi et al. (2014).

Selenium abundances of the MAR basalts span a larger range (88–209 ng/g; N = 18) compared to the PAR basalts (158–219 ng/g; N = 27). All the depleted MORBs from these two localities (N = 31), including both primitive and highly evolved samples (MgO contents 4.52–8.85 wt. %) display apparently linear Se–S and Se–Te co-variation arrays with opposite respective trends (Fig. 3.3). The MAR samples associated with plume influences however show considerable scatter from the depleted MORB array (Fig. 3.3).

The Västervik granitoids have a remarkably narrow range in δ^{82}Se values (+0.18 ± 0.12‰–+0.24 ± 0.12‰; N = 3) with significantly low Se abundances (21–35 ng/g; N = 3). They show similar δ^{82}Se values to the subaerial basalts (all non-glass rock standards), both isotopically heavier than MORB (Fig. 3.1).

3.5 Discussion

3.5.1 Selenium elemental and isotopic variability of MORB

Selenium is a chalcophile element (Peach et al., 1990; Guo et al., 1999; Hattori et al., 2002; Patten et al., 2013; Brenan, 2015; Kiseeva et al., 2017) and its abundance in mantle-derived melts are dominantly controlled by the behavior of sulfide phases present during partial melting and igneous differentiation (Hertogen et al., 1980; Lissner et al., 2014; Yierpan et al., 2019). Previous studies suggested that almost all MORB melts with near-primitive to highly evolved compositions (~9–4.5 wt. %) are sulfide-saturated and thus experience continuous Se removal by sulfide segregation during their magmatic evolution (Fig. 3.3; Lissner et al., 2014; Jenner et al., 2015; Smythe et al., 2017; Yierpan et al., 2019). Compared to the strictly co-genetic PAR basalts that show strong correlation of Se with magmatic differentiation indexes such as MgO and FeO_T and other chalcophile elements such as S and Te (Yierpan et al., 2019), the MAR samples shows little or weak correlation between Se and other indexes (e.g., Fig. 3.3). Only the depleted MAR basalts plot close to the PAR suite with respect to both the Se–S and Se–Te variations. These depleted MORBs (N = 31) follow linear co-variation arrays with opposite respective trends (Fig. 3.3), suggesting that sulfide liquid–silicate melt partitioning of these elements is in the order of Te>Se>S as previously observed (e.g., Brenan, 2015; Wang et al., 2015; Yierpan et al., 2019). The MAR suite shows large scatter around the linear array mainly because (1) the PAR basalts were generated from melting of a first-order homogeneous mantle source devoid of any plume influence (Vlastélic et al., 2000; Hamelin et al., 2010), whereas the

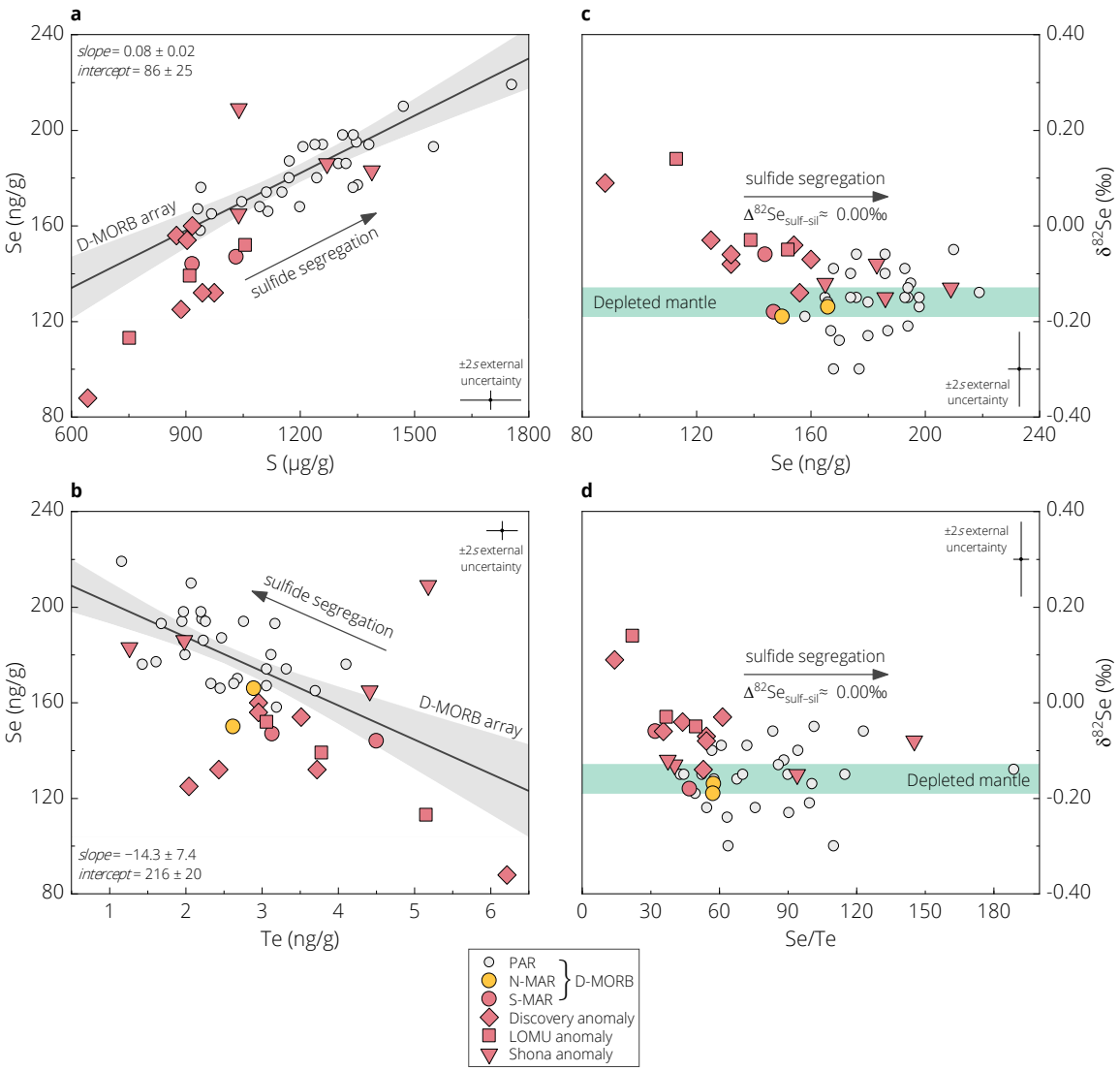

Fig. 3.3 Selenium vs. other chalcophile elements S and Te (a and b) and δ^{82}Se vs. Se abundances and Se/Te ratios (c and d) within the studied MAR suite, in comparison with the recently published data for the PAR basalts (Yierpan et al., 2019). All the depleted MORBs from these two localities (ranging from primitive and highly evolved basalts; MgO contents from 4.52 to 8.85 wt. %) display a linear Se–S (a) and Se–Te (b) co-variation arrays with opposite trends (the grey shaded area around the regression line represents the calculated 95% *CI* envelope).

variably enriched S-MAR basalts were generated from ridge segments that experienced plume-ridge interaction involving melting of plume-derived pyroxenite (le Roux et al., 2002c); (2) the PAR basalts evolved from uniform parental magma composition following a common liquid line of descent at a narrow pressure range (2–5 kbar; Yierpan et al., 2019), whereas the S-MAR basalts are evolved from variable parental magma compositions at a wide pressure range (1 atm–6 kbar; le Roux et al., 2002a). Both elemental abundance and ratios of Se and other chalcophile elements in basalts are readily affected by these complex magmatic processes, and

therefore, they are not a good tracer of mantle source compositions in the context of crustal recycling, despite the elevated abundances of these elements in surface materials relative to mantle-derived melts (e.g., Fig. 3.1a).

On the other hand, Se isotopes do not fractionate during mantle melting or MORB differentiation involving segregation of sulfides (sulfide liquid with/without monosulfide solid solution), as has been previously suggested based on PAR basalts (Yierpan et al., 2019). The MAR samples studied here display random variations between δ^{82}Se values and MgO, FeO_T, and indexes of sulfide segregation such as S (642–1388 μg/g; not shown), Se (88–209 ng/g) and Se/Te ratios (14–145; Fig. 3.3c and d). Similar observations have been made for δ^{34}S vs S abundances (Labidi et al., 2013). The two heaviest δ^{82}Se values (+0.09 ± 0.08‰ and +0.14 ± 0.08‰) characterized by the Discovery and LOMU anomaly MORBs seem to be associated with the lowest S and Se abundances and Se/Te ratios across the entire MAR and PAR suites (Fig. 3.3c and d; Labidi et al., 2013). These MORBs represent the least differentiated samples with the two lowest FeO_T contents (Supplementary Table S3.3), meaning that they experienced the least sulfide segregation. Should all other lighter δ^{82}Se values be caused by further sulfide segregation, one would expect to see continuous decrease of δ^{82}Se with increasing Se content or Se/Te ratio, which is not observed across a wide range of magma composition (Fig. 3.3c and d). We thus confirm the conclusion of Yierpan et al. (2019) that there is no Se isotopic fractionation during igneous processes and that δ^{82}Se of MORB is the mantle source signature. This might be due to the dominant presence of reduced Se^{2-} and therefore lack of redox transition-related isotopic fractionation under the prevailing redox condition of the MORB mantle (ΔQFM = 0.2 ± 0.3; O'Neill et al., 2018; Wykes et al., 2011; Yierpan et al., 2019). Besides, the bonding environment of Se in sulfides and silicate melts (as Fe–Se) might not change significantly during isotope partitioning at pressure and temperature conditions relevant for MORB petrogenesis (Young et al., 2015; Wykes et al., 2015). In this context, the observed δ^{82}Se variability of the MAR basalts (~0.33‰), which cannot be sufficiently accounted for by analytical uncertainties (see Section 3.4), must reflect source heterogeneity. The most ^{82}Se-enriched samples mentioned above also represent the two most enriched MAR basalts with respect to radiogenic isotope ratios (Fig. 3.2), suggesting that heavy Se isotope signature of MORB must be resulted from source enrichment. Indeed, we observe a strong correlation between δ^{82}Se and $^{87}Sr/^{86}Sr$ (Fig. 3.4a; see further discussion below). Therefore, Se isotopes in mantle melts provide a novel tool to trace mantle source heterogeneity.

This, as a prerequisite, requires a robust estimation of the Se isotope composition of the depleted mantle endmember.

3.5.2 Selenium isotope composition of the depleted mantle

The Se isotope compositions of the depleted basalts from the S- and N-MAR fall within the δ^{82}Se range of the PAR (depleted) basalts. Together, they yield a mean δ^{82}Se = −0.16 ± 0.03‰ (95% *CI*, *N* = 31), which is suggested here to represent the depleted mantle Se isotopic composition. The use of 95% *CI* as an uncertainty of the mean is justified by performing the Anderson-Darling normality test, which yields a test statistic of 0.39, smaller than the critical value of 0.73 at α = 0.05 significance level. This suggests that the depleted MORB δ^{82}Se dataset can be adequately described by a normal distribution. Note that the 95% *CI* uncertainty of ±0.03‰ on the deplete mantle δ^{82}Se is identical to that obtained for the average of 9 replicate analyses of a single glass sample (Table 3.1), which shows that the mean δ^{82}Se obtained for the depleted mantle is accurate at ±0.03‰ precision level.

As for the dispersion of δ^{82}Se values within the 31 depleted MORBs, we obtain 2*s* = ±0.13‰, higher than the $2s_p$ external uncertainties of our method (±0.08‰; Section 3.4). The reduced χ^2 for these data is 2.60, well outside the 95% confidence interval of 0.57–1.56 given by the χ^2 statistics. These calculations imply certain isotopic variabilities detectable within the depleted MORB, which cannot be sufficiently accounted for by analytical uncertainties. We note that 2 PAR MORBs show very negative δ^{82}Se values of −0.30 ± 0.08‰ (Fig. 3.3c and d; Yierpan et al., 2019). Isoplot algorithm (Ludwig, 2003) suggests rejection of these data as statistical outlier, and for the remaining 29 samples, it yields lower reduced χ^2 of 1.80. This value still exceeds the 95% confidence interval (χ^2 statistics; see above) but it is very small, indicating that most depleted MORBs have homogenous Se isotope composition (see Teng et al., 2013).

The presence of small statistical δ^{82}Se variations in the depleted upper mantle might reflect intrinsic isotopic heterogeneity, commonly referred to as the marble-cake mantle (Allègre and Turcotte, 1986). For instance, Hamelin et al. (2011) demonstrated that the Pacific depleted mantle (devoid of plume influence) is polluted by small amounts of recycled oceanic crust components with HIMU affinity (Fig. 3.2; Hamelin et al., 2011). Previous studied on S isotopes in global MORB also reported considerable variations in δ^{34}S for different depleted mantle domains (Labidi et al., 2013, 2014, 2016). Only a few δ^{82}Se data are currently available for the

altered oceanic crust and they show significantly negative values of ~−1.3‰ (N = 2; hydrothermally altered basalts at Menez Gwen field; Rouxel et al., 2002). With these regards, presence of variable amounts of recycled oceanic crust in the PAR mantle source could explain the two lightest δ^{82}Se values as well as the statistically subtle δ^{82}Se variability observed among other PAR basalts (Fig. 3.3c and d; Yierpan et al., 2019). Nevertheless, the N-MAR samples, which plot among the most remarkably depleted MORBs across the global dataset (with respect to all radiogenic isotopes shown in Fig. 3.2; White et al., 1978), display identical δ^{82}Se values (−0.17 ± 0.08‰ and −0.19 ± 0.08‰) to the PAR basalt average representing the Pacific depleted mantle (−0.16 ± 0.03‰; 95% *CI*, N = 27; Fig. 3.4 and Fig. 3.5). This further attests to the robustness of the depleted mantle Se isotope composition that is calculated over all the depleted MORB data (N = 31).

3.5.3 Origin of Se isotope heterogeneity in the upper mantle

Localized interactions between the S-MAR and the Discovery and Shona hotspots (Supplementary Fig. S3.1) resulted in significant mantle heterogeneity in the S-MAR mantle source by incorporation of enriched recycled components (Fig. 3.2; Douglass et al., 1999). Moreover, the South Atlantic depleted mantle itself shows intrinsic source enrichments relative to the Pacific/North Atlantic depleted mantle (Fig. 3.2) due to largescale mantle pollution with DUPAL-type mantle components (Douglass et al., 1999; Andres et al., 2002; Escrig et al., 2005). These studies proposed a variety of recycled materials (ancient oceanic crust, sediment, delaminated subcontinental lithospheric mantle, and lower continental crust) to account for the variabilities of radiogenic isotopes in S-MAR basalts (Fig. 3.2; see Section 3.2 for each group of basalts). However, Labidi et al. (2013) argued that the S isotope systematics are mainly accounted for by sediment recycling based on the linear δ^{34}S–^{87}Sr/^{86}Sr trend (Fig. 3.4b), which requires the enriched endmember to be rich in S. The age of the recycled sediments were estimated to be one to two billion years old (Proterozoic) based on both δ^{34}S and mass independent sulfur isotope (Δ^{33}S) considerations.

Our data shows a strong correlation between Se isotope composition and ^{87}Sr/^{86}Sr ratios (r^2 = 0.86), in a remarkably similar manner as S isotope composition (r^2 = 0.85; Labidi et al., 2013; Fig. 3.4a and b). The δ^{82}Se and δ^{34}S values are also correlated with each other (r^2 = 0.64). All the individual δ^{82}Se (N = 45) and δ^{34}S (N = 51) data across the entire MAR and PAR suites (Labidi et al., 2013, 2014; Yierpan et al., 2019; this work) show a highly consistent distribution

patterns (Fig. 3.4c; Supplementary Fig. S3.3). For both isotopes, the Discovery and LOMU anomalies (both influenced by the Discovery mantle plume; see Section 3.2) extend the depleted MORB values towards heavier values, with the Shona anomaly in between (Fig. 3.4). When compared by groups, it clearly shows systematic covariations between the average δ^{82}Se and δ^{34}S values and ^{87}Sr/^{86}Sr ratios of these S-MAR basalts (Supplementary Fig. S3.3). The difference of the average δ^{82}Se between the depleted MORBs and Shona anomaly basalts are not statistically significant (Student's *t*-test, two-tailed *p*-value 0.41), whereas the difference between the depleted MORBs and Discovery + LOMU anomalies are statistically significant (*p*-value 0.02). For the latter comparison, if all the depleted MORBs from the MAR and PAR are considered, the *p*-value becomes extremely small (~0.00001).

The coupled δ^{82}Se–δ^{34}S variations are further illustrated for other geochemical indicators of mantle source enrichment, including radiogenic isotopes such as ^{143}Nd/^{144}Nd and ^{208}Pb*/^{206}Pb* as well as key trace/major elements ratios such as $(La/Sm)_N$, Th/Nb, and K_2O/TiO_2 (Fig. 3.5 and Supplementary Fig. S3.3 and Fig. S3.4; Labidi et al., 2013). These observations, together with the similar elemental/isotopic behavior of Se and S during igneous processes (Section 3.5.1; Labidi et al., 2013, 2014, 2016; Yierpan et al., 2019), argue for an overall similar behavior of these chalcophile stable isotope systems in high-temperature environments. Considering their similarities in low-temperature environments (e.g., Fig. 3.6; Johnson and Bullen, 2004; König et al., 2019), one might expect that the Se isotope mantle heterogeneity beneath the S-MAR also dominantly reflects sediment recycling as in the case of S isotopes (Labidi et al., 2013).

Indeed, variations of δ^{82}Se–^{87}Sr/^{86}Sr and δ^{82}Se–δ^{34}S in the studied MORBs can be explained by a simple binary mixing between the depleted mantle and enriched component that is demonstrated here to be sediments (Fig. 3.4a and c), in accordance with the S isotope constraints (Fig. 3.4b; Labidi et al., 2013). First, the compiled sediment data (Fig. 3.1) yield a mean δ^{82}Se = +0.47 ± 0.88‰ for Proterozoic sediments (1*s*, *N* = 210; Fig. 3.7a), which would readily satisfy the positive slope of the trends (Fig. 3.4). Extrapolations of the linear regressions (calculated by Isoplot; Ludwig, 2003) to the sediment ^{87}Sr/^{86}Sr (0.7203; Rehkämper and Hofmann, 1997) and δ^{34}S (10‰; Labidi et al., 2013) yields δ^{82}Se of +1.44 ± 0.40‰ and +1.15 ± 0.42‰, respectively (95% prediction interval), for the sediment endmember. These values are essentially identical with each other and their mean δ^{82}Se = +1.29 ± 0.41‰ overlap with the mean δ^{82}Se of Proterozoic sediments (Fig. 3.7a). Second, the linear trends require the same Sr/Se and S/Se elemental ratios for both depleted mantle and enriched endmembers. If we

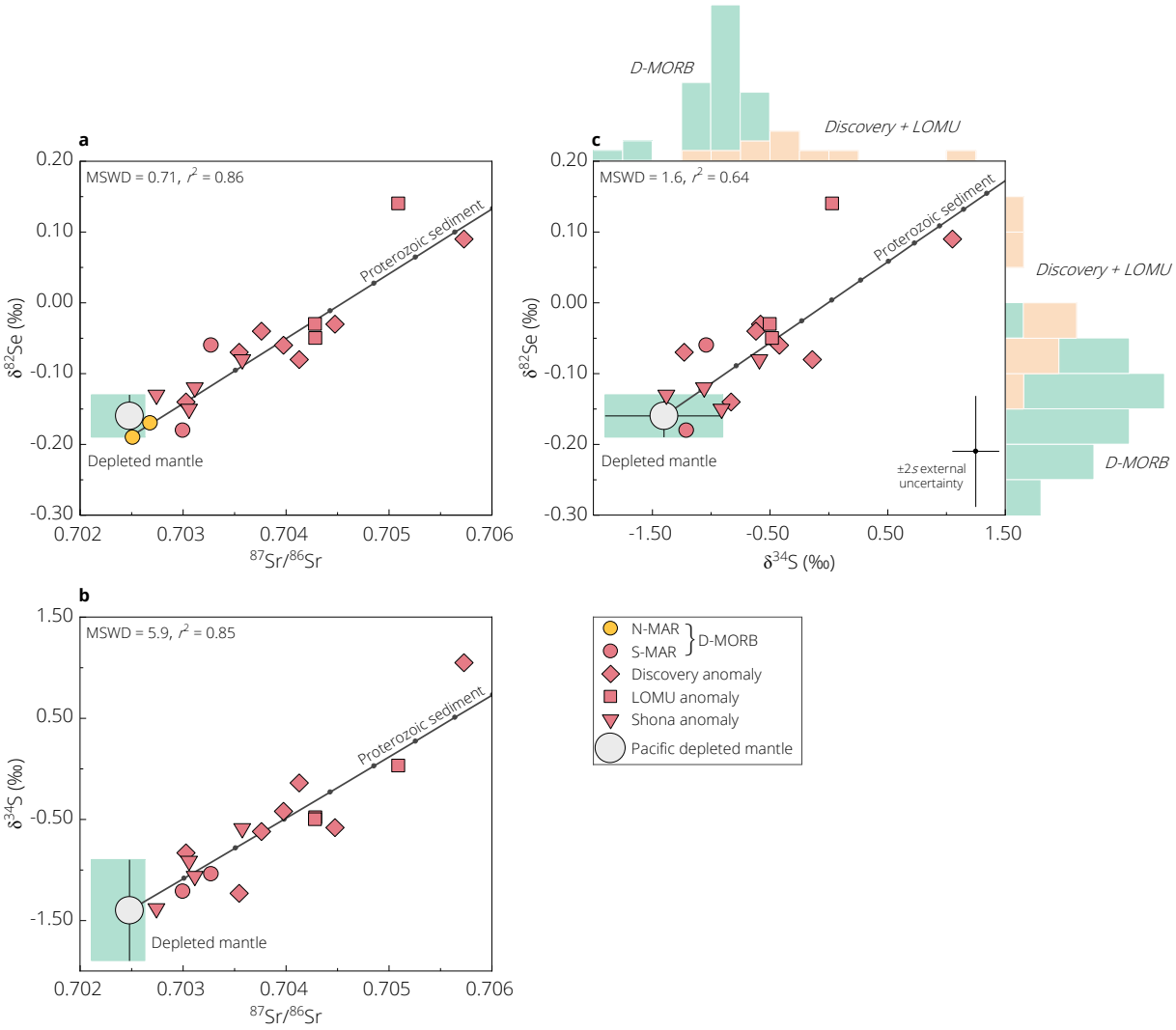

Fig. 3.4 $\delta^{82}Se$ and $\delta^{34}S$ vs. $^{87}Sr/^{86}Sr$ (a and b) and $\delta^{82}Se$ vs $\delta^{34}S$ (c). Selenium isotopes show a strong positive correlation with $^{87}Sr/^{86}Sr$ in a similar manner as S isotopes (Labidi et al., 2013). The pronounced similarity of these stable isotope systems are also expressed by their linear covariation and the consistent distributions of $\delta^{82}Se$ and $\delta^{34}S$ data across the entire MAR and PAR suites (Labidi et al., 2013, 2014; Yierpan et al., 2019; this work). MORBs associated with the Discovery mantle plume (i.e., Discovery and LOMU anomaly basalts) extend the Se and S isotope compositions towards heavier values relative to the depleted MORBs. Variations of the MORB data can be explained by a simple binary mixing between the depleted mantle and enriched component that is argued here to be Proterozoic sediments, in accordance with S isotope constraints (Labidi et al., 2013). The linear mixing trends shown here are calculated using the Pacific ambient depleted mantle or the most depleted MORB composition as an anchor (Table 3.3) and the 'best-fit' sediment end-member composition from a Yorkfit regression (Isoplot; Ludwig, 2003). External uncertainties (2*s*) on the $\delta^{82}Se$ (±0.08‰; $2s_p$) and $\delta^{34}S$ (±0.2‰) data were considered for the regression. Compositions of the (bulk) depleted mantle and Pacific ambient depleted mantle are listed in Table 3.3 (Labidi et al., 2014; Kimura et al., 2017; this work).

take 0.080 ± 0.017 μg/g Se, 9.8 ± 1.9 μg/g Sr, and 200 ± 40 μg/g S for the depleted mantle (Salters and Stracke, 2004; Wang et al., 2013; Palme and O'Neill, 2014; Yierpan et al., 2019), and 300 μg/g Sr and 5700 ± 1000 μg/g S for the Proterozoic subducted sediment (all 1*s*; Rehkämper and Hofmann, 1997; Labidi et al., 2013), the calculated Se contents in the sediments would be 2.45 ± 0.70 and 2.28 ± 0.78 μg/g with the depleted mantle Sr/Se = 123 ± 35 and S/Se = 2500 ± 730, respectively. These values are essentially identical within 1*s* error and yield a mean Se content of 2.36 ± 0.74 μg/g (1*s*). Note that only marine sediments satisfy such a high value and it is well within the range of the compiled dataset, which has a log-normal mean Se content of $1.00^{+3.83}_{-0.80}$ for the Proterozoic sediments (N = 210; Fig. 3.1 and Fig. 3.7b). With this set of mean δ^{82}Se and Se abundance of the sediment endmember obtained from δ^{82}Se–^{87}Sr/^{86}Sr and δ^{82}Se–δ^{34}S variations, we successfully reproduce the mixing curves for δ^{82}Se–^{143}Nd/^{144}Nd (Fig. 3.5a), which has a parabolic rather than linear trends due to the higher Nd/Se ratios of sediments (~36) relative to the depleted mantle (~9; Nd content and isotopic ratios from Salters and Stracke, 2004; Rehkämper and Hofmann, 1997). Because our calculated sediment compositions agree well with the published deep-sea sediment data, we argue for little or minor Se loss from sediments or associated isotopic fractionation during subduction (for S, see Labidi et al., 2013).

Next we consider the possibility of the delaminated subcontinental lithospheric mantle and lower continental crust (EM1- and LOMU-type radiogenic isotope signatures; Fig. 3.2; Douglass et al., 1999; Andres et al., 2002) as carriers of the heave Se isotope signatures in the Discovery plume-influenced basalts. Worldwide peridotites (N = 11) derived from the subcontinental lithospheric mantle have comparable Se contents (mean $0.054^{+0.076}_{-0.032}$ μg/g) to the depleted mantle and a narrow δ^{82}Se range with a mean of ~−0.03‰ (Fig. 3.1b; Varas-Reus et al., 2019). They thus cannot explain the observed ^{82}Se-enrichments by mixing with the depleted mantle (Fig. 3.4). As for the lower continental crust, estimated Se content varies from ~0.05 to 0.2 μg/g in the literature (e.g., Rudnick and Gao, 2003). These values might be potentially lower compared to the Se content of the delaminated lower crust due to the pervasive deep-seated cumulate-hosted sulfides that are enriched in strongly chalcophile elements such as Se (Jenner, 2017). There is no literature Se isotope data for continental crust materials. Based on the δ^{82}Se values of the Proterozoic Västervik granitoids (~0.20‰; Table 3.3) and other mantle-derived melts, it is very likely that the Se isotopic composition of the lower continental crust does not significantly deviate from the range of the igneous inventory (~−0.3‰–+0.3‰; Fig. 3.1b). Therefore, despite the potentially higher Se content relative to the depleted mantle, the

delaminated lower continental crust cannot sufficiently account for the linear relationship between $\delta^{82}Se$ and $^{87}Sr/^{86}Sr$ (Fig. 3.4a).

Furthermore, we do not observe clear correlation between $\delta^{82}Se$ and $^{206}Pb/^{204}Pb$ ratios (Fig. 3.5c), and all the Shona anomaly basalts carrying mild EM1 and HIMU affinities (mildly elevated $^{87}Sr/^{86}Sr$ and $^{206}Pb/^{204}Pb$; Fig. 3.2; also see Section 3.2) show identical $\delta^{82}Se$ values to the depleted mantle composition. Previous studies suggested that the Shona plume consists of subducted oceanic crust with/without sediments (Douglass et al., 1999; Andres et al., 2002). As mentioned in Section 3.5.2, two $\delta^{82}Se$ data published so far for the altered oceanic crust show

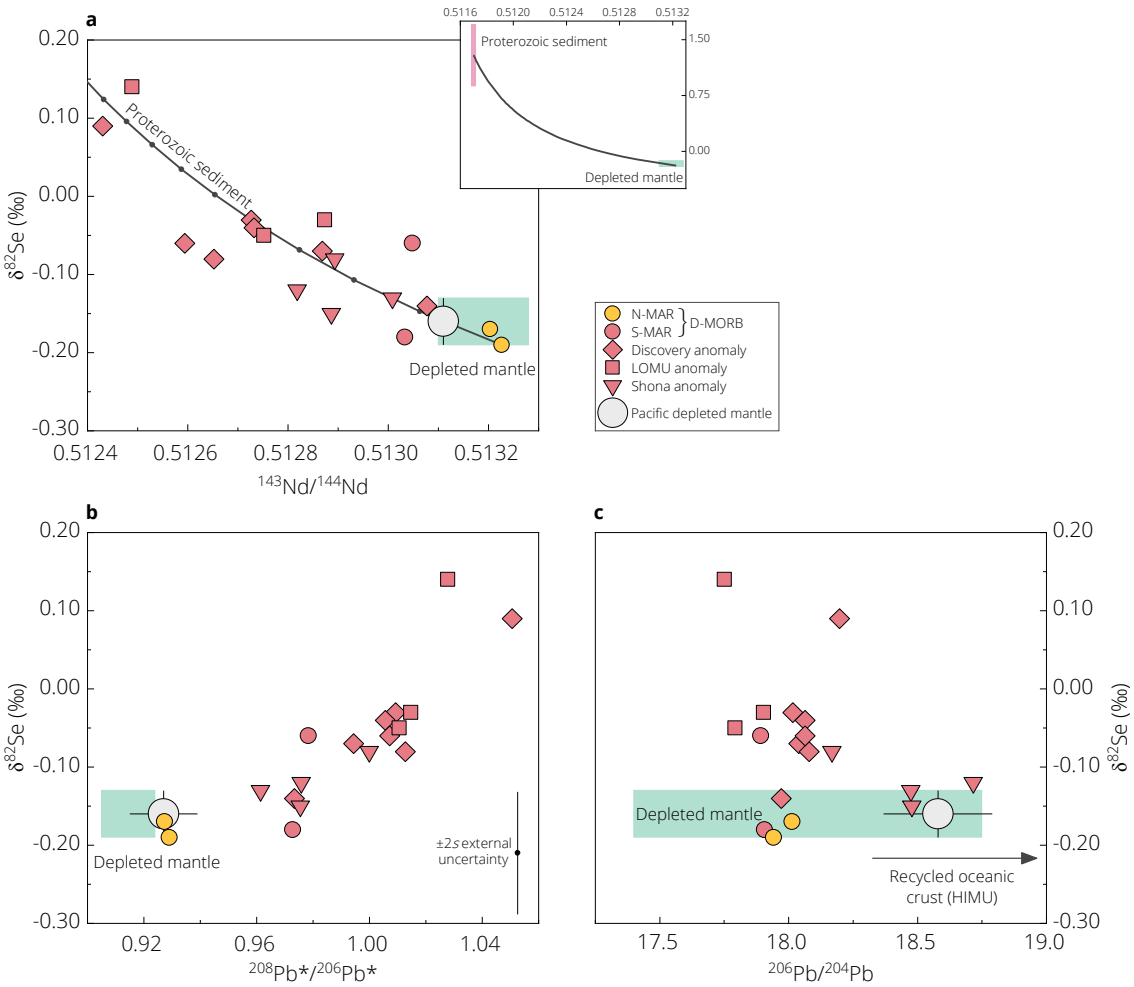

Fig. 3.5 $\delta^{82}Se$ vs. $^{143}Nd/^{144}Nd$, $^{208}Pb^*/^{206}Pb^*$, and $^{206}Pb/^{204}Pb$. It shows that Se isotopes are correlated with radiogenic Nd isotopes and $^{208}Pb^*/^{206}Pb^*$ (as time-integrated Th/U ratios) but not with $^{206}Pb/^{204}Pb$. The mixing trend accounting for the Se–Nd isotopic variation shown in (a) are calculated using the most depleted MORB (TR138 08D-1g; S-MAR basalt) and the average 'best-fit' sediment end-member compositions (see the insert) obtained from the $\delta^{82}Se$–$^{87}Sr/^{86}Sr$ and $\delta^{82}Se$–$\delta^{34}S$ linear mixing relationships in Fig. 3.4. See Section 3.5.3 for more details.

significantly negative values of ~−1.3‰, with anomalously enriched Se contents of ~60 µg/g (Rouxel et al., 2002) that are even higher compared to most sediments. A HIMU plume component carrying this light δ^{82}Se would readily result in lighter δ^{82}Se with increasing $^{206}Pb/^{204}Pb$ in the S-MAR basalts (Fig. 3.5c), which is not observed. Also, with regard to the elemental abundances, it cannot explain the linear δ^{82}Se–δ^{34}S trend (Fig. 3.4c) due to its high Se and low S contents (~175–300 µg/g S based on S isotope systematics; Labidi et al., 2013, 2014). Therefore, the altered oceanic basalts studied by Rouxel et al. (2002) very likely represent exceptionally enriched crust due to their proximity to the hydrothermal field and do not represent a global altered oceanic crust composition. Future studies are needed to constrain the Se elemental and isotopic composition of the HIMU endmember. To summarize, the Se isotope heterogeneity of the mantle recorded by the S-MAR basalts chiefly reflects recycling of marine sediments, as in the case of S isotopes (Labidi et al., 2013).

3.5.4 Atmospheric oxygenation: A selenium record from the mantle perspective

The Se isotopic variability of marine sediments (Fig. 3.1a) mainly results from kinetic isotopic fractionation during reduction of Se oxyanions (SeO_4^{2-} and SeO_3^{2-}) at various redox conditions (Fig. 3.6; Johnson and Bullen, 2004). These soluble and mobile species of Se only occur at relatively high redox potentials such as oxic and suboxic conditions, and therefore, the presence of free atmospheric O_2 enhances release of the reduced Se hosted in continental rocks and their pyrites via oxidative weathering and ultimately its transport to the oceans (Fig. 3.6; Johnson et al., 1999; Johnson, 2004; Johnson and Bullen, 2004; Large et al., 2014; Stüeken, 2017). This makes the Se isotopic and elemental abundances of sediments and their pyrites a tracer of marine–atmosphere oxygenation (Fig. 3.6; Large et al., 2014, 2019; Wen et al., 2014; Stüeken et al., 2015a, b; Pogge von Strandmann et al., 2015; Mitchell et al., 2016; Kipp et al., 2017; Koehler et al., 2018; Mukherjee et al., 2018).

Our compiled dataset in Fig. 3.7 shows, to a first-order, intimate links between Se isotopic/elemental abundances of the surface reservoirs and major secular changes in the composition of the continental crust and atmospheric oxygenation (for other geochemical cycles, see Lee et al., 2016; Smit and Mezger, 2016). The global sediment record does not show changes in δ^{82}Se across the Great Oxidation Event (2400–2100 Ma; Holland, 2002; Lyons et al., 2014), with essentially identical mean δ^{82}Se values of +0.48 ± 0.60‰ and +0.47 ± 0.88‰

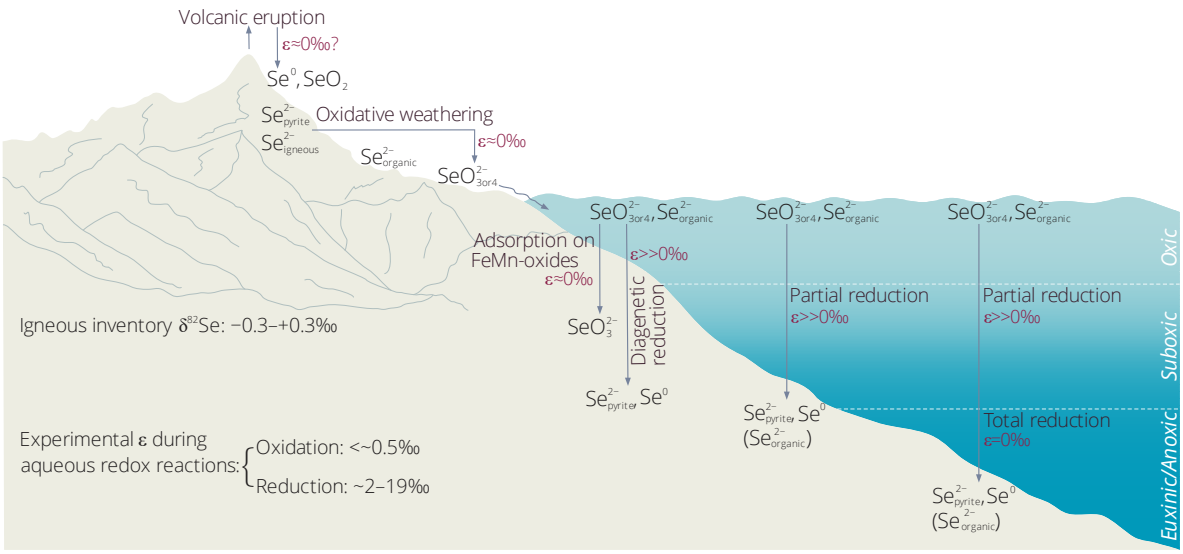

Fig. 3.6 Schematic illustration of the biogeochemical Se cycle. It shows the major processes that control the transport and fate of Se on a continental setting and redox-stratified open ocean (modified after Stüeken et al., 2015a). The experimental kinetic isotopic fractionations ε during low-temperature redox reactions are from Johnson and Bullen (2004). The sense of isotopic fractionation ε between the silicate magma $Se^{2-}_{igneous}$ and gas species Se^0 and SeO_2 (both readily depositing on surface upon cooling; Floor and Román-Ross, 2012) during subaerial volcanic activity remains unknown, but the magnitude might be significantly small compared to the experimentally observed ε based on the relatively limited difference in $\delta^{82}Se$ values between submarine MORBs and subaerial basalts (Fig., 1; Yierpan et al., 2019; this study).

for the Archean and Proterozoic sediments, respectively (Fig. 3.7). However, there is a notable change in $\delta^{82}Se$ towards mostly lighter values after the Neoproterozoic oxygenation event (800–550 Ma; Och and Shields-Zhou, 2012), with a mean $\delta^{82}Se$ of -0.20 ± 0.84‰ for the Phanerozoic sediments (Fig. 3.7). This has been suggested to reflect deep ocean oxygenation and widespread occurrence of Se oxyanions, hence partial reduction-induced isotope fractionation, throughout the deep ocean (Stüeken et al., 2015b). In comparison, the dominant occurrence of positive values in deep-sea sediments during Precambrian reflects quantitative reduction of Se oxyanions under anoxic conditions following partial reduction under suboxic conditions in the ocean and during transport on land (e.g., Fig. 3.6; Stüeken et al., 2015a; Stüeken, 2017). Subsequent transport of these sediments with different ages into the deep mantle through subduction would introduce isotope heterogeneity in the mantle by imparting their Se isotopic signatures. Tracing these surface signatures by mantle samples thus provides a new approach to investigate the secular oxidation of the surface environments from the mantle perspective.

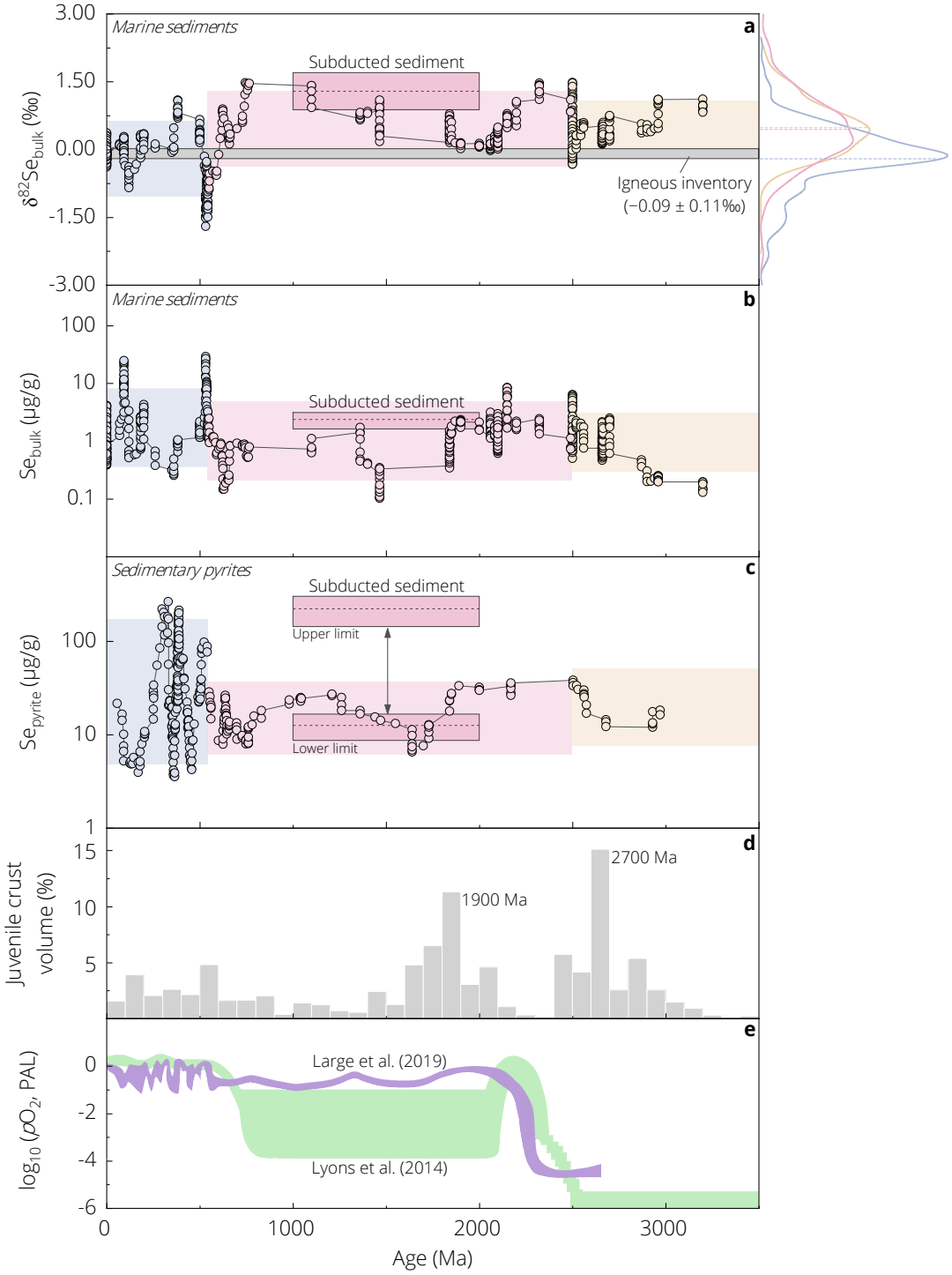

Fig. 3.7 Selenium record of marine sediments and pyrites and atmospheric oxygenation through geological time. $\delta^{82}Se$ and Se abundances of bulk sediments (a and b; N = 699; see Fig. 3.1 for the source literature) and Se abundances of sedimentary pyrites (c; N = 347; Large et al., 2014, 2019; Mukherjee et al., 2018) from the literature are presented as moving averages of 11 single data points in order to highlight longer-term trends. The colour-coded shaded areas in (a–c) are average $\delta^{82}Se$ values with ±1*s* uncertainties calculated for the Archean, Proterozoic, and Phanerozoic. The empirical distribution curves with mean $\delta^{82}Se$ values (dashed lines) of these groups are shown in the right panel of (a) as in Fig. 3.1a. Shown for comparison is the estimated $\delta^{82}Se$ range for the igneous inventory (−0.09 ± 0.11‰; weighted mean, 1*s*). The sediment and pyrite data show rather consistent temporal

changes in δ^{82}Se and Se abundances of sediments and/or their pyrites, in response to the temporal evolution of juvenile continental crust (d; Groves et al., 2005) and atmospheric oxygen level (e; schematic representation after Lyons et al., 2014; Large et al., 2019). The boxes in (a–c) represent the model composition of the recycled sediments calculated based on the linear relationships of δ^{82}Se–^{87}Sr/^{86}Sr and δ^{82}Se–δ^{34}S variations of the studied MORB glasses (see Section 3.5.3 for details). The two boxes in (c) represent the upper and lower limits of the calculated pyrite composition depending on the Se budget of the host phases in sedimentary protoliths (pyrite and other sediment matrix; after Large et al., 2014). See text for further discussion.

As discussed in Section 3.5.3, the recycled sediment endmember for the S-MAR mantle should be of Proterozoic age (~1–2 billion years old) and has δ^{82}Se of +1.29 ± 0.41‰ and Se abundance of 2.36 ± 0.74 μg/g. Although comparable with the published data within uncertainty, this δ^{82}Se value of the recycled sediment seems to be heavier than the Proterozoic sediment average (+0.47 ± 0.88‰; Fig. 3.7). This is in fact what one might expect because the subducted sediments are biased towards those deposited at the deepest seafloor under anoxic conditions (Fig. 3.6). These sediments should be dominantly associated with quantitative reduction of Se oxyanions, leading to the most positive δ^{82}Se values (see above). Because the composition of the recycled sediment represents the average of global sediments deposited over a wide range of geological time interval (e.g., during mid-Proterozoic Fig. 3.7), it yields information regarding the spatial and temporal relationships between the atmospheric oxygen evolution and redox-sensitive trace element chemistry in the ocean on a global scale.

Recently, Large et al. (2019) proposed a much higher atmospheric O_2 level for the entire Proterozoic eon compared to earlier studies (Lyons et al., 2014) using Se/Co ratios in sedimentary pyrites as a proxy. Because pyrite is the major host of Se in marine sediments (Large et al., 2014), our results obtained here may contribute to the new constraints on the atmospheric O_2 evolution (Large et al., 2019) by calculating the Se content of the pyrite in the recycled sediment. Because there is no evidence for significant Se or S loss from the bulk sediments during subduction (see Section 3.5.3; Labidi et al., 2013), the calculated sediment composition should resemble that of the subducting protolith. Assuming that the sedimentary pyrite containing Se is of $FeS_xSe_{(2-x)}$ composition, based on the sediment endmember composition of 2.36 ± 0.74 μg/g Se (see above) and 5700 ± 1000 μg/g S (Labidi et al., 2013), (1) if both Se and S budgets in the bulk subducting protolith are completely contributed by pyrites, we obtain pyrite Se content of 222 ± 79 μg/g; (2) if Se is hosted by both pyrites and other matrices in the subducting protolith, taking the mean pyrite/matrix Se ratio of 5.82 in global pyrites (Large et al., 2014) and mean pyrite S content of ~1 wt. % (log-normal mean) in

global Proterozoic sediments (Poulton et al., 2004), we obtain pyrite Se content of 12.6 ± 3.9 μg/g (Fig. 3.7). These values are similar to or higher than the average pyrite Se content of the mid-Proterozoic pyrite record (15^{+22}_{-9} μg/g, N = 113) that was used to constrain the evolution of atmospheric O_2 level (Large et al., 2014, 2019; Mukherjee et al., 2018). In another words, our results, from the mantle Se isotope record, are in accordance with the high O_2 level throughout the Proterozoic (1–15 wt. %; Large et al., 2019), contrary to earlier conclusions (0.002–2 wt. %; Lyons, et al., 2014; Fig. 3.7e). This would mean that atmospheric O_2 level was not as critical as previously thought for the evolution of complex life on Earth across the 'Boring Billion'; other factors such as the stepwise increase of bio-essential trace-element availability in marine settings need to be considered (Mukherjee et al., 2018; Large et al., 2019).

3.6 Conclusion

We have analyzed Se isotope compositions of a suite of representative MORBs from the northern and southern sections of the Mid-Atlantic ridge. The S-MAR basalts display a wide range of radiogenic isotope/trace element compositional variability due to the localized interaction between the south Atlantic depleted mantle and the Discovery and Shona mantle plumes. The Se isotope composition (δ^{82}Se) of these basalts range between −0.19 ± 0.08‰ and +0.14 ± 0.08‰, with a total variability of ~0.33‰ that cannot be explained by analytical uncertainties and reflect mantle source heterogeneity. The depleted basalts from the S- and N-MAR devoid of plume influence show similar δ^{82}Se values to the PAR depleted basalts. All these depleted basalts yield a mean δ^{82}Se of −0.16 ± 0.03‰ (95% confidence interval, N = 31) that represents the depleted mantle Se isotope composition. The enriched samples, especially the Discovery and LOMU anomaly basalts, show heavier δ^{82}Se values. There are strong correlations between δ^{82}Se and radiogenic isotope ratios $^{87}Sr/^{86}Sr$ and $^{143}Nd/^{144}Nd$ as well as δ^{34}S. We suggest that the observed δ^{82}Se variations in the mantle source of the MAR basalts are mainly accounted for by binary mixing between the depleted mantle and recycled sediments along the linear δ^{82}Se–$^{87}Sr/^{86}Sr$ and δ^{82}Se–δ^{34}S trends. Both the calculated δ^{82}Se value and Se abundance of the sediment endmember fall within the range of Proterozoic sediment composition in the literature, as in the case of S isotopes (Labidi et al., 2013). The Se isotope record of the mantle is further used to provide constraints on a recent model of atmospheric O_2 evolution using Se/Co ratios in sedimentary pyrites (Large et al., 2019). The estimated Se contents of pyrite in the subducting sediment are similar to or higher than the average

Proterozoic pyrites. Within these limits inferred from the Se isotope systematics of mantle melts, our study argues for the high atmospheric O_2 level throughout the Proterozoic eon as proposed by Large et al. (2019). This requires consideration of a critical role of other factors such as availability of nutrient trace elements, together with the atmospheric oxygen, in the progressive evolution of complex life during the 'Boring Billion'.

Outlook

With the analytical method presented in Kurzawa et al. (2017) and Yierpan et al. (2018) (Chapter 1), the currently limited data set of Se isotope compositions in mantle-derived rocks and melts can be further extended. As one of the most important contributions of this work, the new data presented in Chapter 2 and 3 suggest that there is no isotopic fractionation during Se partitioning between sulfide phases and silicate melt in the MORB mantle. This might be due to the dominant presence of reduced Se^{2-} and therefore lack of redox transition-related isotopic fractionation in the mantle (such as those in low-temperature aqueous systems; e.g., Johnson and Bullen, 2004; Stüeken, 2017). It is also postulated here that bonding environment between Se^{2-} dissolved in the silicate melt and Se^{2-} precipitating with sulfides might not significantly vary. Future studies on Se partitioning experiments at relevant mantle conditions would help further constrain the Se isotopic behavior during sulfide–silicate melt partitioning. Besides, as discussed in Chapter 2, there are significant discrepancies on the experimental Se and Te elemental partitioning data between two working groups (Brenan, 2015; Kiseeva et al., 2017), which warrants further experimental work.

Compared to submarine MORB glasses, all the sub-aerial basaltic lavas analyzed so far (this work; Rouxel et al., 2002) display systematically heavier Se isotope compositions. Interestingly, these basalts are derived from a variety of geodynamic settings and have rather uniform $\delta^{82/76}$Se values around +0.20‰. Is this because of potential Se isotopic variability of their mantle sources and/or isotopic fractionation during subaerial volcanic eruption-related Se degassing (e.g., Floor and Román-Ross, 2012)? Unlike S (e.g., Wallace and Edmonds, 2011; Beaudry et al., 2018), Se isotope fractionation during magmatic degassing has not been studied so far. Considering the similarities of Se and S isotopic and elemental behavior in both high- and low-temperature systems (e.g., Chapter 3), it is quite likely that Se isotopic fractionation during magmatic eruption is tightly controlled by the relative fractions of Se redox species (i.e., Se^{2-} and Se oxyanion) in the melt and vapor phases. So far, there is only one study that focused on Se speciation in basalts (Wykes et al., 2011 Goldschmidt Abstracts), which reported that Se^{4+} exists in basaltic melts at moderate to high oxygen fugacities. The Se degassing behavior and associated isotope fractionation need to be explored via future experimental studies and analyses of basaltic suites that include both submarine and sub-aerial basalts. This is important for understanding the Se geochemical cycle in the crust and mantle systems and may provide

new insights into the behavior of sulfide during magmatic outgassing (Edmonds and Mather, 2017).

The Se isotopic heterogeneity recorded by the southern Mid-Atlantic ridge is attributed to the presence of enriched plume components. They must be of sedimentary origin (i.e., Se- and S-rich) to account for the linear mixing trends of $\delta^{82/76}$Se–^{87}Sr/^{86}Sr and $\delta^{82/76}$Se–δ^{34}S. This means that contributions from other recycled components such as altered oceanic crust, delaminated subcontinental lithospheric mantle and lower continental crust are minor with respect to the Se isotopes. Selenium isotope composition of the subcontinental lithospheric mantle is well constrained using worldwide peridotites (Varas-Reus et al., 2019). The lower continental crust $\delta^{82/76}$Se is also likely in the range of the igneous reservoir (Chapter 3). The recycled oceanic crust or HIMU endmember $\delta^{82/76}$Se, on the other hand, needs to be estimated via analyses of a section of altered oceanic crust and ocean-island basalt endmembers. This would also allow a better understanding of the Se mobility during hydrothermal alteration and subduction processes (e.g., Rouxel et al., 2004; Kurzawa et al., 2019).

There is a statistical difference on the model Se isotope composition between the depleted mantle estimated by fresh submarine MORB glasses (this work) and the primitive mantle estimated by subcontinental lithospheric peridotites (Varas-Reus et al., 2019). Because there is no Se isotopic fractionation during MORB differentiation and partial melting involving sulfide–silicate melt partitioning (Chapter 2 and 3), the difference remains to be explained in future studies using different mantle samples such as komatiites in order to confirm the robustness of the primitive mantle $\delta^{82/76}$Se value.

Regarding the Se and Te elemental behavior during core–mantle differentiation, the currently available metal–silicate partition coefficients (*D*) are based on the extrapolation of low-pressure experiments (<20 GPa; Rose-Weston et al., 2009). Recent S partitioning experiments by Suer et al. (2017) conducted at core formation conditions showed that S becomes significantly less siderophile with increasing pressure than previously predicted. Is it possible that the pressure dependence of *D* for Se and Te determined at <20 GPa also becomes lower at higher pressure (or temperature) to some extent as in the case of S, so that some fractions of Se and Te budget in the mantle record metal–silicate differentiaion? If so, it would be critical to investigate the effect of such process on Se isotopic fractionation in order to determine the pre-late veneer mantle composition.

Appendix: Supplementary/Supporting Information

Chapter 1

Chemical sample processing for combined selenium isotope and selenium–tellurium elemental investigation of the Earth's igneous reservoirs

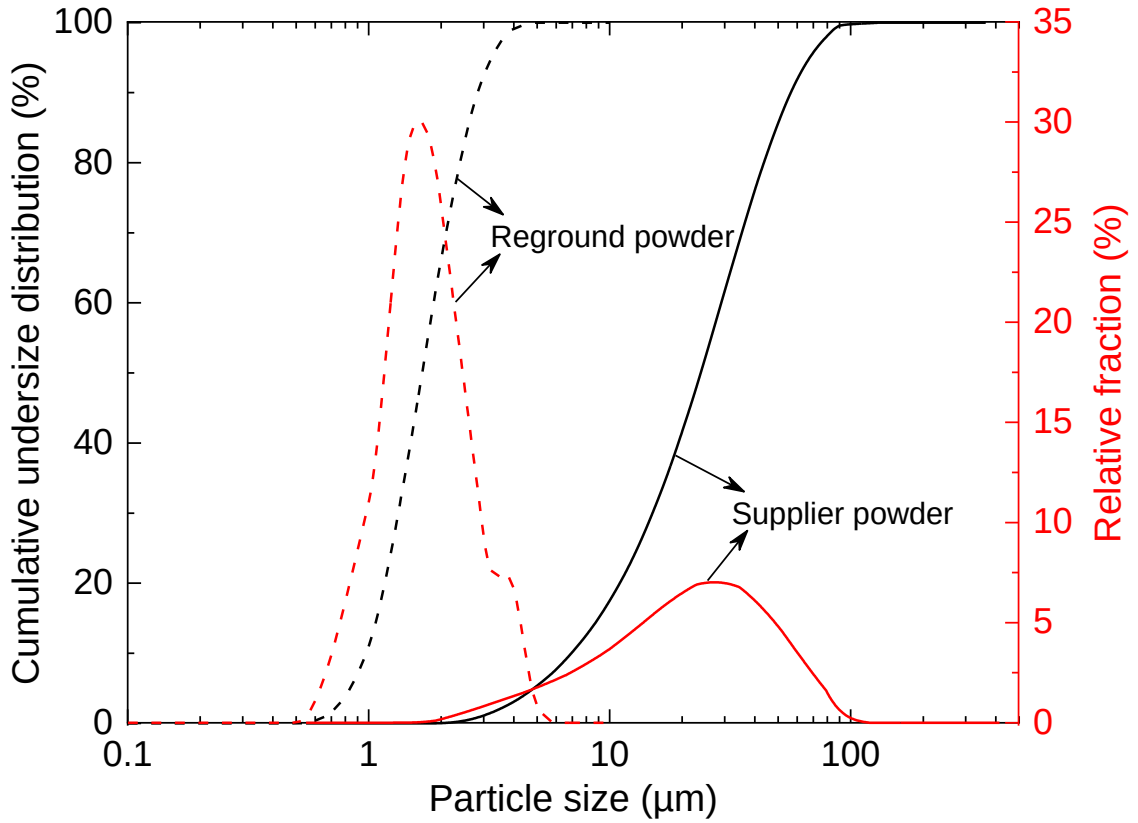

Figure S1.1 Comparison of particle size distribution of BHVO-2 between the supplier powder (provided by Stephen A. Wilson, USGS) and reground powder (analyzed using a laser particle sizer, Analysette 22 NanoTec, in the Application Laboratory of Fritsch, Germany). Note that all the reground powders have particles ≤5 μm. Although the particle size distribution is significantly different between these two rock powders, the same Se–Te extraction efficiency is observed from the HPA-S (inverse *aqua regia*) digestion.

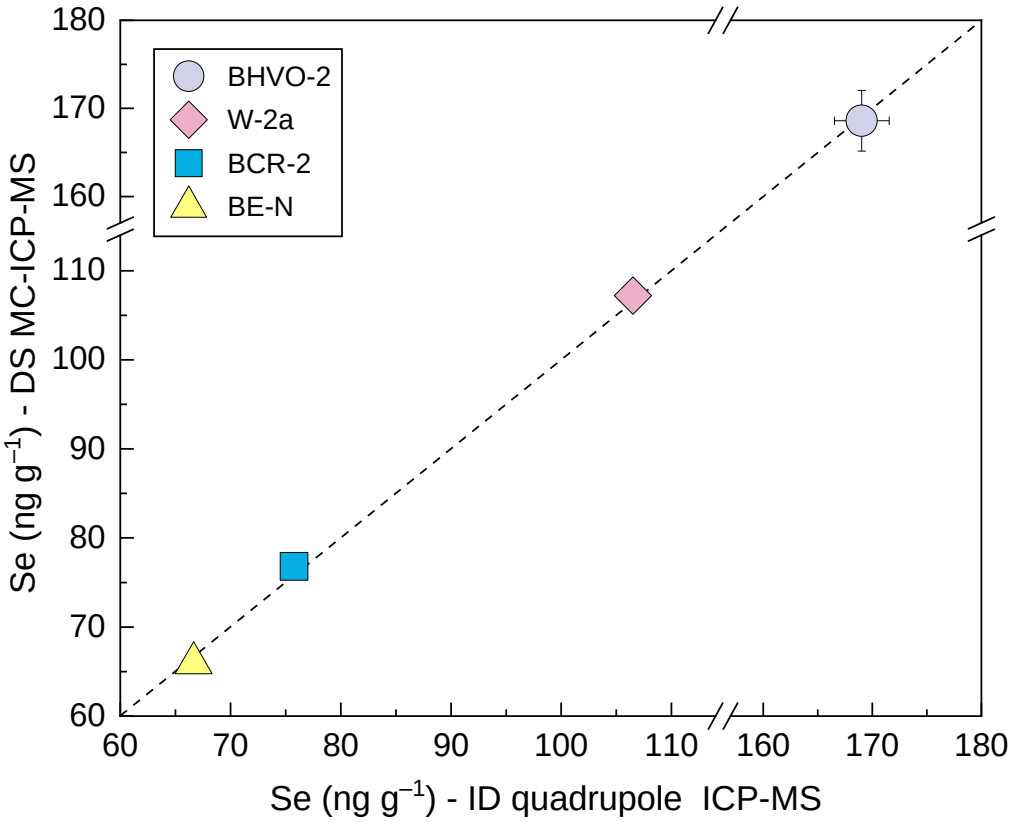

Figure S1.2 Comparison of Se concentrations (± 1 s.d.) determined by hydride generation DS MC-ICP-MS and ID quadrupole ICP-MS using aliquots from the same sample digest (Main text Table 1.1 and supporting information Table S1.6). For all samples, the results are in excellent agreement (within ~3% variation) between both instruments. Note that the 1 s.d. uncertainties for BCR-2, BE-N and W-2a Se data are all smaller than the symbol size. The intermediate precision of our method is obtained from repeated analyses of BHVO-2 (75 analyses from 61 digestions) and is estimated to be ~2% (r.s.d.).

Table S1.1 Se–Te concentrations and/or Se isotope compositions analyzed for BHVO-2 supplier and reground powder with different sample sizes using HPA-S (inverse *aqua regia*) digestion conducted at 100 bar for 16 h. Also shown are Se concentrations analyzed for the undigested residue after the HPA-S procedure using HF digestion.

Sample size (g)	Acid volume[b] (mL)	Digestion temperature (°C)	Se concentration (ng g^{-1})	$\delta^{82/76}$Se (‰)	2 s.e.[c] (‰)	Te concentration (ng g^{-1})	Dissolved powder fraction	Residue Se concentration (ng g^{-1})
Supplier powder								
1.088	10.0	320	125					
0.517	10.0	320	122					
0.618	10.0	320	124					
0.247	2.5	320	137					
0.251	2.5	320	139					
0.246	2.5	320	125					

Sample size (g)	Acid volume[b] (mL)	Digestion temperature (°C)		Se concentration (ng g^{-1})	$\delta^{82/76}$Se (‰)	2 s.e.[c] (‰)	Te concentration (ng g^{-1})	Dissolved powder fraction	Residue Se concentration (ng g^{-1})
0.250	4.0	320		121					
0.250	4.0	320		122					
0.246	4.0	220		118					
0.299	4.0	220		135					
0.301	2.5	220		132					
0.201	2.5	220		118					
0.246	2.5	220		121					
0.252	2.5	320		128	0.17	0.09			
0.251	2.5	220		129	0.27	0.09			
0.250	2.5	220		133	0.19	0.06			
0.250	2.5	220		133	0.15	0.08			
0.257	2.5	220		124	0.21	0.08			
0.307	2.5	220		114	0.22	0.08		15%	41
0.763	10.0	280					12.2	9%	
0.745	7.5	280					12.2	10%	
0.753	7.5	280					12.7	10%	
			Average	127	0.21		12.4		
			Uncertainty[d]	7	0.08		0.3		
Reground powder									
0.302	4.0	220		133	0.32	0.08		17%	35
0.302	2.5	220		132	0.21	0.07		13%	37
0.302	2.5	220		131	0.28	0.08		16%	35
0.307	2.5	220		144	0.18	0.07		15%	40
0.302	2.5	220		137	0.23	0.07		10%	33
0.305	2.5	220		141	0.16	0.06		14%	40
0.756	10.0	280					12.4	9%	
0.764	7.5	280					13.1	9%	
0.759	7.5	280					12.6	10%	
			Average	136	0.23		12.7		
			Uncertainty[d]	5	0.12		0.3		
			Total average	129	0.22		12.5	12%	37
			Uncertainty[d]	8	0.10		0.3	3%	3
			n	25	12		6	13	7

[a] In contrast to data listed in Table 1.1, Te concentration and Se isotope (hence Se isotope concentration) were not determined from the same sample digest from the HPA-S (inverse aqua regia) digestion as the purpose of this experiment is to assess the Se–Te extraction efficiencies.
[b] Acid mixture of 14.5 M HNO_3 and 10.5 M HCl (molar ratio 3:1).
[c] Internal precision of a sample run during Se isotope analysis (over 40 cycles) is reported as 2 standard error (2 s.e.).
[d] Uncertainties are 2 s.d. for $\delta^{82/76}$Se and 1 s.d. for all other data.

Table S1.2 Selenium and tellurium recoveries of BHVO-2 that are determined in this study from different chemical purification procedures following different sample digestion protocols.

Purification chemistry	Chromatography protocol used[a]	HPA-S inverse *aqua regia* digestion		Hotplate HF–HNO_3 digestion	
		Se recovery	Te recovery	Se recovery	Te recovery
TCF and TCP Chemistry[b]		-	-	<20% (n = 26)	-
Ion exchange chromatography					
Anion column chemistry[c]					
	A/B	55–81% (n = 15)	-	28–64% (n = 6)	54–58 % (n = 2)
	C	-	-	-	-
	new column chemistry	-	-	73–87% (n = 5)	85–93% (n = 5)
Cation column chemistry[d]					
	A/B	42–78% (n = 8)	-	-	-
	new column chemistry or C	-	-	92–100% (n = 5)	-
Overall procedural recovery[e]					
	A/B	39–57% (n = 15)	<10% (n = 6)	<20% (n = 6)	<20% (n = 15)
	C	-	-	-	~50% (n = 2)
	new column chemistry	-	-	70–83% (n = 16)	68–89% (n = 11)

[a] Chromatographic purification protocols for Se and/or Te: A = Kurzawa et al. (2017); B = Wang and Becker (2013); C = Wang et al. (2015). Each protocol was followed exactly as described in the original literature.
[b] See the text in detail for the protocol applied. In total, five TCF and 1 TCP batches (freshly-prepared before the purification) were used.
[c] Determined by ID when the sample is spiked after the anion column chemistry.
[d] Determined by signal comparison against NIST SRM 3149 solutions when (1) the sample is spiked after the anion column chemistry or (2) the sample is spiked prior to digestion and Se is measured separately from aliquots after anion- and cation-column chemistry.
[e] Determined by signal comparison of the final solution against NIST SRM 3149 and 3156 standard solutions for Se and Te, respectively. Note that it includes Se–Te recoveries from HCl evaporation at 85 °C, 2-stage column purification and hydride formation.

Table S1.3 Chromatographic separation of Se–Te using our newly established protocol from NIST SRM 3149 and 3156 mixture and BHVO-2 (after the HF digestion), and the relative recovery fractions[a] at each 2.5 mL eluent, which were used to obtain the elution profiles in Figure 1.1 in the main text.

Elution Step	Eluent	Volume[b] (mL)	Cumulative volume (mL)	Se (%)	Te (%)	Se (%)	Te (%)
Eichrom AG1-X8				NIST SRM 3149 and 3156 mixture		BHVO-2	
1	4M HCl	2.5	2.5	-		-	
2	4M HCl	2.5	5.0	25.9		6.0	
3	4M HCl	2.5	7.5	47.2		34.5	
4	4M HCl	2.5	10.0	22.3		34.0	
5	4M HCl	2.5	12.5	1.0		11.3	
6	4M HCl	2.5	15.0	0.1		1.6	

7	4M HCl	2.5	17.5	-		-	-
8	2M HCl–5M HF	5.0	22.5	<0.1	<0.1	-	<0.1
9	2M HCl–5M HF	5.0	27.5	<0.1	-		0.7
10	0.4 M HCl	4.0	31.5	-	0.2		-
11	0.4 M HCl	2.5	34.0		0.3		-
12	0.4 M HCl	2.5	36.5		3.7		-
13	0.4 M HCl	2.5	39.0		58.1		22.4
14	0.4 M HCl	2.5	41.5		35.2		67.6
15	0.4 M HCl	2.5	44.0		0.5		5.0
16	0.4 M HCl	2.5	46.5		-		1.0
17	1 M HNO_3[c]	8.0	54.5		-		-
Recovery				**96.5**	**97.9**	**87.4**	**95.0**

Eichrom AG 50W-X8				NIST SRM 3149	BHVO-2
1	0.1 M HNO_3	2.5	2.5	3.61	0.2
2	0.1 M HNO_3	2.5	5.0	49.1	28.2
3	0.1 M HNO_3	2.5	7.5	43.3	48.5
4	0.1 M HNO_3	2.5	10.0	1.3	20.2
5	0.1 M HNO_3	2.5	12.5	<0.1	0.8
6	0.1 M HNO_3	2.5	15.0	-	-
Recovery				**97.4**	**97.9**

[a] The relative recovery fractions were determined using ID method by spiking each individual eluent fraction after collection. The Se–Te yields were determined twice on some collection cuts and the yield repeatabilities are <1% (r.s.d.).
[b] The eluent fraction was collected at each 2.5 mL for 4 M HCl, 0.4 M HCl and 0.1 M HNO_3, 5 mL for 2M HCl–5M HF and 8 mL for 1M HNO_3.
[c] 1 M HNO_3 was used to check if Te was completely eluted from the resin after the collection of 0.4 M HCl (see Fehr et al., 2004; Wang et al., 2015).

Table S1.4 The hydride (H_2Te) formation efficiencies[a] in the presence of different amount of Fe in 0.5 ng mL^{-1} NIST SRM 3156 standard solutions.

Fe/Te mass ratio	Hydride formation efficiency (%)
1000	82
2000	81
5000	62
10000	49
100000	49
1000000	43

[a]Efficiency of H_2Te formation in the hydride generation system (*hydrideICP*, *ESI*; 0.1 M $NaBH_4$–0.07 M NaOH and 2 M HCl) is calculated relative to Fe-free 0.5 ng mL^{-1} standard solutions.

Table S1.5 The $\delta^{82/76}$Se value of the inter-laboratory standard MH 495 (15 and 30 ng mL^{-1} Se) measured together with the samples in this study.

	15 ng mL^{-1} solution		30 ng mL^{-1} solution	
	$\delta^{82/76}$Se (‰)	2 s.e.[a] (‰)	$\delta^{82/76}$Se (‰)	2 s.e.[a] (‰)
	-3.14	0.07	-3.24	0.04
	-3.27	0.06	-3.30	0.05
	-3.26	0.07	-3.28	0.05
	-3.19	0.06	-3.26	0.04
	-3.20	0.06	-3.22	0.04
	-3.15	0.05	-3.23	0.03
	-3.26	0.06	-3.25	0.04
	-3.21	0.05	-3.26	0.05
	-3.25	0.06	-3.27	0.03
	-3.21	0.07	-3.27	0.05
	-3.18	0.05	-3.20	0.03
	-3.24	0.06	-3.26	0.04
	-3.27	0.06	-3.25	0.03
	-3.29	0.07	-3.23	0.05
	-3.23	0.06	-3.27	0.04
	-3.12	0.06	-3.28	0.04
	-3.17	0.06	-3.26	0.03
	-3.18	0.06	-3.26	0.05
	-3.32	0.08	-3.33	0.05
	-3.26	0.07	-3.24	0.05
	-3.26	0.05	-3.22	0.04
	-3.25	0.05	-3.27	0.04
	-3.34	0.07	-3.26	0.04
	-3.28	0.06	-3.24	0.05
	-3.22	0.06	-3.29	0.05
	-3.19	0.07	-3.27	0.04
	-3.25	0.07	-3.25	0.04
	-3.30	0.06	-3.30	0.04
	-3.30	0.06	-3.31	0.05
	-3.23	0.07	-3.28	0.05
	-3.20	0.07	-3.24	0.05
	-3.20	0.08	-3.23	0.05
	-3.21	0.07		
	-3.19	0.06		
	-3.24	0.07		
	-3.25	0.07		
	-3.27	0.07		
	-3.26	0.07		
	-3.27	0.08		
	-3.17	0.07		
	-3.28	0.06		
	-3.27	0.05		
	-3.24	0.06		
	-3.29	0.07		
	-3.27	0.07		
	-3.21	0.06		
Average	-3.24		-3.26	
2 s.d.	0.10		0.06	
	n = 46		n = 32	

[a] Internal precision of a sample run during Se isotope analysis (over 40 cycles) is reported as 2 standard error (2 s.e.).

Table S1.6 Compilation of Se and/or Te concentrations of BHVO-2, BCR-2, BE-N and W-2a that were measured using DS MC-ICP-MS and/or ID quadrupole ICP-MS from HF digestions using purification protocols existing in the literature and newly established in this study (see Figure 1.1 for details) over the course of 18 months.

Sample	Digestion batch	Sample size (g)	Purification protocol used[b,c]	Se concentration (ng g^{-1})	ICP-MS used for Se analysis	Te concentration (ng g^{-1})
BHVO-2	1	0.243	A (2-stage)	174	Neptune	
BHVO-2	2	0.246	A (2-stage)	173	Neptune	
BHVO-2	3	0.084	A (1st stage)	167	iQAP-Q	
BHVO-2	4	0.084	A (1st stage)	167	iQAP-Q	
BHVO-2	5	0.255	A (1st stage)	165	Neptune	
BHVO-2	6	0.253	A (1st stage)	168	Neptune	
BHVO-2	7	0.252	A (1st stage)	169	Neptune	
	7		A (1st stage)	170	iQAP-Q	
	7		A (2-stage)	170	Neptune	
BHVO-2	8	0.380	A (1st stage)	170	Neptune	
	8		A (1st stage)	170	iQAP-Q	
	8		A (2-stage)	170	Neptune	
	8		A (2-stage)	170	Neptune	
BHVO-2	9	0.251	B (2-stage)	168	Neptune	
BHVO-2	10	0.252	A (2-stage)	166	Neptune	
BHVO-2	11	0.251	A (1st stage)	168	Neptune	
BHVO-2	12	0.253	A (2-stage)	162	Neptune	
BHVO-2	13	0.258	A (1st stage)	172	Neptune	
BHVO-2	14	0.258	A (1st stage)	172	iQAP-Q	
BHVO-2	15	0.206	A (1st stage)	168	iQAP-Q	
	15		A (1st stage)	169	iQAP-Q	
BHVO-2	16	0.218	A (1st stage)	172	iQAP-Q	
BHVO-2	17	0.262	A (1st stage)	173	iQAP-Q	
BHVO-2	18	0.209	A (1st stage)	175	iQAP-Q	
BHVO-2	19	0.251	A (1st stage)	169	iQAP-Q	
BHVO-2	20	0.275	B (2-stage)	170	iQAP-Q	14.5
	20		A (1st stage)	170	iQAP-Q	
BHVO-2	21	0.269	A (1st stage)	169	iQAP-Q	
BHVO-2	22	0.300	A (1st stage)	165	Neptune	
BHVO-2	23	0.262	C			13.6
BHVO-2	24	0.267	C			13.8
BHVO-2	25	0.250	B (1st stage)			14.7
BHVO-2-reground	26	0.250	B (2-stage)	168	iQAP-Q	14.6
	26		A (2-stage)	168	iQAP-Q	
	26		A (2-stage)	171	Neptune	
BHVO-2	27	0.205	TCF	164	Neptune	
BHVO-2	28	0.231	B (1st stage)			14.4
BHVO-2	29	0.229	B (2-stage)	170	iQAP-Q	14.4
	26		A (1st stage)	171	iQAP-Q	
	26		A (1st stage)	170	iQAP-Q	
BHVO-2	30	0.304	A (1st stage)	169	iQAP-Q	
BHVO-2	31	0.247	B (1st stage)	168	iQAP-Q	14.0

Sample	Digestion batch	Sample size (g)	Purification protocol used[b,c]	Se concentration (ng g^{-1})	ICP-MS used for Se analysis	Te concentration (ng g^{-1})
BHVO-2	32	0.104	A (1st stage)	167	iQAP-Q	
BHVO-2	33	0.110	A (1st stage)	171	iQAP-Q	
BHVO-2	34	0.255	B (1st stage)			13.6
BHVO-2	35	1.114	A (2-stage)	169	Neptune	
BHVO-2	36	1.012	TCF	174	Neptune	
BHVO-2	37	1.105	TCF	169	Neptune	
BHVO-2	38	1.035	TCF	166	Neptune	
BHVO-2	39	1.024	TCF	170	Neptune	
BHVO-2	40	0.521	TCF	166	Neptune	
BHVO-2	41	0.510	TCP	163	Neptune	
BHVO-2	42	1.008	TCP	176	Neptune	
BHVO-2	43	1.011	TCP	172	Neptune	
BHVO-2	44	0.501	new column chemistry	167	Neptune	
BHVO-2	45	0.500	new column chemistry	167	Neptune	
BHVO-2	46	0.238	new column chemistry	165	Neptune	
BHVO-2	47	0.101	new column chemistry	173	Neptune	
BHVO-2	48	0.102	new column chemistry	168	Neptune	
BHVO-2-reground	49	0.426	new column chemistry	165	iQAP-Q	14.6
BHVO-2-reground	50	0.405	new column chemistry	167	iQAP-Q	14.6
BHVO-2	51	0.309	new column chemistry	165	Neptune	
BHVO-2	52	0.302	new column chemistry	179	Neptune	
BHVO-2	53	0.204	new column chemistry	168	Neptune	
BHVO-2	54	0.245	new column chemistry	167	Neptune	14.3
	54		new column chemistry	166	iQAP-Q	
BHVO-2	55	0.245	new column chemistry	167	Neptune	14.3
	55		new column chemistry	166	iQAP-Q	
BHVO-2	56	0.248	new column chemistry	166	Neptune	14.0
	56		new column chemistry	166	iQAP-Q	
BHVO-2	57	0.224	new column chemistry	166	Neptune	14.5
BHVO-2	58	0.230	new column chemistry	174	Neptune	14.3
			Average	**169**		**14.3**
			1 s.d.	3		0.3
			n[d]	53		16
BCR-2	1	1.216	A (1st stage)	75	iQAP-Q	
	1		A (1st stage)	75	iQAP-Q	
	1		A (1st stage)	76	iQAP-Q	
	1		A (1st stage)	76	iQAP-Q	
	1		A (1st stage)	76	iQAP-Q	
	1		A (1st stage)	76	iQAP-Q	
	1		A (2-stage)	75	iQAP-Q	
	1		A (2-stage)	75	iQAP-Q	
	1		A (2-stage)	75	iQAP-Q	
	1		A (2-stage)	74	iQAP-Q	
BCR-2	2	0.853	A (1st stage)	75	iQAP-Q	
BCR-2	3	1.019	TCF	75	Neptune	
BCR-2	4	1.100	TCF	76	Neptune	
BCR-2	5	1.036	TCP	78	Neptune	

Sample	Digestion batch	Sample size (g)	Purification protocol used[b,c]	Se concentration (ng g^{-1})	ICP-MS used for Se analysis	Te concentration (ng g^{-1})
BCR-2	6	1.039	TCP	76	Neptune	
BCR-2	7	0.748	new column chemistry	78	Neptune	
BCR-2	8	0.735	new column chemistry	78	Neptune	
BCR-2	9	0.347	new column chemistry	76	Neptune	
BCR-2	10	0.356	new column chemistry	76	Neptune	
BCR-2	11	0.351	new column chemistry	77	Neptune	
	11		new column chemistry	77	iQAP-Q	
BCR-2	12	0.328	new column chemistry	78	iQAP-Q	
BCR-2	13	0.329	new column chemistry	77	iQAP-Q	
			Average	**76**		
			1 s.d.	1		
			n[d]	13		
BE-N	1	0.204	new column chemistry	67	iQAP-Q	
BE-N	2	0.598	new column chemistry	66	Neptune	
BE-N	3	0.602	new column chemistry	67	Neptune	
BE-N	4	0.627	new column chemistry	66	Neptune	
BE-N	5	0.399	new column chemistry	65	Neptune	
BE-N	6	0.399	new column chemistry	65	Neptune	
BE-N	7	0.402	new column chemistry	63	Neptune	
BE-N	8	0.401	new column chemistry	65	Neptune	
BE-N	9	0.865	new column chemistry	67	Neptune	
BE-N	10	0.851	new column chemistry	68	Neptune	
BE-N	11	0.861	new column chemistry	66	Neptune	
BE-N	12	0.429	new column chemistry	66	Neptune	
BE-N	13	0.463	new column chemistry	67	Neptune	
BE-N	14	0.398	new column chemistry	66	Neptune	
BE-N	15	0.386	new column chemistry	67	Neptune	
BE-N	16	0.335	new column chemistry	67	Neptune	
BE-N	17	0.400	new column chemistry	64	Neptune	
BE-N	18	0.517	new column chemistry	66	Neptune	
	18		new column chemistry	66	iQAP-Q	
			Average	**66**		
			1 s.d.	1		
			n[d]	18		
W-2a	1	0.309	new column chemistry	106	iQAP-Q	
W-2a	2	0.275	new column chemistry	107	iQAP-Q	
			Average	**107**		
			1 s.d.	1		
			n[d]	2		

[a] Note that, in this table, the samples processed after the new column chemistry were only analyzed for additional Se concentrations (Se isotopes and/or Te concentration analyses were not performed) for a more reliable evaluation of the accuracy and precision of our routine Se concentration analysis. Se–Te concentrations determined together with the Se isotope composition from the same sample digests are reported in Table 1.1 and are not further included here.

[b] A = Kurzawa et al. (2017); B =Wang and Becker (2013); C = Wang et al. (2015). Each protocol was followed exactly as described in the original literature.

[c] 2-stage = anion + cation exchange column; 1st stage = anion exchange column only.

[d] Number of digestion repeats.

Table S1.7 Se–Te concentrations of BHVO-2 sieved grain separates analyzed by ID quadrupole ICP-MS after the HF digestion and our newly established purification procedure.

BHVO-2 particle separates	Sieved weight fraction[a]		Se (ng g^{-1})	Te (ng g^{-1})
coarse particles (>25 μm)	49%			
			131	11.1
			135	10.3
			134	10.6
			132	
			136	
		Average concentration	134 ± 2[b]	10.6 ± 0.4[b]
		Se/Te	12.6 ± 0.5[b]	
fine particles (<25 μm)	51%			
			197	18.8
			203	19.3
			196	19.4
			193	18.2
			200	
			202	
			208	
		Average concentration	200 ± 5[b]	18.9 ± 0.5[b]
		Se/Te	10.6 ± 0.4[b]	
		Calculated bulk-rock concentration	167 ± 3[b]	14.8 ± 0.3[b]
		Measured bulk-rock concentration[c]	169 ± 3[b]	14.2 ± 0.3[b]
		Measured bulk-rock Se/Te	11.9 ± 0.7[b]	

[a] Normalized to 100%.
[b] All uncertainties are 1 s.d. for the average Se–Te concentrations and the calculated Se/Te ratios.
[c] It is taken from Table 1 in the main text.

Chapter 2

Selenium isotope and S-Se-Te elemental systematics along the Pacific-Antarctic ridge: Role of mantle processes

S2.1 Modelling Se–Te variations during MORB differentiation

The observed major element systematics were first constrained using a simple fractional crystallization model, which is generally considered as a dominant process during low-pressure magmatic evolution, especially in fast spreading ridges (Grove et al., 1992; Sinton and Detrick, 1992; Perfit, 2001) as in the case of the studied PAR segments (see Main Text Section 2.2). The liquid lines of descents (LLDs) were modelled with alphaMELTS front end (MELTS mode; Version 1.8) run in isobaric mode (Ghiorso and Sack, 1995; Smith and Asimow, 2005). Calculations were performed starting from the most primitive glass PAC1 DR12-1g (Table S2.1) at 2–7 kbar along a buffered fO_2 of 0.18 log units below the FMQ buffer (Zhang H. L. et al., 2018). The modelled trends at 2–5 kbar broadly reproduce the observed variations of most major elements (Fig. S2.3), reflecting a comagmatic origin of the entire PAR on-axis (Vlastélic et al., 2000; Hamelin et al., 2010). The observed Se–Te variations were subsequently modelled using FeO_T as an index of differentiation due to their tight covariations as mentioned in Main Text Section 2.5.2 (also see Main Text Fig. 2.6). Note that FeO_T content of the PAR samples monotonically increases with ongoing crystal fractionation prior to magnetite saturation (Fig. S2.3). The modelled LLDs for FeO_T yields the best match with the observed trend at 3 kbar and the resulting parameters were used in the subsequent modelling.

The Se–Te partitioning between the bulk fractionated minerals (i.e., silicate crystals + sulfide phase) and silicate melt ($D^{bulk}_{Se\ or\ Te}$) is described by

$$D^{bulk}_{Se\ or\ Te} = \frac{X_{sulf}}{1-f} D^{sulf–sil}_{Se\ or\ Te} + \frac{X_{cryst}}{1-f} D^{cryst–sil}_{Se\ or\ Te} \quad \text{(s2.1)}$$

where f, X_{sulf}, and X_{cryst} are the mass fractions of remaining silicate melt, fractionated immiscible sulfide phase, and silicate crystals, respectively, relative to the initial system (i.e., PAC1 DR12-1g); $D^{sulf–sil}_{Se\ or\ Te}$ and $D^{cryst–sil}_{Se\ or\ Te}$ are the sulfide phase–silicate melt and silicate crystal–silicate melt partition coefficients, respectively. As Se–Te are essentially incompatible in silicate crystals (assuming $D^{cryst–sil}_{Se\ or\ Te} = 0.001$; Brenan, 2015), Eq. (s2.1) can be approximated as

$$D^{bulk}_{Se\ or\ Te} = \frac{X_{sulf}}{1-f} D^{sulf–sil}_{Se\ or\ Te} \quad \text{(s2.2)}$$

Considering that all fractionated S is exclusively partitioned into sulfide due to its incompatibility in silicate crystals (Labidi et al., 2014), the mass balance allows calculation of X_{sulf} at a given f (directly obtained from alphaMELTS) following

$$X_{sulf} = \frac{C^0_S - fC^l_S}{C^{sulf}_S} \quad \text{(s2.3)}$$

where C^0_S, C^l_S, and C^{sulf}_S are the S concentrations of the initial high-MgO melts (on average 968 ± 26 μg g^{-1}; Main Text Table 2.2 and Fig. 2.6a), remaining melt, and segregated sulfides, respectively. The term $\frac{X_{sulf}}{1-f}$ in Eq. (s2.2) represents the proportion of sulfide in the bulk fractionated minerals ($X^{bulk\ min}_{sulf}$). For the studied PAR glasses that have not experienced magnetite saturation-triggered sulfide segregation (see Main Text Section 2.5.2 and Fig. 2.6a), we obtain $X^{bulk\ min}_{sulf}$ ranging between 0.09 and 0.20 wt.% averaging at 0.14 ± 0.04 wt.%, consistent with the previous estimate for a larger set of samples (0.19 ± 0.07 wt.%; assuming C^{sulf}_S = 35 wt.%; Labidi et al., 2014).

As for $D^{sulf–sil}_{Se\ or\ Te}$, previous studies reported a wide range of values (Peach et al., 1990; Barnes et al., 2009; Patten et al., 2013; Brenan, 2015; Kiseeva et al., 2017). Two partitioning experiments show that $D^{sulf–sil}_{Se\ or\ Te}$ strongly depends on the fractionating sulfide phase (crystalline monosulphide solid solution (MSS) and sulfide liquid) and FeO content of the silicate melt (Brenan, 2015; Kiseeva et al., 2017). Both elements are highly compatible in sulfides relative to silicates, whereas Te is more compatible in sulfide liquid and Se is more compatible in MSS (Brenan, 2015). For sulfide liquid–silicate melt partitioning ($D^{sulf\ liq–sil}_{Se\ or\ Te}$), these studies reported significantly different values. For a basaltic melt with 8–11 wt.% FeO, Kiseeva et al. (2017) reported $D^{sulf\ liq–sil}_{Se}$ = 450–650 and $D^{sulf\ liq–sil}_{Te}$ = 2600–3200, much lower than $D^{sulf\ liq–sil}_{Se}$ = 1050 ± 360–1460 ± 400 and $D^{sulf\ liq–sil}_{Te}$ = 9720 ± 1170–13640 ± 1590 (1 s.d. propagated error) expected from the formula of Brenan (2015), respectively ($D^{sulf\ liq–sil}_{Se\ or\ Te}$ decreases with increasing FeO content of the silicate melt). In the case of the evolving PAR melts with FeO_T from 8.49 to 12.78 wt.% (Main Text Fig. 2.6b and c; MgO from ~8.85–5.5 wt.%; Fig. S2.3), assuming $Fe^{2+}/\Sigma Fe$ = 0.87 (Bézos and Humler, 2005; Zhang H. L. et al., 2018), we obtain 1560 ± 410–

1035 ± 360 for $D_{Se}^{sulf\ liq–sil}$ and 14430 ± 1680–9570 ± 1150 for $D_{Te}^{sulf\ liq–sil}$ (both 1 s.d.) following Brenan (2015). Both these values and $D_{Se\ or\ Te}^{sulf\ liq–sil}$ from Kiseeva et al. (2017), together with $X_{sulf}^{bulk\ min}$ = 0.14 ± 0.04 wt.%, are used to derive $D_{Se\ or\ Te}^{bulk}$ using Eq. (s2.2). Finally, the model Se–Te concentrations were calculated using the fractional (Eq. s2.4) and/or batch crystallization (Eq. s2.5) laws following

$$C_{Se\ or\ Te}^{l} = C_{Se\ or\ Te}^{0} f^{D_{Se\ or\ Te}^{bulk} - 1} \quad \text{(s2.4)}$$

and/or

$$C_{Se\ or\ Te}^{l} = \frac{C_{Se\ or\ Te}^{0}}{f + D_{Se\ or\ Te}^{bulk}(1 - f)} \quad \text{(s2.5)}$$

where $C_{Se\ or\ Te}^{l}$ and $C_{Se\ or\ Te}^{0}$ are Se-Te concentrations of the remaining melt at a given f and the initial melt (PAC1 DR12-1g; Main Text Table 2.2), respectively.

S2.2 Modelling Se–Te variations during partial melting

The variations of Se–Te during partial melting were modelled for a triangular passive-flow near-fractional melting regime, which has been previously used to explain the Se–Te and highly siderophile element systematics of MORB melts (Rehkämper et al., 1999; Bézos et al., 2005; Mungall and Brenan, 2014; Lissner et al., 2014; Brenan, 2015). The procedures of our model basically follow that detailed by Rehkämper et al. (1999) and Brenan (2015). Briefly, we assume a simplified two-phase mineralogy for the mantle source, which consists of sulfides (sulfide liquid with/without MSS) and bulk silicate minerals. The Se–Te concentrations of each melt increment (1%; relative to the initial system mass) and the residue are calculated by the batch melting equation (Shaw, 1970) with $D_{Se\ or\ Te}^{bulk}$ using experimentally determined $D_{Se\ or\ Te}^{sulf\ liq–sil}$ and/or $D_{Se\ or\ Te}^{MSS–sil}$ values while assuming $D_{Se\ or\ Te}^{cryst–sil}$ = 0.001 (Brenan, 2015; Kiseeva et al., 2017; see Section S2.1). After each equilibrium melting step, 0.1% of the fractional melt is retained (by simple batch mixing) to refertilize the residual mantle column and the rest is extracted. The mineral modes (sulfide and silicate) and composition (S–Se–Te contents) of the residue (i.e., the source for the next melting step) are recalculated accordingly. Finally, the polybaric column-melts produced over the entire two-dimensional melting zone are pooled completely and produce the PAR primary melts at a mean extent of melting F_B (defined as the mass fraction of

all melts relative to the initial solid entering the melting region), which is approximated as $\frac{F_{max}}{2}$, where F_{max} is the maximum extent of melting achieved in the central melting column (Langmuir et al., 1992; Plank et al., 1995; Rehkämper et al., 1999). Sulfur contents of the residue and partial melts at each step depend on the initial S content of the source and SCSS of the aggregate melt in a specific melting column. When the S content of the residue is insufficient to keep the equilibrium melt S-saturated, S starts to behave as an incompatible element (with $D_S^{cryst-sil} = 0.001$; Labidi et al., 2014). Upon sulfide exhaustion in a column, S content of the aggregate melt is simply diluted as the subsequent melt increments essentially become S-free. We note that this may be an oversimplification in some cases. For instance, S systematics in the Garrett transform fault lavas, which might have formed by re-melting of a depleted MORB source ($F_B \approx 10\%$ for both melting events; see discussion and Fig. S2.5a for the typical F_B of sulfide undersaturation in aggregate MORB melts), are similar to those observed in global sulfide-saturated MORBs, requiring that their source (after the first MORB melting event) kept the melts sulfide-saturated (Labidi and Cartigny, 2016). However, generally, MORB melts produced in a triangular melting regime typical for fast-spreading ridges (e.g., Langmuir and Forsyth, 2007; Langmuir et al., 1992; Lin and Morgan, 1992; Brown and Lesher, 2016; and references therein) represent a mixture of S-saturated partial melts (coming from low-F sulfide-bearing mantle columns) and S-undersaturated partial melts (from high-F (e.g., ~20%) S-exhausted mantle columns) (also see Ding and Dasgupta, 2017).

The model parameters used here are summarized in Main Text Table 2.3. The melt major element compositions and pressure-temperature (P–T) conditions for calculating the SCSS of the aggregate melt in a melting column (Smythe et al., 2017) and $D_{Se\ or\ Te}^{sulf\ liq-sil}$ (as a function of FeO; for each incremental/equilibrium melt; Brenan, 2015; Kiseeva et al., 2017) were modelled with alphaMELTS front end run in pMELTS mode (Ghiorso et al., 2002; Smith and Asimow, 2005), following a similar approach used by Ding and Dasgupta (2017). The relevant mantle potential temperature (T_P) for the PAR MORBs was estimated based on the previously determined primary melt–mantle equilibration P–T (on average ~10.2 kbar and 1325°C; Main Text Section 2.5.2.2), which falls between 1275 and 1350°C, in accordance with the previous estimates for global MORBs (Main Text Fig. 2.7; Lee et al., 2009; Ding and Dasgupta, 2017). The pMELTS calculation with $T_P = 1350$°C may be adequate for our purpose because each P–T data for the aggregate PAR primary melts represents the weighted average P–T of melt extraction from all mantle parcels across the triangular melting zone and thus lies below the

polybaric melting path (Main Text Fig. 2.7; Asimow and Longhi, 2004; Lee et al., 2009). The composition of the depleted MORB mantle were taken from Salters and Stracke (2004) assuming 0.2 wt.% Fe_2O_3 (e.g., Cottrell and Kelley, 2011). We obtain a range of temperature from 1389 to 1294°C for the extent of melting F from 0 to 20%, with the corresponding extraction pressures 17.5 to 5.4 kbar for the incremental melts and 17.5 to 9.4 kbar for the aggregate melts (1-D integration over a single melting column). Under these conditions, the calculated $D_{Se\ or\ Te}^{sulf\ liq–sil}$ values following Brenan (2015) at each melting step are 1414 ± 401–1900 ± 435 for $D_{Se}^{sulf\ liq–sil}$ and 13199 ± 1541–16811 ± 1940 for $D_{Te}^{sulf\ liq–sil}$ (1 s.d. propagated uncertainty), increasing with progressive melting due to the decreasing FeO content of the fractional melts (~8.34–5.37 wt.%). These values are considerably higher than that used by Brenan (2015) for the melting model, which are 1086 and 8789 for Se and Te, respectively (chosen at an empirical FeO content of 10 wt.%). At this range of FeO content, $D_{Se\ or\ Te}^{sulf\ liq–sil}$ values of Kiseeva et al. (2017) should be 550–850 and 3000–3800 for Se and Te, respectively (see Section S2.1 for the different results between two studies).

As for estimating the average melting degree for the PAR MORBs, we used (incompatible) trace element systematics (Fig. S2.4). The primary melt compositions (on average ~11.8 wt.% MgO and Mg# = 0.73) were obtained by a similar method used for Se–Te (see Main Text Section 2.5.2.2). Briefly, measured concentrations (Table S2.1) were first corrected to MgO content (8.85 wt.%) of the most primitive glass by linear regression. This was followed by correcting for ~8.7% olivine fractionation considering that these elements are highly incompatible in olivine (e.g., Bédard, 2005). The average melting degree was then estimated in two different approaches: (1) by solving the simple batch melting equation for F_B using concentration of each trace element i (C_i^{melt}) for all primary melts (n = 24) and the source (C_i^{mantle}; depleted MORB mantle; Salters and Stracke, 2004) with empirical mantle–melt bulk partition coefficients ($D_i^{mantle–melt}$) following the approach of Kelley et al. (2006):

$$F_B = \frac{\frac{C_i^{mantle}}{C_i^{melt}} - D_i^{mantle–melt}}{1 - D_i^{mantle–melt}} \quad \text{(s2.6)}$$

which yields F_B from ~6.6 to ~11.7% (average 8.5 ± 1.5%; 1 s.d., n = 24); and (2) comparing the results obtained from pMELTS for the accumulated melts (over the entire triangular melting region) to our calculated primary melt concentrations, which gives a best match if F_B ranges

between 6.5 and 9.5% (Fig. S2.4). Both results are in excellent agreement and, meanwhile, consistent with the previous estimates for global MORBs (e.g., Klein and Langmuir, 1987; Salters and Stracke, 2004; Workman and Hart, 2005; Kimura et al., 2017). Besides, our calculated primary melt–mantle equilibration P–T for PAR glasses, together with most global MORBs, fall between 10–20% melt fraction isopleths estimated for a fertile lherzolite (Main Text Fig. 2.7; Katz et al., 2003; Lee et al., 2009). Lower melt fractions would be expected for a depleted MORB source mantle due to its relatively higher solidus (Lee et al., 2009), which may then be broadly consistent with our estimated F_B.

Three different mantle sulfides (Fe–Ni–Cu BMS) were used to calculate the SCSS of the partial melts considering that the equilibrium sulfide chemistry significantly affects the S solubility as FeS activity decreases due to the presence of Ni and Cu, i.e., SCSS decreases with decreasing $X_{Fe} = \frac{\text{Fe}}{\text{Fe + Ni + Cu}}$ (molar ratio) (e.g., Ariskin et al., 2013, 2018; Ding and Dasgupta, 2017; Ding et al., 2018; Smythe et al., 2017). The calculated chemical formulas are shown in Fig. S2.5. Sulfide A has a relatively refractory composition and was used in the melting experiments of Bockrath et al. (2004) and Zhang Z. and Hirschmann (2016) to obtain the sulfide solidus and liquidus as shown in Main Text Fig. 2.7. Sulfide B is calculated assuming 25 wt.% Ni + 5 wt.% Cu (used in the melting model of Ding and Dasgupta (2017)) and metal/S atomic ratio of 0.93 that is typical for shallow mantle sulfides under relatively oxidized conditions (e.g, MORB source mantle; Zhang Z. et al., 2018; also see Lorand and Luguet, 2016). For sulfide C, we first estimated its $\frac{\text{Ni}}{\text{Ni + Fe}}$ molar ratio using the Ni and FeO contents of olivine in the residue (~10.06–9.01 wt.% FeO and ~1964–2349 μg g^{-1} Ni for 0–20% melting; from pMELTS) and sulfide melt–olivine Fe–Ni exchange relations following Zhang Z. et al. (2018):

$$\frac{(Ni/Fe)_{sulf\,liq}}{(Ni/Fe)_{olivine}} = 14.33\frac{Ni}{Ni + Fe} + 39.45 \quad \text{(s2.7)}$$

which yields 0.53–0.60 (increasing with increasing F). The weight fractions of Fe, Ni, and S are then calculated with a constant $\frac{\text{Ni}}{\text{Ni + Fe}}$ = 0.53 while taking metal/S ratio of 0.93 (Zhang Z. et al., 2018) and 5 wt.% Cu (Kiseeva et al., 2017).

Because there are a large number of model parameters, we first validate our model for the variation of chalcophile elements S and Cu during melting (Fig. S2.5) because (1) S and Cu abundances in the mantle are relatively well constrained using different approaches by several

studies (e.g., Mcdonough and Sun, 1995; Salters and Stracke, 2004; Lorand and Luguet, 2016; Lorand et al., 2013; Wang and Becker, 2013, 2015b; Palme and O'Neill, 2014); (2) their behavior during partial melting has been systematically modelled using experimentally determined partition coefficients (e.g., Lee et al., 2009; Li and Audétat, 2012; Kiseeva and Wood, 2013, 2015; Brenan, 2015) and a large number of analyses in MORB melts (e.g., Jenner and O'Neill, 2012; Labidi et al., 2014) with a variety of SCSS models, source contents, and T_P (Lee et al., 2009; Li and Audétat, 2012; Ding and Dasgupta, 2017). The S of contents used for the PAR MORB source mantle ranges from "PM-like" 200 μg g^{-1} (e.g., Lorand et al., 2013; Palme and O'Neill, 2014; Wang and Becker, 2013) to slightly lower 150 μg g^{-1} as estimated for the depleted MORB mantle (e.g., Luguet et al., 2003; Bézos et al., 2005; Nielsen et al., 2014; Lorand and Luguet, 2016). A starting Cu content of 30 ± 6 μg g^{-1} is used, as suggested for the PM (Mcdonough and Sun, 1995; Wang and Becker, 2015b) as well as the depleted MORB mantle (Salters and Stracke, 2004). Partition coefficients of Cu between silicate minerals and melt ($D_{Cu}^{cryst–sil}$) are taken from Lee et al. (2009). $D_{Cu}^{sulf\ liq–sil}$ is taken as 1000 (Li and Audétat, 2012), which has been used in several studies for modelling the behavior of Cu (e.g., Ding and Dasgupta, 2017; Wang and Becker, 2015b). The primary melt S and Cu contents (after correcting for sulfide + crystal fractionation) are calculated by the same approach used for Se and Te contents (Main Text Section 2.5.2.2). Our result (Fig. S2.5) shows that, with the SCSS model of Smythe et al. (2017) and equilibrium sulfide composition B (X_{Fe} = 0.54; $\frac{\text{Ni}}{\text{Ni + Fe}}$ = 0.42; Fig. S2.5a), the PAR primary melt S concentrations are very well reproduced with our partial melting model for the estimated F_B of the samples using a range of source S content (150–200 μg g^{-1}). Note that the chemistry of sulfide B used here is also consistent with typical lherzolite-hosted sulfide compositions (e.g., Lorand and Luguet, 2016) as well as the suggested range of $\frac{\text{Ni}}{\text{Ni + Fe}}$ value for a shallow mantle Cu-free sulfide (0.4–0.6) by Zhang Z. et al. (2018) at the range of melting depth (from ~50 to 20 km from pMELTS; Maint Text Fig. 2.7) and fO_2 (~FMQ; Cottrell and Kelley, 2011; Zhang H. L. et al., 2018) estimated for the Pacific–Antarctic MORB. The corresponding model curves also show a very good fit to the primary melt Cu concentrations with 170–200 μg g^{-1} S and 30 (or 24) μg g^{-1} Cu in the source (Fig. S2.5b and c). The same parameters are then used for the modelling of Se and Te behavior during partial melting and estimation of the Pacific mantle composition (Fig. S2.6 and Main Text Fig. 2.8 and Fig. 2.9).

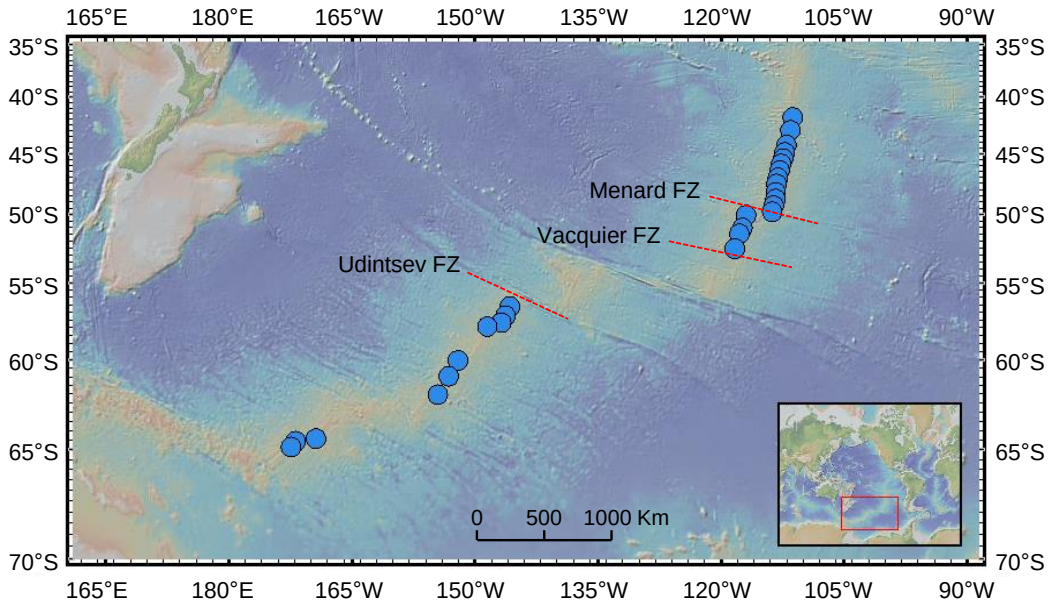

Fig. S2.1 Map showing the location of the studied MORB samples from the Pacific–Antarctic ridge (PAR; 65–56°S (n = 10) and 53–41°S (n = 17)). Also shown are the major fracture zones in the southern and northern ridge sections (Vlastélic et al., 2000; Hamelin et al., 2010). The map is generated using the GeoMapApp (http://www.geomapapp.org; and references therein).

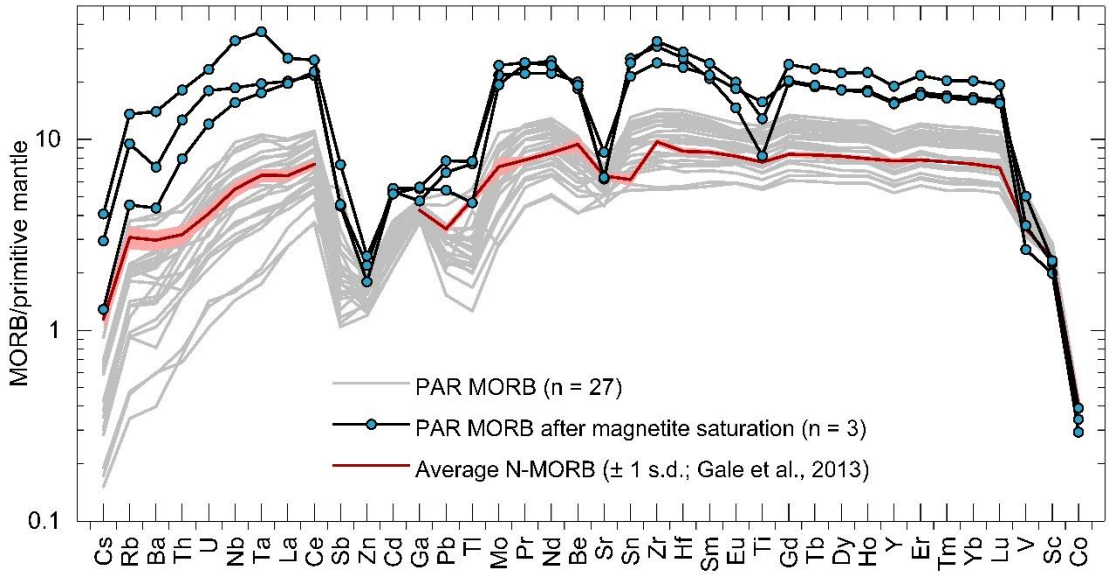

Fig. S2.2 Primitive mantle-normalized (McDonough and Sun, 1995) trace element diagram of the studied PAR MORBs. The element order (with increasing compatibility to the right) is after Hofmann (1988) and Jenner et al. (2012). All samples show typical depleted MORB patterns similar to that of the average N-MORB from Gale et al. (2013). Three most evolved samples (blue line) that have experienced magnetite saturation and magnetite-triggered sulfide precipitation (Fig. S2.3; Main Text Fig. 2.4 and Fig. 2.6) display abrupt drops in apparently compatible elements Zn, Ga, Ti, V, Sc, and Co due to their strong partitioning into fractionating magnetite and/or sulfide (Nielsen et al., 1994; Toplis and Corgne, 2002; Righter et al., 2006; Dare et al., 2012, 2014; Labidi et al., 2014; Jenner et al., 2010, 2012, 2015).

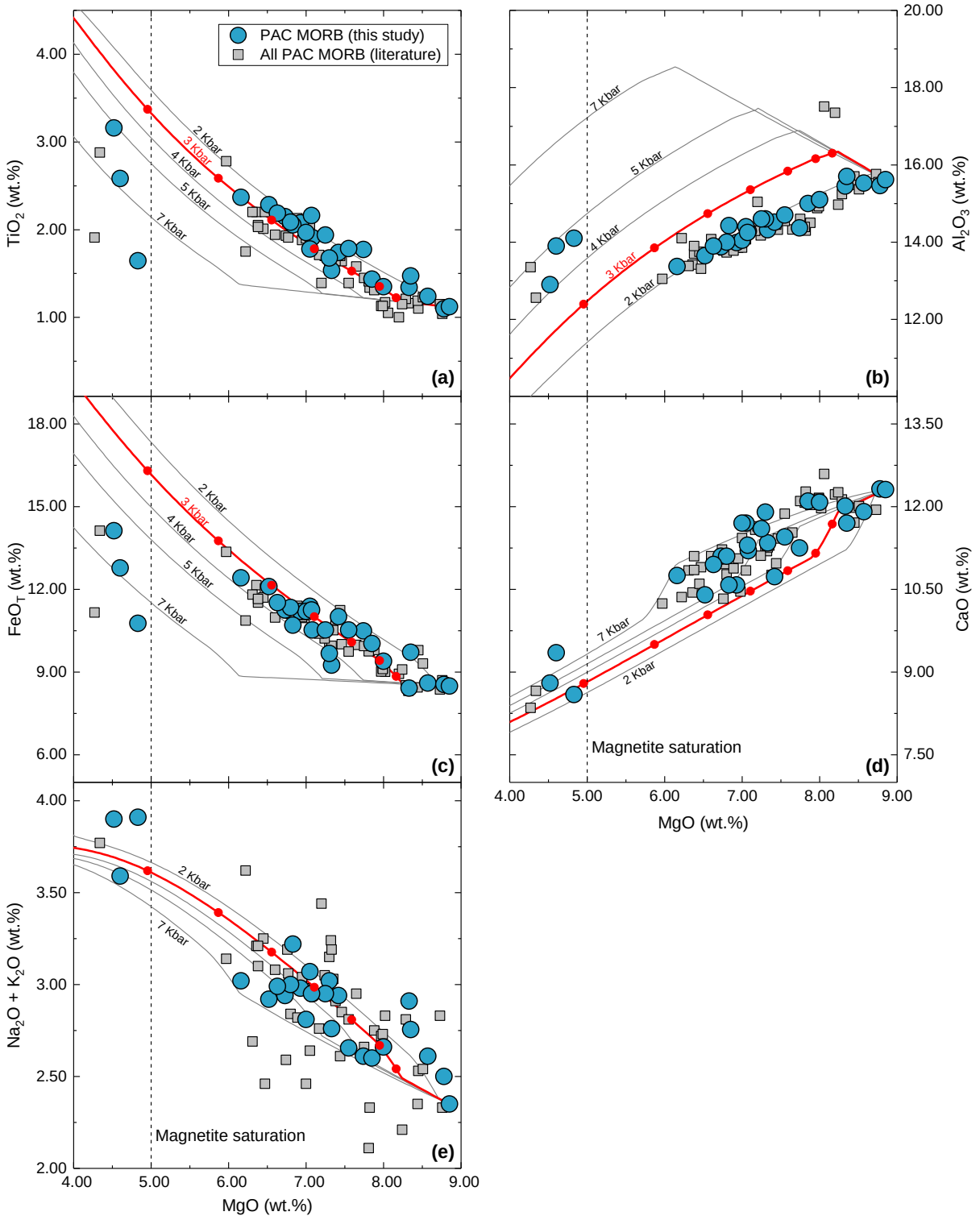

Fig. S2.3 Major element variation diagrams versus MgO for all the PAR on-axis samples (between 65–56°S and 53–41°S; Table S2.1) as well as the modelled liquid lines of descents (LLDs). The TiO_2 data (a) for the studied glasses are obtained in this study together with other trace elements. All other data along the studied ridge segments are reported by Vlastélic et al. (2000) and Hamelin et al. (2010). The differentiation trends (isobaric fractional crystallization) are modelled with alphaMELTS front end (V 1.8; Ghiorso and Sack, 1995; Smith and Asimow, 2005) along a buffered fO_2 of 0.18 log units below the FMQ buffer (Zhang H. L. et al., 2018) at a variety of pressures (2, 3, 4, 5 and 7 kbar), starting from the most primitive glass PAC1 DR12-1g (8.85 wt.% MgO). Each

tick mark indicates 10% crystal fractionation step. Before the magnetite saturation at ~5 wt.% MgO (Vlastélic et al., 2000; Hamelin et al., 2010; Labidi et al., 2014), most major element variations broadly follow the modelled LLDs at 2–5 kbar. The variation of FeO_T is best reproduced at 3 kbar, and the resulting parameters are used in the subsequent modelling in Main Text Fig. 2.6.

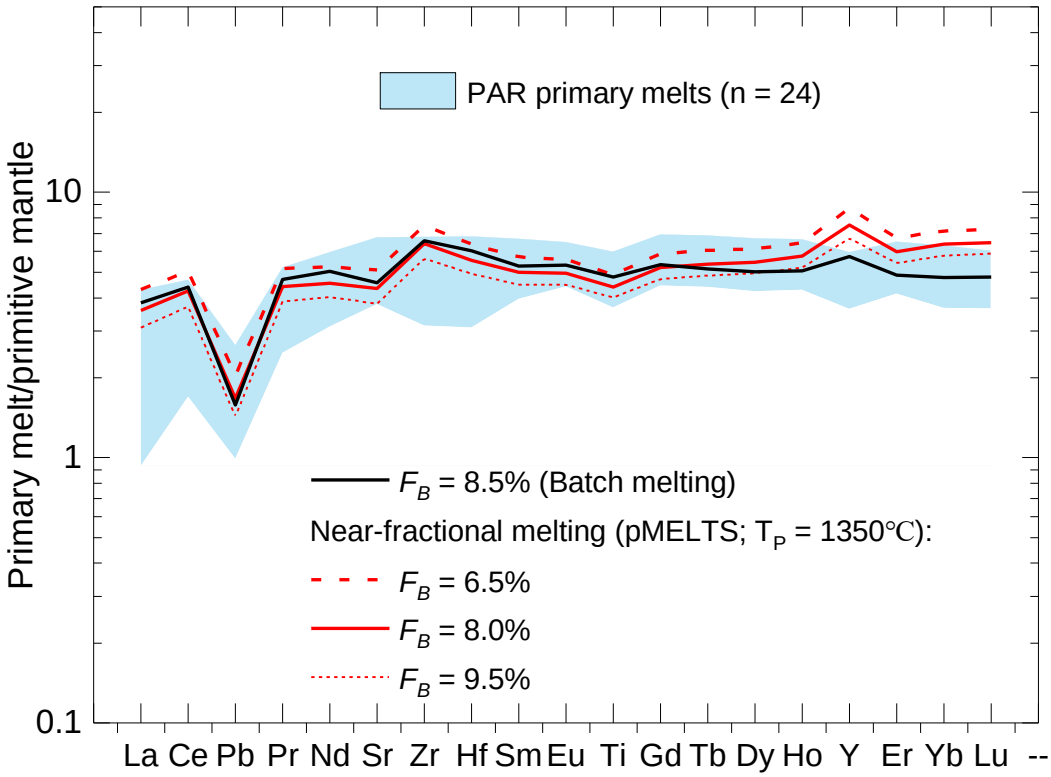

Fig. S2.4 Primitive mantle-normalized (McDonough and Sun, 1995) incompatible trace element pattern for the model PAR primary magmas (n = 24; at Mg# = 0.73) which were obtained after correcting the observed concentrations for fractional crystallization (see the text for details). Three samples (MgO <5 wt.%) that have experienced magnetite saturation were not included (Fig. S2.2 and S2.3 and Main Text Fig. 2.4). The curves show the best-matched primary melt composition obtained from (1) simple batch melting using average F_B (~8.5%) of the samples, which was first obtained by solving the batch melting equation for F_B for each sample (Eq. s2.6; following the approach of Kelley et al. (2006)) and (2) pMELTS (near-fractional melting) for the aggregate melts over the entire triangular melting region (F_B: 6.5, 8.0, and 9.5%). The source trace element compositions and empirical bulk partition coefficients were taken from Salters and Stracke (2004) and Kelley et al. (2006), respectively. Both results are in excellent agreement with each other and used for modelling the Se–Te (additionally S–Cu) behavior during partial melting (Fig. S2.5 and S2.6; Main Text Fig. 2.8).

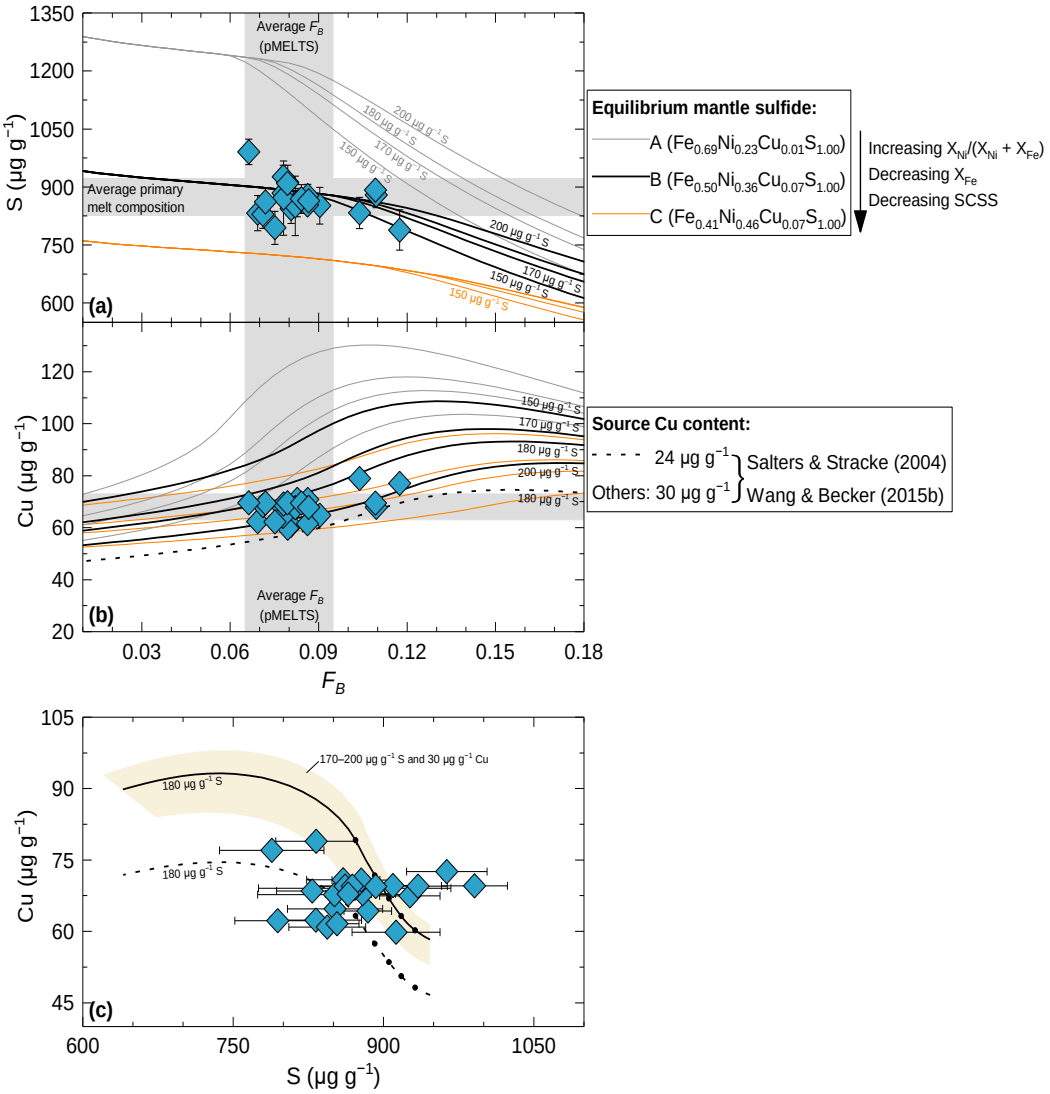

Fig. S2.5 Variations of S (a) and Cu (b) concentrations of the primary PAR melts with their average degree of melting (F_B; estimated by batch melting equation Eq. s2.6 using incompatible trace element systematics; ~6.6–11.7%). The S and Cu concentrations were corrected for sulfide + crystal fractionation by the same approach used for Se and Te concentrations (see Main Text Section 2.5.2.2 for details). The vertical and horizontal shaded field represent the range of F_B (6.5–9.5%; estimated from the forward modelling (near-fractional melting; pMLETS); also see Fig. S2.4) and average primary melt composition (874 ± 48 µg g^{-1} S and 68 ± 5 µg g^{-1} Cu), respectively. Superimposed are modelled S and Cu contents of the primary melt during a near-fractional melting of a depleted MORB mantle in a triangular melting regime (e.g., Rehkämper et al., 1999; Lissner et al., 2014; Brenan, 2015). The major element concentrations, mineral modes, and P–T parameters were obtained from the pMELTS modelling (see Main Text Fig. 2.7) and used for calculating the SCSS of the silicate melts (Smythe et al., 2017) and D_{Cu}^{bulk}. Three different equilibrium BMS compositions were used to calculate the SCSS (Smythe et al., 2017) of the partial melts (see Section S2.2 for details). A range of source S contents (150–200 µg g^{-1}) are used for the PAR MORB source mantle according to previous estimates for the primitive and depleted upper mantle (e.g., Luguet et al., 2003; Lorand et al., 2013; Lorand and Luguet, 2016; Bézos et al., 2005; Wang and Becker, 2013; Nielsen et al., 2014; Palme and O'Neill, 2014). The source Cu concentration used here (30 ± 6 µg g^{-1}) has been suggested for both the PM (Wang and Becker, 2015b) and depleted MORB mantle (Salters and Stracke, 2004).

$D_{Cu}^{cryst-sil}$ (silicate minerals include olivine, orthopyroxene, clinopyroxene, and spinel) from Lee et al. (2009) and $D_{Cu}^{sulf\ liq-sil}$ = 1000 from Li and Audétat (2012). The $D_{Cu}^{sulf\ liq-sil}$ value was used by Ding and Dasgupta (2017) and Wang and Becker (2015) for modelling the behavior of Cu during melting. It shows that our modelled S variation using the SCSS model of Smythe et al. (2017) combined with equilibrium sulfide B (X_{Fe} = 0.54; $\frac{Ni}{Ni+Fe}$ = 0.42) successfully reproduces the primary melt S contents with 150–200 μg g^{-1} S in the mantle source (a); meanwhile, the model curves also perfectly match the Cu contents with 170–200 μg g^{-1} S (b and c; also see the light yellow shaded area in c). Additionally shown in (b) and (c) is the modelled Cu content with 24 μg g^{-1} Cu (previously used in the model of Ding and Dasgupta (2017)) and 180 μg g^{-1} S (dashed black line), in accordance with the source S content used for modelling the Se–Te variation during melting shown in Fig. S2.6 and Main Text Fig. 2.8 and Fig. 2.9.

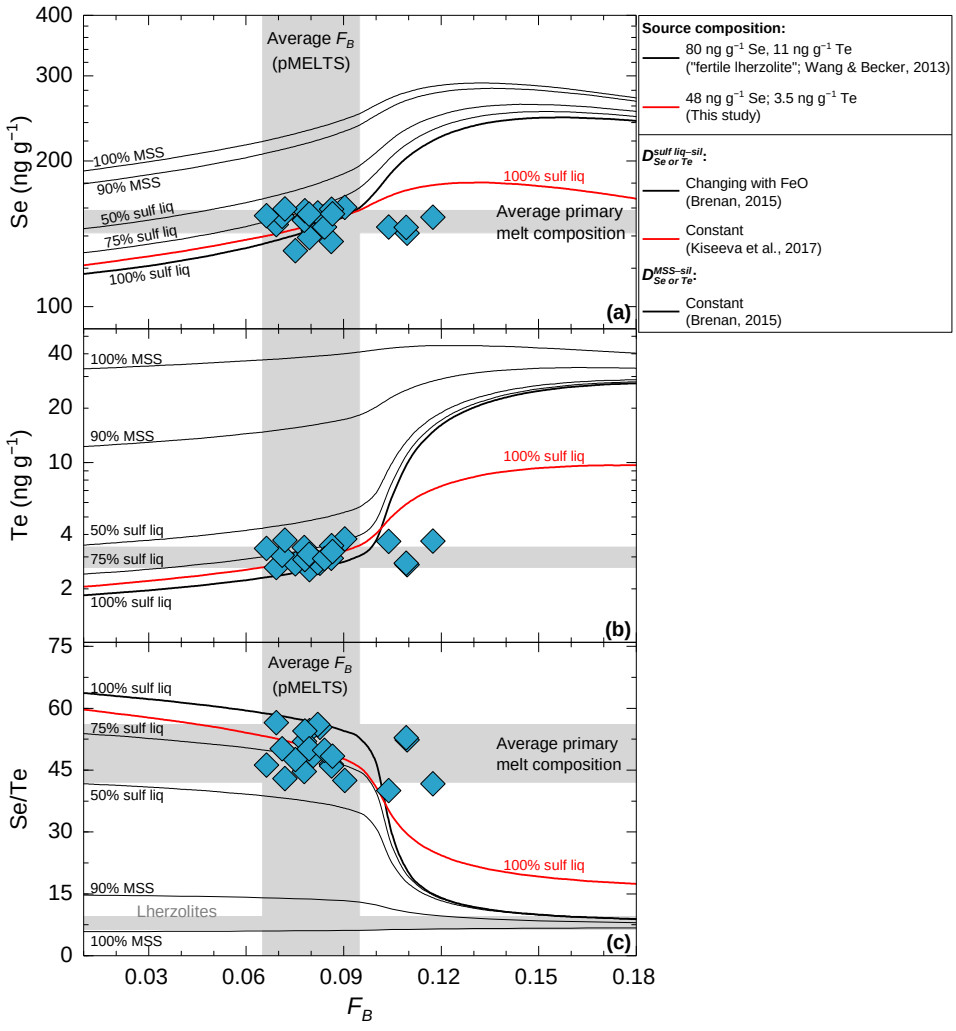

Fig. S2.6 Variations of Se (a) and Te (b) contents and Se/Te ratios (c) of the primary PAR melts with their average degree of melting (F_B). Here, it shows the effect of varying proportions of sulfide phases (i.e., sulfide liquid and crystalline MSS; assuming congruent melting) in the source with 180 μg g^{-1} S. See Main Text Fig. 2.8 for details of the modelling parameters when the source has only sulfide liquid (e.g., different S–Se–Te contents of the mantle source). The grey shaded areas have the same meaning as in Main Text Fig. 2.8. $D_{Se\ or\ Te}^{sulf\ liq-sil}$ values are either

calculated following Brenan (2015) at each incremental melt (black lines) or taken from Kiseeva et al. (2017) (red lines; $D_{Se}^{sulf\ liq–sil}$ = 850 and $D_{Te}^{sulf\ liq–sil}$ = 3800) considering the FeO content of the melt increments (also see Section S2.1 for the difference of $D_{Se\ or\ Te}^{sulf\ liq–sil}$ values between these studies). $D_{Se}^{MSS–sil}$ = 883 and $D_{Te}^{MSS–sil}$ = 729 (both constant) from Brenan (2015). It shows that the Se–Te fractionation during entire F_B interval is limited if MSS is the only residual sulfide due to the similar $D_{Se\ or\ Te}^{MSS–sil}$ values (also see Main Text Fig. 2.9; Brenan, 2015). Sulfide liquid is required to be the dominant (>50%), if not only, residual sulfide phase in order to account for the observed Se–Te variations of the primary MORB melts based on the relative partitioning of these elements in sulfide liquid and crystalline MSS (see Main Text for discussion).

Table. S2.1 Selenium isotope analysis of MH-495 (inter-laboratory standard solution; 30 ng mL^{-1} Se) during the course of this study.

	$\delta^{82/76}$Se (‰)	2 s.e. (‰)[a]
	-3.20	0.04
	-3.19	0.05
	-3.27	0.05
	-3.24	0.04
	-3.22	0.06
	-3.28	0.05
	-3.26	0.05
	-3.21	0.05
	-3.17	0.07
	-3.24	0.05
	-3.24	0.05
	-3.29	0.04
	-3.25	0.06
	-3.28	0.05
	-3.25	0.06
	-3.28	0.04
	-3.17	0.05
	-3.28	0.05
	-3.24	0.05
	-3.23	0.05
Average[b]	**-3.24 ± 0.07**	
Kurzawa et al. (2017)[b]	-3.27 ± 0.13 (n = 100) *(15 ng mL^{-1} Se)*	
Yierpan et al. (2018)[b]	-3.24 ± 0.10 (n = 46) *(15 ng mL^{-1} Se)*	
	-3.26 ± 0.06 (n = 32) *(30 ng mL^{-1} Se)*	

[a] Internal uncertainty of each individual measurement (40 cycles) given in 2 standard error.
[b] Uncertainty on the average given in 2 standard deviation.

Table. S2.2 Compilation of trace element concentrations analyzed in this study (solution iQAP-Qc quadrupole ICP-MS) together with the major/trace element and radiogenic/stable isotope composition in the literature for the studied PAR glasses.

Sample	Latitude (°S)	Longitude (°W)	Dredging Depth (m)	Major elements[a] (wt. %)	SiO_2	TiO_2	Al_2O_3	FeO_T	MnO	MgO	CaO	Na_2O	K_2O	P_2O_5
PAC1 CV02-g	*64.83*	*172.43*	*2936*		*50.8*	*1.77*	*14.4*	*10.5*	*0.19*	*7.74*	*11.3*	*2.55*	*0.06*	
PAC1 CV03-g	*64.53*	*171.88*	*2576*		*50.7*	*1.24*	*15.5*	*8.60*	*0.16*	*8.57*	*11.9*	*2.53*	*0.08*	
PAC1 CV04-g	*64.40*	*169.40*	*2340*		*50.3*	*1.10*	*15.5*	*8.55*	*0.16*	*8.78*	*12.3*	*2.46*	*0.04*	
PAC1 DR05-1g	*62.00*	*154.54*	*2344*		*51.0*	*1.34*	*15.5*	*8.42*	*0.15*	*8.33*	*12.0*	*2.82*	*0.09*	
PAC1 DR06-g	*60.94*	*153.21*	*2527*		*51.0*	*2.08*	*14.0*	*11.2*	*0.20*	*6.93*	*10.6*	*2.86*	*0.12*	
PAC1 DR07-1g	*60.00*	*152.08*	*2362*		*50.8*	*2.05*	*14.4*	*10.7*	*0.22*	*6.83*	*10.6*	*3.03*	*0.19*	
PAC1 DR10-1g	*57.89*	*148.50*	*2319*		*53.8*	*1.65*	*14.1*	*10.8*	*0.21*	*4.83*	*8.59*	*3.43*	*0.48*	
PAC1 DR11-1g	*57.63*	*146.80*	*2500*		*50.2*	*1.53*	*14.3*	*9.25*	*0.17*	*7.33*	*11.3*	*2.70*	*0.06*	
PAC1 DR12-1g	*57.18*	*146.29*	*2539*		*50.9*	*1.12*	*15.6*	*8.49*	*0.15*	*8.85*	*12.3*	*2.32*	*0.03*	
PAC1 DR13-2g	*56.57*	*145.74*	*2674*		*50.5*	*1.74*	*14.5*	*11.0*	*0.19*	*7.42*	*10.7*	*2.85*	*0.09*	
PAC2 DR01-1	*52.53*	*118.35*	*2323*		*50.2*	*1.68*	*14.6*	*9.67*	*0.18*	*7.30*	*11.9*	*2.82*	*0.20*	*0.17*
PAC2 DR04-2	*51.43*	*117.78*	*2409*		*50.4*	*1.91*	*14.3*	*10.5*	*0.20*	*7.08*	*11.2*	*2.83*	*0.12*	*0.18*
PAC2 DR05-2g	*50.98*	*117.40*	*2784*		*49.9*	*2.28*	*13.7*	*12.1*	*0.22*	*6.52*	*10.4*	*2.74*	*0.18*	*0.24*
PAC2 DR08-1	*49.99*	*116.97*	*2221*		*49.4*	*1.78*	*14.4*	*11.4*	*0.20*	*7.05*	*11.7*	*2.87*	*0.20*	*0.17*
PAC2 DR20-1	*49.73*	*113.78*	*2441*		*51.2*	*2.58*	*13.9*	*12.8*	*0.24*	*4.60*	*9.35*	*3.34*	*0.25*	*0.42*
PAC2 DR21-2	*49.26*	*113.60*	*2339*		*50.3*	*2.15*	*13.9*	*11.2*	*0.21*	*6.73*	*11.1*	*2.79*	*0.15*	*0.18*
PAC2 DR22-1	*48.73*	*113.37*	*2413*		*49.9*	*1.94*	*14.6*	*10.5*	*0.20*	*7.25*	*11.6*	*2.78*	*0.17*	*0.18*
PAC2 DR27-1	*48.18*	*113.34*	*2359*		*49.8*	*3.16*	*12.9*	*14.1*	*0.26*	*4.52*	*8.80*	*3.37*	*0.53*	*0.46*
PAC2 DR28-2	*47.51*	*113.25*	*2489*		*49.7*	*1.44*	*15.0*	*10.0*	*0.19*	*7.85*	*12.1*	*2.52*	*0.08*	*0.12*
PAC2 DR29-1	*47.01*	*113.09*	*2407*		*49.9*	*2.37*	*13.4*	*12.4*	*0.23*	*6.16*	*10.8*	*2.83*	*0.19*	*0.23*
PAC2 DR30-1	*46.40*	*112.87*	*2345*		*50.0*	*1.97*	*14.1*	*11.2*	*0.21*	*7.00*	*11.7*	*2.64*	*0.17*	*0.20*
PAC2 DR31-3	*45.85*	*112.69*	*2414*		*49.9*	*1.78*	*14.7*	*10.5*	*0.19*	*7.55*	*11.5*	*2.56*	*0.10*	*0.18*
PAC2 DR32-1	*45.39*	*112.43*	*2384*		*50.5*	*2.08*	*14.0*	*11.3*	*0.21*	*6.80*	*11.1*	*2.84*	*0.16*	*0.21*
PAC2 DR33-1	*44.87*	*112.25*	*2374*		*50.2*	*2.19*	*13.9*	*11.5*	*0.21*	*6.63*	*11.0*	*2.84*	*0.15*	*0.22*
PAC2 DR34-1	*44.24*	*112.04*	*2467*		*50.0*	*1.35*	*15.1*	*9.39*	*0.18*	*8.00*	*12.1*	*2.60*	*0.06*	*0.12*
PAC2 DR36-1	*42.95*	*111.56*	*2503*		*49.6*	*2.16*	*14.3*	*11.2*	*0.20*	*7.07*	*11.3*	*2.80*	*0.15*	*0.21*
PAC2 DR38-1	*41.80*	*111.27*	*2524*		*49.1*	*1.47*	*15.7*	*9.72*	*0.18*	*8.35*	*11.7*	*2.67*	*0.09*	*0.14*

Table. S2.2 continued

Sample	Trace elements[b] (μg g^{-1})	Li	Be	Sc	Ti	V		Cr	Co	Ni	Cu		Zn
	Uncertainty[c] (%)	1	2	1	2	1		1	1	1	1		4
PAC1 CV02-g		7.02	0.43	42	10632	358	*334*	272	44	100	56	*57*	92
PAC1 CV03-g		4.88	0.38	38	7428	261	*255*	413	41	123	65	*72*	68
PAC1 CV04-g		4.69	0.28	39	6585	252	*251*	377	42	110	70	*85*	66
PAC1 DR05-1g		5.29	0.45	42	8041	267	*243*	400	42	91	77	*85*	72
PAC1 DR06-g		7.89	0.60	41	12451	375	*366*	232	43	77	50	*57*	100
PAC1 DR07-1g		6.76	0.69	40	12308	354	*344*	143	41	62	61	*69*	93
PAC1 DR10-1g		11.63	1.36	32	9863	217	*227*	106	31	29	49	*68*	99
PAC1 DR11-1g		6.18	0.43	47	9199	333	*294*	334	45	75	74	*76*	85
PAC1 DR12-1g		5.16	0.28	38	6720	270	*248*	409	43	128	70	*82*	70
PAC1 DR13-2g		7.03	0.47	41	10433	325	*309*	219	45	92	59	*64*	95
PAC2 DR01-1		5.56	0.50	44	10050	310		289	40	67	67	*82*	74
PAC2 DR04-2		7.39	0.52	43	11451	343		224	42	73	55	*65*	86
PAC2 DR05-2g		8.45	0.62	42	13690	391		163	42	63	47	*66*	104
PAC2 DR08-1		6.31	0.53	44	10660	323		207	42	60	67	*88*	85
PAC2 DR20-1		11.16	1.25	36	15485	290		58	36	30	40	*52*	120
PAC2 DR21-2		7.46	0.59	46	12873	375		134	44	54	59	*62*	94
PAC2 DR22-1		6.96	0.57	44	11625	359		263	43	79	63	*76*	85
PAC2 DR27-1		11.40	1.30	38	18926	414		18	41	21	39	*29*	135
PAC2 DR28-2		5.91	0.37	45	8601	308		335	45	86	77	*93*	77
PAC2 DR29-1		8.53	0.71	46	14192	427		94	45	48	55	*71*	108
PAC2 DR30-1		7.19	0.56	45	11799	371		251	43	74	60	*69*	90
PAC2 DR31-3		6.72	0.48	42	10688	351		320	44	98	64	*73*	85
PAC2 DR32-1		7.37	0.63	46	12493	389		175	43	63	59	*66*	95
PAC2 DR33-1		7.70	0.66	46	13113	401		135	43	57	56	*63*	97
PAC2 DR34-1		5.82	0.34	42	8091	294		340	43	105	70	*74*	75
PAC2 DR36-1		7.58	0.64	45	12952	385		298	43	72	60	*67*	94
PAC2 DR38-1		5.54	0.40	40	8824	285		322	46	124	68	*67*	75

Table. S2.2 continued

Sample	Ga	Rb	Sr		Y		Zr		Nb		Mo		Cd	Sn
	1	1	1		1		2		1		15		1	2
PAC1 CV02-g	17	0.55	89		38	*37*	101	*105*	1.90	*2.13*	0.20		0.12	1.22
PAC1 CV03-g	15	0.81	132		25	*24*	76	*77*	2.42	*2.21*	0.19	*0.18*	0.09	0.88
PAC1 CV04-g	15	0.29	101		23	*23*	57	*64*	1.08	*1.03*	0.14		0.08	0.70
PAC1 DR05-1g	16	1.33	149		26	*25*	82	*86*	3.54	*3.43*	0.26		0.10	0.97
PAC1 DR06-g	19	1.09	107		43	*42*	132	*140*	3.57	*3.65*	0.38		0.13	1.53
PAC1 DR07-1g	18	2.06	145		41	*40*	141	*148*	5.64	*5.77*	0.54		0.14	1.61
PAC1 DR10-1g	19	5.70	124		67	*71*	323	*355*	12.26	*13.62*	1.09		0.21	3.45
PAC1 DR11-1g	17	0.70	122		32	*29*	90	*89*	2.09	*1.93*	0.26	*0.19*	0.11	1.07
PAC1 DR12-1g	15	0.28	91		24	*24*	59	*62*	0.95	*0.82*	0.14		0.08	0.76
PAC1 DR13-2g	17	1.25	106		37	*35*	102	*107*	2.86	*2.86*	0.28	*0.26*	0.11	1.25
PAC2 DR01-1	17	1.20	137	*144*	32	*39*	104	*112*	3.76	*3.74*	0.33	*0.32*	0.12	1.13
PAC2 DR04-2	17	0.81	114	*116*	38	*43*	115	*120*	2.90	*3.13*	0.28		0.12	1.27
PAC2 DR05-2g	18	2.24	113	*115*	45	*50*	142	*153*	6.38	*6.83*	0.45		0.15	1.53
PAC2 DR08-1	17	2.23	145	*142*	33	*36*	109	*116*	5.89	*6.03*	0.36		0.12	1.30
PAC2 DR20-1	22	2.72	126	*137*	82	*89*	342	*305*	10.28	*10.70*	0.97	*0.80*	0.22	3.27
PAC2 DR21-2	18	1.25	122	*123*	41	*44*	131	*139*	4.60	*4.92*	0.39		0.13	1.45
PAC2 DR22-1	18	1.15	127	*122*	39	*43*	124	*128*	4.05	*4.28*	0.37	*0.46*	0.13	1.38
PAC2 DR27-1	23	8.15	170	*164*	66	*72*	265	*279*	21.66	*22.42*	1.22	*1.19*	0.21	2.79
PAC2 DR28-2	17	0.55	101	*103*	30	*32*	80	*83*	1.96	*2.36*	0.21		0.10	0.92
PAC2 DR29-1	19	1.34	119	*117*	47	*51*	152	*161*	4.77	*5.12*	0.47		0.15	1.70
PAC2 DR30-1	18	1.20	115	*119*	40	*45*	125	*133*	4.04	*4.40*	0.37		0.13	1.38
PAC2 DR31-3	17	0.80	104	*102*	37	*41*	110	*117*	2.98	*3.15*	0.30	*0.28*	0.11	1.25
PAC2 DR32-1	18	1.29	132	*138*	40	*45*	132	*138*	4.52	*4.61*	0.43		0.14	1.48
PAC2 DR33-1	18	1.24	131	*130*	42	*47*	139	*145*	4.44	*4.79*	0.43		0.14	1.54
PAC2 DR34-1	16	0.21	102	*93*	28	*32*	73	*77*	1.05	*1.17*	0.16		0.09	0.85
PAC2 DR36-1	18	0.85	124	*124*	43	*49*	140	*149*	3.87	*4.23*	0.45	*0.39*	0.14	1.55
PAC2 DR38-1	16	0.58	127	*131*	29	*33*	86	*91*	2.32	*2.32*	0.29	*0.23*	0.10	0.99

Table. S2.2 continued

Sample	Sb	Cs	Ba	La		Ce		Pr		Nd		Sm		Eu	
	10	1	1	1		1		1		1		1		2	
PAC1 CV02-g	0.009	0.006	5.36	3.00	*3.01*	10.27	*10.5*	1.88		10.55		3.83	*4.03*	1.32	
PAC1 CV03-g	0.009	0.009	9.49	2.98	*2.88*	9.14	*8.7*	1.55		8.20		2.78	*2.83*	1.03	
PAC1 CV04-g	0.006	0.004	3.92	1.79	*1.97*	6.08	*6.3*	1.12		6.28		2.31	*2.51*	0.91	
PAC1 DR05-1g	0.010	0.015	17.46	3.64	*3.77*	10.61		1.75		9.20		3.05	*3.08*	1.15	
PAC1 DR06-g	0.011	0.012	11.65	4.68	*4.58*	14.65	*5.2*	2.54		13.66		4.64	*4.67*	1.58	
PAC1 DR07-1g	0.019	0.025	23.53	6.42	*6.11*	18.08	*10.5*	2.94		15.09		4.86	*5.02*	1.64	
PAC1 DR10-1g	0.025	0.062	47.21	13.05	*14.27*	36.30	*39.6*	5.62		27.84		8.48	*9.50*	2.25	
PAC1 DR11-1g	0.008	0.007	11.58	3.22	*3.11*	10.30	*9.6*	1.83		9.95		3.48	*3.45*	1.27	
PAC1 DR12-1g	0.012	0.004	3.97	1.78	*1.87*	6.17	*6.0*	1.14		6.42		2.42	*2.58*	0.91	
PAC1 DR13-2g	0.007	0.013	12.30	3.54	*3.79*	11.42	*11.1*	2.02		11.10		3.92	*3.92*	1.39	
PAC2 DR01-1	0.014	0.013	14.54	4.49	*4.94*	13.29	*14.4*	2.19	*2.22*	11.38	*12.32*	3.78	*3.94*	1.38	*1.56*
PAC2 DR04-2	0.009	0.009	9.27	4.16	*3.98*	13.15	*12.8*	2.30	*2.14*	12.34	*11.94*	4.27	*4.13*	1.54	*1.54*
PAC2 DR05-2g	0.014	0.024	25.32	6.50	*6.37*	18.58	*17.6*	3.02	*2.82*	15.52	*15.10*	5.12	*4.89*	1.72	*1.74*
PAC2 DR08-1	0.010	0.019	26.74	5.77	*5.57*	16.05	*15.8*	2.53	*2.41*	12.76	*12.29*	4.00	*3.87*	1.47	*1.38*
PAC2 DR20-1	0.025	0.027	28.83	12.72	*11.92*	38.04	*34.2*	6.27	*5.69*	32.38	*28.95*	10.16	*9.29*	3.07	*2.78*
PAC2 DR21-2	0.008	0.012	15.16	5.34	*4.64*	16.31	*14.0*	2.78	*2.32*	14.63	*12.61*	4.82	*4.41*	1.71	*1.60*
PAC2 DR22-1	0.011	0.013	13.98	4.81	*4.81*	14.84	*14.6*	2.54	*2.41*	13.33	*12.94*	4.46	*4.42*	1.58	*1.55*
PAC2 DR27-1	0.041	0.085	92.44	17.27	*16.13*	43.61	*40.3*	6.41	*5.87*	30.53	*28.60*	8.82	*8.49*	2.84	*2.65*
PAC2 DR28-2	0.006	0.006	6.87	2.78	*2.77*	8.98	*8.6*	1.59	*1.50*	8.73	*8.40*	3.10	*3.02*	1.19	*1.19*
PAC2 DR29-1	0.016	0.014	16.79	5.86	*5.61*	17.94	*17.1*	3.04	*2.79*	16.12	*14.87*	5.33	*5.14*	1.87	*1.78*
PAC2 DR30-1	0.010	0.013	14.64	4.84	*4.79*	14.97	*14.9*	2.53	*2.43*	13.45	*13.16*	4.55	*4.51*	1.59	*1.60*
PAC2 DR31-3	0.009	0.008	9.13	3.93	*3.91*	12.55	*12.7*	2.19	*2.09*	11.73	*11.46*	4.05	*4.00*	1.43	*1.42*
PAC2 DR32-1	0.012	0.014	15.84	5.33	*5.26*	16.21	*16.2*	2.71	*2.68*	14.24	*14.33*	4.72	*4.77*	1.67	*1.70*
PAC2 DR33-1	0.012	0.013	14.13	5.48	*5.44*	16.79	*16.2*	2.81	*2.70*	14.70	*14.32*	4.85	*4.83*	1.70	*1.70*
PAC2 DR34-1	0.006	0.003	2.63	2.23	*2.27*	7.76	*8.1*	1.42	*1.43*	8.04	*8.24*	2.93	*3.03*	1.14	*1.19*
PAC2 DR36-1	0.011	0.008	9.90	5.09	*5.15*	16.13	*16.2*	2.77	*2.75*	14.78	*14.80*	4.97	*4.99*	1.71	*1.74*
PAC2 DR38-1	0.030	0.007	7.52	3.07	*3.14*	9.89	*10.2*	1.74	*1.74*	9.44	*9.64*	3.26	*3.34*	1.23	*1.29*

Table. S2.2 continued

Sample	Gd		Tb		Dy		Ho		Er		Tm	Yb		Lu	
	1		1		2		1		1		2	2		2	
PAC1 CV02-g	5.54		0.99		6.59		1.47		4.23		0.63	4.09		0.60	
PAC1 CV03-g	3.75		0.67		4.31		0.95		2.72		0.40	2.57		0.38	
PAC1 CV04-g	3.31		0.60		3.96		0.88		2.51		0.37	2.39		0.35	
PAC1 DR05-1g	4.10		0.72		4.65		1.02		2.91		0.42	2.70		0.40	
PAC1 DR06-g	6.36		1.12		7.37		1.62		4.61		0.69	4.38		0.65	
PAC1 DR07-1g	6.40		1.13		7.31		1.61		4.57		0.66	4.25		0.63	
PAC1 DR10-1g	10.87		1.87		12.29		2.70		7.74		1.15	7.32		1.08	
PAC1 DR11-1g	4.95		0.87		5.84		1.29		3.67		0.54	3.45		0.51	
PAC1 DR12-1g	3.52		0.64		4.36		0.96		2.77		0.41	2.61		0.39	
PAC1 DR13-2g	5.68		1.02		6.77		1.52		4.33		0.64	4.12		0.60	
PAC2 DR01-1	5.11	*5.00*	0.90	*0.93*	5.88	*6.22*	1.29	*1.32*	3.70	*3.71*	0.55	3.48	*3.72*	0.51	*0.50*
PAC2 DR04-2	6.02	*5.63*	1.06	*1.03*	7.03	*6.89*	1.56	*1.51*	4.44	*4.33*	0.67	4.18	*4.10*	0.63	*0.60*
PAC2 DR05-2g	7.08	*6.57*	1.23	*1.20*	8.15	*8.03*	1.81	*1.76*	5.14	*5.07*	0.76	4.84	*4.78*	0.73	*0.69*
PAC2 DR08-1	5.31	*5.01*	0.93	*0.90*	6.07	*5.96*	1.35	*1.30*	3.81	*3.69*	0.55	3.50	*3.49*	0.53	*0.50*
PAC2 DR20-1	13.46	*11.64*	2.32	*2.11*	15.04	*14.10*	3.34	*3.08*	9.50	*8.82*	1.38	8.93	*8.26*	1.31	*1.24*
PAC2 DR21-2	6.68	*5.73*	1.18	*1.04*	7.65	*7.13*	1.72	*1.57*	4.85	*4.50*	0.70	4.53	*4.22*	0.68	*0.63*
PAC2 DR22-1	5.95	*5.64*	1.05	*1.02*	6.91	*6.81*	1.52	*1.50*	4.32	*4.29*	0.64	4.11	*3.98*	0.61	*0.60*
PAC2 DR27-1	11.06	*10.50*	1.90	*1.82*	12.24	*11.81*	2.63	*2.54*	7.47	*7.23*	1.12	7.11	*6.80*	1.04	*0.99*
PAC2 DR28-2	4.47	*3.97*	0.81	*0.77*	5.43	*5.40*	1.20	*1.13*	3.48	*3.30*	0.52	3.31	*3.18*	0.49	*0.48*
PAC2 DR29-1	7.32	*6.83*	1.29	*1.26*	8.48	*8.26*	1.86	*1.78*	5.29	*5.21*	0.79	5.06	*4.85*	0.74	*0.72*
PAC2 DR30-1	6.16	*6.16*	1.10	*1.11*	7.24	*7.31*	1.60	*1.60*	4.53	*4.62*	0.68	4.36	*4.47*	0.64	*0.65*
PAC2 DR31-3	5.59	*5.38*	0.99	*0.99*	6.58	*6.65*	1.45	*1.43*	4.13	*4.20*	0.62	3.97	*3.97*	0.58	*0.57*
PAC2 DR32-1	6.30	*6.19*	1.12	*1.13*	7.30	*7.52*	1.61	*1.59*	4.54	*4.58*	0.67	4.37	*4.29*	0.63	*0.63*
PAC2 DR33-1	6.49	*6.21*	1.15	*1.13*	7.50	*7.59*	1.66	*1.64*	4.70	*4.85*	0.70	4.47	*4.48*	0.65	*0.64*
PAC2 DR34-1	4.22	*4.12*	0.76	*0.78*	5.06	*5.21*	1.12	*1.14*	3.18	*3.28*	0.47	3.02	*3.17*	0.44	*0.45*
PAC2 DR36-1	6.75	*6.58*	1.19	*1.21*	7.85	*7.97*	1.73	*1.71*	4.90	*4.87*	0.73	4.68	*4.71*	0.69	*0.67*
PAC2 DR38-1	4.47	*4.41*	0.80	*0.82*	5.26	*5.41*	1.15	*1.17*	3.29	*3.37*	0.49	3.13	*3.24*	0.46	*0.46*

Table. S2.2 continued

Sample	Hf		Ta		W	Tl	Pb		Th		U		$(La/Sm)_N$
	3		2		20	8	6		5		4		
PAC1 CV02-g	2.74		0.13		0.11	0.007	0.37		0.12		0.04		0.490
PAC1 CV03-g	1.92		0.15		0.09	0.007	0.34		0.16		0.05		0.671
PAC1 CV04-g	1.56		0.07		0.09	0.015	0.32		0.06		0.03		0.485
PAC1 DR05-1g	2.08		0.21		0.11	0.008	0.43		0.22		0.06		0.747
PAC1 DR06-g	3.37		0.23		0.09	0.009	0.47		0.22		0.09		0.632
PAC1 DR07-1g	3.53		0.36		0.12	0.019	0.68		0.37		0.14		0.828
PAC1 DR10-1g	7.53		0.72		0.14	0.026	1.01		1.01		0.37		0.965
PAC1 DR11-1g	2.36		0.14		0.06	0.009	0.48		0.13		0.05		0.579
PAC1 DR12-1g	1.61		0.06		0.08	0.004	0.23		0.05		0.02		0.461
PAC1 DR13-2g	2.78		0.19		0.06	0.008	0.37		0.16		0.06		0.566
PAC2 DR01-1	2.70	*2.89*	0.24		0.04	0.008	0.36	*6.51*	0.21	*0.27*	0.09	*0.10*	0.744
PAC2 DR04-2	3.16	*3.23*	0.18	*0.32*	1.17	0.011	0.42	*0.46*	0.15	*0.20*	0.07	*0.07*	0.610
PAC2 DR05-2g	3.84	*3.86*	0.39	*0.29*	0.06	0.010	0.54	*1.35*	0.37	*0.43*	0.13	*0.16*	0.796
PAC2 DR08-1	2.85	*2.98*	0.38	*0.52*	0.07	0.008	0.43	*0.63*	0.33	*0.38*	0.11	*0.14*	0.904
PAC2 DR20-1	8.14	*7.87*	0.65	*0.62*	0.15	0.016	0.81	*1.04*	0.63	*0.69*	0.24	*0.25*	0.785
PAC2 DR21-2	3.59	*3.69*	0.30	*0.88*	0.09	0.012	0.45	*0.60*	0.24	*0.29*	0.10	*0.10*	0.693
PAC2 DR22-1	3.29	*3.36*	0.26	*0.41*	0.04	0.010	0.47	*0.51*	0.25	*0.26*	0.10	*0.10*	0.675
PAC2 DR27-1	6.73	*6.66*	1.36	*0.36*	0.23	0.027	1.16	*1.31*	1.44	*1.41*	0.47	*0.43*	1.227
PAC2 DR28-2	2.20	*2.15*	0.14	*1.35*	0.59	0.008	0.33	*0.34*	0.12	*0.12*	0.05	*0.06*	0.562
PAC2 DR29-1	4.03	*4.18*	0.32	*0.15*	0.07	0.017	0.78	*0.59*	0.29	*0.29*	0.12	*0.12*	0.688
PAC2 DR30-1	3.34	*3.55*	0.26	*0.44*	0.10	0.009	0.46	*0.47*	0.25	*0.26*	0.10	*0.10*	0.667
PAC2 DR31-3	2.97	*3.13*	0.20	*0.34*	1.37	0.008	0.38	*0.44*	0.18	*0.19*	0.08	*0.08*	0.608
PAC2 DR32-1	3.48	*3.56*	0.30	*0.27*	0.80	0.012	0.51	*0.62*	0.26	*0.28*	0.11	*0.11*	0.708
PAC2 DR33-1	3.59	*3.75*	0.29	*0.35*	1.23	0.012	0.52	*0.53*	0.25	*0.27*	0.11	*0.11*	0.708
PAC2 DR34-1	2.05	*2.13*	0.08	*0.48*	0.71	0.006	0.30	*0.42*	0.06	*0.06*	0.03	*0.06*	0.476
PAC2 DR36-1	3.75	*3.74*	0.27	*0.10*	1.39	0.010	0.47	*0.49*	0.21	*0.22*	0.09	*0.09*	0.642
PAC2 DR38-1	2.33	*2.40*	0.16	*0.31*	0.02	0.008	0.34	*0.61*	0.13	*0.13*	0.06	*0.12*	0.590

Table. S2.2 continued

Sample	Se (ng g^{-1})	1 s.d. (ng g^{-1})	Te (ng g^{-1})	1 s.d. (ng g^{-1})	S (µg g^{-1})	1 s.d. (ng g^{-1})	Cl (µg g^{-1})	Cl/K	Radiogenic[d] and stable isotopes	$\delta^{82/76}Se_{SRM\ 3149}$ (‰)	2 s.d. (‰)	$\delta^{34}S_{V\text{-}CDT}$ (‰)[d]	1 s.d. (‰)[d]
PAC1 CV02-g	180	4	1.99	0.06	*1171*	*50*	*49*	*0.10*		-0.23	0.09	*-0.91*	*0.14*
PAC1 CV03-g	158	1	3.19	0.10	*938*	*42*	*38*	*0.06*		-0.19	0.09	*-0.72*	*0.02*
PAC1 CV04-g	176	4	4.10	0.12	*940*	*52*	*75*	*0.22*		-0.15	0.09	*-0.83*	*0.04*
PAC1 DR05-1g	167	3	3.06	0.09	*932*	*40*	*47*	*0.06*		-0.22	0.09	*-0.94*	
PAC1 DR06-g	177	2	1.61	0.05	*1351*	*48*	*290*	*0.29*		-0.30	0.09	*-0.89*	*0.05*
PAC1 DR07-1g	186	4	2.23	0.07	*1301*	*33*	*494*	*0.31*		-0.06	0.09	*-0.95*	*0.01*
PAC1 DR10-1g	170	3	2.68	0.08	*1047*	*39*	*2163*	*0.54*		-0.24	0.09	*-0.14*	*0.03*
PAC1 DR11-1g	174	3	3.06	0.09	*1153*	*44*	*162*	*0.32*		-0.10	0.09	*-0.29*	*0.03*
PAC1 DR12-1g	165	3	3.70	0.11	*968*	*26*	*36*	*0.14*		-0.15	0.09	*-0.31*	*0.01*
PAC1 DR13-2g	194	2	1.95	0.06	*1259*	*84*	*75*	*0.10*		-0.21	0.09	*-0.65*	*0.10*
PAC2 DR01-1	166	3	2.45	0.07	*1116*	*36*	*225*	*0.13*		-0.16	0.09	*-0.81*	*0.14*
PAC2 DR04-2	168	3	2.33	0.07	*1199*	*24*	*264*	*0.26*		-0.09	0.09	*-0.80*	
PAC2 DR05-2g	176	4	1.43	0.04	*1339*	*47*	*292*	*0.19*		-0.06	0.09	*-0.78*	*0.04*
PAC2 DR08-1	194	4	2.76	0.08	*1239*	*57*	*266*	*0.16*		-0.15	0.09	*-0.77*	*0.02*
PAC2 DR20-1	193	4	1.68	0.05	*1550*	*50*	*1475*	*0.71*		-0.15	0.09	*0.60*	*0.10*
PAC2 DR21-2	198	4	1.97	0.06	*1312*	*105*	*287*	*0.23*		-0.17	0.09	*-0.42*	*0.03*
PAC2 DR22-1	187	4	2.47	0.07	*1172*	*39*	*281*	*0.20*		-0.22	0.09	*-0.83*	*0.05*
PAC2 DR27-1	219	4	1.16	0.03	*1755*	*14*	*1047*	*0.24*		-0.14	0.09	*-0.10*	*0.08*
PAC2 DR28-2	174	3	3.32	0.10	*1112*	*44*	*223*	*0.33*		-0.15	0.09	*-0.80*	*0.01*
PAC2 DR29-1	210	4	2.07	0.06	*1471*	*32*	*404*	*0.25*		-0.05	0.09	*-0.20*	*0.01*
PAC2 DR30-1	195	1	2.21	0.07	*1348*	*21*	*373*	*0.26*		-0.12	0.09	*-0.72*	
PAC2 DR31-3	193	4	3.17	0.10	*1208*	*37*	*435*	*0.52*		-0.09	0.09	*-1.02*	*0.01*
PAC2 DR32-1	186	4	1.97	0.06	*1321*	*41*	*335*	*0.25*		-0.10	0.09	*-0.70*	*0.04*
PAC2 DR33-1	199	1	2.20	0.05	*1340*	*25*	*277*	*0.22*		-0.15	0.09	*-0.86*	*0.01*
PAC2 DR34-1	168	1	2.63	0.08	*1094*	*22*	*77*	*0.15*		-0.30	0.09	*-0.99*	*0.30*
PAC2 DR36-1	194	1	2.26	0.07	*1381*	*32*	*514*	*0.41*		-0.13	0.09	*-1.11*	*0.08*
PAC2 DR38-1	180	1	3.12	0.09	*1244*	*36*	*141*	*0.19*		-0.16	0.09	*-1.12*	*0.02*

Table. S2.2 continued

Sample	$^{87}Sr/^{86}Sr$	$^{143}Nd/^{144}Nd$	$^{176}Hf/^{177}Hf$	$^{3}He/^{4}He$ (R/Ra)	$^{206}Pb/^{204}Pb$	$^{207}Pb/^{204}Pb$	$^{208}Pb/^{204}Pb$
PAC1 CV02-g	*0.702568*	*0.513135*	*0.283175*	*7.6*	*18.395*	*15.491*	*37.916*
PAC1 CV03-g	*0.702406*	*0.513117*	*0.283170*		*18.497*	*15.498*	*38.093*
PAC1 CV04-g	*0.702512*	*0.513144*	*0.283173*	*8.1*	*18.152*	*15.453*	*37.596*
PAC1 DR05-1g	*0.702407*	*0.513132*	*0.283168*		*18.491*	*15.507*	*37.998*
PAC1 DR06-g	*0.702502*	*0.513126*		*8.0*	*18.504*	*15.505*	*37.987*
PAC1 DR07-1g	*0.702472*	*0.513099*	*0.283144*		*18.632*	*15.498*	*38.074*
PAC1 DR10-1g	*0.702473*	*0.513112*	*0.283149*		*18.435*	*15.510*	*37.968*
PAC1 DR11-1g	*0.702435*	*0.513125*	*0.283171*		*18.401*	*15.494*	*37.862*
PAC1 DR12-1g	*0.702310*	*0.513150*	*0.283235*		*18.015*	*15.473*	*37.506*
PAC1 DR13-2g	*0.702556*	*0.513142*	*0.283204*	*7.6*	*18.500*	*15.497*	*37.966*
PAC2 DR01-1	*0.702422*	*0.513090*	*0.283133*	*7.6*	*18.822*	*15.547*	*38.199*
PAC2 DR04-2	*0.702367*	*0.513134*	*0.283163*	*7.7*	*18.531*	*15.513*	*37.942*
PAC2 DR05-2g	*0.702524*	*0.513098*	*0.283135*	*7.5*	*18.634*	*15.504*	*38.024*
PAC2 DR08-1	*0.702483*	*0.513077*	*0.283132*	*7.3*	*18.796*	*15.550*	*38.237*
PAC2 DR20-1	*0.702493*	*0.513092*	*0.283126*	*7.1*	*18.749*	*15.540*	*38.168*
PAC2 DR21-2	*0.702483*	*0.513088*	*0.283125*	*7.1*	*18.768*	*15.544*	*38.189*
PAC2 DR22-1	*0.702465*	*0.513100*	*0.283131*	*7.25*	*18.726*	*15.539*	*38.153*
PAC2 DR27-1	*0.702643*	*0.513035*	*0.283094*	*6.1*	*19.174*	*15.585*	*38.634*
PAC2 DR28-2	*0.702468*	*0.513070*	*0.283102*	*7.1*	*18.725*	*15.539*	*38.121*
PAC2 DR29-1	*0.702504*	*0.513059*	*0.283117*	*7.2*	*18.798*	*15.538*	*38.208*
PAC2 DR30-1	*0.702472*	*0.513060*	*0.283106*	*6.8*	*18.887*	*15.565*	*38.311*
PAC2 DR31-3	*0.702479*	*0.513066*	*0.283112*	*7.3*	*18.858*	*15.580*	*38.300*
PAC2 DR32-1	*0.702516*	*0.513078*	*0.283100*	*7.2*	*18.809*	*15.539*	*38.202*
PAC2 DR33-1	*0.702488*	*0.513082*	*0.283111*	*7.3*	*18.817*	*15.562*	*38.236*
PAC2 DR34-1	*0.702392*	*0.513108*	*0.283145*	*7.3*	*18.798*	*15.549*	*38.234*
PAC2 DR36-1	*0.702479*	*0.513066*	*0.283119*	*7.5*	*18.724*	*15.538*	*38.117*
PAC2 DR38-1	*0.702465*	*0.513108*	*0.283125*	*7.2*	*18.671*	*15.533*	*38.039*

Note: All literature data are shown in italics.
[a] From Vlastélic et al. (2000) and Hamelin et al. (2010).
[b] Literature trace element data are mostly from Vlastelic et al. (2000) and Hamelin et al. (2010); Cu, S and Cl data from Labidi et al. (2014); Mo data from Bezard et al. (2016). Ce data for PAC1 samples are from Clog et al. (2013).
[c] Uncertainties (Li to U) are estimated using relative standard deviations (r.s.d.) from 14 analyses of 6 BHVO-2 digestions (4 digested together with the PAR samples; see Table S2.3).
[d] From Labidi et al. (2014).
[e] From Vlastélic et al. (2000), Moreira et al. (2008) and Hamelin et al. (2010, 2011).

Table. S2.3 Trace element concentrations of BHVO-2 (USGS reference material) analyzed in this study as a quality control standard.

Trace elements	Concentration[a] (ng g^{-1})	Uncertainty[b] (%)
Li	4536	1
Be	1019	2
Sc	32716	1
Ti	16994990	2
V	325386	1
Cr	309103	1
Co	45747	1
Ni	119380	1
Cu	125876	1
Zn	100302	4
Ga	21049	1
Rb	9131	1
Sr	397697	1
Y	24508	1
Zr	165858	2
Nb	18450	1
Mo	4114	15
Cd	121	1
Sn	2016	2
Sb	101	10
Cs	96	1
Ba	131906	1
La	15330	1
Ce	37955	1
Pr	5421	1
Nd	24686	1
Sm	6098	1
Eu	2073	2
Gd	6307	1
Tb	944	1
Dy	5308	2
Ho	1012	1
Er	2547	1
Tm	341	2
Yb	1999	2
Lu	278	2
Hf	4302	3
Ta	1151	2
W	229	20
Tl	19	8
Pb	1580	6
Th	1159	5
U	416	4

[a] Average concentration of 14 analyses of 6 separate digestions (4 digested together with PAR glasses).
[b] Expressed as relative standard deviation.

Chapter 3

Deep mantle Se isotope record of atmospheric oxygenation

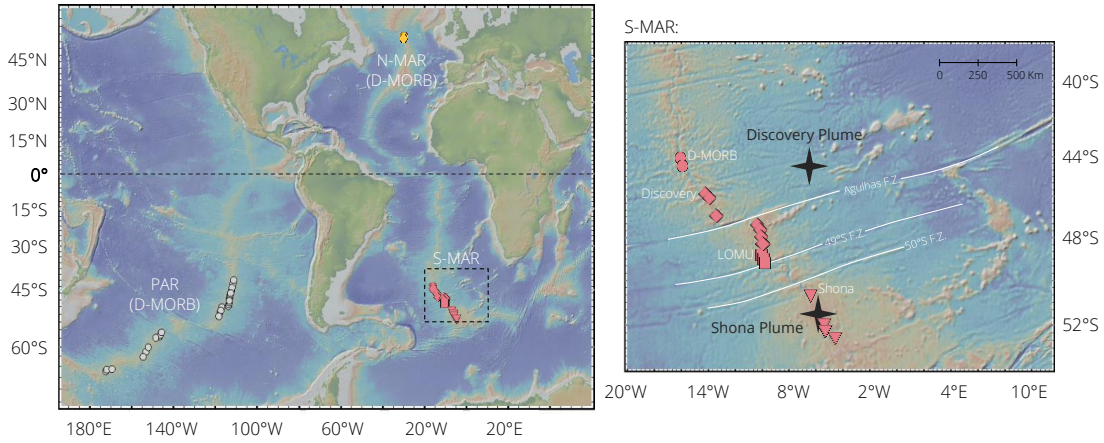

Fig. S3.1 Maps of the dredged sample locations along the N- and S-MAR (*N* = 18; this work) and the PAR (*N* = 27; Yierpan et al., 2019). Also shown in detail are the locations of the off-ridge Discovery plume and ridge-centered Shona plume, as well as the principle first-order tectonic discontinues (fracture zones; F.Z.) across the studied S-MAR sections. Samples associated with different plume contributions are displayed with different symbols. The regional map is generated by the GeoMapApp (http://www.geomapapp.org).

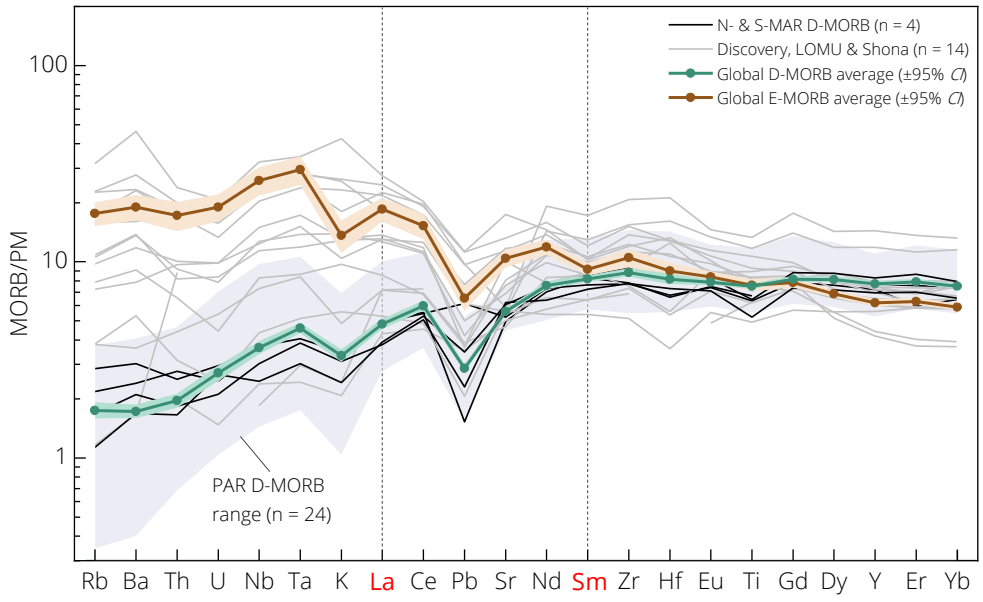

Fig. S3.2 Primitive mantle-normalized trace element patterns of the studied N- and S-MAR glasses. Normalizing values are from McDonough and Sun (1995). The depleted MORBs (black solid lines; $(La/Sm)_N$ 0.457–0.643) and enriched MORBs (grey solid lines; $(La/Sm)_N$ 0.670–2.681, mostly >1) are plotted as two separate groups. Shown

for comparison are the PAR MORB range (after excluding highly fractionated basalts; Yierpan et al., 2019) and global MORB averages (±95% *CI*) of Gale et al. (2013).

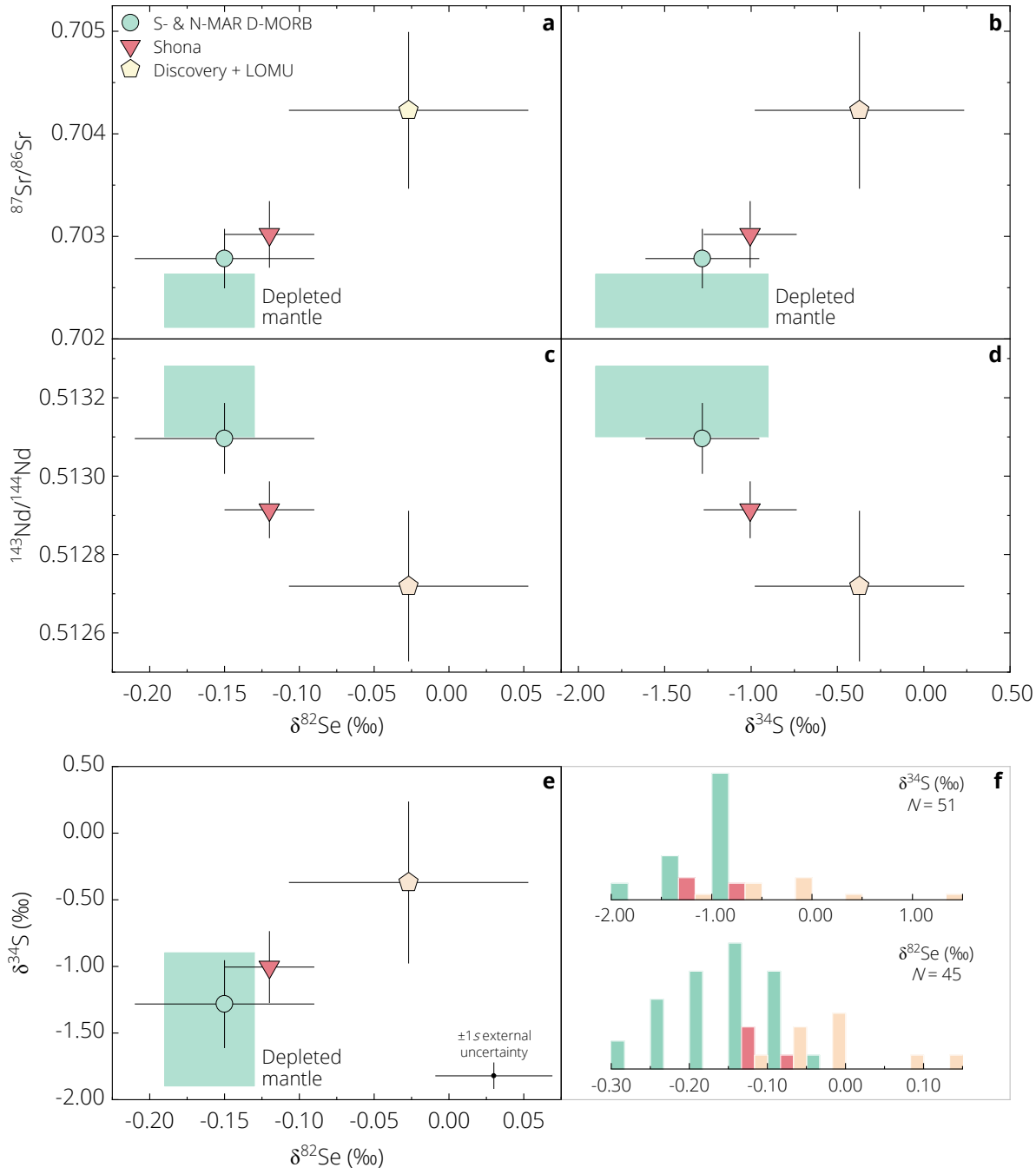

Fig. S3.3 Average Se and S isotope compositions of the three groups of samples (MAR depleted MORB, Shona anomaly, and Discovery + LOMU anomalies) plotted against their Sr and Nd radiogenic isotope ratios (a–d). Both $\delta^{82}Se$ and $\delta^{34}S$ show strong systematic correlations with $^{87}Sr/^{86}Sr$ and $^{143}Nd/^{144}Nd$ across these groups. The most heavy $\delta^{82}Se$ and $\delta^{34}S$ values are all associated with the samples influenced by the Discovery plume (i.e., Discovery + LOMU anomaly basalts). (e) shows the correlation between $\delta^{82}Se$ and $\delta^{34}S$. Additional S, Sr, and Nd isotope data for the S-MAR (Labidi et al., 2013, 2014) are also included in the calculation of the group means and the

uncertainties are ±1*s* of the mean for all isotopes. The depleted mantle compositions are from Labidi et al. (2014), Kimura et al. (2017), and this work (Table 3.3). (f) shows the distribution histogram for the entire dataset of the MAR and PAR MORBs (bin width 0.05‰ for δ^{82}Se and 0.5‰ for δ^{34}S).

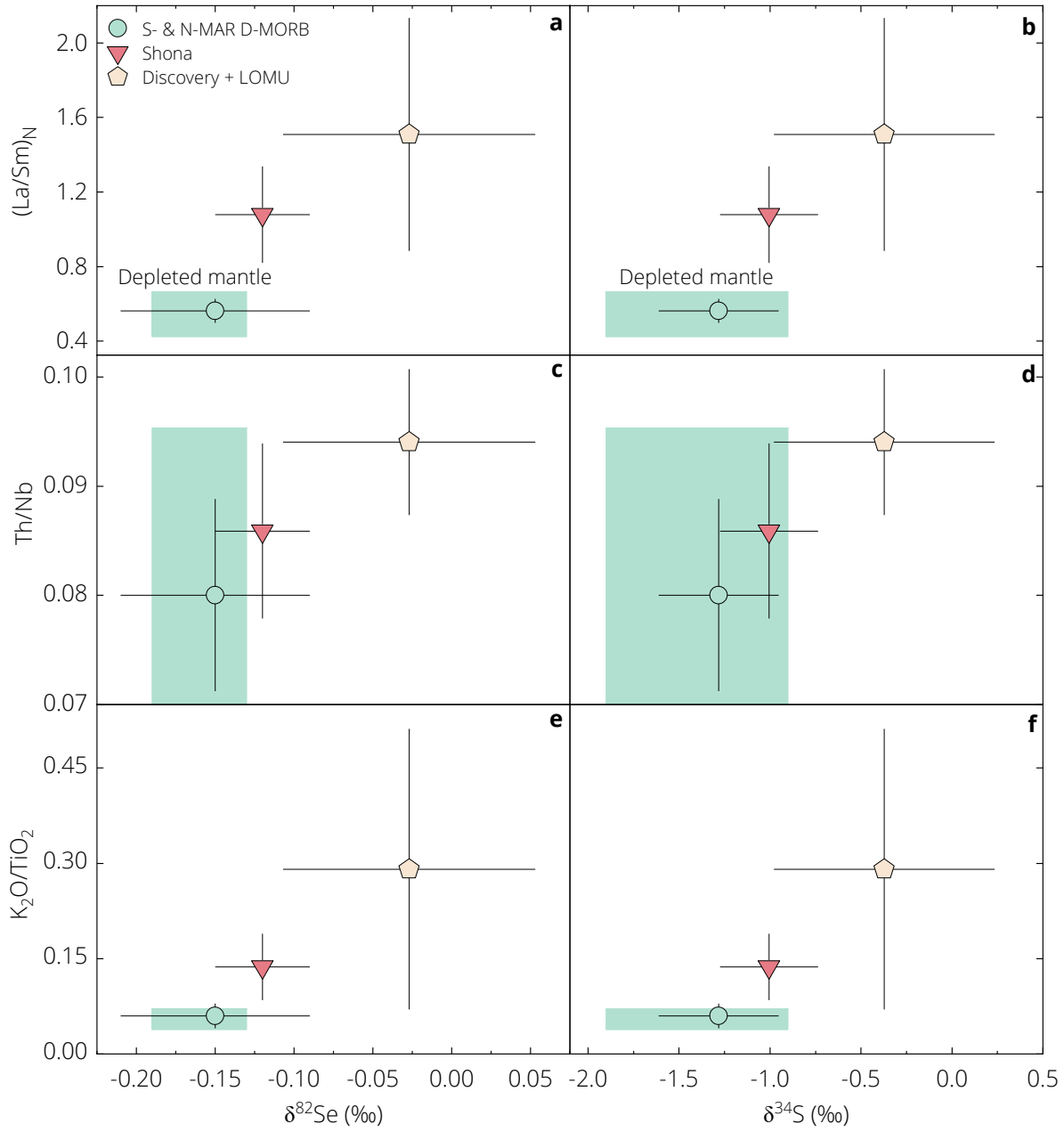

Supplementary Fig. S3.4 Average Se and S isotope compositions of the three groups of samples (MAR depleted MORB, Shona anomaly, and Discovery + LOMU anomalies) plotted against key trace/major element ratios $(La/Sm)_N$, Th/Nb, and K_2O/TiO_2 as indicators of mantle source heterogeneity. Both δ^{82}Se and δ^{34}S show strong and systematic correlations with these trace element ratios, as observed for their variations with radiogenic isotopes in the Supplementary Fig. S5. Additional S isotope and trace element data for the S-MAR (Labidi et al., 2013, 2014) are also included when calculating the group means and the uncertainties are ±1*s* of the mean. The depleted

mantle compositions are from Salters and Stracke (2004) (reported uncertainties are propagated for the presented trace element ratios), Labidi et al. (2014), and this work.

Table S3.1 Selenium isotope and elemental abundances of international rock standards analyzed over the course of the study and literature data.

		Individual measurement				Mean[d]						
Rock standard/Type	Location	Sample weight digested (mg)	δ^{82}Se (‰)	Internal error (95% *CI*)[c]	Se (ng/g)	δ^{82}Se (‰)	2*s*	95% *CI*	*n*	Se (ng/g)	2*s*	*n*
BHVO-2, USGS (ocean island basalt)	Hawaii, USA	399.96	0.20	0.03	170	0.14	0.10		4	171	7	4
		319.14[a]	0.11	0.04	165							
		422.70[a]	0.18	0.04	171							
		353.88[a, b]	0.13	0.06	174							
		353.88[a, b]	0.08	0.06	174							
Yierpan et al. (2019)						0.10	0.11		4	165	4	4
Yierpan et al. (2018)						0.18	0.10		8	169	6	61
Wang et al. (2015)										170	45	3
König et al. (2012)										169	6	3
Grand mean						**0.15**	**0.11**	**0.03**	**16**	**169**	**7**	**69**
BCR-2, USGS (continental flood basalt)	Columbia River, USA	1019.16[a]	0.27	0.05	78					78	3	1
Yierpan et al. (2019)						0.17	0.11		2	79	3	2
Yierpan et al. (2018)						0.29	0.10		5	76	2	18
Kurzawa et al. (2017)						0.18	0.11		3	71	8	3
Lissner et al. (2014)										78	6	5
Grand mean						**0.23**	**0.13**	**0.04**	**11**	**76**	**3**	**24**
BE-N, CRPG (continental basalt)	near Essey-la-côte, France											
Yierpan et al. (2018)						**0.15**	**0.10**	**0.06**	**5**	**66**	**2**	**23**
Rouxel et al. (2002)						0.37	0.32		1	57		1
König et al. (2014)										67	6	3
Lissner et al. (2014)										65	1	3
BIR-1a, USGS (Icelandic basalt)	near Reykjavik, Iceland	1529.38[a]	0.33	0.06	15					15	1	1
Yierpan et al. (2018)						0.28	0.11		5	15	1	5
König et al. (2012)										14	1	3
Grand mean						**0.29**	**0.10**	**0.05**	**6**	**15**	**1**	**6**

		Individual measurement				Mean[d]						
Rock standard/Type	Location	Sample weight digested (mg)	δ^{82}Se (‰)	Internal error (95% *CI*)[c]	Se (ng/g)	δ^{82}Se (‰)	2*s*	95% *CI*	*n*	Se (ng/g)	2*s*	*n*
JB-2, GSJ (basalt)	Oshima, Japan											
Kurzawa et al. (2019)						**-0.19**	**0.12**		**3**	**153**	**10**	**6**
JB-3, GSJ (basalt)	Narusawa-mura, Japan											
Kurzawa et al. (2019)						**0.16**	**0.12**		**2**	**67**	**4**	**2**
JGb-1, GSJ (gabbro)	Funehiji-machi, Japan	401.92[b]	-0.23	0.07	178	**-0.25**	**0.12**		**1**	**178**	**7**	**1**
		401.92[b]	-0.27	0.09	178							
Terashima & Imai (2000)										159	10	
MRG-1, CCRMP (gabbro)	Montreal, Canada	211.68[b]	0.08	0.06	214	**0.09**	**0.12**		**1**	**214**	**9**	**1**
		211.68[b]	0.10	0.07	214							
Marin et al. (2001)										210	20	
Wang et al. (2015)										212	8	
JA-3, GSJ (andesite)	Tsumagoi-mura, Japan	625.57	0.26	0.06	58	**0.26**	**0.12**		**1**	**58**	**2**	**1**
Terashima & Imai (2000)										50	8	
W-2a, USGS (diabase)	near Centreville, USA	401.76	-0.01	0.06	106	-0.05	0.10		2	106	4	2
		273.05	-0.08	0.05	106							
Yierpan et al. (2018, 2019)						-0.07	0.12		7	107	2	9
Grand mean						**-0.07**	**0.11**	**0.04**	**9**	**107**	**4**	**11**

Note: the recommended values for the rock standards (highlighted in bold) are calculated using the data (in this work and the literature) obtained under intermediate precision conditions (i.e., in Uni. Tübingen).

[a] Sample digests processed through the new 'HF chemistry'. All other sample digests were processed through the 'HCl chemistry' following Yierpan et al. (2018).

[b] Different aliquots of a single sample digest measured separately.

[c] Internal error (95% confidence interval; *CI*) based on 40 cycles of integration in each individual measurement.

[d] 2*s* uncertainties on the recommended δ^{82}Se are directly calculated if the total number of digestions $n>3$, or estimated with the $2s_p$ external reproducibility of 0.11‰ (calculated for non-glass matrices; see Section 3.3.2) if $n\leq3$. Uncertainties on Se abundance are 4% two relative standard deviation (Yierpan et al., 2018). The δ^{82}Se data of Rouxel et al. (2002) is converted relative to NIST SRM 3149 following Carignan and Wen (2007).

Table S3.2 Selenium isotope composition of the inter-laboratory standard solution MH-495 (30 ng/mL Se) analyzed over the course of the study.

MH-495 solution[a]	$^{77}Se/^{78}Se$	$\delta^{82}Se$ (‰)	Internal error (95% *CI*)[b]	Mean $\delta^{82}Se$ (‰)	2*s*	95% *CI*	*n*
#1	2.30	-3.28	0.06				
#2	2.32	-3.33	0.04				
	2.23	-3.30	0.04				
#3	2.24	-3.24	0.06				
	2.24	-3.21	0.06				
	2.24	-3.23	0.05				
	2.24	-3.25	0.08				
	2.25	-3.27	0.07				
	2.24	-3.29	0.06				
	2.24	-3.31	0.06				
	2.24	-3.26	0.07				
	2.24	-3.23	0.07				
	2.25	-3.21	0.04				
	2.25	-3.27	0.04				
	2.24	-3.21	0.05				
	2.24	-3.22	0.04				
	2.24	-3.28	0.05				
	2.24	-3.21	0.05				
	2.24	-3.24	0.04				
#4	2.33	-3.28	0.05				
	2.33	-3.22	0.05				
	2.33	-3.25	0.03				
	2.33	-3.26	0.04				
	2.33	-3.22	0.04				
	2.33	-3.22	0.04				
	2.33	-3.33	0.03				
	2.33	-3.25	0.04				
	2.33	-3.25	0.04				
	2.33	-3.28	0.04				
	2.33	-3.27	0.03				
	2.33	-3.23	0.03				
	2.33	-3.22	0.03				
	2.33	-3.24	0.05				
	2.33	-3.24	0.04				

MH-495 solution[a]	$^{77}Se/^{78}Se$	$\delta^{82}Se$ (‰)	Internal error (95% *CI*)[b]	Mean $\delta^{82}Se$ (‰)	2*s*	95% *CI*	*n*
	2.33	-3.24	0.03				
#5	2.29	-3.20	0.05				
	2.28	-3.22	0.03				
	2.28	-3.28	0.04				
	2.28	-3.23	0.04				
	2.28	-3.28	0.04				
	2.28	-3.19	0.04				
	2.28	-3.28	0.04				
#6	2.33	-3.26	0.05				
	2.33	-3.22	0.03				
	2.33	-3.28	0.04				
	2.33	-3.29	0.04				
	2.33	-3.18	0.06				
	2.33	-3.28	0.04				
	2.33	-3.17	0.04				
	2.33	-3.26	0.04				
	2.33	-3.20	0.04				
	2.33	-3.27	0.04				
	2.33	-3.20	0.04				
This study				-3.25	0.07	0.01	53
Yierpan et al. (2018)				-3.26	0.06	0.01	32
Yierpan et al. (2019)				-3.24	0.07	0.02	20
Kurzawa et al. (2019)				-3.25	0.08	0.02	26
Varas-Reus et al. (2019)				-3.25	0.08	0.01	69
Grand mean[c]				**-3.25**	**0.07**	**0.01**	**200**

[a] Different MH-495 solution splits prepared from a stock solution with ~1880 ng/g Se.
[b] Internal error (95% *CI*) based on 40 cycles of integration in each individual measurement.
[c] The 2*s* analytical precision of 0.07‰ is evaluated from 200 measurements of MH-495 (listed here) under intermediate precision conditions over the course of 24 months.

Table S3.3 Compilation of Se isotope and Se–Te abundances (from this work) and major/trace element and radiogenic/stable isotope compositions (in the literature) of the studied Mid-Atlantic ridge glasses.

	Sample	Latitude (°S)	Longitude (°W)	Dredging Depth (m)	SiO_2	TiO_2	Al_2O_3	FeO_T	MnO	MgO	CaO	Na_2O	K_2O	P_2O_5
Southern MAR	EW9309 41D-1g	44.02	16.08	3522	50.4	1.35	15.8	9.63	0.14	8.36	11.6	2.77	0.10	0.13
	EW9309 40D-1g	44.41	15.91	3488	51.1	1.27	15.1	9.32	0.15	8.30	11.5	2.85	0.10	0.11
	EW9309 34D-1g	45.85	14.19	3443	49.9	1.25	16.5	10.15	0.17	8.35	11.2	2.77	0.06	0.10
	EW9309 33D 1g	45.99	14.08	3381	49.9	1.66	16.0	9.16	0.17	7.83	10.3	3.35	0.74	0.27
	EW9309 28D-1g	46.90	13.45	3417	51.0	1.24	14.9	8.98	0.14	8.22	11.9	2.87	0.07	0.12
	EW9309 25D-1g	47.35	10.32	2032	54.0	1.43	15.8	8.38	0.14	7.51	8.7	3.41	0.28	0.11
	EW9309 2D-1g	47.55	10.19	2494	51.7	2.14	14.9	9.86	0.16	6.24	10.42	3.35	0.76	0.25
	EW9309 4D-3g	47.97	10.08	2895	51.2	1.57	15.3	9.03	0.14	7.60	11.1	2.70	0.40	0.21
	EW9309 5D 5g	48.24	10.00	3453	51.1	1.86	15.6	9.21	0.15	7.08	10.5	3.14	0.67	0.24
	EW9309 7D-1g	48.76	10.07	3218	51.2	1.53	16.4	7.88	0.14	6.79	10.5	3.15	1.22	0.27
	EW9309 8D-1g	48.97	9.97	3894	52.1	1.68	15.0	9.68	0.14	7.38	10.9	3.10	0.37	0.16
	EW9309 9D-3g	49.15	9.91	3892	49.3	0.99	15.2	10.1	0.15	8.67	11.9	2.58	0.16	0.08
	EW9309 15D-1g	50.58	6.43	2980	50.1	1.64	14.6	10.8	0.17	7.81	11.5	2.49	0.14	0.13
	EW9309 21D-1g	51.82	5.50	2025	50.8	1.79	14.8	10.1	0.16	7.10	11.4	2.65	0.38	0.19
	EW9309 23D-1g	52.16	5.34	2609	50.8	2.35	13.6	12.6	0.15	6.09	9.99	3.03	0.30	0.27
	EW9309 22D-3g	52.46	4.57	3059	51.4	2.68	13.4	13.6	0.16	4.83	9.2	3.18	0.52	0.36
Northern MAR	TR138 09D-2g	-51.56	29.92	3710	50.5	1.29	16.9	8.87	0.16	7.45	11.88	2.72	0.07	0.13
	TR138 08D-1g	-51.28	30.02	3500	50.4	1.05	17.9	7.51	0.13	7.24	12.5	2.67	0.09	0.10

Table S3.3 Continued

	Sample	**δ^{82}Se (‰)**	**2*s***	**Se (ng/g)**	**2*s***	$\delta^{34}S_{V\text{-}CDT}$ (‰)	S (μg/g)	**Te (ng/g)**	**2*s***	$^{87}Sr/^{86}Sr$	$^{143}Nd/^{144}Nd$	$^{176}Hf/^{177}Hf$	$^{206}Pb/^{204}Pb$	$^{207}Pb/^{204}Pb$	$^{208}Pb/^{204}Pb$	$^{208}Pb^*/^{206}Pb^*$
Southern MAR	EW9309 41D-1g	**-0.06**	**0.08**	**144**	**4**	-1.04	917	**4.50**	**0.27**	0.703273	0.513048	0.283191	17.892	15.499	37.874	0.978
	EW9309 40D-1g	**-0.18**	**0.08**	**147**	**4**	-1.21	1032	**3.13**	**0.19**	0.702997	0.513033	0.283242	17.906	15.490	37.840	0.973
	EW9309 34D-1g	**-0.07**	**0.08**	**160**	**5**	-1.23	917	**2.95**	**0.18**	0.703544	0.512868	0.283028	18.039	15.517	38.158	0.994
	EW9309 33D 1g	**-0.03**	**0.08**	**125**	**4**	-0.58	887	**2.04**	**0.12**	0.704475	0.512726	0.282954	18.015	15.550	38.265	1.009
	EW9309 28D-1g	**-0.14**	**0.08**	**156**	**5**	-0.83	875	**2.95**	**0.18**	0.703028	0.513077	0.283178	17.970	15.511	37.908	0.973
	EW9309 25D-1g	**0.09**	**0.08**	**88**	**3**	1.05	642	**6.21**	**0.37**	0.705728	0.512430	0.282700	18.196	15.639	38.814	1.051
	EW9309 2D-1g	**-0.08**	**0.04**	**132**	**4**	-0.14	974	**2.43**	**0.15**	0.704127	0.512652	0.282891	18.079	15.534	38.360	1.013
	EW9309 4D-3g	**-0.04**	**0.08**	**154**	**5**	-0.62	903	**3.51**	**0.21**	0.703762	0.512732	0.282994	18.063	15.531	38.280	1.006
	EW9309 5D 5g	**-0.06**	**0.08**	**132**	**4**	-0.42	943	**3.72**	**0.22**	0.703976	0.512594	0.282909	18.063	15.522	38.294	1.007
	EW9309 7D-1g	**0.14**	**0.08**	**113**	**3**	0.03	752	**5.15**	**0.31**	0.705093	0.512489	0.282728	17.751	15.585	38.154	1.028
	EW9309 8D-1g	**-0.05**	**0.08**	**152**	**5**	-0.48	1056	**3.06**	**0.18**	0.704286	0.512752	0.282979	17.792	15.572	38.050	1.011
	EW9309 9D-3g	**-0.03**	**0.04**	**139**	**4**	-0.50	910	**3.78**	**0.23**	0.704284	0.512873	0.282971	17.903	15.574	38.198	1.015
	EW9309 15D-1g	**-0.13**	**0.08**	**209**	**6**	-1.38	1039	**5.18**	**0.31**	0.702741	0.513008	0.283132	18.474	15.542	38.289	0.961
	EW9309 21D-1g	**-0.12**	**0.08**	**165**	**5**	-1.06	1038	**4.41**	**0.26**	0.703115	0.512818	0.282958	18.716	15.598	38.657	0.976
	EW9309 23D-1g	**-0.15**	**0.08**	**186**	**6**	-0.91	1270	**1.98**	**0.12**	0.703058	0.512886	0.283027	18.478	15.564	38.422	0.975
	EW9309 22D-3g	**-0.08**	**0.08**	**183**	**5**	-0.59	1388	**1.26**	**0.08**	0.703576	0.512893	0.283008	18.168	15.546	38.336	1.000
Northern MAR	TR138 09D-2g	**-0.17**	**0.08**	**166**	**5**			**2.89**	**0.17**	0.702680	0.513203	0.283324	18.013	15.451	37.549	0.927
	TR138 08D-1g	**-0.19**	**0.08**	**150**	**4**			**2.62**	**0.16**	0.702510	0.513226	0.283301	17.942	15.443	37.498	0.929

Table S3.3 Continued

	Sample	Sc	V	Cr	Co	Ni	Cu	Zn	Rb	Sr	Y	Zr	Nb	Ba	La	Ce
Southern MAR	EW9309 41D-1g	44	241	328	47	107	56	73	1.31	99	33	82	2.4	16	3.3	9.3
	EW9309 40D-1g	42	239	364	44	122	56	72	1.71	104	31	81	2.3	20	3.2	9.2
	EW9309 34D-1g	41				124			0.98	100	32	72	1.6	12	2.8	7.6
	EW9309 33D 1g	37	226	292	45	113	52	80	13.60	233	31	129	15.8	154	11.8	23.0
	EW9309 28D-1g	28				77			0.70	108	28	77	1.2	11	4.7	12.2
	EW9309 25D-1g	23	150	449	48	132	51	93	4.72	199	18	79	5.5	60	5.5	11.4
	EW9309 2D-1g	38	245	198	43	43	47	90	13.70	263	30	159	15.7	183	16.0	32.0
	EW9309 4D-3g	40				78			6.32	151	26	99	8.4	90	8.2	18.5
	EW9309 5D 5g	33				86			10.50	227	26	144	13.4	152	14.1	29.0
	EW9309 7D-1g	30	178	262	39	70	55	67	19.00	347	19	126	21.2	305	17.8	34.0
	EW9309 8D-1g	40	284	281	44	82	55	86	6.49	137	32	118	7.5	91	8.5	18.9
	EW9309 9D-3g	45	148	322	46	84	72	50	2.29	112	24	54	2.9	35	3.4	8.1
	EW9309 15D-1g	44	306	299	51	89	66	88	2.28	93	34	95	4.8	24	4.6	11.6
	EW9309 21D-1g	45	269	275	42	68	56	81	5.85	160	31	117	9.8	78	8.9	19.8
	EW9309 23D-1g	47	359	104	47	47	51	115	4.35	111	51	162	8.2	52	8.4	21.0
	EW9309 22D-3g	46	363	77	43	33	37	128	9.47	117	62	218	14.9	106	14.6	33.0
Northern MAR	TR138 09D-2g	41	277	284	42	109	66	82	0.68	121	36	97	1.6	11	2.53	8.9
	TR138 08D-1g	38	244	370	40	121	67	70	1.01	123	30	81	2.0	14	2.45	8.5

Table S3.3 Continued

	Sample	Nd	Sm	Eu	Gd	Dy	Er	Yb	Hf	Ta	Pb	Th	U
Southern MAR	EW9309 41D-1g	8.8	3.36	1.15			3.31	3.28	1.87	0.15	0.23	0.22	0.05
	EW9309 40D-1g	9.2	3.10	1.14	4.27	5.12	2.61	2.83	1.91	0.17	0.92	0.20	0.06
	EW9309 34D-1g	7.2	2.61	0.75			3.03	3.48		0.09	0.53	0.16	0.03
	EW9309 33D 1g	15.4	4.31	1.51			3.10	2.94	3.02	1.05	1.15	1.48	0.33
	EW9309 28D-1g	8.2	2.60	1.09	3.96	4.67	2.78	2.86	1.52	0.11		0.70	
	EW9309 25D-1g	9.8	3.57	1.36	4.28	3.48	1.63	1.63	1.58	0.32	0.56	0.52	0.09
	EW9309 2D-1g	19.8	4.91	1.76	5.39	5.35	2.73	2.67	3.64	1.03	1.68	1.59	0.34
	EW9309 4D-3g	12.4	3.47	1.30	4.04	4.40	2.57	2.56	3.53	0.51	0.63	0.73	0.16
	EW9309 5D 5g	17.2	4.20	1.65	4.86	4.92	2.54	2.54	3.61	0.88	1.45	1.38	0.27
	EW9309 7D-1g	18.2	4.16	1.56	3.85	3.74	1.76	1.73	3.76	1.27	1.69	1.90	0.42
	EW9309 8D-1g	13.5	4.05	1.37	4.61	5.34	3.22	3.24	3.10	0.44	0.75	0.65	0.17
	EW9309 9D-3g	6.7	2.19	0.85	3.09	3.75	2.55	2.66	1.02	0.19	0.31	0.25	0.05
	EW9309 15D-1g	10.4	3.46	1.31	4.45	5.88	3.52	3.50	2.24	0.31	0.58	0.35	0.11
	EW9309 21D-1g	13.7	3.73	1.36	5.16	5.61	3.01	3.28	2.71	0.64	0.55	0.80	0.20
	EW9309 23D-1g	17.9	5.26	2.06	7.61	8.00	4.91	5.09	4.57	0.56	0.92	0.77	0.20
	EW9309 22D-3g	24.0	6.98	2.24	9.62	9.62	5.98	5.82	6.00	0.93	1.46	1.42	0.32
Northern MAR	TR138 09D-2g	9.3	3.47	1.27	4.79	5.89	3.79	3.50	2.48	0.112	0.520	0.132	0.054
	TR138 08D-1g	8.0	2.94	1.09	4.00	4.85	3.07	2.88	2.07	0.142	0.345	0.146	0.043

Note:

1. New data reported in this work are given in bold. Uncertainties on δ^{82}Se are 95% *CI* if the number of analyses n_i>3, or the $2s_p$ external reproducibility of 0.08‰ (estimated for glass matrices) if $n_i \leq 3$ (see Sections 3.3.2 and 3.4). Uncertainties on Se and Te abundances are ~2% and 3% two relative standard deviation (external reproducibility for glass matrices; this work and Yierpan et al., 2019), respectively.
2. Literature data are from White et al. (1978), Schilling et al. (1983), Douglass et al. (1999), Andres et al. (2002), le Roux et al. (2002a, b, c), Blichert-Toft et al. (2005), Escrig et al. (2005), Kelley et al. (2013), and Labidi et al. (2013).

References

Adams R. D. (1964). Thickness Of The Earth's Crust Beneath The Pacific-Antarctic Ridge. *New Zealand Journal of Geology and Geophysics*, **7**(3), 529-542.

Agranier A., Blichert-Toft J., Graham D., Debaille V., Schiano P. and Albarede F. (2005). The spectra of isotopic heterogeneities along the mid-Atlantic Ridge. *Earth and Planetary Science Letters*, **238**(1-2), 96-109.

Akio MAKISHIMA, Ryoji TANAKA and NAKAMURA E. (2009). Precise Elemental and Isotopic Analyses in Silicate Samples Employing ICP-MS: Application of Hydrofluoric Acid Solution and Analytical Techniques. *Analytical Sciences*, **25**, 1181-1187.

Albarède F. (2009). Volatile accretion history of the terrestrial planets and dynamic implications. *Nature*, **461**(7268), 1227-1233.

Albut G., Babechuk M. G., Kleinhanns I. C., Benger M., Beukes N. J., Steinhilber B., Smith A. J. B., Kruger S. J. and Schoenberg R. (2018). Modern rather than Mesoarchaean oxidative weathering responsible for the heavy stable Cr isotopic signatures of the 2.95 Ga old Ijzermijn iron formation (South Africa). *Geochimica et Cosmochimica Acta*, **228**, 157-189.

Allègre C., Manhes G. and Lewin E. (2001). Chemical composition of the Earth and the volatility control on planetary genetics. *Earth and Planetary Science Letters*, **185**(1-2), 49-69.

Allègre C. J. and Turcotte D. L. (1986). Implications of a two-component marble-cake mantle. *Nature*, **323**(6084), 123-127.

Andersen M. B., Elliott T., Freymuth H., Sims K. W., Niu Y. and Kelley K. A. (2015). The terrestrial uranium isotope cycle. *Nature*, **517**(7534), 356-9.

Andres M., Blichert-Toft J. and Schilling J.-G. (2002). Hafnium isotopes in basalts from the southern Mid-Atlantic Ridge from 40°S to 55°S: Discovery and Shona plume-ridge interactions and the role of recycled sediments. *Geochemistry Geophysics Geosystems*, **3**, 1-25.

Ariskin A. A., Bychkov K. A., Nikolaev G. S. and Barmina G. S. (2018). The COMAGMAT-5: Modeling the Effect of Fe–Ni Sulfide Immiscibility in Crystallizing Magmas and Cumulates. *Journal of Petrology*, **59**(2), 283-298.

Asimow P. D. and Longhi J. (2004). The significance of multiple saturation points in the context of polybaric near-fractional melting. *Journal of Petrology*, **45**(12), 2349-2367.

Babechuk M. G., Kamber B. S., Greig A., Canil D. and Kodolanyi J. (2010). The behaviour of tungsten during mantle melting revisited with implications for planetary differentiation time scales. *Geochimica et Cosmochimica Acta*, **74**(4), 1448-1470.

Ballhaus C. (1993). Redox states of lithospheric and asthenospheric upper mantle. *Contributions to Mineralogy and Petrology*, **114**(3), 331-348.

Ballhaus C., Bockrath C., Wohlgemuth-Ueberwasser C., Laurenz V. and Berndt J. (2006). Fractionation of the noble metals by physical processes. *Contributions to Mineralogy and Petrology*, **152**(6), 667-684.

Barnes S.-J., Savard D., Bédard L. P. and Maier W. D. (2009). Selenium and sulfur concentrations in the Bushveld Complex of South Africa and implications for formation

of the platinum-group element deposits. *Mineralium Deposita*, **44**(6), 647-663.

Beaudry P., Longpre M. A., Economos R., Wing B. A., Bui T. H. and Stix J. (2018). Degassing-induced fractionation of multiple sulphur isotopes unveils post-Archaean recycled oceanic crust signal in hotspot lava. *Nat Commun*, **9**(1), 5093.

Bédard J. H. (2005). Partitioning coefficients between olivine and silicate melts. *Lithos*, **83**(3-4), 394-419.

Bezard R., Fischer-Godde M., Hamelin C., Brennecka G. A. and Kleine T. (2016). The effects of magmatic processes and crustal recycling on the molybdenum stable isotopic composition of Mid-Ocean Ridge Basalts. *Earth and Planetary Science Letters*, **453**, 171-181.

Bézos A. and Humler E. (2005). The Fe3+/ΣFe ratios of MORB glasses and their implications for mantle melting. *Geochimica et Cosmochimica Acta*, **69**(3), 711-725.

Bézos A., Lorand J. P., Humler E. and Gros M. (2005). Platinum-group element systematics in Mid-Oceanic Ridge basaltic glasses from the Pacific, Atlantic, and Indian Oceans. *Geochimica et Cosmochimica Acta*, **69**(10), 2613-2627.

Blichert-Toft J., Agranier A., Andres M., Kingsley R., Schilling J.-G. and Albarède F. (2005). Geochemical segmentation of the Mid-Atlantic Ridge north of Iceland and ridge-hot spot interaction in the North Atlantic. *Geochemistry, Geophysics, Geosystems*, **6**(1).

Bockrath C., Ballhaus C. and Holzheid A. (2004). Fractionation of the platinum-group elements during mantle melting. *Science*, **305**(5692), 1951-3.

Bodinier J. L. and Godard M., 2014. Orogenic, Ophiolitic, and Abyssal Peridotites. In: Holland, H.D., Turekian, K.K. (Eds.), Treatise on Geochemistry. Elsevier, Oxford, pp. 103-167.

Brenan J. M. (2015). Se–Te fractionation by sulfide–silicate melt partitioning: Implications for the composition of mantle-derived magmas and their melting residues. *Earth and Planetary Science Letters*, **422**, 45-57.

Brown E. L. and Lesher C. E. (2016). REEBOXPRO: A forward model simulating melting of thermally and lithologically variable upwelling mantle. *Geochemistry, Geophysics, Geosystems*, **17**(10), 3929-3968.

Carignan J. and Wen H. J. (2007). Scaling NIST SRM 3149 for Se isotope analysis and isotopic variations of natural samples. *Chemical Geology*, **242**(3-4), 347-350.

Castillo P. R., Natland J. H., Niu Y. and Lonsdale P. F. (1998). Sr, Nd and Pb isotopic variation along the Pacific–Antarctic risecrest, 53–57°S: Implications for the composition and dynamics of the South Pacific upper mantle. *Earth and Planetary Science Letters*, **154**(1-4), 109-125.

Chau Y. K. and Riley J. P. (1965). The determination of selenium in sea water, silicates and marine organisms. *Analytica Chimica Acta*, **33**, 36-49.

Chew D. M., Donelick R. A., Donelick M. B., Kamber B. S. and Stock M. J. (2014). Apatite Chlorine Concentration Measurements by LA-ICP-MS. *Geostandards and Geoanalytical Research*, **38**(1), 23-35.

Choi N. and Cho W. D. (1997). Distribution behavior of cobalt, selenium, and tellurium between nickel-copper-iron matte and silica-saturated iron silicate slag. *Metallurgical and Materials Transactions B*, **28**(3), 429-438.

Chou C.-L., 1978. Fractionation ofsiderophileelementsinthe Earth'suppermantle, Proc. Lunar

Planet. Sci. Conf 9th, pp. 219-230.

Clark S. K. and Johnson T. M. (2010). Selenium Stable Isotope Investigation into Selenium Biogeochemical Cycling in a Lacustrine Environment: Sweitzer Lake, Colorado. *Journal of Environmental Quality*, **39**(6), 2200-2210.

Class C. and le Roex A. P. (2008). Ce anomalies in Gough Island lavas — Trace element characteristics of a recycled sediment component. *Earth and Planetary Science Letters*, **265**(3-4), 475-486.

Clog M., Aubaud C., Cartigny P. and Dosso L. (2013). The hydrogen isotopic composition and water content of southern Pacific MORB: A reassessment of the D/H ratio of the depleted mantle reservoir. *Earth and Planetary Science Letters*, **381**, 156-165.

Cotta A. J. B. and Enzweiler J. (2012). Classical and New Procedures of Whole Rock Dissolution for Trace Element Determination by ICP-MS. *Geostandards and Geoanalytical Research*, **36**(1), 27-50.

Cutter G. A. and Bruland K. W. (1984). The marine biogeochemistry of selenium: A re-evaluation1. *Limnology and Oceanography*, **29**(6), 1179-1192.

Cutter G. A. and Cutter L. S. (2001). Sources and cycling of selenium in the western and equatorial Atlantic Ocean. *Deep-Sea Research Part II: Topical Studies in Oceanography*, **48**(13), 2917-2931.

Dale C. W., Macpherson C. G., Pearson D. G., Hammond S. J. and Arculus R. J. (2012). Inter-element fractionation of highly siderophile elements in the Tonga Arc due to flux melting of a depleted source. *Geochimica et Cosmochimica Acta*, **89**, 202-225.

Dare S. A. S., Barnes S. J. and Beaudoin G. (2012). Variation in trace element content of magnetite crystallized from a fractionating sulfide liquid, Sudbury, Canada: Implications for provenance discrimination. *Geochimica et Cosmochimica Acta*, **88**, 27-50.

Dare S. A. S., Barnes S. J., Beaudoin G., Méric J., Boutroy E. and Potvin-Doucet C. (2014). Trace elements in magnetite as petrogenetic indicators. *Mineralium Deposita*, **49**(7), 785-796.

Day J. M. D., Waters C. L., Schaefer B. F., Walker R. J. and Turner S. (2016). Use of Hydrofluoric Acid Desilicification in the Determination of Highly Siderophile Element Abundances and Re-Pt-Os Isotope Systematics in Mafic-Ultramafic Rocks. *Geostandards and Geoanalytical Research*, **40**(1), 49-65.

Ding S. and Dasgupta R. (2017). The fate of sulfide during decompression melting of peridotite implications for sulfur inventory of the MORB-source depleted upper mantle. *Earth and Planetary Science Letters*, **459**, 183-195.

Dixon J. E., Leist L., Langmuir C. and Schilling J.-G. (2002). Recycled dehydrated lithosphere observed in plume-influenced mid-ocean-ridge basalt. *Nature*, **420**(6914), 385-389.

Douglass J., Schilling J.-G. and Fontignie D. (1999). Plume-ridge interactions of the Discovery and Shona mantle plumes with the southern Mid-Atlantic Ridge (40°-55°S). *Journal of Geophysical Research*, **104**(B2), 2941.

Douglass J., Schilling J.-G. and Kingsley R. H. (1995). Influence of the Discovery and Shona Mantle Plumes on the Southern Mid-Atlantic Ridge - Rare-Earth Evidence. *Geophysical Research Letters*, **22**(21), 2893-2896.

Edmonds M. and Mather T. A. (2017). Volcanic Sulfides and Outgassing. *Elements*, **13**(2), 105-

110.

Ellis A. S., Johnson T. M., Herbel M. J. and Bullen T. D. (2003). Stable isotope fractionation of selenium by natural microbial consortia. *Chemical Geology*, **195**(1-4), 119-129.

Elrashidi M. A., Adriano D. C., Workman S. M. and Lindsay W. L. (1987). Chemical Equilibria of Selenium in Soils. *Soil Science*, **144**(2), 141-152.

Elwaer N. and Hintelmann H. (2008). Selective separation of selenium (IV) by thiol cellulose powder and subsequent selenium isotope ratio determination using multicollector inductively coupled plasma mass spectrometry. *Journal of Analytical Atomic Spectrometry*, **23**(5), 733-743.

Escrig S., Schiano P., Schilling J.-G. and Allègre C. (2005). Rhenium–osmium isotope systematics in MORB from the Southern Mid-Atlantic Ridge (40°–50° S). *Earth and Planetary Science Letters*, **235**(3-4), 528-548.

Falconer R. K. H. (1972). The Indian-Antarctic-Pacific triple junction. *Earth and Planetary Science Letters*, **17**(1), 151-158.

Fang L. and Lynch D. C. (1987). Evaluation of the Behavior of Selenium in Silicate Slag. *Metallurgical Transactions B-Process Metallurgy*, **18**(1), 181-187.

Faris J. P. (1960). Adsorption of Elements from Hydrofluoric Acid by Anion Exchange. *Analytical Chemistry*, **32**(4), 520-522.

Fehr M. A., Rehkamper M. and Halliday A. N. (2004). Application of MC-ICPMS to the precise determination of tellurium isotope compositions in chondrites, iron meteorites and sulfides. *International Journal of Mass Spectrometry*, **232**(1), 83-94.

Fehr M. A., Rehkämper M., Halliday A. N., Wiechert U., Hattendorf B., Günther D., Ono S., Eigenbrode J. L. and Rumble D. (2005). Tellurium isotopic composition of the early solar system—A search for effects resulting from stellar nucleosynthesis, 126Sn decay, and mass-independent fractionation. *Geochimica et Cosmochimica Acta*, **69**(21), 5099-5112.

Floor G. H., Millot R., Iglesias M. and Negrel P. (2011). Influence of methane addition on selenium isotope sensitivity and their spectral interferences. *J Mass Spectrom*, **46**(2), 182-8.

Floor G. H. and Román-Ross G. (2012). Selenium in volcanic environments: A review. *Applied Geochemistry*, **27**(3), 517-531.

Fonseca R. O. C., Laurenz V., Mallmann G., Luguet A., Hoehne N. and Jochum K. P. (2012). New constraints on the genesis and long-term stability of Os-rich alloys in the Earth's mantle. *Geochimica et Cosmochimica Acta*, **87**, 227-242.

Fornadel A. P., Spry P. G., Jackson S. E., Mathur R. D., Chapman J. B. and Girard I. (2014). Methods for the determination of stable Te isotopes of minerals in the system Au–Ag–Te by MC-ICP-MS. *J. Anal. At. Spectrom.*, **29**(4), 623-637.

Forrest A., Kingsley R. and Schilling J. G. (2009). Determination of Selenium and Tellurium in Basalt Rock Reference Materials by Isotope Dilution Hydride Generation-Inductively Coupled Plasma-Mass Spectrometry (ID-HG-ICP-MS). *Geostandards and Geoanalytical Research*, **33**(2), 261-269.

Francheteau J., Yelles-Chaouche A. and Craig H. (1987). The Juan Fernandez microplate north of the Pacific-Nazca-Antarctic plate junction at 35°S. *Earth and Planetary Science Letters*, **86**(2-4), 253-268.

Gale A., Dalton C. A., Langmuir C. H., Su Y. and Schilling J.-G. (2013). The mean composition of ocean ridge basalts. *Geochemistry, Geophysics, Geosystems*, **14**(3), 489-518.

Géli L., Bougault H., Aslanian D., Briais A., Dosso L., Etoubleau J., LeFormal J. P., Maia M., Ondreas H., Olivet J. L., Richardson C., Sayanagi K., Seama N., Shah A., Vlastelic I. and Yamamoto M. (1997). Evolution of the Pacific-Antarctic Ridge south of the Udintsev fracture zone. *Science*, **278**(5341), 1281-1284.

Ghiorso M. S., Hirschmann M. M., Reiners P. W. and Kress V. C. (2002). The pMELTS: A revision of MELTS for improved calculation of phase relations and major element partitioning related to partial melting of the mantle to 3 GPa. *Geochemistry, Geophysics, Geosystems*, **3**(5), 1-35.

Ghiorso M. S. and Sack R. O. (1995). Chemical mass transfer in magmatic processes IV. A revised and internally consistent thermodynamic model for the interpolation and extrapolation of liquid-solid equilibria in magmatic systems at elevated temperatures and pressures. *Contributions to Mineralogy and Petrology*, **119**(2-3), 197-212.

Grove T. L., Kinzler R. J. and Bryan W. B., 1992. Fractionation of Mid-Ocean Ridge Basalt (MORB). In: P., M.J., K., B.D., M., S.J. (Eds.), Mantle Flow and Melt Generation at Mid-Ocean Ridges. Geophysical Monograph Series. American Geophysical Union, Washington, DC, pp. 281-310.

Groves D. I., Vielreicher R. M., Goldfarb R. J., Hronsky J. M. A. and Condie K. C., 2005. Tectonic and lithospheric controls on the heterogeneous temporal distribution of mineral deposits. Mineral Deposit Research: Meeting the Global Challenge. Springer Berlin Heidelberg, Berlin, Heidelberg, pp. 11-14.

Guo J. F., Griffin W. L. and O'Reilly S. Y. (1999). Geochemistry and origin of sulphide minerals in mantle xenoliths: Qilin, southeastern China. *Journal of Petrology*, **40**(7), 1125-1149.

Hall G. E. M. and Pelchat J.-C. (1997a). Analysis of Geological Materials for Bismuth, Antimony, Selenium and Tellurium by Continuous Flow Hydride Generation Inductively Coupled Plasma Mass Spectrometry Part 2. Methodology and Results. *Journal of Analytical Atomic Spectrometry*, **12**(1), 103-106.

Hall G. E. M. and Pelchat J.-C. (1997b). Determination of As, Bi, Sb, Se and Te in Fifty Five Reference Materials by Hydride Generation ICP-MS. *Geostandards and Geoanalytical Research*, **21**(1), 85-91.

Hamelin C., Dosso L., Hanan B., Barrat J.-A. and Ondréas H. (2010). Sr-Nd-Hf isotopes along the Pacific Antarctic Ridge from 41 to 53°S. *Geophysical Research Letters*, **37**(10), n/a-n/a.

Hamelin C., Dosso L., Hanan B. B., Moreira M., Kositsky A. P. and Thomas M. Y. (2011). Geochemical portray of the Pacific Ridge: New isotopic data and statistical techniques. *Earth and Planetary Science Letters*, **302**(1-2), 154-162.

Hannington M. D., Petersen S., Herzig P. M. and Jonasson I. R. (2004). A global database of seafloor hydrothermal systems, including a digital database of geochemical analyses of seafloor polymetallic sulfides. *Geological Survey of Canada Open File, 4598 . , 9 pp.*

Hart S. R. and Gaetani G. A. (2006). Mantle Pb paradoxes: the sulfide solution. *Contributions to Mineralogy and Petrology*, **152**(3), 295-308.

Harvey J., König S. and Luguet A. (2015). The effects of melt depletion and metasomatism on highly siderophile and strongly chalcophile elements: S-Se-Te-Re-PGE systematics of peridotite xenoliths from Kilbourne Hole, New Mexico. *Geochimica et Cosmochimica*

Acta, **166**, 210-233.

Hattori K. H., Arai S. and Clarke D. B. (2002). Selenium, tellurium, arsenic and antimony contents of primary mantle sulfides. *Canadian Mineralogist*, **40**, 637-650.

He Y., Meng X., Ke S., Wu H., Zhu C., Teng F.-Z., Hoefs J., Huang J., Yang W., Xu L., Hou Z., Ren Z.-Y. and Li S. (2019). A nephelinitic component with unusual δ56Fe in Cenozoic basalts from eastern China and its implications for deep oxygen cycle. *Earth and Planetary Science Letters*, **512**, 175-183.

Helmy H. M., Ballhaus C., Wohlgemuth-Ueberwasser C., Fonseca R. O. C. and Laurenz V. (2010). Partitioning of Se, As, Sb, Te and Bi between monosulfide solid solution and sulfide melt - Application to magmatic sulfide deposits. *Geochimica et Cosmochimica Acta*, **74**(21), 6174-6179.

Herbel M. J., Johnson T. M., Oremland R. S. and Bullen T. D. (2000). Fractionation of selenium isotopes during bacterial respiratory reduction of selenium oxyanions. *Geochimica et Cosmochimica Acta*, **64**(21), 3701-3709.

Herbel M. J., Johnson T. M., Tanji K. K., Gao S. and Bullen T. D. (2002). Selenium stable isotope ratios in California agricultural drainage water management systems. *J Environ Qual*, **31**(4), 1146-56.

Hertogen J., Janssens M. J. and Palme H. (1980). Trace elements in ocean ridge basalt glasses: implications for fractionations during mantle evolution and petrogenesis. *Geochimica et Cosmochimica Acta*, **44**(12), 2125-2143.

Hill S. J., Pitts L. and Worsfold P. (1995). Investigation into the Kinetics of Selenium(Vi) Reduction Using Hydride Generation Atomic Fluorescence Detection. *Journal of Analytical Atomic Spectrometry*, **10**(5), 409-411.

Hin R. C., Coath C. D., Carter P. J., Nimmo F., Lai Y. J., von Strandmann P. A. E. P., Willbold M., Leinhardt Z. M., Walter M. J. and Elliott T. (2017). Magnesium isotope evidence that accretional vapour loss shapes planetary compositions. *Nature*, **549**(7673), 511-+.

Hofmann A. W. (1988). Chemical Differentiation of the Earth: the Relationship between Mantle, Continental-Crust, and Oceanic-Crust. *Earth and Planetary Science Letters*, **90**(3), 297-314.

Holland H. D. (2002). Volcanic gases, black smokers, and the Great Oxidation Event. *Geochimica et Cosmochimica Acta*, **66**(21), 3811-3826.

Howard J. H. (1977). Geochemistry of selenium: formation of ferroselite and selenium behavior in the vicinity of oxidizing sulfide and uranium deposits. *Geochimica et Cosmochimica Acta*, **41**(11), 1665-1678.

Ishikawa A., Senda R., Suzuki K., Dale C. W. and Meisel T. (2014). Re-evaluating digestion methods for highly siderophile element and 187Os isotope analysis: Evidence from geological reference materials. *Chemical Geology*, **384**, 27-46.

Jagoutz E., Palme H., Baddenhausen H., Blum K., Cendales M., Dreibus G., Spettel B., Waenke H. and Lorenz V. (1979). The abundances of major, minor and trace elements in the earth's mantle as derived from primitive ultramafic nodules. *Lunar and Planetary Science Conference Proceedings*, **10**, 2031-2050.

Jain J. C., Field M. P., Neal C. R., Ely J. C. and Sherrell R. M. (2000). Determination of the REE in Geological Reference Materials DTS-1 (Dunite) and PCC-1 (Peridotite) by Ultrasonic and Microconcentric Desolvating Nebulisation ICP-MS. *Geostandards and*

Geoanalytical Research, **24**(1), 65-72.

Jenner F. E. (2017). Cumulate causes for the low contents of sulfide-loving elements in the continental crust. *Nature Geoscience*, **10**(7), 524-+.

Jenner F. E., Arculus R. J., Mavrogenes J. A., Dyriw N. J., Nebel O. and Hauri E. H. (2012). Chalcophile element systematics in volcanic glasses from the northwestern Lau Basin. *Geochemistry, Geophysics, Geosystems*, **13**(6), Q06014.

Jenner F. E., Hauri E. H., Bullock E. S., König S., Arculus R. J., Mavrogenes J. A., Mikkelson N. and Goddard C. (2015). The competing effects of sulfide saturation versus degassing on the behavior of the chalcophile elements during the differentiation of hydrous melts. *Geochemistry, Geophysics, Geosystems*, **16**(5), 1490-1507.

Jenner F. E. and O'Neill H. S. (2012). Analysis of 60 elements in 616 ocean floor basaltic glasses. *Geochemistry, Geophysics, Geosystems*, **13**(2), Q02005.

Jenner F. E., O'Neill H. S. C., Arculus R. J. and Mavrogenes J. A. (2010). The Magnetite Crisis in the Evolution of Arc-related Magmas and the Initial Concentration of Au, Ag and Cu. *Journal of Petrology*, **51**(12), 2445-2464.

Jochum K. P., Nohl L., Herwig K., Lammel E., Stoll B. and Hofmann A. W. (2005). GeoReM: A new geochemical database for reference materials and isotopic standards. *Geostandards and Geoanalytical Research*, **29**(3), 333-338.

Johnson T. M. (2004). A review of mass-dependent fractionation of selenium isotopes and implications for other heavy stable isotopes. *Chemical Geology*, **204**(3-4), 201-214.

Johnson T. M. and Bullen T. D. (2003). Selenium isotope fractionation during reduction by Fe(II)-Fe(III) hydroxide-sulfate (green rust). *Geochimica et Cosmochimica Acta*, **67**(3), 413-419.

Johnson T. M. and Bullen T. D. (2004). Mass-dependent fractionation of selenium and chromium isotopes in low-temperature environments. *Geochemistry of Non-Traditional Stable Isotopes*, **55**(1), 289-317.

Johnson T. M., Herbel M. J., Bullen T. D. and Zawislanski P. T. (1999). Selenium isotope ratios as indicators of selenium sources and oxyanion reduction. *Geochimica et Cosmochimica Acta*, **63**(18), 2775-2783.

Kadlag Y. and Becker H. (2015). Fractionation of highly siderophile and chalcogen elements in components of EH3 chondrites. *Geochimica et Cosmochimica Acta*, **161**, 166-187.

Kadlag Y. and Becker H. (2016). 187Re–187Os systematics, highly siderophile element, S–Se–Te abundances in the components of unequilibrated L chondrites. *Geochimica et Cosmochimica Acta*, **172**, 225-246.

Katz R. F., Spiegelman M. and Langmuir C. H. (2003). A new parameterization of hydrous mantle melting. *Geochemistry, Geophysics, Geosystems*, **4**(9).

Keith M., Haase K. M., Klemd R., Schwarz-Schampera U. and Franke H. (2017). Systematic variations in magmatic sulphide chemistry from mid-ocean ridges, back-arc basins and island arcs. *Chemical Geology*, **451**, 67-77.

Kelley K. A., Kingsley R. and Schilling J.-G. (2013). Composition of plume-influenced mid-ocean ridge lavas and glasses from the Mid-Atlantic Ridge, East Pacific Rise, Galápagos Spreading Center, and Gulf of Aden. *Geochemistry, Geophysics, Geosystems*, **14**(1), 223-242.

Kelley K. A., Plank T., Grove T. L., Stolper E. M., Newman S. and Hauri E. (2006). Mantle melting as a function of water content beneath back-arc basins. *Journal of Geophysical Research*, **111**(B9).

Kimura J.-I., Gill J. B., van Keken P. E., Kawabata H. and Skora S. (2017). Origin of geochemical mantle components: Role of spreading ridges and thermal evolution of mantle. *Geochemistry, Geophysics, Geosystems*, **18**(2), 697-734.

Kimura K., Lewis R. S. and Anders E. (1974). Distribution of gold and rhenium between nickel-iron and silicate melts: implications for the abundance of siderophile elements on the Earth and Moon. *Geochimica et Cosmochimica Acta*, **38**(5), 683-701.

Kinzler R. J. and Grove T. L. (1993). Corrections and further discussion of the primary magmas of mid-ocean ridge basalts, 1 and 2. *Journal of Geophysical Research: Solid Earth*, **98**(B12), 22339-22347.

Kipp M. A., Stueken E. E., Bekker A. and Buick R. (2017). Selenium isotopes record extensive marine suboxia during the Great Oxidation Event. *Proc Natl Acad Sci*, **114**(5), 875-880.

Kiseeva E. S. and Wood B. J. (2013). A simple model for chalcophile element partitioning between sulphide and silicate liquids with geochemical applications. *Earth and Planetary Science Letters*, **383**, 68-81.

Kiseeva E. S. and Wood B. J. (2015). The effects of composition and temperature on chalcophile and lithophile element partitioning into magmatic sulphides. *Earth and Planetary Science Letters*, **424**, 280-294.

Kiseeva E. S. and Wood B. J. (2017). Partitioning of As, Se, Te and Bi between sulphide and silicate liquids. Paper presented at Annual V.M. Goldschmidt Conference. Geochemical Society and European Association of Geochemistry, Paris, France.

Kiseeva E. S., Fonseca R. O. C. and Smythe D. J. (2017). Chalcophile Elements and Sulfides in the Upper Mantle. *Elements*, **13**(2), 111-116.

Klein E. M. and Langmuir C. H. (1987). Global Correlations of Ocean Ridge Basalt Chemistry with Axial Depth and Crustal Thickness. *Journal of Geophysical Research-Solid Earth and Planets*, **92**(B8), 8089-8115.

Kleinhanns I. C., Whitehouse M. J., Nolte N., Baero W., Wilsky F., Hansen B. T. and Schoenberg R. (2015). Mode and timing of granitoid magmatism in the Västervik area (SE Sweden, Baltic Shield): Sr–Nd isotope and SIMS U–Pb age constraints. *Lithos*, **212-215**, 321-337.

Klingelhoefer F., Ondréas H., Briais A., Hamelin C. and Dosso L. (2006). New structural and geochemical observations from the Pacific-Antarctic Ridge between 52°45′S and 41°15′S. *Geophysical Research Letters*, **33**(21).

Koehler M. C., Buick R., Kipp M. A., Stueken E. E. and Zaloumis J. (2018). Transient surface ocean oxygenation recorded in the approximately 2.66-Ga Jeerinah Formation, Australia. *Proc Natl Acad Sci*, **115**(30), 7711-7716.

König S., Eickmann B., Zack T., Yierpan A., Wille M., Taubald H. and Schoenberg R. (2019). Redox induced sulfur-selenium isotope decoupling recorded in pyrite. *Geochimica et Cosmochimica Acta*, **244**, 24-39.

König S., Lissner M., Lorand J. P., Bragagni A. and Luguet A. (2015a). Mineralogical control of selenium, tellurium and highly siderophile elements in the Earth's mantle: Evidence from mineral separates of ultra-depleted mantle residues. *Chemical Geology*, **396**, 16-

24.

König S., Lorand J. P., Luguet A. and Pearson D. G. (2014). A non-primitive origin of near-chondritic S–Se–Te ratios in mantle peridotites; implications for the Earth's late accretionary history. *Earth and Planetary Science Letters*, **385**, 110-121.

König S., Luguet A., Lorand J.-P., Lissner M. and Graham Pearson D. (2015b). Reply to the comment on "A non-primitive origin of near-chondritic S–Se–Te ratios in mantle peridotites: Implications for the Earth's late accretionary history" by König S. et al. [Earth Planet. Sci. Lett. 385 (2014) 110–121]. *Earth and Planetary Science Letters*, **417**, 167-169.

König S., Luguet A., Lorand J.-P., Wombacher F. and Lissner M. (2012). Selenium and tellurium systematics of the Earth's mantle from high precision analyses of ultra-depleted orogenic peridotites. *Geochimica et Cosmochimica Acta*, **86**, 354-366.

Krouse H. R. and Thode H. G. (1962). Thermodynamic Properties and Geochemistry of Isotopic Compounds of Selenium. *Canadian Journal of Chemistry*, **40**(2), 367-375.

Kurzawa T., König S., Alt J. C., Yierpan A. and Schoenberg R. (2019). The role of subduction recycling on the selenium isotope signature of the mantle: Constraints from Mariana arc lavas. *Chemical Geology*, **513**, 239-249.

Kurzawa T., König S., Labidi J., Yierpan A. and Schoenberg R. (2017). A method for Se isotope analysis of low ng-level geological samples via double spike and hydride generation MC-ICP-MS. *Chemical Geology*, **466**, 219-228.

Labidi J. and Cartigny P. (2016). Negligible sulfur isotope fractionation during partial melting: Evidence from Garrett transform fault basalts, implications for the late-veneer and the hadean matte. *Earth and Planetary Science Letters*, **451**, 196-207.

Labidi J., Cartigny P., Hamelin C., Moreira M. and Dosso L. (2014). Sulfur isotope budget (32S, 33S, 34S and 36S) in Pacific–Antarctic ridge basalts: A record of mantle source heterogeneity and hydrothermal sulfide assimilation. *Geochimica et Cosmochimica Acta*, **133**, 47-67.

Labidi J., Cartigny P. and Jackson M. G. (2015). Multiple sulfur isotope composition of oxidized Samoan melts and the implications of a sulfur isotope 'mantle array' in chemical geodynamics. *Earth and Planetary Science Letters*, **417**, 28-39.

Labidi J., Cartigny P. and Moreira M. (2013). Non-chondritic sulphur isotope composition of the terrestrial mantle. *Nature*, **501**(7466), 208-211.

Langmuir C. H. and Forsyth D. W. (2007). Mantle Melting Beneath Mid-Ocean Ridges. *Oceanography*, **20**(1), 78-89.

Langmuir C. H., Klein E. M. and Plank T., 1992. Petrological Systematics of Mid-Ocean Ridge Basalts: Constraints on Melt Generation Beneath Ocean Ridges, Mantle Flow and Melt Generation at Mid-Ocean Ridges. Geophysical Monograph Series. American Geophysical Union, Washington, D. C., pp. 183-280.

Langmyhr F. J. (1967). Removal of Hydrofluoric Acid by Evaporation in Presence of Sulfuric or Perchloric Acids. *Analytica Chimica Acta*, **39**(4), 516-&.

Langner B. E., 2000. Selenium and Selenium Compounds, Ullmann's Encyclopedia of Industrial Chemistry.

Large R. R., Halpin J. A., Danyushevsky L. V., Maslennikov V. V., Bull S. W., Long J. A., Gregory D. D., Lounejeva E., Lyons T. W., Sack P. J., McGoldrick P. J. and Calver C.

R. (2014). Trace element content of sedimentary pyrite as a new proxy for deep-time ocean–atmosphere evolution. *Earth and Planetary Science Letters*, **389**, 209-220.

Large R. R., Mukherjee I., Gregory D., Steadman J., Corkrey R. and Danyushevsky L. V. (2019). Atmosphere oxygen cycling through the Proterozoic and Phanerozoic. *Mineralium Deposita*.

Layton-Matthews D., Leybourne M. I., Peter J. M. and Scott S. D. (2006). Determination of selenium isotopic ratios by continuous-hydride-generation dynamic-reaction-cell inductively coupled plasma-mass spectrometry. *Journal of Analytical Atomic Spectrometry*, **21**(1), 41-49.

Layton-Matthews D., Leybourne M. I., Peter J. M., Scott S. D., Cousens B. and Eglington B. M. (2013). Multiple sources of selenium in ancient seafloor hydrothermal systems: Compositional and Se, S, and Pb isotopic evidence from volcanic-hosted and volcanic-sediment-hosted massive sulfide deposits of the Finlayson Lake District, Yukon, Canada. *Geochimica et Cosmochimica Acta*, **117**, 313-331.

le Roux P. J., le Roex A. and Schilling J.-G. (2002a). Crystallization processes beneath the southern Mid-Atlantic Ridge (40–55°S), evidence for high-pressure initiation of crystallization. *Contributions to Mineralogy and Petrology*, **142**(5), 582-602.

le Roux P. J., le Roex A. and Schilling J.-G. (2002c). MORB melting processes beneath the southern Mid-Atlantic Ridge (40–55°S): a role for mantle plume-derived pyroxenite. *Contributions to Mineralogy and Petrology*, **144**(2), 206-229.

le Roux P. J., le Roex A. P., Schilling J.-G., Shimizu N., Perkins W. W. and Pearce N. J. G. (2002b). Mantle heterogeneity beneath the southern Mid-Atlantic Ridge: trace element evidence for contamination of ambient asthenospheric mantle. *Earth and Planetary Science Letters*, **203**(1), 479-498.

Le Roux V., Bodinier J. L., Alard O., O'Reilly S. Y. and Griffin W. L. (2009). Isotopic decoupling during porous melt flow: A case-study in the Lherz peridotite. *Earth and Planetary Science Letters*, **279**(1-2), 76-85.

Le Roux V., Tommasi A. and Vauchez A. (2008). Feedback between melt percolation and deformation in an exhumed lithosphere–asthenosphere boundary. *Earth and Planetary Science Letters*, **274**(3-4), 401-413.

Lee C. T. A., Luffi P., Plank T., Dalton H. and Leeman W. P. (2009). Constraints on the depths and temperatures of basaltic magma generation on Earth and other terrestrial planets using new thermobarometers for mafic magmas. *Earth and Planetary Science Letters*, **279**(1-2), 20-33.

Lee C. T. A., Yeung L. Y., McKenzie N. R., Yokoyama Y., Ozaki K. and Lenardic A. (2016). Two-step rise of atmospheric oxygen linked to the growth of continents. *Nature Geoscience*, **9**(6), 417-+.

Lee D. S. and Edmond J. M. (1985). Tellurium Species in Seawater. *Nature*, **313**(6005), 782-785.

Li J., Zhao P.-P., Liu J., Wang X.-C., Yang A. Y., Wang G.-Q. and Xu J.-F. (2015). Reassessment of Hydrofluoric Acid Desilicification in the Carius Tube Digestion Technique for Re-Os Isotopic Determination in Geological Samples. *Geostandards and Geoanalytical Research*, **39**(1), 17-30.

Li Y. and Audétat A. (2012). Partitioning of V, Mn, Co, Ni, Cu, Zn, As, Mo, Ag, Sn, Sb, W, Au, Pb, and Bi between sulfide phases and hydrous basanite melt at upper mantle

conditions. *Earth and Planetary Science Letters*, **355**, 327-340.

Li Y. and Audétat A. (2013). Gold solubility and partitioning between sulfide liquid, monosulfide solid solution and hydrous mantle melts: Implications for the formation of Au-rich magmas and crust–mantle differentiation. *Geochimica et Cosmochimica Acta*, **118**, 247-262.

Lin J. and Morgan J. P. (1992). The spreading rate dependence of three-dimensional mid-ocean ridge gravity structure. *Geophysical Research Letters*, **19**(1), 13-16.

Liu J. G., Touboul M., Ishikawa A., Walker R. J. and Pearson D. G. (2016). Widespread tungsten isotope anomalies and W mobility in crustal and mantle rocks of the Eoarchean Saglek Block, northern Labrador, Canada: Implications for early Earth processes and W recycling. *Earth and Planetary Science Letters*, **448**, 13-23.

Liu Y. and Brenan J. (2015). Partitioning of platinum-group elements (PGE) and chalcogens (Se, Te, As, Sb, Bi) between monosulfide-solid solution (MSS), intermediate solid solution (ISS) and sulfide liquid at controlled fO2–fS2 conditions. *Geochimica et Cosmochimica Acta*, **159**, 139-161.

Lodders K. (2003). Solar system abundances and condensation temperatures of the elements. *Astrophysical Journal*, **591**(2), 1220-1247.

Lodders K., Palme H., & Gail, H.P., 2009. Abundances of the elements in the Solar System.

Long G. L. and Winefordner J. D. (2012). Limit of Detection A Closer Look at the IUPAC Definition. *Analytical Chemistry*, **55**(07), 712A-724A.

Lonsdale P. (1994). Geomorphology and structural segmentation of the crest of the southern (Pacific-Antarctic) East Pacific Rise. *Journal of Geophysical Research: Solid Earth*, **99**(B3), 4683-4702.

Lorand J. P. (1990). Are spinel Iherzolite xenoliths representative of the abundance of sulfur in the upper mantle? *Geochimica et Cosmochimica Acta*, **54**(5), 1487-1492.

Lorand J. P. (1991). Sulphide Petrology and Sulphur Geochemistry of Orogenic Lherzolites: A Comparative Study of the Pyrenean Bodies (France) and the Lanzo Massif (Italy). *Journal of Petrology*, **Special Volume, Issue 2**, 77-95.

Lorand J. P. and Alard O. (2010). Determination of selenium and tellurium concentrations in Pyrenean peridotites (Ariege, France): New insight into S/Se/Te systematics of the upper in mantle samples. *Chemical Geology*, **278**(1-2), 120-130.

Lorand J. P., Alard O. and Luguet A. (2010). Platinum-group element micronuggets and refertilization process in Lherz orogenic peridotite (northeastern Pyrenees, France). *Earth and Planetary Science Letters*, **289**(1-2), 298-310.

Lorand J. P., Alard O., Luguet A. and Keays R. R. (2003). Sulfur and selenium systematics of the subcontinental lithospheric mantle: Inferences from the Massif Central xenolith suite (France). *Geochimica et Cosmochimica Acta*, **67**(21), 4137-4151.

Lorand J. P., Delpech G., Gregoire M., Moine B., O'Reilly S. Y. and Cottin J. Y. (2004). Platinum-group elements and the multistage metasomatic history of Kerguelen lithospheric mantle (South Indian Ocean). *Chemical Geology*, **208**(1-4), 195-215.

Lorand J. P., Luguet A. and Alard O. (2013). Platinum-group element systematics and petrogenetic processing of the continental upper mantle: A review. *Lithos*, **164**, 2-21.

Lorand J.-P. and Luguet A. (2016). Chalcophile and Siderophile Elements in Mantle Rocks:

Trace Elements Controlled By Trace Minerals. *Reviews in Mineralogy and Geochemistry*, **81**(1), 441-488.

Loss R. D., Rosman K. J. R. and Delaeter J. R. (1990). The Isotopic Composition of Zinc, Palladium, Silver, Cadmium, Tin, and Tellurium in Acid-Etched Residues of the Allende Meteorite. *Geochimica et Cosmochimica Acta*, **54**(12), 3525-3536.

Luais B. (2012). Germanium chemistry and MC-ICPMS isotopic measurements of Fe–Ni, Zn alloys and silicate matrices: Insights into deep Earth processes. *Chemical Geology*, **334**, 295-311.

Luguet A., Behrens M., Pearson D. G., König S. and Herwartz D. (2015). Significance of the whole rock Re–Os ages in cryptically and modally metasomatised cratonic peridotites: Constraints from HSE–Se–Te systematics. *Geochimica et Cosmochimica Acta*, **164**, 441-463.

Luguet A., Lorand J. P., Alard O. and Cottin J. Y. (2004). A multi-technique study of platinum group element systematic in some Ligurian ophiolitic peridotites, Italy. *Chemical Geology*, **208**(1-4), 175-194.

Luguet A., Lorand J. P. and Seyler M. (2003). Sulfide petrology and highly siderophile element geochemistry of abyssal peridotites: A coupled study of samples from the Kane Fracture Zone (45°W 23°20N, MARK Area, Atlantic Ocean). *Geochimica et Cosmochimica Acta*, **67**(8), 1553-1570.

Luguet A., Shirey S. B., Lorand J. P., Horan M. F. and Carlson R. W. (2007). Residual platinum-group minerals from highly depleted harzburgites of the Lherz massif (France) and their role in HSE fractionation of the mantle. *Geochimica et Cosmochimica Acta*, **71**(12), 3082-3097.

Lyons T. W., Reinhard C. T. and Planavsky N. J. (2014). The rise of oxygen in Earth's early ocean and atmosphere. *Nature*, **506**(7488), 307-15.

Makishima A. and Nakamura E. (2009). Determination of Ge, As, Se and Te in Silicate Samples Using Isotope Dilution-Internal Standardisation Octopole Reaction Cell ICP-QMS by Normal Sample Nebulisation. *Geostandards and Geoanalytical Research*, **33**(3), 369-384.

Marin L., Lhomme J. and Carignan J. (2001). Determination of selenium concentration in sixty five reference materials for geochemical analysis by GFAAS after separation with thiol cotton. *Geostandards Newsletter-the Journal of Geostandards and Geoanalysis*, **25**(2-3), 317-324.

Mcdonough W. F. and Sun S.-S. (1995). The Composition of the Earth. *Chemical Geology*, **120**(3-4), 223-253.

McNeal J. M. and Balistrieri L. S., 1989. Geochemistry and Occurrence of Selenium: An Overview, Selenium in Agriculture and the Environment. SSSA Special Publication. Soil Science Society of America and American Society of Agronomy, Madison, WI, pp. 1-13.

Mcphail D. C. (1995). Thermodynamic Properties of Aqueous Tellurium Species between 25 and 350 °C. *Geochimica et Cosmochimica Acta*, **59**(5), 851-866.

Meija J., Coplen T. B., Berglund M., Brand W. A., De Bievre P., Groning M., Holden N. E., Irrgeher J., Loss R. D., Walczyk T. and Prohaska T. (2016). Isotopic compositions of the elements 2013 (IUPAC Technical Report). *Pure and Applied Chemistry*, **88**(3), 293-306.

Meisel T. and Horan M. F. (2016). Analytical Methods for the Highly Siderophile Elements. *Highly Siderophile and Strongly Chalcophile Elements in High-Temperature Geochemistry and Cosmochemistry*, **81**(1), 89-106.

Meisel T., Reisberg L., Moser J., Carignan J., Melcher F. and Brügmann G. (2003). Re–Os systematics of UB-N, a serpentinized peridotite reference material. *Chemical Geology*, **201**(1-2), 161-179.

Menzies M., Blanchard D., Brannon J. and Korotev R. (1977). Rare-Earth Geochemistry of Fused Ophiolitic and Alpine Lherzolites .2. Beni Bouchera, Ronda and Lanzo. *Contributions to Mineralogy and Petrology*, **64**(1), 53-74.

Michael P. J. and Cornell W. C. (1998). Influence of spreading rate and magma supply on crystallization and assimilation beneath mid-ocean ridges: Evidence from chlorine and major element chemistry of mid-ocean ridge basalts. *Journal of Geophysical Research: Solid Earth*, **103**(B8), 18325-18356.

Mitchell K., Mansoor S. Z., Mason P. R. D., Johnson T. M. and Van Cappellen P. (2016). Geological evolution of the marine selenium cycle: Insights from the bulk shale delta Se-82/76 record and isotope mass balance modeling. *Earth and Planetary Science Letters*, **441**, 178-187.

Mitchell K., Mason P. R. D., Van Cappellen P., Johnson T. M., Gill B. C., Owens J. D., Diaz J., Ingall E. D., Reichart G. J. and Lyons T. W. (2012). Selenium as paleo-oceanographic proxy: A first assessment. *Geochimica et Cosmochimica Acta*, **89**, 302-317.

Moore J. G. and Calk L. (1971). Sulfide Spherules in Vesicles of Dredged Pillow Basalt. *American Mineralogist*, **56**(3-4), 476-&.

Moore J. G. and Fabbi B. P. (1971). An estimate of the juvenile sulfur content of basalt. *Contributions to Mineralogy and Petrology*, **33**(2), 118-127.

Moore J. G. and Schillin.Jg (1973). Vesicles, Water, and Sulfur in Reykjanes Ridge Basalts. *Contributions to Mineralogy and Petrology*, **41**(2), 105-118.

Moreira M., Staudacher T., Sarda P., Schilling J.-G. and Allègre C. J. (1995). A primitive plume neon component in MORB: The Shona ridge-anomaly, South Atlantic (51–52°S). *Earth and Planetary Science Letters*, **133**(3-4), 367-377.

Moreira M. A., Dosso L. and Ondréas H. (2008). Helium isotopes on the Pacific-Antarctic ridge (52.5°–41.5°S). *Geophysical Research Letters*, **35**(10).

Morgan J. W. (1986). Ultramafic xenoliths: Clues to Earth's late accretionary history. *Journal of Geophysical Research*, **91**(B12), 12375-12387.

Mukherjee I., Large R. R., Corkrey R. and Danyushevsky L. V. (2018). The Boring Billion, a slingshot for Complex Life on Earth. *Sci Rep*, **8**(1), 4432.

Mungall J. E. and Brenan J. M. (2014). Partitioning of platinum-group elements and Au between sulfide liquid and basalt and the origins of mantle-crust fractionation of the chalcophile elements. *Geochimica et Cosmochimica Acta*, **125**, 265-289.

Nagamori M. and Mackey P. J. (1977). Distribution equilibria of Sn, Se and Te between FeO-Fe2O3-SiO2-AI2O3-CuO0.5 slag and metallic copper. *Metallurgical Transactions B*, **8**(1), 39-46.

Nebel O., Sossi P. A., Bénard A., Arculus R. J., Yaxley G. M., Woodhead J. D., Rhodri Davies D. and Ruttor S. (2019). Reconciling petrological and isotopic mixing mechanisms in the Pitcairn mantle plume using stable Fe isotopes. *Earth and Planetary Science Letters*,

521, 60-67.

Nielsen R. L., Forsythe L. M., Gallahan W. E. and Fisk M. R. (1994). Major- and trace-element magnetite-melt equilibria. *Chemical Geology*, **117**(1-4), 167-191.

Nielsen S. G., Shimizu N., Lee C.-T. A. and Behn M. D. (2014). Chalcophile behavior of thallium during MORB melting and implications for the sulfur content of the mantle. *Geochemistry, Geophysics, Geosystems*, **15**(12), 4905-4919.

Niu Y. and Batiza R. (1991). An empirical method for calculating melt compositions produced beneath mid-ocean ridges: Application for axis and off-axis (seamounts) melting. *Journal of Geophysical Research: Solid Earth*, **96**(B13), 21753-21777.

Nolte N., Kleinhanns I. C., Baero W. and Hansen B. T. (2011). Petrography and whole-rock geochemical characteristics of Västervik granitoids to syenitoids, southeast Sweden: constraints on petrogenesis and tectonic setting at the southern margin of the Svecofennian domain. *Gff*, **133**(3-4), 173-196.

Och L. M. and Shields-Zhou G. A. (2012). The Neoproterozoic oxygenation event: Environmental perturbations and biogeochemical cycling. *Earth-Science Reviews*, **110**(1-4), 26-57.

Ondréas H., Aslanian D., Géli L., Olivet J.-L. and Briais A. (2001). Variations in axial morphology, segmentation, and seafloor roughness along the Pacific-Antarctic Ridge between 56°S and 66°S. *Journal of Geophysical Research: Solid Earth*, **106**(B5), 8521-8546.

O'Neill H. S. C., Berry A. J. and Mallmann G. (2018). The oxidation state of iron in Mid-Ocean Ridge Basaltic (MORB) glasses: Implications for their petrogenesis and oxygen fugacities. *Earth and Planetary Science Letters*, **504**, 152-162.

Palme H. and O'Neill H. S. C., 2014. Cosmochemical Estimates of Mantle Composition. In: Holland, H.D., Turekian, K.K. (Eds.), Treatise on Geochemistry (Second Edition). Elsevier, Oxford, pp. 1-39.

Patten C., Barnes S. J. and Mathez E. A. (2012). Textural Variations in Morb Sulfide Droplets Due to Differences in Crystallization History. *Canadian Mineralogist*, **50**(3), 675-692.

Patten C., Barnes S. J., Mathez E. A. and Jenner F. E. (2013). Partition coefficients of chalcophile elements between sulfide and silicate melts and the early crystallization history of sulfide liquid: LA-ICP-MS analysis of MORB sulfide droplets. *Chemical Geology*, **358**, 170-188.

Patten C. G. C., Pitcairn I. K., Teagle D. A. H. and Harris M. (2016). Sulphide mineral evolution and metal mobility during alteration of the oceanic crust: Insights from ODP Hole 1256D. *Geochimica et Cosmochimica Acta*, **193**, 132-159.

Peach C. L., Mathez E. A. and Keays R. R. (1990). Sulfide melt-silicate melt distribution coefficients for noble metals and other chalcophile elements as deduced from MORB: Implications for partial melting. *Geochimica et Cosmochimica Acta*, **54**(12), 3379-3389.

Perfit M. R., 2001. Mid-Ocean Ridge Geochemistry and Petrology. In: Steele, J.H. (Ed.), Encyclopedia of Ocean Sciences. Academic Press, Oxford, pp. 815-825.

Plank T., Spiegelman M., Langmuir C. H. and Forsyth D. W. (1995). The meaning of "mean F": Clarifying the mean extent of melting at ocean ridges. *Journal of Geophysical Research*, **100**(B8), 15045-15052.

Pogge von Strandmann P. A. E., Coath C. D., Catling D. C., Poulton S. W. and Elliott T. (2014).

Analysis of mass dependent and mass independent selenium isotope variability in black shales. *J. Anal. At. Spectrom.*, **29**(9), 1648-1659.

Pogge von Strandmann P. A. E., Stüeken E. E., Elliott T., Poulton S. W., Dehler C. M., Canfield D. E. and Catling D. C. (2015). Selenium isotope evidence for progressive oxidation of the Neoproterozoic biosphere. *Nat. Commun.*, **6**(10157).

Poulton S. W., Fralick P. W. and Canfield D. E. (2004). The transition to a sulphidic ocean approximately 1.84 billion years ago. *Nature*, **431**(7005), 173-7.

Rashid K. and Krouse H. R. (1985). Selenium isotopic fractionation during reduction to Se0 and H2Se. *Canadian Journal of Chemistry*, **63**(11), 3195-3199.

Rees C. E. and Thode H. G. (1966). Selenium Isotope Effects in the Reduction of Sodium Selenite and of Sodium Selenate. *Canadian Journal of Chemistry*, **44**(4), 419-427.

Rehkämper M., Halliday A. N., Fitton J. G., Lee D. C., Wieneke M. and Arndt N. T. (1999). Ir, Ru, Pt, and Pd in basalts and komatiites: New constraints for the geochemical behavior of the platinum-group elements in the mantle. *Geochimica et Cosmochimica Acta*, **63**(22), 3915-3934.

Rehkämper M. and Hofmann A. W. (1997). Recycled ocean crust and sediment in Indian Ocean MORB. *Earth and Planetary Science Letters*, **147**(1-4), 93-106.

Righter K., Leeman W. P. and Hervig R. L. (2006). Partitioning of Ni, Co and V between spinel-structured oxides and silicate melts: Importance of spinel composition. *Chemical Geology*, **227**(1-2), 1-25.

Rose-Weston L., Brenan J. M., Fei Y. W., Secco R. A. and Frost D. J. (2009). Effect of pressure, temperature, and oxygen fugacity on the metal-silicate partitioning of Te, Se, and S: Implications for earth differentiation. *Geochimica et Cosmochimica Acta*, **73**(15), 4598-4615.

Rouxel O., Galy A. and Elderfield H. (2006). Germanium isotopic variations in igneous rocks and marine sediments. *Geochimica et Cosmochimica Acta*, **70**(13), 3387-3400.

Rouxel O., Ludden J., Carignan J., Marin L. and Fouquet Y. (2002). Natural variations of Se isotopic composition determined by hydride generation multiple collector inductively coupled plasma mass spectrometry. *Geochimica et Cosmochimica Acta*, **66**(18), 3191-3199.

Rouxel O., Fouquet Y., Ludden J.N. (2004). Subsurface processes at the lucky strike hydrothermal field, Mid-Atlantic ridge: evidence from sulfur, selenium, and iron isotopes. *Geochimica et Cosmochimica Acta*, **68**(10), 2295-2311.

Rudnick R. L. and Gao S., 2003. Composition of the Continental Crust. In: Holland, H.D., Turekian, K.K. (Eds.), Treatise on Geochemistry. Pergamon, Oxford, pp. 1-64.

Saal A. E., Hauri E. H., Langmuir C. H. and Perfit M. R. (2002). Vapour undersaturation in primitive mid-ocean-ridge basalt and the volatile content of Earth's upper mantle. *Nature*, **419**, 451.

Salters V. J. M. and Stracke A. (2004). Composition of the depleted mantle. *Geochemistry, Geophysics, Geosystems*, **5**(5), Q05B07.

Sarda P., Moreira M., Staudacher T., Schilling J.-G. and Allègre C. J. (2000). Rare gas systematics on the southernmost Mid-Atlantic Ridge: Constraints on the lower mantle and the Dupal source. *Journal of Geophysical Research*, **105**(B3), 5973.

Savard D., Bedard L. P. and Bames S. J. (2009). Selenium Concentrations in Twenty-Six Geological Reference Materials: New Determinations and Proposed Values. *Geostandards and Geoanalytical Research*, **33**(2), 249-259.

Schaefer L. and Fegley B. (2010). Volatile element chemistry during metamorphism of ordinary chondritic material and some of its implications for the composition of asteroids. *Icarus*, **205**(2), 483-496.

Schilling J.-G., Zajac M., Evans R., Johnston T., White W., Devine J. D. and Kingsley R. (1983). Petrologic and Geochemical Variations Along the Mid-Atlantic Ridge from 29°N to 73°N. *American Journal of Science*, **283**(6), 510-586.

Schilling K., Johnson T. M. and Mason P. R. D. (2014). A sequential extraction technique for mass-balanced stable selenium isotope analysis of soil samples. *Chemical Geology*, **381**, 125-130.

Schilling K., Johnson T. M. and Wilcke W. (2011a). Isotope Fractionation of Selenium During Fungal Biomethylation by Alternaria alternata. *Environmental Science & Technology*, **45**(7), 2670-2676.

Schilling K., Johnson T. M. and Wilcke W. (2011b). Selenium Partitioning and Stable Isotope Ratios in Urban Topsoils. *Soil Science Society of America Journal*, **75**(4), 1354.

Schirmer T., Koschinsky A. and Bau M. (2014). The ratio of tellurium and selenium in geological material as a possible paleo-redox proxy. *Chemical Geology*, **376**, 44-51.

Schoenberg R. and von Blanckenburg F. (2005). An assessment of the accuracy of stable Fe isotope ratio measurements on samples with organic and inorganic matrices by high-resolution multicollector ICP-MS. *International Journal of Mass Spectrometry*, **242**(2-3), 257-272.

Schönbächler M. and Fehr M. A. (2014). Basics of Ion Exchange Chromatography for Selected Geological Applications. 123-146.

Seyler M., Lorand J. P., Dick H. J. B. and Drouin M. (2006). Pervasive melt percolation reactions in ultra-depleted refractory harzburgites at the Mid-Atlantic Ridge, 15° 20′N: ODP Hole 1274A. *Contributions to Mineralogy and Petrology*, **153**(3), 303-319.

Shaw D. M. (1970). Trace element fractionation during anatexis. *Geochimica et Cosmochimica Acta*, **34**(2), 237-243.

Shore A. J. T., 2010. Selenium geochemistry and isotopic composition of sediments from the Cariaco Basin and the Bermuda Rise: a comparison between a restricted basin and the open ocean over the last 500 ka, University of Leicester, Leicester, UK.

Sinton J. M. and Detrick R. S. (1992). Mid-ocean ridge magma chambers. *Journal of Geophysical Research*, **97**(B1), 197-216.

Small C. (1995). Observations of Ridge-Hotspot Interactions in the Southern-Ocean. *Journal of Geophysical Research-Solid Earth*, **100**(B9), 17931-17946.

Smit M. A. and Mezger K. (2017). Earth's early O2 cycle suppressed by primitive continents. *Nature Geoscience*, **10**, 788.

Smith P. M. and Asimow P. D. (2005). Adiabat_1ph: A new public front-end to the MELTS, pMELTS, and pHMELTS models. *Geochemistry, Geophysics, Geosystems*, **6**(2), Q02004.

Smythe D. J., Wood B. J. and Kiseeva E. S. (2017). The S content of silicate melts at sulfide

saturation: New experiments and a model incorporating the effects of sulfide composition. *American Mineralogist*, **102**(4), 795-803.

Stracke A. (2012). Earth's heterogeneous mantle: A product of convection-driven interaction between crust and mantle. *Chemical Geology*, **330-331**, 274-299.

Stüeken E. E. (2017). Selenium Isotopes as a Biogeochemical Proxy in Deep Time. *Reviews in Mineralogy and Geochemistry*, **82**(1), 657-682.

Stüeken E. E., Buick R. and Anbar A. D. (2015a). Selenium isotopes support free O2 in the latest Archean. *Geology*, **43**(3), 259-262.

Stüeken E. E., Buick R., Bekker A., Catling D., Foriel J., Guy B. M., Kah L. C., Machel H. G., Montanez I. P. and Poulton S. W. (2015b). The evolution of the global selenium cycle: Secular trends in Se isotopes and abundances. *Geochimica et Cosmochimica Acta*, **162**, 109-125.

Stüeken E. E., Foriel J., Nelson B. K., Buick R. and Catling D. C. (2013). Selenium isotope analysis of organic-rich shales: advances in sample preparation and isobaric interference correction. *Journal of Analytical Atomic Spectrometry*, **28**(11), 1734-1749.

Suer T.-A., Siebert J., Remusat L., Menguy N. and Fiquet G. (2017). A sulfur-poor terrestrial core inferred from metal–silicate partitioning experiments. *Earth and Planetary Science Letters*, **469**, 84-97.

Takei H., Okayama U., Tetsuya Y., Okayama U., Akio M., max@misasa.okayama u. a. j., Institute for Planetary M., Eizo N., eizonak@misasa.okayama u. a. j. and Institute for P. (2001). Formation and suppression of AlF3 during HF digestion of rock samples in Teflon bomb for precise trace element analyses by ICP-MS and ID-TIMS. *Proceedings of the Japan Academy Series B: Physical and Biological Sciences*, **77**(1), 13-17.

Tao G. H. and Sturgeon R. E. (1999). Sample nebulization for minimization of transition metal interferences with selenium hydride generation ICP-AES. *Spectrochimica Acta Part B-Atomic Spectroscopy*, **54**(3-4), 481-489.

Teng F. Z., Dauphas N., Huang S. C. and Marty B. (2013). Iron isotopic systematics of oceanic basalts. *Geochimica et Cosmochimica Acta*, **107**, 12-26.

Terashima S. and Imai N. (2000). Determination of selenium in fifty two geochemical reference materials by hydride generation atomic absorption spectrometry. *Geostandards Newsletter-the Journal of Geostandards and Geoanalysis*, **24**(1), 83-86.

Tokunaga K., Yokoyama Y. and Takahashi Y. (2013). Estimation of Se(VI)/Se(IV) ratio in water by the ratio recorded in barite. *Geochemistry Geophysics Geosystems*, **14**(11), 4826-4834.

Toplis M. J. and Corgne A. (2002). An experimental study of element partitioning between magnetite, clinopyroxene and iron-bearing silicate liquids with particular emphasis on vanadium. *Contributions to Mineralogy and Petrology*, **144**(1), 22-37.

Varas-Reus M. I., König S., Yierpan A., Lorand J.-P. and Schoenberg R. (2019). Selenium isotopes as tracers of a late volatile contribution to Earth from the outer Solar System. *Nature Geoscience*.

Vijan P. N. and Leung D. (1980). Reduction of Chemical Interference and Speciation Studies in the Hydride Generation Atomic-Absorption Method for Selenium. *Analytica Chimica Acta*, **120**(Nov), 141-146.

Vlastelic I., Aslanian D., Dosso L., Bougault H., Olivet J. L. and Geli L. (1999). Large-scale

chemical and thermal division of the Pacific mantle. *Nature*, **399**(6734), 345-350.

Vlastélic I., Dosso L., Bougault H., Aslanian D., Géli L., Etoubleau J., Bohn M., Joron J.-L. and Bollinger C. (2000). Chemical systematics of an intermediate spreading ridge: The Pacific-Antarctic Ridge between 56°S and 66°S. *Journal of Geophysical Research*, **105**(B2), 2915-2936.

Vollstaedt H., Mezger K. and Leya I. (2016). The isotope composition of selenium in chondrites constrains the depletion mechanism of volatile elements in solar system materials. *Earth and Planetary Science Letters*, **450**, 372-380.

Wallace P. J. and Edmonds M. (2011). The Sulfur Budget in Magmas: Evidence from Melt Inclusions, Submarine Glasses, and Volcanic Gas Emissions. *Sulfur in Magmas and Melts: Its Importance for Natural and Technical Processes*, **73**(1), 215-246.

Wang Z. and Becker H. (2013). Ratios of S, Se and Te in the silicate Earth require a volatile-rich late veneer. *Nature*, **499**(7458), 328-31.

Wang Z. and Becker H. (2014). Abundances of Sulfur, Selenium, Tellurium, Rhenium and Platinum-Group Elements in Eighteen Reference Materials by Isotope Dilution Sector-Field ICP-MS and Negative TIMS. *Geostandards and Geoanalytical Research*, **38**(2), 189-209.

Wang Z. and Becker H. (2015a). Fractionation of highly siderophile and chalcogen elements during magma transport in the mantle: Constraints from pyroxenites of the Balmuccia peridotite massif. *Geochimica et Cosmochimica Acta*, **159**, 244-263.

Wang Z. and Becker H. (2015b). Abundances of Ag and Cu in mantle peridotites and the implications for the behavior of chalcophile elements in the mantle. *Geochimica et Cosmochimica Acta*, **160**, 209-226.

Wang Z. and Becker H. (2017). Chalcophile elements in Martian meteorites indicate low sulfur content in the Martian interior and a volatile element-depleted late veneer. *Earth and Planetary Science Letters*, **463**, 56-68.

Wang Z., Becker H. and Gawronski T. (2013). Partial re-equilibration of highly siderophile elements and the chalcogens in the mantle: A case study on the Baldissero and Balmuccia peridotite massifs (Ivrea Zone, Italian Alps). *Geochimica et Cosmochimica Acta*, **108**, 21-44.

Wang Z., Becker H. and Wombacher F. (2015). Mass Fractions of S, Cu, Se, Mo, Ag, Cd, In, Te, Ba, Sm, W, Tl and Bi in Geological Reference Materials and Selected Carbonaceous Chondrites Determined by Isotope Dilution ICP-MS. *Geostandards and Geoanalytical Research*, **39**(2), 185-208.

Wasson J. T. and Kallemeyn G. W. (1988). Compositions of Chondrites. *Philosophical Transactions of the Royal Society A: Mathematical, Physical and Engineering Sciences*, **325**(1587), 535-544.

Watts A. B., Weissel J. K., Duncan R. A. and Larson R. L. (1988). Origin of the Louisville Ridge and its relationship to the Eltanin Fracture Zone System. *Journal of Geophysical Research*, **93**(B4), 3051-3077.

Welz B. and Melcher M. (1984). Mechanisms of transition metal interferences in hydride generation atomic-absorption spectrometry. Part 1. Influence of cobalt, copper, iron and nickel on selenium determination. *The Analyst*, **109**(5), 569.

Wen H. J., Carignan J., Chu X. L., Fan H. F., Cloquet C., Huang J., Zhang Y. X. and Chang H.

J. (2014). Selenium isotopes trace anoxic and ferruginous seawater conditions in the Early Cambrian. *Chemical Geology*, **390**, 164-172.

White W. M. and Schilling J.-G. (1978). The nature and origin of geochemical variation in Mid-Atlantic Ridge basalts from the Central North Atlantic. *Geochimica et Cosmochimica Acta*, **42**(10), 1501-1516.

Willbold M. and Elliott T. (2017). Molybdenum isotope variations in magmatic rocks. *Chemical Geology*, **449**, 253-268.

Williams H. M. and Bizimis M. (2014). Iron isotope tracing of mantle heterogeneity within the source regions of oceanic basalts. *Earth and Planetary Science Letters*, **404**, 396-407.

Wood B. J., Smythe D. J. and Harrison T. (2019). The condensation temperatures of the elements: A reappraisal. *American Mineralogist*, **104**(6), 844-856.

Workman R. K. and Hart S. R. (2005). Major and trace element composition of the depleted MORB mantle (DMM). *Earth and Planetary Science Letters*, **231**(1-2), 53-72.

Wykes J. L., O'Neill H. S. C. and Mavrogenes J. A. (2015). The Effect of FeO on the Sulfur Content at Sulfide Saturation (SCSS) and the Selenium Content at Selenide Saturation of Silicate Melts. *Journal of Petrology*, **56**(7), 1407-1424.

Wykes, J. L., O'Neill, H. C. & Mavrogenes, J. A. (2011). XANES investigation of selenium speciation in silicate glasses. Paper presented at Annual V. M. Goldschmidt Conference, Prague, Czech Republic.

Xu G. P., Hannah J. L., Bingen B., Georgiev S. and Stein H. J. (2012). Digestion methods for trace element measurements in shales: Paleoredox proxies examined. *Chemical Geology*, **324**, 132-147.

Yamamoto M. (1976). Relationship between Se/S and sulfur isotope ratios of hydrothermal sulfide minerals. *Mineralium Deposita*, **11**(2), 197-209.

Yang A. Y., Zhou M. F., Zhao T. P., Deng X. G., Qi L. and Xu J. F. (2014). Chalcophile elemental compositions of MORBs from the ultraslow-spreading Southwest Indian Ridge and controls of lithospheric structure on S-saturated differentiation. *Chemical Geology*, **382**, 1-13.

Yi W., Halliday A. N., Alt J. C., Lee D.-C., Rehkämper M., Garcia M. O., Langmuir C. H. and Su Y. (2000). Cadmium, indium, tin, tellurium, and sulfur in oceanic basalts: Implications for chalcophile element fractionation in the Earth. *Journal of Geophysical Research*, **105**(B8), 18927.

Yi W., Halliday A. N., Lee D. C. and Rehkamper M. (1998). Precise determination of cadmium, indium and tellurium using multiple collector ICP-MS. *Geostandards Newsletter-the Journal of Geostandards and Geoanalysis*, **22**(2), 173-179.

Yierpan A., König S., Labidi J., Kurzawa T., Babechuk M. G. and Schoenberg R. (2018). Chemical Sample Processing for Combined Selenium Isotope and Selenium-Tellurium Elemental Investigation of the Earth's Igneous Reservoirs. *Geochemistry, Geophysics, Geosystems*, **19**(2), 516-533.

Yierpan A., König S., Labidi J. and Schoenberg R. (2019). Selenium isotope and S-Se-Te elemental systematics along the Pacific-Antarctic ridge: Role of mantle processes. *Geochimica et Cosmochimica Acta*, **249**, 199-224.

Yokoyama T., Makishima A. and Nakamura E. (1999). Evaluation of the coprecipitation of incompatible trace elements with fluoride during silicate rock dissolution by acid

digestion. *Chemical Geology*, **157**(3-4), 175-187.

Young E. D., Manning C. E., Schauble E. A., Shahar A., Macris C. A., Lazar C. and Jordan M. (2015). High-temperature equilibrium isotope fractionation of non-traditional stable isotopes: Experiments, theory, and applications. *Chemical Geology*, **395**, 176-195.

Yu L. L., Fassett J. D. and Guthrie W. F. (2002). Detection limit of isotope dilution mass spectrometry. *Anal Chem*, **74**(15), 3887-91.

Yu M. Q., Liu G. Q. and Jin Q. (1983). Determination of Trace Arsenic, Antimony, Selenium and Tellurium in Various Oxidation-States in Water by Hydride Generation and Atomic-Absorption Spectrophotometry after Enrichment and Separation with Thiol Cotton. *Talanta*, **30**(4), 265-270.

Zhang Z. and Hirschmann M. M. (2016). Experimental constraints on mantle sulfide melting up to 8 GPa. *American Mineralogist*, **101**(1-2), 181-192.

Zhang Z., von der Handt A. and Hirschmann M. M. (2018). An experimental study of Fe–Ni exchange between sulfide melt and olivine at upper mantle conditions: implications for mantle sulfide compositions and phase equilibria. *Contributions to Mineralogy and Petrology*, **173**(3), 19.

Zhu J.-M., Johnson T. M., Clark S. K. and Zhu X.-K. (2008). High Precision Measurement of Selenium Isotopic Composition by Hydride Generation Multiple Collector Inductively Coupled Plasma Mass Spectrometry with a 74Se-77Se Double Spike. *Chinese Journal of Analytical Chemistry*, **36**(10), 1385-1390.

Zhu J.-M., Johnson T. M., Clark S. K., Zhu X.-K. and Wang X. L. (2014). Selenium redox cycling during weathering of Se-rich shales: A selenium isotope study. *Geochimica et Cosmochimica Acta*, **126**, 228-249.

Curriculum Vitae: Aierken Yierpan (ئەيرپان ئەركىن)

PERSONAL

Address	Isotopengeochemie, Universität Tübingen Wilhelmstr. 56, 72074 Tübingen +49-(0)7071-29-78907 aierken.yierpan@uni-tuebingen.de
Date of Birth	01.04.1989
Place of Birth	Xinjiang Uyghur Autonomous Region, China
Marital Status	Married

EDUCATION

May 2015–Present	*Ph.D. Student*, Isotopengeochemie, Universität Tübingen, Germany	
	Dissertation	Selenium isotope systematics of mid-ocean-ridge basalts and implications for the long-term volatile and chalcophile record of the crust–mantle system
	Supervisors	Dr. Stephan König, Prof. Dr. Ronny Schoenberg
Oct. 2012–Feb. 2015	*M.Sc.* (110/110 cum laude), Sezione di Geologia, Università di Camerino, Italy	
	Thesis	Geochemistry of mantle xenoliths from Salt Lake Crater, O`ahu, Hawaii: an LA-ICP-MS Study
	Supervisors	Prof. Michael R. Carroll, Prof. Munir Humayun
	Co-supervisor	Prof. Eleonora Paris
Sept. 2008–June 2012	*B.Eng.* (major in Geological Engineering), School of Earth Sciences and Engineering, Nanjing University, China	
	Thesis	Study on the heat affected range of ground heat exchangers
	Supervisor	Prof. Xiaobao Zhao

PROFESSIONAL EXPERIENCE

Aug. 2014–Nov. 2014	Visiting Graduate Student, Geochemistry Group, National High Magnetic Field Laboratory, Florida State University, USA (supervised by Prof. Munir Humayun)
Oct. 2013–Aug. 2014	Teaching Assistant, Geomaterials Laboratory (GEO06), Università di Camerino
Feb. 2014–July 2014	Teaching Assistant, Geochemistry and Petrogenesis (GEO07), Università di Camerino
May 2013–Aug. 2014	Lab Assistant, X-ray Diffraction Laboratory and Mineralogy Laboratory, Università di Camerino

HONOURS AND AWARDS

Aug. 2014–Nov. 2014	'Third-country' Research Grant (Università di Camerino): Visiting Graduate Student at the National High Magnetic Field Laboratory, Florida State University, USA

Oct. 2012–Dec. 2014	Borsa di studio (Università di Camerino): Full scholarship for M.Sc. program
2009–2011	Zhu Yicai Scholarship (Nanjing University)

LABORATORY SKILLS

MC-ICP-MS, iCAP Qc ICP-MS, clean lab, chemical separation; experienced with LA-ICP-MS, XRD

LANGUAGE SKILLS

Uyghur (native speaker), English (professional working proficiency), Chinese (professional working proficiency), Uzbek (elementary proficiency), German (elementary proficiency A1)

COMPUTER SKILLS

Microsoft Office Suite, CorelDRAW, OriginLab, alphaMELTS (with MELTS/pMELTS models), Photoshop; experienced with C Language, MATLAB, ArcGIS, ANSYS simulation, 3ds Max, Illustrator

SERVICES

Sept. 2013	Poster presentation and introduction during the Lab Day for new students, Università di Camerino
Sept. 2013	Student Tutor for new Master's students, Università di Camerino
Sept. 2008–Nov. 2009	Office Assistant at Geology Laboratory, Nanjing University

FIELD EXPERIENCE

Nov 2016	Sample campaign to Cyprus (with Dr. Stephan König, Universität Tübingen)
Apr–July 2013	Field trips to Apennine umbro-marchigiano, Italy (Structural Geology and Stratigraphy; with Prof. Claudio Di Celma and Dr. Pietro Paolo, Università di Camerino)
Aug 2010	Field trips to Chaohu, Anhui, China (junction of the North China Plate and Yangtze Plate; Regional Geology; with Prof. Bin Shi, Nanjing University)
Aug 2009	Field trips to Hushan, Nanjing and Lianyungang coastal areas, China (Regional Geology; Prof. Junqi Wu, Nanjing University)

THESIS CO-SUPERVISION

Johannes Redlinger	M.Sc. 2019, Universität Tübingen (*Selenium isotope and Se- & Te-elemental systematics along the Reykjanes Ridge to Iceland*)
	B.Sc. 2016, Universität Tübingen (*Modell zum Verhalten von Selen und Tellur in der Marianen-Subduktionszone*)
Mona Schiller	M.Sc. 2019, Universität Tübingen (*Geochemical Constraints on Sources of Ocean Island Basalts from French Polynesia*)

CONFERENCE ABSTRACTS

Yierpan A., König S., Labidi J., Varas-Reus M. I., Redlinger J. and Schoenberg R. (2019). Tracing atmospheric oxygenation with selenium isotopes in mantle melts. Talk, *GeoMünster*, Münster, Germany

Yierpan A., König S., Labidi J., Varas-Reus M. I., Redlinger J. and Schoenberg R. (2019) Selenium isotopes trace crustal recycling in the upper mantle. Talk, *Goldschmidt Annual Meeting*, Barcelona, Spain

Varas-Reus M. I., König S., **Yierpan A.**, Garrido C. J., Marchesi C. and Schoenberg R. (2019). Selenium isotope variations in orogenic garnet pyroxenites. Talk, *Goldschmidt Annual Meeting*, Barcelona, Spain

Yierpan A., König S., Labidi J., Redlinger J., Varas-Reus M. I. and Schoenberg R. (2019) Tracing crustal recycling with selenium isotopes. Poster, *Annual meeting of DMG-sections Geochemistry as well as Petrology & Petrophysics*, Heidelberg, Germany

Varas-Reus M. I., König S., **Yierpan A.**, Kurzawa T., Schönberg R. and Lorand J.-P. (2019). Selenium isotope constraints on the volatile nature of the late veneer. Talk, *Annual meeting of DMG-sections Geochemistry as well as Petrology & Petrophysics*, Heidelberg, Germany

Yierpan A., König S., Labidi J., Kurzawa T., Redlinger J. and Schoenberg R. (2018). Selenium isotope and Se–Te elemental systematics of the Pacific–Antarctic ridge basalts. Talk, *Goldschmidt Annual Meeting*, Boston, USA

König S., Eickmann B., Zack T., **Yierpan A.**, Taubald H. and Schoenberg R. (2018). Redox-record from sulfur-selenium isotope decoupling at the sulfide scale. Poster, *Goldschmidt Annual Meeting*, Boston, USA

Kurzawa T., König S., Jeffrey A., Yierpan A . and Schoenberg R. (2018). The Se isotope signature of Mariana arc lavas. Talk, *Goldschmidt Annual Meeting*, Boston, USA

Varas-Reus M. I., König S., **Yierpan A.**, Kurzawa T., Schönberg R. and Lorand J.-P. (2018). Selenium isotope composition of mantle peridotites. Talk, *Goldschmidt Annual Meeting*, Boston, USA

Labidi J., König S., Bennett N., Kurzawa T., **Yierpan A.**, Shahar A. and Schoenberg R. (2016). Testing the Late-Veneer hypothesis with selenium isotopes. Poster, *AGU Fall Meeting*, San Francisco, USA

Yierpan A., König S., Labidi J., Huber F., Kurzawa T. and Schoenberg R. (2016). The elemental S-Se-Te and Se isotopic signature of Pacific-Antarctic MORB. Talk, *4th International Workshop on Highly Siderophile Element Geochemistry*, Durham, UK

PUBLICATIONS

Varas-Reus M. I., König S., **Yierpan A.**, Lorand J.-P. and Schoenberg R. (2019). Selenium isotopes as tracers of a late volatile contribution to Earth from the outer Solar System. *Nature Geoscience*.

Kurzawa T., König S., Alt J. C., **Yierpan A.** and Schoenberg R. (2019). The role of subduction recycling on the selenium isotope signature of the mantle: Constraints from Mariana arc lavas. *Chemical Geology*, 513, 239–249.

Yierpan A., König S., Labidi J. and Schoenberg R. (2019). Selenium isotope and S-Se-Te elemental systematics along the Pacific-Antarctic ridge: Role of mantle processes. *Geochimica et Cosmochimica Acta*, 249, 199–224.

König S., Eickmann B., Zack T., **Yierpan A.**, Wille M., Taubald H. and Schoenberg R. (2019). Redox induced sulfur-selenium isotope decoupling recorded in pyrite. *Geochimica et Cosmochimica Acta*, 244, 24–39.

Yierpan A., König S., Labidi J., Kurzawa T., Babechuk M. G. and Schoenberg R. (2018). Chemical Sample Processing for Combined Selenium Isotope and Selenium-Tellurium Elemental Investigation of the Earth's Igneous Reservoirs. *Geochemistry, Geophysics, Geosystems*, 19, 516–533.

Labidi J., König S., Kurzawa T., **Yierpan A.** and Schoenberg R. (2018). The selenium isotopic variations in chondrites are mass-dependent; Implications for sulfide formation in the early solar system. *Earth and Planetary Science Letters*, 481, 212–222.

Kurzawa T., König S., Labidi J., **Yierpan A.** and Schoenberg R. (2017). A method for Se isotope analysis of low ng-level geological samples via double spike and hydride generation MC-ICP-MS. *Chemical Geology*, 466, 219–228.

AGU PUBLICATIONS

Geochemistry, Geophysics, Geosystems

RESEARCH ARTICLE
10.1002/2017GC007299

Key Points:
- High-precision Se stable isotope and Se-Te concentration analyses from the same sample digest
- New Se isotope data for five international silicate reference materials and Se isotopic difference between basalts and chondrites
- Potential to study the Earth's igneous reservoirs and mantle perspective on the volatile evolution

Supporting Information:
- Supporting Information S1
- Table S1
- Table S5
- Table S6

Correspondence to:
A. Yierpan,
aierken.yierpan@uni-tuebingen.de

Citation:
Yierpan, A., König, S., Labidi, J., Kurzawa, T., Babechuk, M. G., & Schoenberg, R. (2018). Chemical sample processing for combined selenium isotope and selenium-tellurium elemental investigation of the Earth's igneous reservoirs. *Geochemistry, Geophysics, Geosystems*, *19*, 516–533. https://doi.org/10.1002/2017GC007299

Received 20 OCT 2017
Accepted 25 JAN 2018
Accepted article online 1 FEB 2018
Published online 27 FEB 2018

Chemical Sample Processing for Combined Selenium Isotope and Selenium-Tellurium Elemental Investigation of the Earth's Igneous Reservoirs

Aierken Yierpan[1], Stephan König[1], Jabrane Labidi[1], Timon Kurzawa[1], Michael G. Babechuk[2], and Ronny Schoenberg[1]

[1]Isotope Geochemistry, Department of Geosciences, University of Tübingen, Tübingen, Germany, [2]Department of Earth Sciences, Memorial University of Newfoundland, St. John's, Newfoundland and Labrador, Canada

Abstract The redox-sensitive, chalcophile, and volatile Se stable isotope system offers new perspectives to investigate the origin and evolution of terrestrial volatiles and the roles of magmatic and recycling processes in the development of the redox contrast between Earth's reservoirs. Selenium isotope systematics become more robust in a well-constrained petrogenetic context as can be inferred from Se-Te elemental signatures of sulfides and igneous rocks. In this study, we present a high-yield chemical sample processing method that allows the determination of Se-Te concentrations and Se isotope composition from the same sample digest of silicate rocks by hydride generation isotope dilution (ID) quadrupole inductively coupled plasma mass spectrometry (ICP-MS) and double spike (DS) multicollector (MC)-ICP-MS, respectively. Our procedure yields ~80% Se-Te recoveries with quantitative separation of relevant interfering elements such as Ge and HG-buffering metals. Replicate analyses of selected international reference materials yield uncertainties better than 0.11‰ (2 s.d.) on $\delta^{82/76}$Se and 3% (r.s.d.) on Se concentration for DS MC-ICP-MS determinations for as low as ~10 ng sample Se. The precision of Se-Te concentration measurements by ID ICP-MS is better than 3% and 5% (r.s.d.) for total amounts of ~0.5–1 ng Se and ~0.2–0.5 ng Te, respectively. The basaltic reference materials have variable Se-Te contents, but their $\delta^{82/76}$Se values are rather uniform (on average 0.23 ± 0.14‰; 2 s.d.) and different from the chondritic value. This altogether provides the methodology and potential to extend the limited data set of coupled Se isotope and Se-Te elemental systematics of samples relevant to study the terrestrial igneous inventory.

1. Introduction

Selenium and tellurium are moderately volatile (Lodders, 2003) and chalcophile elements (Guo et al., 1999; Hattori et al., 2002). They are present in the mantle at 2–3 orders of magnitude higher concentrations than expected from metal-silicate partitioning experiments performed at low pressure (<20 GPa; Rose-Weston et al., 2009). The broadly chondritic S-Se-Te elemental ratios in fertile peridotites (Wang & Becker, 2013) have been attributed to late accretion (i.e., the late veneer; Kimura et al., 1974; McDonough & Sun, 1995; Morgan, 1986). However, the subchondritic δ^{34}S of the silicate Earth indicates that the mantle S budget probably records core formation with limited sulfide incorporation rather than a post-core formation accretionary S addition (Labidi & Cartigny, 2016; Labidi et al., 2013, 2016). Moreover, some authors argue that the observed Se-Te signature of fertile peridotites are not primitive features of the mantle because peridotites are generally affected by secondary magmatic processes (Harvey et al., 2015; König et al., 2014, 2015a, 2015b; Luguet et al., 2015).

Systematics of Se isotopes may contribute to placing constraints on these possible scenarios. If the Se budget was dominated by late-accreted materials and if no subsequent Se isotope fractionation of the upper mantle occurred, a chondritic Se isotope composition (Labidi et al., 2018; Vollstaedt et al., 2016) would be expected for the upper mantle. However, the scarcity of data sets regarding Se isotopes in mantle-derived rocks limits reasonable conclusions regarding either process. In order to evaluate the origin of Se isotope signatures in igneous rocks, the Se-Te elemental systematics are very useful. This is because of the chalcophile behaviors of both Se and Te with complementary partitioning into residual monosulfide solid solution versus metasomatic sulfide liquid, respectively (Brenan, 2015; König et al., 2014). Using Se-Te elemental

systematics thus helps interpret isotopic signatures of Se in a constrained petrogenetic context, including partial melting, magmatic differentiation and metasomatic addition of base metal sulfides (e.g., Harvey et al., 2015; König et al., 2014; Jenner et al., 2015; Lissner et al., 2014; Luguet et al., 2015). Therefore, a combination of the Se-Te abundances and Se isotope analysis of igneous rocks may be useful for investigating the intrinsic origin and budget of these elements in the silicate Earth and during evolution of its reservoirs. Yet, to date, no such combined studies exist.

Following pioneering studies (Hertogen et al., 1980; Lorand & Alard, 2010; Morgan, 1986), analytical advancements for combined Se-Te elemental analyses of silicate rocks have been made by hydride generation (HG) isotope dilution (ID) inductively coupled plasma mass spectrometry (ICP-MS) measurements coupled with chemical purification such as thiol cotton fiber/powder (TCF/TCP) chemistry (König et al., 2012) and ion exchange chromatography (Wang et al., 2013). Different sample digestion techniques have been used: (1) inverse *aqua regia* digestion in a high-pressure asher (HPA-S) for peridotites (König et al., 2012; Wang & Becker, 2013, 2014; Wang et al., 2013), pyroxenites (Wang & Becker, 2015), and basalts (Wang et al., 2013); (2) hotplate HF digestion in perfluoroalkoxy alkane (PFA) beakers for peridotites (König et al., 2012, 2014, 2015a; Luguet et al., 2015) and basalts (Forrest et al., 2009; König et al., 2014; Lissner et al., 2014); (3) HF digestion in HPA-S or pressure bombs for a wide range of matrices, including peridotites, basalts, and Martian meteorites (Wang & Becker, 2017; Wang et al., 2015); (4) inverse *aqua regia* (HPA-S) digestion followed by a hotplate HF-desilicification for peridotites (Harvey et al., 2015; König et al., 2012). While there are several rather comprehensive studies regarding different chemical sample processing and associated limitations for analyses of highly siderophile element (HSE) abundances in mafic and ultramafic rocks (e.g., Dale et al., 2012; Day et al., 2016; Ishikawa et al., 2014; Li et al., 2015; Meisel et al., 2003), few studies conducted comparative sample digestion experiments for Se-Te analyses (König et al., 2012, Wang & Becker, 2014; Wang et al., 2015).

Due to significant isotopic fractionation during Se oxyanion reduction (Krouse & Thode, 1962; Rees & Thode, 1966), Se isotope measurements have received increasing interest in biogeochemistry (Clark & Johnson, 2010; Ellis et al., 2003; Herbel et al., 2000, 2002; Johnson et al., 1999; Schilling et al., 2011a) and paleoenvironmental studies (Kipp et al., 2017; Layton-Matthews et al., 2013; Mitchell et al., 2012, 2016; Pogge Von Strandmann et al., 2015; Rouxel et al., 2004; Stüeken et al., 2015a, 2015b; Zhu et al., 2014). Following important analytical advancements (Elwaer & Hintelmann, 2008; Layton-Matthews et al., 2006; Pogge von Strandmann et al., 2014; Rouxel et al., 2002; Stüeken et al., 2013; Zhu et al., 2008), Kurzawa et al. (2017) provided a precise and accurate measuring method for $\delta^{82/76}$Se with a consumption of as low as 5 ng Se, which allows the Se isotope determination of geological samples with low ng g^{-1} Se levels. To do so, it is necessary to establish a matrix-matched sample digestion and purification method that necessarily includes (1) complete Se extraction, (2) high chemistry recovery, and (3) quantitative separation of HG-buffering transition metals and Ge that potentially causes significant isobaric interferences on ^{74}Se (e.g., Pogge von Strandmann et al., 2014; Stüeken et al., 2013).

In this study, we aim to combine the instrumental protocol for Se isotope analysis described by Kurzawa et al. (2017) with Se-Te concentration determinations by ID ICP-MS from a single digest of igneous rocks. We report on a series of comparative experiments on the international basaltic reference material BHVO-2 and discuss some of the major issues regarding sample digestion, such as sample heterogeneity, Se-Te extraction efficiency, sample-spike equilibration and Se-Te volatility. We present a suitable sample digestion and refined chemical purification method with high Se-Te recoveries, which enables precise and accurate Se isotope and Se-Te elemental analyses from the same rock digest using small amounts of sample materials. Our ultimate goal is to extend the limited data set of Se isotope composition and Se-Te concentrations of mantle-derived rocks in order to place firm constraints on the behavior of these elements in magmatic processes and their message regarding the origin and evolution of Earth's volatiles.

2. Reagents, Samples, and Method

2.1. Reagents

Hydrochloric, hydrofluoric, and nitric acids (Emsure®, Merck) used in this study were distilled using Savillex DST-1000 subboiling Teflon stills. All diluted acids were prepared with 18.2 MΩ·cm water and titrated on a molarity basis. All PFA vials were fluxed successively in reagent grade 3 M HCl, 5 M HNO_3 and 18.2 MΩ·cm

H_2O at 120°C for more than 48 h prior to use. The reducing solution for HG (0.1 M $NaBH_4$ in 0.07 M NaOH) was prepared fresh before each analytical session by dissolving sodium borohydride (analytical grade, Merck) and sodium hydroxide monohydrate (Suprapur®, Merck) in 18.2 MΩ·cm H_2O. Selenium standard solutions of NIST SRM 3149 and MH 495 (in 2 M HCl) were used for MC-ICP-MS analysis with concentrations of 15 or 30 ng mL^{-1}. The standard solutions used for ID ICP-MS measurements were diluted from NIST SRM 3149 and NIST SRM 3156 stock solutions to 0.5 ng mL^{-1}. A calibrated Se double spike (~52% ^{74}Se and ~47% ^{77}Se in 0.1 M HNO_3; Kurzawa et al., 2017) and Te single spike (~92% ^{125}Te in 1 M HNO_3; König et al., 2012) were used for our analyses.

2.2. Samples

Given the few studies regarding Se isotopes in mantle geochemistry, limited data of igneous reference materials measured by several working groups are available so far. In this study, we mainly used the international reference material BHVO-2 (Hawaiian basalt; splits #2375, #2481, and #3323) from the United States Geological Survey (USGS) for our sample digestion and chemical purification experiments because relatively consistent isotope dilution Se-Te concentration data are recently published for this material by different laboratories (König et al., 2012; Wang et al., 2015). The newly established sample processing scheme was then applied to other reference materials such as BCR-2 (Columbia River flood basalt, USGS), BE-N (continental intraplate basalt, Service d'Analyse des Roches et des Minéraux, France), BIR-1a (Icelandic basalt, USGS), and W-2a (diabase, USGS) to allow inter-laboratory comparison of future studies on a larger number of natural samples.

All reference materials used were supplied as finely ground powders. The BHVO-2 standard has a fairly wide range of particle sizes (supporting information Figure S1). To compare the Se-Te extraction efficiency of the HPA-S digestion between sample powders with different particle sizes, we reground two independent BHVO-2 splits (~6 g each) using a micro mill (Fritsch Pulverisette 7 classic line). Particle size distribution of the reground material was determined using a laser particle sizer (Analysette 22 NanoTec) in the Application Laboratory of Fritsch, Germany. König et al. (2015a) demonstrated large whole-rock Se-Te concentration heterogeneities in peridotites. This was investigated for basalts in this study by the analysis of BHVO-2 sieved fractions of <25 and >25 μm. Both fractions were further reground to preclude any potential sampling and digestion bias. All reground powders have particles ≤ 5 μm (supporting information Figure S1).

2.3. Sample Digestion

The extraction efficiency of the HPA-S technique for coupled Se isotope and Se-Te concentration analyses from the same sample digest was assessed using BHVO-2 under varying conditions, including sample size, acid volume, digestion temperature (supporting information Table S1), and particle size (supporting information Figure S1). A conventional hotplate HF digestion (König et al., 2012) was performed in parallel for comparison. We additionally carried out a series of extensive HF digestion experiments on BHVO-2 and BCR-2 following different protocols to evaluate some of the most common digestion related issues such as sample heterogeneity, sample-spike equilibration, effect of insoluble fluoride complexes, and Se-Te volatility, with the aim to identify the most suitable digestion method for our routine analyses.

2.3.1. HPA-S (Inverse *aqua regia*) Digestion

The HPA-S (Anton Paar™, Graz) digestion was performed following the basic procedure outlined by Kurzawa et al. (2017). Briefly, about 0.2–1.1 g of BHVO-2 powder ($n = 31$) together with Se DS or Te single spike solutions were weighed into quartz glass vials and mixed with 2.5–10 mL inverse *aqua regia* (14.5 M HNO_3 and 10.5 M HCl, molar ratio 3:1). The digestion was carried out at 100 bar and different temperatures (220, 280, and 320°C) with a constant duration of 16 h. After the digestion, the supernatant was processed for Se-Te purification based on the protocol of Wang et al. (2013). The solid residue ($n = 7$) was analyzed for its Se content in order to assess Se extraction efficiency from the rock powder and potential Se degassing during ashing. To do so, the residue was first fluxed multiple (1–3) times with 18.2 MΩ·cm water in an ultrasonic bath for 30 min. After centrifugation for 15 min, the supernatant water was discarded and the residue was then transferred to a PFA beaker and dried down at 65°C. The dry residue was carefully weighed with Se DS and processed following the HF digestion protocols described below.

2.3.2. Hotplate HF Digestion

Sample powders ranging in weight from 0.05 to 1.2 g were mixed with Se and Te spike solutions and digested using a HF-HNO_3 mixture (1:5 volume ratio) in PFA beakers on a hotplate at 120°C or 85°C for 24 h.

Solutions were subsequently evaporated at 65°C. After this point, BHVO-2 and BCR-2 samples that were digested at 120°C (n = 50 and 11, respectively) were processed following the protocol used by König et al. (2012) before the chemical purification. Briefly, the dry dissolved samples were taken up in 6 M HCl, heated at 100–130°C for >24 h, dried down at 65°C, and re-dissolved in 6 M HCl. The fluoride precipitates were removed via centrifugation and the supernatant solution was used for the subsequent TCF/TCP chemistry or chromatography. In order to examine the effect of insoluble fluorides for Se-Te analysis, additional HCl, HNO_3, and $HClO_4$ treatments were performed for several BHVO-2 (n = 4) in high-pressure PTFE vials with pressure bombs in an oven at 190°C for 48 h to fully dissolve fluoride complexes (Cotta & Enzweiler, 2012; Langmyhr, 1967; Yokoyama et al., 1999). All HCl and HNO_3 solutions were evaporated to complete dryness at 65°C. The $HClO_4$ solution was evaporated at 130°C until ~10% solution remained in order to avoid potential Se loss (Stüeken et al., 2013) and directly taken up in 4 M HCl before chromatographic purification.

For all other samples that were digested at 85°C, a modified protocol (i.e., our routine procedure) was used in combination with our ion exchange chromatography. The dry sample residues were dissolved and heated in 8 mL 6 M HCl at 130°C on a hotplate for a minimum of 48 h, during which they were treated twice in an ultrasonic bath for 30 min. No visible fluoride precipitates were inspected at this point (for up to 0.55 g sample). Samples were subsequently evaporated to dryness at 85°C, followed by two successive dissolutions and complete evaporations with 1 mL 10.5 M HCl. Finally, samples were taken up in 5 mL 4 M HCl and centrifuged for 10 min to separate transparent silica gels (e.g., Luais, 2012; Rouxel et al., 2006) prior to chromatographic purification.

In order to quantify and compare potential loss of Se-Te during the evaporation of HCl solutions, seven BHVO-2 samples were digested and spiked only after the evaporation of 8 mL 6 M HCl and 2 mL 10.5 M HCl solutions to complete dryness at 65 (n = 4) or 85°C (n = 3).

2.4. Chemical Purification of Se and Te

2.4.1. TCF and TCP Chemistry

Several BHVO-2 (n = 26) and BCR-2 (n = 4) samples with weights 0.25–1 g were digested with HF-HNO_3 and used for Se separation via TCF or TCP chemistry. The TCF and TCP batches (n = 5 and 1, respectively) were prepared from commercially available medical-grade cotton fiber and powder with analytical-grade thioglycolic acid, acetic anhydride, acetic acid, and sulfuric acid (Merck) based on the methods described by König et al. (2012). Selenium was purified through columns filled with 0.15–0.3 g TCF and TCP (depending on the sample size) following the procedure of Rouxel et al. (2002) and Vollstaedt et al. (2016), respectively. After the separation and evaporation at 65°C, a dark residue was observed. It was repeatedly treated with ~200 μL of 14.5 M HNO_3 and 30% H_2O_2 to remove residual organic matter. This step was followed by dissolution of the Se fractions in 1 mL 2 M HCl and centrifugation for 15 min. The supernatant was passed through a precleaned 0.45 μm syringe filter (Millex®, Merck) to further eliminate residual fine organic particles (Vollstaedt et al., 2016) and then measured for Se isotope composition.

2.4.2. Ion Exchange Chromatography

When comparing the Se-Te extraction efficiencies of the HPA-S (inverse *aqua regia*) and hotplate HF digestions, BHVO-2 samples were purified for Se and/or Te using the ion exchange chromatography developed by Wang et al. (2013). This method was recently demonstrated to be applicable to high-precision analysis of Se isotopes in shales and basalts after the HPA-S digestion (Kurzawa et al., 2017). In contrast to HPA-S (inverse *aqua regia*) digestion that produces a relatively simple matrix (only ~12 wt.% of the BHVO-2 powder was dissolved; n = 13; supporting information Table S1; also see Xu et al., 2012), HF digestion results in whole-rock dissolution, posing additional difficulties on the ion exchange chromatography in terms of Se-Te recovery and separation of interference elements.

We tested existing purification protocols (supporting information Table S2) and propose an improved method in combination with our established HF digestion procedure. The new method utilized polypropylene columns (0.9 cm diameter and 8 cm bed height; Triskem, France) filled with 7 mL resin bed volume of Eichrom AG1-X8 (100–200 mesh chloride form) and Eichrom AG 50W-X8 (100–200 mesh hydrogen form) anion and cation exchange resins, respectively. A fresh resin bed, precleaned following a general laboratory procedure (e.g., successive cleaning with H_2O, HNO_3, and HCl), was used for each separation procedure. The columns were calibrated with 7 mL resin for up to 0.45 g mafic matrix. A complete procedure and elution

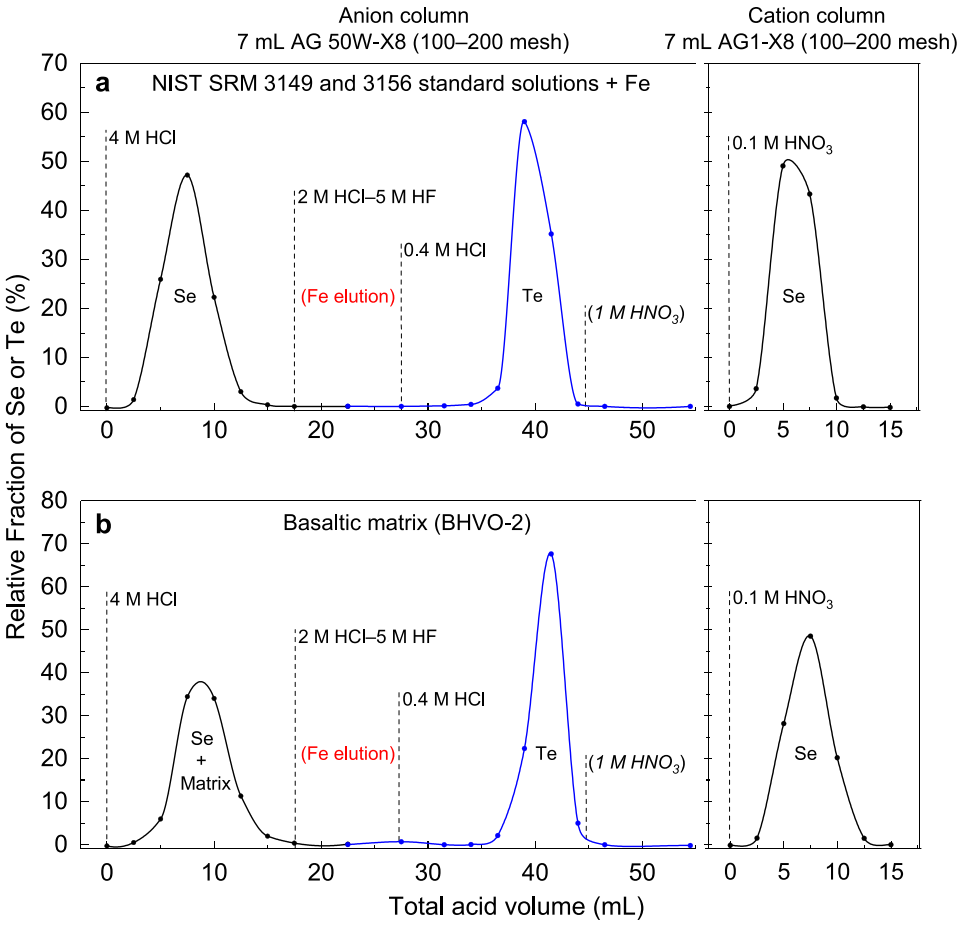

Figure 1. Elution profiles for Se (black line) and Te (blue line) from (a) standard solutions NIST SRM 3149 and 3156 and (b) BHVO-2 after the hotplate HF digestion using 7 mL of AG1-X8 and AG 50W-X8 anion and cation resins (100–200 mesh) following the newly established protocol in this study. The dashed lines represent the eluent we used. The relative fractions of Se and Te were determined at each 2.5 mL eluent (for 2 M HCl–5 M HF and 1 M HNO_3, 5 and 8 mL of fractions were collected, respectively) using ID method (supporting information Table S3). The Se-Te yields were determined twice on some collection cuts and the yield repeatabilities are $<$1% (r.s.d.). The Te elution with 1 M HNO_3 (Fehr et al., 2004; Wang et al., 2013) was additionally performed to check the complete desorption of Te from the resin during the column calibration.

profiles of Se-Te from NIST SRM 3149 and 3156 as well as BHVO-2 for each individual fraction (2.5 mL) are shown in Figure 1 and supporting information Table S3.

In the first stage, the anion exchange resin was cleaned with 10 mL 18.2 MΩ·cm water and conditioned with 10 mL 4 M HCl. The sample solution (5 mL 4 M HCl) was then loaded onto the column, followed by an addition of 9 mL 4 M HCl. Tellurium and iron are strongly retained by the resin in $\geq$2 M HCl (Fehr et al., 2004; Fornadel et al., 2014; Loss et al., 1990; Yi et al., 1998), whereas selenium is not adsorbed at HCl molarities of 4–7 M (Schönbächler & Fehr, 2014; Wang & Becker, 2014; Wang et al., 2015). The Se fraction was collected in 14 mL 4 M HCl together with most matrix elements and subsequently evaporated at 85°C to complete dryness. Rinsing the resin with 10 mL of 2 M HCl–5 M HF mixture eluted almost all Fe while assuring complete retention of Te, probably as chloro-complex and fluoro-complex. The resin was further rinsed with 4 mL 0.4 M HCl to elute residual Fe before collecting Te with 14 mL 0.4 M HCl. Separation of Fe may also be achieved by elution with 5 M HF only (Faris, 1960; Fehr et al., 2004; Wang et al., 2013), but we found that in that case, large amounts of eluent ($>$25 mL of 0.4 M HCl or 1 M HNO_3) were necessary to quantitatively elute Te. Besides, weak HCl was preferred over HNO_3 for Te elution as the latter more readily destroys the persistent $FeCl_4^-$ complex in the resin (Schoenberg & von Blanckenburg, 2005), resulting in more Fe in the Te eluate. Finally, the Te fractions were dried down at 85°C to incipient dryness and directly taken up in 1 mL 2 M HCl for concentration analysis.

Complete separation of Fe from Te eluate is crucial as Fe significantly inhibits H_2Te formation during the analysis, reducing signal intensity (Yu et al., 1983). This effect was quantified by analyses of Fe-doped (ICP Fe standard solution, 1,000 μg mL^{-1}) NIST SRM 3156 solutions (0.5 ng mL^{-1}), with Fe/Te mass ratio ranging between $\sim10^3$ and 10^6 (supporting information Table S4).

In the second stage, the dry Se fraction was dissolved in 5 mL 0.1 M HNO_3 and placed in an ultrasonic bath for 30 min. When observed, insoluble fluorides were separated via 10 min centrifugation. Selenium was then purified through the cation column following the procedure established by Wang et al. (2015) with small modifications. Briefly, the resin was rinsed with water and conditioned with 0.1 M HNO_3. The sample solution was then loaded onto the column, and Se was collected with another 9 mL 0.1 M HNO_3. In these conditions, other species such as the HG-buffering transition metals Co^{2+}, Ni^{2+}, Cu^{2+}, and Pb^{2+} (Vijan & Leung, 1980; Welz & Melcher, 1984; Yu et al., 1983) are quantitatively retained on the resin (Davies, 2012). The Se fractions were dried down at 85°C, followed by another complete dry-down in 2 mL 10.5 M HCl to remove extant NO_3^-. Finally, they were taken up in 1 mL 2 M HCl, from which an aliquot (100 μL) was measured to verify that all Ge was removed (see section 2.5.1). In case of remaining Ge, the dry-down step at 85°C was repeated (1–2 times) until a final 1 mL 2 M HCl solution was ready for Se isotope analysis. Note that in dependence on PFA beaker size, hotplate heating increments, and laminar flow cooling effects, the specific temperature settings required for adequate hotplate temperatures may slightly vary in different laboratories. At this stage, we emphasize that the optimum temperature window (between 85°C and 90°C) is crucial for eliminating Ge from the sample solution while minimizing Se loss (see section 4.2).

2.5. Instrumental Analysis

2.5.1. DS MC-ICP-MS Analysis

Analysis of Se isotope composition was performed on a ThermoFisher Scientific NeptunePlus™ MC-ICP-MS coupled with a HGX-200 (Cetac) hydride generator at the laboratory of the Isotope Geochemistry Group, University of Tübingen, Germany. Measurements were run in low-resolution mode with a Ni-Jet sample cone and Ni skimmer H-cone. Typical operating parameters, analytical procedure, interference corrections, and double-spike inversion protocols were previously described in detail by Kurzawa et al. (2017). For most analyses in this study, ~10–35 ng mL^{-1} sample Se was used, which generated ^{82}Se signal intensities of ~350–1,150 mV using a 10^{11} Ω amplifier resistor with an uptake rate of 0.181 mL min^{-1} under typical running conditions. The background level (typically ~3 mV on ^{82}Se) was determined on pure 2 M HCl before each standard and sample solution for on-peak-zero corrections. Washout times were typically 5 min. Selenium isotope ratios are expressed in the δ-notation relative to NIST SRM 3149 as per mil (‰) deviation following:

$$\delta^{82/76}\mathrm{Se}_{\mathrm{Sample}} = \left(\frac{^{82/76}\mathrm{Se}_{\mathrm{Sample}}}{^{82/76}\mathrm{Se}_{\mathrm{NIST\ SRM\ 3149}}}\right) \times 1{,}000$$

The $\delta^{82/76}$Se values of sample and inter-laboratory standard MH 495 are always corrected against the average $\delta^{82/76}$Se value of two bracketing (concentration-matched) NIST SRM 3149 standards with 15 and 30 ng mL^{-1} Se. Kurzawa et al. (2017) reported a long-term external reproducibility of 0.11‰ (2 s.d.) on $\delta^{82/76}$Se using 15 ng mL^{-1} NIST SRM 3149 standard solution. The MH 495 standard analyzed together with the samples in this study yields mean $\delta^{82/76}$Se values of -3.24 ± 0.10‰ (2 s.d., n = 46) and -3.26 ± 0.06‰ (2 s.d., n = 32) for 15 and 30 ng mL^{-1} solutions, respectively (supporting information Table S5). This is in accordance with the value of -3.27 ± 0.13‰ (2 s.d., n = 100; on 15 ng mL^{-1} solution) reported by Kurzawa et al. (2017) and is within the range of previously published values (Carignan & Wen, 2007; Vollstaedt et al., 2016; Zhu et al., 2008).

Germanium is the main isobaric interference from the sample matrix in Se isotope analysis, but it cannot be fully separated from Se by our chromatography with the range of eluent molarities tested (e.g., 4–7 M HCl and 0.06–0.2 M HNO_3; but see Schilling et al., 2011b, 2014). However, it is efficiently eliminated during the evaporation of all HCl solutions at 85°C (see section 4.2). As a result, we observed ^{72}Ge/^{82}Se signal ratios <0.0002 (i.e., Ge/Se <0.0001) from all sample solutions with digested sample sizes <0.45 g, allowing us to fully neglect a ^{74}Ge interference correction. Note that the occurrence of As, Se, and Br hydrides could also represent significant interferences (Pogge von Strandmann et al., 2014; Stüeken et al., 2013; Vollstaedt et al., 2016). However, all relevant hydride interferences are suppressed to undetectable levels by adding a

controlled flux of methane in the plasma during the measurement (for details, see Floor et al., 2011; Kurzawa et al., 2017), and no further corrections were made after the on-peak-zero correction.

2.5.2. ID ICP-MS Analysis

The Se and Te ID concentration measurements were carried out on a ThermoFisher Scientific iCAP-Qc quadrupole ICP-MS at the laboratory of the Isotope Geochemistry Group, University of Tübingen, Germany. For most analyses, aliquots of purified Se and Te fractions were prepared separately in 1 mL 2 M HCl to have 0.5–1.0 ng mL^{-1} Se and 0.15–0.5 ng mL^{-1} Te. Some sample unknowns were analyzed for Se concentrations directly after removing only Fe by the anion resin in order to swiftly obtain Se concentrations for adequate spiking for Se isotope analysis on new digests. The sample solutions were mixed with 2 M HCl and 0.1 M $NaBH_4$–0.07 M NaOH in a hydrideICP HG system (ESI) to reduce Se^{4+} and Te^{4+} oxyanions to their hydride forms, which were transported by Ar (~1.08 L min^{-1}) to the plasma through a quartz cyclonic spray chamber. Measurements were performed in the iCAP-Qc STD mode to maximize signal sensitivity on the analyte isotopes, due to the reduction in sensitivity that can accompany the use of He kinetic energy discrimination (Chew et al., 2014). Each individual analysis consisted of 420 measurements of 3 points per peak of ^{77}Se and ^{78}Se for Se and ^{125}Te and ^{126}Te for Te with a dwell time of 0.03 s starting from the point of signal stabilization, which was usually achieved after ~1.2 min from the start of sample uptake. Every analytical session includes four standard solutions (0.5 ng mL^{-1} NIST SRM 3149 and 3156) measured before and after the sample unknowns. Under typical operating conditions with an uptake rate of ~0.41 mL/min, these standard solutions yield intensities of ~40,000 cps on ^{78}Se and ~55,000 cps on ^{126}Te, whereas the reagent blank (i.e., pure 2 M HCl) generally yields less than 13% and 3% of the respective signals. Unlike the HPA-S vial blanks that can sometimes be up to ~1 ng (Kurzawa et al., 2017), total procedural blanks (n = 10) from our established sample preparation procedures always yielded Se-Te signals that are indistinguishable from the background level on pure 2 M HCl. Taking the detection limit of the quadrupole ICP-MS as three times the standard deviation for each measured isotope in the reagent blank (Long & Winefordner, 1983), the maximum detection limits of the isotope dilution analysis calculated following the approach of Yu et al. (2002) are ~0.05 and ~0.007 ng mL^{-1} for Se and Te, respectively (for the comparison of ID detection limits on an Element XR sector field ICP-MS, see Wang & Becker, 2014).

A typical washout time of 2.5 min for solutions with Se concentrations of up to 5 ng mL^{-1} Se efficiently flushed the HG system. On the contrary, efficiency of Te washout was in some cases compromised by memory effects after ~10 samples. Elevated background levels may occur (up to 10 times the initial level), especially when Te fractions contain residual Fe after the purification. Note that our refined chromatographic protocol for Fe separation (by a HF-HCl mixture) efficiently addressed this issue (see section 2.4.2). When still necessary in some cases, a prolonged >45 min washout was performed. Fehr et al. (2005) also reported long washout times of up to 60 min during Te isotope analysis using a desolvating nebulizer system. The primary source of the memory was identified as Te accumulation on the quartz injector and torch, which were cleaned with 0.1 M of HNO_3 or 0.5 M HCl for ~24 h after every 2 analytical sessions in order to ensure Te concentration data quality.

Selenium and tellurium concentrations of the samples were calculated using $^{77}Se/^{78}Se$ and $^{125}Te/^{126}Te$ ratios obtained after on-peak-zero and instrumental mass bias correction using the measured and natural ratios (Meija et al., 2016) of the NIST SRM 3149 and 3156 solutions. Although the Se and Te concentrations of these standards (both 0.5 ng mL^{-1}) in some cases do not overlap with the full range of sample concentrations (0.5–1.0 ng mL^{-1} Se and 0.15–0.5 ng mL^{-1} Te), we did not observe any associated uncertainty propagation on the corrected isotopic ratios, although the blank levels on each of the monitored masses are different. This might be due to the high washout efficiency for both Se and Te (with <10 samples in a session). The Se-Te analysis may in theory be affected by multiple isobaric and polyatomic interferences at monitored masses, but no further corrections were considered necessary. This is because any existing matrix-based oxides (e.g., $^{62}Ni^{16}O$, $^{109}Ag^{16}O$, $^{110}Pd^{16}O$, and $^{110}Cd^{16}O$) are prevented from entering the plasma by the hydride generator, whereas interferences from the carrier gas, analyte and cones (e.g., $^{40}Ar^{37}Cl$, $^{40}Ar^{38}Ar$, ^{78}Kr, $^{86}Kr^{40}Ar$, ^{126}Xe, and $^{62}Ni^{16}O$) are considered to be constant over the course of a session and hence eliminated by the on-peak-zero correction. To evaluate the quantities of potential hydride interferences such as ^{76}GeH, ^{77}SeH, ^{124}SnH, and ^{125}TeH, we monitored signal intensities at m/z 82, 83, 130, and 131 for ^{82}Se, ^{82}SeH, ^{130}Te, and ^{130}TeH in three standard and BHVO-2 solutions containing 0.5–1.5 ng mL^{-1} Se and Te. The signals obtained at m/z 83 and 131 were identical to background levels within the Se

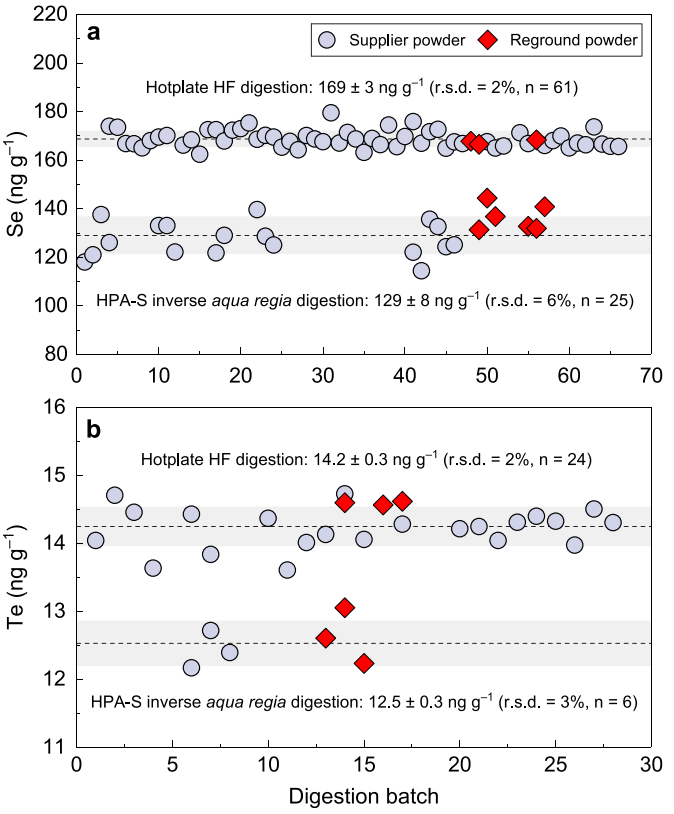

Figure 2. BHVO-2 Se and Te concentrations analyzed from the HPA-S (inverse *aqua regia*) and different hotplate HF digestion procedures over the course of 18 months. These samples cover a wide range of sample sizes (~0.08–1.1 g). The sample size distributions are reported in supporting information Tables S1 and S6. Note that the reground sample powder shows the same Se and Te extraction efficiencies from the HPA-S digestion with the original/supplier powder, although they show quite distinct particle size distributions (supporting information Figure S1).

and Te concentration range tested. Assuming $SeH^+/Se^+ = GeH^+/Ge^+$ and $TeH^+/Te^+ = SnH^+/Sn^+$, our results suggest that negligible interferences are generated from these hydrides.

The precision of the Se-Te concentration analyses is evaluated by replicate analyses of BHVO-2 with a wide range of sample sizes (~0.08–1.10 g) from different HF digestion batches (n = 61 and 24 for Se and Te, respectively) and chemical separation procedures (Figure 2 and supporting information Table S6). Despite these different methods applied, BHVO-2 yields consistent Se-Te concentrations with an average of 169 ± 3 ng g^{-1} Se (1 s.d., n = 61) and 14.2 ± 0.3 ng g^{-1} Te (1 s.d., n = 24; Figure 2). Based on these replicate analyses, the intermediate precision of our method for Se-Te concentration determination is estimated to be ~2% (expressed in r.s.d.). For comparison, some Se concentrations were determined on both quadrupole ICP-MS (by ID) and MC-ICP-MS (by DS inversion) using aliquots from the same sample digest and show excellent agreement (within ~3% variation) for all samples (supporting information Figure S2).

3. Results

3.1. Recoveries of Se and Te

Selenium and tellurium recoveries for BHVO-2 at different stages after digestion and chemical purification procedures are determined by the ID approach and/or comparing signal intensities against NIST SRM 3149 and 3156 standard solutions. Results are listed in supporting information Table S2. Selenium recoveries from the TCF and TCP chemistry are systematically low for BHVO-2 (<20%, n = 26) as well as BCR-2 (<15%, n = 4). Only Se concentrations were analyzed for these samples. Although this purification chemistry has the advantage of quantitatively separating Ge from Se (Rouxel et al., 2002), this technique was not pursued for subsequent Se isotope analysis due to the poor and variable Se recoveries obtained for basalts by several TCF and TCP batches (n = 5 and 1, respectively).

Selenium recoveries for BHVO-2 (digested with HF-HNO_3) from the new chromatographic purification procedure are 73–87% (n = 5) and 92–100% (n = 5) from the anion and cation exchange column, respectively, with a total procedural recovery of 70–83% (n = 16). The observed and expected signal intensities from samples relative to NIST SRM 3149 standard solutions show that the H_2Se formation efficiency exceeds 90% for all sample solutions after the two-stage purification, indicating a near-quantitative removal of HG-buffering metals.

For Te in BHVO-2, we obtain 85–93% (n = 5) and 68–89% (n = 11) column chemistry and overall recovery, respectively. The lower overall recovery is mainly caused by the residual Fe that in some cases was not fully separated from Te, thereby inhibiting H_2Te formation. Analysis of Fe-doped standard solutions (see section 2.4.2) shows that Te signals are highly sensitive to the amount of Fe: up to 40% signal loss can occur with Fe/Te = 5,000 (Figure 3 and supporting information Table S4). Based on the difference between the (anion) column and overall recovery (i.e., ~15% signal suppression), an average Fe/Te ratio of ~1,000–2,000 is estimated for the BHVO-2 Te fraction. Low Te recoveries (10–30%) from peridotites observed by Wang et al. (2013) might also be due to the incomplete separation of Fe.

Overall, total procedural recoveries of Se and Te for all other samples (<0.45 g) are ~80% and ~75%, respectively. The Se and Te elution peaks can shift in the presence of matrix (see NIST SRM 3149 and 3156 versus BHVO-2 in Figure 1). However, in comparison to pure standard solution, the Se recoveries for BHVO-2 are only ~10% lower after anion and identical after cation column chemistry. The Te column recovery is even identical between standard and matrix-bearing solutions (supporting information Table S3). This tentatively suggests that our chromatographic purification method is only slightly (if any) matrix-dependent.

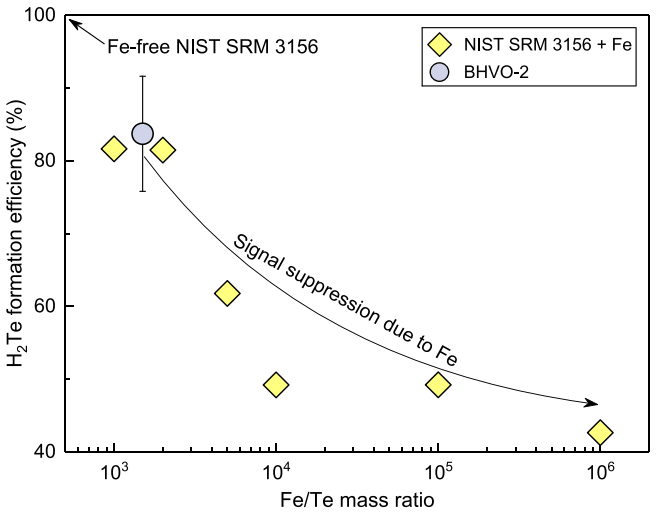

Figure 3. Effect of Fe on the hydride (H_2Te) formation efficiency in the hydride generator. The H_2Te formation yields of Fe-doped solutions are calculated by comparing signal intensities against those of pure NIST SRM 3156 standard solutions (0.5 ng mL^{-1}). It shows that H_2Te formation is highly sensitive to the amount of coexisting Fe. Based on this, the purified Te fraction from BHVO-2 (~15% difference between the column and overall recovery) is estimated to have residual Fe with Fe/Te mass ratio of ~1,000–2,000, which mainly accounts for the ~15% signal suppression.

As for the HCl evaporation experiments (see section 2.3.2), we obtain 99–103% (n = 4) and 87–91% (n = 3) Se recoveries (determined by the ID method) from BHVO-2 when performing the evaporation at 65°C and 85°C, respectively. Two BHVO-2 samples spiked after the evaporation with ~10% Se loss at 85°C yield higher $\delta^{82/76}$Se (0.42 ± 0.04‰; 2 s.d.) compared to our average value of BHVO-2 that are spiked prior to the digestion (Table 1). We obtain Te recoveries of ~100% at both evaporation temperatures for BHVO-2 (n = 5), as well as NIST SRM 3156 standard solutions (n = 5).

3.2. Se-Te Concentrations

The BHVO-2 supplier and reground powders from the HPA-S digestions were analyzed for Se isotopes (hence also Se concentrations) or Te concentrations in order to evaluate Se and Te extraction efficiencies (supporting information Table S1). They yield average concentrations of 129 ± 8 ng g^{-1} Se (1 s.d., n = 25) and 12.5 ± 0.3 ng g^{-1} Te (1 s.d., n = 6). The reground powder alone yields 136 ± 5 ng g^{-1} Se (1 s.d., n = 6) and 12.7 ± 0.3 ng g^{-1} Te (1 s.d., n = 3), indistinguishable from the HPA-S total averages. These values display higher variations and are distinctly lower compared to the values from the HF-based digestions of BHVO-2 with average concentrations of 169 ± 3 ng g^{-1} Se (1 s.d., n = 61) and 14.2 ± 0.3 ng g^{-1} Te (1 s.d., n = 24; Figure 2). Note that the Se concentration of the solid residue after the HPA-S procedure is on average 37 ± 3 ng g^{-1} (1 s.d., n = 7; supporting information Table S1). When added to the HPA-S extracted fractions, this yields 173 ± 7 ng g^{-1} (1 s.d., n = 7), which matches the bulk BHVO-2 average (169 ± 3 ng g^{-1}; 1 s.d., n = 61) obtained from the HF digestion.

The Se-Te concentrations of reference materials obtained after the newly established sample digestion and purification protocols are listed in Table 1. Additional Se-Te concentration data for BHVO-2 and Se

Table 1
Combined Selenium Isotope Compositions and Se-Te Concentrations of Selected International Reference Materials Analyzed From the Same Sample Digests Following the Newly Established Hotplate HF Digestion and Chromatographic Purification Protocols in This Study

Samples		Se concentration[a] (ng g^{-1})	Se analyzed (ng)	$\delta^{82/76}$Se (‰)	2 s.e.[b] (‰)	Te concentration (ng g^{-1})
BHVO-2 (basalt)		171	14	0.21	0.06	14.3
		170	36	0.26	0.04	14.3
		167	12	0.18	0.11	14.3
		168	35	0.10	0.04	14.1
		168	37	0.14	0.04	14.2
		166	9	0.20	0.11	14.0
		166	20	0.16	0.06	14.1
		166	23	0.16	0.06	14.4
	Average	*169*		0.18		*14.2*
	Uncertainty[c]	*3*		0.10		*0.3*
König et al. (2012)		169 ± 3				11.9 ± 0.7
Wang et al. (2015)		170 ± 22				14.4 ± 0.3
BCR-2 (basalt)		76	15	0.28	0.06	2.50
		77	14	0.31	0.07	2.53
		78	13	0.36	0.07	2.46
		78	16	0.23	0.06	2.66
		77	17	0.25	0.06	2.52
	Average	*76*		0.29		2.54
	Uncertainty[c]	*1*		0.10		0.08

Table 1. (continued)

Samples		Se concentration[a] (ng g^{-1})	Se analyzed (ng)	$\delta^{82/76}$Se (‰)	2 s.e.[b] (‰)	Te concentration (ng g^{-1})
Makishima and Nakamura (2009)		82 ± 7				3.20 ± 0.04
Lissner et al. (2014)		78 ± 3				2.73 ± 0.06
Kurzawa et al. (2017)		71 ± 4		0.18 ± 0.03		
BE-N (basalt)		65	19	0.18	0.06	1.06
		66	20	0.16	0.05	1.04
		66	20	0.14	0.06	1.05
		65	20	0.20	0.05	1.03
		65	19	0.07	0.06	0.94
	Average	*66*		0.15		1.02
	Uncertainty[c]	*1*		0.10		0.05
Rouxel et al. (2002)		57		0.37 ± 0.32[d]		
Savard et al. (2009)		70 ± 9				
Lissner et al. (2014)		65 ± 1				0.82 ± 0.01
König et al. (2014)		67 ± 3				0.78 ± 0.10
BIR-1a (basalt)		14.9	18	0.25	0.08	5.86
		14.5	10	0.31	0.08	5.81
		15.4	18	0.28	0.08	5.85
		15.5	19	0.22	0.07	5.62
		14.5	12	0.36	0.08	5.98
	Average	15.0		0.28		5.82
	Uncertainty[c]	0.5		0.11		0.13
Yi et al. (1998)						5.70 ± 0.15
Forrest et al. (2009)		11–11.2				3.5–5.3
König et al. (2012)		14.2 ± 1.0				4.79 ± 0.17
W-2a (diabase)		107	21	−0.04	0.05	1.64
		108	27	−0.13	0.04	1.67
		108	41	−0.09	0.04	1.68
		107	30	−0.10	0.04	1.69
		108	18	−0.15	0.07	1.83
		106	24	0.00	0.05	1.75
	Average	*107*		−0.09		1.71
	Uncertainty[c]	*1*		0.11		0.07
Yi et al. (1998)						1.84 ± 0.05
Savard et al. (2009)		91 ± 13				
Forrest et al. (2009)		5.2				1.6

Note. Italics refer to the average Se and Te concentrations and 1 s.d. calculated using the data in this table and all the additional Se and/or Te concentrations analyzed in this study from supporting information Table S6. [a]Selenium concentrations in this table are obtained from the double-spike inversion. [b]Internal precision of a sample run (over 40 cycles) is reported as 2 standard error (2 s.e.). [c]All uncertainties are 2 s.d. and 1 s.d. for the average $\delta^{82/76}$Se and Se-Te concentrations, respectively. [d]$\delta^{82/76}$Se data from Rouxel et al. (2002) is converted relative to NIST SRM 3149 following the approach of Carignan and Wen (2007).

concentration data for BCR-2, BE-N, and W-2a from the HF-based digestion experiments using different purification protocols can be found in supporting information Table S6. The calculated uncertainties (r.s.d.) on all samples are better than ~3% and ~5% for Se and Te concentrations, respectively. Despite limited literature data, our BHVO-2 Se-Te concentrations overlap with the values of ~170 ng g^{-1} Se and ~11.9–14.4 ng g^{-1} Te reported by König et al. (2012) and Wang et al. (2015). The reason why these two studies obtained similar Se (169 ± 3 and 170 ± 22 ng g^{-1}; 1 s.d.) but different Te concentrations (11.9 ± 0.7 and 14.4 ± 0.3 ng g^{-1}; 1 s.d.) for BHVO-2 remains unclear. We therefore compared our data with the combined range of these published data. Overall, our Se-Te concentrations of most samples are fairly comparable to the published data, but some significant differences are also observed (Table 1). For example, W-2a in this study yields Se concentration (107 ± 1 ng g^{-1}; 1 s.d., n = 8) that is significantly different from the published value of 5.2 ng g^{-1} (Forrest et al., 2009) but similar to the average value of 91 ± 13 ng g^{-1} (1 s.d.) from Savard et al. (2009). Also, BE-N Te concentration (1.02 ± 0.05 ng g^{-1}) is ~25–30% higher than those published by Lissner et al. (2014) and König et al.

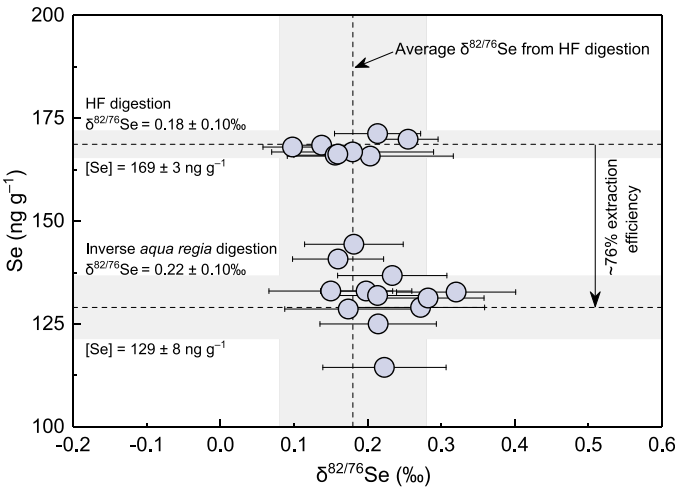

Figure 4. The $\delta^{82/76}$Se value and Se concentrations of BHVO-2 obtained from the HPA-S (inverse *aqua regia*) and hotplate HF digestions. Horizontal error bars are internal precisions (2 s.e.) on $\delta^{82/76}$Se for a single analysis (40 cycles). The horizontal dashed lines and shaded fields represent average ID concentrations ± 1 s.d. obtained using each digestion method (Figure 1). The vertical dashed line and shaded field represent the bulk-rock average $\delta^{82/76}$Se value ± 2 s.d. that is obtained from HF digestions. Despite the systematically low Se extraction efficiency of the HPA-S digestion (~76% relative to the HF digestion), the extracted fraction yields identical $\delta^{82/76}$Se value to that of the bulk rock.

(2014). About ~7% relative difference is observed for BCR-2 Te data between this study and Lissner et al. (2014).

The BHVO-2 grain separates of >25 and <25 μm analyzed after the HF digestion yields distinct concentrations: 134 ± 2 and 200 ± 5 ng g^{-1} Se and 10.6 ± 0.4 and 18.9 ± 0.5 ng g^{-1} Te (all 1 s.d.; supporting information Table S7). Mass balance calculation of the bulk-rock Se-Te concentrations using weight fractions of these separates yields 167 ± 3 ng g^{-1} Se (1 s.d.) and 14.8 ± 0.3 ng g^{-1} Te (1 s.d.), in agreement with the average measured concentrations.

3.3. Selenium Isotopic Composition

The Se isotope compositions of BHVO-2 analyzed using the HPA-S and HF digestion techniques are listed in Table 1 and supporting information Table S1 and presented in Figure 4. Although the ID concentrations are significantly different as mentioned above, the $\delta^{82/76}$Se values for the bulk-rock BHVO-2 from the HF digestion and extracted fractions from the HPA-S digestion are indistinguishable: 0.18 ± 0.10‰ (2 s.d., n = 8) and 0.22 ± 0.10‰ (2 s.d., n = 12), respectively.

The bulk-rock Se isotope compositions of all international reference materials processed following the newly established sample processing scheme are listed in Table 1 and presented in Figure 5. Existing literature data for silicates, chondrites, and troilites are also shown for comparison (Kurzawa et al., 2017; Labidi et al., 2018; Rouxel et al., 2002; Vollstaedt et al., 2016). The 2 s.d. uncertainties on $\delta^{82/76}$Se estimated over at least five different sample digestion batches are ≤0.11‰ for all samples. When the ^{82}Se signal is below 200 mV (~6.5 ng mL^{-1} Se), the internal precision (2 standard error, 2 s.e.) becomes higher than the analytical uncertainty. However, a minimum of 6.5 ng Se still permits a high-precision Se isotope analysis (e.g., Kurzawa et al., 2017). In this study, more than 15 ng Se (up to 40 ng) was used for most analyses and the internal precision of a sample run is generally better than 0.06‰ (over 40 cycles). The $\delta^{82/76}$Se values of these reference materials range between −0.09 ± 0.11‰ (W-2a; 2 s.d., n = 6) and 0.29 ± 0.10‰ (BCR-2; 2 s.d., n = 5). The $\delta^{82/76}$Se value obtained for BE-N is 0.15 ± 0.10‰ (2 s.d., n = 5), similar within uncertainties to the previously published value of 0.37 ± 0.32‰ (relative to NIST SRM 3149; 2 s.d., n = 1; Rouxel et al., 2002; for the conversion, see Carignan & Wen, 2007). After HF digestion, BCR-2 yields comparable $\delta^{82/76}$Se within uncertainty to that obtained from HPA-S (inverse *aqua regia*) digestion (0.18 ± 0.03‰; 2 s.d., n = 3) by Kurzawa et al. (2017). The diabase W-2a yields distinctly lower $\delta^{82/76}$Se that does not overlap with any basaltic values.

4. Discussion

4.1. Comparison of the HPA-S (Inverse *aqua regia*) and Hotplate HF Digestion

4.1.1. Se-Te Extraction Efficiency

Selenium and tellurium are chalcophile elements and considered to be primarily hosted by base metal sulfides and platinum group minerals in mantle rocks (Guo et al., 1999; Hattori et al., 2002; König et al., 2015a; Lorand & Alard, 2010). As these accessory phases are easily dissolved in inverse *aqua regia* at high temperature (e.g., Day et al., 2016; Li et al., 2015), a complete extraction of Se-Te from peridotites would be expected after HPA-S digestion. Despite heterogeneous distribution of sulfides in peridotites, several authors reported similar Se and/or Te abundances for peridotites using HPA-S or HF-based digestions (König et al., 2012, 2014, 2015a; Lissner et al., 2014; Wang & Becker, 2014; Wang et al., 2013, 2015). It is noteworthy that these groups analyzed UB-N (serpentinized lherzolite, SARM) as a reference material and obtained similar Se-Te abundances within uncertainties, regardless of whether silicate phases were dissolved by HF. This observation, together with the analytical results of a harzburgite sample (König et al., 2012), strongly argues for the quantitative control of the peridotite Se-Te budget by sulfides. In chondrites, Se also appears to be fully hosted by sulfides (Labidi et al., 2018; Vollstaedt et al., 2016, and references therein). The HPA-S (inverse *aqua regia*) digestion thus has been employed as an ideal digestion technique for combined determination

of S-Se-Te and HSE abundances of mantle rocks, bulk chondrites, and components of chondrites (Kadlag & Becker, 2015, 2016; Wang & Becker, 2013).

On the other hand, few comparative digestion experiments have been done on basalts. The basaltic reference material BHVO-1 (no longer commercially available from USGS) yields similar Se-Te ID concentrations from HPA-S (inverse *aqua regia*) and HF-based digestions (Makishima & Nakamura, 2009; Wang & Becker, 2014; Wang et al., 2015). Two previous studies (Kurzawa et al., 2017; Lissner et al., 2014) and this study obtain similar Se ID concentrations within uncertainty for another basaltic reference material BCR-2 (USGS) using these digestion techniques. However, basalts can have crystalline and glassy components. Selenium and tellurium, similar to sulfur, may be exsolved in sulfides and/or dissolved in the glassy matrices (e.g., Wykes et al., 2011, 2015). In this case, liberation of the dissolved Se-Te fractions requires HF-desilicification.

Relative to our BHVO-2 Se-Te concentrations obtained from HF digestion, the HPA-S digestion extracted 76 ± 5% and 88 ± 3% (1 s.d.) of the bulk-rock Se and Te, respectively (Figure 2). Note that the Se concentrations of the solid residue and extracted fractions of BHVO-2 after the HPA-S procedure sum up to the BHVO-2 bulk-rock average obtained after hotplate HF digestion (section 3.2). The extraction efficiency of the HPA-S for Se seems independent from the sample size (~0.08–1.1 g), acid volume (2.5–10 mL) and ashing temperature (220–320°C; see supporting information Table S1). Some sulfides can be enclosed in coarse silicate grains and remain shielded from acid digestion (Day et al., 2016). However, we observed nearly identical Se-Te extraction efficiency on both the supplier and reground powders (Figure 2 and supporting information Figure S1). This suggests that the population of exposed sulfides does not increase with decreasing particle sizes of the powder. Unless the sulfide grains are systematically smaller than silicate grains in the reground powder that ranges between 0.5 and 5 μm (Moore & Calk, 1971), our observation might suggest that most sulfides in BHVO-2 are quantitatively dissolved during the digestion. Similarly, all oxide phases are sufficiently dissolved in inverse *aqua regia* at high-temperature (Li et al., 2015). Therefore, we suggest that the unextracted portions of Se and Te from BHVO-2, which systematically represent ~25% and ~12% of the bulk-rock budget, are either dissolved in the glass matrix or hosted in the crystal lattice of silicate minerals (also see Chau & Riley, 1965; Hall & Pelchat, 1997a).

The results of this study support that the extraction of Se and Te from basalts using inverse *aqua regia* may depend on the sample matrix and partitioning of these elements between silicate phases (crystals and glass) and sulfides (e.g., Brenan, 2015; Kiseeva et al., 2017; Kiseeva & Wood, 2017), as previously suggested for some HSEs (e.g., Dale et al., 2012; Ishikawa et al., 2014; Li et al., 2015). Therefore, the HPA-S (inverse *aqua regia*) digestion without HF-desilicification has to be used with caution for analyses of bulk-rock Se-Te concentrations and/or Se isotope composition of basalts and potentially other silicate melts.

4.1.2. Effect of Insoluble Fluorides During HF Digestion

A typical disadvantage associated with HF-based digestion compared to the inverse *aqua regia* digestion is that many elements tend to coprecipitate with fluorides (e.g, Cotta & Enzweiler, 2012; Meisel et al., 2003; Takei et al., 2001; Yokoyama et al., 1999). Some authors speculated that Se and Te do not coprecipitate with fluorides but are dissolved in the supernatant HF solution as oxyanions (Makishima & Nakamura, 2009). Indeed, we did not observe any measurable Se or Te from fluoride precipitates ($n = 5$) that were separated and completely dissolved by multiple HCl treatments. Moreover, the low uncertainties and consistency of the BHVO-2 Se-Te ID concentrations obtained between different HF digestion procedures (see section 2.3.2) seem to suggest a complete sample-spike equilibrium in the presence of fluoride precipitates, supporting that Se and Te do not coprecipitate with fluorides.

4.2. Volatile Loss of Se-Te During the Sample Processing

Accurate determination of Se-Te and other volatile elements (such as S, Ge, As, and Sb) in silicate rocks can be compromised by evaporative loss during solution treatment as hydride or halide species (Makishima et al., 2009). Formation of these species can be suppressed by the addition of strongly oxidizing HCl-HNO_3 or HBr-HNO_3 mixtures to the digestion acid (e.g., Hall & Pelchat, 1997a, 1997b; Makishima & Nakamura, 2009). A combination of the inverse *aqua regia* digestion in HPA-S and the ID method may thus promote sample-spike equilibration and minimize analytical bias associated with the effects of Se-Te loss (König et al., 2012; Wang & Becker, 2014). In our experiment, the Se concentrations of the dissolved phases and

residue of BHVO-2 from the HPA-S procedure sum up to 97 ± 6% (1 s.d., n = 7) of the bulk-rock Se concentration by ID. This suggests that Se degassing, if any, is efficiently prevented before equilibration of the dissolved sample fraction and spike.

Following HF digestion, Se and Te are probably present as aqueous oxyanions of Se^{4+} and/or Se^{6+} and Te^{4+} in the solution (Hall & Pelchat, 1997a; Kuldvere, 1989; Stüeken et al., 2013). During subsequent evaporation at 65°C, these species may not be prone to degassing as volatile fluorides in the presence of rock matrix and HNO_3 (Marin et al., 2001; Makishima & Nakamura, 2009; but see Yi et al., 1998). Note that our HCl evaporation experiment conducted at 65°C (after the evaporation of HF-HNO_3) yields full Se-Te recoveries from BHVO-2. This observation, together with the intermediate precision of our BHVO-2 Se-Te concentration data (r.s.d. = 2%; Figure 2), suggests that both elements are not subject to evaporative losses following the HF digestion.

As for the subsequent HCl treatment for dissolving insoluble fluorides and converting total Se to Se^{4+} (Hill et al., 1995; Hall & Pelchat, 1997a), Se loss may indeed occur (Chau & Riley, 1965). This might be due to the formation of (1) volatile Se compounds such as hydride (H_2Se) and chlorides (Kurzawa et al., 2017; Schirmer et al., 2014; Vollstaedt et al., 2016) and/or (2) insoluble Se^0 (Langner, 2000; Marin et al., 2001; Tokunaga et al., 2013) that is unreactive with $NaBH_4$ during the analysis (Hall & Pelchat, 1997a). It has been suggested that evaporation of HCl solutions needs to be conducted below 80°C to prevent Se loss (Layton-Matthews et al., 2006; Rouxel et al., 2002). However, despite the potential Se losses, we necessarily dried down all HCl solutions to complete dryness at 85°C in order to quantitatively eliminate Ge as volatile $GeCl_4$ (boiling point 84°C; see Lopez-Molinero et al., 2001; Luais, 2012; Makishima & Nakamura, 2009; Rouxel et al., 2006). Note that the double spike approach corrects for any isotopic fractionation associated with loss of Se as detailed by Kurzawa et al. (2017). We observed between negligible and up to 10% Se losses from BHVO-2 after multiple evaporations of HCl solutions at 65°C and 85°C, respectively (see section 3.1). Kurzawa et al. (2017) reported large Se losses (up to 51%) from NIST SRM 3149 solution even at 65°C. This indicates that the behavior of Se species in HCl in fact largely depends on the presence of sample matrix. On the other hand, we observed negligible evaporative Te losses from both standard (NIST SRM 3156) and BHVO-2 matrix solutions at 65°C and 85°C, reflecting different chemical behaviors of Se and Te in aqueous solutions (McPhail, 1995).

4.3. Sample Heterogeneity

The reproducibility of HSE analysis is known to be compromised by sample heterogeneity (Meisel & Horan, 2016, and references therein). Similarly, based on the literature, Se-Te concentrations for a given sample can show large variabilities between replicate digestions (e.g., Forrest et al., 2009; König et al., 2012; Wang et al., 2015). This is more pronounced in peridotites even with a large sample size (up to 3 g; König et al., 2012). Furthermore, grain size experiments on a harzburgite showed that coarse and fine fractions have quite different Se-Te concentrations and Se/Te ratios, emphasizing the importance of the mineralogy and sample size selection for precise Se-Te determinations in peridotites (König et al., 2015a).

The Se-Te concentrations of our BHVO-2 sieved fractions of >25 and <25 μm illustrate a similar sample heterogeneity in this basaltic reference material (supporting information Table S7). The Se/Te ratio of the fine fraction (10.6 ± 0.4) is lower than that of the coarse fraction (12.6 ± 0.5) and the bulk rock (11.9 ± 0.7; all 1 s.d.). For peridotites, the complementary Se/Te ratios in different grain separates are explained by the predominant stabilization of metasomatic Te-rich phases (e.g., tellurides) along interstitial grain boundaries after melt depletion (König et al., 2015a). In the case of basalt BHVO-2, it probably indicates predominant settling of tellurides or other high Te-bearing host phases (with lower Se/Te) along grain boundaries during cooling and crystallization of the melt.

Despite the heterogeneous distribution of Se-Te-rich phases within the matrix, the variabilities of Se-Te concentrations obtained for bulk-rock BHVO-2 powders are always lower than ~3% (r.s.d.) at a range of sample sizes (~0.08–1.1 g; see supporting information Table S6 and Figure 2). Although the level of heterogeneity is predicted to be sample specific (Wang et al., 2015), low variabilities are also observed under intermediate precision conditions for the measured Se-Te concentrations (r.s.d. <5%) and $\delta^{82/76}$Se values (2 s.d. ≤0.11‰) in all reference materials with a wide range of Se-Te contents (~15–170 ng g^{-1} Se and ~1–14 ng g^{-1} Te). This suggests that the effect of sample heterogeneity might not be significant in Se-Te analysis of a melt-like matrix with digestion of down to 0.1 g sample powder.

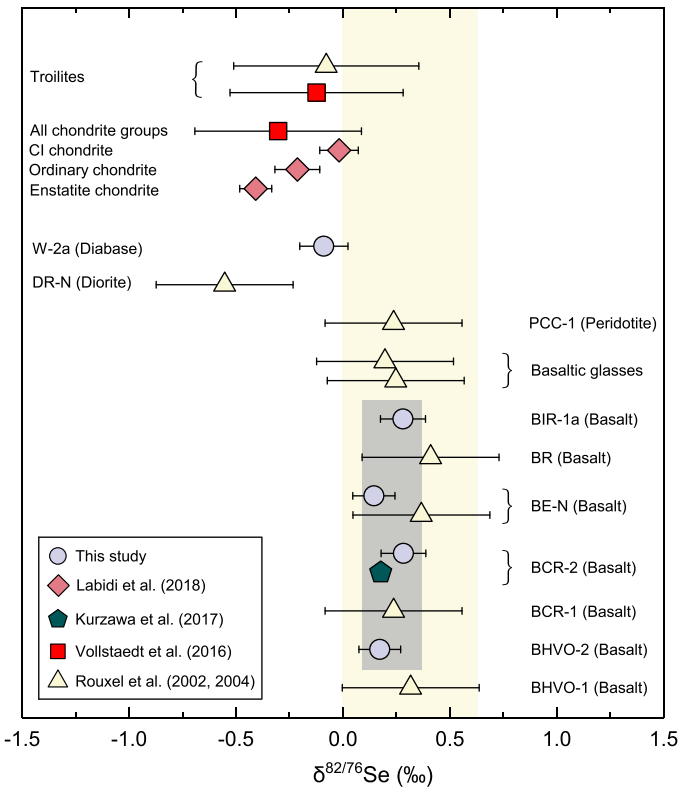

Figure 5. The $\delta^{82/76}$Se values of reference materials analyzed using our newly established HF digestion and chromatographic purification protocols. Also shown for comparison are literature data for silicate rocks (Kurzawa et al., 2017; Rouxel et al., 2002, 2004), chondrites and troilites (Rouxel et al., 2002; Vollstaedt et al., 2016), as well as each chondrite group (Labidi et al., 2018). Literature data are converted to $\delta^{82/76}$Se relative to NIST SRM 3149 (Carignan & Wen, 2007). Horizontal error bars on our data represent 2 s.d. uncertainties estimated over at least five digestion batches and are well within our analytical precision of ~0.11‰. The grey shaded box represents the range for $\delta^{82/76}$Se values of analyzed basalts (0.23 ± 0.14‰), which is smaller but still falls in the previously constrained range (light-yellow shaded field) for the igneous silicate Earth (0.33 ± 0.32‰; Rouxel et al., 2002). Note that the range conservatively takes into account the 2 s.d. of the mean or, where larger, 2 s.d. analytical uncertainty.

4.4. The Se Isotopic Composition of Igneous Rocks

Identical $\delta^{82/76}$Se values after the HPA-S (inverse *aqua regia*) and hotplate HF digestions might indicate a Se isotopic homogeneity within a basaltic matrix (e.g., BHVO-2), despite seemingly different Se host phases as indicated by systematically lower and relatively variable Se concentrations obtained after the HPA-S digestion (Figure 4). However, for accurate analyses of combined Se isotope and Se concentration of bulk basalts, the use of HF is required to achieve complete Se extraction (see section 4.1.1).

With the method presented, the $\delta^{82/76}$Se values of all analyzed reference materials are indistinguishable within 2 s.d. uncertainties from the previous estimate for the igneous silicate Earth (0.33 ± 0.32‰; 2 s.d. analytical precision; Rouxel et al., 2002; Figure 5). Based on the basaltic reference materials and refined analytical precision (~0.11‰; 2 s.d.), we obtain an estimate of 0.23 ± 0.14‰ (2 s.d. of the mean). Interestingly, the basalts displaying this narrow range of $\delta^{82/76}$Se are from diverse geodynamic settings (e.g., ocean islands, plume-influenced mid-ocean ridges, and continental settings). Despite markedly different Se-Te elemental systematics of these basalts (Table 1), their similar Se isotopic compositions overlapping with those of a peridotite (Rouxel et al., 2002) and basaltic glasses (from a lava lake near the Lucky Strike hydrothermal field; Rouxel et al., 2004) may either reflect their isotopically homogeneous source or secondary processes (e.g., Lissner et al., 2014; Jenner et al., 2015) that result in similar Se isotope and different Se-Te elemental signatures. On the same note, we point out that the resolvable differences of $\delta^{82/76}$Se values between these basalts and a diabase (W-2a) as well as a diorite (DR-N; Rouxel et al., 2002; Figure 5) require further investigation of different types of igneous rocks in order to assess if and how the respective emplacements or subtle petrogenetic differences have an effect on Se isotopes.

Despite some overlap within uncertainties, we note that the average $\delta^{82/76}$Se of basalts analyzed so far are higher than the average chondritic values of −0.30 ± 0.39‰ (2 s.d.; Vollstaedt et al., 2016) and −0.21 ± 0.31‰ (2 s.d.; Labidi et al., 2018). Perhaps more significantly, some basalts (BHVO-2 and BE-N) show $\delta^{82/76}$Se values similar to the estimate for carbonaceous chondrites (−0.01 ± 0.09‰; 2 s.d.), but all basalts show Se isotope signatures significantly different from those of ordinary and enstatite chondrites (−0.21 ± 0.10‰ and −0.40 ± 0.07‰, respectively; 2 s.d.; Labidi et al., 2018). However, a substantially extended data set on terrestrial melts and mantle rocks is still required to fully understand Se isotope variations in magmatic systems before constraining the isotopic composition of the bulk silicate Earth (BSE). This is a prerequisite for understanding the Se isotope and Se-Te elemental perspective on the origin and evolution of the Earth's volatiles.

5. Conclusion

This study presents a new and simplified chemical sample processing scheme that enables combined high-precision analyses of Se stable isotopes and Se-Te elemental abundances from the same rock digest of significantly small sample amounts using as low as ~6.5 ng Se by DS MC-ICP-MS (Kurzawa et al., 2017) and ~0.5 ng Se and ~0.15 ng Te by ID (quadrupole) ICP-MS. The method includes a hotplate HF digestion and refined chromatographic purification that yields low blanks and high procedural recoveries of Se and Te (~80%). A complete separation of isobarically interfering Ge from Se is achieved via evaporation of HCl solutions at 85°C. At the same time, previous equilibration of sample and ^{77}Se–^{74}Se double spike enables

correction for any Se isotopic fractionation associated with minor Se losses. Low variability under intermediate precision conditions was obtained for each sample over at least five digestion batches, with calculated uncertainties better than ~0.11‰ (2 s.d.) on $\delta^{82/76}$Se and 3% and 5% (r.s.d.) on Se and Te concentrations, respectively. The selected reference materials (BHVO-2, BIR-1a, BCR-2, BE-N, and W-2a) are therefore considered to be rather homogeneous when digested strategically and recommended as Se isotope reference materials in future studies concerning igneous systems.

Although an identical $\delta^{82/76}$Se value of BHVO-2 is observed using the HPA-S (inverse *aqua regia*) and HF digestion techniques, the former cannot fully extract Se and Te depending on the sample matrix and has to be used with caution in bulk-rock Se isotope and/or Se-Te abundance analyses of basaltic matrices. The presented sample preparation procedure in this study is optimized for basalts, but may be readily applied to other silicate matrices (e.g., ultramafic samples with resistant alloys) by employing HPA-S digestion followed by a hotplate HF-desilicification.

The basalts analyzed in this study have markedly distinct Se and Te contents, yet their Se isotopic compositions fall within the range of the igneous silicate Earth previously estimated by Rouxel et al. (2002) but exhibit a smaller variation with an average of 0.23 ± 0.14‰ (2 s.d.). Despite the demonstrated differences of $\delta^{82/76}$Se between these basalts and main chondrite groups (Labidi et al., 2018; Vollstaedt et al., 2016), more systematic studies are required to investigate natural Se isotope variations in igneous systems in order to place firm constraints on the BSE and planetary-scale processes. At this point, the observed $\delta^{82/76}$Se variations indicate the potential of Se isotopes as a future tracer for the origin and evolution of volatiles in the mantle.

Acknowledgments
This work was funded by an ERC Starting Grant (O_2RIGIN, 636808) to Stephan König. We thank Elmar Reitter, Martin Wille, and Johannes Redlinger for their support during sample preparation and mass spectrometry analysis, and Marcus Burnham for providing insight into hydride generation quadrupole ICP-MS analysis with his experience. We also thank Stephen A. Wilson (USGS) for providing the BHVO-2 particle size information and Fritsch (Germany) for the particle size analysis. We greatly appreciate insightful reviews by Frances E. Jenner, Philip A.E. Pogge von Strandmann, Graeme M. Poole, and Anne Trinquier, as well as the editorial handling of Janne Blichert-Toft. All data used in this study are available in tables in the main text, supporting information, and references.

References

Brenan, J. M. (2015). Se-Te fractionation by sulfide-silicate melt partitioning: Implications for the composition of mantle-derived magmas and their melting residues. *Earth and Planetary Science Letters*, *422*, 45–57. https://doi.org/10.1016/j.epsl.2015.04.011

Carignan, J., & Wen, H. J. (2007). Scaling NIST SRM 3149 for Se isotope analysis and isotopic variations of natural samples. *Chemical Geology*, *242*(3–4), 347–350. https://doi.org/10.1016/j.chemgeo.2007.03.020

Chau, Y. K., & Riley, J. P. (1965). The determination of selenium in sea water, silicates and marine organisms. *Analytica Chimica Acta*, *33*, 36–49. https://doi.org/10.1016/s0003-2670(01)84852-2

Chew, D. M., Donelick, R. A., Donelick, M. B., Kamber, B. S., & Stock, M. J. (2014). Apatite chlorine concentration measurements by LA-ICP-MS. *Geostandards and Geoanalytical Research*, *38*(1), 23–35. https://doi.org/10.1111/j.1751-908X.2013.00246.x

Clark, S. K., & Johnson, T. M. (2010). Selenium stable isotope investigation into selenium biogeochemical cycling in a lacustrine environment: Sweitzer Lake, Colorado. *Journal of Environmental Quality*, *39*(6), 2200–2210. https://doi.org/10.2134/jeq2009.0380

Cotta, A. J. B., & Enzweiler, J. (2012). Classical and new procedures of whole rock dissolution for trace element determination by ICP-MS. *Geostandards and Geoanalytical Research*, *36*(1), 27–50. https://doi.org/10.1111/j.1751-908X.2011.00115.x

Dale, C. W., Macpherson, C. G., Pearson, D. G., Hammond, S. J., & Arculus, R. J. (2012). Inter-element fractionation of highly siderophile elements in the Tonga Arc due to flux melting of a depleted source. *Geochimica et Cosmochimica Acta*, *89*, 202–225. https://doi.org/10.1016/j.gca.2012.03.025

Davies, C. M. (2012). *Determination of distribution coefficients for cation exchange resin and optimisation of ion exchange chromatography for chromium separation for geological materials* (Master's thesis). UK: The University of Manchester.

Day, J. M. D., Waters, C. L., Schaefer, B. F., Walker, R. J., & Turner, S. (2016). Use of hydrofluoric acid desilicification in the determination of highly siderophile element abundances and Re-Pt-Os isotope systematics in mafic-ultramafic rocks. *Geostandards and Geoanalytical Research*, *40*(1), 49–65. https://doi.org/10.1111/j.1751-908X.2015.00367.x

Ellis, A. S., Johnson, T. M., Herbel, M. J., & Bullen, T. D. (2003). Stable isotope fractionation of selenium by natural microbial consortia. *Chemical Geology*, *195*(1–4), 119–129. https://doi.org/10.1016/S0009-2541(02)00391-1

Elwaer, N., & Hintelmann, H. (2008). Selective separation of selenium (IV) by thiol cellulose powder and subsequent selenium isotope ratio determination using multicollector inductively coupled plasma mass spectrometry. *Journal of Analytical Atomic Spectrometry*, *23*(5), 733–743. https://doi.org/10.1039/b801673a

Faris, J. P. (1960). Adsorption of elements from hydrofluoric acid by anion exchange. *Analytical Chemistry*, *32*(4), 520–522. https://doi.org/10.1021/ac60160a019

Fehr, M. A., Rehkamper, M., & Halliday, A. N. (2004). Application of MC-ICPMS to the precise determination of tellurium isotope compositions in chondrites, iron meteorites and sulfides. *International Journal of Mass Spectrometry*, *232*(1), 83–94. https://doi.org/10.1016/j.ijms.2003.11.006

Fehr, M. A., Rehkämper, M., Halliday, A. N., Wiechert, U., Hattendorf, B., Günther, D., et al. (2005). Tellurium isotopic composition of the early solar system—A search for effects resulting from stellar nucleosynthesis, ^{126}Sn decay, and mass-independent fractionation. *Geochimica et Cosmochimica Acta*, *69*(21), 5099–5112. https://doi.org/10.1016/j.gca.2005.04.020

Floor, G. H., Millot, R., Iglesias, M., & Negrel, P. (2011). Influence of methane addition on selenium isotope sensitivity and their spectral interferences. *Journal of Mass Spectrometry*, *46*(2), 182–188. https://doi.org/10.1002/jms.1880

Fornadel, A. P., Spry, P. G., Jackson, S. E., Mathur, R. D., Chapman, J. B., & Girard, I. (2014). Methods for the determination of stable Te isotopes of minerals in the system Au-Ag-Te by MC-ICP-MS. *Journal of Analytical Atomic Spectrometry*, *29*(4), 623–637. https://doi.org/10.1039/C3JA50237F

Forrest, A., Kingsley, R., & Schilling, J. G. (2009). Determination of selenium and tellurium in basalt rock reference materials by isotope dilution hydride generation-inductively coupled plasma-mass spectrometry (ID-HG-ICP-MS). *Geostandards and Geoanalytical Research*, *33*(2), 261–269. https://doi.org/10.1111/j.1751-908X.2009.00841.x

Guo, J., Griffin, W. L., & O'Reilly, S. Y. (1999). Geochemistry and origin of sulphide minerals in mantle xenoliths: Qilin, southeastern China. *Journal of Petrology*, *40*(7), 1125–1149. https://doi.org/10.1093/petroj/40.7.1125

Hall, G. E. M., & Pelchat, J.-C. (1997a). Analysis of geological materials for bismuth, antimony, selenium and tellurium by continuous flow hydride generation inductively coupled plasma mass spectrometry Part 2. Methodology and results. *Journal of Analytical Atomic Spectrometry*, *12*(1), 103–106. https://doi.org/10.1039/a605399h

Hall, G. E. M., & Pelchat, J.-C. (1997b). Determination of As, Bi, Sb, Se and Te in fifty five reference materials by hydride generation ICP-MS. *Geostandards and Geoanalytical Research*, *21*(1), 85–91. https://doi.org/10.1111/j.1751-908X.1997.tb00534.x

Harvey, J., König, S., & Luguet, A. (2015). The effects of melt depletion and metasomatism on highly siderophile and strongly chalcophile elements: S-Se-Te-Re-PGE systematics of peridotite xenoliths from Kilbourne Hole, New Mexico. *Geochimica et Cosmochimica Acta*, *166*, 210–233. https://doi.org/10.1016/j.gca.2015.06.028

Hattori, K. H., Arai, S., & Clarke, D. B. (2002). Selenium, tellurium, arsenic and antimony contents of primary mantle sulfides. *Canadian Mineralogist*, *40*(2), 637–650. https://doi.org/10.2113/gscanmin.40.2.637

Herbel, M. J., Johnson, T. M., Oremland, R. S., & Bullen, T. D. (2000). Fractionation of selenium isotopes during bacterial respiratory reduction of selenium oxyanions. *Geochimica et Cosmochimica Acta*, *64*(21), 3701–3709. https://doi.org/10.1016/S0016-7037(00)00456-7

Herbel, M. J., Johnson, T. M., Tanji, K. K., Gao, S., & Bullen, T. D. (2002). Selenium stable isotope ratios in California agricultural drainage water management systems. *Journal of Environmental Quality*, *31*(4), 1146–1156. https://doi.org/10.2134/jeq2002.1146

Hertogen, J., Janssens, M. J., & Palme, H. (1980). Trace-elements in ocean ridge basalt glasses: Implications for fractionations during mantle evolution and petrogenesis. *Geochimica et Cosmochimica Acta*, *44*(12), 2125–2143. https://doi.org/10.1016/0016-7037(80)90209-4

Hill, S. J., Pitts, L., & Worsfold, P. (1995). Investigation into the kinetics of selenium(VI) reduction using hydride generation atomic fluorescence detection. *Journal of Analytical Atomic Spectrometry*, *10*(5), 409–411. https://doi.org/10.1039/ja9951000409

Ishikawa, A., Senda, R., Suzuki, K., Dale, C. W., & Meisel, T. (2014). Re-evaluating digestion methods for highly siderophile element and ^{187}Os isotope analysis: Evidence from geological reference materials. *Chemical Geology*, *384*, 27–46. https://doi.org/10.1016/j.chemgeo.2014.06.013

Jenner, F. E., Hauri, E. H., Bullock, E. S., König, S., Arculus, R. J., Mavrogenes, J. A., et al. (2015). The competing effects of sulfide saturation versus degassing on the behavior of the chalcophile elements during the differentiation of hydrous melts. *Geochemistry, Geophysics, Geosystems*, *16*(5), 1490–1507. https://doi.org/10.1002/2014GC005670

Johnson, T. M., Herbel, M. J., Bullen, T. D., & Zawislanski, P. T. (1999). Selenium isotope ratios as indicators of selenium sources and oxyanion reduction. *Geochimica et Cosmochimica Acta*, *63*(18), 2775–2783. https://doi.org/10.1016/S0016-7037(99)00279-3

Kadlag, Y., & Becker, H. (2015). Fractionation of highly siderophile and chalcogen elements in components of EH3 chondrites. *Geochimica et Cosmochimica Acta*, *161*, 166–187. https://doi.org/10.1016/j.gca.2015.04.022

Kadlag, Y., & Becker, H. (2016). ^{187}Re-^{187}Os systematics, highly siderophile element, S-Se-Te abundances in the components of unequilibrated L chondrites. *Geochimica et Cosmochimica Acta*, *172*, 225–246. https://doi.org/10.1016/j.gca.2015.09.026

Kimura, K., Lewis, R. S., & Anders, E. (1974). Distribution of gold and rhenium between nickel-iron and silicate melts: Implications for the abundance of siderophile elements on the Earth and Moon. *Geochimica et Cosmochimica Acta*, *38*(5), 683–701. https://doi.org/10.1016/0016-7037(74)90144-6

Kipp, M. A., Stüeken, E. E., Bekker, A., & Buick, R. (2017). Selenium isotopes record extensive marine suboxia during the Great Oxidation Event. *Proceedings of the National Academy of Sciences of the United States of America*, *114*(5), 875–880. https://doi.org/10.1073/pnas.1615867114

Kiseeva, E. S., Fonseca, R. O. C., & Smythe, D. J. (2017). Chalcophile elements and sulfides in the Upper Mantle. *Elements*, *13*(2), 111–116. https://doi.org/10.2113/gselements.13.2.111

Kiseeva, E. S., & Wood, B. J. (2017). *Partitioning of As, Se, Te and Bi between sulphide and silicate liquids*. Paper presented at Annual V.M. Goldschmidt Conference. Geochemical Society and European Association of Geochemistry, Paris, France.

König, S., Lissner, M., Lorand, J. P., Bragagni, A., & Luguet, A. (2015a). Mineralogical control of selenium, tellurium and highly siderophile elements in the Earth's mantle: Evidence from mineral separates of ultra-depleted mantle residues. *Chemical Geology*, *396*, 16–24. https://doi.org/10.1016/j.chemgeo.2014.12.015

König, S., Lissner, M., Lorand, J.-P., Bragagni, A., & Luguet, A. (2015b). Reply to the comment on "A non-primitive origin of near-chondritic S-Se-Te ratios in mantle peridotites: Implications for the Earth's late accretionary history" by König S. et al. [Earth Planet. Sci. Lett. 385 (2014) 110–121]. *Earth and Planetary Science Letters*, *417*, 167–169. https://doi.org/10.1016/j.epsl.2013.10.036

König, S., Lorand, J. P., Luguet, A., & Pearson, D. G. (2014). A non-primitive origin of near-chondritic S-Se-Te ratios in mantle peridotites: Implications for the Earth's late accretionary history. *Earth and Planetary Science Letters*, *385*, 110–121. https://doi.org/10.1016/j.epsl.2013.10.036

König, S., Luguet, A., Lorand, J. P., Wombacher, F., & Lissner, M. (2012). Selenium and tellurium systematics of the Earth's mantle from high precision analyses of ultra-depleted orogenic peridotites. *Geochimica et Cosmochimica Acta*, *86*, 354–366. https://doi.org/10.1016/j.gca.2012.03.014

Krouse, H. R., & Thode, H. G. (1962). Thermodynamic properties and geochemistry of isotopic compounds of selenium. *Canadian Journal of Chemistry*, *40*(2), 367–375. https://doi.org/10.1139/v62-055

Kuldvere, A. (1989). Extraction of geological-materials with mineral acids for the determination of arsenic, antimony, bismuth and selenium by hydride generation atomic-absorption spectrometry. *Analyst*, *114*(2), 125–131. https://doi.org/10.1039/an9891400125

Kurzawa, T., König, S., Labidi, J., Yierpan, A., & Schoenberg, R. (2017). A method for Se isotope analysis of low ng-level geological samples via double spike and hydride generation MC-ICP-MS. *Chemical Geology*, *466*, 219–228. https://doi.org/10.1016/j.chemgeo.2017.06.012

Labidi, J., & Cartigny, P. (2016). Negligible sulfur isotope fractionation during partial melting: Evidence from Garrett transform fault basalts, implications for the late-veneer and the hadean matte. *Earth and Planetary Science Letters*, *451*, 196–207. https://doi.org/10.1016/j.epsl.2016.07.012

Labidi, J., Cartigny, P., & Moreira, M. (2013). Non-chondritic sulphur isotope composition of the terrestrial mantle. *Nature*, *501*(7466), 208–211. https://doi.org/10.1038/nature12490

Labidi, J., König, S., Kurzawa, T., Yierpan, A., & Schoenberg, R. (2018). The selenium isotopic variations in chondrites are mass-dependent: Implications for sulfide formation in the early solar system. *Earth and Planetary Science Letters*, *481*, 212–222. https://doi.org/10.1016/j.epsl.2017.10.032

Labidi, J., Shahar, A., Le Losq, C., Hillgren, V. J., Mysen, B. O., & Farquhar, J. (2016). Experimentally determined sulfur isotope fractionation between metal and silicate and implications for planetary differentiation. *Geochimica et Cosmochimica Acta*, *175*, 181–194. https://doi.org/10.1016/j.gca.2015.12.001

Langmyhr, F. J. (1967). Removal of hydrofluoric acid by evaporation in presence of sulfuric or perchloric acids. *Analytica Chimica Acta*, *39*(4), 516. https://doi.org/10.1016/S0003-2670(01)80548-1

Langner, B. E. (2000). Selenium and selenium compounds. In *Ullmann's encyclopedia of industrial chemistry*. Germany: Wiley-VCH. https://doi.org/10.1002/14356007.a23_525

Layton-Matthews, D., Leybourne, M. I., Peter, J. M., & Scott, S. D. (2006). Determination of selenium isotopic ratios by continuous-hydride-generation dynamic-reaction-cell inductively coupled plasma-mass spectrometry. *Journal of Analytical Atomic Spectrometry*, *21*(1), 41–49. https://doi.org/10.1039/b501704A

Layton-Matthews, D., Leybourne, M. I., Peter, J. M., Scott, S. D., Cousens, B., & Eglington, B. M. (2013). Multiple sources of selenium in ancient seafloor hydrothermal systems: Compositional and Se, S, and Pb isotopic evidence from volcanic-hosted and volcanic-sediment-hosted massive sulfide deposits of the Finlayson Lake District, Yukon, Canada. *Geochimica et Cosmochimica Acta*, *117*, 313–331. https://doi.org/10.1016/j.gca.2013.05.002

Li, J., Zhao, P. P., Liu, J. G., Wang, X. C., Yang, A. Y., Wang, G. Q., & Xu, J. F. (2015). Reassessment of hydrofluoric acid desilicification in the carius tube digestion technique for Re-Os isotopic determination in geological samples. *Geostandards and Geoanalytical Research*, *39*(1), 17–30. https://doi.org/10.1111/j.1751-908X.2014.00299.x

Lissner, M., König, S., Luguet, A., Le Roux, P. J., Schuth, S., Heuser, A., et al. (2014). Selenium and tellurium systematics in MORBs from the southern Mid-Atlantic Ridge (47–50°S). *Geochimica et Cosmochimica Acta*, *144*, 379–402. https://doi.org/10.1016/j.gca.2014.08.023

Lodders, K. (2003). Solar system abundances and condensation temperatures of the elements. *Astrophysical Journal*, *591*(2), 1220–1247. https://doi.org/10.1086/375492

Long, G. L., & Winefordner, J. D. (1983). Limit of detection a closer look at the IUPAC definition. *Analytical Chemistry*, *55*(7), 712A–724A. https://doi.org/10.1021/ac00258a724

Lopez-Molinero, A., Villareal, A., Andia, D., Velilla, C., & Castillo, J. R. (2001). Volatile germanium tetrachloride for sample introduction and germanium determination by inductively coupled plasma atomic emission spectroscopy. *Journal of Analytical Atomic Spectrometry*, *16*(7), 744–749. https://doi.org/10.1039/b009937F

Lorand, J. P., & Alard, O. (2010). Determination of selenium and tellurium concentrations in Pyrenean peridotites (Ariege, France): New insight into S/Se/Te systematics of the upper in mantle samples. *Chemical Geology*, *278*(1–2), 120–130. https://doi.org/10.1016/j.chemgeo.2010.09.007

Loss, R. D., Rosman, K. J. R., & de Laeter, J. R. (1990). The isotopic composition of zinc, palladium, silver, cadmium, tin, and tellurium in acid-etched residues of the allende meteorite. *Geochimica et Cosmochimica Acta*, *54*(12), 3525–3536. https://doi.org/10.1016/0016-7037(90)90302-2

Luais, B. (2012). Germanium chemistry and MC-ICPMS isotopic measurements of Fe-Ni, Zn alloys and silicate matrices: Insights into deep Earth processes. *Chemical Geology*, *334*, 295–311. https://doi.org/10.1016/j.chemgeo.2012.10.017

Luguet, A., Behrens, M., Pearson, D. G., König, S., & Herwartz, D. (2015). Significance of the whole rock Re-Os ages in cryptically and modally metasomatised cratonic peridotites: Constraints from HSE-Se-Te systematics. *Geochimica et Cosmochimica Acta*, *164*, 441–463. https://doi.org/10.1016/j.gca.2015.06.016

Makishima, A., & Nakamura, E. (2009). Determination of Ge, As, Se and Te in silicate samples using isotope dilution-internal standardisation octopole reaction cell ICP-QMS by normal sample nebulisation. *Geostandards and Geoanalytical Research*, *33*(3), 369–384. https://doi.org/10.1111/j.1751-908X.2009.00014.x

Makishima, A., Tanaka, R., & Nakamura, E. (2009). Precise elemental and isotopic analyses in silicate samples employing ICP-MS: Application of hydrofluoric acid solution and analytical techniques. *Analytical Sciences*, *25*(10), 1181–1187. https://doi.org/10.2116/analsci.25.1181

Marin, L., Lhomme, J., & Carignan, J. (2001). Determination of selenium concentration in sixty five reference materials for geochemical analysis by GFAAS after separation with thiol cotton. *Geostandards and Geoanalytical Research*, *25*(2–3), 317–324. https://doi.org/10.1111/j.1751-908X.2001.tb00608.x

Mcdonough, W. F., & Sun, S. S. (1995). The composition of the Earth. *Chemical Geology*, *120*(3–4), 223–253. https://doi.org/10.1016/0009-2541(94)00140-4

Mcphail, D. C. (1995). Thermodynamic properties of aqueous tellurium species between 25 and 350°C. *Geochimica et Cosmochimica Acta*, *59*(5), 851–866. https://doi.org/10.1016/0016-7037(94)00353-X

Meija, J., Coplen, T. B., Berglund, M., Brand, W. A., De Bievre, P., Groning, M., et al. (2016). Isotopic compositions of the elements 2013 (IUPAC Technical Report). *Pure and Applied Chemistry*, *88*(3), 293–306. https://doi.org/10.1515/pac-2015-0503

Meisel, T., & Horan, M. F. (2016). Analytical methods for the highly siderophile elements. *Reviews in Mineralogy and Geochemistry*, *81*(1), 89-106. https://doi.org/10.2138/rmg.2016.81.02

Meisel, T., Reisberg, L., Moser, J., Carignan, J., Melcher, F., & Brügmann, G. (2003). Re-Os systematics of UB-N, a serpentinized peridotite reference material. *Chemical Geology*, *201*(1–2), 161–179. https://doi.org/10.1016/s0009-2541(03)00234-1

Mitchell, K., Mansoor, S. Z., Mason, P. R. D., Johnson, T. M., & Van Cappellen, P. (2016). Geological evolution of the marine selenium cycle: Insights from the bulk shale $\delta^{82/76}$Se record and isotope mass balance modeling. *Earth and Planetary Science Letters*, *441*, 178–187. https://doi.org/10.1016/j.epsl.2016.02.030

Mitchell, K., Mason, P. R. D., Van Cappellen, P., Johnson, T. M., Gill, B. C., Owens, J. D., et al. (2012). Selenium as paleo-oceanographic proxy: A first assessment. *Geochimica et Cosmochimica Acta*, *89*, 302–317. https://doi.org/10.1016/j.gca.2012.03.038

Moore, J. G., & Calk, L. (1971). Sulfide spherules in vesicles of dredged pillow basalt. *American Mineralogist*, *56*(3–4), 476–488.

Morgan, J. W. (1986). Ultramafic xenoliths: Clues to Earth's late accretionary history. *Journal of Geophysical Research*, *91*(B12), 12375–12387. https://doi.org/10.1029/JB091iB12p12375

Pogge von Strandmann, P. A. E., Coath, C. D., Catling, D. C., Poulton, S. W., & Elliott, T. (2014). Analysis of mass dependent and mass independent selenium isotope variability in black shales. *Journal of Analytical Atomic Spectrometry*, *29*(9), 1648–1659. https://doi.org/10.1039/C4JA00124A

Pogge von Strandmann, P. A., Stüeken, E. E., Elliott, T., Poulton, S. W., Dehler, C. M., Canfield, D. E., et al. (2015). Selenium isotope evidence for progressive oxidation of the Neoproterozoic biosphere. *Nature Communications*, *6*(1), 10157. https://doi.org/10.1038/ncomms10157

Rees, C. E., & Thode, H. G. (1966). Selenium isotope effects in the reduction of sodium selenite and of sodium selenate. *Canadian Journal of Chemistry*, *44*(4), 419–427. https://doi.org/10.1139/v66-057

Rose-Weston, L., Brenan, J. M., Fei, Y. W., Secco, R. A., & Frost, D. J. (2009). Effect of pressure, temperature, and oxygen fugacity on the metal-silicate partitioning of Te, Se, and S: Implications for earth differentiation. *Geochimica et Cosmochimica Acta*, *73*(15), 4598–4615. https://doi.org/10.1016/j.gca.2009.04.028

Rouxel, O., Galy, A., & Elderfield, H. (2006). Germanium isotopic variations in igneous rocks and marine sediments. *Geochimica et Cosmochimica Acta*, *70*(13), 3387–3400. https://doi.org/10.1016/j.gca.2006.04.025

Rouxel, O., Fouquet, Y., & Ludden, J. N. (2004). Subsurface processes at the Lucky Strike hydrothermal field, Mid-Atlantic Ridge: Evidence from sulfur, selenium, and iron isotopes. *Geochimica et Cosmochimica Acta*, *68*(10), 2295–2311. https://doi.org/10.1016/j.gca.2003.11.029

Rouxel, O., Ludden, J., Carignan, J., Marin, L., & Fouquet, Y. (2002). Natural variations of Se isotopic composition determined by hydride generation multiple collector inductively coupled plasma mass spectrometry. *Geochimica et Cosmochimica Acta*, *66*(18), 3191–3199. https://doi.org/10.1016/S0016-7037(02)00918-3

Savard, D., Bédard, L. P., & Barnes, S.-J. (2009). Selenium concentrations in twenty-six geological reference materials: New determinations and proposed values. *Geostandards and Geoanalytical Research*, *33*(2), 249–259. https://doi.org/10.1111/j.1751-908X.2009.00003.x

Schilling, K., Johnson, T. M., & Mason, P. R. D. (2014). A sequential extraction technique for mass-balanced stable selenium isotope analysis of soil samples. *Chemical Geology*, *381*, 125–130. https://doi.org/10.1016/j.chemgeo.2014.04.014

Schilling, K., Johnson, T. M., & Wilcke, W. (2011a). Isotope fractionation of selenium during fungal biomethylation by Alternaria alternata. *Environmental Science & Technology*, *45*(7), 2670–2676. https://doi.org/10.1021/es102926p

Schilling, K., Johnson, T. M., & Wilcke, W. (2011b). Selenium partitioning and stable isotope ratios in urban topsoils. *Soil Science Society of America Journal*, *75*(4), 1354. https://doi.org/10.2136/sssaj2010.0377

Schirmer, T., Koschinsky, A., & Bau, M. (2014). The ratio of tellurium and selenium in geological material as a possible paleo-redox proxy. *Chemical Geology*, *376*, 44–51. doi:10.1016/j.chemgeo.2014.03.005

Schoenberg, R., & von Blanckenburg, F. (2005). An assessment of the accuracy of stable Fe isotope ratio measurements on samples with organic and inorganic matrices by high-resolution multicollector ICP-MS. *International Journal of Mass Spectrometry*, *242*(2–3), 257–272. https://doi.org/10.1016/j.ijms.2004.11.025

Schönbächler, M., & Fehr, M. A. (2014). Basics of ion exchange chromatography for selected geological applications. In *Treatise on geochemistry* (2nd ed., Vol. 15, pp. 123–146). Amsterdam, Netherlands: Elsevier. https://doi.org/10.1016/b978-0-08-095975-7.01408-x

Stüeken, E. E., Buick, R., & Anbar, A. D. (2015). Selenium isotopes support free O_2 in the latest Archean. *Geology*, *43*(3), 259–262. https://doi.org/10.1130/g36218.1

Stüeken, E. E., Buick, R., Bekker, A., Catling, D., Foriel, J., Guy, B. M., et al. (2015). The evolution of the global selenium cycle: Secular trends in Se isotopes and abundances. *Geochimica et Cosmochimica Acta*, *162*, 109–125. https://doi.org/10.1016/j.gca.2015.04.033

Stüeken, E. E., Foriel, J., Nelson, B. K., Buick, R., & Catling, D. C. (2013). Selenium isotope analysis of organic-rich shales: Advances in sample preparation and isobaric interference correction. *Journal of Analytical Atomic Spectrometry*, *28*(11), 1734–1749. https://doi.org/10.1039/c3ja50186h

Takei, H., Yokoyama, T., Makishima, A., & Nakamura, E. (2001). Formation and suppression of AlF_3 during HF digestion of rock samples in Teflon bomb for precise trace element analyses by ICP-MS and ID-TIMS. *Proceedings of the Japan Academy Series B: Physical and Biological Sciences*, *77*(1), 13–17.

Tokunaga, K., Yokoyama, Y., & Takahashi, Y. (2013). Estimation of Se(VI)/Se(IV) ratio in water by the ratio recorded in barite. *Geochemistry, Geophysics, Geosystems*, *14*(11), 4826–4834. https://doi.org/10.1002/ggge.20295

Vijan, P. N., & Leung, D. (1980). Reduction of chemical interference and speciation studies in the hydride generation atomic-absorption method for selenium. *Analytical Chimica Acta*, *120*(Nov), 141–146. https://doi.org/10.1016/S0003-2670(01)84356-7

Vollstaedt, H., Mezger, K., & Leya, I. (2016). The isotope composition of selenium in chondrites constrains the depletion mechanism of volatile elements in solar system materials. *Earth and Planetary Science Letters*, *450*, 372–380. https://doi.org/10.1016/j.epsl.2016.06.052

Wang, Z., & Becker, H. (2013). Ratios of S, Se and Te in the silicate Earth require a volatile-rich late veneer. *Nature*, *499*(7458), 328–331. https://doi.org/10.1038/nature12285

Wang, Z., & Becker, H. (2014). Abundances of sulfur, selenium, tellurium, rhenium and platinum-group elements in eighteen reference materials by isotope dilution sector-field ICP-MS and negative TIMS. *Geostandards and Geoanalytical Research*, *38*(2), 189–209. https://doi.org/10.1111/j.1751-908X.2013.00258.x

Wang, Z., & Becker, H. (2015). Fractionation of highly siderophile and chalcogen elements during magma transport in the mantle: Constraints from pyroxenites of the Balmuccia peridotite massif. *Geochimica et Cosmochimica Acta*, *159*, 244–263. https://doi.org/10.1016/j.gca.2015.03.036

Wang, Z., & Becker, H. (2017). Chalcophile elements in Martian meteorites indicate low sulfur content in the Martian interior and a volatile element-depleted late veneer. *Earth and Planetary Science Letters*, *463*, 56–68. https://doi.org/10.1016/j.epsl.2017.01.023

Wang, Z., Becker, H., & Gawronski, T. (2013). Partial re-equilibration of highly siderophile elements and the chalcogens in the mantle: A case study on the Baldissero and Balmuccia peridotite massifs (Ivrea Zone, Italian Alps). *Geochimica et Cosmochimica Acta*, *108*, 21–44. https://doi.org/10.1016/j.gca.2013.01.021

Wang, Z., Becker, H., & Wombacher, F. (2015). Mass fractions of S, Cu, Se, Mo, Ag, Cd, In, Te, Ba, Sm, W, Tl and Bi in geological reference materials and selected carbonaceous chondrites determined by isotope dilution ICP-MS. *Geostandards and Geoanalytical Research*, *39*(2), 185–208. https://doi.org/10.1111/j.1751-908X.2014.00312.x

Welz, B., & Melcher, M. (1984). Mechanisms of transition metal interferences in hydride generation atomic-absorption spectrometry Part 1. Influence of cobalt, copper, iron and nickel on selenium determination. *The Analyst*, *109*(5), 569. https://doi.org/10.1039/an9840900569

Wykes, J. L., O'neill, H. C., & Mavrogenes, J. A. (2011). *XANES investigation of selenium speciation in silicate glasses*. Paper presented at Annual V. M. Goldschmidt Conference. Geochemical Society and European Association of Geochemistry, Prague, Czech Republic.

Wykes, J. L., O'neill, H. S. C., & Mavrogenes, J. A. (2015). The effect of FeO on the Sulfur Content at Sulfide Saturation (SCSS) and the selenium content at selenide saturation of silicate melts. *Journal of Petrology*, *56*(7), 1407–1424. https://doi.org/10.1093/petrology/egv041

Xu, G. P., Hannah, J. L., Bingen, B., Georgiev, S., & Stein, H. J. (2012). Digestion methods for trace element measurements in shales: Paleoredox proxies examined. *Chemical Geology*, *324–325*, 132–147. https://doi.org/10.1016/j.chemgeo.2012.01.029

Yi, W., Halliday, A. N., Lee, D. C., & Rehkamper, M. (1998). Precise determination of cadmium, indium and tellurium using multiple collector ICP-MS. *Geostandards and Geoanalytical Research*, *22*(2), 173–179. https://doi.org/10.1111/j.1751-908X.1998.tb00689.x

Yokoyama, T., Makishima, A., & Nakamura, E. (1999). Evaluation of the coprecipitation of incompatible trace elements with fluoride during silicate rock dissolution by acid digestion. *Chemical Geology*, *157*(3–4), 175–187. https://doi.org/10.1016/S0009-2541(98)00206-X

Yu, L. L., Fassett, J. D., & Guthrie, W. F. (2002). Detection limit of isotope dilution mass spectrometry. *Analytical Chemistry*, *74*(15), 3887–3891. https://doi.org/10.1021/ac011254l

Yu, M. Q., Liu, G. Q., & Jin, Q. (1983). Determination of trace arsenic, antimony, selenium and tellurium in various oxidation-states in water by hydride generation and atomic-absorption spectrophotometry after enrichment and separation with thiol cotton. *Talanta*, *30*(4), 265–270. https://doi.org/10.1016/0039-9140(83)80060-5

Zhu, J.-M., Johnson, T. M., Clark, S. K., & Zhu, X.-K. (2008). High precision measurement of selenium isotopic composition by hydride generation multiple collector inductively coupled plasma mass spectrometry with a ^{74}Se-^{77}Se double spike. *Chinese Journal of Analytical Chemistry*, *36*(10), 1385–1390. https://doi.org/10.1016/s1872-2040(08)60075-4

Zhu, J.-M., Johnson, T. M., Clark, S. K., Zhu, X.-K., & Wang, X.-L. (2014). Selenium redox cycling during weathering of Se-rich shales: A selenium isotope study. *Geochimica et Cosmochimica Acta*, *126*, 228–249. https://doi.org/10.1016/j.gca.2013.11.004

Available online at www.sciencedirect.com

ScienceDirect

Geochimica et Cosmochimica Acta 249 (2019) 199–224

Geochimica et Cosmochimica Acta

www.elsevier.com/locate/gca

Selenium isotope and S-Se-Te elemental systematics along the Pacific-Antarctic ridge: Role of mantle processes

Aierken Yierpan [a,*], Stephan König [a], Jabrane Labidi [a,b], Ronny Schoenberg [a,c]

[a] Isotope Geochemistry, Department of Geosciences, Eberhard Karls University of Tübingen, Wilhelmstrasse 56, 72074 Tübingen, Germany
[b] Department of Earth, Planetary, and Space Sciences, University of California Los Angeles, Los Angeles, CA, USA
[c] Department of Geology, University of Johannesburg, P.O. Box 524, Auckland Park 2006, South Africa

Received 20 June 2018; accepted in revised form 21 January 2019; Available online 29 January 2019

Abstract

The selenium stable isotope system emerges as a new potential tracer of volatile origin and evolution of the terrestrial planets. Accurate determination of the mantle Se isotope composition requires an assessment of Se isotopic behavior in magmatic processes and potential variations across all mantle reservoirs. Here we report the first high-precision Se isotope and Se–Te abundance data for a suite of basaltic glasses from the Pacific–Antarctic ridge. These MORBs display a narrow range in $\delta^{82/76}$Se values (deviation of ^{82}Se/^{76}Se relative to NIST SRM 3149) between -0.30 ± 0.09‰ and -0.05 ± 0.09‰, with an average of -0.16 ± 0.13‰ (2 s.d., $n = 27$). We quantify the main processes relevant to MORB petrogenesis in order to better understand the Se–Te elemental behavior in the mantle and investigate if these are systematically related to Se isotope variations.

We show that both Se isotopes and S–Se–Te abundances of MORB melts remain unaffected by assimilation of high-temperature hydrothermal fluids and sulfides, whereas the latter has been shown to overprint the ^{34}S/^{32}S ratios. MORB differentiation involving sulfide segregation (sulfide liquid and monosulfide solid solution) significantly fractionates Se and Te (Se/Te ratio ~ 45–190), with no systematic Se isotope variation. The Se–Te contents of the primary MORB melt corrected for magmatic differentiation can be successfully reproduced by near-fractional decompression melting of a mantle with 170–200 μg g^{-1} S (as sulfide liquid), which has either (1) "fertile lherzolite-like" Se and Te contents (80 ± 17 and 11 ± 1.7 ng g^{-1}, respectively; 1 s.d.) or (2) distinctly lower Se (49 ± 11 ng g^{-1}) and Te (3.5 ± 1.3 ng g^{-1}) contents depending on the choice of experimental partition coefficients published by different studies. Regardless, our model shows that Se-Te systematics of "fertile" lithospheric peridotites preserve little primary melt depletion signatures and reflect significant, if not complete, metasomatic overprinting. Finally, based on the observed negligible Se isotopic fractionation between sulfide phase and silicate melt, we suggest that MORBs preserve their mantle source isotopic signature ($\delta^{82/76}$Se = -0.16 ± 0.13‰). Our MORB average is similar within uncertainty to chondritic values but significantly lighter than previously published $\delta^{82/76}$Se data for basalts from a variety of geodynamic settings. The subtle but significant Se isotope variation observed within the investigated MORB suite (up to ~0.25‰) and between other mantle samples analyzed so far may reflect intrinsic source heterogeneity and potential isotopic differences across various mantle reservoirs.

Keywords: Selenium; Se isotopes; Tellurium; Sulfur; Late veneer; MORB; Pacific-Antarctic ridge; Mantle melting; Chalcophile element partitioning; Sulfide liquid; Monosulfide solid solution

* Corresponding author.
E-mail address: aierken.yierpan@uni-tuebingen.de (A. Yierpan).

https://doi.org/10.1016/j.gca.2019.01.028
0016-7037/

1. INTRODUCTION

The current primitive mantle (PM) abundances of the moderately volatile and chalcophile elements Se (~80 ng g^{-1}) and Te (~11 ng g^{-1}) are 35–45 times lower compared to the Earth's general volatile depletion trend (McDonough and Sun, 1995; Allègre et al., 2001; McDonough, 2014; Wang and Becker, 2013; Palme and O'Neill, 2014). Because extrapolation of metal–silicate partitioning experiments at 1–19 GPa to core formation conditions predicts near-complete Se–Te removal from the silicate mantle (Rose-Weston et al., 2009), the mantle abundances of Se–Te, together with that of S, have been explained to be established by a chondritic late veneer addition after core formation (Morgan, 1986; McDonough and Sun, 1995; Rose-Weston et al., 2009; Wang and Becker, 2013). However, the non-chondritic $^{34}S/^{32}S$ ratio of the mantle and recent S partitioning experiments suggest that a major fraction of mantle S budget reflects metal–silicate equilibration (Labidi et al., 2013; Suer et al., 2017). Meanwhile, it has been debated whether the broadly-chondritic relative abundances of S–Se–Te in lherzolites are representative of the PM composition (Wang and Becker, 2013) since these samples from the lithospheric mantle are often considered metasomatized, especially by Se–Te-rich base metal sulfides and associated platinum-group minerals (Lorand et al., 2003, 2004, 2010; Luguet et al., 2003, 2004, 2015; Lorand and Alard, 2010; König et al., 2014, 2015; Harvey et al., 2015). In this context, mantle-derived melts such as mid-ocean ridge basalts (MORBs) may provide a complementary and broader picture regarding the composition of the asthenospheric mantle, provided that Se–Te elemental behavior in mantle processes is well constrained.

There are only few studies concerning Se and/or Te elemental systematics in MORB (Hertogen et al., 1980; Yi et al., 2000; Jenner et al., 2010, 2015; Lissner et al., 2014). Because of their strong partitioning into base metal sulfides (Peach et al., 1990; Guo et al., 1999; Hattori et al., 2002; Barnes et al., 2009; Patten et al., 2013; Brenan, 2015; Kiseeva et al., 2017), Se–Te abundances and ratios in basaltic melts are strongly controlled by sulfide phase–silicate melt partitioning (Hertogen et al., 1980; Lissner et al., 2014). Hertogen et al. (1980) first observed distinctly higher Se/Te ratios and broadly similar Te contents in worldwide MORBs compared to mantle rocks and suggested a higher apparent compatibility of Te relative to Se during partial melting. This appears consistent with observations from lherzolites, pyroxenites (Wang et al., 2013; Wang and Becker, 2013, 2015a), and sulfides in sub-arc mantle xenoliths (Hattori et al., 2002), but inconsistent with observations from refractory harzburgites and platinum group minerals (König et al., 2012, 2014, 2015). Lissner et al. (2014) investigated the Se–Te systematics in enriched- and depleted-MORBs from a restricted section of the southern Mid-Atlantic Ridge and suggested an incompatible behavior of both elements and a higher incompatibility of Te during partial melting. This relative partitioning seems to be reversed during magmatic differentiation (Lissner et al., 2014). These observations might be partly attributed to contrasting relative partitioning of Se–Te in different sulfide phases and platinum-group minerals (e.g., Helmy et al., 2010; Liu and Brenan, 2015; Brenan, 2015; König et al., 2015) during different mantle processes. Previous evidence for Se and Te behavior in MORB petrogenesis remains ambiguous and warrants further work.

On the other hand, Se isotopes might provide new perspectives on the origin of S–Se–Te as well as other highly siderophile or volatile elements on Earth. Due to analytical difficulties (e.g., Yierpan et al. 2018), only few studies reported Se isotope composition ($\delta^{82/76}$Se; deviation of $^{82}Se/^{76}Se$ relative NIST SRM 3149) of mantle rocks/melts, which are limited to geological reference materials (Rouxel et al., 2002; Kurzawa et al., 2017; Yierpan et al., 2018). Compared to the chondrite average $\delta^{82/76}$Se of -0.30 ± 0.39‰ (Vollstaedt et al., 2016) and -0.21 ± 0.31‰ (2 s.d.; Labidi et al., 2018), previously analyzed basalts ($n = 9$) and one peridotite show heavier $\delta^{82/76}$Se with some marginal overlap. Labidi et al. (2018) reported resolvable mass-dependent Se isotope variations among main chondrite groups, ranging between -0.40 ± 0.07‰ (enstatite chondrite) and -0.01 ± 0.09‰ (CI-chondrite). Recent high-precision Se isotope analyses on a small number of different basalts show a rather restricted range in $\delta^{82/76}$Se ($+0.21 \pm 0.15$‰, $n = 4$; Kurzawa et al., 2017; Yierpan et al., 2018). These rocks originate from a variety of geodynamic settings and cover a wide range of Se contents (~15–170 ng g^{-1}) and Se/Te ratios (~3–65), indicating various mantle sources and/or igneous differentiation histories (Yierpan et al., 2018). It thus remains unclear whether their $\delta^{82/76}$Se values readily represent a mantle source signature.

In this study, we present the first Se isotope compositions and new Se–Te abundances for a total of 27 fresh MORB glasses collected from the Pacific–Antarctic ridge (65–56°S and 53–41°S). Compared to the sampling areas in previous Se–Te studies (Hertogen et al., 1980; Lissner et al., 2014), these ridge sections are free of plume influence and represent melts derived from a source with first-order major element homogeneity (Vlastélic et al., 2000; Moreira et al., 2008; Hamelin et al., 2010). It is thus an ideal sample set for (1) better understanding Se–Te elemental behavior during mantle processes using recently published experimental sulfide–silicate melt partitioning data and (2) investigating effects of such processes on potential Se isotope fractionation in order to constrain the isotopic composition of the depleted mantle.

2. SAMPLES AND GEOLOGICAL BACKGROUND

We have analyzed 27 on-axis MORB glasses from two sections of the Pacific–Antarctic ridge (PAR): 65–56°S ($n = 10$) and 53–41°S ($n = 17$) (Supplementary Fig. S1). These samples were collected from the PAR by the French research vessel *L'Atalante* during the cruises PACANTARCTIC 1 (65–56°S; Géli et al., 1997; Vlastélic et al., 1999) and PACANTARCTIC 2 (53–41°S; Klingelhoefer et al., 2006; Moreira et al., 2008; Hamelin et al., 2010). The PAR extends southward from the southern end of the Juan Fernandez microplate at 35°S,110°W (Francheteau et al., 1987) to the Macquarie triple junction at 62°S, 161°E (Falconer, 1972). The studied ridge sections are

located to the north of the Vacquier Fracture Zone (FZ; ~53°S) and south of Udintsev FZ (~56–57°S; Supplementary Fig. S1), respectively, with the Eltanin FZ System in between (Watts et al., 1988; Geli et al., 1997; Castillo et al., 1998). The northern section is separated by the Menard FZ (~50°S), which is the major geological feature along the sampling area (Hamelin et al., 2010). Two ridge sections have half-spreading rates of 46–50 mm/year between 52 and 42°S (Lonsdale, 1994) and 27–37 mm/year between 65 and 55°S (Hamelin et al., 2010). The northern ridge section is one of the fastest spreading mid-ocean ridges (Moreira et al., 2008) and, therefore, shows a uniform axial high morphology along the crest (Klingelhoefer et al., 2006). In contrast, the southern section (slow to intermediate spreading ridge) displays variable axis morphologies, ranging from axial valley to axial high (Vlastélic et al., 2000; Ondréas et al., 2001). The oceanic crust beneath the PAR is estimated to be 6–7 km (Adams, 1964).

Previous analyses of He, Sr, Nd, Hf, and Pb isotopes show that the studied PAR sections are free from any plume-ridge interactions and reflect a regional-scale first-order mantle source homogeneity (Vlastélic et al., 1999, 2000; Moreira et al., 2008; Hamelin et al., 2010, 2011). However, the ridge sections display clear latitudinal variations of radiogenic isotopes, with gradually increasing recycled crust component northwards (Hamelin et al., 2011). This is interpreted to be a subtle yet intrinsic source heterogeneity resulting from progressive mixing of a depleted MORB mantle and recycled oceanic crust. Besides, almost all PAR samples have experienced contamination by Cl-rich brines and/or hydrothermally altered crust during low-pressure magmatic differentiation, which results in significantly heavier S isotope composition if it is associated with hydrothermal sulfide assimilation (Clog et al., 2013; Labidi et al., 2014; Bezard et al., 2016).

3. ANALYTICAL METHODS

3.1. Selenium isotope and Se–Te elemental analyses

Most of the studied PAR basalts are in the form of fresh glass fragments. A few samples have plagioclase phenocrysts (<3 mm) and slightly altered yellowish crusts. After they were crushed, fresh chips (1–5 mm) were picked, washed with 18.2 MΩ·cm water in an ultrasonic bath and ground to fine powders. At least 2.5 g sample was used for grinding in order to preclude any potential effect of sample heterogeneity (Wang et al., 2015; Yierpan et al., 2018). One sample (PAC2 DR01-1) is represented by both glass rims and pillow interior, which were processed and analyzed separately.

All analyses were conducted at the University of Tübingen. Selenium isotope and Se–Te concentrations were determined from the same sample digest. Details of the chemistry and instrumental procedures are given in Kurzawa et al. (2017) and Yierpan et al. (2018). Briefly, Se contents of most sample unknowns were first determined via isotope dilution by estimating a spike–sample ratio of ~1 based on a general Se vs MgO or S trend previously shown for MORB (Lissner et al., 2014). For this procedure, only ~0.025 g of sample was digested and analyzed directly after separating Fe (see below; but with 2.5 mL resin and 6 N HCl). After Se content was determined, ~0.15–0.4 g of sample was mixed with ^{74}Se–^{77}Se double spike and ^{125}Te single spike to yield Se and Te spike–sample ratios of ~1 and ~0.6–1, respectively. Samples were then digested in a HF–HNO_3 mixture at 85 °C and evaporated at 65 °C. This is followed by heating in 6 N HCl at 130 °C and complete evaporation at 85 °C. In order to remove Ge while minimizing evaporative Se losses, samples were additionally dissolved and dried down twice with 10.5 N HCl at 85 °C in the presence of rock matrix. Selenium was purified by a two-stage column chemistry using 7 mL of Eichrom AG1-X8 and AG 50W-X8 (both 100–200 mesh) ion exchange resins (collected in 4 N HCl and 0.1 N HNO_3, respectively). The dry Se cuts were subsequently dissolved and evaporated in 10.5 N HCl. Tellurium was collected in 0.4 N HCl from the first column after eluting Se and most matrix elements with 4 N HCl and Fe with a 2 N HCl–5 N HF mixture. Finally, the dry Se and Te fractions were taken up in 1 mL 2 N HCl for analysis. Total procedural recoveries of Se and Te for MORBs are systematically ~85–95%, higher than that for reference materials (~80%; Yierpan et al., 2018). Procedural blanks ($n = 5$) yield signal intensities for each isotope indistinguishable from the background (2 N HCl), which are equivalent to ~0.05 and 0.01 ng for Se and Te, respectively.

Selenium isotopes were measured on a ThermoFisher Scientific NeptunePlus multi-collector inductively coupled plasma mass spectrometer (MC-ICP-MS) connected to a HGX-200 hydride generator. The double spike method was used to correct for isotopic fractionation during the chemistry and instrumental analysis. Each analysis was bracketed by 30 ng mL^{-1} spiked NIST SRM 3149 standard. The Se isotope composition is expressed using δ-notation relative to the international reference material NIST SRM 3149 following:

$$\delta^{82/76}\mathrm{Se}_{\mathrm{Sample}} = \frac{\left(^{82}\mathrm{Se}/^{76}\mathrm{Se}\right)_{\mathrm{Sample}}}{\left(^{82}\mathrm{Se}/^{76}\mathrm{Se}\right)_{\mathrm{NIST\ SRM\ 3149}}} - 1 \quad (1)$$

$\delta^{82/76}$Se values are reported in ‰ units by multiplication with a factor of 1000. In order to fully eliminate residual Ge that represents a significant isobaric interference (Stüeken et al., 2013; Pogge von Strandmann et al., 2014), post-chemistry Se fractions were additionally evaporated (1–2 times) in HCl at 85–90 °C and monitored for Ge using sample aliquots before analysis (Luais, 2012; Yierpan et al., 2018). Each analyzed sample yields ^{72}Ge/^{82}Se < 0.0002 (with <~10% evaporative Se loss). Hydride interferences of Se, Br, and ArAr are generally insignificant owing to the methane addition (Floor et al., 2011; Kurzawa et al., 2017) and associated corrections (mainly SeH) on $\delta^{82/76}$Se are typically ≤ 0.04‰. For most sample analyses, ~20–40 ng Se was used and the internal error (2 standard error, 2 s.e.) of a single measurement over 40 cycles is mostly < 0.05‰. Analytical accuracy and precision were monitored by analyses of inter-laboratory standard MH-495 (30 ng mL^{-1}; Supplementary Table S1) and three reference materials (Table 1; Fig. 1). The MH-495 yields an average $\delta^{82/76}$Se of −3.24 ± 0.07‰ (2 s.d., $n = 20$), in excellent agreement with literature values (Zhu et al., 2008;

Table 1
Selenium isotope composition and Se–Te abundances of geological reference materials and a randomly selected PAR MORB glass reported in this study and literature.

Sample	Weight (g)	$\delta^{82/76}$Se (‰)	2 s.e.[a] (‰)	Se[b] (ng g^{-1})	Te (ng g^{-1})
BHVO-2	0.193	0.13	0.07	164	14.4
	0.201	0.15	0.05	168	14.2
	0.238	0.04	0.08	164	14.0
	0.400	0.06	0.08	165	14.3
Average		0.10 ± 0.11		165 ± 2	14.2 ± 0.2
Rouxel et al. (2002)[c]		0.32 ± 0.32 ($n = 1$)		74 ($n = 1$)	
Wang et al. (2015)				170 ± 22 ($n = 3$)	14.4 ± 0.3 ($n = 3$)
Yierpan et al. (2018)		0.18 ± 0.10 ($n = 8$)		169 ± 3 ($n = 61$)	14.2 ± 0.3 ($n = 24$)
BCR-2	0.406	0.18	0.09	78	2.65
	0.450	0.15	0.07	79	2.54
Rouxel et al. (2002)[c]		0.24 ± 0.32 ($n = 1$)		90 ($n = 1$)	
Lissner et al. (2014)				78 ± 3 ($n = 5$)	2.73 ± 0.06 ($n = 5$)
Kurzawa et al. (2017)		0.18 ± 0.11 ($n = 3$)		71 ± 4 ($n = 3$)	
Yierpan et al. (2018)		0.29 ± 0.10 ($n = 5$)		76 ± 1 ($n = 18$)	2.54 ± 0.08 ($n = 5$)
W-2a	0.454	0.00	0.04	105	1.78
Yierpan et al. (2018)		-0.09 ± 0.11 ($n = 6$)		107 ± 1 ($n = 8$)	1.71 ± 0.07 ($n = 6$)
PAC2 DR33-1	0.150	−0.16	0.03	201	2.14
	0.210 (a)[d]	−0.10	0.04	198	2.20
	0.210 (b)[d]	−0.11	0.07	198	
	0.232	−0.16	0.03	198	2.18
	0.238	−0.19	0.04	198	
	0.241	−0.18	0.03	197	2.23
	0.255	−0.22	0.03	199	2.27
	0.402 (a)[d]	−0.12	0.04	201	2.17
	0.402 (b)[d]	−0.10	0.05	201	
Average		-0.15 ± 0.09		199 ± 2	2.20 ± 0.05

Note: Uncertainties are 2 s.d. for $\delta^{82/76}$Se and 1 s.d. for Se–Te concentrations; numbers in parentheses denote different sample digestions; $\delta^{82/76}$Se data from Rouxel et al. (2002) are converted relative to NIST SRM 3149 (Carignan and Wen, 2007) considering error propagation (analytical and conversion errors); quoted uncertainties on $\delta^{82/76}$Se are conservatively represented by either the external reproducibility of the sample $\delta^{82/76}$Se or analytical precision as reported in the literature, whichever is larger.

[a] Internal uncertainty of each individual measurement (over 40 cycles) given in 2 standard error (2 s.e.).

[b] Selenium concentrations listed here were obtained by double spike inversion.

[c] Rouxel et al. (2002) analyzed BHVO-1 and BCR-1.

[d] Replicate analyses of the final sample solutions from the same digestion.

Kurzawa et al., 2017; Labidi et al., 2018; Yierpan et al., 2018). The $\delta^{82/76}$Se values of BHVO-2 ($+0.10 \pm 0.11$‰; 2 s.d., $n = 4$) and W-2a (0.00 ± 0.04‰; 2 s.e., $n = 1$) are comparable to the previously reported values of $+0.18 \pm 0.10$‰ (2 s.d., $n = 8$) and -0.09 ± 0.11‰ (2 s.d., $n = 6$), respectively (Yierpan et al., 2018; Fig. 1). Two BCR-2 digestions yield $\delta^{82/76}$Se values ($+0.18 \pm 0.09$‰ and $+0.15 \pm 0.07$ ‰; 2 s.e.) that are identical to the average value from Kurzawa et al. (2017) ($+0.18 \pm 0.11$‰; 2 s.d., $n = 3$) but somewhat lower than that from Yierpan et al. (2018) ($+0.29 \pm 0.10$‰; 2 s.d., $n = 5$; Fig. 1). BCR-2 yields an overall average $\delta^{82/76}$Se of $+0.23 \pm 0.14$‰ (2 s.d., $n = 10$), whose uncertainty is slightly higher than a typical external reproducibility of 0.10–0.12‰ (2 s.d.) on other reference materials (Fig. 1; Yierpan et al., 2018). Note that all these analyses were performed in the same lab (Fig. 1). Considering potentially smaller sample heterogeneity in a glass matrix relevant to this study, the external reproducibility for MORB was assessed by replicate analyses of a randomly selected moderately evolved sample (PAC2 DR33-1; 6.63 wt.% MgO) with different sample amounts (0.15–0.4 g; Table 1). We obtain a 2 s.d. uncertainty of 0.09‰ from 7 digestions and 9 measurements (4 different sessions over 6 months).

The isotope dilution concentrations for Te (and when necessary, also for Se; Table 2) were determined on a ThermoFisher Scientific iCAP-Qc quadrupole ICP-MS connected to an ESI hydrideICP hydride generator. Only ~0.1–0.3 ng Te and 0.5–1 ng Se (in 1 mL 2 N HCl) were used for each analysis. The analytical precision of our method was previously reported to be ~2–3% r.s.d. (relative standard deviation) for both Se and Te. All reference materials yield Se–Te concentrations that are in general agreement with the recently published data (Table 1; Lissner et al., 2014; Wang et al., 2015; Yierpan et al., 2018). The Se concentrations of MORBs obtained by double spike inversion and isotope dilution are always comparable within 2% and both reproduce at ~2% r.s.d. (Tables 1 and 2).

3.2. Trace element analysis

Only a few trace element data have been published for the PAC1 samples (latitude 65–56°S), whereas the data for PAC2 samples (latitude 53–41°S) are relatively complete

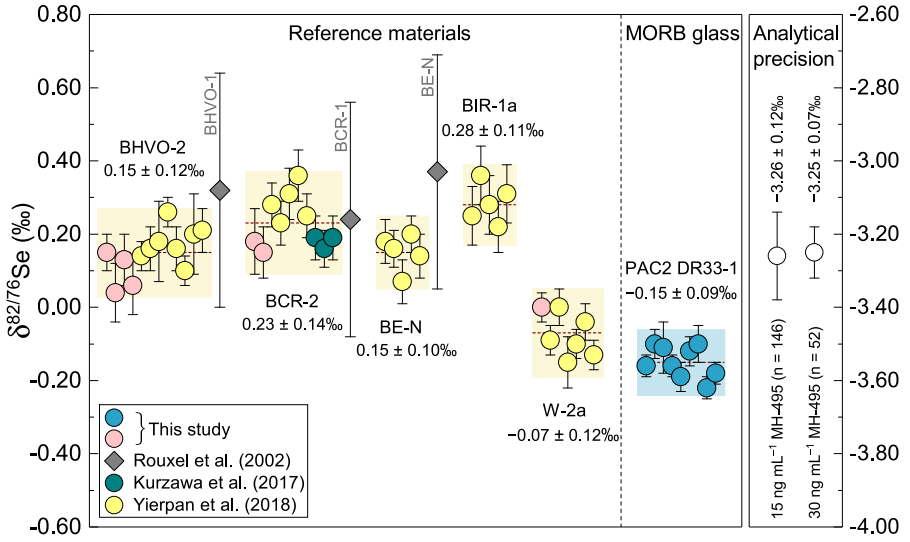

Fig. 1. Measurements of geological reference materials and a randomly selected moderately evolved PAR glass (PAC2 DR33-1; 6.63 wt.% MgO; Table 1) for assessing the external reproducibility (2 s.d.) on the sample $\delta^{82/76}$Se (left panel). Each symbol represents an individual measurement with the associated internal precision (2 s.e.; over 40 cycles). All sample digests were analyzed once, except for two MORB glass digestions that were aliquoted and analyzed twice. Our analytical accuracy and precision is evaluated by the long-term reproducibility of inter-laboratory standard MH-495 (open circles; right panel), which yields -3.26 ± 0.12‰ and -3.25 ± 0.07‰ (2 s.d.) for 15 and 30 ng mL^{-1} solutions, respectively (Supplementary Table S1; this study; Kurzawa et al., 2017; Yierpan et al., 2018). Shown for comparison are literature data on reference materials reported by Kurzawa et al. (2017), Yierpan et al. (2018) (measurements in both studies were performed over the course of ~18 months at the University of Tübingen; all circles), and Rouxel et al. (2002) (diamonds). Interlaboratory comparison of $\delta^{82/76}$Se data on silicate samples remains difficult due to the limited Se isotope studies, and therefore BHVO-2 and BCR-2 are compared here with BHVO-1 and BCR-1 (only BE-N has been analyzed by two working groups). $\delta^{82/76}$Se from Rouxel et al. (2002) that were originally reported relative to MERCK standard are converted relative to NIST SRM 3149 following Carignan and Wen (2007) considering error propagation (analytical and conversion errors of 0.25‰ and 0.20‰, respectively). (For interpretation of the references to color in the figures, the reader is referred to the web version of this article.)

(Supplementary Table S2; Vlastélic et al., 2000; Hamelin et al., 2010; Clog et al., 2013; Labidi et al., 2014; Bezard et al., 2016). To fully characterize the samples, we report a more complete set of trace element data (43 elements). The measurements were performed at the University of Tübingen by solution ICP-MS following the method previously described by Babechuk et al. (2010) and Albut et al. (2018). About 0.02 g of sample powder was digested and diluted with 2% HNO_3 containing an internal standard solution (^{6}Li, In, Re, and Bi) to the analyte solution with a final dilution factor of ~10,000. Reproducibility and accuracy of trace element determinations were evaluated from the average data of BHVO-2 (quality control standard) from 14 analyses of 6 separate digestions (4 digested together with the PAR samples). Our BHVO-2 results (Supplementary Table S3) show uncertainties better than ~5% r.s.d. for all elements except for Mo, Sb, W, and Tl (~8–20%). Most data agree within ~5% with previously reported values (GeoReM; Jochum et al., 2005).

4. RESULTS

4.1. Major/trace element composition

The trace element concentrations determined here, together with all available major/trace element, radiogenic/stable isotope data, are compiled in Supplementary Table S2. All samples are typical N-MORB (normal MORB) with $(La/Sm)_N$ ratios of 0.461–0.965 (normalized to PM; McDonough and Sun, 1995), except PAC2 DR27-1 ($(La/Sm)_N = 1.227$), which is the most evolved sample (4.52 wt.% MgO) and dredged from a seamount-ridge transition zone (Hamelin et al., 2010). The PM-normalized trace element patterns of PAR glasses are similar to that of the average N-MORB compiled by Gale et al. (2013) (Supplementary Fig. S2). Variations in major element compositions of the studied samples span the entire spectrum observed in PAR basalts from 65–56°S and 53–41°S, with MgO content from 8.85 to 4.52 wt.% (Supplementary Fig. S3). This MgO range is larger than that of MORBs previously investigated for Se–Te systematics (7.02–9.23 wt.%; Hertogen et al., 1980; Lissner et al., 2014). The most evolved glasses (MgO < 5 wt.%; $n = 3$) have experienced titanomagnetite fractionation, evidenced by a decrease in Ti and Fe from the general trend after 5 wt.% MgO (Supplementary Fig. S3; Vlastélic et al., 2000; Hamelin et al., 2010). Similar abrupt drops are also consistently observed for concentrations of Zn, Ga, Mn (not shown), V, Sc, and Co in these evolved samples (e.g., Supplementary Fig. S2), probably resulted from the magnetite saturation and/or the induced sulfide segregation due to their strong partitioning into these phases (Nielsen et al., 1994; Toplis and Corgne, 2002; Righter et al., 2006; Jenner et al., 2010, 2012, 2015; Dare et al., 2012, 2014; Labidi et al., 2014).

Table 2
Selenium isotope composition, S–Se–Te abundances, and selected major element composition of the studied PAR glasses.

Sample	$\delta^{82/76}$Se (‰)	2 s.e.[a] (‰)	n[b]	Se (ng g^{-1})	s.d.[c] (ng g^{-1})	n[d]	Te (ng g^{-1})	s.d.[c] (ng g^{-1})	Se/Te	s.d.	S (μg g^{-1})	MgO (wt.%)	FeO_T (wt.%)
PAC1 CV02-g	−0.23	0.05	1	180	4	2	1.99	0.06	90	3	1171	7.74	10.5
PAC1 CV03-g	−0.19	0.05	1	158	1	3	3.19	0.10	50	2	938	8.57	8.60
PAC1 CV04-g	−0.15	0.04	1	176	4	1	4.10	0.12	43	2	940	8.78	8.55
PAC1 DR05-1g	−0.22	0.04	1	167	3	1	3.06	0.09	55	2	932	8.33	8.42
PAC1 DR06-g	−0.30	0.05	1	177	2	3	1.61	0.05	110	4	1351	6.93	11.2
PAC1 DR07-1g	−0.06	0.05	1	186	4	2	2.23	0.07	83	3	1301	6.83	10.7
PAC1DR10-1g	−0.24	0.08	1	170	3	3	2.68	0.08	63	2	1047	4.83	10.8
PAC1 DR11-1g	−0.10	0.05	1	174	3	1	3.06	0.09	57	2	1153	7.33	9.25
PAC1 DR12-1g	−0.15	0.04	1	165	3	2	3.70	0.11	45	2	968	8.85	8.49
PAC1 DR13-2g	−0.21	0.05	2	194	2	5	1.95	0.06	99	3	1259	7.42	11.0
PAC2 DR01-1 glass	−0.13	0.04	1	166	3	1	2.52	0.08	66	2	1116	7.30	9.67
PAC2 DR01-1 basalt	−0.18	0.05	1	167	3	1	2.39	0.07	70	2			
PAC2 DR04-2	−0.09	0.03	1	168	3	1	2.33	0.07	72	3	1199	7.08	10.5
PAC2 DR05-2g	−0.06	0.04	2	176	4	2	1.43	0.04	123	4	1339	6.52	12.1
PAC2 DR08-1	−0.15	0.04	1	194	4	1	2.76	0.08	70	2	1239	7.05	11.4
PAC2 DR20-1	−0.15	0.06	2	193	4	2	1.68	0.05	115	4	1550	4.60	12.8
PAC2 DR21-2	−0.17	0.04	2	198	4	2	1.97	0.06	101	4	1312	6.73	11.3
PAC2 DR22-1	−0.22	0.02	1	187	4	1	2.47	0.07	76	3	1172	7.25	10.5
PAC2 DR27-1	−0.14	0.04	2	219	4	2	1.16	0.03	189	6	1755	4.52	14.1
PAC2 DR28-2	−0.15	0.05	2	174	3	2	3.32	0.10	52	2	1112	7.85	10.0
PAC2 DR29-1	−0.05	0.07	1	210	4	2	2.07	0.06	101	4	1471	6.16	12.4
PAC2 DR30-1	−0.12	0.07	2	195	1	4	2.21	0.07	88	3	1348	7.00	11.2
PAC2 DR31-3	−0.09	0.07	2	193	4	2	3.17	0.10	61	2	1208	7.55	10.5
PAC2 DR32-1	−0.10	0.07	1	186	4	1	1.97	0.06	94	4	1321	6.80	11.3
PAC2 DR33-1	−0.15	0.08	7	199	1	9	2.20	0.05	90	2	1340	6.63	11.5
PAC2 DR34-1	−0.30	0.05	1	168	1	3	2.63	0.08	64	2	1094	8.00	9.39
PAC2 DR36-1	−0.13	0.08	2	194	1	5	2.26	0.07	86	3	1381	7.07	11.3
PAC2 DR38-1	−0.16	0.05	2	180	1	4	3.12	0.09	58	2	1244	8.35	9.72

Note: S data from Labidi et al. (2014); MgO and FeO_T (total Fe expressed as FeO) data from Vlastélic et al. (2000) and Hamelin et al. (2010).
[a] For replicate digestions, the highest 2 s.e. is reported.
[b] Number of digestions for combined Se isotope and Te concentration analyses.
[c] Uncertainties are 1 s.d. of the mean for $n \geq 3$ and conservatively estimated using the long-term external reproducibility of ~3% (Yierpan et al., 2018) for $n < 3$.
[d] Total number of Se concentration determinations by double spike inversion and isotope dilution.

4.2. Selenium isotope composition and Se–Te abundances

The selenium isotope composition and Se–Te concentrations of the studied PAR samples are reported in Table 2 together with S (Labidi et al., 2014) and selected major element data. The uncertainties on $\delta^{82/76}$Se and Se–Te abundances throughout the text are given in 2 and 1 s.d., respectively. The PAR glasses display $\delta^{82/76}$Se values ranging between -0.30 ± 0.09‰ and -0.05 ± 0.09‰, with an average of $\delta^{82/76}Se = -0.16 \pm 0.13$‰ ($n = 27$; Figs. 2 and 3). The differences in $\delta^{82/76}$Se between sample duplicates ($n = 12$) never exceeded the 2 s.d. external reproducibility of 0.09‰ (Table 1). The glassy rim and pillow interior of PAC2 DR01-1 that were analyzed separately yield identical $\delta^{82/76}$Se values within uncertainty (-0.13 ± 0.09‰ and -0.18 ± 0.09‰, respectively; Table 2). However, small but resolvable isotopic variations (up to 0.25 ± 0.13‰ in $\delta^{82/76}$Se) are observed between different samples (e.g., between PAC1 DR06-g and PAC2 DR29-1, with $\delta^{82/76}$Se of -0.30 ± 0.09‰ and -0.05 ± 0.09‰, respectively). These variations are not systematically related to the sample latitude or ridge axial depth (Fig. 2a and b). The average $\delta^{82/76}$Se of the two PAR sections (Fig. 2a) are identical within uncertainty: -0.14 ± 0.12‰ north of the Vacquier FZ ($n = 17$) and -0.19 ± 0.14‰ south of the Udintsev FZ ($n = 10$). $\delta^{82/76}$Se values of the samples are fairly constant over the wide range of Se abundances observed (158–219 ng g^{-1}; Fig. 2c).

The MORBs show systematic offset towards lighter Se isotope composition compared to all previously analyzed basalts (average $\delta^{82/76}$Se between $+0.21 \pm 0.15$‰ and $+0.30 \pm 0.32$‰; $n = 9$) and one peridotite ($+0.24 \pm 0.32$‰), with some marginal overlap with the latter (Fig. 3; Rouxel et al., 2002, 2004; Kurzawa et al., 2017; Yierpan et al., 2018; this study). The MORB average $\delta^{82/76}$Se (-0.16 ± 0.13‰) lies in the range of chondritic values of -0.30 ± 0.39‰ ($n = 14$; Vollstaedt et al., 2016) and -0.21 ± 0.31‰ ($n = 20$; Labidi et al., 2018) (Fig. 3). Specifically, it is similar within uncertainty to $\delta^{82/76}$Se values of ordinary chondrites (-0.21 ± 0.10‰; $n = 9$) and CO (-0.19 ± 0.07‰; $n = 2$), CV (-0.25 ± 0.12‰; $n = 2$), and CI (-0.01 ± 0.09‰; $n = 2$) carbonaceous chondrites, but distinct from that of enstatite chondrites (-0.40 ± 0.07‰; $n = 3$; Labidi et al., 2018; Fig. 3).

Fig. 4 presents the variation of Se, Te, S, and Cu abundances and/or their ratios versus MgO contents of PAR

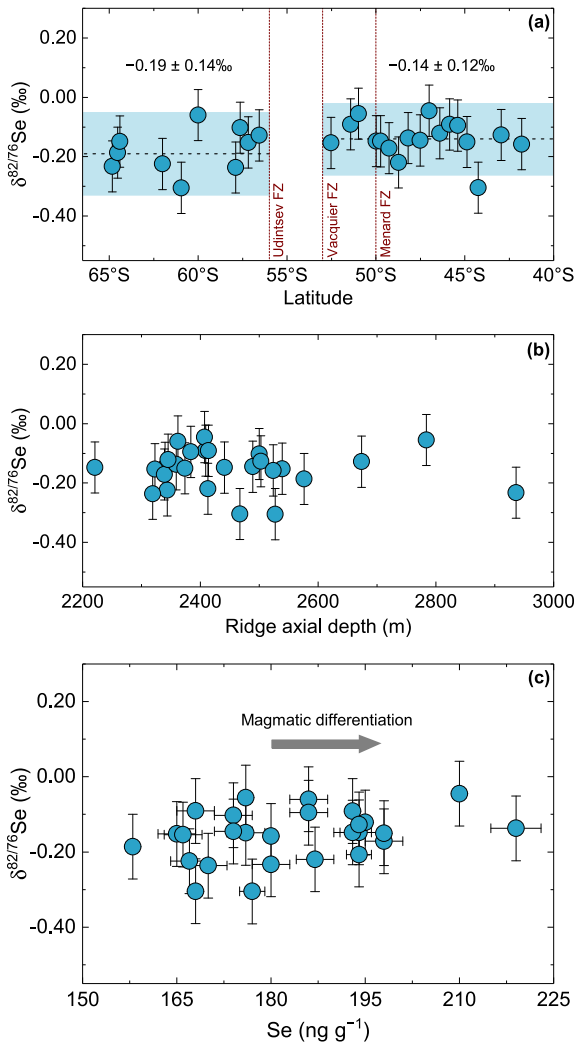

Fig. 2. Variation of Se isotope composition of PAR glasses with (a) sample latitude, (b) dredging depth, and (c) Se abundance. Two ridge sections (north of the Vacquier FZ and south of the Udintsev FZ) display identical average $\delta^{82/76}$Se values within uncertainty (a).

basalts. The generally negative correlation of Se (from 158 ± 1 to 219 ± 4 ng g^{-1}) and positive correlations Te (from 4.10 ± 0.12 to 1.16 ± 0.03 ng g^{-1}) with MgO show their apparently contrasting compatibilities (Fig. 4a and b), which result in significant Se/Te fractionation (increasing from 42.9 ± 1.1 to 188.8 ± 4.7 with decreasing MgO content; Fig. 4c). Selenium in PAR MORBs seems to behave as an apparently incompatible element, opposite to observations from the southern Mid-Atlantic Ridge (SMAR) basalts (Lissner et al., 2014). At a given MgO, PAR MORBs tend to have higher Se content than SMAR N-MORBs (Fig. 4a). Two samples from the Indian ocean have anomalously high Se contents (~330 ng g^{-1}) compared to the range in PAR and SMAR, but these samples have probably been affected by assimilation of wall-rock sulfide cumulates (Fig. 4a; Hertogen et al., 1980). Tellurium displays similarly apparent compatibility in a global context (Fig. 4b; Hertogen et al., 1980; Yi et al., 2000; Lissner et al., 2014). It is noteworthy, however, that Te contents in SMAR E-MORBs (i.e., enriched- and transitional-type MORBs) are generally higher than in N-MORBs, attributed to Te enrichment (relative to Se) in an E-MORB mantle source (Lissner et al., 2014). This is in agreement with the distinctly lower Se/Te and S/Te ratios of E-MORBs compared to N-MORBs over almost the entire melt evolution in both PAR and SMAR (Fig. 4c and e). Besides, the S/Se variations in these settings (Fig. 4d) appear to follow two distinct trends, with Se being more compatible relative to S in the SMAR melts than in PAR melts. The Cu/Se ratios in both PAR and SMAR for MgO contents above ~7–7.5 wt.% remain fairly constant and identical (418 ± 24 and 408 ± 22, respectively; Fig. 4f). The constant Cu/Se ratios were previously interpreted to reflect a similar geochemical behavior of these elements based on a relatively small data set (MgO ~ 7–9 wt.%; Lissner et al., 2014). Below ~7 wt.% MgO, the Cu/Se ratios of PAR basalts smoothly decrease from 346 to 178, indicating an overall higher compatibility of Cu.

5. DISCUSSION

5.1. Effects of non-magmatic processes on Se isotopes and S–Se–Te abundances

Non-magmatic processes that may potentially affect the S–Se–Te systematics of MORB melts generally include eruption-related degassing and assimilation of hydrothermal fluids during and/or after MORB differentiation in crustal magma chambers (Jenner et al., 2010; Floor and Román-Ross, 2012; Labidi et al., 2014; Lissner et al., 2014). All the studied PAR glasses are sulfide saturated as evidenced by the systematically observed immiscible sulfide droplets and the correlation between S and FeO contents (Labidi et al., 2014). The latter, together with the lack of correlation between S content and eruption depth (~2220–2950 m; Supplementary Table S2), also argues against eruptive S degassing (Moore and Fabbi, 1971; Moore and Schilling, 1973; Mathez, 1976; Wallace and Edmonds, 2011; Labidi et al., 2014). Little is known about the Se–Te gaseous species and their formation conditions in igneous systems. Similar to S, Se and Te are possibly dissolved in a silicate melt as Se^{2-} and Te^{2-} and/or Se^{4+} and Te^{4+} depending on the prevailing oxygen fugacity (e.g., Nagamori and Mackey, 1977; Fang and Lynch, 1987; Choi and Cho, 1997; Wykes et al., 2011). In the case of (PAR) MORB, S occurs almost exclusively as reduced S^{2-} and retained in the glass during submarine quenching (Labidi et al., 2014). Since transition of selenide and telluride to oxyanions requires higher redox potential relative to sulfide (Se > Te > S at a given temperature and pH; Yamamoto 1976; Brookins, 1988; McPhail, 1995; Johnson, 2004; König et al., 2019), we suggest that Se and Te are dissolved in MORB melts in the form of Se^{2-} and Te^{2-} and are (also) unlikely to degas during submarine eruption (also see Yi et al., 2000; Jenner et al., 2010; Lissner et al., 2014). This would be in accordance with the lack of a systematic variation of Se isotopes (Fig. 2b) and Se–Te contents (not shown) with the ridge axial depth (>2220 m).

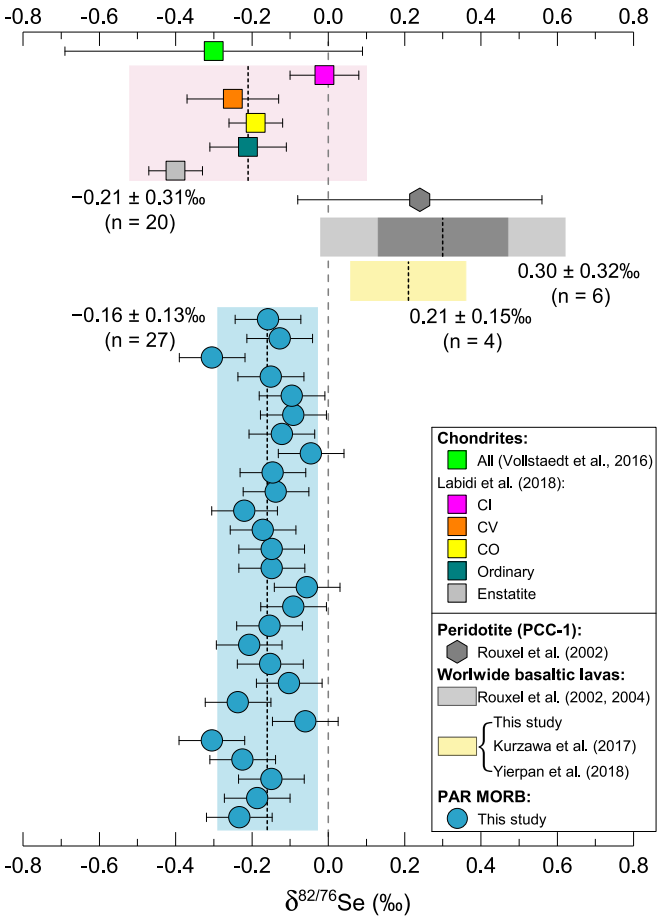

Fig. 3. Compilation of Se isotope compositions of PAR MORBs, terrestrial rock standards (7 basalts and 1 peridotite; Rouxel et al., 2002; Kurzawa et al., 2017; Yierpan et al., 2018; this study), basalts from a lava lake near the Lucky Strike hydrothermal field ($n = 2$; Rouxel et al., 2004), and main chondrite classes (Vollstaedt et al., 2016; Labidi et al., 2018). See Fig. 1 and Yierpan et al. (2018) for details on the measured basaltic rock standards. The peridotite analyzed by Rouxel et al. (2002) is a partially serpentinized harzburgite (PCC-1; Jain et al., 2000). Each shaded field represents the average $\delta^{82/76}$Se (black dashed line) with 2 s.d. uncertainties of chondrite and terrestrial rocks. Red dashed line denotes $\delta^{82/76}Se = 0‰$. The overall chondrite average $\delta^{82/76}$Se from Labidi et al. (2018) includes all chondrite groups analyzed (enstatite, ordinary, and carbonaceous) except three weathered CV chondrites. The data from Rouxel et al. (2002, 2004) is converted relative to NIST SRM 3149 following the approach of Carignan and Wen (2007) while considering error propagation (analytical and conversion uncertainties); the light and dark grey fields represent the uncertainties of the mean with (0.32‰) and without (0.17‰) error prorogation, respectively.

The majority of PAR basalts have experienced interaction with chlorine-rich brines and/or hydrothermally altered materials during magmatic differentiation (Clog et al., 2013; Labidi et al., 2014). We have examined the potential effect of hydrothermal fluid contamination on Se isotopes and Se–Te concentrations using Cl/K ratio as an indicator of the extent of chlorine contamination because Cl and K are not fractionated during magmatic processes (Fig. 5; Michael and Cornell, 1998; Clog et al., 2013; Labidi et al., 2014). Previous studies on PAR samples show that this process did not significantly affect D/H ratios and stable Mo isotope compositions (Clog et al., 2013; Bezard et al., 2016), but systematically shifted the S isotope compositions towards heavier values (>−0.5‰ in $\delta^{34}S_{V\text{-}CDT}$) when the chlorine contamination was associated with high-temperature (>300 °C) hydrothermal sulfide assimilation (Fig. 5a; Labidi et al., 2014). Volcanogenic massive sulfides from sediment-starved environments (such as hydrothermal systems at mid-ocean ridges) show highly variable and mostly negative $\delta^{82/76}$Se values from −4.75‰ to +0.7‰ (Rouxel et al., 2002, 2004; Layton-Matthews et al., 2013). However, we do not observe any systematic deviations in $\delta^{82/76}$Se values of the samples that show variable S assimilation (i.e., $\delta^{34}S_{V\text{-}CDT}$ heavier than −0.5‰; $n = 7$) from the general variation trend along Cl/K or $\delta^{34}S_{V\text{-}CDT}$ (Fig. 5b and d). The sample PAC2 DR20-1 with the highest $\delta^{34}S_{V\text{-}CDT}$ value of +0.60 ± 0.10‰ (1 s.d.; Supplementary Table S2), which represents the highest amount of S assimilation, shows "typical" $\delta^{82/76}$Se of −0.15 ± 0.09‰ (Table 2; Fig. 5d). Average $\delta^{82/76}$Se values of the two sample subsets (i.e., with and without sulfide assimilation) are identical within 2 s.d. uncertainty (−0.14 ± 0.12‰ and −0.16 ± 0.14‰, respectively). Also, there is no clear covariation between the Se isotope composition and degree of Cl contamination (Fig. 5b).

On the other hand, there seems to be an apparent increase in S/Se ratio with Cl/K from 0.06 to 0.41

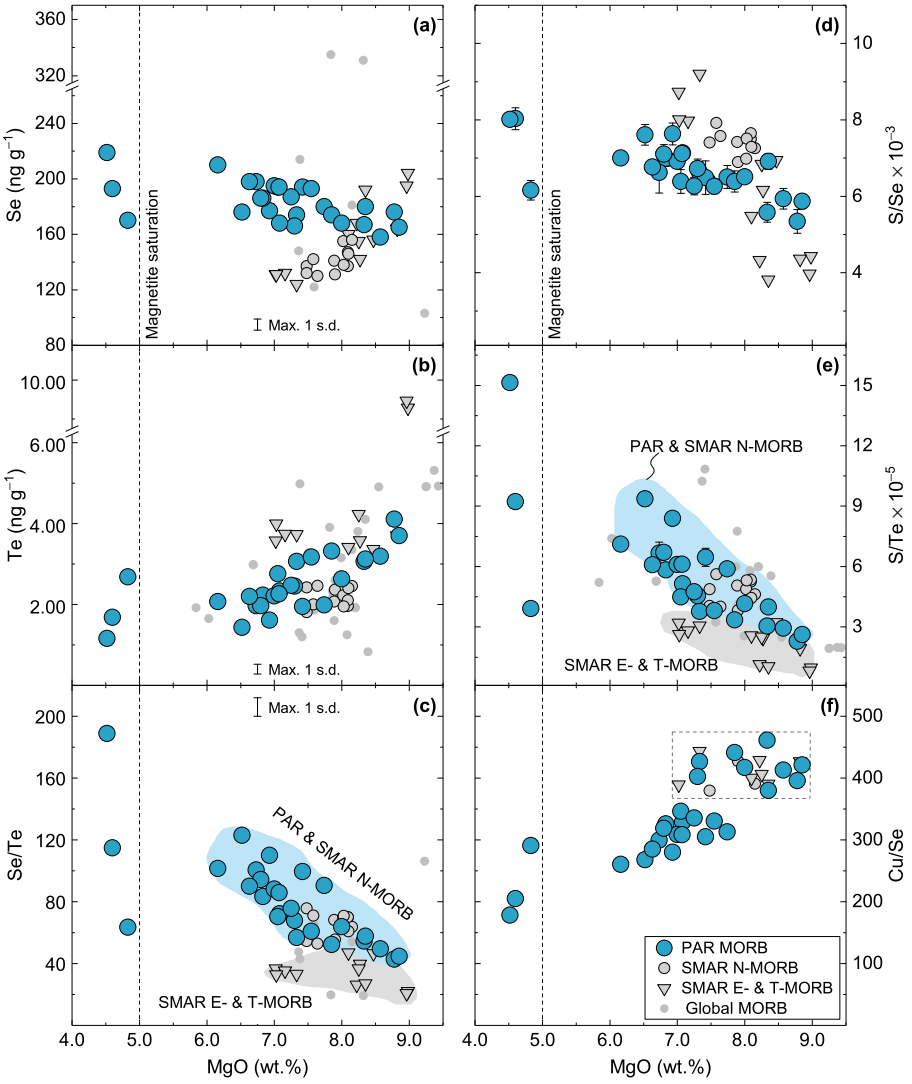

Fig. 4. Variations of Se, Te, S, and Cu abundances and/or their ratios with MgO content. Also shown for comparison are SMAR N- and E-MORBs (Lissner et al., 2014; E-MORB refers to all enriched- and transitional-type MORBs), as well as global MORBs from Hertogen et al. (1980) and Yi et al. (2000). The SMAR E-MORBs display distinctly lower Se/Te and S/Te ratios than that of N-MORBs from both PAR and SMAR over almost the entire magmatic differentiation (c and e), reflecting the Te-enrichment in E-MORB mantle source (Lissner et al., 2014). The Cu/Se ratio (f) in PAR and SMAR remains fairly constant and remarkably similar prior to ~7–7.5 wt.% MgO and PAR samples show a smooth decrease afterwards. The change of relative compatibility of Cu–Se may be related to the FeO content of the silicate melt as noted by Brenan (2015). The vertical dashed lines represent the onset of magnetite saturation (5 wt.% MgO) and associated sulfide segregation. Prior to this, the observed apparent compatibilities of these chalcophile elements (Te > Cu > Se > S) in the PAR suite indicate that they are predominantly controlled by fractionation of sulfide liquid, consistent with previous studies. At magnetite saturation, except the most evolved sample (PAC2 DR27-1) whose S solubility remains largely unaffected (Labidi et al., 2014), other two samples show consistent decrease in Se (a) and increase in Te (b) from the general trend (note the consistent decreases in FeO_T and TiO_2; Supplementary Fig. S3). The strong abrupt decrease in their Se/Te and S/Te ratios (c and e) is argued here as an indicator of the predominant appearance of crystalline MSS in the segregating sulfide assemblage from the MORB melt (see the text for details).

(Fig. 5c). Highest S/Se ratios (~8000) are also observed in two samples (PAC2 DR20-1 and PAC2 DR27-1) that have experienced S assimilation (Fig. 4d and c). Compared to MORBs (~3800–9200; Fig. 4d; Lissner et al., 2014; this study) and magmatic sulfides (~2700–8700; Patten et al., 2013, 2016), massive sulfides from sediment-starved hydrothermal systems have much more variable S/Se ratios (500–500,000), with lower values typical for sulfides near mid-ocean ridges due to the formation of selenide or Se-rich sulfides at high temperature conditions (Rouxel et al., 2004; Hannington et al., 2004; Layton-Matthews et al., 2008, 2013; Keith et al., 2016). Sulfide assimilation would not increase S abundance (hence S/Se ratio) of the melt due to sulfide saturation (Labidi et al., 2014; also see Section 5.2.2), but it may potentially increase the Se abundance because a MORB melt with ~8–14 wt.% FeO can dissolve ~0.15–0.25 wt.% Se (Wykes et al., 2015). Labidi et al. (2014) showed that the highest $\delta^{34}S_{V\text{-}CDT}$ value (+0.60 ± 0.10‰; 1 s.d.) can be reproduced by mixing a MORB melt having 1000 μg g^{-1} S and $\delta^{34}S_{V\text{-}CDT} = -1$‰ with a

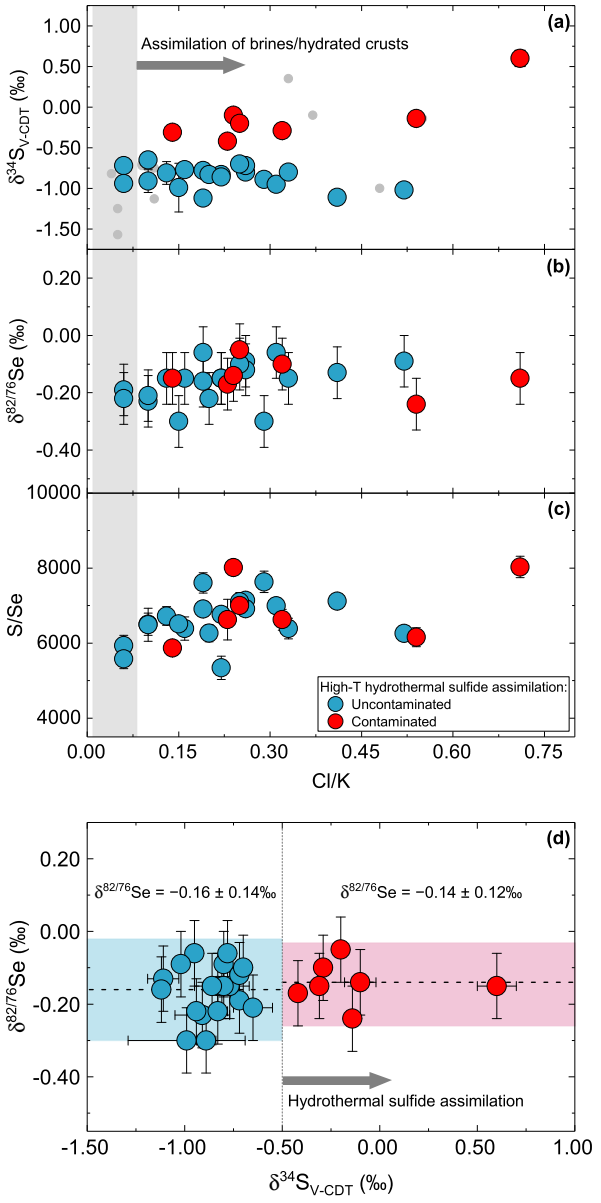

Fig. 5. Variations of $\delta^{34}S_{V\text{-}CDT}$ (a), $\delta^{82/76}Se$ (b) and S/Se ratios (c) with Cl/K that is used as a proxy for the extent of Cl contamination due to the interaction of the magma with brines and hydrothermally altered materials during magmatic differentiation (Michael and Cornell, 1998; Clog et al., 2013; Labidi et al., 2014). Note that Cl/K The grey shaded field represents the Cl/K ratio (0.01–0.08) of global MORBs that are unaffected by hydrothermal fluid assimilation (Michael and Cornell, 1998). The studied PAR basalts that have experienced high-T hydrothermal sulfide assimilation based on S isotope systematics (Labidi et al., 2014) are shown in red. Other PAR glass data (Labidi et al., 2014) are shown in grey circles (a). (d) shows the variation of $\delta^{82/76}Se$ with $\delta^{34}S_{V\text{-}CDT}$. Two shaded fields in (d) represent the average $\delta^{82/76}Se$ of two subsets of samples with and without assimilating hydrothermal sulfides.

maximum of 3.5 wt.% wall-rock having 10,000 μg g^{-1} S and $\delta^{34}S_{V\text{-}CDT} = +5‰$. Assuming that the original melt has ~168 ng g^{-1} Se (at 1000 μg g^{-1} S; from the general S–Se covariation), a final melt with the lowest S/Se = 5867 ($\delta^{34}S_{V\text{-}CDT} = -0.31‰$) observed in the contaminated samples (Fig. 5a and c) would require only ~3 ng g^{-1} increase in Se concentration to be associated with an assimilation of ~1.35 wt.% wall-rock. Note that a typical uncertainty of MORB Se concentration is also ~3 ng g^{-1} (Table 2). Therefore, we argue that the observed variation in S/Se ratios of PAR basalts (Fig. 5c) are not influenced by high-temperature hydrothermal sulfide assimilation but rather reflects magmatic differentiation (Fig. 4d; see below). Note that Cl contamination broadly scales with the degree of magmatic differentiation (Labidi et al., 2014), which readily accounts for the seemingly increasing S/Se with increasing Cl/K (Fig. 5c). The same conclusion may be reached for S/Te ratios (not shown) and hence the observed Te abundances. Lastly, alteration by seawater after the eruption (e.g., Lissner et al., 2014) or during magmatic differentiation are not likely to influence the Se isotope or Se–Te elemental systematics of MORBs because of extremely low Se and Te concentrations in modern seawater at relevant depths (~200 and ~0.2 ng kg^{-1}, respectively; Measures and Burton, 1980; Cutter and Bruland, 1984; Lee and Edmond, 1985; Cutter and Cutter, 2001).

5.2. Se–Te elemental systematics during MORB differentiation

As chalcophile elements, Se and Te, together with S and Cu, are sensitive to progressive MORB differentiation involving a concurrent precipitation of immiscible sulfides (Fig. 4). This process accounts for the observed abundances and relative fractionation of Se–Te–S–Cu (Fig. 4) because these elements are all highly incompatible in silicate minerals but show different partitioning into sulfides (Barnes et al., 2009; Patten et al., 2013; Labidi et al., 2014; König et al., 2015; Brenan, 2015; Wang and Becker, 2015a; Kiseeva et al., 2017). Our data shows a relative compatibility into sulfides (prior to magnetite saturation; see below) in the order of Te > Cu > Se > S (Fig. 4; Cu/Te ratio increases with decreasing MgO; not shown), consistent with earlier studies. The difference in the relative compatibility of Se and Cu above and below ~7 wt.% MgO (see Section 4.2 and Fig. 4f) may be attributed to different FeO content of the silicate melt (Brenan, 2015).

All these elements are affected by magnetite saturation-triggered sulfide segregation after ~5 wt.% MgO (Fig. 4; also see Section 4.1), as previously observed for S in PAR MORB (Fig. 6a; Labidi et al., 2014) and other chalcophile elements in glasses from worldwide arc settings (Jenner et al., 2010, 2012, 2015) and Kilauea Iki lava lake (Greaney et al., 2017). One exception is PAC2 DR27-1, which is the most evolved sample (MgO 4.52 wt.%; Table 2) yet remains largely unaffected (Labidi et al., 2014). Compared to the extrapolated general differentiation trends prior to 5 wt.% MgO, there is a consistent decrease in S–Se and increase in Te concentrations in samples that have experienced magnetite-induced sulfide segregation (Figs. 4a, b, and 6a; Supplementary Fig. S3). This is amplified by consistent and abrupt decrease in Se/Te and S/Te (Fig. 4c and e).

Selenium and tellurium likely segregate from the silicate melt as Fe–Se and Fe–Te complexes analogous to Fe–S and

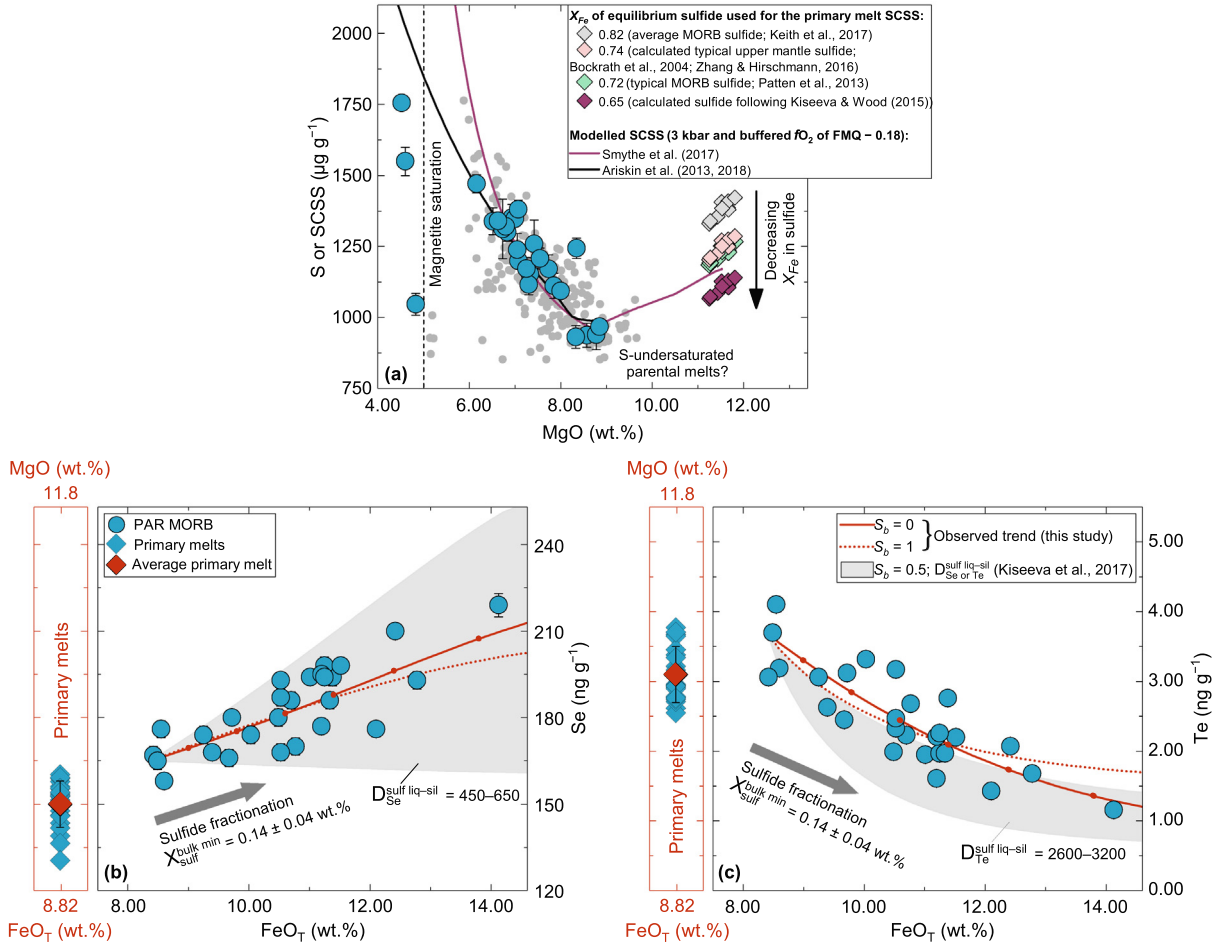

Fig. 6. Variations of S, Se, and Te abundances with MgO and/or FeO_T contents in PAR glasses. (a) shows the calculated SCSS (Smythe et al., 2017) for the primary melts ($n = 10$) as well as across the entire PAR magmatic differentiation following a similar approach of Ding and Dasgupta (2017). The primary melt major element compositions and their P–T conditions (on average ~10.2 kbar and 1325 °C) of last equilibration with mantle olivine (Mg# = 0.90) are calculated using the algorithm of Lee et al. (2009). At this condition, their SCSS are calculated in combination with a variety of equilibrium sulfide compositions ($X_{Fe} = 0.65$–0.82; $X_{Fe} = Fe/(Fe + Ni + Cu)$ atomic ratio) that might be found in the shallow mantle. It shows that even the lowest SCSS value with $X_{Fe} = 0.63$ (calculated sulfide composition in equilibrium with the most primitive glass PAC1 DR12-1g following Kiseeva and Wood (2015)) is still higher than the observed S contents of primitive PAR MORBs, implying that primary melts may be sulfide-undersaturated. The modelled SCSS (Smythe et al., 2017) across the entire PAR magmatic differentiation (from ~11.8 wt.% MgO) is calculated at 3 kbar (also see Fig. 7 and Supplementary Fig. S3) with $X_{Fe} = 0.65$ using major element compositions from alphaMELTS. Also shown for comparison is the SCSS from COMAGMAT (Ariskin et al., 2013, 2018) for the observed magmatic differentiation using Ni contents of the silicate melts (other parameters from alphaMELTS; Supplementary Fig. S3). Both models are in good agreement with the observed S abundances in sulfide-saturated MORBs from the PAR and global oceanic spreading ridges (Jenner et al., 2012, 2015; Labidi et al., 2014; global MORB data from Jenner and O'Neill (2012); $n = 233$). (b) and (c) show the modelled Se–Te variations with the calculated $X_{sulf}^{bulk\ min}$ (based on S systematics; Labidi et al., 2014) and the experimentally determined $D_{Se\ or\ Te}^{sulf\ liq–sil}$ for basaltic melts with 8–11 wt.% FeO from Kiseeva et al. (2017), which well reproduces the observed Se–Te variations. Calculation assumes that Se–Te partitioning between the fractionated sulfide liquid and silicate melt is an intermediate equilibrium process between fractional and batch partitioning, with $S_b = 0.5$ (Rehkämper et al., 1999). The observed/empirical trends using the observed $D_{Se\ or\ Te}^{bulk}$ values with S_b of 0 and 1 were shown for comparison. Each tick mark represents 10% crystal fractionation step. Also shown in (b) and (c) are the primary PAR melt (~11.8 wt.% MgO) Se–Te contents corrected for sulfide + crystal fractionation during later differentiation (sulfide-saturated; MgO < 8.85 wt.%) and for olivine fractionation during early differentiation (sulfide-undersaturated; 11.8–8.85 wt.% MgO).

thus their abundances in the melt should (also) be directly related to the FeO content. This is evidenced by the significant effect of FeO on the Se solubility in silicate melts (Fang and Lynch, 1987; Wykes et al., 2015) and on the partitioning of Se–Te between sulfide and silicate melts (Choi and Cho, 1997; Brenan, 2015; Kiseeva et al., 2017). Indeed, PAR MORBs display strong covariations between FeO_T and Se–Te contents (Fig. 6b and c), similar to that observed for S (Labidi et al., 2014). Note that FeO_T monotonically increases with deceasing MgO prior to magnetite saturation (Supplementary Fig. S3). In the following sections, we first model Se–Te variations during MORB differentiation using

FeO_T content as an index of crystal fractionation. We then estimate the primary melt Se–Te contents by correcting the observed concentrations for crystal + sulfide fractionation.

5.2.1. Modelling Se–Te variations and implications for chalcophile element partitioning

Details of the model calculations are given in Supplementary Material. Major element variations were modelled by alphaMELTS (fractional crystallization; Ghiorso and Sack, 1995; Smith and Asimow, 2005). The model curves for FeO_T yield the best match with the observed variation at 3 kbar and the resulting parameters were used subsequently (Supplementary Fig. S3). Bulk partition coefficients of Se and Te ($D^{bulk}_{Se\ or\ Te}$) were calculated using the mean sulfide fraction in the bulk segregated minerals ($X^{bulk\ min}_{sulf} = 0.14 \pm 0.04$ wt.%; based on S systematics; Labidi et al., 2014) and two sets of experimentally determined sulfide liquid–silicate melt partition coefficients ($D^{sulf\ liq–sil}_{Se\ or\ Te}$) considering the range of FeO contents of our samples: 450–650 for Se and 2600–3200 for Te (Kiseeva et al., 2017) and 1560 ± 410–1035 ± 360 for Se and $14{,}430 \pm 1680$–9570 ± 1150 for Te (1 s.d.; $D^{sulf\ liq–sil}_{Se\ or\ Te}$ decreases with increasing FeO; Brenan, 2015). The Se–Te variations were then modelled by a combination of the fractional and batch crystallization laws because partitioning of a chalcophile element between the fractionated sulfide and silicate melt is probably an intermediate (between pure fractional and batch) equilibrium process (Rehkämper et al., 1999; Bézos et al., 2005; Yang et al., 2014; Lissner et al., 2014; Kiseeva and Wood, 2015). The partitioning mode is described by the parameter S_b, which is the mass fraction of sulfide displaying batch partitioning (Rehkämper et al., 1999).

Dependency of the modelled Se–Te variations on the mode of sulfide–silicate melt partitioning (i.e., S_b) is relatively small compared to that of other highly chalcophile elements (e.g., Rehkämper et al., 1999). This is indicated by similar observed sulfide phase–silicate melt partition coefficients ($D^{sulf–sil}_{Se\ or\ Te}$) at S_b of 0 and 1 (by inversion; Supplementary Material Eqs. (2), (4), and (5); also see Bézos et al., 2005; Lissner et al.,2014), which yields $D^{sulf–sil}_{Se}$ of $\sim 560 \pm 190$ and 530 ± 180 and $D^{sulf–sil}_{Te}$ of $\sim 1600 \pm 600$ and 2200 ± 950, respectively (1 s.d.). With $S_b = 0.5$ and $D^{sulf\ liq–sil}_{Se\ or\ Te}$ from Kiseeva et al. (2017), the calculated trends well reproduce the observed Se–Te variations across the PAR magmatic differentiation (Fig. 6b and c). On the other hand, the modelled trends using $D^{sulf\ liq–sil}_{Se\ or\ Te}$ from Brenan (2015) predict much higher $D^{bulk}_{Se\ or\ Te}$ and cannot properly describe the observed patterns with any S_b values (not shown). Based on the experiments of Brenan (2015), a lower apparent $D^{sulf–sil}_{Te}$ can be predicted if a significant fraction of the segregating sulfides is crystalline monosulfide solid solution (MSS) in which Te is significantly more incompatible relative to sulfide liquid ($D^{MSS–sulf\ liq}_{Te} \approx 0.02$–$0.08$ and $D^{MSS–sil}_{Te} = 729$; also see Helmy et al., 2010; Liu and Brenan, 2015); in this case, our observed $D^{sulf–sil}_{Te}$ at $S_b = 1$ would require $87 \pm 6\%$ of the sulfide phase to be MSS using an average $D^{sulf\ liq–sil}_{Te} = 11{,}960 \pm 1400$ (see above). Such a high MSS fraction is however unlikely. At a pressure–temperature (P–T) range relevant to MORB differentiation (e.g., from ~1280 to 1160 °C at 2–5 kbar until ~70% crystallization in most PAR melts; Fig. 7), segregated sulfide is at its liquidus near ~1050–1125 °C according to sulfide

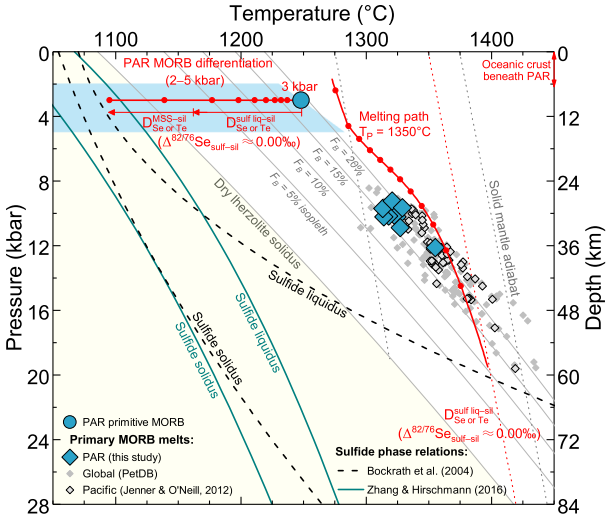

Fig. 7. P–T diagram showing the sulfide phase relations determined on a single sulfide composition ($X_{Fe} = 0.74$, metal/S = 0.93, and Ni/(Fe + Ni) = 0.25 molar ratio; Bockrath et al., 2004; Zhang and Hirschmann, 2016) and modelled conditions of PAR MORB differentiation (isobaric fractional crystallization; also see Supplementary Fig. S3) and near-fractional isentropic decompression melting path of a depleted MORB mantle (Salters and Stracke, 2004) to the base of the PAR crust (6.5 Km; alphaMELTS; Ghiorso and Sack, 1995; Ghiorso et al., 2002; Smith and Asimow, 2005). Each tick mark indicates 10% crystal fractionation or 2% melting extent. Anhydrous lherzolite solidus and bulk melt fraction (F_B) isopleths are calculated after Katz et al. (2003). The P–T condition of primary melt–mantle equilibration was obtained by the thermobarometer of Lee et al. (2009) using primitive PAR MORBs (>8.5 wt.% MgO; $n = 10$; Vlastelic et al., 2000; Hamelin et al., 2010), suggesting that melting at a mantle potential temperature (T_P) of 1350 °C (also see Ding and Dasgupta (2017) for other MORBs) may be adequate for our modelling purpose because each data point for an aggregate primary melt represents weighted average P–T of melt extraction from all mantle parcels across the triangular melting zone and thus lies below the polybaric melting path (Asimow and Longhi, 2004; Lee et al., 2009). The primary melt P–T of MORBs from the Pacific ($n = 55$; Jenner and O'Neill, 2012) and other spreading-ridges ($n = 157$; PetDB) is shown for comparison. Both sulfide melting experiments (Bockrath et al., 2004; Zhang and Hirschmann, 2016) suggest that sulfide liquid is the dominant fractionating phase across much of low-P MORB differentiation (red arrow), consistent with previous inferences from behavior of chalcophile elements (see Section 5.2.1). However, the sulfide liquidi estimated by these experiments distinctly vary at P–T conditions relevant to melting of a depleted mantle with typical T_P between ~1275 °C and 1400 °C. Under these conditions, a mantle sulfide may have similar metal/S ratio but much higher Ni/(Fe + Ni) (~0.40–0.65) compared to the sulfide mentioned above, resulting in an even lower solidus (Zhang and Hirschmann, 2016; Z. Zhang et al., 2018). This implies that chalcophile element behavior during decompression melting is entirely controlled by sulfide liquid–silicate melt fractionation rather than MSS–sulfide liquid or MSS–silicate melt fractionation.

melting experiments (Bockrath et al., 2004; Zhang and Hirschmann, 2016) and empirical approximations on natural sulfides in MORB glasses (Patten et al., 2012). Although there is geochemical evidence that a certain proportion of MSS needs to be present in fractionating sulfides to explain the variations of some chalcophile elements (Li and Audétat, 2012), sulfide liquid is still the main (if not dominant) sulfide phase during much of MORB differentiation that occurs above the sulfide liquidus (e.g., Bézos et al., 2005; Jenner et al., 2010; Li and Audétat, 2012; Lissner et al., 2014; Brenan, 2015). Besides, the fact that the observed Se–Te variations are well reproduced with $D^{sulf\ liq-sil}_{Se\ or\ Te}$ from Kiseeva et al. (2017) argues against a significant control of MSS fractionation on Se–Te systematics of PAR glasses. Another alternative explanation for the observed low $D^{sulf-sil}_{Te}$ compared to $D^{sulf\ liq-sil}_{Te}$ from Brenan (2015) could be poor equilibration between sulfides and silicate melt (i.e., $R_{eff} < 1$) as previously proposed for partitioning of platinum-group elements in MORBs (Rehkämper et al., 1999; Bézos et al., 2005; Yang et al., 2014). However, the extent of sulfide–silicate equilibration in our case might not be properly assessed due to the difference in the experimental $D^{sulf\ liq-sil}_{Se\ or\ Te}$ published by Brenan (2015) and Kiseeva et al. (2017) for the range of FeO content of PAR basalts.

Finally, only for the highly evolved MORB melts (PAC1 DR10-1g and PAC2 DR20-1) that have experienced > 70% crystallization and magnetite-triggered sulfide segregation (Fig. 6a; Supplementary Fig. S3), we suggest crystalline MSS to be the dominant fractionating sulfide phase to account for the observed abrupt drop in Se/Te (and S/Te) ratios (Fig. 4), considering $D^{sulf\ liq-sil}_{Se} < D^{sulf\ liq-sil}_{Te}$ and $D^{MSS-sil}_{Se} > D^{MSS-sil}_{Te}$ (Brenan, 2015). This was previously proposed for sulfide-saturated arc magmas based on Cu–Ag systematics (Jenner et al., 2010, 2012, 2015).

5.2.2. Primary melt Se–Te contents: Consideration of sulfide saturation

The primary melt major element composition was calculated following Lee et al. (2009) by adding liquidus olivine back into primitive samples with MgO > ~8.5 wt.% ($n = 10$; Vlastélic et al., 2000; Hamelin et al., 2010) until the melts reach equilibrium with mantle olivine containing Mg# = 0.90 (Mg#: molar $Mg/(Mg + Fe^{2+})$). Assuming the glasses have $Fe^{2+}/\Sigma Fe = 0.87$ (e.g., Bézos and Humler, 2005; H.L. Zhang et al., 2018), we obtain an average primary melt composition of ~11.8 wt.% MgO and ~8.8 wt.% FeO_T at ~10.2 kbar and ~1325 °C after ~8.7% olivine addition. For the Se–Te contents, we applied a two-step correction. Considering all studied glasses are sulfide-saturated, based on the strong covariation paths of Se–Te with FeO_T (Fig. 6b and c) and FeO_T with MgO (Supplementary Fig. S3), the Se–Te contents were first corrected to FeO_T content (8.49 wt.%) of the most primitive sample (PAC1 DR12-1g; 8.85 wt.% MgO) following a linear regression scheme previously used for other elements (e.g., Klein and Langmuir, 1987; Bézos et al., 2005; Kelley et al., 2006; Lissner et al., 2014). This yields 164 ± 8 and 3.4 ± 0.4 ng g^{-1} Se and Te, respectively (melts experiencing magnetite saturation were excluded; see Fig. 4 and Supplementary Fig. S2 and S3). Further corrections (from 8.85 to 11.8 wt.% MgO) along some linear slope with MgO or Mg# depend on whether the more primitive melts are sulfide-saturated. Several global MORBs with MgO > 9 wt.% (Jenner and O'Neill, 2012; Jenner et al., 2015) seem to display a clear absence of fractionation between chalcophile elements that have quite different $D^{sulf\ liq-sil}$ (e.g., Cu, As, Se, Ag, In, Sn, Tl, and Pb; Li and Audétat, 2012; Patten et al., 2013; Kiseeva and Wood, 2015; Kiseeva et al., 2017), which might indicate a sulfide undersaturation in high-MgO basalts (also see Ding and Dasgupta, 2017).

In this regard, we calculated the S solubilities of the primary PAR melts at their last equilibration with the mantle (see above) using the recent sulfur content at sulfide saturation (SCSS) model of Smythe et al. (2017) while taking into account the effect of equilibrium sulfide chemistry (Fig. 6a). It shows that, with a wide range of sulfide compositions (42–51 wt.% Fe, 9–18 wt.% Ni, and 0.4–10 wt.% Cu; Bockrath et al., 2004; Patten et al., 2013; Kiseeva and Wood, 2015; Zhang and Hirschmann, 2016; Keith et al., 2017), SCSS of the primary melts range from 1117 ± 44 to 1394 ± 55 μg g^{-1}, which decreases with decreasing X_{Fe} in sulfides ($X_{Fe} = Fe/(Fe + Ni + Cu)$ molar ratio). Even the lowest SCSS seems to be still higher than the S contents of the primitive PAR glasses (932–968 μg g^{-1}; Labidi et al., 2014), implying that primary melts might be sulfide-undersaturated. The modelled SCSS (Smythe et al., 2017) across the entire magmatic evolution (with $X_{Fe} = 0.65$ at 3 kbar and fO_2 of FMQ − 0.18; Supplementary Material) shows that MORBs may have reached sulfide saturation during early differentiation (P from ~10.2 to 3 kbar and T from ~1325 to 1248 °C; Fig. 7) due to the decreasing S solubility as well as olivine crystallization; they then remained sulfide-saturated, which also matches the model of Ariskin et al. (2013, 2018) that considers the effect of sulfide chemistry using Ni contents of the silicate melts (Fig. 6a). Both predictions are consistent with the observed sulfide saturation in the PAR as well as global spreading-ridge glasses (Jenner et al., 2012, 2015; Labidi et al., 2014; Smythe et al., 2017; but see Shimizu et al., 2016). Although primitive basalts (MgO > 9–10 wt.%) were also suggested to be sulfide undersaturated based on a variety of S solubility models, these models can result in significant differences in SCSS (up to 1000 μg g^{-1}) at a given condition (Saal et al., 2002; Ding and Dasgupta, 2017; and references therein). The model of Smythe et al. (2017), which we applied for our model primary melts, also carries large uncertainties (~25%). Here, we tentatively assume that parental PAR melts (MgO > 8.85wt.%) are sulfide undersaturated and accordingly the Se–Te concentrations after the first-step correction were further corrected for ~8.7% olivine fractionation only. This yields average Se and Te concentrations of 150 ± 8 and 3.1 ± 0.4 ng g^{-1}, respectively, for PAR primary melts (Se/Te = 48.4 ± 6.8; $n = 24$; Fig. 6b and c). This Se/Te ratio would represent an upper limit if the primary melts are sulfide saturated. These estimates are significantly lower than for the SMAR N-MORB primary melts (230–254 and 9.0–11.3 ng g^{-1}, respectively; Se/Te = 22–26; Lissner et al., 2014). This discrepancy may be

attributed to the difference in the observed Se–Te variations (Fig. 4a, b, and c; Section 4.2) as well as the correction approach used between two studies. Additional uncertainties may also result from other complexities during MORB differentiation (e.g., O'Neill and Jenner, 2012; Coogan and Dosso, 2016; Lissenberg and MacLeod, 2016). Most importantly, the clear negative slope in Te versus MgO in PAR MORBs is not resolved in SMAR N-MORBs (Lissner et al., 2014) due to the smaller MgO range of the latter (Fig. 4b). A wider compositional range of N-MORB now proves to be more appropriate (this study) than coupled N- and E-MORB arrays (Lissner et al., 2014) in order to adequately correct for differentiation and recover the primary melt Se–Te contents.

5.3. Role of partial melting on Se–Te systematics and inferences on composition of the upper mantle

5.3.1. Partitioning behavior of Se–Te during mantle melting

In the upper mantle, Se and Te are mainly hosted by Fe–Ni–Cu base metal sulfides and platinum-group minerals (Guo et al., 1999; Hattori et al., 2002; Lorand and Alard, 2010; König et al., 2015; Lorand and Luguet, 2016). The behavior of Se–Te during mantle melting is thus predominantly controlled by fractionation between these phases and silicate melt. However, their absolute and relative partitioning during melting has been debated. Based on the apparent variation in Se–Te abundances of peridotites, some authors suggest a slightly more incompatible behavior of Se compared to Te, with both being moderately incompatible (Wang and Becker, 2013; Wang et al., 2013). This relative partitioning is however opposite to observations from highly depleted harzburgites (König et al., 2012, 2014, 2015; Luguet et al., 2015). Hertogen et al. (1980), from the MORB perspective, suggest that Se is much more incompatible than Te during melting, with Te being rather compatible. This was based on the observed lack of clear Se/Te fractionation during magmatic differentiation and distinctly higher Se/Te ratios of global MORBs compared to mantle rocks (Hertogen et al., 1980; and references therein). In fact, as shown for PAR and SMAR MORBs (Fig. 4c), significant Se/Te fractionation occurs during MORB differentiation. This was not evident from the relatively small sample suite of Hertogen et al. (1980) probably due to (1) different source composition (Section 4.2) and (2) different mode and rate of sulfide fractionation during low-P magmatic differentiation in different spreading ridges (e.g., Bézos et al., 2005; Yang et al., 2014; Lissner et al., 2014), which may result in different apparent fractionation of Se/Te among genetically unrelated samples. Lissner et al. (2014) propose that both Se–Te are apparently incompatible during melting, with Te being more incompatible, although the empirical $D^{sulf\ liq–sil}_{Se\ or\ Te}$ they applied for modelling seem to suggest the opposite at low- to moderate-degree melting. Besides, both PAR and SMAR MORB data show that Te is much more compatible than Se during magmatic differentiation (Fig. 4c; Section 5.2.1), in accordance with experimental or empirical constraints (Peach et al., 1990; Patten et al., 2013; Lissner et al., 2014; Brenan, 2015; Wang and Becker, 2015a; Kiseeva et al., 2017).

These discrepancies have been explained by the presence of different equilibrium sulfide assemblages (sulfide liquid and crystalline MSS) during MORB differentiation and mantle melting, which involve sulfide liquid–silicate melt partitioning and MSS–sulfide liquid/silicate melt partitioning, respectively (Lorand and Alard, 2010; Lissner et al., 2014; König et al., 2014, 2015; Brenan, 2015). This is because Te is much more incompatible in MSS relative to sulfide liquid than Se (with $D^{MSS–sulf\ liq}_{Se\ or\ Te}$ of ~0.56–0.75 and ~0.02–0.08 for Se and Te, respectively; Helmy et al., 2010; Liu and Brenan, 2015; Brenan, 2015). The presence of MSS in the MORB mantle was also experimentally shown and used to explain the partitioning behavior of chalcophile and highly siderophile elements during melting (e.g., Bockrath et al., 2004; Bézos et al., 2005; Ballhaus et al., 2006; Fischer-Gödde et al., 2011; Brenan, 2015). However, the sulfide liquidus (Fig. 7) determined by Bockrath et al. (2004) has been questioned (Hart and Gaetani, 2006; Fonseca et al., 2012; Mungall and Brenan, 2014; Zhang and Hirschmann, 2016). Recent sulfide melting experiments using the same sulfide composition as in Bockrath et al. (2004) show that crystalline MSS is not stable in the convecting upper mantle (Fig. 7; Zhang and Hirschmann, 2016; Z. Zhang et al., 2018), which indicates that behavior of chalcophile elements during the partial melting might be entirely controlled by sulfide liquid–silicate melt partitioning, in favour of earlier conclusions based on Cu–Ag systematics of mantle rocks and melts (Wang and Becker, 2015b; Jenner et al., 2015).

5.3.2. Melting model

In order to further understand the role of partial melting on the Se–Te systematics of MORB melts and mantle residues, we modelled the behavior of Se–Te in a triangular passive-flow near-fractional melting regime, which was previously used to explain the Se–Te and highly siderophile element systematics of MORBs (e.g., Rehkämper et al., 1999; Lissner et al., 2014; Brenan, 2015). The modelling procedures and parameters are detailed in Supplementary Material and summarized in Table 3. Briefly, the melt major element compositions and P–T conditions for calculating the SCSS (Smythe et al., 2017) and $D^{sulf\ liq–sil}_{Se\ or\ Te}$ (as a function of FeO; Brenan, 2015; Kiseeva et al., 2017) were modelled with alphaMELTS front end (pMELTS mode; Ghiorso et al., 2002; Smith and Asimow, 2005) at a mantle potential temperature of 1350 °C following a similar approach used by Ding and Dasgupta (2017) (Fig. 6). The depleted mantle composition was taken from Salters and Stracke (2004) assuming 0.2 wt.% Fe_2O_3 (e.g., Cottrell and Kelley, 2011). The average melting degree (F_B; Langmuir et al., 1992; Plank et al., 1995) of the samples was estimated using differentiation-corrected incompatible trace element concentrations by (1) solving the simple batch melting equation for F_B (e.g., Kelley et al., 2006) and (2) comparing the concentrations to the result from pMELTS (near-fractional melting). These two approaches yield consistent F_B of ~6.6–11.7% (average 8.5 ± 1.5%) and 6.5–9.5% (Supplementary Fig. S4), respectively, in agreement with the previous estimates for global MORBs (e.g., Klein and Langmuir, 1987; Salters and

Table 3
Summary of model parameters used for the near-fractional melting of a MORB mantle.

		Note
PAR primary melts		
Major elements	~11.8 wt.% MgO, ~8.8 wt.% FeO_T, and Mg# = 73 (calculated average; $n = 10$)	Following Lee et al. (2009)
fO_2	$\Delta FMQ = -0.18$ ($Fe^{2+}/\Sigma Fe = 0.87$)	Bézos and Humler (2005); H.L. Zhang et al. (2018)
Equilibration P–T with Fo_{90} olivine	~10.2 kbar and ~1325 °C (calculated average; $n = 10$)	Thermobarometer of Lee et al. (2009); Fig. 7
Equilibrium sulfide	Natural and calculated sulfide compositions ($X_{Fe} = 0.82$–0.65)	Fig. 6
S–Se–Te	874 ± 48 μg g^{-1} S, 150 ± 8 ng g^{-1} Se, and 3.1 ± 0.4 ng g^{-1} Te (1 s.d., $n = 24$)	Fig. 8 and 9; Supplementary Fig. S5 and S6
Se/Te	48.4 ± 6.8 (1 s.d., $n = 24$)	
Mantle source		
Major/trace elements	Depleted MORB Mantle (with 0.2 wt.% Fe_2O_3)	Salters and Stracke (2004); Cottrell and Kelley (2011)
Potential temperature (T_P)	1350 °C	Following Lee et al. (2009); also see Ding and Dasgupta (2017)
Extraction P–T for each 1% melt increment	17.5–5.4 kbar and 1389–1294 °C (for F 0–20%; pMELTs)	Ghiorso et al. (2002); Smith and Asimow (2005); Fig. 7
S	170–200 μg g^{-1}	E.g., Lorand and Luguet (2016)
Se–Te (Potential Source 1)	80 ng g^{-1} Se and 11 ng g^{-1} Te (fertile lherzolite)	Wang and Becker (2013)
Se–Te (Potential Source 2)	49 ± 11 ng g^{-1} Se and 3.5 ± 1.3 ng g^{-1} Te (resulting best-fit abundances)	Figs. 8–10
Experimental partition coefficients:		
$D^{sulf\ liq-sil}$	(1) 1414–1900 for Se and 13,199–16,811 for Te (for equilibrium melts at F 0–20%)	Following Brenan (2015); increasing with decreasing FeO
$D^{sulf\ liq-sil}$	(2) 850 for Se and 3800 for Te	Kiseeva et al. (2017)
$D^{MSS-sil}$	883 for Se and 729 for Te	Brenan (2015)
Equilibrium sulfide	$Fe_{0.50}Ni_{0.36}Cu_{0.07}S_{1.00}$ (calculated "sulfide B"; $X_{Fe} = 0.54$; Ni/(Ni + Fe) = 0.42)	Supplementary Fig. S5
SCSS of the partial melts	960–821 μg g^{-1} (for an aggregate column-melt at F 0–20%)	Smythe et al. (2017); Supplementary Fig. S5
F_B	(1) 8.5 ± 1.5% (from trace element systematics; $n = 24$)	Following Kelley et al. (2006); Supplementary Fig. S4
F_B	(2) 6.5–9.5% (pMELTs forward modelling)	Fig. 8; Supplementary Fig. S4–S6

Stracke, 2004; Workman and Hart, 2005; Kimura et al., 2017). Three different upper mantle sulfide compositions were considered when calculating the SCSS of the partial melts ($X_{Fe} = 0.44$–0.74 and Ni/(Fe + Ni) = 0.25–0.53 at a constant (Fe + Ni + Cu)/S = 0.93; Supplementary Fig. S5). Considering a large number of input parameters in our model, in order to assure an internal consistency and reliability of our MORB mantle Se–Te estimates, we first modelled the variation of S and Cu during partial melting (Supplementary Fig. S5) because their mantle abundances (McDonough and Sun, 1995; Salters and Stracke, 2004; Lorand et al., 2013; Wang and Becker, 2013, 2015b; Palme and O'Neill, 2014; Lorand and Luguet, 2016) and behavior during mantle melting are relatively well established (e.g., Lee et al., 2009; Li and Audétat, 2012; Kiseeva and Wood, 2013, 2015; Ding and Dasgupta, 2017).

Our result shows that the PAR primary melt S concentrations are well reproduced for the estimated F_B of the samples using a range of source S content from "PM-like" 200 μg g^{-1} (e.g., Wang and Becker, 2013; Palme and O'Neill, 2014) to slightly lower 150 μg g^{-1} as estimated for the depleted MORB mantle (e.g., Luguet et al., 2003; Bézos et al., 2005; Nielsen et al., 2014; Lorand and Luguet, 2016) in combination with the SCSS model of Smythe et al. (2017) and equilibrium "sulfide B" (Supplementary Fig. S5a). Note that this sulfide chemistry is typical for lherzolite-hosted sulfides (e.g., Lorand and Luguet, 2016; Kiseeva et al., 2017) and consistent with the suggested range of Ni/(Fe + Ni) value for a shallow mantle Cu-free sulfide liquid (0.4–0.6) by recent experiments (Z. Zhang et al., 2018) at the range of melting depth (~50–20 km; Fig. 7) and fO_2 (~FMQ; Cottrell and Kelley, 2011; H.L. Zhang et al., 2018) estimated for the PAR basalts. The corresponding model curves also show an excellent fit to the primary melt Cu concentrations with 170–200 μg g^{-1} S and 30 (or 24) μg g^{-1} Cu in the source (Supplementary Fig. S5b and c).

5.3.3. Modelling Se–Te variations in mantle melts and residues

Figs. 8 and 9a show that the Se–Te systematics of PAR primary melts (150 ± 8 and 3.1 ± 0.4 ng g^{-1} Se and Te, respectively; Se/Te = 48.4 ± 6.8; $n = 24$) can be successfully reproduced by melting of a sulfide liquid-bearing MORB

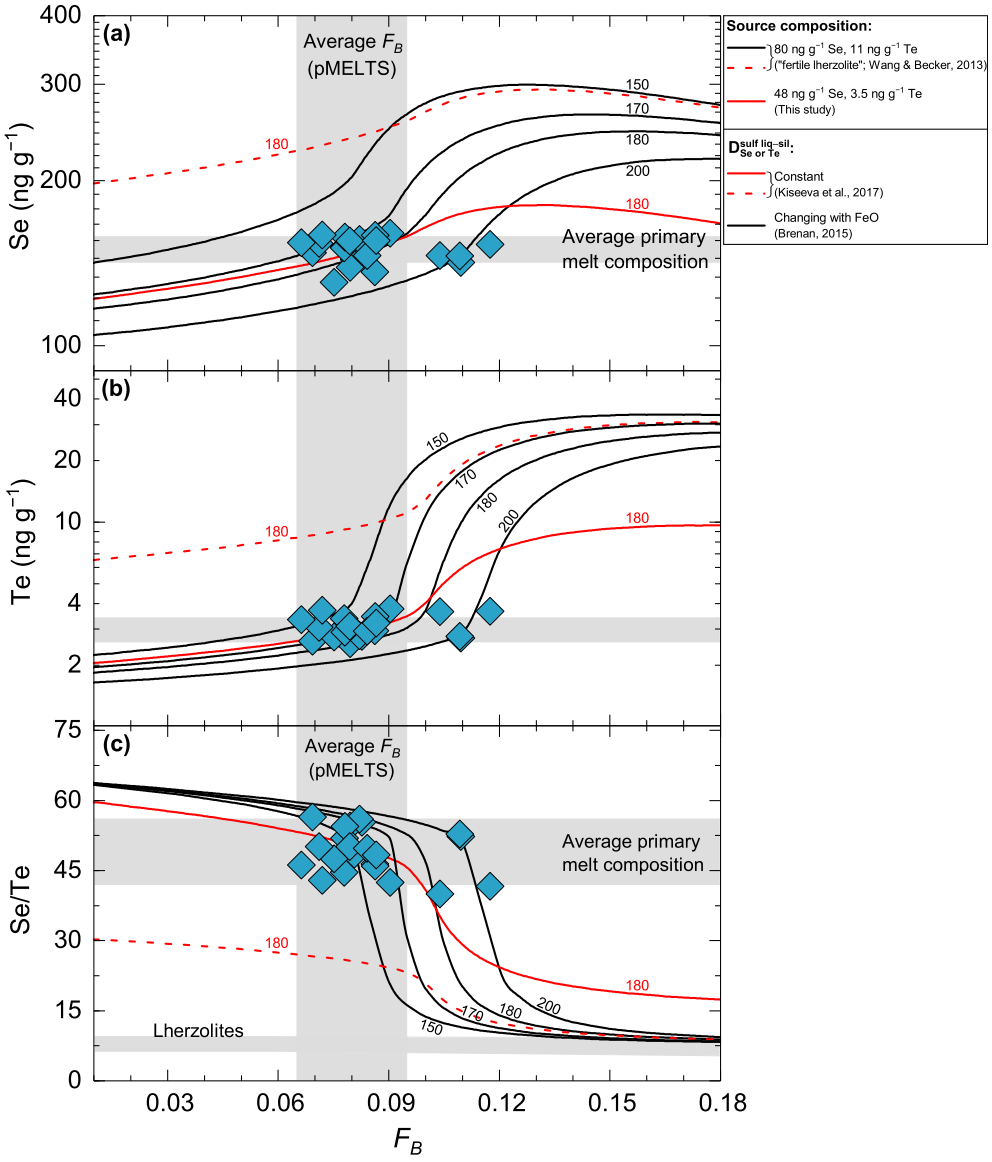

Fig. 8. Variations of Se (a) and Te (b) contents and Se/Te ratios (c) of the primary PAR melts (also see Fig. 6b and c) with their average degree of melting (F_B) estimated by batch melting equation using incompatible trace element systematics (~6.6–11.7%; Supplementary Fig. S4). The vertical and horizontal shaded field represent the range of F_B (6.5–9.5%) estimated from the forward modelling (near-fractional melting; pMLETS) and average primary melt composition (150 ± 8 and 3.1 ± 0.4 ng g^{-1} Se and Te, respectively; Se/Te = 48.4 ± 6.8). The variation in Se–Te concentrations were modelled for a triangular near-fractional melting regime (e.g., Rehkämper et al., 1999; Lissner et al., 2014; Brenan, 2015) using "fertile lherzolite-like" Se and Te contents (80 and 11 ng g^{-1}; Wang and Becker, 2013) and a range of S contents (150–200 μg g^{-1}) previously estimated for the primitive and/or depleted upper mantle (e.g., Luguet et al., 2003; Lorand et al., 2013; Lorand and Luguet, 2016; Bézos et al., 2005; Wang and Becker, 2013; Nielsen et al., 2014; Palme and O'Neill, 2014). $D^{sulf\ liq-sil}_{Se\ or\ Te}$ values are from Brenan (2015) and Kiseeva et al. (2017) (Table 3). The melt major element compositions and P–T conditions were modelled with pMELTS (see Fig. 7) and used to calculate $D^{sulf\ liq-sil}_{Se\ or\ Te}$ (as a function of FeO content of each equilibrium melt) and SCSS of the melt (Smythe et al., 2017) assuming the melt is in equilibrium with a calculated upper mantle sulfide ($Fe_{0.50}Ni_{0.36}Cu_{0.07}S_{1.00}$; Supplementary Fig. S5). (a), (b), and (c) show that the Se–Te systematics of the primary PAR melts can be broadly reproduced using the selected "fertile lherzolite-like" Se–Te contents (with 170–200 μg g^{-1} S) and $D^{sulf\ liq-sil}_{Se\ or\ Te}$ from Brenan (2015) (black lines). Sulfide undersaturation in the aggregate melt occurs at slightly different F_B (~9.5% to 11.5%) depending on the source S content (see Supplementary Fig. S5a). With the same starting composition, calculation using $D^{sulf\ liq-sil}_{Se\ or\ Te}$ of Kiseeva et al. (2017) overestimates the Se–Te contents of the melts (only shown for 180 μg g^{-1} S in the source for simplicity; red dashed lines) and only reproduces the observed variations with a significantly lowered source Se and Te contents (48 and 3.5 ng g^{-1}, respectively; red solid lines).

mantle which has "fertile lherzolite-like" Se and Te contents (80 and 11 ng g^{-1}, respectively; estimated at 3.52 wt. % Al_2O_3; Wang and Becker, 2013) using experimental $D^{sulf\ liq-sil}_{Se\ or\ Te}$ from Brenan (2015) calculated at each 1% equilibrium melting (Table 3). With the same SCSS, the polybaric aggregate melts reach sulfide undersaturation at F_B from

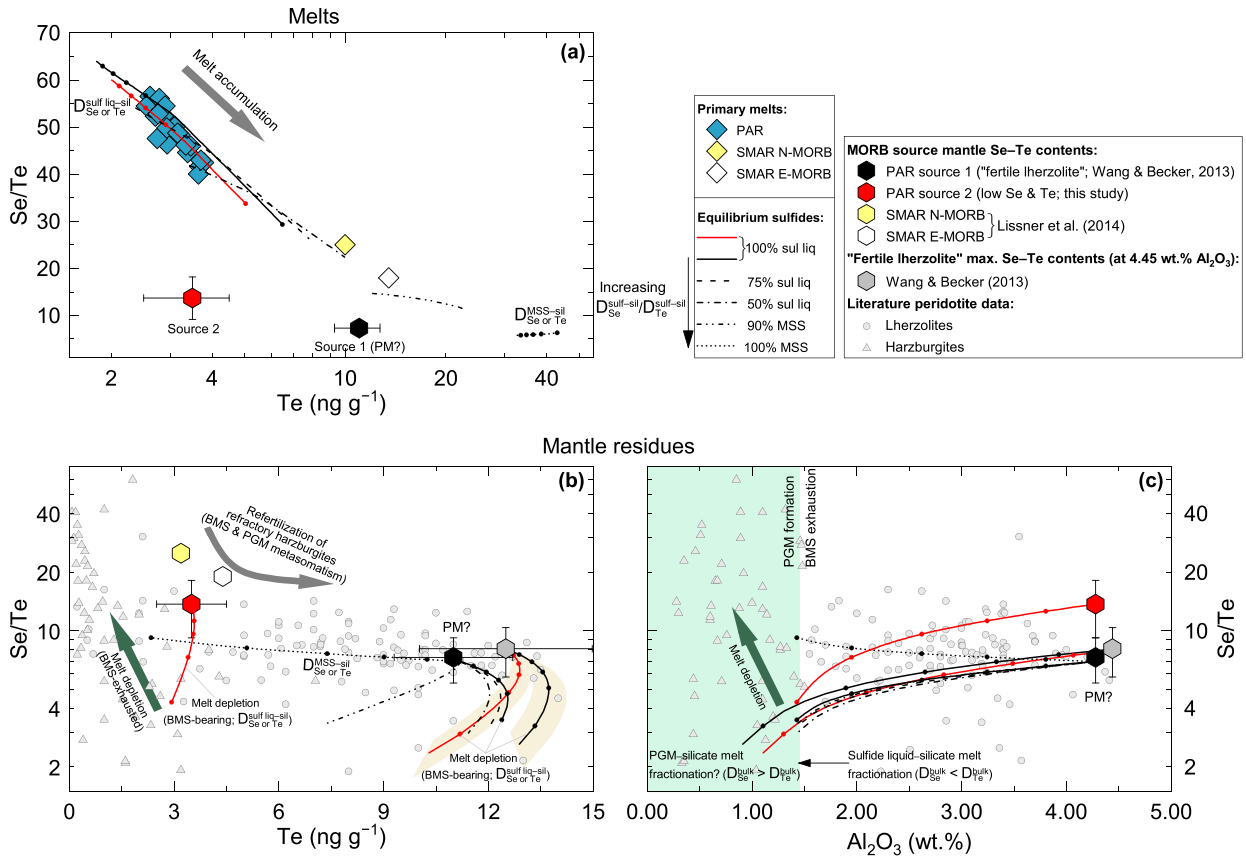

Fig. 9. Variations of Se/Te against (a) Te contents of the primary aggregate melts and (b) Te and (c) Al_2O_3 contents of the mantle residue. The red solid lines and all black lines correspond to the modelled melt composition with different proportions of sulfide liquid and crystalline MSS in the mantle having 180 μg g^{-1} S but two distinct Se and Te concentrations: (1) 80 ± 17 and 11 ± 1.7 ng g^{-1}, respectively (“fertile mantle”; estimated at 3.52 wt.% Al_2O_3; Wang and Becker, 2013), in combination with $D^{sulf\ liq–sil}_{Se\ or\ Te}$ (changing as a function of FeO contents of equilibrium melts) and/or $D^{MSS–sil}_{Se\ or\ Te}$ (constant) from Brenan (2015); and (2) 48 ± 8 and 3.5 ± 0.9 ng g^{-1}, respectively, which are the best-fit values from the modelling in combination with $D^{sulf\ liq–sil}_{Se\ or\ Te}$ (constant) from Kiseeva et al. (2017) (see Fig. 8 and Supplementary Fig. S6 for the modelling of partial melt composition). Each tick mark indicates 2% F_B (average degree of melting over a triangular melting zone) for the melts and 4% melting for a residual melting column (only shown for curves with 100% sulfide liquid or MSS). The modelling results are only shown until a mantle column becomes sulfide-exhausted, after which the remaining Se–Te budget is controlled by platinum-groups minerals (PGM; see the light blue shaded area in (c); Luguet et al., 2007; König et al., 2015). Additionally shown are the melting curves of a source with the maximum “fertile mantle” Se and Te contents (101 and 12.5 ng g^{-1}, respectively; estimated at 4.45 wt.% Al_2O_3 by Wang and Becker (2013)) using experimental $D^{sulf\ liq–sil}_{Se\ or\ Te}$ of (1) 1086 and 8789 (used in the melting model of Brenan (2015)) and (2) 850 and 3800 (same as above; Kiseeva et al., 2017) for Se and Te, respectively. For this modelling, major element compositions are from PM of McDonough and Sun (1995) and SCSS is calculated accordingly using parameters from pMELTS. The light yellow shaded areas in (c) are the range of residue compositions with a typical fertile mantle S content (200 ± 40 μg g^{-1}; e.g., Lorand, 1991; Palme and O’Neill, 2014). Our result shows that, regardless of the choice of source Se–Te contents and experimental $D^{sulf\ liq–sil}_{Se\ or\ Te}$ data, the Se–Te pattern displayed by lherzolites is inconsistent with melt depletion involving sulfide liquid–silicate melt fractionation (all solid black and red lines; b and c), which is suggested here to control Se–Te partitioning during mantle melting ($D^{bulk}_{Se} << D^{bulk}_{Te}$; see text for more details). Shown for comparison are the Se–Te contents for the SMAR N- and E-MORB primary melts and mantle sources (Lissner et al., 2014). Lherzolite (>1.5 wt.% Al_2O_3) and harzburgite (<1.5 wt.% Al_2O_3) data are from Morgan (1986), Lorand and Alard (2010), Wang and Becker (2013), Wang et al. (2013), König et al. (2012, 2014, 2015), Luguet et al. (2015), and Harvey et al. (2015).

~9.5% to 11.5%, increasing with increasing initial S content from 170 to 200 μg g^{-1} (also see Supplementary Fig. S5a). This corresponds to an extent of melting F from ~19% to 23% in the central melting column (i.e., F_{max}; Supplementary Material) and is consistent with the conclusion of previous studies using other empirical or experimental SCSS models (Luguet et al., 2003; Bézos et al., 2005; Lee et al., 2012; Lissner et al., 2014; Brenan, 2015). In the case of 180 μg g^{-1} S, a mantle column becomes sulfide-exhausted after ~20% melting. At any stage before sulfide exhaustion, Se is apparently much more incompatible than Te, with contrasting $D^{bulk}_{Se\ or\ Te}$ values of ~0.69–0.01 and ~6.38–0.11 for Se and Te, respectively (decreasing with ongoing partial melting). Therefore, a large Se/Te fractionation occurs between the melt and residue as long as sulfide liquid is present in the system (Fig. 8c). The estimated F_B for PAR MORBs (~6.6–11.7%) indicates that the primary aggregate melt is a mixture of melt increments derived from both sulfide-bearing (low-F) and sulfide-exhausted (high-F) mantle columns (also see Ding and Dasgupta, 2017), and there-

fore, the observed Se/Te fractionation in primary melts with respect to their source is largely accounted for by melting. This is in contrast to the observations from the primary SMAR melts, in which the relative partitioning of Se and Te is suggested to have played a minor role on the observed Se–Te variation (Lissner et al., 2014). This is because the SMAR partial melts are mostly derived from sulfide-free mantle owing to the relatively high F_B (12.8–17.2%) estimated by the authors, whereas sulfide exhaustion in their model occurs at around $F_B \approx 9\%$. However, as noted by Kinzler and Grove (1993), the model of Niu and Batiza (1991) applied by Lissner et al. (2014) to estimate the melting extent of the SMAR MORB tends to produce somewhat higher values compared to other models using major element systematics. This may partly explain the different observations between our study and Lissner et al. (2014) regarding the effect of partial melting on the observed Se/Te fractionation in MORB.

The modelling was also performed using experimental $D^{\text{sulf liq–sil}}_{\text{Se or Te}}$ of Kiseeva et al. (2017), from which the highest values were taken (850 and 3800 for Se and Te, respectively) considering the FeO content of the equilibrium melts (8.3–5.4 wt.%; Supplementary Material). However, these $D^{\text{sulf liq–sil}}_{\text{Se or Te}}$ overestimate the Se–Te contents of the melts with a "fertile lherzolite-like" starting Se–Te contents (with 180 μg g^{-1} S; Fig. 8a and b). A good match is obtained only after the source Se and Te contents are lowered to 48^{+5}_{-8} and $3.5^{+0.5}_{-0.9}$ ng g^{-1}, respectively (Figs. 8 and 9a). With this set of $D^{\text{sulf liq–sil}}_{\text{Se or Te}}$, we obtain 49 ± 11 ng g^{-1} Se and 3.5 ± 1.3 ng g^{-1} Te on average for the PAR mantle having 170–200 μg g^{-1} S. Considering the difference in experimental $D^{\text{sulf liq–sil}}_{\text{Se or Te}}$ between Brenan (2015) and Kiseeva et al. (2017), it is uncertain which Se–Te contents actually represent the mantle source composition (Fig. 9a).

The role of MSS–silicate melt partitioning on the behavior of Se–Te was investigated by incorporating varying proportions of MSS and sulfide liquid into the bulk sulfide assemblage in the mantle (180 μg g^{-1} S) using experimental $D^{\text{MSS–sil}}_{\text{Se or Te}}$ from Brenan (2015) and "fertile lherzolite-like" Se–Te contents for consistency (Supplementary Fig. S6). Due to the similar $D^{\text{MSS–sil}}_{\text{Se or Te}}$ of Se and Te (883 and 729, respectively), there is little Se/Te fractionation during the entire melting interval if crystalline MSS is the only controlling sulfide phase (also see Brenan, 2015); besides, both Se–Te concentrations are highly overestimated owing to their high apparent incompatibilities, with $D^{\text{bulk}}_{\text{Se or Te}}$ values of ~0.43–0.01 and 0.35–0.01 for Se and Te, respectively (Supplementary Fig. S6). It shows that Se–Te systematics of the melt can only be reproduced if sulfide liquid is the major controlling phase (>50%; in the case of 180 μg g^{-1} S in the source; Fig. 9a and Supplementary Fig. S6).

On the other hand, the modelled Se–Te contents of the residue shows that the variations of Se–Te abundances and Se/Te ratios of worldwide lherzolites (Fig. 9b and c) can be reproduced only when MSS is the dominant, if not only, sulfide phase (>90%) in the mantle. In this case, both Se and Te would be (apparently) incompatible, with Te being more incompatible (e.g., Brenan, 2015). As mentioned earlier, this absolute and relative partitioning during partial melting are in line with the conclusion of some studies (Lissner et al., 2014; König et al., 2014, 2015) but cannot be reconciled with our observations from the perspective of partial melts, which does not require the presence of "residual" crystalline MSS controlling Se–Te partitioning (Fig. 9a) as previously suggested by the Cu–Ag systematics (Jenner et al., 2015; Wang and Becker, 2015b) as well as recent sulfide melting experiments (Zhang and Hirschmann, 2016; Z. Zhang et al., 2018; Fig. 7; Section 5.3.1). We argue that, from the melt perspective, secondary refertilization processes such as addition of metasomatic base metal sulfides and platinum-group minerals have significantly, if not completely, overprinted the original melt depletion signature of lherzolites (i.e., sulfide liquid–silicate melt fractionation; Fig. 9b and c), in line with the conclusions from studies of peridotites (Lorand and Alard, 2010; König et al., 2014, 2015; Luguet et al., 2015; Harvey et al., 2015). Note that this argument is independent of the choice of source Se–Te contents and published experimental $D^{\text{sulf liq–sil}}_{\text{Se or Te}}$. For instance, the residue composition was also calculated with a source having the maximum "fertile mantle" Se and Te contents (101 and 12.5 ng g^{-1}, respectively; estimated at 4.45 wt.% Al_2O_3; Wang and Becker, 2013) using $D^{\text{bulk}}_{\text{Se or Te}}$ from both studies (Brenan, 2015; Kiseeva et al., 2017). Results show that the modelled residue composition still hardly reconciles with the observed Se–Te variation in lherzolites, which likely represent a post-melt depletion refertilization trend (Fig. 9b and c). As for the highly depleted residue after sulfide exhaustion, little is known regarding the quantitative control of Se–Te host phases. Nevertheless, the increasing Se/Te ratios (>15; suprachondritic relative to CI chondrites; Lodders et al., 2009) with progressive melt depletion in refractory harzburgites, which represent the least metasomatically influenced peridotites (König et al., 2014; Luguet et al., 2015), probably reflects the relatively compatible behavior of Se that is preferentially incorporated in platinum-group minerals formed upon sulfide exhaustion (Luguet et al., 2007; Fonseca et al., 2012; König et al., 2015; Luguet and Reisberg, 2016).

5.4. Role of magmatic processes on Se isotope systematics of MORB

Having established the Se (and Te) elemental behavior during partial melting and MORB differentiation, we now discuss the role of these magmatic processes on Se isotopes and estimate a reliable mantle source composition. Note that none of the (secondary) non-magmatic processes, including high-T hydrothermal fluid/sulfide assimilation during magmatic differentiation and volcanic degassing, have measurable effects on Se isotope composition of PAR glasses (Section 5.1).

Previous experiments reported significant Se isotopic fractionation (up to 19‰ in $^{82}Se/^{76}Se$) during abiotic reduction of Se oxyanions (SeO_3^{2-} and SeO_4^{2-}) at low temperature conditions (e.g., Krouse and Thode, 1962; Rees and Thode, 1966; Rashid and Krouse, 1985; Johnson et al., 1999;

Johnson and Bullen, 2003; Mitchell et al., 2013). In contrast, there is relatively little isotopic fractionation (<0.5‰) associated with oxidation of reduced Se species (Johnson et al., 1999; Johnson, 2004). As discussed in Section 5.1, Se is very likely dissolved in MORB melts as reduced Se^{2-}. Since MORB forms and evolves at fO_2 around FMQ buffer (Ballhaus, 1993; Bézos and Humler, 2005; Cottrell and Kelley, 2011; Labidi et al., 2014; H.L. Zhang et al., 2018), transition between Se^{4+} (with/without Se^{6+}) and Se^{2-} and hence associated Se isotopic fractionation, if any, is expected to be very subtle across the entire MORB evolution starting from the mantle source region.

Despite the narrow range in $\delta^{82/76}$Se values of the PAR glasses (-0.16 ± 0.13‰ on average), subtle but resolvable differences (up to ~0.25‰ vs the external reproducibility of 0.09‰) is observed between some samples (Fig. 3). These differences seem to be unrelated to the sample latitude, tectonic discontinuity, or ridge axial depth (Fig. 2a and b; Supplementary Fig. S1). Hamelin et al. (2011) demonstrated clear latitudinal variations in radiogenic isotopes (He–Sr–Nd–Hf–Pb) along the studied PAR segments (65–56°S and 53–41°S), which is interpreted to result from progressive mixing of the depleted Pacific upper mantle and gradually increasing amount of recycled oceanic crust component northwards. However, Se isotope compositions of the northern and southern PAR segments are essentially the same (-0.14 ± 0.12‰ and -0.19 ± 0.14‰, respectively; 2 s.d.) and show no clear latitudinal variation (Fig. 2a). There is also no covariation between $\delta^{82/76}$Se (or Se–Te contents) and radiogenic isotope ratios of the samples (not shown). Furthermore, the Se isotopic variations are not correlated with (1) Se content of the melt (158–219 ng g^{-1}; Fig. 2c), (2) magmatic differentiation index Mg# (0.68–0.40; Fig. 10a), or (3) Se/Te ratio (~43–189) that is demonstrated above as a direct indicator of sulfide liquid–silicate melt fractionation (Figs. 4c and 10b; Section 5.2.1). Besides, two highly evolved PAR glasses that show clear evidence of magnetite-triggered sulfide fractionation (PAC1DR10-1g and PAC2 DR20-1; Fig. 4c and e) have Se isotope compositions (-0.24 ± 0.09‰ and -0.15 ± 0.09‰) indistinguishable from those of less evolved samples (MgO > 5wt.%). As discussed earlier, the predominantly fractionating sulfide phase in response to liquidus magnetite appearance after MgO < 5wt.% is very likely crystalline MSS. Altogether, we suggest that there is no resolvable Se isotopic fractionation within uncertainty (0.09‰; 2 s.d.) during shallow-level magmatic differentiation that involves segregation of silicate crystals and sulfide liquid and/or MSS (i.e., $\Delta^{82/76}Se_{sulf-sil} \approx 0.00$‰). Effects of pressure on Se isotopic partitioning at mantle conditions relevant to MORB petrogenesis (Fig. 7) is expected to be negligible (Young et al., 2015), as in the case of S isotopes (Labidi and Cartigny, 2016). We therefore argue that there is negligible $^{82}Se/^{76}Se$ fractionation during partial melting of the upper mantle, which also involves equilibrium partitioning of Se between sulfide liquid (probably without MSS) and silicate melt (Figs. 8 and 9; Supplementary Fig. S5; see Section 5.3.3). Accordingly, we use the observed PAR MORB average $\delta^{82/76}$Se (-0.16 ± 0.13‰; $n = 27$) to represent the Se isotope composition of the primary melts

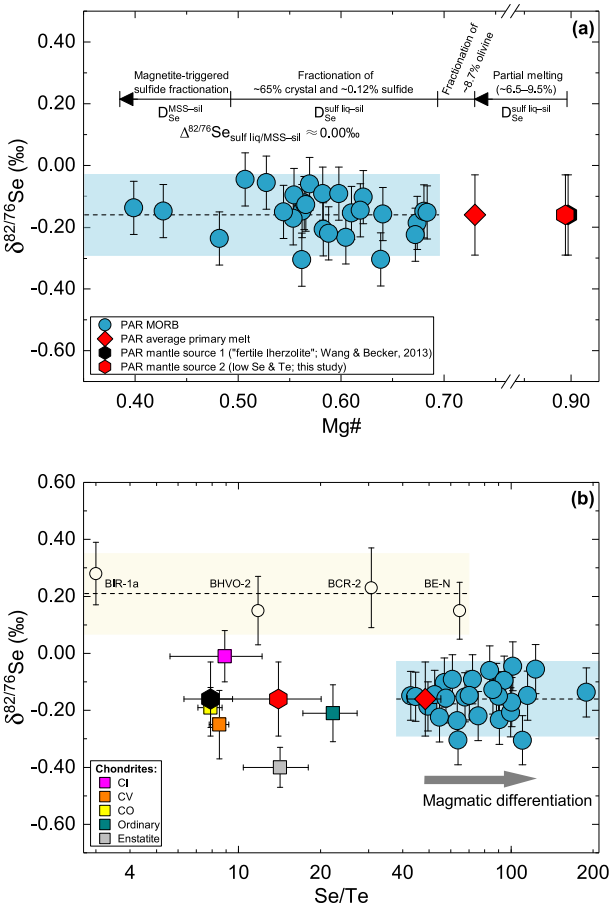

Fig. 10. $\delta^{82/76}$Se plotted against (a) Mg# and (b) Se/Te ratio across the entire MORB evolution according to our models of magmatic differentiation and partial melting. Also shown for comparison are $\delta^{82/76}$Se (±2 s.d.) and Se/Te (±1 s.d.) data for basaltic reference materials and main chondrite groups (also see Fig. 3). Each shaded field represents the average $\delta^{82/76}$Se with 2 s.d. uncertainty and range of Mg# (a) or Se/Te (b). The mass fractions of the fractionated crystals and sulfides are relative to the initial primary melt (a). Selenium isotope compositions of the primary PAR melt and MORB mantle source are represented by the average $\delta^{82/76}$Se value of all PAR glasses (-0.16 ± 0.13‰; 2 s.d., $n = 27$) based on the demonstrated absence of Se isotope fractionation during Se partitioning between sulfide (liquid and/or crystalline MSS) and silicate melt ($\Delta^{82/76}Se_{sulf-sil} \approx 0.00$‰). Both mantle source compositions estimated for PAR MROBs were shown: 80 ± 17 and 11 ± 1.7 ng g^{-1} (source 1) and 49 ± 11 and 3.5 ± 1.3 ng g^{-1} (source 2) Se and Te, respectively (also see Figs. 8 and 9; symbols in (a) were slightly staggered for clarity). $\delta^{82/76}$Se and Se/Te ratios of all basaltic reference materials are from this study and Yierpan et al. (2018) and $\delta^{82/76}$Se of BCR-2 is also taken from Kurzawa et al. (2017) (also see Fig. 1). For chondrites, $\delta^{82/76}$Se are from Labidi et al. (2018) and the Se/Te ratios from Wasson and Kallemeyn (1988), Lodders et al. (2009), Schaefer and Fegley (2010), and Wang and Becker (2013).

(Mg# = 0.73) as well as the mantle source (Fig. 10a and b). The apparent Se isotope variation along the PAR (up to 0.25 ± 0.13‰; e.g., Figs. 2 and 3) thus likely reflects intrinsic mantle heterogeneity.

The $\delta^{82/76}$Se values of the PAR MORBs are systematically lighter than that of all other basaltic lavas from vari-

ous geological settings (e.g., oceanic/continental intraplate basalts and plume-influenced ocean ridge basalts; Fig. 3; Rouxel et al., 2002; Kurzawa et al., 2017; Yierpan et al., 2018; this study). Four subaerial basalts analyzed by the same technique as in this study have variable Se (~15–170 ng g^{-1}) and Te (1.0–14.2 ng g^{-1}) contents with Se/Te ratios ~3–65 (Fig. 10b; Yierpan et al., 2018), implying that they may have different source compositions and/or experienced different degrees of partial melting and igneous differentiation (see Section 5.2 and 5.3). These petrogenetic processes however should result in no Se isotopic fractionation as discussed above. Their non-chondritic and significantly heavier $\delta^{82/76}$Se (+0.21 ± 0.15‰) compared to MORB could thus reflect (1) so far unidentified effects of non-magmatic processes (such as subaerial eruption-related degassing; e.g., Floor and Román-Ross, 2012; Floor et al., 2013) and/or (2) Se isotopic variability among terrestrial igneous reservoirs ($\delta^{82/76}$Se between −0.16 ± 0.13‰ and +0.21 ± 0.15‰; Figs. 3 and 10b).

5.5. Implications for the origin of Se and Te in the mantle

The upper mantle abundances of Se, Te, and S have been suggested to be primarily established by addition of volatile-rich chondritic late veneer after core formation (Wang and Becker, 2013) because these elements are predicted to behave as highly siderophile elements during core–mantle differentiation based on the extrapolation of low-P (1–19 GPa) metal–silicate partitioning experiments (Rose-Weston et al., 2009; Steenstra et al., 2017). However, this simple late-veneer origin of S cannot explain the non-chondritic S isotope composition of the mantle, which requires a significant portion of S in the pre-late veneer mantle (Labidi et al., 2013, 2016). This is further supported by more recent partitioning experiments on S (Boujibar et al., 2014; Suer et al., 2017). Suer et al. (2017) showed that S becomes less siderophile with increasing pressure than previously predicted, with the observed $D_S^{metal-silicate}$ of ~10–55 versus ~1000 predicted by Rose-Weston et al. (2009), at core forming condition (~40–55 GPa; Jackson et al., 2018). In this context, if the late veneer consisted of volatile-rich materials (e.g., McDonough and Sun, 1995; Wang and Becker, 2013), suprachondritic S/Se and S/Te ratios should be expected for the mantle because the Se–Te budget was primarily accounted for by late veneer; alternatively, if the pressure dependence of $D_{Se\ or\ Te}^{metal-silicate}$ determined at <20 GPa (Rose-Weston et al., 2009; Steenstra et al., 2017) was lowered at higher pressure (or temperature) to some extent as in the case of S (Suer et al., 2017) and other elements (e.g., Siebert et al., 2013), the possibility that mantle Se–Te budget represents metal–silicate equilibration would remain open (as suggested for the Moon; Steenstra et al., 2017).

As discussed earlier, lithospheric lherzolites that were used to estimate PM Se–Te abundances (Wang and Becker, 2013) preserve little primary melt depletion signature and very likely represent refertilized (previously-depleted) harzburgites (Fig. 9b and c; also see Le Roux et al., 2007; König et al., 2014). Unlike Cu and Ag that show limited fractionation during different petrogenetic processes (e.g., mantle melting, refertilization, and melt transport; Wang and Becker, 2015b), different and non-systematic Se–Te fractionation occurs during these processes depending on the host assemblages controlling the Se–Te behavior (Figs. 4, 6, and, 9b and c; Section 5.3.3). This implies that the near-chondritic Se/Te ratios (7.9 ± 1.6) in worldwide "fertile lherzolites", despite the broad correlation between Se–Te and lithophile elements such as Al and Ca (Wang and Becker, 2013), should be considered with great caution as primitive signature of PM.

Mantle melts provide an alternative approach to estimate composition of the asthenospheric mantle. The MORB mantle abundances of Se–Te and other strongly chalcophile elements (e.g., Cu; Supplementary Fig. S5) would be essentially identical to that of PM (Fig. 9b and c) because average depleted MORB mantle is only ~2–3% melt-depleted from PM (Menzies et al., 1977; Salters and Stracke, 2004; Workman and Hart, 2005; Bodinier and Godard, 2014). However, this approach critically depends on the modelling parameters (Sections 5.2.2 and 5.3.3) and hence leads to different results (Figs. 8 and 9). We obtain two distinct possible source compositions for the PAR MORB: 80 ± 17 ng g^{-1} Se and 11 ± 1.7 ng g^{-1} Te (source 1; "fertile lherzolite-like"; Wang and Becker, 2013) vs 49 ± 11 ng g^{-1} Se and 3.5 ± 1.3 ng g^{-1} Te (source 2) due to the difference in $D_{Se\ or\ Te}^{sulf\ liq-sil}$ published by Brenan (2015) and Kiseeva et al. (2017), respectively (Table 3; Figs. 9 and 10). It is noteworthy that only $D_{Se\ or\ Te}^{sulf\ liq-sil}$ from the latter study successfully reproduces the observed Se–Te variation during MORB differentiation (Fig. 6b and c; Section 5.2.1).

On the other hand, $\delta^{82/76}$Se of PAR MORB mantle (−0.16 ± 0.13‰) is well within the range of chondritic values of −0.30 ± 0.39‰ (Vollstaedt et al., 2016) and −0.21 ± 0.31‰ (Labidi et al., 2018) (Fig. 3). Combined with the possible Se/Te ratios (7.9 ± 1.6 and 14.0 ± 6.1 for source 1 and 2, respectively), $\delta^{82/76}$Se of the PAR mantle appears to overlap with that of both CI chondrites and volatile-depleted carbonaceous (CV and CO) and ordinary chondrites but show a significant offset from enstatite chondrites (Fig. 10b). Yet, the latter have been suggested to be the main constituent of the late veneer based on Ru and Os isotopes (e.g., Meisel et al., 1996; Dauphas, 2017; Fischer-Gödde and Kleine, 2017). Interestingly, all terrestrial rocks/melts show distinctly heavier $\delta^{82/76}$Se relative to enstatite chondrites (Fig. 3). At this stage, it is difficult to link the late veneer material to certain chondrite groups because a robust mantle $\delta^{82/76}$Se value remains to be established and little is known regarding the role of planetary processes on moderately volatile Se isotopes (e.g., metal–silicate equilibration and vapor loss during accretionary growth of small planetesimals; Labidi et al., 2016; Hin et al., 2017; Norris and Wood, 2017). Our result obtained here however highlights the potential of Se isotopes to contribute new constraints on planetary accretion models regarding the Earth's volatile delivery.

6. CONCLUSION

We present the first high-precision Se isotope and Se–Te elemental data for MORB glasses from the PAR (65–56°S and 53–41°S) using recently developed analytical tech-

niques (Kurzawa et al., 2017; Yierpan et al., 2018). Almost all PAR basalts have experienced high-temperature hydrothermal fluid assimilation during magmatic differentiation, which significantly overprints the S isotope composition when it is associated with assimilation of hydrothermal sulfides (Labidi et al., 2014). However, neither of these processes affects the Se isotope composition and S–Se–Te abundances. The observed S–Se–Te variations are dominantly controlled by MORB differentiation involving segregation of immiscible sulfide liquid, which is successfully reproduced using the experimentally determined $D^{sulf\ liq–sil}_{Se\ or\ Te}$ values from Kiseeva et al. (2017); in the highly evolved melts at magnetite saturation, the dominant fractionating sulfide phase is very likely crystalline MSS, indicated by the abrupt drop in Se/Te and S/Te ratios. The differentiation-corrected Se–Te contents of the primary MORB melts are well reproduced by near-fractional decompression melting of a mantle using experimental $D^{sulf\ liq–sil}_{Se\ or\ Te}$ (Brenan, 2015; Kiseeva et al., 2017) with a mantle source containing 170–200 μg g^{-1} S but distinct Se–Te contents ("fertile lherzolite-like" 80 ± 17 and 11 ± 1.7 ng g^{-1} vs 49 ± 11 and 3.5 ± 1.3 ng g^{-1} Se and Te, respectively) due to the significant difference in $D^{sulf\ liq–sil}_{Se\ or\ Te}$ reported by these groups. Nevertheless, our model suggests that sulfide liquid–silicate melt partitioning, rather than MSS–sulfide liquid or MSS–silicate melt partitioning, predominantly controls the partitioning behavior of chalcophile elements during melting of a MORB mantle, in accordance with recent sulfide melting experiments (Zhang and Hirschmann, 2016; Z. Zhang et al., 2018). This reinforces the notion that Se–Te variations (with broadly-chondritic Se/Te ratios) in "static" lithospheric lherzolites reflect significant, if not complete, metasomatic overprinting (e.g., König et al., 2014), which in turn requires a reassessment of the current PM composition (Wang and Becker, 2013).

The observed Se isotope variation along the PAR (between -0.30 ± 0.09‰ and -0.05 ± 0.09‰; 2 s.d., $n = 27$) is not systematically related to magmatic differentiation involving sulfide liquid/MSS–silicate melt partitioning or other geochemical parameters, indicating negligible $^{82}Se/^{76}Se$ fractionation within uncertainty during decompression melting. The Se isotope composition of the Pacific mantle is thus represented by the average $\delta^{82/76}Se$ of all MORBs (-0.16 ± 0.13‰). This value is significantly lighter than previously reported $\delta^{82/76}Se$ for basalts and one peridotite from diverse geodynamic settings (Rouxel et al., 2002; Kurzawa et al., 2017; Yierpan et al., 2018); meanwhile, it overlaps with $\delta^{82/76}Se$ of carbonaceous (CI and volatile depleted CV and CO) and ordinary chondrites but shows a distinct offset from that of enstatite chondrites (Labidi et al., 2018). Selenium isotope variations between different mantle reservoirs and in additional non-magmatic processes can be resolved and further investigated in order to contribute constraints on the accretion history of terrestrial volatiles.

ACKNOWLEDGEMENTS

This work was supported by the ERC Starting Grant, O2RIGIN (636808), to Stephan König. We thank Timon Kurzawa, Martin Wille, Elmar Reitter, and Ilka Kleinhanns for their generous support in the lab, and Bernd Steinhilber and Johannes Redlinger for the trace element analysis. Laure Dosso kindly provided the PAR MORB samples. The manuscript greatly benefited from careful reviews and constructive comments by three anonymous reviewers as well as editors Shichun Huang, Marc Norman, and Jeffrey Catalano.

APPENDIX A. SUPPLEMENTARY MATERIAL

Supplementary data to this article can be found online at https://doi.org/10.1016/j.gca.2019.01.028.

REFERENCES

Adams R. D. (1964) Thickness of the Earth's crust beneath the Pacific-Antarctic ridge. *N. Z. J. Geol. Geophys.* **7**(3), 529–542.

Albut G., Babechuk M. G., Kleinhanns I. C., Benger M., Beukes N. J., Steinhilber B., Smith A. J. B., Kruger S. J. and Schoenberg R. (2018) Modern rather than Mesoarchaean oxidative weathering responsible for the heavy stable Cr isotopic signatures of the 2.95 Ga old Ijzermijn iron formation (South Africa). *Geochim. Cosmochim. Acta* **228**, 157–189.

Allègre C., Manhes G. and Lewin E. (2001) Chemical composition of the Earth and the volatility control on planetary genetics. *Earth Planet. Sci. Lett.* **185**(1–2), 49–69.

Ariskin A. A., Danyushevsky L. V., Bychkov K. A., McNeill A. W., Barmina G. S. and Nikolaev G. S. (2013) Modeling solubility of Fe-Ni sulfides in basaltic magmas: the effect of nickel. *Econ. Geol.* **108**(8), 1983–2003.

Ariskin A. A., Bychkov K. A., Nikolaev G. S. and Barmina G. S. (2018) The COMAGMAT-5: modeling the effect of Fe–Ni sulfide immiscibility in crystallizing magmas and cumulates. *J. Petrol.* **59**(2), 283–298.

Asimow P. D. and Longhi J. (2004) The significance of multiple saturation points in the context of polybaric near-fractional melting. *J. Petrol.* **45**(12), 2349–2367.

Babechuk M. G., Kamber B. S., Greig A., Canil D. and Kodolanyi J. (2010) The behaviour of tungsten during mantle melting revisited with implications for planetary differentiation time scales. *Geochim. Cosmochim. Acta* **74**(4), 1448–1470.

Ballhaus C. (1993) Redox states of lithospheric and asthenospheric upper mantle. *Contrib. Miner. Petrol.* **114**(3), 331–348.

Ballhaus C., Bockrath C., Wohlgemuth-Ueberwasser C., Laurenz V. and Berndt J. (2006) Fractionation of the noble metals by physical processes. *Contrib. Miner. Petrol.* **152**(6), 667–684.

Barnes S.-J., Savard D., Bédard L. P. and Maier W. D. (2009) Selenium and sulfur concentrations in the Bushveld Complex of South Africa and implications for formation of the platinum-group element deposits. *Miner. Deposita* **44**(6), 647–663.

Bezard R., Fischer-Gödde M., Hamelin C., Brennecka G. A. and Kleine T. (2016) The effects of magmatic processes and crustal recycling on the molybdenum stable isotopic composition of Mid-Ocean Ridge Basalts. *Earth Planet. Sci. Lett.* **453**, 171–181.

Bézos A. and Humler E. (2005) The $Fe^{3+}/\Sigma Fe$ ratios of MORB glasses and their implications for mantle melting. *Geochim. Cosmochim. Acta* **69**(3), 711–725.

Bézos A., Lorand J. P., Humler E. and Gros M. (2005) Platinum-group element systematics in Mid-Oceanic Ridge basaltic glasses from the Pacific, Atlantic, and Indian Oceans. *Geochim. Cosmochim. Acta* **69**(10), 2613–2627.

Bockrath C., Ballhaus C. and Holzheid A. (2004) Fractionation of the platinum-group elements during mantle melting. *Science* **305**(5692), 1951–1953.

Bodinier J.-L. and Godard M. (2014) Orogenic, ophiolitic, and abyssal peridotites. In *Treatise on Geochemistry* (eds. H. D. Holland and K. K. Turekian), second ed. Elsevier, Oxford, pp. 103–167.

Boujibar A., Andrault D., Bouhifd M. A., Bolfan-Casanova N., Devidal J.-L. and Trcera N. (2014) Metal–silicate partitioning of sulphur, new experimental and thermodynamic constraints on planetary accretion. *Earth Planet. Sci. Lett.* **391**, 42–54.

Brenan J. M. (2015) Se–Te fractionation by sulfide–silicate melt partitioning: implications for the composition of mantle-derived magmas and their melting residues. *Earth Planet. Sci. Lett.* **422**, 45–57.

Brookins D. G. (1988) *Eh-pH Diagrams for Geochemistry*. Springer-Verlag, Berlin, Heidelberg.

Carignan J. and Wen H. J. (2007) Scaling NIST SRM 3149 for Se isotope analysis and isotopic variations of natural samples. *Chem. Geol.* **242**(3–4), 347–350.

Castillo P. R., Natland J. H., Niu Y. and Lonsdale P. F. (1998) Sr, Nd and Pb isotopic variation along the Pacific-Antarctic risecrest, 53–57°S: implications for the composition and dynamics of the South Pacific upper mantle. *Earth Planet. Sci. Lett.* **154**(1–4), 109–125.

Choi N. and Cho W. D. (1997) Distribution behavior of cobalt, selenium, and tellurium between nickel-copper-iron matte and silica-saturated iron silicate slag. *Metall. Mater. Trans. B* **28**(3), 429–438.

Clog M., Aubaud C., Cartigny P. and Dosso L. (2013) The hydrogen isotopic composition and water content of southern Pacific MORB: a reassessment of the D/H ratio of the depleted mantle reservoir. *Earth Planet. Sci. Lett.* **381**, 156–165.

Coogan L. A. and Dosso S. E. (2016) Quantifying parental MORB trace element compositions from the eruptive products of realistic magma chambers: parental EPR MORB are depleted. *J. Petrol.* **57**(11–12), 2105–2126.

Cottrell E. and Kelley K. A. (2011) The oxidation state of Fe in MORB glasses and the oxygen fugacity of the upper mantle. *Earth Planet. Sci. Lett.* **305**(3–4), 270–282.

Cutter G. A. and Bruland K. W. (1984) The marine biogeochemistry of selenium: a re-evaluation1. *Limnol. Oceanogr.* **29**(6), 1179–1192.

Cutter G. A. and Cutter L. S. (2001) Sources and cycling of selenium in the western and equatorial Atlantic Ocean. *Deep-Sea Res. Part II: Top. Stud. Oceanogr.* **48**(13), 2917–2931.

Dauphas N. (2017) The isotopic nature of the Earth's accreting material through time. *Nature* **541**, 521.

Dare S. A. S., Barnes S. J. and Beaudoin G. (2012) Variation in trace element content of magnetite crystallized from a fractionating sulfide liquid, Sudbury, Canada: Implications for provenance discrimination. *Geochim. Cosmochim. Acta* **88**, 27–50.

Dare S. A. S., Barnes S. J., Beaudoin G., Meric J., Boutroy E. and Potvin-Doucet C. (2014) Trace elements in magnetite as petrogenetic indicators. *Miner. Deposita* **49**(7), 785–796.

Ding S. and Dasgupta R. (2017) The fate of sulfide during decompression melting of peridotite implications for sulfur inventory of the MORB-source depleted upper mantle. *Earth Planet. Sci. Lett.* **459**, 183–195.

Falconer R. K. H. (1972) The Indian-Antarctic-Pacific triple junction. *Earth Planet. Sci. Lett.* **17**(1), 151–158.

Fang L. and Lynch D. C. (1987) Evaluation of the Behavior of Selenium in Silicate Slag. *Metall. Trans. B-Process Metall.* **18**(1), 181–187.

Fischer-Gödde M. and Kleine T. (2017) Ruthenium isotopic evidence for an inner Solar System origin of the late veneer. *Nature* **541**, 525.

Fischer-Gödde M., Becker H. and Wombacher F. (2011) Rhodium, gold and other highly siderophile elements in orogenic peridotites and peridotite xenoliths. *Chem. Geol.* **280**, 365–383.

Floor G. H. and Román-Ross G. (2012) Selenium in volcanic environments: a review. *Appl. Geochem.* **27**(3), 517–531.

Floor G. H., Margui E., Hidalgo M., Queralt I., Kregsamer P., Streli C. and Román-Ross G. (2013) Study of selenium sorption processes in volcanic ash using Total Reflection X-ray Fluorescence (TXRF). *Chem. Geol.* **352**, 19–26.

Floor G. H., Millot R., Iglesias M. and Negrel P. (2011) Influence of methane addition on selenium isotope sensitivity and their spectral interferences. *J. Mass Spectrom.* **46**(2), 182–188.

Fonseca R. O. C., Laurenz V., Mallmann G., Luguet A., Hoehne N. and Jochum K. P. (2012) New constraints on the genesis and long-term stability of Os-rich alloys in the Earth's mantle. *Geochim. Cosmochim. Acta* **87**, 227–242.

Francheteau J., Yelles-Chaouche A. and Craig H. (1987) The Juan Fernandez microplate north of the Pacific-Nazca-Antarctic plate junction at 35°S. *Earth Planet. Sci. Lett.* **86**(2–4), 253–268.

Gale A., Dalton C. A., Langmuir C. H., Su Y. and Schilling J.-G. (2013) The mean composition of ocean ridge basalts. *Geochem. Geophys. Geosyst.* **14**, 489–518.

Géli L., Bougault H., Aslanian D., Briais A., Dosso L., Etoubleau J., LeFormal J. P., Maia M., Ondreas H., Olivet J. L., Richardson C., Sayanagi K., Seama N., Shah A., Vlastelic I. and Yamamoto M. (1997) Evolution of the Pacific-Antarctic Ridge south of the Udintsev fracture zone. *Science* **278**(5341), 1281–1284.

Ghiorso M. S., Hirschmann M. M., Reiners P. W. and Kress V. C. (2002) The pMELTS: a revision of MELTS for improved calculation of phase relations and major element partitioning related to partial melting of the mantle to 3 GPa. *Geochem. Geophys. Geosyst.* **3**, 1–35.

Ghiorso M. S. and Sack R. O. (1995) Chemical mass transfer in magmatic processes IV. A revised and internally consistent thermodynamic model for the interpolation and extrapolation of liquid-solid equilibria in magmatic systems at elevated temperatures and pressures. *Contrib. Miner. Petrol.* **119**(2–3), 197–212.

Greaney A. T., Rudnick R. L., Helz R. T., Gaschnig R. M., Piccoli P. M. and Ash R. D. (2017) The behavior of chalcophile elements during magmatic differentiation as observed in Kilauea Iki lava lake, Hawaii. *Geochim. Cosmochim. Acta* **210**, 71–96.

Guo J. F., Griffin W. L. and O'Reilly S. Y. (1999) Geochemistry and origin of sulphide minerals in mantle xenoliths: Qilin, southeastern China. *J. Petrol.* **40**(7), 1125–1149.

Hamelin C., Dosso L., Hanan B., Barrat J.-A. and Ondréas H. (2010) Sr-Nd-Hf isotopes along the Pacific Antarctic Ridge from 41 to 53°S. *Geophys. Res. Lett.* **37**(10).

Hamelin C., Dosso L., Hanan B. B., Moreira M., Kositsky A. P. and Thomas M. Y. (2011) Geochemical portray of the Pacific Ridge: new isotopic data and statistical techniques. *Earth Planet. Sci. Lett.* **302**(1–2), 154–162.

Hannington M. D., Peterson S., Herzig P.M. and Jonasson I. R. (2004) A global database of seafloor hydrothermal systems, including a digital database of geochemical analyses of seafloor polymetallic sulfides. Geological Survey of Canada, Open File, Report 4598, 1 CD-ROM.

Hart S. R. and Gaetani G. A. (2006) Mantle Pb paradoxes: the sulfide solution. *Contrib. Miner. Petrol.* **152**(3), 295–308.

Harvey J., König S. and Luguet A. (2015) The effects of melt depletion and metasomatism on highly siderophile and strongly chalcophile elements: S-Se–Te–Re–PGE systematics of peridotite xenoliths from Kilbourne Hole, New Mexico. *Geochim. Cosmochim. Acta* **166**, 210–233.

Hattori K. H., Arai S. and Clarke D. B. (2002) Selenium, tellurium, arsenic and antimony contents of primary mantle sulfides. *Can. Mineral.* **40**, 637–650.

Helmy H. M., Ballhaus C., Wohlgemuth-Ueberwasser C., Fonseca R. O. C. and Laurenz V. (2010) Partitioning of Se, As, Sb, Te and Bi between monosulfide solid solution and sulfide melt - Application to magmatic sulfide deposits. *Geochim. Cosmochim. Acta* **74**(21), 6174–6179.

Hertogen J., Janssens M. J. and Palme H. (1980) Trace elements in ocean ridge basalt glasses: implications for fractionations during mantle evolution and petrogenesis. *Geochim. Cosmochim. Acta* **44**(12), 2125–2143.

Hin R. C., Coath C. D., Carter P. J., Nimmo F., Lai Y. J., von Strandmann P. A. E. P., Willbold M., Leinhardt Z. M., Walter M. J. and Elliott T. (2017) Magnesium isotope evidence that accretional vapour loss shapes planetary compositions. *Nature* **549**(7673), 511–515.

Jackson C. R. M., Bennett N. R., Du Z., Cottrell E. and Fei Y. (2018) Early episodes of high-pressure core formation preserved in plume mantle. *Nature* **553**(7689), 491–495.

Jain J. C., Field M. P., Neal C. R., Ely J. C. and Sherrell R. M. (2000) Determination of the REE in geological reference materials DTS-1 (Dunite) and PCC-1 (Peridotite) by ultrasonic and microconcentric desolvating nebulisation ICP-MS. *Geostand. Geoanal. Res.* **24**(1), 65–72.

Jenner F. E. and O'Neill H. S. (2012) Analysis of 60 elements in 616 ocean floor basaltic glasses. *Geochem. Geophys. Geosyst.* **13**, Q02005.

Jenner F. E., Arculus R. J., Mavrogenes J. A., Dyriw N. J., Nebel O. and Hauri E. H. (2012) Chalcophile element systematics in volcanic glasses from the northwestern Lau Basin. *Geochem. Geophys. Geosyst.* **13**, Q06014.

Jenner F. E., Hauri E. H., Bullock E. S., König S., Arculus R. J., Mavrogenes J. A., Mikkelson N. and Goddard C. (2015) The competing effects of sulfide saturation versus degassing on the behavior of the chalcophile elements during the differentiation of hydrous melts. *Geochem. Geophys. Geosyst.* **16**, 1490–1507.

Jenner F. E., O'neill H. S. C., Arculus R. J. and Mavrogenes J. A. (2010) The magnetite crisis in the evolution of arc-related magmas and the initial concentration of Au Ag and Cu. *J. Petrol.* **53**(5), 1089-1089.

Jochum K. P., Nohl L., Herwig K., Lammel E., Stoll B. and Hofmann A. W. (2005) GeoReM: a new geochemical database for reference materials and isotopic standards. *Geostand. Geoanal. Res.* **29**(3), 333–338.

Johnson T. M. (2004) A review of mass-dependent fractionation of selenium isotopes and implications for other heavy stable isotopes. *Chem. Geol.* **204**(3–4), 201–214.

Johnson T. M. and Bullen T. D. (2003) Selenium isotope fractionation during reduction by Fe(II)-Fe(III) hydroxide-sulfate (green rust). *Geochim. Cosmochim. Acta* **67**(3), 413–419.

Johnson T. M., Herbel M. J., Bullen T. D. and Zawislanski P. T. (1999) Selenium isotope ratios as indicators of selenium sources and oxyanion reduction. *Geochim. Cosmochim. Acta* **63**(18), 2775–2783.

Katz R. F., Spiegelman M. and Langmuir C. H. (2003) A new parameterization of hydrous mantle melting. *Geochem. Geophys. Geosyst.* **4**, 1073.

Keith M., Haase K. M., Klemd R., Krumm S. and Strauss H. (2016) Systematic variations of trace element and sulfur isotope compositions in pyrite with stratigraphic depth in the Skouriotissa volcanic-hosted massive sulfide deposit, Troodos ophiolite, Cyprus. *Chem. Geol.* **423**, 7–18.

Keith M., Haase K. M., Klemd R., Schwarz-Schampera U. and Franke H. (2017) Systematic variations in magmatic sulphide chemistry from mid-ocean ridges, back-arc basins and island arcs. *Chem. Geol.* **451**, 67–77.

Kelley K. A., Plank T., Grove T. L., Stolper E. M., Newman S. and Hauri E. (2006) Mantle melting as a function of water content beneath back-arc basins. *J. Geophys. Res.* **111**(B9).

Kimura J.-I., Gill J. B., van Keken P. E., Kawabata H. and Skora S. (2017) Origin of geochemical mantle components: Role of spreading ridges and thermal evolution of mantle. *Geochem. Geophys. Geosyst.* **18**(2), 697–734.

Kinzler R. J. and Grove T. L. (1993) Corrections and further discussion of the primary magmas of mid-ocean ridge basalts, 1 and 2. *J. Geophys. Res. Solid Earth* **98**(B12), 22339–22347.

Kiseeva E. S., Fonseca R. O. C. and Smythe D. J. (2017) Chalcophile elements and sulfides in the upper mantle. *Elements* **13**(2), 111–116.

Kiseeva E. S. and Wood B. J. (2013) A simple model for chalcophile element partitioning between sulphide and silicate liquids with geochemical applications. *Earth Planet. Sci. Lett.* **383**, 68–81.

Kiseeva E. S. and Wood B. J. (2015) The effects of composition and temperature on chalcophile and lithophile element partitioning into magmatic sulphides. *Earth Planet. Sci. Lett.* **424**, 280–294.

Klein E. M. and Langmuir C. H. (1987) Global correlations of ocean ridge basalt chemistry with axial depth and crustal thickness. *J. Geophys. Res.-Solid Earth Planets* **92**(B8), 8089–8115.

Klingelhoefer F., Ondréas H., Briais A., Hamelin C. and Dosso L. (2006) New structural and geochemical observations from the Pacific-Antarctic Ridge between 52°45′S and 41°15′S. *Geophys. Res. Lett.* **33**(21).

König S., Eickmann B., Zack T., Yierpan A., Wille M., Taubald H. and Schoenberg R. (2019) Redox induced sulfur-selenium isotope decoupling recorded in pyrite. *Geochim. Cosmochim. Acta* **244**, 24–39.

König S., Lissner M., Lorand J. P., Bragagni A. and Luguet A. (2015) Mineralogical control of selenium, tellurium and highly siderophile elements in the Earth's mantle: evidence from mineral separates of ultra-depleted mantle residues. *Chem. Geol.* **396**, 16–24.

König S., Lorand J. P., Luguet A. and Pearson D. G. (2014) A non-primitive origin of near-chondritic S-Se–Te ratios in mantle peridotites; implications for the Earth's late accretionary history. *Earth Planet. Sci. Lett.* **385**, 110–121.

König S., Luguet A., Lorand J.-P., Wombacher F. and Lissner M. (2012) Selenium and tellurium systematics of the Earth's mantle from high precision analyses of ultra-depleted orogenic peridotites. *Geochim. Cosmochim. Acta* **86**, 354–366.

Krouse H. R. and Thode H. G. (1962) Thermodynamic properties and geochemistry of isotopic compounds of selenium. *Can. J. Chem.* **40**(2), 367–375.

Kurzawa T., König S., Labidi J., Yierpan A. and Schoenberg R. (2017) A method for Se isotope analysis of low ng-level geological samples via double spike and hydride generation MC-ICP-MS. *Chem. Geol.* **466**, 219–228.

Labidi J., Cartigny P., Hamelin C., Moreira M. and Dosso L. (2014) Sulfur isotope budget (^{32}S, ^{33}S, ^{34}S and ^{36}S) in Pacific-Antarctic ridge basalts: a record of mantle source heterogeneity and hydrothermal sulfide assimilation. *Geochim. Cosmochim. Acta* **133**, 47–67.

Labidi J. and Cartigny P. (2016) Negligible sulfur isotope fractionation during partial melting: evidence from Garrett transform fault basalts, implications for the late-veneer and the hadean matte. *Earth Planet. Sci. Lett.* **451**, 196–207.

Labidi J., Cartigny P. and Moreira M. (2013) Non-chondritic sulphur isotope composition of the terrestrial mantle. *Nature* **501**(7466), 208–211.

Labidi J., König S., Kurzawa T., Yierpan A. and Schoenberg R. (2018) The selenium isotopic variations in chondrites are mass-dependent; implications for sulfide formation in the early solar system. *Earth Planet. Sci. Lett.* **481**, 212–222.

Labidi J., Shahar A., Le Losq C., Hillgren V. J., Mysen B. O. and Farquhar J. (2016) Experimentally determined sulfur isotope fractionation between metal and silicate and implications for planetary differentiation. *Geochim. Cosmochim. Acta* **175**, 181–194.

Langmuir C. H., Klein E. M. and Plank T. (1992) Petrological systematics of mid-ocean ridge basalts: constraints on melt generation beneath ocean ridges. In *Mantle Flow and Melt Generation at Mid-Ocean Ridges, Geophysical Monograph Series* (eds. J. P. Morgan, D. K. Blackman and J. M. Sinton). American Geophysical Union, Washington, D. C., pp. 183–280.

Layton-Matthews D., Peter J. M., Scott S. D. and Leybourne M. I. (2008) Distribution, mineralogy, and geochemistry of selenium in felsic volcanic-hosted massive sulfide deposits of the Finlayson Lake district, Yukon Territory, Canada. *Econ. Geol.* **103** (1), 61–88.

Layton-Matthews D., Leybourne M. I., Peter J. M., Scott S. D., Cousens B. and Eglington B. M. (2013) Multiple sources of selenium in ancient seafloor hydrothermal systems: compositional and Se, S, and Pb isotopic evidence from volcanic-hosted and volcanic-sediment-hosted massive sulfide deposits of the Finlayson Lake District, Yukon, Canada. *Geochim. Cosmochim. Acta* **117**, 313–331.

Le Roux V., Bodinier J. L., Tommasi A., Alard O., Dautri J. M., Vauchez A. and Riches A. J. V. (2007) The Lherz spinel lherzolite: refertilised rather than pristine mantle. *Earth Planet. Sci. Lett.* **259**, 599–612.

Lee C. T. A., Luffi P., Plank T., Dalton H. and Leeman W. P. (2009) Constraints on the depths and temperatures of basaltic magma generation on Earth and other terrestrial planets using new thermobarometers for mafic magmas. *Earth Planet. Sci. Lett.* **279**(1–2), 20–33.

Lee C. T., Luffi P., Chin E. J., Bouchet R., Dasgupta R., Morton D. M., Le Roux V., Yin Q. Z. and Jin D. (2012) Copper systematics in arc magmas and implications for crust-mantle differentiation. *Science* **336**(6077), 64–68.

Lee D. S. and Edmond J. M. (1985) Tellurium species in seawater. *Nature* **313**(6005), 782–785.

Li Y. and Audétat A. (2012) Partitioning of V, Mn Co, Ni, Cu, Zn, As, Mo, Ag, Sn, Sb, W, Au, Pb, and Bi between sulfide phases and hydrous basanite melt at upper mantle conditions. *Earth Planet. Sci. Lett.* **355**, 327–340.

Lissenberg C. J. and MacLeod C. J. (2016) A reactive porous flow control on mid-ocean ridge magmatic evolution. *J. Petrol.* **57** (11–12), 2195–2220.

Lissner M., König S., Luguet A., le Roux P. J., Schuth S., Heuser A. and le Roex A. P. (2014) Selenium and tellurium systematics in MORBs from the southern Mid-Atlantic Ridge (47–50°S). *Geochim. Cosmochim. Acta* **144**, 379–402.

Liu Y. and Brenan J. (2015) Partitioning of platinum-group elements (PGE) and chalcogens (Se, Te, As, Sb, Bi) between monosulfide-solid solution (MSS), intermediate solid solution (ISS) and sulfide liquid at controlled fO_2–fS_2 conditions. *Geochim. Cosmochim. Acta* **159**, 139–161.

Lodders K., Palme H. and Gail H. P. (2009) Abundances of the elements in the solar system. In *Landolt-Bornstein* (ed. J. E. Trumper). Springer-Verlag, New Series, Berlin, Heidelberg, New York, pp. 560–630.

Lonsdale P. (1994) Geomorphology and structural segmentation of the crest of the southern (Pacific-Antarctic) East Pacific Rise. *J. Geophys. Res. Solid Earth* **99**(B3), 4683–4702.

Lorand J. P. (1991) Sulphide petrology and sulphur geochemistry of orogenic lherzolites: a comparative study of the pyrenean bodies (France) and the Lanzo, Massif (Italy). *J. Petrol.* **Special Volume**(2), 77–95.

Lorand J. P. and Alard O. (2010) Determination of selenium and tellurium concentrations in Pyrenean peridotites (Ariege, France): new insight into S/Se/Te systematics of the upper in mantle samples. *Chem. Geol.* **278**(1–2), 120–130.

Lorand J. P. and Luguet A. (2016) Chalcophile and siderophile elements in mantle rocks: trace elements controlled by trace minerals. *Rev. Mineral. Geochem.* **81**(1), 441–488.

Lorand J. P., Alard O., Luguet A. and Keays R. R. (2003) Sulfur and selenium systematics of the subcontinental lithospheric mantle: Inferences from the Massif Central xenolith suite (France). *Geochim. Cosmochim. Acta* **67**(21), 4137–4151.

Lorand J. P., Delpech G., Gregoire M., Moine B., O'Reilly S. Y. and Cottin J. Y. (2004) Platinum-group elements and the multistage metasomatic history of Kerguelen lithospheric mantle (South Indian Ocean). *Chem. Geol.* **208**(1–4), 195–215.

Lorand J. P., Alard O. and Luguet A. (2010) Platinum-group element micronuggets and refertilization process in Lherz orogenic peridotite (northeastern Pyrenees, France). *Earth Planet. Sci. Lett.* **289**(1–2), 298–310.

Lorand J. P., Luguet A. and Alard O. (2013) Platinum-group element systematics and petrogenetic processing of the continental upper mantle: a review. *Lithos* **164**, 2–21.

Luais B. (2012) Germanium chemistry and MC-ICPMS isotopic measurements of Fe–Ni, Zn alloys and silicate matrices: Insights into deep Earth processes. *Chem. Geol.* **334**, 295–311.

Luguet A. and Reisberg L. (2016) Highly siderophile element and ^{187}Os signatures in non-cratonic basalt-hosted peridotite xenoliths: unravelling the origin and evolution of the post-archean lithospheric mantle. *Rev. Mineral. Geochem.* **81**(1), 305–367.

Luguet A., Behrens M., Pearson D. G., König S. and Herwartz D. (2015) Significance of the whole rock Re–Os ages in cryptically and modally metasomatised cratonic peridotites: constraints from HSE–Se–Te systematics. *Geochim. Cosmochim. Acta* **164**, 441–463.

Luguet A., Lorand J. P. and Seyler M. (2003) Sulfide petrology and highly siderophile element geochemistry of abyssal peridotites: a coupled study of samples from the Kane Fracture Zone (45° W 23°20N, MARK Area, Atlantic Ocean). *Geochim. Cosmochim. Acta* **67**(8), 1553–1570.

Luguet A., Lorand J. P., Alard O. and Cottin J. Y. (2004) A multi-technique study of platinum group element systematic in some Ligurian ophiolitic peridotites, Italy. *Chem. Geol.* **208**(1–4), 175–194.

Luguet A., Shirey S. B., Lorand J. P., Horan M. F. and Carlson R. W. (2007) Residual platinum-group minerals from highly depleted harzburgites of the Lherz massif (France) and their role in HSE fractionation of the mantle. *Geochim. Cosmochim. Acta* **71**(12), 3082–3097.

Mathez E. A. (1976) Sulfur solubility and magmatic sulfides in submarine basalt glass. *J. Geophys. Res.* **81**(23), 4269–4276.

McDonough W. F. (2014) Compositional model for the Earth's Core. In *Treatise on Geochemistry* (eds. H. D. Holland and K. K. Turekian), second ed. Elsevier, Oxford, pp. 559–577.

Mcdonough W. F. and Sun S. S. (1995) The composition of the Earth. *Chem. Geol.* **120**(3–4), 223–253.

Mcphail D. C. (1995) Thermodynamic properties of aqueous tellurium species between 25 and 350°C. *Geochim. Cosmochim. Acta* **59**(5), 851–866.

Measures C. I. and Burton J. D. (1980) The vertical-distribution and oxidation-states of dissolved selenium in the northeast atlantic-ocean and their relationship to biological processes. *Earth Planet. Sci. Lett.* **46**(3), 385–396.

Meisel T., Walker R. J. and Morgan J. W. (1996) The osmium isotopic composition of the Earth's primitive upper mantle. *Nature* **383**, 517–520.

Menzies M., Blanchard D., Brannon J. and Korotev R. (1977) Rare-earth geochemistry of fused ophiolitic and alpine lherzolites. II. Beni Bouchera, Ronda and Lanzo. *Contrib. Miner. Petrol.* **64**(1), 53–74.

Michael P. J. and Cornell W. C. (1998) Influence of spreading rate and magma supply on crystallization and assimilation beneath mid-ocean ridges: evidence from chlorine and major element chemistry of mid-ocean ridge basalts. *J. Geophys. Res. Solid Earth* **103**(B8), 18325–18356.

Mitchell K., Couture R.-M., Johnson T. M., Mason P. R. D. and Cappellen P. V. (2013) Selenium sorption and isotope fractionation: Iron(III) oxides versus iron(II) sulfides. *Chem. Geol.* **342**, 21–28.

Moore J. G. and Fabbi B. P. (1971) An estimate of the juvenile sulfur content of basalt. *Contrib. Miner. Petrol.* **33**(2), 118–127.

Moore J. G. and Schilling J.-G. (1973) Vesicles, water, and sulfur in Reykjanes ridge Basalts. *Contrib. Miner. Petrol.* **41**(2), 105–118.

Moreira M. A., Dosso L. and Ondréas H. (2008) Helium isotopes on the Pacific-Antarctic ridge (52.5°–41.5°S). *Geophys. Res. Lett.* **35**(10).

Morgan J. W. (1986) Ultramafic xenoliths: clues to Earth's late accretionary history. *J. Geophys. Res.* **91**(B12), 12375–12387.

Mungall J. E. and Brenan J. M. (2014) Partitioning of platinum-group elements and Au between sulfide liquid and basalt and the origins of mantle-crust fractionation of the chalcophile elements. *Geochim. Cosmochim. Acta* **125**, 265–289.

Nagamori M. and Mackey P. J. (1977) Distribution equilibria of Sn, Se and Te between FeO-Fe_2O_3-SiO_2-Al_2O_3-$CuO_{0.5}$ slag and metallic copper. *Metall. Trans. B* **8**(1), 39–46.

Nielsen R. L., Forsythe L. M., Gallahan W. E. and Fisk M. R. (1994) Major-element and trace-element magnetite-melt equilibria. *Chem. Geol.* **117**(1–4), 167–191.

Nielsen S. G., Shimizu N., Lee C.-T. A. and Behn M. D. (2014) Chalcophile behavior of thallium during MORB melting and implications for the sulfur content of the mantle. *Geochem. Geophys. Geosyst.* **15**, 4905–4919.

Niu Y. and Batiza R. (1991) An empirical method for calculating melt compositions produced beneath mid-ocean ridges: application for axis and off-axis (seamounts) melting. *J. Geophys. Res. Solid Earth* **96**(B13), 21753–21777.

Norris C. A. and Wood B. J. (2017) Earth's volatile contents established by melting and vaporization. *Nature* **549**(7673), 507–510.

Ondréas H., Aslanian D., Géli L., Olivet J.-L. and Briais A. (2001) Variations in axial morphology, segmentation, and seafloor roughness along the Pacific-Antarctic Ridge between 56°S and 66°S. *J. Geophys. Res. Solid Earth* **106**(B5), 8521–8546.

O'Neill H. S. and Jenner F. E. (2012) The global pattern of trace-element distributions in ocean floor basalts. *Nature* **491**(7426), 698–704.

Palme H. and O'Neill H. S. C. (2014) Cosmochemical estimates of Mantle composition. In *Treatise on Geochemistry* (eds. H. D. Holland and K. K. Turekian), second ed. Elsevier, Oxford, pp. 1–39.

Patten C., Barnes S. J. and Mathez E. A. (2012) Textural variations in MORB sulfide droplets due to differences in crystallization history. *Can. Mineral.* **50**(3), 675–692.

Patten C., Barnes S. J., Mathez E. A. and Jenner F. E. (2013) Partition coefficients of chalcophile elements between sulfide and silicate melts and the early crystallization history of sulfide liquid: LA-ICP-MS analysis of MORB sulfide droplets. *Chem. Geol.* **358**, 170–188.

Patten C. G. C., Pitcairn I. K., Teagle D. A. H. and Harris M. (2016) Sulphide mineral evolution and metal mobility during alteration of the oceanic crust: insights from ODP Hole 1256D. *Geochim. Cosmochim. Acta* **193**, 132–159.

Peach C. L., Mathez E. A. and Keays R. R. (1990) Sulfide melt-silicate melt distribution coefficients for noble metals and other chalcophile elements as deduced from MORB: Implications for partial melting. *Geochim. Cosmochim. Acta* **54**(12), 3379–3389.

Plank T., Spiegelman M., Langmuir C. H. and Forsyth D. W. (1995) The meaning of "mean F": clarifying the mean extent of melting at ocean ridges. *J. Geophys. Res.* **100**(B8), 15045–15052.

Pogge von Strandmann P. A. E., Coath C. D., Catling D. C., Poulton S. W. and Elliott T. (2014) Analysis of mass dependent and mass independent selenium isotope variability in black shales. *J. Anal. At. Spectrom.* **29**(9), 1648–1659.

Rashid K. and Krouse H. R. (1985) Selenium isotopic fractionation during SeO_3^{2-} reduction to Se^0 and H_2Se. *Can. J. Chem.* **63** (11), 3195–3199. https://doi.org/10.1139/v85-528.

Rees C. E. and Thode H. G. (1966) Selenium isotope effects in the reduction of sodium selenite and of sodium selenate. *Can. J. Chem.* **44**(4), 419–427.

Rehkämper M., Halliday A. N., Fitton J. G., Lee D. C., Wieneke M. and Arndt N. T. (1999) Ir, Ru, Pt, and Pd in basalts and komatiites: new constraints for the geochemical behavior of the platinum-group elements in the mantle. *Geochim. Cosmochim. Acta* **63**(22), 3915–3934.

Righter K., Leeman W. P. and Hervig R. L. (2006) Partitioning of Ni, Co and V between spinel-structured oxides and silicate melts: importance of spinel composition. *Chem. Geol.* **227**(1–2), 1–25.

Rose-Weston L., Brenan J. M., Fei Y. W., Secco R. A. and Frost D. J. (2009) Effect of pressure, temperature, and oxygen fugacity on the metal-silicate partitioning of Te, Se, and S: Implications for earth differentiation. *Geochim. Cosmochim. Acta* **73**(15), 4598–4615.

Rouxel O., Fouquet Y. and Ludden J. N. (2004) Subsurface processes at the Lucky Strike hydrothermal field, Mid-Atlantic Ridge: evidence from sulfur, selenium, and iron isotopes. *Geochim. Cosmochim. Acta* **68**(10), 2295–2311.

Rouxel O., Ludden J., Carignan J., Marin L. and Fouquet Y. (2002) Natural variations of Se isotopic composition determined by hydride generation multiple collector inductively coupled plasma mass spectrometry. *Geochim. Cosmochim. Acta* **66**(18), 3191–3199.

Saal A. E., Hauri E. H., Langmuir C. H. and Perfit M. R. (2002) Vapour undersaturation in primitive mid-ocean-ridge basalt and the volatile content of Earth's upper mantle. *Nature* **419**, 451.

Salters V. J. M. and Stracke A. (2004) Composition of the depleted mantle. *Geochem. Geophys. Geosyst.* **5**, Q05B07.

Schaefer L. and Fegley B. (2010) Volatile element chemistry during metamorphism of ordinary chondritic material and some of its implications for the composition of asteroids. *Icarus* **205**(2), 483–496.

Shimizu K., Saal A. E., Myers C. E., Nagle A. N., Hauri E. H., Forsyth D. W., Kamenetsky V. S. and Niu Y. L. (2016) Two-component mantle melting-mixing model for the generation of mid-ocean ridge basalts: implications for the volatile content of the Pacific upper mantle. *Geochim. Cosmochim. Acta* **176**, 44–80.

Siebert J., Badro J., Antonangeli D. and Ryerson F. J. (2013) Terrestrial accretion under oxidizing conditions. *Science* **339** (6124), 1194–1197.

Smith P. M. and Asimow P. D. (2005) Adiabat_1ph: a new public front-end to the MELTS, pMELTS, and pHMELTS models. *Geochem. Geophys. Geosyst.* **6**, Q02004.

Smythe D. J., Wood B. J. and Kiseeva E. S. (2017) The S content of silicate melts at sulfide saturation: new experiments and a model incorporating the effects of sulfide composition. *Am. Mineral.* **102**(4), 795–803.

Steenstra E. S., Lin Y., Dankers D., Rai N., Berndt J., Matveev S. and van Westrenen W. (2017) The lunar core can be a major reservoir for volatile elements S, Se, Te and Sb. *Sci. Rep.* **7**(1), 14552.

Stüeken E. E., Foriel J., Nelson B. K., Buick R. and Catling D. C. (2013) Selenium isotope analysis of organic-rich shales: advances in sample preparation and isobaric interference correction. *J. Anal. At. Spectrom.* **28**(11), 1734–1749.

Suer T.-A., Siebert J., Remusat L., Menguy N. and Fiquet G. (2017) A sulfur-poor terrestrial core inferred from metal–silicate partitioning experiments. *Earth Planet. Sci. Lett.* **469**, 84–97.

Toplis M. J. and Corgne A. (2002) An experimental study of element partitioning between magnetite, clinopyroxene and iron-bearing silicate liquids with particular emphasis on vanadium. *Contrib. Miner. Petrol.* **144**(1), 22–37.

Vlastélic I., Aslanian D., Dosso L., Bougault H., Olivet J. L. and Geli L. (1999) Large-scale chemical and thermal division of the Pacific mantle. *Nature* **399**(6734), 345–350.

Vlastélic I., Dosso L., Bougault H., Aslanian D., Géli L., Etoubleau J., Bohn M., Joron J.-L. and Bollinger C. (2000) Chemical systematics of an intermediate spreading ridge: the Pacific-Antarctic Ridge between 56°S and 66°S. *J. Geophys. Res.* **105**(B2), 2915–2936.

Vollstaedt H., Mezger K. and Leya I. (2016) The isotope composition of selenium in chondrites constrains the depletion mechanism of volatile elements in solar system materials. *Earth Planet. Sci. Lett.* **450**, 372–380.

Wallace P. J. and Edmonds M. (2011). The Sulfur Budget in Magmas: Evidence from Melt Inclusions, Submarine Glasses, and Volcanic Gas Emissions. Sulfur in Magmas and Melts: Its Importance for Natural and Technical Processes, vol. 73(1), pp. 215–246.

Wang Z. and Becker H. (2013) Ratios of S, Se and Te in the silicate Earth require a volatile-rich late veneer. *Nature* **499**(7458), 328–331.

Wang Z., Becker H. and Gawronski T. (2013) Partial re-equilibration of highly siderophile elements and the chalcogens in the mantle: a case study on the Baldissero and Balmuccia peridotite massifs (Ivrea Zone, Italian Alps). *Geochim. Cosmochim. Acta* **108**, 21–44.

Wang Z. and Becker H. (2015a) Fractionation of highly siderophile and chalcogen elements during magma transport in the mantle: constraints from pyroxenites of the Balmuccia peridotite massif. *Geochim. Cosmochim. Acta* **159**, 244–263.

Wang Z. and Becker H. (2015b) Abundances of Ag and Cu in mantle peridotites and the implications for the behavior of chalcophile elements in the mantle. *Geochim. Cosmochim. Acta* **160**, 209–226.

Wang Z., Becker H. and Wombacher F. (2015) Mass Fractions of S, Cu, Se, Mo, Ag, Cd, In, Te, Ba, Sm, W, Tl and Bi in geological reference materials and selected carbonaceous chondrites determined by isotope dilution ICP-MS. *Geostand. Geoanal. Res.* **39**(2), 185–208.

Wasson J. T. and Kallemeyn G. W. (1988) Compositions of chondrites. *Philos. Trans. Roy. Soc. A: Math., Phys. Eng. Sci.* **325**(1587), 535–544.

Watts A. B., Weissel J. K., Duncan R. A. and Larson R. L. (1988) Origin of the Louisville Ridge and its relationship to the Eltanin Fracture Zone System. *J. Geophys. Res.* **93**(B4), 3051–3077.

Workman R. K. and Hart S. R. (2005) Major and trace element composition of the depleted MORB mantle (DMM). *Earth Planet. Sci. Lett.* **231**(1–2), 53–72.

Wykes J. L., O'Neill H. S. C. & Mavrogenes, J. A. (2011). XANES investigation of selenium speciation in silicate glasses. Paper presented at Annual V. M. Goldschmidt Conference, Prague, Czech Republic.

Wykes J. L., O'Neill H. S. C. and Mavrogenes J. A. (2015) The effect of FeO on the sulfur content at sulfide saturation (SCSS) and the selenium content at selenide saturation of silicate melts. *J. Petrol.* **56**(7), 1407–1424.

Yamamoto M. (1976) Relationship between Se/S and sulfur isotope ratios of hydrothermal sulfide minerals. *Miner. Deposita* **11**(2), 197–209.

Yang A. Y., Zhou M. F., Zhao T. P., Deng X. G., Qi L. and Xu J. F. (2014) Chalcophile elemental compositions of MORBs from the ultraslow-spreading Southwest Indian Ridge and controls of lithospheric structure on S-saturated differentiation. *Chem. Geol.* **382**, 1–13.

Yi W., Halliday A. N., Alt J. C., Lee D.-C., Rehkämper M., Garcia M. O., Langmuir C. H. and Su Y. (2000) Cadmium, indium, tin, tellurium, and sulfur in oceanic basalts: implications for chalcophile element fractionation in the Earth. *J. Geophys. Res.* **105**(B8), 18927.

Yierpan A., König S., Labidi J., Kurzawa T., Babechuk M. G. and Schoenberg R. (2018) Chemical sample processing for combined selenium isotope and selenium-tellurium elemental investigation of the Earth's igneous reservoirs. *Geochem. Geophys. Geosyst.* **19**, 516–533.

Young E. D., Manning C. E., Schauble E. A., Shahar A., Macris C. A., Lazar C. and Jordan M. (2015) High-temperature equilibrium isotope fractionation of non-traditional stable isotopes: experiments, theory, and applications. *Chem. Geol.* **395**, 176–195.

Zhang H. L., Cottrell E., Solheid P. A., Kelley K. A. and Hirschmann M. M. (2018) Determination of Fe^{3+} /ΣFe of XANES basaltic glass standards by Mössbauer spectroscopy and its application to the oxidation state of iron in MORB. *Chem. Geol.* **497**, 166–175.

Zhang Z. and Hirschmann M. M. (2016) Experimental constraints on mantle sulfide melting up to 8 GPa. *Am. Mineral.* **101**(1–2), 181–192.

Zhang Z., von der Handt A. and Hirschmann M. M. (2018) An experimental study of Fe–Ni exchange between sulfide melt and olivine at upper mantle conditions: implications for mantle sulfide compositions and phase equilibria. *Contrib. Miner. Petrol.* **173**(3), 19.

Zhu J.-M., Johnson T. M., Clark S. K. and Zhu X.-K. (2008) High precision measurement of selenium isotopic composition by hydride generation multiple collector inductively coupled plasma mass spectrometry with a ^{74}Se-^{77}Se double spike. *Chin. J. Anal. Chem.* **36**(10), 1385–1390.

Associate editor: Shichun Huang